Journal of Nanomaterials

Nanomaterials for Sustainable Development: the UN 2030 goals

Lead Guest Editor: R. Lakshmipathy
Guest Editors: Mohan Kumar Kesarla and S.K. Khadheer Pasha

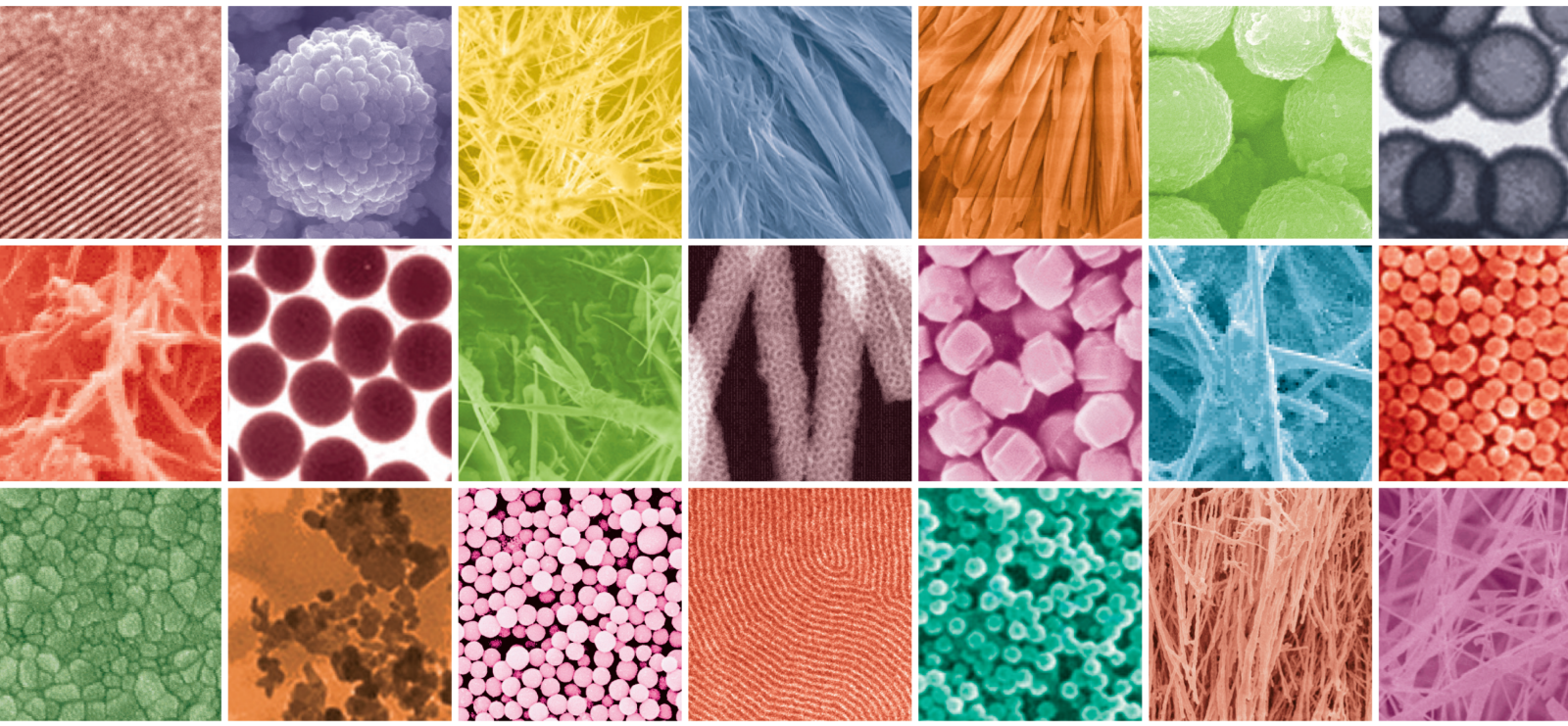

Nanomaterials for Sustainable Development: the UN 2030 goals

Journal of Nanomaterials

Nanomaterials for Sustainable Development: the UN 2030 goals

Lead Guest Editor: R. Lakshmipathy
Guest Editors: Mohan Kumar Kesarla and S.K. Khadheer Pasha

Copyright © 2022 Hindawi Limited. All rights reserved.

This is a special issue published in “Journal of Nanomaterials.” All articles are open access articles distributed under the Creative Commons Attribution License, which permits unrestricted use, distribution, and reproduction in any medium, provided the original work is properly cited.

Chief Editor

Stefano Bellucci, Italy

Associate Editors

Ilaria Armentano, Italy
Stefano Bellucci, Italy
Paulo Cesar Morais, Brazil
William Yu, USA

Academic Editors

Buzuayehu Abebe, Ethiopia
Domenico Acierno, Italy
Sergio-Miguel Acuña-Nelson, Chile
Katerina Aifantis, USA
Omer Alawi, Malaysia
Nageh K. Allam, USA
Muhammad Wahab Amjad, USA
Martin Andersson, Sweden
Hassan Azzazy, Egypt
Ümit Ağbulut, Turkey
Vincenzo Baglio, Italy
Lavinia Balan, France
Nasser Barakat, Egypt
Thierry Baron, France
Carlos Gregorio Barreras-Urbina, Mexico
Andrew R. Barron, USA
Enrico Bergamaschi, Italy
Sergio Bietti, Italy
Raghvendra A. Bohara, India
Mohamed Bououdina, Saudi Arabia
Victor M. Castaño, Mexico
Albano Cavaleiro, Portugal
Kondareddy Cherukula, USA
Shafiul Chowdhury, USA
Yu-Lun Chueh, Taiwan
Elisabetta Comini, Italy
David Cornu, France
Miguel A. Correa-Duarte, Spain
P. Davide Cozzoli, Italy
Anuja Datta, India
Loretta L. Del Mercato, Italy
Yong Ding, USA
Kaliannan Durairaj, Republic of Korea
Ana Espinosa, France
Claude Estournès, France
Giuliana Faggio, Italy
Andrea Falqui, Saudi Arabia
Matteo Ferroni, Italy
Chong Leong Gan, Taiwan
Siddhartha Ghosh, Singapore
Filippo Giubileo, Italy
Iaroslav Gnilitskyi, Ukraine
Hassanien Gomaa, Egypt
Fabien Grasset, Japan
Jean M. Greneche, France
Kimberly Hamad-Schifferli, USA
Simo-Pekka Hannula, Finland
Michael Harris, USA
Hadi Hashemi Gahruie, Iran
Yasuhiko Hayashi, Japan
Michael Z. Hu, USA
Zhengwei Huang, China
Zafar Iqbal, USA
Balachandran Jeyadevan, Japan
Xin Ju, China
Antonios Kelarakis, United Kingdom
Mohan Kumar Kesarla Kesarla, Mexico
Ali Khorsand Zak, Iran
Avvaru Praveen Kumar, Ethiopia
Prashant Kumar, United Kingdom
Jui-Yang Lai, Taiwan
Saravanan Lakshmanan, India
Meiyong Liao, Japan
Shijun Liao, China
Silvia Licoccia, Italy
Zainovia Lockman, Malaysia
Jim Low, Australia
Rajesh Kumar Manavalan, Russia
Yingji Mao, China
Ivan Marri, Italy
Laura Martinez Maestro, United Kingdom
Sanjay R. Mathur, Germany
Tony McNally, United Kingdom
Pier Gianni Medaglia, Italy
Paul Munroe, Australia
Jae-Min Myoung, Republic of Korea
Rajesh R. Naik, USA
Albert Nasibulin, Russia
Ngoc Thinh Nguyen, Vietnam
Hai Nguyen Tran, Vietnam
Hiromasa Nishikiori, Japan

Sherine Obare, USA
Abdelwahab Omri, Canada
Dillip K. Panda, USA
Sakthivel Pandurengan, India
Dr. Asisa Kumar Panigrahy, India
Mazeyar Parvinzadeh Gashti, Canada
Edward A. Payzant, USA
Alessandro Pegoretti, Italy
Oscar Perales-Pérez, Puerto Rico
Anand Babu Perumal, China
Suresh Perumal, India
Thathan Premkumar, Republic of Korea
Helena Prima-García, Spain
Alexander Pyatenko, Japan
Xiaoliang Qi, China
Haisheng Qian, China
Baskaran Rangasamy, Zambia
Soumyendu Roy, India
Fedlu Kedir Sabir, Ethiopia
Lucien Saviot, France
Shu Seki, Japan
Senthil Kumaran Selvaraj, India
Donglu Shi, USA
Muhammad Hussnain Siddique, Pakistan
Bhanu P. Singh, India
Jagpreet Singh, India
Jagpreet Singh, India
Surinder Singh, USA
Thangjam Ibomcha Singh, Republic of Korea
Vidya Nand Singh, India
Vladimir Sivakov, Germany
Tushar Sonar, Russia
Pingan Song, Australia
Adolfo Speghini, Italy
Kishore Sridharan, India
Marinella Striccoli, Italy
Andreas Stylianou, Cyprus
Fengqiang Sun, China
Ashok K. Sundramoorthy, India
Bo Tan, Canada
Leander Tapfer, Italy
Dr. T. Sathish Thanikodi, India
Arun Thirumurugan, Chile
Roshan Thotagamuge, Sri Lanka
Valeri P. Tolstoy, Russia
Muhammet S. Toprak, Sweden
Achim Trampert, Germany
Tamer Uyar, USA
Cristian Vacacela Gomez, Ecuador
Luca Valentini, Italy
Viet Van Pham, Vietnam
Antonio Vassallo, Italy
Ester Vazquez, Spain
Ajayan Vinu, Australia
Ruibing Wang, Macau
Magnus Willander, Sweden
Guosong Wu, China
Ping Xiao, United Kingdom
Zhi Li Xiao, USA
Yingchao Yang, USA
Hui Yao, China
Dong Kee Yi, Republic of Korea
Jianbo Yin, China
Hesham MH Zakaly, Russia
Michele Zappalorto, Italy
Mauro Zarrelli, Italy
Osman Ahmed Zelekew, Ethiopia
Wenhui Zeng, USA
Renyun Zhang, Sweden

Contents

Contents

Hindawi
Journal of Nanomaterials
Volume 2022, Article ID 3167809, 14 pages
https://doi.org/10.1155/2022/3167809

Research Article

Tin Oxide/Nitrogen-Doped Graphene Quantum Dots Composite Nanotubes: An Efficient Electrode for Supercapacitors

Seshendra Reddy Ch,[1] Ravindra N. Bulakhe,[2,3] Jeevan Kumar Reddy Modigunta,[2] G. Murali,[2] Reddy Sivasankar A.,[1] Jiyeong Kim,[2] Eunji Park,[2] Byungin Kang,[2] Insik In,[2] Arup Kumer Roy,[4] Kiruthiga Ramakrishnan,[5] and Udayabhaskar Rednam[5]

[1]*Department of Physics, Vikrama Simhapuri University P.G. Centre, Kavali, 524201 Andhra Pradesh, India*
[2]*Department of Polymer Science and Engineering, Department of IT-Energy Convergence (BK21 FOUR), Chemical Industry Institute, Korea National University of Transportation, Chungju 27469, Republic of Korea*
[3]*Soft Energy Systems and Laser Applications Laboratory, School of Mechanical Engineering, Chung-Ang University, Seoul 06974, Republic of Korea*
[4]*Department of Chemistry, Chittagong University of Engineering & Technology, Chittagong-4349, Bangladesh*
[5]*Instituto de Investigaciónes Científicas Y Tecnológicas (IDICTEC), Vicerrectoría de Investigación Y Postgrado, Universidad de Atacama, Avenida Copayapu, 485 Copiapó, Chile*

Correspondence should be addressed to Arup Kumer Roy; arupkumer@cuet.ac.bd

Received 10 September 2021; Revised 28 December 2021; Accepted 23 May 2022; Published 13 July 2022

Academic Editor: Antonios Kelarakis

Copyright © 2022 Seshendra Reddy Ch et al. This is an open access article distributed under the Creative Commons Attribution License, which permits unrestricted use, distribution, and reproduction in any medium, provided the original work is properly cited.

Tin oxide (SnO_2) and nitrogen-doped graphene quantum dots (N-GQDs) composite nanotubes (SnO_2/N-GQD NTs) were fabricated by the electrospinning technique and followed by the thermal annealing method for the application in supercapacitor as an electrode. SnO_2/N-GQD NTs with different ratio of N-GQDs were prepared by adding different ratios of N-GQDs along with tin chloride during the electrospinning process. The prepared composite's structure and morphological properties were characterized by using different techniques like XRD, FE-SEM, TEM, and XPS. The supercapacitor performance of the SnO_2/N-GQD NTs composite was analyzed by the electrochemical studies such as cyclic voltammetry and galvanostatic charge-discharge (GCD) measurement in 2 M KOH solution as electrolyte. The electrochemical analyses of SnO_2/N-GQD NTs was tested at different scan rates and current densities. SnO_2/N-GQD NTs prepared using 3 wt.% of N-GQDs showed an excellent capacity retention even after 5000 GCD cycles and exhibited a maximum specific capacitance of 420 mF g^{-1} at a current density of 8 mA cm^{-2} in comparison to pure SnO_2 NTs (230 mF cm^{-2}).

1. Introduction

In the past few decades, the continuous growth in the demand for energy thrived researchers to find an alternative energy storage and conversion systems for the depleting fossil fuels which are affecting the global environment. Among various available energy storage and conversion devices, such as batteries, fuel cells, and supercapacitors (SCs), SCs provide an instant high-power density for the required applications [1–5]. SCs have gained a wide attention in the interdisciplinary fields due to their amazing characteristics like, high efficiency at prolonged cycles [6], high-power density, and high-energy density [7, 8]. In general most of the metal oxide semiconductors (MOS) such as RuO_2 [9, 10], NiO [11], SnO_2 [12], MnO_2 [13, 14], Fe_3O_4 [15], CuO [16], ZnO [17], and CoO [18] are having a significant contribution for the SC applications [19]. Tin oxide (SnO_2) is well-known among MOS due to its vast applications such as in gas sensors [20, 21], biosensors [22, 23], solar cells [24, 25], Li-ion battery materials [26, 27], photocatalytic applications [28],

and SCs [29, 30]. Among the MOS, SnO_2 is a non-toxic and easily synthesizable nanomaterial [31]. Although SnO_2 performs well for SCs, the limiting factors such as poor electrical conductivity, poor transportation of electrolyte ions within the SnO_2 matrix, and huge volume expansion hinder its practical applicability [32]. In order to improve SnO_2 as an efficient electrode material for the SCs, the combination of SnO_2 with other conductive materials containing a high surface area and good morphologies is one of the most suitable choices. The composites made of a conductive material such as carbon-based materials with SnO_2 and related composites are one of the good choices among many available methods in order to enhance the performance as electrode for SCs.

In recent years, carbon-based materials are among the eco-friendly, low-cost, and easily available sources for improving the conductivity of MOS along with different morphologies with high surface area [33]. Carbon-based nanomaterials and MOS nanocomposites have been reported to be good electrode materials for energy conversion and storage applications [26, 34]. The preparation of 2D fiber or tube-like morphologies supports the improvement of internal conductivity in the materials which contains interconnecting branching networks in the structures. These type of morphologies can be easily fabricated using the electrospinning method [35].

The composites of carbon-based materials contribute to the improvement of the pseudocapacitance of the materials in electrochemical analysis. In recent times, heteroatom-doped carbon-based materials such as N-doped graphene and N-doped graphene quantum dots (N-GQDs) are among the carbon nanostructures that have been studied majorly [36–38]. N-GQDs are used as the electrodes for SCs and found that they exhibited superior capacitance and rate performance [39]. These properties make N-GQDs as one of the suitable materials for making composites with MOS for improving the electrochemical performance. The fabrication of these nanotube (NT) composite materials with nanometer scale morphology is one of the challenging processes to obtain a highly active sites and good conductive networks. However, the N-GQDs incorporated SnO_2 NTs can be a good suitable electrode material for the improvement of electrochemical performance of SnO_2 in SC applications.

In this work, the SnO_2 NTs and SnO_2/N-GQD NTs have been prepared by two-step process in which first the solution of tin chloride and N-GQDs (with 3 and 5 wt.%) along with polyvinylpyrrolidone in DMF solutions was subjected to electrospinning followed by thermal annealing. This process is cheaper, easy to handle, and has the advantage of easy morphological control. The electrochemical performance of synthesized SnO_2/N-GQD NTs was studied by fabricating a SC device with a three-electrode system configuration and aqueous potassium hydroxide as electrolyte.

2. Experimental

2.1. Materials. Tin (II) chloride dihydrate ($SnCl_2{\cdot}2H_2O$), *N*, *N*-dimethylformamide (DMF), ethanol, polyvinylpyrrolidone (PVP, $M_w = 1{,}300{,}000\,g\,mol^{-1}$), citric acid monohydrate, urea, polyvinylidene fluoride (PVdF), and N-methyl pyrrolidone (NMP) were procured from Sigma Aldrich, USA. Conductive additive super p carbon and Ni-foam were procured from MTI Corporation, South Korea. All the chemicals purchased were used as received without any further purification.

2.2. Synthesis of N-GQDs. Citric acid monohydrate (0.42 g) and urea (0.36 g) were mixed in 12 mL deionized water and sonicated for 60 min. The mixture was then transferred to a Teflon-lined autoclave (50 mL) and heated at 180 °C for 3 h. After cooling the autoclave to room temperature, the resultant product was filtered and washed with ethanol and centrifuged at 8000 rpm for 5 min. The solid precipitate obtained was dried at 50 °C for 10 h to obtain the nitrogen-doped graphene quantum dots (N-GQDs) [38].

2.3. Synthesis of SnO_2 Nanotubes and N-GQD Incorporated SnO_2 Nanotubes. $SnCl_2{\cdot}2H_2O$ (0.7 g) was dissolved in 4.2 mL ethanol and sonicated adequately for 1 h; simultaneously, 0.44 g of PVP was dissolved in DMF and stirred for 3 h. Finally, both clear solutions were mixed and stirred for 4 h to obtain the precursor liquid for electrospinning. N-GQDs (3 and 5 wt.%) incorporated tin chloride NTs were prepared by adding the solution of tin chloride with pre-prepared N-GQD solution with stirring for several hours until the solution becomes uniform. The obtained solution was loaded into the syringe and electrospinned. For the preparation of the pristine tin chloride and N-GQD incorporated tin chloride NTs, a constant voltage of 12 kV and 15 kV was applied, respectively. The distance between the syringe needle and the electrospun mat collector was fixed at 12 cm. The specimens were collected and dried in vacuum oven for overnight. Pure SnO_2 and N-GQDs incorporated SnO_2 nanotube composites were obtained by annealing the dried electrospun mats at 600 °C for 2 h and 500 °C for 4 h, respectively. The samples were denoted as S1 for pure SnO_2 NTs, S2 for SnO_2 NTs with 3 wt.% of N-GQDs, and S3 for SnO_2 NTs with 5 wt.% N-GQDs-loaded samples. The detailed synthesis procedure is shown in Scheme 1.

2.4. Materials Characterization. The structural properties of the prepared samples (S1, S2, and S3) were characterized by the patterns obtained from X-ray diffraction (Bruker, D8 ADVANCE, USA). The surface morphology and microstructure of the samples were characterized by field emission scanning electron spectroscopy (FE-SEM, JEOL, JSM-6700F, Japan) and transmission electron microscopy (TEM, Tecnai G2 F20, FEI Corporation, Japan). The chemical bonds in the samples were characterized using X-ray photoelectron spectra (XPS, Scientific Sigma Probe Multi-2000 spectrometer, Thermo VG Scientific Co., USA).

2.5. Electrochemical Characterization. The electrochemical analyses were carried by using a Ni foam electrode coated with the prepared active materials. For electrode preparation, 80 wt.% active material, 10 wt.% polyvinylidene fluoride (PVDF) and 10 wt.% conductive carbon were mixed in n-methyl-2-pyrrolidone (NMP). The mixture was made as fine slurry, and then, it was coated on Ni foam (1 × 4 cm) in

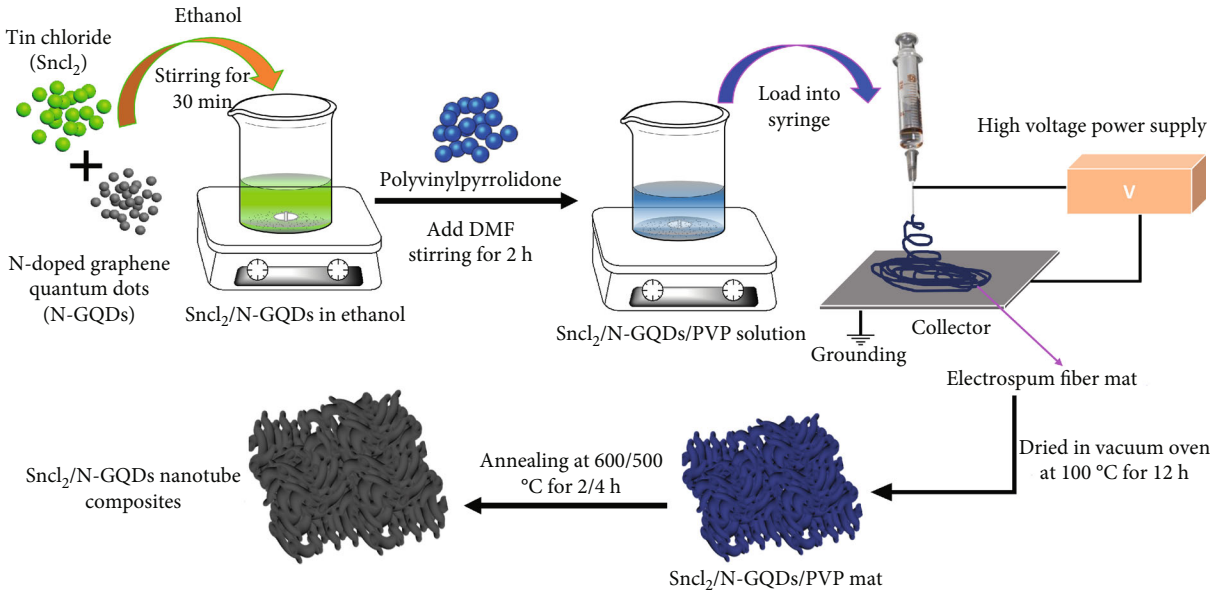

Scheme 1: Schematic diagram for the synthesis of SnO_2 nanotubes and N-GQDs incorporated SnO_2 nanotubes by electrospinning followed by thermal annealing.

1×1 cm size and then dried in vacuum oven for 12 h at 100 °C. The loading of the active material in the electrodes is approximately 2.5 mg cm^{-2}. Electrochemical measurements such as cyclic voltammetry (CV) and galvanostatic charge–discharge (GCD) were performed at room temperature with the help of Wonatech, Korea, instrument using three-electrode configuration in 2 M KOH electrolyte solution. Electrochemical impedance spectra (EIS) analyses were performed using frequency range between 0 Hz and 50 kHz. CV was carried out at various scan rates (5 to 100 mV/s) in the potential window of 0-0.5 V. GCD was performed at different current densities (1 to 8 mA g^{-1}) in the voltage window of 0-0.5 V. The specific capacitance of the SCs is calculated by using the formula:

$$\text{Specific capacitance}\left(C_{\text{sp}}\right) = \frac{I \times \Delta t}{m \times \Delta V}, \quad (1)$$

where $I\,(A)$ is discharge current, $\Delta t\,(s)$ is the discharge time consumed for in the potential range of V, $m\,(g)$ is the mass of the active material, and $\Delta V\,(V)$ is the potential window used for the charge-discharge. Energy density and power density of the fabricated materials are determined by using the following equations:

$$\text{Energy density}(E) = \frac{C_{sp} \times \Delta V^2}{2}, \quad (2)$$

where C_{sp} $(F\,g^{-1})$ is the specific capacitance calculated from charge-discharge process and ΔV is the potential window used in the charge-discharge process.

$$\text{Power Density}(P) = \frac{E}{\Delta t}, \quad (3)$$

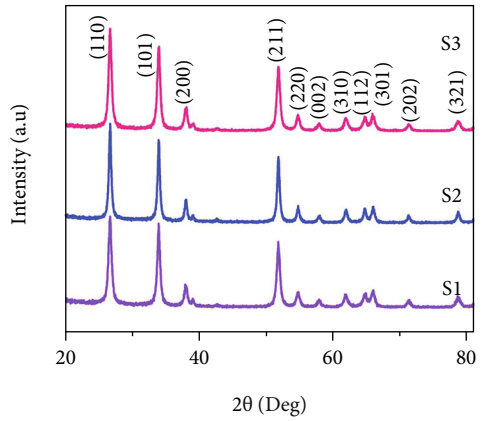

Figure 1: XRD spectral data of S1 (SnO_2) nanotubes, S2 (SnO_2/N-GQDs-3 wt.%) nanotubes, and S3 (SnO_2/N-GQDs-5 wt.%) nanotubes.

where E is the energy density calculated from the specific capacitance and Δt discharge time of the supercapacitor.

3. Results and Discussions

Figure 1 Shows the XRD patterns of S1, S2, and S3 NTs with the major peaks corresponding to the (110), (101), (200), (211), (220), (002), (310), (112), (301), (202), and (321) lattice planes of the rutile structure of SnO_2. XRD patterns are in good agreement with the reference patterns of SnO_2 with JCPDS number 41-1445, which are compatible with previous reports [40]. The lack of N-GQD peaks in XRD might be due to the dominant concentration of the SnO_2 matrix in the samples. The effect of N-GQDs incorporation into the samples is studied by considering the (110) diffraction peak as reference candidate to calculate the crystallite

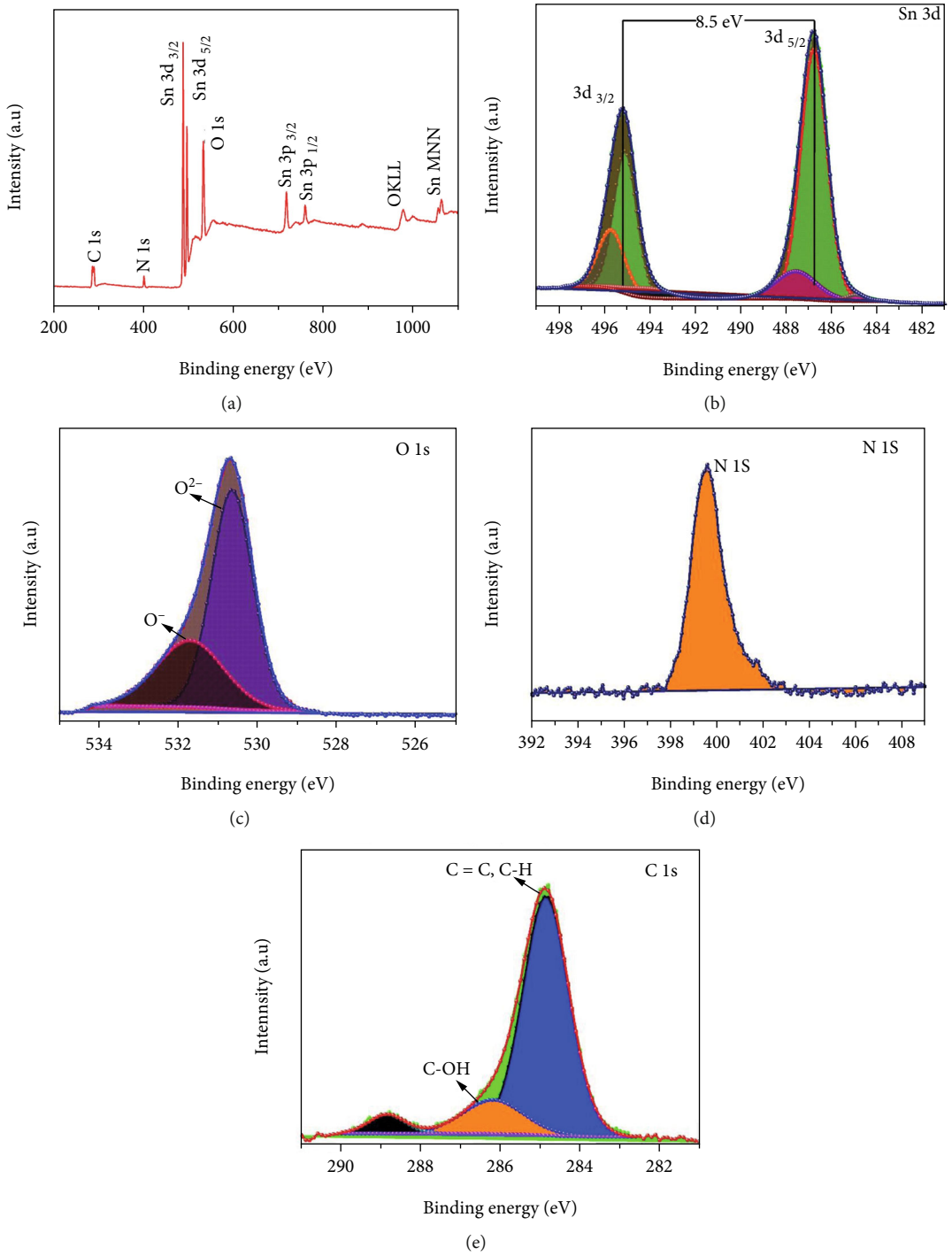

Figure 2: XPS (a) survey scan spectrum and high resolution deconvoluted spectra for (b) Sn 3d, (c) O 1s, (d) N 1s, and (e) C 1s, of sample S2 (SnO_2/N-GQDs-3 wt.%).

size. The crystallite size of the samples is calculated using the Scherrer's formula. The calculated average crystallite size of the S1, S2, and S3 are 10.1 nm, 12.3 nm, and 14.5 nm, respectively, showing change in the crystallite size caused by the N-GQDs incorporation during the synthesis process.

The surface elemental composition of the S2 is analyzed by XPS as shown in Figure 2. The survey scan spectrum (Figure 2(a)) detected elements Sn, C, N, and O. The peaks of Sn 3d, Sn 3p, and MNN were detected from SnO_2. The Sn 3d ($3d_{3/2}$ and $3d_{5/2}$) peaks were observed at 495.2 and 486.7 eV (Figure 2(b)) corresponding to Sn^{4+} in the rutile SnO_2 structure. In Figure 2(c), the O 1s spectra of the S2 shows the peaks at 532.1, 531.2, and 530.4 eV; corresponding to oxygen absorption (O_2^-), oxygen vacancy (O^-), and oxygen binding (O_2^-), this designates the formation of oxygen vacancies in S2. XPS spectra of the S2 sample have an obvious peak at 399.8 eV corresponding to N 1s (Figure 2(d)) due to the presence of nitrogen functional groups (from N-

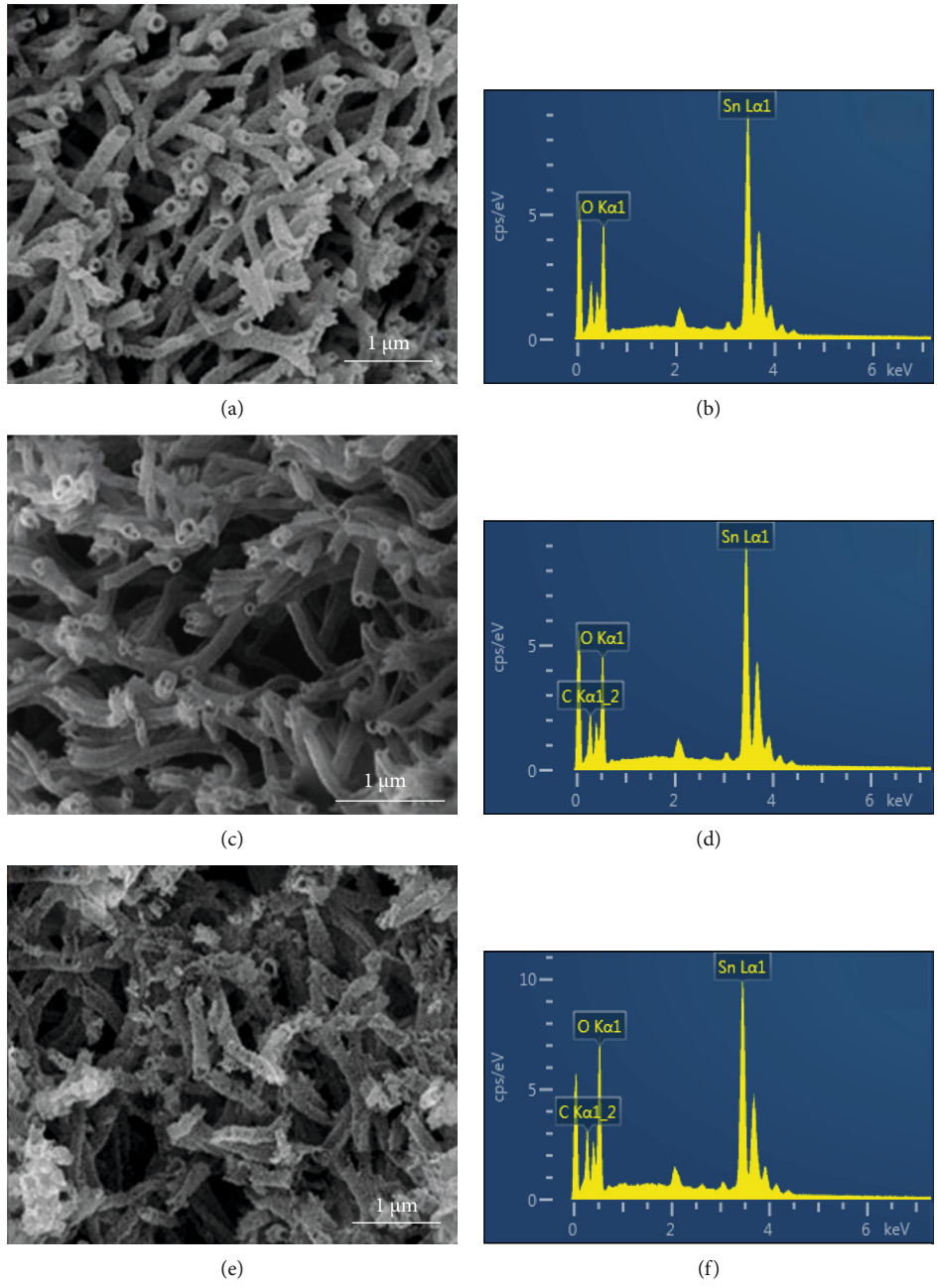

FIGURE 3: FE-SEM images and EDS spectrum of samples (a, b) S1 (pure SnO_2 nanotubes), (c, d) S2 (SnO_2/N-GQDs-3 wt.% nanotubes), and (e, f) S3 (SnO_2/N-GQDs-5 wt.% nanotubes).

GQDs). The peak of C1s can be attributed mainly to GQDs as shown in Figure 2(e). The C1s spectrum shows a strong peak center at 284.9 eV that is attributed for the C=C/C–C bonds, and peaks at 285.5 and 286.7 eV revealing the presence of C=N (sp^2) and C–N (sp^3) bonds, respectively. The XPS analysis provides evidence for the formation of N-doped GQDs and their composites in combination with SnO_2 [41].

FE-SEM and EDS spectral images of S1, S2, and S3 NTs are shown in Figures 3(a)–3(f). In all samples, NTs are randomly oriented in all directions with the rough surface. Figures 3(a)–3(b), Figures 3(c)–3(d), and Figures 3(e)–3(f) represent the FE-SEM images and EDS spectra of S1, S2, and S3 samples after calcination, respectively. The elemental composition of pristine and composite SnO_2 NTs is determined by EDS analysis that indicates the presence of Sn, O, and C elements as shown in Figure 3. Pristine and N-GQDs incorporated SnO_2 long NTs are having the diameter in the range of 15–40 nm. From FE-SEM and EDS results, it is observed that almost there were no trances of PVP-based amorphous carbon after thermal annealing. Although PVP created some porous vacancies during the annealing process, the nanotube structures were retained during the calcination process due to the crystallization of SnO_2. From FE-SEM images, it can also be observed that the S1 and S2 are thin and almost uniform. In the case of S3 sample, as the N-

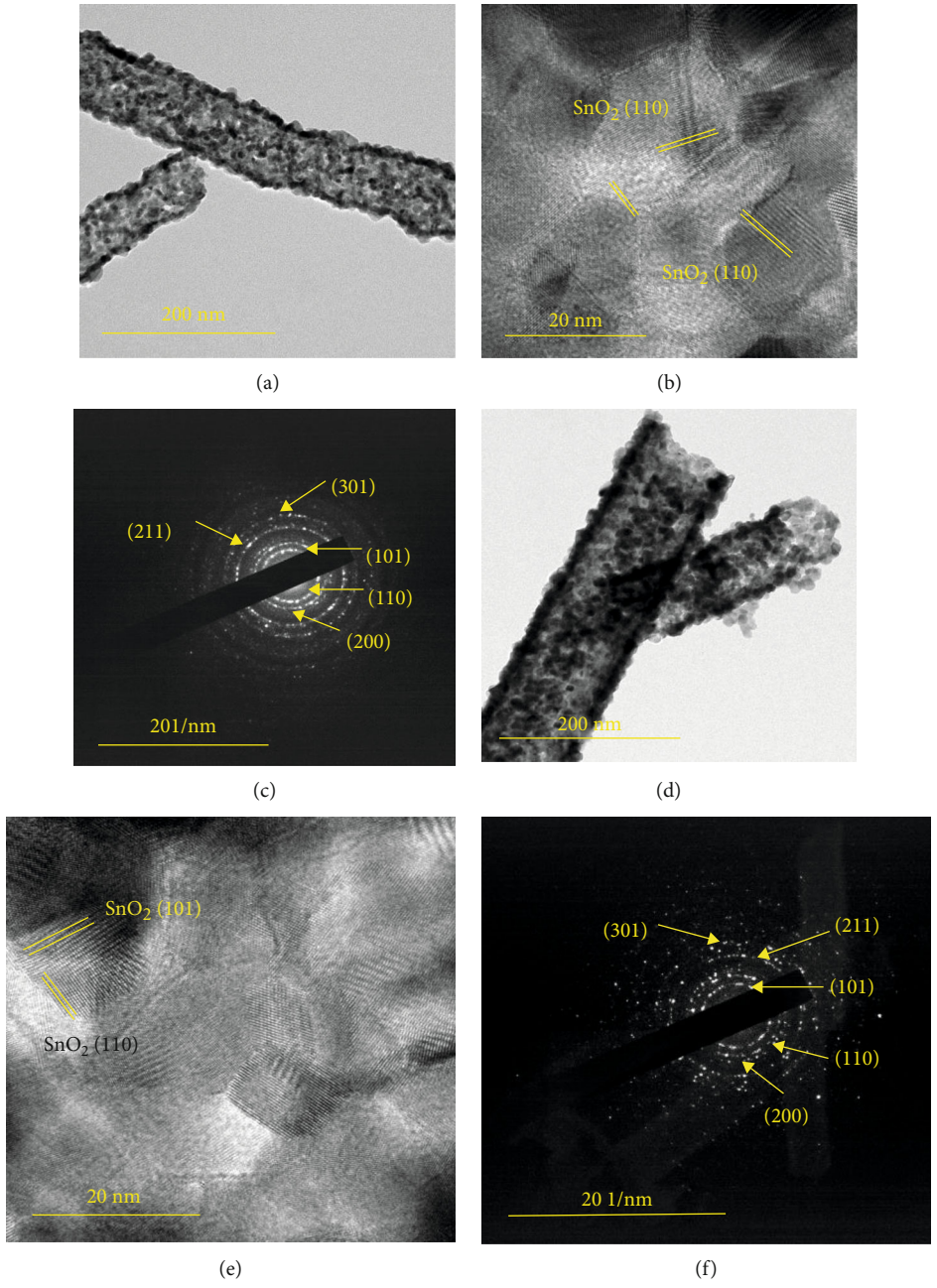

Figure 4: TEM, HR-TEM, and SAED pattern images of (a–c) SnO_2 (S1) and (d–f) SnO_2/N-GQDs composite material (S2).

GQDs concentration is about 5 wt.%, the NTs were broken, and this may be due to the increase in the viscosity of the electrospinning precursor solution.

Figure 4 shows the TEM, HR-TEM, and SAED images of S1 and S2 samples. Figures 4(a)–4(c) display the TEM, HR-TEM, and SAED images of S1, i.e., pristine SnO_2 NTs. The size of pristine SnO_2 nanoparticles is about 20 nm. The nanoparticle network has been continued in the form of nanotube by the mutual sharing of the crystal edges of each particle. The crystal structure of S2, i.e., SnO_2/N-GQD NTs (Figures 4(d)–4(f)), could be verified in the high-resolution TEM. The SnO_2 NTs consist of crystalline nanoparticles-shaped SnO_2, and the N-GQDs were tightly incorporated in the SnO_2 NTs. Moreover, the HR-TEM images demonstrate clear lattice fringes with *d*-space of 0.34 nm and 0.27 nm, which are in good agreement with that of the (101) and (110) planes of SnO_2. The SAED images of the S1 and S2 represent the monocrystalline structure and that is in good agreement with the XRD analysis as discussed earlier.

The electrochemical analysis of the prepared samples was investigated using CV, EIS, and GCD cycling through a three-electrode configuration. In the three-electrode system devices, active material-loaded Ni foam is used as working electrode, Ag/AgCl as the reference electrode, and platinum strip as

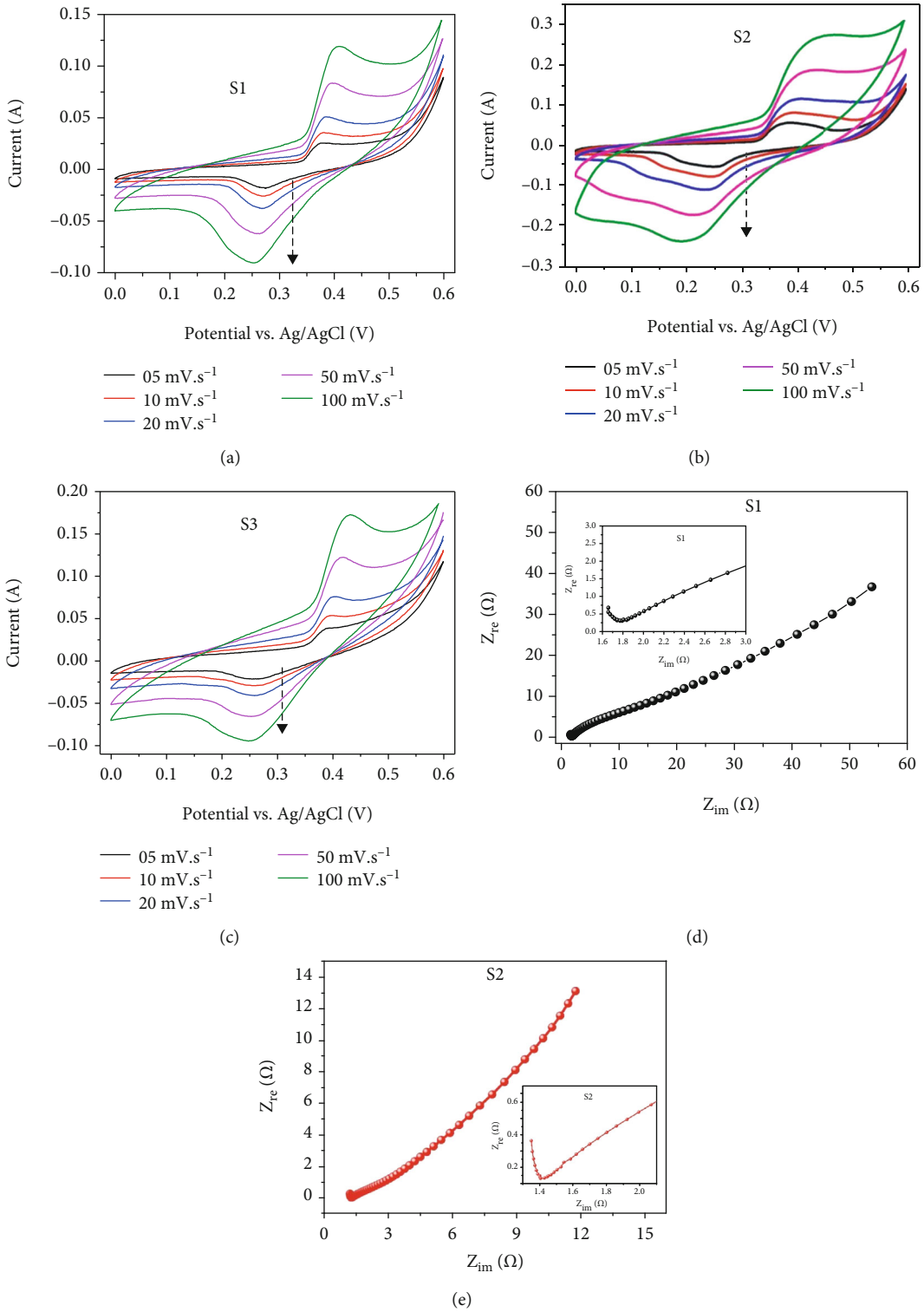

Figure 5: Continued.

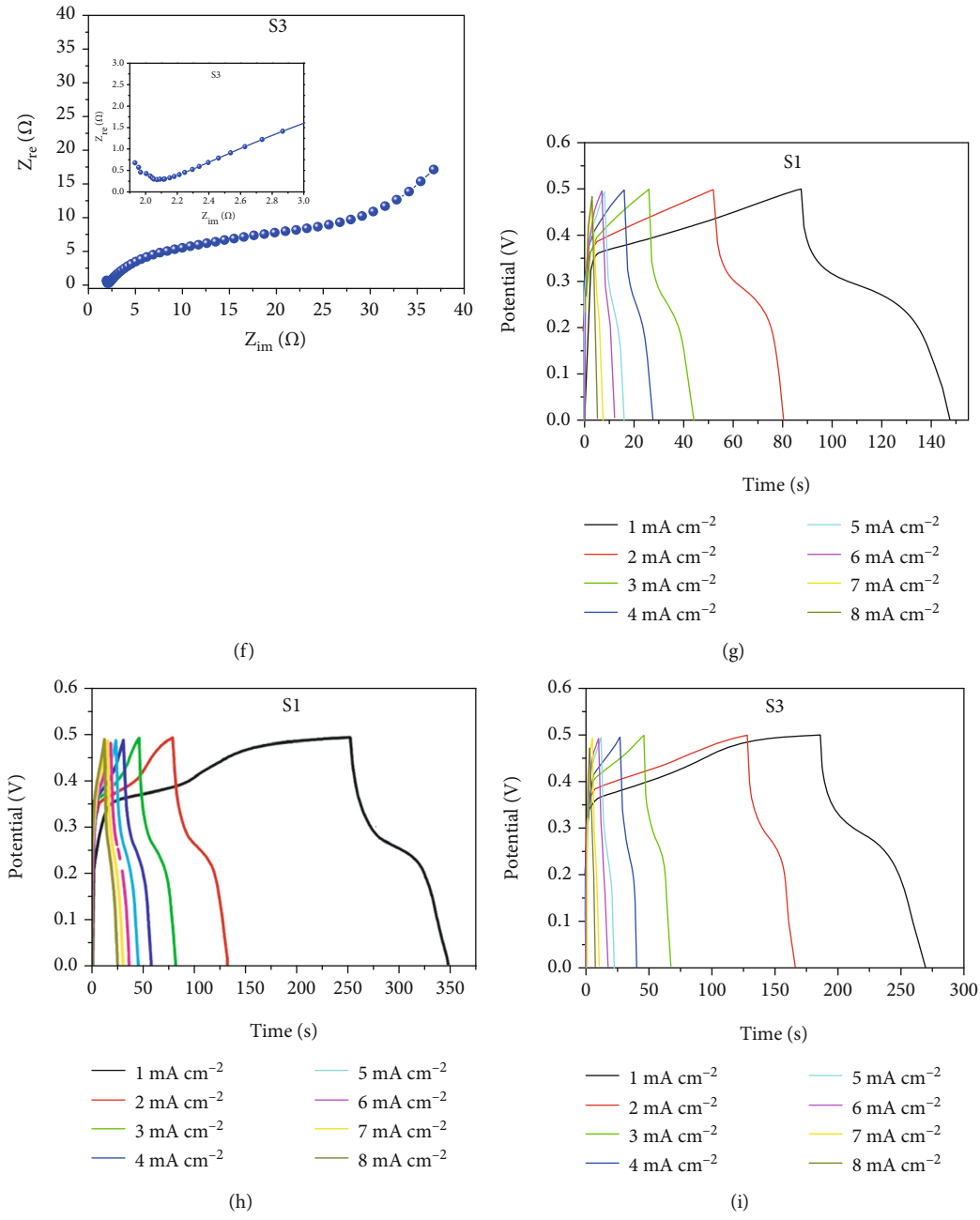

Figure 5: Electrochemical performance evolution of the S1, S2, and S3 electrodes: (a–c) cyclic voltammetry (CV) curves at different scan rates from 5 to 100 mV s^{-1}, (d–f) Nyquist plots (EIS) analyzed in the frequency range 0.1 to 10 kHz (inset, selective magnified scale in the high-frequency region), and (g–i) galvanostatic charge-discharge (GCD) curves at different current densities from 1 to 8 mA cm^{-2}.

counter electrode. Aqueous 2 M KOH was used as the electrolyte for the analyses. The CV, EIS, and GCD analysis results for S1, S2, and S3 are shown in Figure 5.

Figures 5(a)–5(c) show the CV curves of S1, S2, and S3 electrodes for comparison in the potential window of 0 to 0.6 V in 2 M KOH aqueous electrolyte at different scan rates from 5 to 100 mV s^{-1}. CV curves of S1, S2, and S3 have shown noticeable redox peaks at ~0.38 and 0.27 V. The CV curve for S1 electrode has clearly shown the characteristic redox peaks for SnO_2 material (Figure 5(a)). The CV curves of S2 has shown well-defined redox peaks similar to S1, indicating the presence of quasi-reversible faradaic reactions at different scan rates as shown in Figure 5(b). The redox peaks of S2 sample are broadened with increase of the scan rate from 5 to 100 mV s^{-1} might be due to the fact that the quasi-reversible redox reactions at the surface of SnO_2 material along with the conductive N-GQDs in the electrodes that might help to enhance the internal conductivity of the electrodes. Whereas in the case S3 electrode, the CV redox peak positions were similar to the previous electrodes, but the peak broadening was not observed as that of S2 (Figure 5(c)). The possible redox reactions of the SnO_2/N-GQD NT electrodes during the CV process (between Sn(III)/

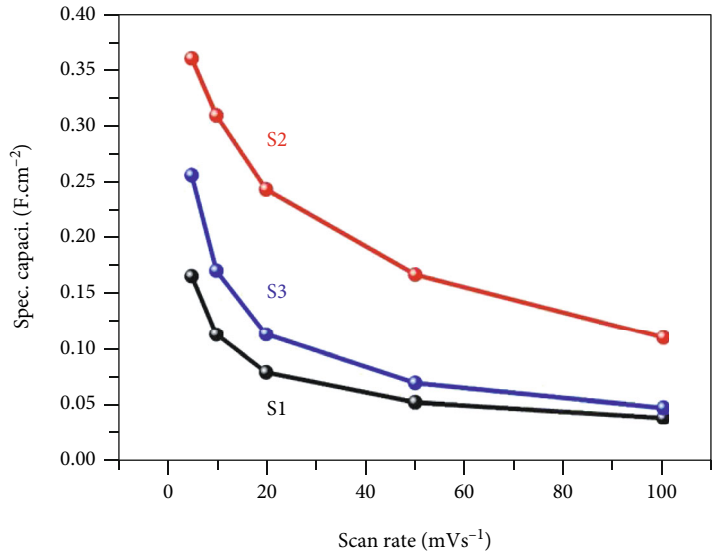

(a)

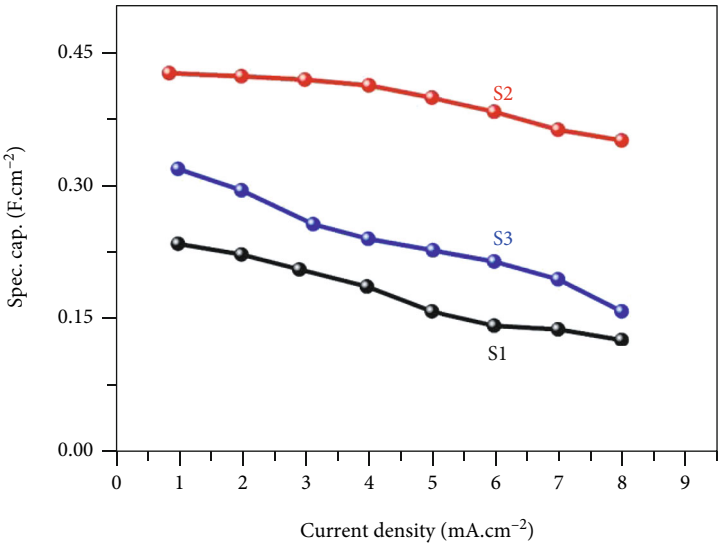

(b)

Figure 6: Continued.

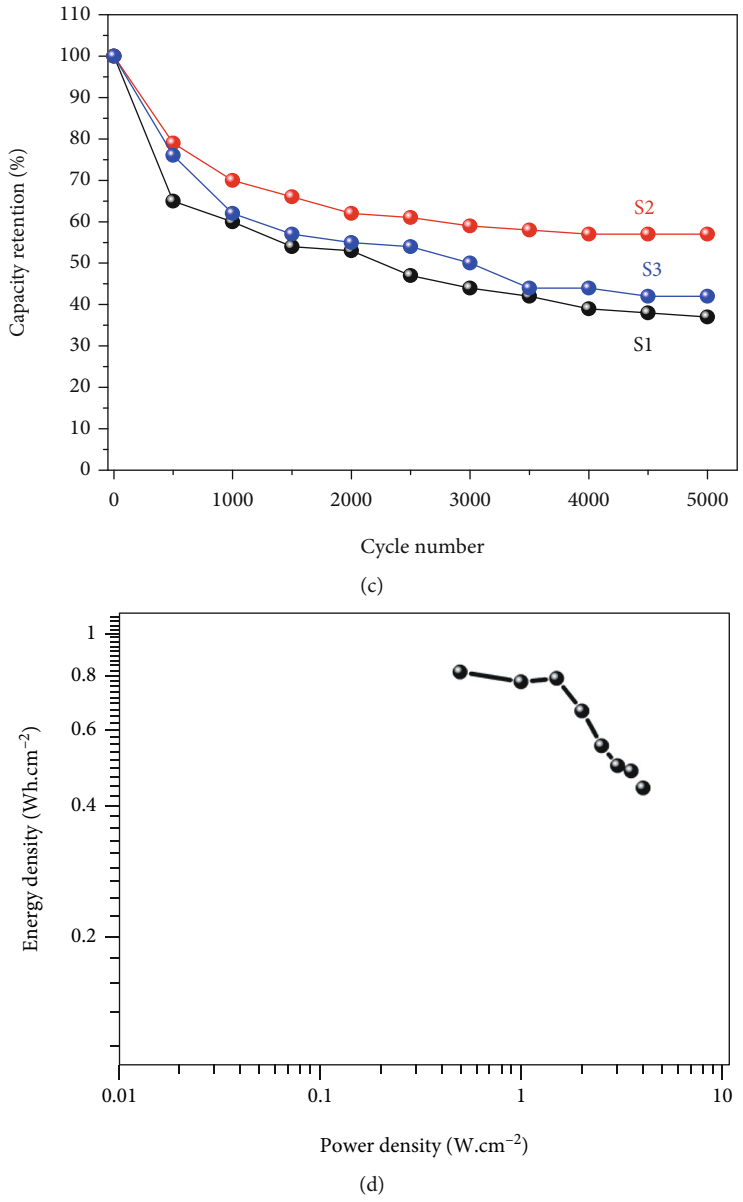

Figure 6: Electrochemical performance of S1 (SnO_2 NTs), S2 (SnO_2/N-GQD-3 wt.% NTs), and S3 (SnO_2/N-GQD-5 wt.% NTs) electrodes: (a) specific capacitance vs. scan rate, (b) plots of specific capacitance vs. current density, and (c) capacity retention efficiency with respect to cycle number. (d) Ragone plot of energy density vs. power density for supercapacitor with S2 electrodes.

Sn(IV) in reaction with OH^-) are described in Equations (4) and (5) [42].

$$SnO_2 + OH^- \leftrightarrow SnOOH + e^- \quad (4)$$

$$SnOOH + OH^- \leftrightarrow SnO_2 + H_2O + e^- \quad (5)$$

The electron/ion transport behavior of the nanocomposites is understood by using EIS measurements. EIS measurements also carried to compare the resistance at the interface of the electrode materials interface and the electrolyte in the devices fabricated using electrodes made-up of S1, S2, and S3 materials as shown in Figures 5(d)–5(f). The Nyquist plots of the nanocomposites were showing the semi-half circle followed by the immediate raise in the diffusion resistance in the high-frequency region (as shown in the inset of Figures 5(d)–5(f)) and a linear slope in the low-frequency region. The charge transfer resistance (R_{ct}) was observed for all the samples, and the inclined line is attributed to the anomalous diffusion of the ions in the electrolyte to the modified electrode. The R_{ct} of the electrodes indicates the presence of more resistance due to the semiconducting SnO_2 in S1, whereas the R_{ct} value decreases for S2 electrodes and further increases for S3 as shown in Figures 5(d)–5(f). The device with S2 electrode showed a least resistance in comparison to S1 and S3. The above electrochemical results imply that S2 electrode is a high

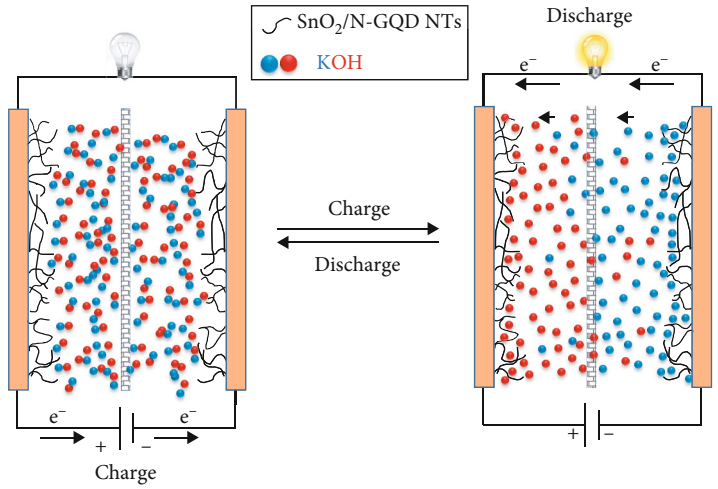

Figure 7: The schematic of the possible mechanism involved in the SnO_2/N-GQD NT composite electrodes during the charge-discharge processes.

potential candidate for the application of SCs in comparison to the S1 and S3 electrodes.

The N-GQDs will not take part in the redox reaction directly, and it will enhance the electrical/ionic conductivity of the composites with faster kinetics of positive ions during the redox process by means of electric double layer (EDL) formation. The GCD profiles of S1, S2, and S3 electrodes at different current densities ranging from 1 to 8 mA cm^{-2} are shown in Figures 5(g)–5(i). The corresponding areal capacitance values at different current densities were calculated, and the results were compared for S1, S2, and S3. The areal capacitances of the S2 electrode are calculated at different current densities from 1 to 8 mA cm^2 and are varying from 420 to 200 mF cm^{-2}, respectively, as shown in Figure 5(h). S2 electrode delivers higher areal capacitance of 420 mF cm^{-2} at current density of 1 mA cm^{-2}, as compared to S1 (230 mF cm^{-2}) and S3 (320 mF cm^{-2}) as shown in Figures 5(g)–5(i). The S2 electrode revealed good electrochemical performance in comparison to S1 and S3 electrodes; this might be due to the improved conductivity of the S2 electrode. The CV curves with redox peaks and charge-discharge plots with lower internal resistance indicate that the materials are suitable for SC applications.

Figure 6(a) shows the specific capacitance of the electrodes S1, S2, and S3 with respect to scan rates used in the CV analysis. Similarly, Figure 6(b) shows the specific capacitance with change in current densities varied from 1 to 8 mA cm^{-2}. From these electrochemical analyses, it can be corroborated that electrodes prepared using S2 sample are having the best possible combination of N-GQDs and SnO_2 NTs for the application in SCs.

The specific capacitance is decreased at higher scan rates, which could be due to the approach of positive ions (K^+) only at the outer surface of the electrode during the EDL formation and/or quasi-reversible reactions. Whereas at lower scan rates, positive ions could easily diffuse into all the available spaces of electrode, thus leading to sufficient insertion reaction to form quasi-reversible reactions and/or EDL formation or to show a high specific capacitance [43, 44]. The capacitance retention of S1, S2, and S3 electrodes studied by the GCD measurements at 10 mA cm^{-2} current density for 5000 cycles is shown in Figure 6(c). The capacitance retention for S2 electrode (65%) is higher in comparison to S1 (51%) and S3 (44%) as shown in Figure 6(c). These results indicate the higher electrochemical cycling stability of S2 composite electrode. Figure 6(d) shows the Ragone plot of energy density vs. power density of the SC with S2 electrode. The energy density of 820 mWh cm^{-2} and the power density of 4.10 W cm^{-2} were obtained for the S2 electrode. Similar work was reported by Barik et al., which is found to have the energy density of 80 mWh cm^{-2} and power density of 4.87 W cm^{-2} for SnO_2@carbon nanofiber synthesized by the electrospinning method [45]. The schematic for the possible mechanism involved in the SnO_2/N-GQD NT composite electrodes during charge-discharge process is shown in Figure 7.

The schematic mechanism (Figure 7) shows the movement of ions in electrolyte during the charge-discharge process of the SnO_2/N-GQD NT electrodes. The K^+ and OH^- ions in the electrolyte move towards the opposite charged electrodes. The electrons in the OH^- ions adsorbed onto the surface of SnO_2/N-GQD electrodes undergo chemical reactions as discussed above in Equations (4) and (5). Whereas the K^+ ions adsorbed on the surface of the electrodes take electron released during SnO_2 reversible reactions and form an EDL during the charge process, in the charging process, both EDL and reversible chemical reactions both occur at the surface of the electrodes. The reversible reactions during the discharge process will retain the ionic combination of electrolyte resulting in neutral bulk electrolyte. The performance enhancement of S2 electrodes can be attributed to spacer effect of SnO_2 particles in the NTs incorporated with N-GQDs. The highly reversible faradaic redox process of SnO_2 also enhances the performance of SCs. The specific capacitance performance of the S2 electrode was higher in comparison to S1 and S3 and might be due to the factors discussed above such as spacer effect, good conductivity of N-GQDs, and good internal contacts between SnO_2 particles

and N-GQDs in the NTs. In the case of S1 electrodes, there are no additional conducting agents such as N-GQDs, whereas for S3 electrode, the N-GQDs concentration has hindered the adhesive property between SnO_2 crystals leading to damage of NT structures subsequently losing the conductivity advantage. In contrast, S2 has shown a good structural stability and enhanced conductivity for electrodes along with more suitable sites for the surface chemical reactions on SnO_2, therefore resulted as a good performing electrode than others.

From the above experimental results, the N-GQDs incorporated SnO_2 NTs have shown a considerable better improvement in the areal capacitance of the SnO_2 NTs due to the enhanced electrons and ionic diffusion with increase of more active sites. The moderate (3 wt.%) addition of N-GQDs into SnO_2 NTs has demonstrated an excellent electrochemical behavior due to the tubular porous morphology along with decrease in electrical resistance compared to pure SnO_2 NTs and higher N-GQDs containing samples. The improved capacitive behavior could be attributed to the decrease in the resistance of the electrodes and increase in the ionic diffusion from the bulk electrolyte solution to the surface of the electrodes due to the incorporation of N-GQDs. Based on these above studies, it is evident that SnO_2 NTs and N-GQDs composites are one of the good futuristic materials for the energy storage and conversion application and in many other interdisciplinary fields.

4. Conclusions

In summary, a simple and cost-effective one-step electrospinning technique followed by thermal annealing was adopted for the fabrication of pristine and N-GQDs incorporated SnO_2 NTs. The structural, morphology, and elemental studies of as-prepared samples were analyzed by different techniques. The combination of tubular microstructures, chemical stability, and electrochemical properties of the S2 (SnO_2/N-GQDs-3 wt.%) composite showed a good performance as an electrode in the supercapacitor device. This work demonstrates a simple and facile synthesis method for the preparation of SnO_2 NTs and their composites that can be efficiently used in the energy storage and conversion applications.

Data Availability

The data used to support the findings of this study are included in the article.

Conflicts of Interest

The authors declare that they have no conflicts of interest.

Acknowledgments

This research was supported by the Basic Science Research Program through the National Research Foundation of Korea (NRF) funded by the Ministry of Education (2018R1A6A1A03023788, 2021R1I1A1A01055790, and 2022R1I1A1A01070368) and the Korea Institute for Advancement of Technology (KIAT) grant funded by the Korean Government (MOTIE) (P00008500, the Competency Development Program for Industry Specialist). This research was also supported by the R&D Program of Ministry of Culture, Sports and Tourism and Korea Creative Content Agency (Development of K-Black Ink containing the Traditional Muk Material and its use in Digital Printing Technology, Project Number: R2020040047).

References

[1] Y. Zhang, S. Yu, G. Lou et al., "Review of macroporous materials as electrochemical supercapacitor electrodes," *Journal of Materials Science*, vol. 52, no. 19, pp. 11201–11228, 2017.

[2] R. Dubey and V. Guruviah, "Review of carbon-based electrode materials for supercapacitor energy storage," *Ionics*, vol. 25, no. 4, pp. 1419–1445, 2019.

[3] S. C. Shin, J. Kim, J. K. R. Modigunta et al., "Bio-mimicking organic-inorganic hybrid ladder-like polysilsesquioxanes as a surface modifier for polyethylene separator in lithium-ion batteries," *Journal of Membrane Science*, vol. 620, p. 118886, 2021.

[4] S. Najib and E. Erdem, "Current progress achieved in novel materials for supercapacitor electrodes: mini review," *Nanoscale Advances*, vol. 1, no. 8, pp. 2817–2827, 2019.

[5] U. Male, J. K. R. Modigunta, and D. S. Huh, "Design and synthesis of polyaniline-grafted reduced graphene oxide via azobenzene pendants for high-performance supercapacitors," *Polymer*, vol. 110, pp. 242–249, 2017.

[6] B. Zhao, D. Chen, X. Xiong et al., "A high-energy, long cycle-life hybrid supercapacitor based on graphene composite electrodes," *Energy Storage Materials*, vol. 7, pp. 32–39, 2017.

[7] C. Portet, P. L. Taberna, P. Simon, E. Flahaut, and C. Laberty-Robert, "High power density electrodes for carbon supercapacitor applications," *Electrochimica Acta*, vol. 50, no. 20, pp. 4174–4181, 2005.

[8] G. Murali, J. Rawal, J. K. R. Modigunta et al., "A review on MXenes: new-generation 2D materials for supercapacitors," *Sustainable Energy & Fuels*, vol. 5, no. 22, pp. 5672–5693, 2021.

[9] S. Jeon, J. H. Jeong, H. Yoo, H. K. Yu, B.-H. Kim, and M. H. Kim, "RuO2 nanorods on electrospun carbon nanofibers for supercapacitors," *ACS Applied Nano Materials*, vol. 3, no. 4, pp. 3847–3858, 2020.

[10] D. Majumdar, T. Maiyalagan, and Z. Jiang, "Recent progress in ruthenium oxide-based composites for supercapacitor applications," *ChemElectroChem*, vol. 6, no. 17, pp. 4343–4372, 2019.

[11] J. Cheng, B. Zhao, W. Zhang et al., "High-performance supercapacitor applications of NiO-nanoparticle-decorated millimeter-long vertically aligned carbon nanotube arrays via an effective supercritical CO2-assisted method," *Advanced Functional Materials*, vol. 25, no. 47, pp. 7381–7391, 2015.

[12] V. Bonu, B. Gupta, S. Chandra, A. Das, S. Dhara, and A. K. Tyagi, "Electrochemical supercapacitor performance of SnO_2 quantum dots," *Electrochimica Acta*, vol. 203, pp. 230–237, 2016.

[13] D. Wu, X. Xie, Y. Zhang et al., "MnO_2/carbon composites for supercapacitor: synthesis and electrochemical performance," *Frontiers in Materials*, vol. 7, no. 2, 2020.

[14] L. Demarconnay, E. Raymundo-Piñero, and F. Béguin, "Adjustment of electrodes potential window in an asymmetric

carbon/MnO2 supercapacitor," *Journal of Power Sources*, vol. 196, no. 1, pp. 580–586, 2011.

[15] S. Xu, L. You, P. Zhang, Y. Zhang, J. Guo, and C. Wang, "Fe_3O_4@coordination polymer microspheres with self-supported polyoxometalates in shells exhibiting high-performance supercapacitive energy storage," *Chemical Communications*, vol. 49, no. 24, pp. 2427–2429, 2013.

[16] C. Xue, Y. Lv, F. Zhang, L. Wu, and D. Zhao, "Copper oxide activation of soft-templated mesoporous carbons and their electrochemical properties for capacitors," *Journal of Materials Chemistry*, vol. 22, no. 4, pp. 1547–1555, 2012.

[17] T. Lu, L. Pan, H. Li et al., "Microwave-assisted synthesis of graphene–ZnO nanocomposite for electrochemical supercapacitors," *Journal of Alloys and Compounds*, vol. 509, no. 18, pp. 5488–5492, 2011.

[18] C.-A. Tseng, P. K. Sahoo, C.-P. Lee, Y.-T. Lin, J.-H. Xu, and Y.-T. Chen, "Synthesis of CoO-decorated graphene hollow nanoballs for high-performance flexible supercapacitors," *ACS Applied Materials & Interfaces*, vol. 12, no. 36, pp. 40426–40432, 2020.

[19] C. E. Shuck, M. Han, K. Maleski et al., "Effect of Ti3AlC2MAX phase on structure and properties of resultant Ti3C2TxM-Xene," *ACS Applied Nano Materials*, vol. 2, no. 6, pp. 3368–3376, 2019.

[20] S. R. Ch, L. Zhang, Y. Qiu, Y. Chen, and S. R. Dugasani, "Investigation of hydrogen sensing properties of graphene/Al- SnO_2 composite nanotubes derived from electrospinning," *Journal of Industrial and Engineering Chemistry*, vol. 63, pp. 411–419, 2018.

[21] J. C. Briones, G. Castillon, M. P. Delmo, and G. N. C. Santos, "Magnetic-field-enhanced morphology of tin oxide nanomaterials for gas sensing applications," *Journal of Nanomaterials*, vol. 2017, Article ID 4396723, 11 pages, 2017.

[22] S. Choudhury, R. Nautiyal, D. K. Thakkar, and C. A. Betty, "Thickness dependence of nanocrystalline tin oxide thin films in capacitive biosensor characterization," *Journal of Electroanalytical Chemistry*, vol. 877, p. 114742, 2020.

[23] A. Gabriunaite, T. S. Valiūnienė, and G. Valincius, "Mixed silane-based self-assembled monolayers deposited on fluorine doped tin oxide as model system for development of biosensors for toxin detection," *Electroanalysis*, vol. 33, no. 5, pp. 1315–1324, 2021.

[24] Z. Guo, A. K. Jena, I. Takei et al., "VOC over 1.4 V for amorphous tin-oxide-based dopant-free $CsPbI_2Br$ perovskite solar cells," *Journal of the American Chemical Society*, vol. 142, no. 21, pp. 9725–9734, 2020.

[25] J. A. Smith, O. S. Game, J. E. Bishop et al., "Rapid scalable processing of tin oxide transport layers for perovskite solar cells," *ACS Applied Energy Materials*, vol. 3, no. 6, pp. 5552–5562, 2020.

[26] M. J. K. Reddy, S. H. Ryu, and A. M. Shanmugharaj, "Synthesis of SnO_2 pillared carbon using long chain alkylamine grafted graphene oxide: an efficient anode material for lithium ion batteries," *Nanoscale*, vol. 8, no. 1, pp. 471–482, 2016.

[27] F. Zoller, D. Böhm, T. Bein, and D. Fattakhova-Rohlfing, "Tin oxide based nanomaterials and their application as anodes in lithium-ion batteries and beyond," *ChemSusChem*, vol. 12, no. 18, pp. 4140–4159, 2019.

[28] J. C. M. Brokken-Zijp, O. L. J. van Asselen, W. E. Kleinjan, R. van de Belt, and G. de With, "Photocatalytic properties of tin oxide and antimony-doped tin oxide nanoparticles," *Journal of Nanotechnology*, vol. 2011, Article ID 106254, 15 pages, 2011.

[29] C. Mevada and M. Mukhopadhyay, "Electrochemical performance of aqueous asymmetric supercapacitor based on synthesized tin oxide positive and commercial titanium dioxide negative electrodes," *Journal of Energy Storage*, vol. 33, p. 102058, 2021.

[30] R. Kumar, R. K. Nekouei, and V. Sahajwalla, "In-situ carbon-coated tin oxide (ISCC-SnO2) for micro-supercapacitor applications," *Carbon Letters*, vol. 30, no. 6, pp. 699–707, 2020.

[31] B. Varshney, M. J. Siddiqui, A. H. Anwer et al., "Synthesis of mesoporous SnO_2/NiO nanocomposite using modified sol-gel method and its electrochemical performance as electrode material for supercapacitors," *Scientific Reports*, vol. 10, no. 1, p. 11032, 2020.

[32] V. Velmurugan, U. Srinivasarao, R. Ramachandran, M. Saranya, and A. N. Grace, "Synthesis of tin oxide/graphene (SnO_2/G) nanocomposite and its electrochemical properties for supercapacitor applications," *Materials Research Bulletin*, vol. 84, pp. 145–151, 2016.

[33] R. B. Rakhi, W. Chen, D. Cha, and H. N. Alshareef, "High performance supercapacitors using metal oxide anchored graphene nanosheet electrodes," *Journal of Materials Chemistry*, vol. 21, no. 40, pp. 16197–16204, 2011.

[34] H. M. Jeong, K. M. Choi, T. Cheng et al., "Rescaling of metal oxide nanocrystals for energy storage having high capacitance and energy density with robust cycle life," *Proceedings of the National Academy of Sciences*, vol. 112, no. 26, pp. 7914–7919, 2015.

[35] X. Lu, C. Wang, F. Favier, and N. Pinna, "Electrospun nanomaterials for supercapacitor electrodes: designed architectures and electrochemical performance," *Advanced Energy Materials*, vol. 7, no. 2, p. 1601301, 2017.

[36] K.-A. Tsai, P.-Y. Hsieh, T.-H. Lai et al., "Nitrogen-doped graphene quantum dots for remarkable solar hydrogen production," *ACS Applied Energy Materials*, vol. 3, no. 6, pp. 5322–5332, 2020.

[37] S. Kang, Y. K. Jeong, J. H. Ryu et al., "Pulsed laser ablation based synthetic route for nitrogen-doped graphene quantum dots using graphite flakes," *Applied Surface Science*, vol. 506, p. 144998, 2020.

[38] G. Murali, M. Reddeppa, C. Seshendra Reddy et al., "Enhancing the charge carrier separation and transport via nitrogen-doped graphene quantum Dot-TiO_2 nanoplate hybrid structure for an efficient NO gas sensor," *ACS Applied Materials & Interfaces*, vol. 12, no. 11, pp. 13428–13436, 2020.

[39] S. Zhang, Y. Li, H. Song et al., "Graphene quantum dots as the electrolyte for solid state supercapacitors," *Scientific Reports*, vol. 6, no. 1, p. 19292, 2016.

[40] C. S. Reddy, G. Murali, A. S. Reddy, S. Park, and I. In, "GO incorporated SnO_2 nanotubes as fast response sensors for ethanol vapor in different atmospheres," *Journal of Alloys and Compounds*, vol. 813, p. 152251, 2020.

[41] L. Tang, R. Ji, X. Li, K. S. Teng, and S. P. Lau, "Energy-level structure of nitrogen-doped graphene quantum dots," *Journal of Materials Chemistry C*, vol. 1, no. 32, pp. 4908–4915, 2013.

[42] S. Raj, P. Kar, and P. Roy, "Ammonia-assisted growth of CoSn(OH)6 nanostructures and their electrochemical performances for supercapacitor," *Journal of Nanoscience and Nanotechnology*, vol. 19, no. 5, pp. 2755–2761, 2019.

[43] R. N. Bulakhe, S. A. Arote, B. Kwon, S. Park, and I. In, "Facile synthesis of nickel cobalt sulfide nano flowers for high performance supercapacitor applications," *Materials Today Chemistry*, vol. 15, p. 100210, 2020.

[44] K.-K. Liu, Q. Jiang, C. Kacica, H. G. Derami, P. Biswas, and S. Singamaneni, "Flexible solid-state supercapacitor based on tin oxide/reduced graphene oxide/bacterial nanocellulose," *RSC Advances*, vol. 8, no. 55, pp. 31296–31302, 2018.

[45] R. Barik, V. Tanwar, R. Kumar, and P. P. Ingole, "A high energy density and high rate capability flexible supercapacitor based on electro-spun highly porous SnO_2@carbon nanofibers," *Journal of Materials Chemistry A*, vol. 8, no. 30, pp. 15110–15121, 2020.

Hindawi
Journal of Nanomaterials
Volume 2022, Article ID 9870753, 1 page
https://doi.org/10.1155/2022/9870753

Corrigendum

Corrigendum to "Nanotechnology-Based Sensitive Biosensors for COVID-19 Prediction Using Fuzzy Logic Control"

Vikas Maheshwari,[1] Md Rashid Mahmood,[1] Sumukham Sravanthi,[2] N. Arivazhagan,[3] A. ParimalaGandhi,[4] K. Srihari,[5] R. Sagayaraj,[6] E. Udayakumar,[4] Yuvaraj Natarajan,[7] Prashant Bachanna,[8] and Venkatesa Prabhu Sundramurthy[9]

[1]*Department of ECE, Guru Nanak Institutions Technical Campus, Ibrahimpatnam, Dist R.R., Hyderabad, Telangana State 501506, India*
[2]*Department of CSE, Kakatiya Institute of Technology and Science, Warangal, India*
[3]*Department of Computational Intelligence, SRM Institute of Science and Technology, SRM Nagar, Kattankulathur 603203, India*
[4]*Department of ECE, KIT-Kalaignarkarunanidhi Institute of Technology, Coimbatore, India*
[5]*CSE, SNSCT, India*
[6]*Department of EEE, Muthayammal Engineering College, Namakkal, India*
[7]*Research and Development, ICT Academy, 600096 Chennai, India*
[8]*Department of ECE, Bharat Institute of Engineering and Technology, Telangana, 501510, Hyderabad, India*
[9]*Department of Chemical Engineering & Center of Excellence for Bioprocess and Biotechnology, College of Biological and Chemical Engineering, Addis Ababa Science and Technology University, P.O. Box 16417, Addis Ababa, Ethiopia*

Correspondence should be addressed to Venkatesa Prabhu Sundramurthy; venkatesa.prabhu@aastu.edu.et

Received 8 June 2022; Accepted 8 June 2022; Published 27 June 2022

Copyright © 2022 Vikas Maheshwari et al. This is an open access article distributed under the Creative Commons Attribution License, which permits unrestricted use, distribution, and reproduction in any medium, provided the original work is properly cited.

In the article titled "Nanotechnology-Based Sensitive Biosensors for COVID-19 Prediction Using Fuzzy Logic Control" [1], there was a spelling error in affiliation nine. The correct affiliation is "Department of Chemical Engineering, Addis Ababa Science and Technology University, Ethiopia," and it is corrected above.

References

[1] V. Maheshwari, M. R. Mahmood, S. Sravanthi et al., "Nanotechnology-Based Sensitive Biosensors for COVID-19 Prediction Using Fuzzy Logic Control," *Journal of Nanomaterials*, vol. 2021, Article ID 3383146, 8 pages, 2021.

Hindawi
Journal of Nanomaterials
Volume 2022, Article ID 8731429, 18 pages
https://doi.org/10.1155/2022/8731429

Review Article

Synthesis of Three-Dimensional Reduced-Graphene Oxide from Graphene Oxide

Rasmeet Singh,[1] **Sajid Ullah**,[2] **Nikita Rao**,[1] **Mandeep Singh**,[3] **Indrajit Patra**,[4] **Daniel Amoako Darko**,[5] **C. Prince Jebedass Issac**,[6] **Keyvan Esmaeilzadeh-Salestani**,[7] **Rahul Kanaoujiya**,[8] **and V. Vijayan**[9]

[1]*Dr. S.S. Bhatnagar University Institute of Chemical Engineering & Technology, Panjab University, Chandigarh 160014, India*
[2]*Department of Water and Environmental Engineering, Nangarhar University, Jalalabad 2600, Afghanistan*
[3]*School of Mechanical and Mechatronic Engineering, University of Technology Sydney, NSW 2007, Australia*
[4]*Independent Researcher, National Institute of Technology Durgapur, Durgapur, West Bengal 713209, India*
[5]*Institute for Environment and Sanitation Studies, College of Basic and Applied Sciences, University of Ghana, Legon, Accra, Ghana*
[6]*Department of Chemistry, Voorhees College, Vellore 632001, Tamil Nadu, India*
[7]*Chair of Crop Science and Plant Biology, Institute of Agricultural and Environmental Sciences, Estonian University of Life Sciences, Friedrich Reinhold Kreutzwaldi 1, 51014 Tartu, Estonia*
[8]*Synthetic Inorganic and Metallo-Organic Research Laboratory, Department of Chemistry, University of Allahabad, Prayagraj 211002, Uttar Pradesh, India*
[9]*Department of Mechanical Engineering, K. Ramakrishnan College of Technology, Samayapuram, Trichy 621112, India*

Correspondence should be addressed to Rasmeet Singh; srasmeet9@gmail.com and Daniel Amoako Darko; dadarko@ug.edu.gh

Received 23 August 2021; Accepted 22 September 2021; Published 3 March 2022

Academic Editor: Lakshmipathy R

Copyright © 2022 Rasmeet Singh et al. This is an open access article distributed under the Creative Commons Attribution License, which permits unrestricted use, distribution, and reproduction in any medium, provided the original work is properly cited.

Carbon materials and their allotropes have been involved significantly in our daily lives. Zero-dimensional (0D) fullerenes, one-dimensional (1D) carbon materials, and two-dimensional (2D) graphene materials have distinctive properties and thus received immense attention from the early 2000s. To meet the growing demand for these materials in applications like energy storage, electrochemical catalysis, and environmental remediation, the special category, i.e., three-dimensional (3D) structures assembled from graphene sheets, has been developed. Graphene oxide is a chemically altered graphene, the desired building block for 3D graphene matter (i.e., 3D graphene macrostructures). A simple synthesis route and pore morphologies make 3D reduced-graphene oxide (rGO) a major candidate for the 3D graphene group. To obtain target-specific 3D rGO, its synthesis mechanism plays an important role. Hence, in this article, we will discuss the general mechanism for 3D rGO synthesis, vital procedures for fabricating advanced 3D rGO, and important aspects controlling the growth of 3D rGO.

1. Introduction

Graphene is a 2D monolayer carbon, one-atom-thick material with superior thermal, mechanical, electronic, and optical properties [1–3]. Graphene along with its derivatives has shown immense applications in low-dimensional physics, energy storage, electronic devices, catalysis, sensors, medical equipment, etc. [4–6]. The excellent properties of graphene are important at nanoscale and must be harnessed for macroscopic applications. To become fully aware of the advanced properties of a single graphene sheet, it is important to integrate 2D graphene materials into 3D architectures [7]. For instance, in electrode materials and energy conversion devices, the 2D graphene sheets undergo restacking and their distinctive properties become less effective, leading to less efficiency than the theoretical values [8]. The way to overcome this drawback is to convert 2D layers into consistent and interconnected 3D frameworks that can be employed without concerning the restacking by retaining the distinctive properties of 2D graphene materials. In order

to fully uncover the prospectus of graphene, both large scale production and conversion of individual graphene sheets into state-of-the-art multifunctional frameworks are required [8, 9].

The key step in manufacturing 3D graphene material (i.e., 3D rGO) and modulating its final structures and characteristics is the reduction of GO [10]. The reduction of GO is a chemical method to eliminate oxygen-containing parts on the GO plane. Majority of researches between the year 2006 and 2010 were focused on synthesizing high-quality graphene sheets from GO [11]. Different strategies have been employed to reduce GO, together with swift thermal reduction in inert atmosphere [12, 13]; chemical reduction through series of reducing agents like hydrazine [14, 15], hydroquinone [16], $NaBH_4$ [17], dimethylhydrazine [18], hot alkaline [19], ascorbic acid [20], etc. [21]; photocatalytic reduction [22]; hydro-/solvothermal technique [23, 24]; laser/flash light irradiation [25–27]; electrochemical reduction [28]; hydrogen-plasma/arc-discharge [29, 30]; microwave treatment [31], and combination of these techniques [32, 33].

A series of experiments have been conducted in the past few decades to study the methods for developing 3D rGO [34–36]. Reduction through thermal, chemical, hydrothermal, electrochemical, and photoinduced paths is a few of the effective techniques for the reduction of 3D GO or GO suspension with concurrent 3D construction. Freeze-casting can be used for tuning the inside structure of GO or rGO gels along the developing ice as the in situ template. The annealing conditions are essential for the structural properties of obtained rGO sheets. The H atoms drive deoxygenation through a series of chemical reactions. The temperatures employed in this kind of process are generally higher than 500°C [29]. With exposure to reducing agents, the chemical reduction of GO proceeds with deoxygenation at low temperatures. However, the reducing agents may sometimes only reduce a certain class of oxygen-containing groups selectively (e.g., hydrazine was selective towards the epoxy groups) [37]. The majority of graphene materials obtained from GO exhibit a substantial number of holes, curvatures, functional groups, and defects on carbon sheets, resulting in a functionalized graphene with a C/O ratio less than 1.5. Moreover, the defective graphene sheets obtained through thermal and chemical reduction display high agglomeration due to the presence of forces of attraction between layers and the reduction in hydrophilicity [13, 14].

Although the past few years have experienced rapid growth of 3D graphene materials and their several new synthesis techniques, still, the clear explanation and classification of 3D architectures have not yet been made. Furthermore, 3D graphene materials fabricated through various methods show distinctive properties and varying levels of performance for different applications. For tuning advanced 3D graphene structures for specific requirements, it is important to infer the relationship between 3D graphene properties and its performance, the mechanism involved in its formation, and key components determining the properties. In the last few years, there have been excellent and enormous review articles dealing with the synthesis of macroscopic 3D graphene [4, 7, 9, 38–41]. The reviews generally focus on 3D graphene-based materials concerning the specific applications [42–46]. An overview of the 3D graphene family is still missing. Hence in this paper, we will discuss recently developed engineering strategies for synthesizing 3D graphene. Considering that a lot of work has been previously published in the field, we will present a detailed collection of advanced fabrication processes for 3D graphene. The primary focus is on the design considerations, formation principles, and engineering of 3D graphene-based architectures.

2. Synthesis of 3D rGO

2.1. Photoinduced Reduction. Photoreduction is a chemical-free process for the reduction of GO with little physical contact, high efficiency, and high processing speed. In early 2008, photon energy was employed for reduction of GO in solutions with the involvement of semiconductor photocatalysts (like TiO_2) under the irradiation of ultraviolet light [22]. This technique came out to be successful for developing the graphene/semiconductor composite. Further, it was established that GO reduction in a solution or over a substrate can be done directly under ultraviolet light with the side formation of CO, O_2, H_2O, and CO_2 [47]. Meanwhile, xenon lamp-equipped photographic camera lights and laser lights were found to be capable of deoxygenating GO photos thermally. In such early reports, photoreduction of GO in dilute solutions only formed rGO suspension and not the desirable 3D rGO [47, 48], whereas with photoreduction of the GO film, a pore-rich 3D rGO was obtained. This also showed high conductivity and an expanded interlayer spacing [25–27].

Reduction of GO via photoenergy follows two types of mechanisms, i.e., photothermal effect and photochemical reduction. By principal, the GO reduction with irradiation of ultraviolet light with wavelength less than 390 nm is referred to as photochemical reduction [47]. For wavelengths longer than 390 nm, the reduction of GO follows the photothermal effect. Because the photothermal effect involves high temperatures of 200-230°C, the reduction of GO becomes effective. In case of laser lights, it creates an intensive heat zone by focusing the laser beam on the specific point. A large number of photons get absorbed upon strong irradiation by a pulsed laser and get converted to heat, leading to the rise of temperature on the sheet [49, 50]. However, photochemical processes can also occur via laser at long wavelengths (i.e., 1064 nm) because of strong electron photon coupling and multiple photon absorption [51]. In both the mechanism paths, strong excitation of the GO surface renders the quick ejection of particles and leads to formation of plasma plumes. When energy transfers from plume to lattice, the oxygen group leaves GO with plume expansion. Thereafter, with formation of CO and CO_2 and evaporation of internal water an interlayer pressure is produced which leads to the expansion of the rGO layer to form a porous structure [27, 52, 53].

The photon-induced reduction is another method applicable on chemically reduced GO films. The energy of

photons decomposes the residual chemical substances present in partially reduced GO. Among several sources of photon energy, laser lights are widely used due to their consistency, strong intensity, tunable power, and flexible pattering [52, 54, 55]. Laser scribing can easily achieve synchronous reduction with a GO film pattern [56, 57]. The reduction degree of the GO film can be administered by varying the laser-processing variables (i.e., intensity, shifting pitch, scanning pitch) [58, 59]. The 3D graphene patterns resulting from laser scribing have recently shown a great potential in biomedical applications like tissue engineering and cell culture [58]. Kaner and his research group [56, 57] fabricated 3D porous graphene sheets via laser-induced reduction of GO films. The process utilized a commercially available LightScribe DVD optical drive. Figure 1(a) shows the illustration for the whole process followed. Reduction with LightScribe gave 3D exfoliated sheets of 1520 m^2/g specific surface area and 1738 S/m electrical conductivity.

Atmosphere is an important factor for laser-induced GO reduction to control the degree of reduction of the resulting rGO film. The degree of reduction can be highly improved in an oxygen-free environment [60]. If the GO precursor is immersed in liquid nitrogen for laser reduction, the thermal expansion will be suppressed, resulting in a 3D rGO film with fewer defects and high conductivity compared to the film obtained in nitrogen [51]. Apart from the reduction of dense GO films/foams, laser intensity can also be directly employed for assembling 3G rGO in crystalline GO suspension. As shown in Figure 1(b), when the nematic lyotropic liquid crystal GO sheet is used as the precursor to be dispersed and ordered, by adjusting the focus and intensity of the laser, the arbitrary homogeneous 3D structures of the inside surface can be noticed [54]. Complex 3D assemblies like trefoil knots can be produced through voxel-by-voxel micropatterning of laser beams in both simple plane and across the thickness of the sample. This arrangement is different from laser-induced reduction of H_2O-reduced GO films and is favorable for error-free 3D localization in electronics and photonics.

2.2. Chemical Reduction. Reduction of GO through chemical routes is another major facile approach. In early research, hydrazine was used to obtain rGO dispersions to reduce dilute GO suspensions [11, 14, 61]. At a later stage, 3D graphene hydrogels/aerogels were synthesized with higher GO concentrated colloidal solution under mild reducing agents [35, 62, 63]. The reducing temperature is kept between 60 and 100°C. The residue (i.e., reagent) and absorbed water are then removed by washing and lyophilization. A variety of reducing agents have been used to simultaneously reduce and construct 3D GO. These may include Na_2S, HI [64], H_3PO_4/I_2 [65], gelatin, and sodium ascorbate [66]. Shi and coworkers [64, 67] employed sodium ascorbate for the reduction of GO to develop a 3D graphene framework. Chen and Yan [64] and Zhang and Shi [68] used $NaHSO_3$, Na_2S, Vit. C, HI, and hydroquinone for reducing GO into 3D rGO. Both these researches claimed that the π-π interlinkage among sheets may be a governing factor in deriving self-assembly of chemically reduced GO. This observation came in a similar manner to the hydrothermal approaches. Few research groups also claimed that function groups attached with reducing agents can be determined in 3D rGO sheet construction [69–71]. As the covalent bonds form between GO sheets and reducing agents, a few of the oxygen-containing hydroxyl and epoxy groups are substituted and the GO sheet is cross-linked [66, 72, 73]. To stimulate the cross-linking, carboxylic groups of reducing agents (i.e., oxalic acid and mercaptoacetic acid) can speed up the development of interlayer hydrogen bonds [74, 75]. As stated by Liu et al. [66], gelatin amino groups induce the electrostatic attractions, ring opening reaction, and multiple hydrogen bonds of epoxy groups to collectively enhance the 3D development of rGO.

The evolution of CO and CO_2 is usual in GO's chemical reduction. Evolution of favorable amounts of these gases helps in restacking of GO and rGO sheets and modulates the pore structure of 3D compounds. Furthermore, along with interactions among GO and reducing agents, water bubbles can additionally be introduced through a monitored heating temperature [76]. The total number of bubbles is important throughout the process. Less number of bubbles fails to suppress the restacking, while excess numbers can affect the self-assembly of rGO sheets. When GO/$NaHCO_3$ suspension is heated at 100°C in an open beaker, the number of bubbles accredited to the boiling of water is generated. On using concentrated reducing agents (i.e., hydrazine and $NaBH_4$), microscopic voided irregular gels and rGO particles were seen because of substantial generation of gases [64, 77]. Hence, hydrazine is more favorable in reduction of GO into 3D structure.

Active metals like Al, Cu, Al, Fe, and Co can also be used as reducing agents for simultaneous reduction and formation of GO sheet 3D assembly on their surface. On the basis of redox reactions among metals and GO, the process of reduction, as well as assembly of GO, happens instantly at room temperature. However, the temperature can be raised to 60°C to speed up the process. Surprisingly, if a conductive substance is placed on the active metal substrate, no reduction in the development of 3D rGO assembly is seen (Figure 2) [78]. This favors the development of unique graphene structures like microtubes and micropatterns. Through slight tuning of the shape of metal deposited, these further can be fabricated into binder-free high performance rechargeable Li-ion batteries. In addition, flexible rGO 3D thin film devices can also be prepared by depositing active thin layers of metal substances on flexible substrates.

In addition, the vapors obtained from reducing agents can also be effectively employed in the reduction of both dried GO films and the sponges with side-by-side alterations in 3D structures. When a dense GO film is used as a precursor, its 3D configuration can be significantly altered during vapor-based reduction. Niu et al. [79] performed the reduction of filtrated GO film by positioning it on the top of a hydrazine monohydrate solution at 90°C for 10 hours (Figure 3). By controlling the concentration of the hydrazine monohydrate solution, the open pore structure can be tuned.

In spite of successful development of chemical reduction of GO, the changes involved in GO during the

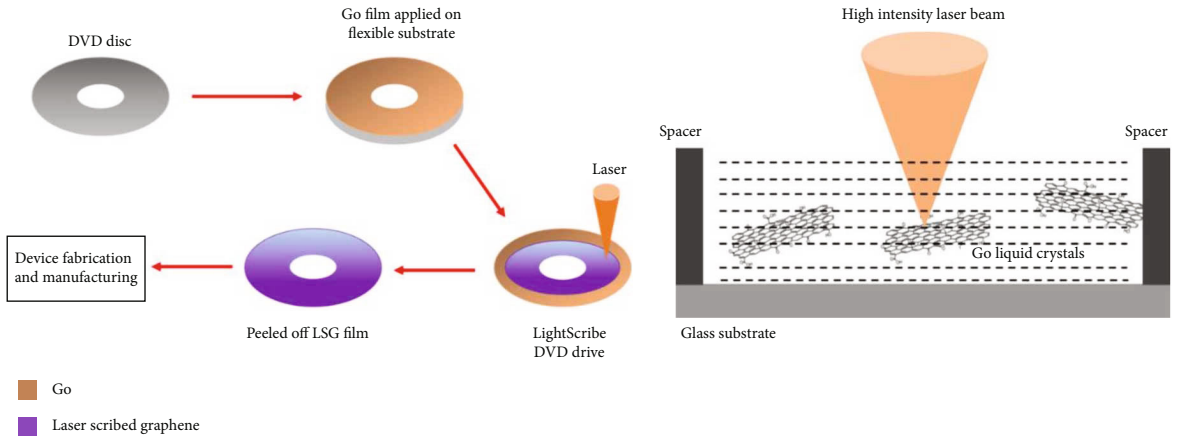

Figure 1: (a) A staggered representation of the laser-induced reduction of GO films. Adapted from [56], copyright 2012, American Association for the Advancement of Science. (b) Representation of ordered lyotropic nematic liquid crystal dispersion with GO leaf as precursor [54].

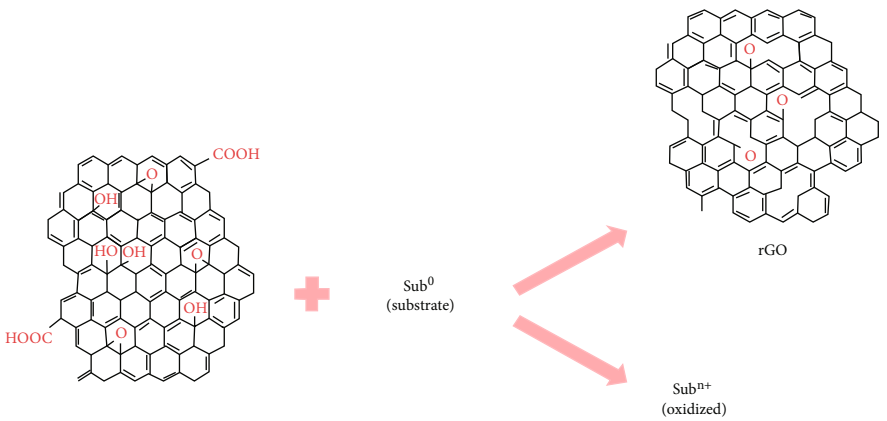

Figure 2: Diagram for substrate-assisted GO reduction and assembly. The active metal substrate (Sub^0) undergoes electron loss and gets oxidized to (Sub^{n+}) ions [78].

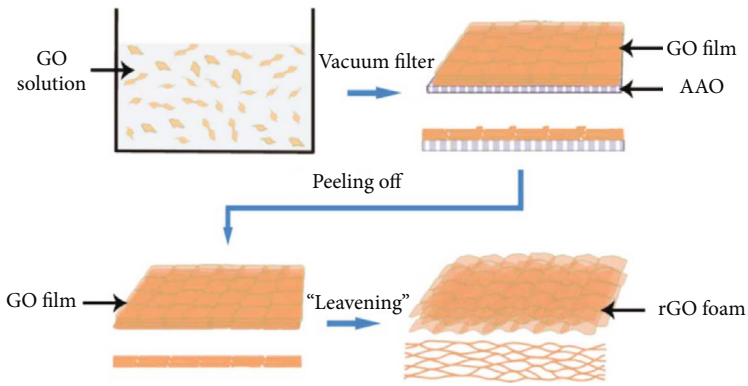

Figure 3: The figure illustrates the fermentation process to prepare rGO foam. Reprinted with permission from [79], copyright 2012, Wiley-VCH Verlag GmbH and Co. KGaA, Weinheim.

reduction process are still not fully understood. Hence, an effective method to minimize the amount of noncarbon impurities is required.

2.3. Electrochemical Reduction. This type of GO reduction is a popular method to directly synthesize electrodes with 3D graphene for electrochemical devices and electrochemical

modifications (Figure 4) [62, 80–82]. The dispersed GO electrochemically reduces to precipitate on the cathode. Instead of packing in a face-to-face manner, the layers reinforce each other up, making a 3D graphene network rigidly stacked to the electrode [62, 81, 83]. This is also referred to as the direct growth of rGO sheets from the electrode surface. Producing a 3D graphene scaffold instead of a solid graphite layer means that a rapid reduction and acceleration process between the initial hydrophobic rGO layer and the GO hydrophobic layer is formed at a later stage. Along with this, hydrogen evolution happens under bias voltage, developing high porosity inside the deposited sheets [84].

Sheng and coworkers were the first ones to fabricate a graphene web on silver foil under -1.2 V and 3 mg/mL GO suspension with 0.1 M $LiCLO_4$. This prototype showed outstanding performance in an electric layer double capacitor having a capacitance of 283 mF/cm^2 [62].

In electrochemically prepared 3D rGO materials, the electrodes are considered the most important components for 3D frameworks. Different materials like stainless steel mesh [82], Pt foil, Ni foam [81], and Au fiber [83] can be utilized as electrode bases. When graphene paper was employed as an electrode base, the highly porous rGO-layered structure was tightly attached to the substrate. This led to an all carbon electrode with excellent applications in flexible devices. On using Ni foam as the electrode substrate, the inner voids were filled with rGO, creating an orderly porous structure having pore sizes in 100s of micrometers or submicrometers in the case of rGO sheets. The 3D rGO structures with varying hierarchical 3D frameworks can be prepared through preobtained 3D rGO materials as electrode bases.

The electrochemical method can also be employed to reduce electrode-precasted GO films [84, 86]. By doing so, the stacking of the GO sheet will be better controlled during the casting step and will ensure that the electrochemical process is effectively slowed down.

2.4. Thermal Expansion of GO Bulk. Thermal reduction or annealing at temperatures between 800 and 1000°C is the most standard, simple, and effective pathway to remove oxygen functional groups from GO. In the case of 3D graphene, annealing at high temperatures may result in thermal exfoliation, which further results in an expansion of dried and preshaped GO bulk precursors. GO precursors by thermal exfoliation include granular GO [87], irregularly aligned GO film [88], tape casting [10], and bulk GO materials [89].

In the process of thermal growth of bulk GO, the groups having oxygen (carboxyl, hydroxyl, carbonyl, and ether) are completely or partially eliminated or are transformed into stable bonds (i.e., anhydrides, quinone, and lactones) with the traces of CO_2, CO, and H_2O [90, 91]. The clear-up amount of the graphene surface rises with increasing annealing temperature. At 1000°C, traces of C–O, OH, and C=O are used to remove thermally unstable oxygen. Therefore, the conductivity of the GO sheet is greatly improved. In the meantime, the GO mass is transformed into the honeycomb 3D nanostructures with microscopic sheets and abundant pores. After undergoing this type of expansion, the distinct surface area could be further enhanced. Based on the precursor used and the reaction that followed, the surface area of 3D rGO frameworks could be maintained between 400 and 800 m^2/g [90, 91].

Thermal annealing is also employed for the reduction of 3D partially reduced GO and 3D GO architecture due to dry treatment and strong reduction. In such cases, the tuning of 3D structures becomes secondary. However, subjecting GO precursors instantly to high temperature regions by avoiding the ramping procedure with violet gas evolution might result in richer in-wall pores, resulting in high surface area. In certain situations, a thermal shock of 400°C can help crumpled graphene spheres to obtain a surface area of approximately 567 m^2/g, and heating the sample at the same temperature ensures a lower surface area of 344 m^2/g [92].

2.5. Solvothermal and Hydrothermal Reduction. This reduction process was first developed to reduce GO into rGO sheets [23, 24]. As shown in Figure 5, Xu et al. [93] used a concentrated GO suspension to see reduction as well as self-assembly of GO in macroscopic 3D rGO hydrogels. Since then, these methods (i.e., hydrothermal and solvothermal) became well-liked methods for 3D graphene monolith production from GO sheets [34, 80, 94–96]. The reaction temperature is generally between 100 and 250°C in autoclave. Thermally induced supercritical water acts as a reducing agent in hydrothermal processes [97].

At the beginning of the hydrothermal process, the reduction in surface changes is noticed due to less carboxylic groups, attracting them to those with charges [98]. On extending the time of reaction, majority of carboxylic groups are removed and the hydrophobicity, π-π stacking interactions, and electrostatic attractions are enhanced, making the rGO sheet assembly tightly interconnected as a 3D framework (Figure 6) [93]. As the oxygen-based groups decrease, CO_2 becomes a predominant product along with traces of CO and fragments of organic acids [99, 100].

Although GO sheets are not completely removed after water heat treatment, as a result, both hydrogen bonds and π-π interactions among oxygen-functional groups add to the cross-linking of 3D sheets in monoliths [101]. Also, the size, concentration, and surface of GO sheets in the first GO suspension could be significant in enhancing the density and structure of final 3D rGO gels.

Replacing H_2O with another organic solvent by solvent thermal reduction of GO lowers the temperature and hardly induces the self-assembly properties of the GO sheet [102, 103]. When compared to the hydrothermal technique, the high self-generated pressure and low surface energy of the solvent in solvothermal processes could result in high efficiency fabrication and reduction of GO sheets [103, 104]. Hence, the 3D rGO materials resulting from solvothermal reduction display higher conductivities with lower surface areas and thick walls. Solvothermal reduction employing ethanol as a solvent results in the development of 3D rGO aerogel. An important observation noted was that the super-elasticity and Poisson's ratio of this material became almost zero, which can never be achieved with water as a solvent at the same reaction conditions [105]. However, the

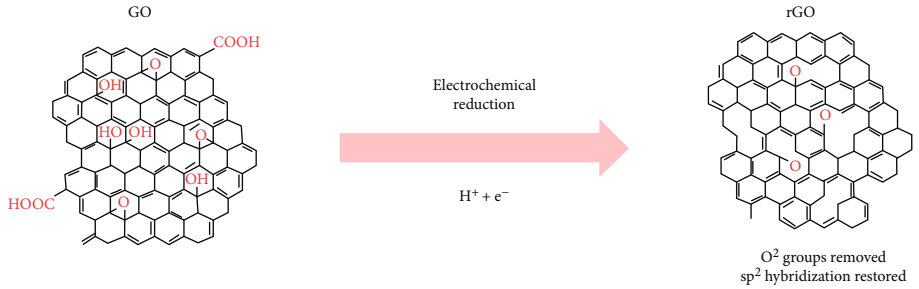

Figure 4: Idea behind the electrochemical reduction of GO into rGO [85].

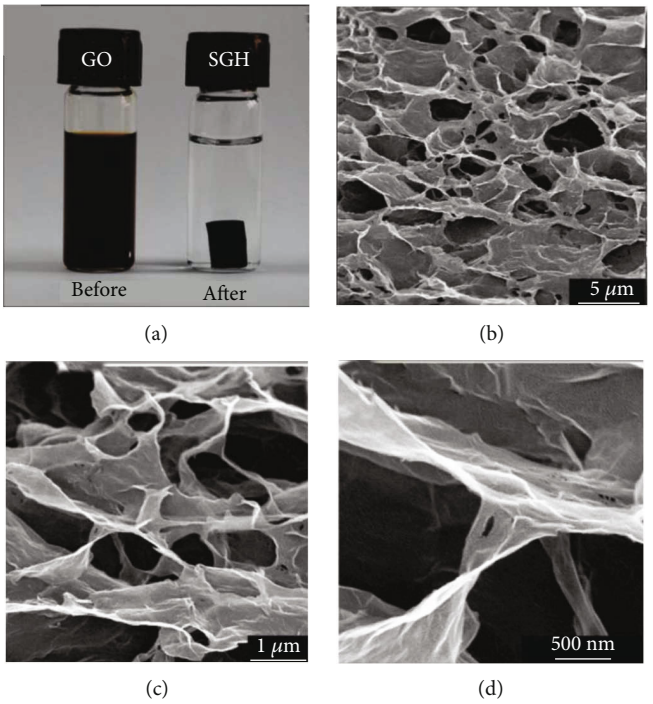

Figure 5: (a) A homogeneous aqueous dispersion of 2 mg/mL GO before and after hydrothermal reduction at a temperature of 180°C for 12 h. (b–d) SEM images at different magnifications of the microstructure inside self-organized graphene hydrogels. Reproduced from [93], copyright 2010, American Chemical Society.

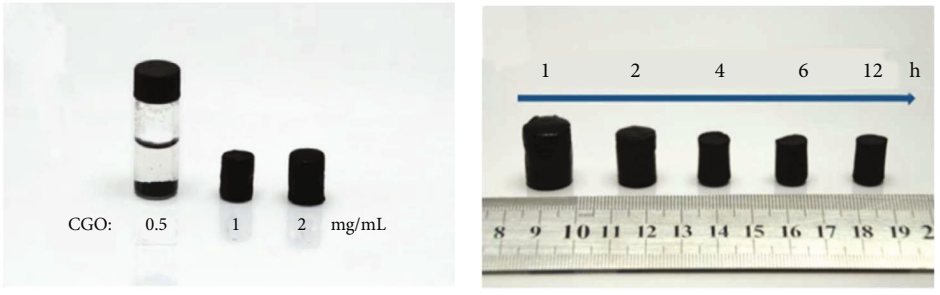

Figure 6: (a) A product manufactured by hot water reducing a GO dispersion at 180°C for 12 hours at different C_{GO}s. (b) Photographs of products manufactured by hydrothermal reduction of 2 mg/mL GO at 180°C varying time limits. Reproduced from [93], copyright 2010, American Chemical Society.

interaction mechanism between GO sheets and solvents in the solvothermal process still remains to be explored.

The drying path of hydrothermally and solvothermally reducing GO is an important factor in deciding the final 3D structure. If processed under general thermal conditions, the 3D rGO hydrogel will bear the acute volume shrinkage and structural cracking. This happens mainly because of large capillary pressure from solvent evaporation and the structural thickness. The capillary pressure is controlled by either freeze-drying or supercritical CO_2 drying. Here, H_2O is replaced by ice or supercritical CO_2 liquid. This is all because they do not react well with graphene walls [77]. The capillary pressure of solvent evaporation is correlated with solvent surface tension, angle of contact, and pore radius in accordance with the Laplace formula. Various schemes can be implemented to achieve ambient drying while maintaining the 3D structure. Meanwhile, the stiffness of the materials depending on wall thickness and the inter-sheet linkage firmness can be improved by resisting the capillary pressure [106].

Further, the hydrothermal and solvothermal processes are efficient in reducing and activating GO with performed 3D structures [107]. In such cases, the 3D structures will be minutely affected by reduction, which normally are determined during the preshaping process. However, the degree of reduction of final 3D rGO materials is slightly low due to the low temperature of hydrothermal and solvothermal reactions. To further eliminate the functional groups, annealing or chemical reduction can be used as a posttreatment reaction. This will also help to restore the π-conjugation and improve the electrical conductivity [105, 107].

The hydrothermal and solvothermal processes can also be used to produce 3D graphene-based composites. This may include 3D graphene doped with nanoparticles like Fe_3O_4 and Co_3O_4 on a composite layer [108]. Compared with the hydrothermal pathway, under the influence of the solvent, the nanoparticles are more uniformly wrapped by the solvothermal pathway in situ by binding with ethanol, resulting in more intimate contact with 3D rGO.

2.6. Freeze-Casting Process (Pre- or Post-reduction). Freeze-casting is a widely used, readily accessible solution phase method for casting GO and partially rGO suspensions or gel forms. It depends on the ice crystallization point. During the procedure, phase separation leads to the repulsion of GO/partially reduced GO sheets from developing ice crystals and gets accumulated in a continuous 3D manner at the interspaces between developed ice [109–111]. The concentration of GO/partially rGO sheets must outgrow the percolation threshold in order to build an interconnected structure. After obtaining a porous GO monolith through freeze-casting, further reduction is required to get a 3D rGO framework. The reduction operation is important to adjust the surface properties of the sheet. However, since the porous composition of 3D rGO is stationed in the freeze-casting process, this may slightly affect the microscopic morphology.

In suspensions, the chemical properties of GO sheets play another major role in the freeze-casting process. Direct freezing yields GO randomly oriented brittle monoliths [112, 113], while a super-elastic honeycomb-like cellular orientation results when freeze-drying is done either for GO-filtered gel or specific partially reduced GO dispersion [106, 109]. This difference among monoliths of GO and partially reduced GO occurs due to improved π-π attractions of partially reduced GO sheets [106]. Additionally, as shown in equation (1), as per the lowest energy principle, for GO or partially reduced GO particles hindered due to the growth of ice, the free energy of interface related with GO/partially reduced GO (σ_i) has to be greater than the sum of both water-GO/partially reduced GO (σ_w) and ice-water interface (σ_{iw}).

$$\Delta\sigma = \sigma_i - (\sigma_w + \sigma_{iw}) > 0. \quad (1)$$

After partial reduction, micro-3D partially reduced GO architects were seen in place of lamellar 2D GO sheets. Thus, a strong deriving force ($\Delta\sigma$) to accumulate building blocks at ice solidification form was produced in the arrangement with partially reduced GO (Figure 7). This further helped in the super-elastic structure of the partially reduced GO monolith [109]. Also, the hydrophobic properties of the partially rGO sheet can be adsorbed on the surface of the ice by the abundant oxygen-containing groups and dominate the growth of ice crystals [114, 115]. As the water solidification in partially reduced GO suspensions gets completed, the 3D crystals are positioned and will interchange a little in thawing and future reductions. The 3D rGO prepared this way is able to maintain its structural integrity with a load, i.e., 450,000 times its own weight with instant recovery from 480% compression [106].

Also, the freezing point is essential to tune the 3D structure of freeze-casting rGO. It directly gets involved with the manipulation of the growth behavior of ice crystals. At high temperatures, the growth of crystals gets more favorable and leads to the production of large lamellar ice crystals. However, at lower temperatures, nucleation of ice dominates and spreads ice crystal nuclei throughout the material. Hence, the wall thickness, total size, and pore structure can be highly influenced by monitoring the freezing temperature [116, 117].

In addition, through monitoring the temperature distribution in the freezing system, Bai's research group successfully developed a bidirectional freezing technology and tried it on synthesizing 3D rGO with a biomimetic lamellar structure [118, 119]. Recently, Wang and coworkers adopted this unique bidirectional temperature control method to achieve a fan-shaped arrangement of GO [115]. The vessel used a copper rod with a cylindrical hole. Because the bottom of the cylinder was immersed in liquid nitrogen, the top was cold so the inside GO suspension had a two-way temperature gradient (i.e., "bottom to top" and "outside to inside") (Figure 8). The distinctive temperature gradients enabled the crystallization in a different manner than a conventional freezing process. To get the desired GO aerogel (i.e., radially aligned channels), a small quantity of ethanol was further added. After reduction by hydrazine vapor and drying in a complete vacuum, the prepared rGO aerogel

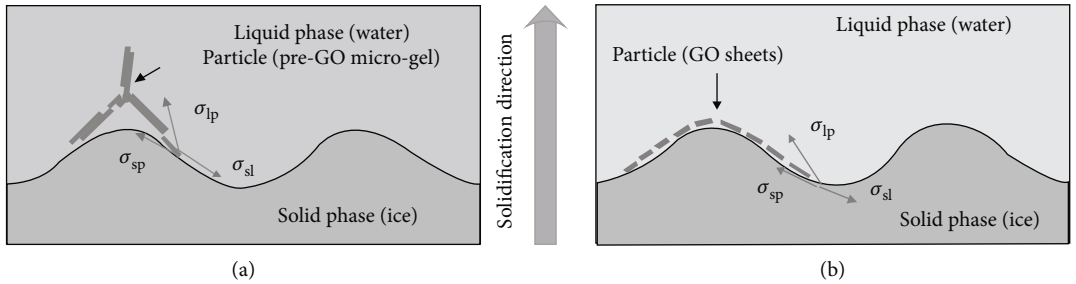

Figure 7: Diagram of the interfacial free energy between the solidification surface of the solvent and the particles present in the suspension. (a) Prereduced GO microgel system. (b) GO sheet system. Reproduced with permission from [109], copyright 2016, Wiley-VCH Verlag GmbH and Co. KGaA, Weinheim.

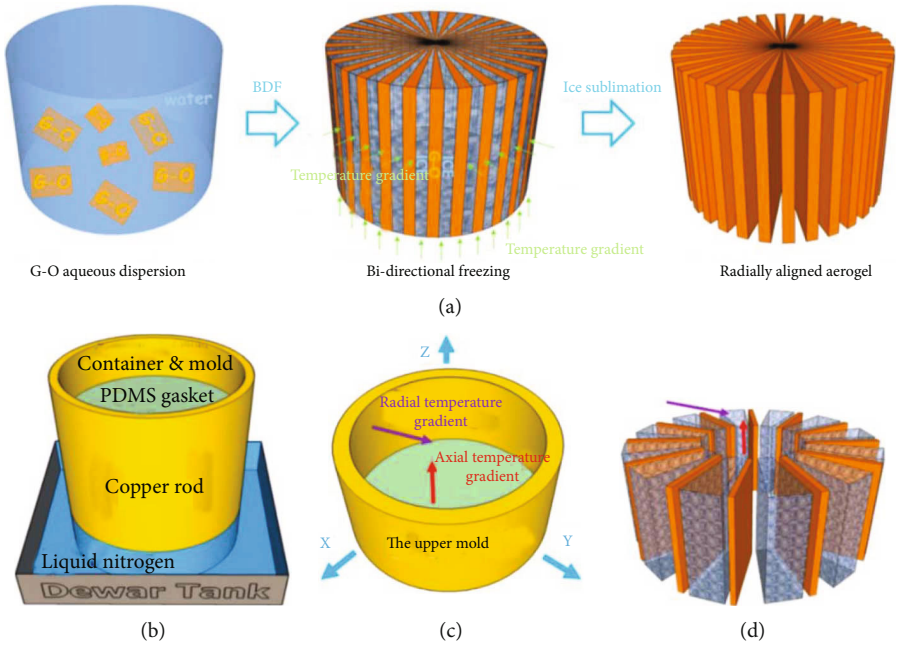

Figure 8: (a) Manufacturing process planning. (b) A refrigeration unit to create a radial structure with a Cu rod with a hollow top. (c) Two temperature gradients caused by the Cu type present upside. (d) Model of ice crystals developing along the radial direction under the influence of two temperature gradients. Orange sheets represent dispersed GO sheets. Reproduced from [115], copyright 2018, American Chemical Society.

displayed high porosity and specific pore orientation and was highly ordered. After 1000 compression cycles with 50% strain, only 8% of the total structural permanent deformation was noted. To further promote the surface activation, KOH solution was used to combine ultralightness and excellent mechanical strength. This substance may selectively adsorb organic pollutants present in water.

Additionally, other solvents can also be employed for the freeze-casting process. These may include organic solvents with high vapor pressure and melting point slightly higher than the room temperature (for example room-temperature freeze gelation) [120]. In comparison to freeze-drying using water, the room-temperature freeze gelation highly reduces the energy consumption. However, the cost of organic solvents could be an issue for this to develop.

2.7. 3D Printing before Reduction. Compared to other strategies, 3D printing prepares a 3D rGO architecture with more complex shapes. Extrusion-based 3D printing is the preferred printing strategy for 3D rGO synthesis [121, 122]. A newly developed technology, optical 3D printing, controls structures more precisely down to the micrometer scale [123].

2.7.1. Extrusion-based 3D Printing. This technique has recently become popular in the on-demand engineering of graphene and composite 3D macrostructures. 3D printing can also be called robot-assisted deposition, robocasting, direct ink writing, and continuous extrusion [124]. Wet-spinning technology can be used for printing of 500 nm graphene nanowires [125], but this is more often used to get

compounded 3D structures through filaments extruded from nozzles, which merge together via a "layer-by-layer method" [126]. Procuring a GO suspension with specific rheology is very important to use 3D printing to its fullest. The extruded filaments are expected to behave as a shear-thinning fluid with viscoelastic characteristics that adhere with neighboring layers while maintaining the shape after printing and pressing upon by printed filaments [122].

Fragment size and GO concentration play important roles in the elastic properties of GO inks. The elastic property (y) for a concentrated GO suspension is denoted by [127, 128]

$$y = k\left(\frac{\Phi \times D_{\text{sheet}} \times S_{\text{sa}} \times \rho}{3} - 1\right)^{x}, \quad (2)$$

where k is the constant, x is the scaling factor, Φ is the GO concentration, ρ is the density of the solvent, D_{sheet} is the lateral size of the GO sheet, and S_{sa} is the specific surface area of the GO sheet.

Zhu and team stated that the GO suspension with 150-400 nm lateral size behaves as a non-Newtonian fluid at a 20 mg/mL concentration [121]. Increase in concentration further improves the GO viscosity and enhances its printability. At similar concentration, the 5-50 μm flake size GO shows high viscosity and forms a robust 3D structure [129, 130].

In order to further improve the printability of GO suspensions, modified GO suspensions together with additives are widely used as printing inks [122, 131]. García-Tuñon et al. [122] developed a pH-sensitive polymer functionalized with GO suspension to apply in 3D printing for the preparation of the 3D rGO monolith. Therefore, the suspension can be adjusted by adjusting the pH for accurate 3D printing. Optimized suspension produces a branched polymer/GO surfactant network formed by noncovalent interactions. This network possesses shear-thinning behavior and predominates with solid-like characteristics up to 1% of strain, enabling easy flow of gels in nozzles of diameter of 100 μm. Since silica powder can transmit additional shear-thinning behavior and shear-yield stress, Zhu and coworkers further used hydrophobic fumed silica powder as fillers to improve the viscosity of GO ink [121, 131]. In addition, the team also introduced basic compounds, such as $(NH_4)_2CO_3$ and RF catalyst compounds, to effectively regulate the cross-linking of GO sheets by adjusting the surface charge and covalent bond formation.

These polymers and solid additives can interfere with the mechanical properties and conductivity of printed rGO structures. Furthermore, treatments to recover the solid add-ons are rather tedious. Hence, greener ionic additives (i.e., Ca^{2+}, Mg^{2+}, Fe^{3+}, etc.) are investigated to see the rheological behavior of the GO ink. A minute amount of Ca^{2+} ions enhanced the viscosity and viscoelasticity of GO dispersion [132]. With increasing Ca^{2+} concentration, the yield modulus and storage of GO also increases. GO sheets with mild ammonium-induced cross-linking can be obtained by adding urea into the GO suspension [133]. These mixtures are easily pushed and converted into tough filaments that exhibit high viscosity and shear behavior.

Apart from adding additives, a special type of solvents can also be employed to obtain printable GO ink. These solvents are liquid and solid at moderately high temperatures (i.e., 50-120°C) and room temperature, respectively [120]. Hence, just mild temperature monitoring is required for tuning the rheology of the suspension to get the required 3D printing. Finally, the solvent is evaporated in a vacuum (even at room temperature), leaving a pure GO framework.

The filaments in extrusion-based 3D printing nozzles are typically extruded in air [122, 130] or liquid [121]. In liquid baths, organic solvents are preferred due to their lesser density than water and immiscibility with aqueous ink [131]. Zhang et al. [134] used an ice bath at -25°C for the ink. The low temperature quickly solidifies the ejected GO suspension, so that a lower concentration of 110 mg/mL of GO precursor can be applied. This process achieves a fine 3D structure due to melting and fusion operations with few voids.

2.7.2. Optical 3D Printing of rGO. The combination of photoexcited polymerization with layer-by-layer 3D printing can be used to synthesize complex macro-3D architectures of rGO [123]. As shown in Figure 9, firstly, a 1 wt.% dilute GO dispersion was mixed with 12 wt.% photocurable acrylates and 2-4 wt.% photoinitiator to get a specific type of photocurable resin. This resin is able to solidify instantly under light-initiated polymerization. A thin layer of resin forms on it when a substrate is placed on it. Then, the top resin layer is cross-linked and solidified by patterned light irradiation. A further top layer of suspension was seen for further patterning and reduction targets. A light of 405 nm wavelength was rearranged with a spatial light-modulator where the targeted 2D image patterns were sliced and 3D structures were the input. Hence, such a process could lead to arbitrary complex 3D structures with controlled size at the micron scale. The resolution of the signal wire is maintained at approximately 10 μm with a guide hole size of 60 nm [123].

2.8. Wet-Spinning before Reduction. The wet-spinning of GO before undergoing chemical, hydrothermal, and thermal reduction is a popular method for developing 3D rGO structures like 3D rGO fabrics, films, cylinders, spheres, and fibers [86, 135–137]. Xu and Gao were the first ones to synthesize continuous graphene fibers independent of any support surfactant or polymer through a wet-spinning GO chiral liquid crystal technique in a coagulation bath containing 5 wt.% $NaOH/CH_3OH$ solution. Further, a chemical reduction method using 40% HI solution was followed. GO's liquid crystal follows the twisted boundary phase as the model. The obtained graphene fibers exhibited 7.7 GPa Young's modulus, 140 MPa fracture strength, an approximate 5.8% fracture elongation, and 25,000 S/m of high conductivity [138].

In the spinning process, the GO suspension concentration is an important factor for the development of continuous fibers. The lamellar structured liquid crystals of GO

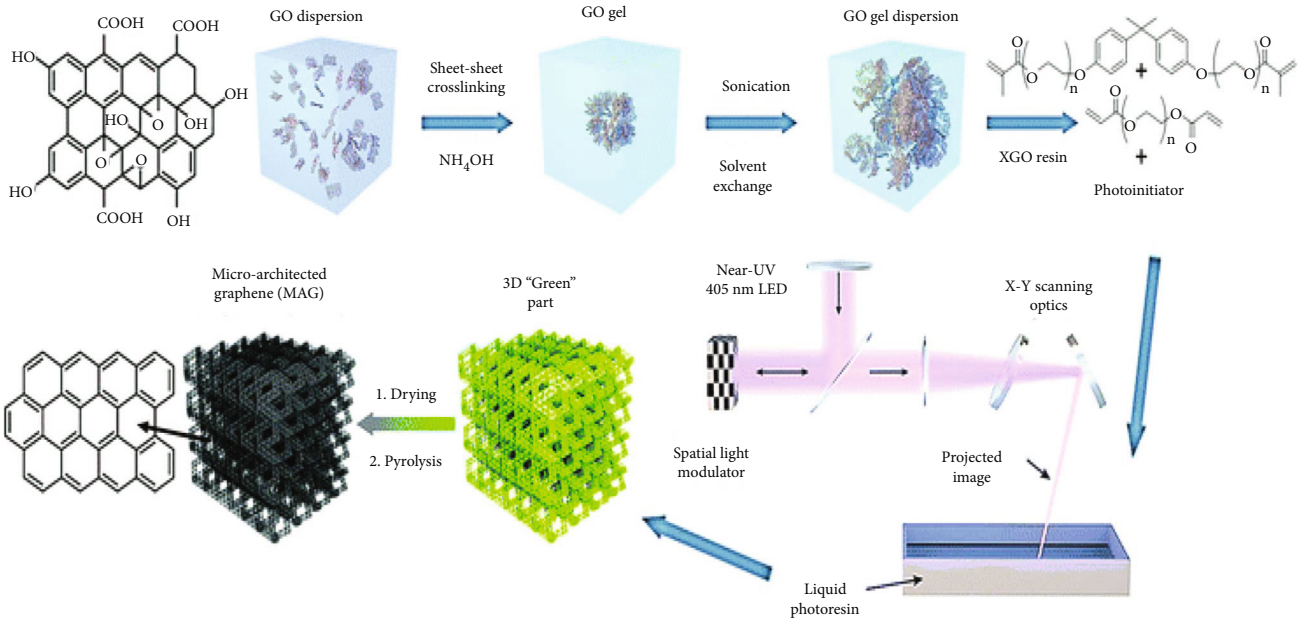

Figure 9: Optical 3D printing process flowchart. Reproduced with permission from [123], copyright 2018, Royal Society of Chemistry.

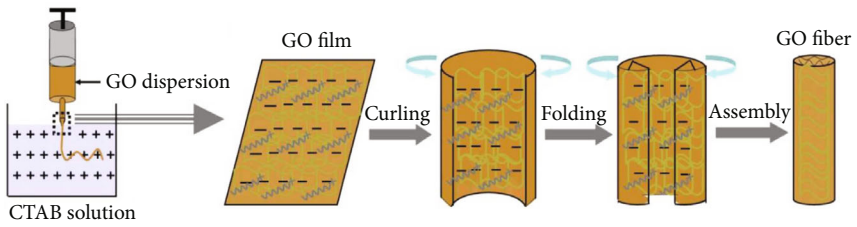

Figure 10: (a) Typical apparatus representation for wet-spinning GO fibers. (b) Illustration of the assembly mechanism of the GO fiber. Reproduced with permission from [136], copyright 2012, Springer Nature.

enables the dispersion at high concentration, leading to strong interactions among GO sheets, thus stimulating the alignment and coagulation of formed sheets. Otherwise, brittle fibers and collapsed belts can result from low concentrations of GO. The spun liquids are targeted in the coagulation bath, where they exert influence on external and internal formations of spun GO fibers. Figure 10 proposes the mechanism for the formation of graphene fibers. A multilayer GO film is first produced through the repulsions among negatively charged GO sheets. Further, as the charge neutralizes between adsorbed low-concentration hexadecyltrimethylammonium bromide solution and the GO sheets, the film turns into a bent and folded form. Continuous curling and folding eventually result in highly aligned fine particles. Spinning liquid GO crystals in liquid nitrogen and additional freeze-drying produces single-core dense-shell graphene fibers [135]. The internal arrangement of the GO/rGO sheet is uniform, and the porous fiber exhibits a high specific surface area of about 884 m^2/g, a tensile strength close to 188 kNm/kg, and a high electrical conductivity of 300 kNm/m of 4900 S/m.

From the perspective of wet-spinning instrument design, the size and shape of the nozzle is an important factor to define the comprehensive shape of final GO/rGO fibers [135]. The 60 μm nozzle generates porous graphene fibers with a diameter of 100 μm, while the 1 cm nozzle results in 1 cm diameter graphene hollow fibers (Figure 11). A double capillary coaxial spinneret can produce graphene-based hollow fibers, while collar-shaped fibers can be obtained by GO suspension (Figure 12) [128]. A geometrically confined flat nozzle of line-shape can give continuous GO hydrogen films [139, 140].

The rotation process can also be manipulated to obtain 3D graphene materials of various shapes and structures. Figure 13 shows the blending of super-elastic graphene aerogel millispheres via spinning the liquid crystals of GO into a rotating coagulation bath. The shear force on the small nozzle makes the outer surface of the hydrogel have an obvious orientation, and after drying and annealing, a continuous shell and core of the cellular structure are formed. The resulting rGO millispheres show high mechanical strength and pressure flight behavior, with high jumping speed. However, a low specific surface area of 37 m^2/g was seen, indicating the presence of bulky/graphene walls.

The reduction after wet-spinning is important for evaluating the characteristics of 3D rGO materials [86, 109, 140].

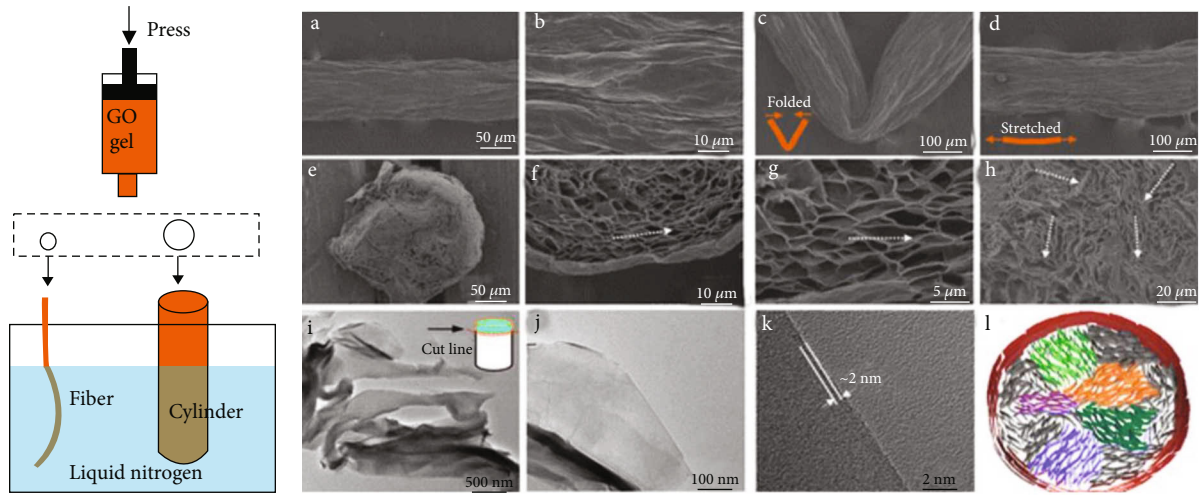

(a) (b)

Figure 11: (a) Manufacturing plan for GO porous fiber and GO porous cylinder. (b) SEM images of the surface of reduced graphene porous fibers (a, b) and folded/stretched reduced graphene porous fibers (c, d). (e–h) SEM image of the fractured form of reduced graphene porous fibers. The arrow indicates the direction of sorting the reduced graphene sheet. (i–k) TEM image of destroyed reduced graphene porous fibers embedded in epoxy resin. (l) Schematic core of reduced graphene porous fibers and GO porous fiber-shell structure model. Reproduced from [135], copyright 2012, American Chemical Society.

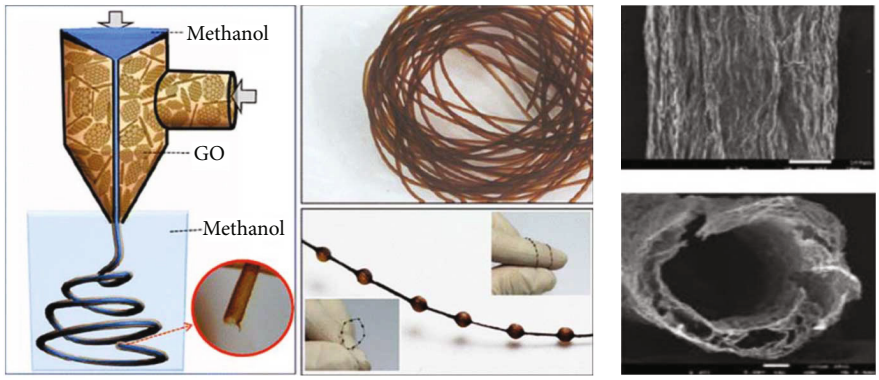

(a) (b)

Figure 12: (a) Double-capillary spinneret to straightly spin GO hollow fiber conversion setup. (b) SEM representation of the fiber surface with section. Reproduced from [137], copyright 2013, American Chemical Society.

Optimization of the reduction process increased the specific surface area of hydrothermally activated graphene fiber fabrics by 370% and also highly influenced its conductivity [107].

2.9. Antisolvent and Capillary Shaping before Reduction. Crushing one or several GO sheets into spherical particles is another way to minimize sheet accumulation under compression. In order to achieve crumpling, forces from the external environment must be applied to the static GO suspension. Desired particles can be obtained through antisolvent methods and the capillary compression [92, 141–143].

Antisolvent precipitation is considered as an effective method to produce crumpled GO papers. The GO sheets are randomly distributed in the aqueous solution, because the oxygen-containing functional groups on the surface of GO can physically and chemically bind with H_2O molecules. Later, after drying, these sheets are arranged in a uniformly stacked GO film. Hexane is considered a nonpolar aprotic antisolvent which prohibits interacting with functional groups present on GO. On its addition into the GO/ethanol suspension, it replaces the ethanol molecules present around GO, resulting in sturdy in-plane interactions of functional groups leading to crumpling of GO sheets; hence, the nonstacked GO gets formed with a large pore volume [142]. The thermally reduced nonstacked rGO shows a stable structure and 1435 m^2/g of surface area, which is much higher than the rGO produced without using an antisolvent (i.e., ~311 m^2/g). Wu et al. [144] developed a similar antisolvent precipitation method using precursor as a GO-based Na_2SO_4 mixture, alcohol as an antisolvent, and NaOH as a neutralizer. After the experiment, it was concluded that not

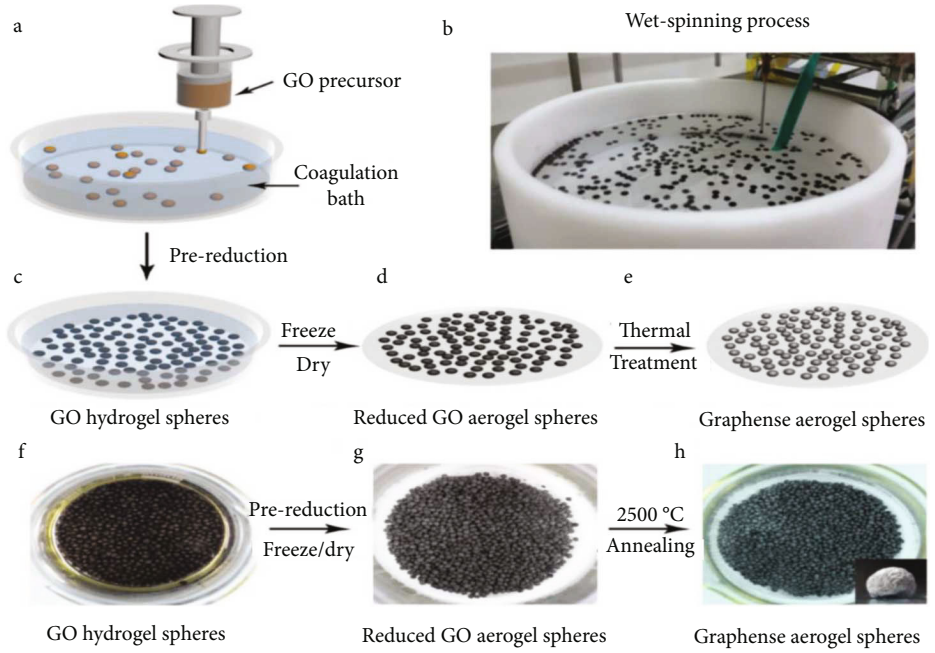

Figure 13: (a, b) Wet-spinning process represented for GO hydrogel spheres. (c–e) Synthesis process of graphene aerogel spheres using GO hydrogel spheres. (f) Newly obtained GO hydrogel spheres. (g) rGO aerogel spheres. (h) Graphene aerogel spheres after 2500°C annealing. Reproduced with permission from [140], copyright 2017, Wiley-VCH Verlag GmbH and Co. KGaA, Weinheim.

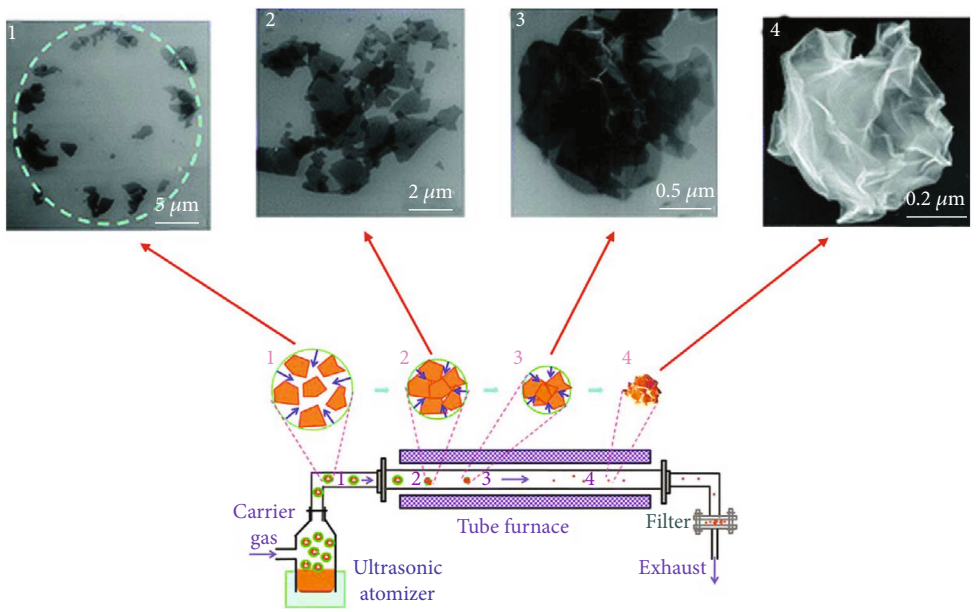

Figure 14: Illustration of experimental setup with evaporation-induced crumpling process and SEM photographs at each sample. Reproduced from [92], copyright 2011, American Chemical Society.

all combinations of solvents and antisolvents can be used to generate robust crumpled rGO as the C_6H_{14}-C_2H_6O system [142].

Capillary force can also be used to obtain crumpled GO sheets. It is introduced during the evaporation process for removing water from GO aerosols [92, 145, 146]. Figure 14 shows the typical apparatus for fabricating capillary crumpled GO/rGO [92]. The aerosolization of GO suspension using spray techniques supplies separate GO sheet groups. Meantime, the employed drying process induces the compression of capillary to deform the GO sheets present in aerosols. In evaporation, GO sheets undergo several morphological changes (i.e., from the coffee ring design in aerosol → titles + clustered sheets → loosely packed + wrinkled sheets having minor water quantities → dry + crumpled ball-like structure having multiple ridges and vertices).

Temperatures beyond 500°C can be used for simultaneous reduction of GO. However, the reduction process affects the crumpling conformations [146].

The GO/rGO structure obtained by capillary wrinkling is stabilized by plastically deformed π-π stacked ridges. These have a thickness of around 10s of nanometers and oppose the unfolding and collapsing as normal GO sheets on running under solution, microwave heating, compression, vapor treatment with hydrazine, and thermal shock [92]. Controlled palletization within 55 MPa may reduce the flat graphene sheet surface area from 407 m^2/g to 66 m^2/g, whereas the surface area during capillary crumpled rGO varies only from 567 m^2/g to 255 m^2/g. The capillary crumpled rGO balls show tight packing without any reduction in the accessible surface area. This enables less dependence on gravimetric capacitance in electrode mass loading [146]. However, the surface area loss caused by load-bearing compression and large load-dependent capacitances still significantly limited the use of expansion.

3. Conclusion and Future Research Directions

The past few decades have reported the evolution of (i) macroscopic (macrofoams, millispheres, fibers, and films) and (ii) microscopic (3D honeycomb-like graphene, hollow spheres, strutted nanostructures, and crumpled sheets) 3D graphene materials. The macroscopic 3D graphene structures can be employed as free-standing units, while the microscopic ones can be turned into arbitrary forms without detailing the restacking issue. As per preconstructed 3D morphologies responsible for preventing the restacking of sheets, the engineering 3D graphene structures and materials are widely used in energy storage applications, environmental remediation, sensors, etc. The macroscopic structure, convenient surface area, conductivities, pore distribution, mechanical properties, and site density are crucial factors in designing 3D graphene for particular application. The 3D structure prepared through 3D self-assembly and reduction is dominating because of its ease of manipulation. Factors like shape, microstructures, functional groups, and dopants of 3D rGO can be achieved by manipulating the GO precursor properties, controlling reaction and reduction conditions, involving additives, and using templates. However, connections between stochastic physical sheets and overstacking of sheets are some of the important issues of the 3D rGO architecture.

Considerable efforts are needed to precisely manage the defects in resulting 3D materials. Its unique topology and external flaws serve as an active seat for a variety of applications. However, apprehending the role of various disordered sites in different applications is undoubtedly limited. Furthermore, there is still a point of doubt among rich active sites, high conductivities (thermal and electrical), and strong mechanical strength. An accurate control over faulty sites in 3D graphene-based material is key to stabilize this equilibrium and attain an optimum performance.

The versatility of 3D graphene also requires exploration for new and promising application areas. 3D graphene films can be utilized in thermal or electromagnetic cloaking. With high transmittance, exceptional mechanical properties, and low sheet resistance, the graphene materials are considered next-generation conduction materials for developing transparent electrodes to be applied into strain sensors, touch screens, optoelectronic devices, organic resistive memory, LCDs, LEDs, flexible electronics, and thin-film photovoltaics [147–152]. However, the applicability of graphene layers in other fields gets limited because the sheets tend to restack, resulting in a decrease of surface area and unique characteristics belonging to thin layers. The 3D graphene structures deliberately eliminate the possibility of face-to-face restacking, expanding the usage of graphene in a broad range of fields. 3D graphene structures can be promising in electrochemical applications like supercapacitors, sensors, fuel cells, hydrogen storage, and flexible electronics [5, 153–160]. Furthermore, 3D graphene materials can be effectively employed as support catalysts in chemical and electrochemical reactions, especially in environmental remedy, where macroscopic structures are advantageous in recycling and recovery.

Also, the microscopic architectures can prove important in scaling the future devices. Various 3D graphene materials also show the scalability of the industry in terms of production and utilization. More importance can be given towards upscaling the lab-based facilities to minimize the production cost. There are high possibilities for 3D graphene materials to overtake markets in the coming years.

Data Availability

The data used to support the study is included in the article.

Conflicts of Interest

The authors declare that they have no known competing financial interests or personal relationships that could have appeared to influence the work reported in this paper.

Authors' Contributions

R.S. was responsible for conceptualization, data curation, formal analysis, methodology, writing of the original draft, and review and editing; N.K., N.R., M.S., D.A.D., and K.E-S. were responsible for data curation and review and editing; I.P., C.P.J.I., R.K., and V.V. were responsible for the formal analysis. All authors have read and agreed to the published version of the manuscript.

Acknowledgments

The authors are grateful to the Dr. S.S. Bhatnagar University Institute of Chemical Engineering & Technology, Panjab University, India, for their support and assistance with the study. All authors wish everyone a good and healthy life in these tough times of COVID-19.

References

[1] K. S. Novoselov, A. K. Geim, S. V. Morozov et al., "Electric field effect in atomically thin carbon films," *Science*, vol. 306, no. 5696, pp. 666–669, 2004.

[2] A. Balandin, S. Ghosh, W. Bao et al., "Superior thermal conductivity of single-layer graphene," *Nano Letters*, vol. 8, no. 3, pp. 902–907, 2008.

[3] C. Lee, X. Wei, J. Kysar, and J. Hone, "Measurement of the elastic properties and intrinsic strength of monolayer graphene," *Science*, vol. 321, no. 5887, pp. 385–388, 2008.

[4] N. Rao, R. Singh, and L. Bashambu, "Carbon-based nanomaterials: synthesis and prospective applications," *Materials Today: Proceedings*, vol. 44, pp. 608–614, 2021.

[5] R. Singh, "Advancements in energy storage through graphene," in *Advances in Materials Processing and Manufacturing Applications. iCADMA 2020*, Lecture Notes in Mechanical Engineering, A. Patnaik, E. Kozeschnik, and V. Kukshal, Eds., pp. 165–173, Springer, Singapore, 2021.

[6] R. Singh, M. Singh, N. Kumari, Janak, S. Maharana, and P. Maharana, "A comprehensive review of polymeric wastewater purification membranes," *J. Compos. Sci*, vol. 5, no. 6, p. 162, 2021.

[7] M. Zeng, W. Wang, and X. Bai, "Preparing three-dimensional graphene architectures: review of recent developments," *Chinese Physics B*, vol. 22, no. 9, p. 098105, 2013.

[8] Z. Sun, S. Fang, and Y. Hu, "3D graphene materials: from understanding to design and synthesis control," *Chemical Reviews*, vol. 120, no. 18, pp. 10336–10453, 2020.

[9] Q. Fang, Y. Shen, and B. Chen, "Synthesis, decoration and properties of three-dimensional graphene-based macrostructures: a review," *Chemical Engineering Journal*, vol. 264, pp. 753–771, 2015.

[10] S. Korkut, J. Roy-Mayhew, D. Dabbs, D. Milius, and I. Aksay, "High surface area tapes produced with functionalized graphene," *ACS Nano*, vol. 5, no. 6, pp. 5214–5222, 2011.

[11] S. Pei and H. Cheng, "The reduction of graphene oxide," *Carbon*, vol. 50, no. 9, pp. 3210–3228, 2012.

[12] H. Schniepp, J. Li, M. McAllister et al., "Functionalized single graphene sheets derived from splitting graphite oxide," *The Journal Of Physical Chemistry B.*, vol. 110, no. 17, pp. 8535–8539, 2006.

[13] M. McAllister, J. Li, D. Adamson et al., "Single sheet functionalized graphene by oxidation and thermal expansion of graphite," *Chemistry Of Materials.*, vol. 19, no. 18, pp. 4396–4404, 2007.

[14] S. Stankovich, D. Dikin, R. Piner et al., "Synthesis of graphene-based nanosheets via chemical reduction of exfoliated graphite oxide," *Carbon*, vol. 45, no. 7, pp. 1558–1565, 2007.

[15] V. Tung, M. Allen, Y. Yang, and R. Kaner, "High-throughput solution processing of large-scale graphene," *Nature Nanotechnology*, vol. 4, pp. 25–29, 2008.

[16] G. Wang, J. Yang, J. Park et al., "Facile synthesis and characterization of graphene nanosheets," *The Journal Of Physical Chemistry C.*, vol. 112, no. 22, pp. 8192–8195, 2008.

[17] R. Muszynski, B. Seger, and P. Kamat, "Decorating graphene sheets with gold nanoparticles," *The Journal Of Physical Chemistry C.*, vol. 112, pp. 5263–5266, 2008.

[18] S. Stankovich, D. Dikin, G. Dommett et al., "Graphene-based composite materials," *Nature*, vol. 442, no. 7100, pp. 282–286, 2006.

[19] X. Fan, W. Peng, Y. Li et al., "Deoxygenation of exfoliated graphite oxide under alkaline conditions: a green route to graphene preparation," *Advanced Materials*, vol. 20, no. 23, pp. 4490–4493, 2008.

[20] M. Fernández-Merino, L. Guardia, J. Paredes et al., "Vitamin C is an ideal substitute for hydrazine in the reduction of graphene oxide suspensions," *The Journal Of Physical Chemistry C.*, vol. 114, no. 14, pp. 6426–6432, 2010.

[21] S. Pei, J. Zhao, J. Du, W. Ren, and H. Cheng, "Direct reduction of graphene oxide films into highly conductive and flexible graphene films by hydrohalic acids," *Carbon*, vol. 48, pp. 4466–4474, 2010.

[22] G. Williams, B. Seger, and P. Kamat, "TiO2-Graphene Nanocomposites. UV-assisted photocatalytic reduction of graphene oxide," *ACS Nano*, vol. 2, no. 7, pp. 1487–1491, 2008.

[23] Y. Zhou, Q. Bao, L. Tang, Y. Zhong, and K. Loh, "Hydrothermal dehydration for the "green" reduction of exfoliated graphene oxide to graphene and demonstration of tunable optical limiting properties," *Chemistry of Materials*, vol. 21, pp. 2950–2956, 2009.

[24] H. Wang, J. Robinson, X. Li, and H. Dai, "Solvothermal reduction of chemically exfoliated graphene sheets," *Journal of the American Chemical Society*, vol. 131, pp. 9910-9911, 2009.

[25] L. Cote, R. Cruz-Silva, and J. Huang, "Flash reduction and patterning of graphite oxide and its polymer composite," *Journal of the American Chemical Society*, vol. 131, pp. 11027–11032, 2009.

[26] S. Gilje, S. Dubin, A. Badakhshan, J. Farrar, S. Danczyk, and R. Kaner, "Photothermal deoxygenation of graphene oxide for patterning and distributed ignition applications," *Advanced Materials*, vol. 22, pp. 419–423, 2010.

[27] D. Sokolov, K. Shepperd, and T. Orlando, "Formation of graphene features from direct laser-induced reduction of graphite oxide," *Journal of Physical Chemistry Letters*, vol. 1, pp. 2633–2636, 2010.

[28] A. Viinikanoja, Z. Wang, J. Kauppila, and C. Kvarnström, "Electrochemical reduction of graphene oxide and its in situ spectroelectrochemical characterization," *Physical Chemistry Chemical Physics*, vol. 14, p. 14003, 2012.

[29] Z. Wu, W. Ren, L. Gao et al., "Synthesis of graphene sheets with high electrical conductivity and good thermal stability by hydrogen arc discharge exfoliation," *ACS Nano*, vol. 3, no. 2, pp. 411–417, 2009.

[30] C. Gómez-Navarro, R. Weitz, A. Bittner et al., "Electronic transport properties of individual chemically reduced graphene oxide sheets," *Nano Letters*, vol. 7, no. 11, pp. 3499–3503, 2007.

[31] Y. Zhu, S. Murali, M. Stoller, A. Velamakanni, R. Piner, and R. Ruoff, "Microwave assisted exfoliation and reduction of graphite oxide for ultracapacitors," *Carbon*, vol. 48, pp. 2118–2122, 2010.

[32] Y. Si and E. Samulski, "Synthesis of water soluble graphene," *Nano Letters*, vol. 8, pp. 1679–1682, 2008.

[33] W. Gao, L. Alemany, L. Ci, and P. Ajayan, "New insights into the structure and reduction of graphite oxide," *Nature Chemistry*, vol. 1, pp. 403–408, 2009.

[34] C. Li and G. Shi, "Three-dimensional graphene architectures," *Nanoscale*, vol. 4, pp. 5549–5563, 2012.

[35] V. Chabot, D. Higgins, A. Yu, X. Xiao, Z. Chen, and J. Zhang, "A review of graphene and graphene oxide sponge: material synthesis and applications to energy and the environment," *Energy & Environmental Science*, vol. 7, p. 1564, 2014.

[36] H. Ahn, J. Jang, M. Seol et al., "Self-assembled foam-like graphene networks formed through nucleate boiling," *Scientific Reports*, vol. 3, no. 1, p. 1396, 2013.

[37] X. Gao, J. Jang, and S. Nagase, "Hydrazine and thermal reduction of graphene oxide: reaction mechanisms, product structures, and reaction design," *The Journal Of Physical Chemistry C.*, vol. 114, pp. 832–842, 2009.

[38] S. Yin, Z. Niu, and X. Chen, "Assembly of graphene sheets into 3D macroscopic structures," *Small*, vol. 8, pp. 2458–2463, 2012.

[39] S. Nardecchia, D. Carriazo, M. Ferrer, M. Gutiérrez, and F. del Monte, "Three dimensional macroporous architectures and aerogels built of carbon nanotubes and/or graphene: synthesis and applications," *Chemical Society Reviews*, vol. 42, pp. 794–830, 2013.

[40] X. Cao, Z. Yin, and H. Zhang, "Three-dimensional graphene materials: preparation, structures and application in supercapacitors," *Energy & Environmental Science*, vol. 7, pp. 1850–1865, 2014.

[41] Y. Ma and Y. Chen, "Three-dimensional graphene networks: synthesis, properties and applications," *National Science Review*, vol. 2, pp. 40–53, 2014.

[42] H. Wang, X. Yuan, G. Zeng et al., "Three dimensional graphene based materials: synthesis and applications from energy storage and conversion to electrochemical sensor and environmental remediation," *Advances in Colloid and Interface Science*, vol. 221, pp. 41–59, 2015.

[43] H. Qiu, Y. Guan, P. Luo, and Y. Wang, "Recent advance in fabricating monolithic 3D porous graphene and their applications in biosensing and biofuel cells," *Biosensors & Bioelectronics*, vol. 89, pp. 85–95, 2017.

[44] M. Rethinasabapathy, S. M. Kang, S. C. Jang, and Y. S. Huh, "Three-dimensional porous graphene materials for environmental applications," *Carbon Lett.*, vol. 22, pp. 1–13, 2017.

[45] Y. Lu, Y. Ma, T. Zhang, Y. Yang, L. Wei, and Y. Chen, "Monolithic 3D cross-linked polymeric graphene materials and the likes: preparation and their redox catalytic applications," *Journal of the American Chemical Society*, vol. 140, pp. 11538–11550, 2018.

[46] Y. Xia, R. Li, R. Chen, J. Wang, and L. Xiang, "3D architectured graphene/metal oxide hybrids for gas sensors: a review," *Sensors*, vol. 18, p. 1456, 2018.

[47] V. Smirnov, A. Arbuzov, Y. Shul'ga et al., "Photoreduction of graphite oxide," *High Energy Chemistry*, vol. 45, no. 1, pp. 57–61, 2011.

[48] V. Abdelsayed, S. Moussa, H. Hassan, H. Aluri, M. Collinson, and M. El-Shall, "Photothermal deoxygenation of graphite oxide with laser excitation in solution and graphene-aided increase in water temperature," *Journal of Physical Chemistry Letters*, vol. 1, pp. 2804–2809, 2010.

[49] P. Willmott and J. Huber, "Pulsed laser vaporization and deposition," *Reviews of Modern Physics*, vol. 72, pp. 315–328, 2000.

[50] L. Huang, Y. Liu, L. Ji, Y. Xie, T. Wang, and W. Shi, "Pulsed laser assisted reduction of graphene oxide," *Carbon*, vol. 49, pp. 2431–2436, 2011.

[51] Y. Guan, Y. Fang, G. Lim, H. Zheng, and M. Hong, "Fabrication of laser-reduced graphene oxide in liquid nitrogen environment," *Scientific Reports*, vol. 6, p. 28913, 2016.

[52] W. Gao, N. Singh, L. Song et al., "Direct laser writing of micro-supercapacitors on hydrated graphite oxide films," *Nature Nanotechnology*, vol. 6, no. 8, pp. 496–500, 2011.

[53] H. Tian, Y. Yang, D. Xie et al., "Wafer-scale integration of graphene-based electronic, optoelectronic and electroacoustic devices," *Scientific Reports*, vol. 4, no. 1, p. 3598, 2015.

[54] B. Senyuk, N. Behabtu, A. Martinez et al., "Three-dimensional patterning of solid microstructures through laser reduction of colloidal graphene oxide in liquid-crystalline dispersions," *Nature Communications*, vol. 6, no. 1, pp. 1–7, 2015.

[55] Y. Zhang, L. Guo, H. Xia, Q. Chen, J. Feng, and H. Sun, "Photoreduction of graphene oxides: methods, properties, and applications," *Advanced Optical Materials*, vol. 2, pp. 10–28, 2013.

[56] M. El-Kady, V. Strong, S. Dubin, and R. Kaner, "Laser scribing of high-performance and flexible graphene-based electrochemical capacitors," *Science*, vol. 335, pp. 1326–1330, 2012.

[57] V. Strong, S. Dubin, M. F. el-Kady et al., "Patterning and electronic tuning of laser scribed graphene for flexible all-carbon devices," *ACS Nano*, vol. 6, no. 2, pp. 1395–1403, 2012.

[58] J. Lu, X. Zhang, Q. Zhu et al., "Highly tunable and scalable fabrication of 3D flexible graphene micropatterns for directing cell alignment," *ACS Applied Materials & Interfaces*, vol. 10, no. 21, pp. 17704–17713, 2018.

[59] D. Bhattacharjya, C. Kim, J. Kim, I. You, J. In, and S. Lee, "Fast and controllable reduction of graphene oxide by low-cost CO_2 laser for supercapacitor application," *Applied Surface Science*, vol. 462, pp. 353–361, 2018.

[60] D. Sokolov, C. Rouleau, D. Geohegan, and T. Orlando, "Excimer laser reduction and patterning of graphite oxide," *Carbon*, vol. 53, pp. 81–89, 2013.

[61] C. Chua and M. Pumera, "Chemical reduction of graphene oxide: a synthetic chemistry viewpoint," *Chemical Society Reviews*, vol. 43, pp. 291–312, 2014.

[62] K. Sheng, Y. Sun, C. Li, W. Yuan, and G. Shi, "Ultrahigh-rate supercapacitors based on eletrochemically reduced graphene oxide for ac line-filtering," *Scientific Reports*, vol. 2, p. 247, 2012.

[63] W. Chen, P. Xiao, H. Chen, H. Zhang, Q. Zhang, and Y. Chen, "Polymeric graphene bulk materials with a 3D cross-linked monolithic graphene network," *Advanced Materials*, vol. 31, p. 1802403, 2018.

[64] W. Chen and L. Yan, "In situ self-assembly of mild chemical reduction graphene for three-dimensional architectures," *Nanoscale*, vol. 3, pp. 3132–3137, 2011.

[65] H. Pham, V. Pham, T. Cuong et al., "Synthesis of the chemically converted graphene xerogel with superior electrical conductivity," *Chemical Communications*, vol. 47, no. 34, pp. 9672–9674, 2011.

[66] C. Liu, H. Liu, A. Xu, K. Tang, Y. Huang, and C. Lu, "In situ reduced and assembled three-dimensional graphene aerogel for efficient dye removal," *Journal of Alloys and Compounds*, vol. 714, pp. 522–529, 2017.

[67] K. Sheng, Y. Xu, C. Li, and G. Shi, "High-performance self-assembled graphene hydrogels prepared by chemical reduction of graphene oxide," *New Carbon Materials*, vol. 26, pp. 9–15, 2011.

[68] L. Zhang and G. Shi, "Preparation of highly conductive graphene hydrogels for fabricating supercapacitors with high rate capability," *Journal of Physical Chemistry C*, vol. 115, pp. 17206–17212, 2011.

[69] W. Wei, K. Sun, and Y. Hu, "Synthesis of mesochannel carbon nanowall material from CO_2 and its excellent

performance for perovskite solar cells," *Industrial and Engineering Chemistry Research*, vol. 56, pp. 1803–1809, 2017.

[70] L. Chang, D. Stacchiola, and Y. Hu, "Design and synthesis of 3D potassium-ion pre-intercalated graphene for supercapacitors," *Industrial and Engineering Chemistry Research*, vol. 57, pp. 3610–3616, 2018.

[71] Z. Xing, B. Wang, W. Gao et al., "Reducing CO_2 to dense nanoporous graphene by Mg/Zn for high power electrochemical capacitors," *Nano Energy*, vol. 11, pp. 600–610, 2015.

[72] X. Zhang, D. Liu, L. Yang, L. Zhou, and T. You, "Self-assembled three-dimensional graphene-based materials for dye adsorption and catalysis," *Journal of Materials Chemistry A*, vol. 3, pp. 10031–10037, 2015.

[73] J. Luo, J. Lai, N. Zhang, Y. Liu, R. Liu, and X. Liu, "Tannic acid induced self-assembly of three-dimensional graphene with good adsorption and antibacterial properties," *ACS Sustainable Chemistry & Engineering*, vol. 4, pp. 1404–1413, 2016.

[74] L. Zhang, G. Chen, M. Hedhili, H. Zhang, and P. Wang, "Three-dimensional assemblies of graphene prepared by a novel chemical reduction-induced self-assembly method," *Nanoscale*, vol. 4, pp. 7038–7045, 2012.

[75] M. Chen, C. Zhang, X. Li et al., "A one-step method for reduction and self-assembling of graphene oxide into reduced graphene oxide aerogels," *Journal of Materials Chemistry A*, vol. 1, no. 8, pp. 2869–2877, 2013.

[76] S. Yang, L. Zhang, Q. Yang et al., "Graphene aerogel prepared by thermal evaporation of graphene oxide suspension containing sodium bicarbonate," *Journal of Materials Chemistry A*, vol. 3, no. 15, pp. 7950–7958, 2015.

[77] X. Zhang, Z. Sui, B. Xu et al., "Mechanically strong and highly conductive graphene aerogel and its use as electrodes for electrochemical power sources," *Journal of Materials Chemistry*, vol. 21, no. 18, pp. 6494–6497, 2011.

[78] C. Hu, X. Zhai, L. Liu, Y. Zhao, L. Jiang, and L. Qu, "Spontaneous Reduction and assembly of graphene oxide into three-dimensional graphene network on arbitrary conductive substrates," *Scientific Reports*, vol. 3, p. 2065, 2013.

[79] Z. Niu, J. Chen, H. Hng, J. Ma, and X. Chen, "A leavening strategy to prepare reduced graphene oxide foams," *Advanced Materials*, vol. 24, pp. 4144–4150, 2012.

[80] Y. Xu, G. Shi, and X. Duan, "Self-assembled three-dimensional graphene macrostructures: synthesis and applications in supercapacitors," *Accounts of Chemical Research*, vol. 48, pp. 1666–1675, 2015.

[81] K. Chen, L. Chen, Y. Chen, H. Bai, and L. Li, "Three-dimensional porous graphene-based composite materials: electrochemical synthesis and application," *Journal of Materials Chemistry*, vol. 22, pp. 20968–20976, 2012.

[82] V. Pham, T. Gebre, and J. Dickerson, "Facile electrodeposition of reduced graphene oxide hydrogels for high-performance supercapacitors," *Nanoscale*, vol. 7, pp. 5947–5950, 2015.

[83] Y. Li, K. Sheng, W. Yuan, and G. Shi, "A high-performance flexible fibre-shaped electrochemical capacitor based on electrochemically reduced graphene oxide," *Chemical Communications*, vol. 49, pp. 291–293, 2013.

[84] T. Purkait, G. Singh, D. Kumar, M. Singh, and R. Dey, "High-performance flexible supercapacitors based on electrochemically tailored three-dimensional reduced graphene oxide networks," *Scientific Reports*, vol. 8, p. 640, 2018.

[85] J. Quezada-Renteria, C. Ania, L. Chazaro-Ruiz, and J. Rangel-Mendez, "Influence of protons on reduction degree and defect formation in electrochemically reduced graphene oxide," *Carbon*, vol. 149, pp. 722–732, 2019.

[86] C. Wu, X. Wang, Q. Zhuo et al., "A facile continuous wet-spinning of graphene oxide fibers from aqueous solutions at high pH with the introduction of ammonia," *Carbon*, vol. 138, pp. 292–299, 2018.

[87] C. Chen, Q. Zhang, M. Yang, C. Huang, Y. Yang, and M. Wang, "Structural evolution during annealing of thermally reduced graphene nanosheets for application in supercapacitors," *Carbon*, vol. 50, pp. 3572–3584, 2012.

[88] C. Chen, Q. Zhang, C. Huang et al., "Macroporous 'bubble' graphene film via template-directed ordered-assembly for high rate supercapacitors," *Chemical Communications*, vol. 48, no. 57, pp. 7149–7151, 2012.

[89] W. Liu, H. Li, Q. Zeng et al., "Fabrication of ultralight three-dimensional graphene networks with strong electromagnetic wave absorption properties," *Journal of Materials Chemistry A*, vol. 3, no. 7, pp. 3739–3747, 2015.

[90] J. Huang, X. Liu, Q. Zhang et al., "Entrapment of sulfur in hierarchical porous graphene for lithium-sulfur batteries with high rate performance from −40 to 60 °C," *Nano Energy*, vol. 2, no. 2, pp. 314–321, 2013.

[91] R. Fang, S. Zhao, S. Pei et al., "Toward more reliable lithium–sulfur batteries: an all-graphene cathode structure," *ACS Nano*, vol. 10, no. 9, pp. 8676–8682, 2016.

[92] J. Luo, H. Jang, T. Sun et al., "Compression and aggregation-resistant particles of crumpled soft sheets," *ACS Nano*, vol. 5, no. 11, pp. 8943–8949, 2011.

[93] Y. Xu, K. Sheng, C. Li, and G. Shi, "Self-assembled graphene hydrogel via a one-step hydrothermal process," *ACS Nano*, vol. 4, pp. 4324–4330, 2010.

[94] Y. Xu, Z. Lin, X. Zhong et al., "Holey graphene frameworks for highly efficient capacitive energy storage," *Nature Communications*, vol. 5, no. 1, 2014.

[95] Z. Sui and B. Han, "Effect of surface chemistry and textural properties on carbon dioxide uptake in hydrothermally reduced graphene oxide," *Carbon*, vol. 82, pp. 590–598, 2015.

[96] Z. Wu, Y. Sun, Y. Tan, S. Yang, X. Feng, and K. Müllen, "Three-dimensional graphene-based macro- and mesoporous frameworks for high-performance electrochemical capacitive energy storage," *Journal of the American Chemical Society*, vol. 134, pp. 19532–19535, 2012.

[97] J. Kim, J. Oh, M. Kotal, N. Koratkar, and I. Oh, "Self-assembly and morphological control of three-dimensional macroporous architectures built of two-dimensional materials," *Nano Today*, vol. 14, pp. 100–123, 2017.

[98] H. Bi, K. Yin, X. Xie et al., "Low temperature casting of graphene with high compressive strength," *Advanced Materials*, vol. 24, no. 37, pp. 5124–5129, 2012.

[99] K. Hu, X. Xie, T. Szkopek, and M. Cerruti, "Understanding hydrothermally reduced graphene oxide hydrogels: from reaction products to hydrogel properties," *Chemistry of Materials*, vol. 28, pp. 1756–1768, 2016.

[100] A. Goldstein, W. Mickelson, A. Machness et al., "Simultaneous sheet cross-linking and deoxygenation in the graphene oxide sol–gel transition," *Journal of Physical Chemistry C*, vol. 118, no. 49, pp. 28855–28860, 2014.

[101] X. Wu, J. Zhou, W. Xing et al., "High-rate capacitive performance of graphene aerogel with a superhigh C/O molar

ratio," *Journal of Materials Chemistry*, vol. 22, no. 43, pp. 23186–23193, 2012.

[102] J. Ma, J. Wang, Y. He et al., "A solvothermal strategy: one-step in situ synthesis of self-assembled 3D graphene-based composites with enhanced lithium storage capacity," *Journal of Materials Chemistry A*, vol. 2, no. 24, pp. 9200–9207, 2014.

[103] J. Ma, Y. He, W. Zhang et al., "An experimental insight into the advantages of _in situ_ solvothermal route to construct 3D graphene-based anode materials for lithium-ion batteries," *Nano Energy*, vol. 16, pp. 235–246, 2015.

[104] Y. Sun, Q. Wu, and G. Shi, "Supercapacitors based on self-assembled graphene organogel," *Physical Chemistry Chemical Physics*, vol. 13, pp. 17249–17254, 2011.

[105] Y. Wu, N. Yi, L. Huang et al., "Three-dimensionally bonded spongy graphene material with super compressive elasticity and near-zero Poisson's ratio," *Nature Communications*, vol. 6, no. 1, p. 6141, 2015.

[106] L. Qiu, J. Liu, S. Chang, Y. Wu, and D. Li, "Biomimetic superelastic graphene-based cellular monoliths," *Nature Communications*, vol. 3, p. 1241, 2012.

[107] Z. Li, T. Huang, W. Gao et al., "Hydrothermally activated graphene fiber fabrics for textile electrodes of supercapacitors," *ACS Nano*, vol. 11, no. 11, pp. 11056–11065, 2017.

[108] C. Nethravathi and M. Rajamathi, "Chemically modified graphene sheets produced by the solvothermal reduction of colloidal dispersions of graphite oxide," *Carbon*, vol. 46, pp. 1994–1998, 2008.

[109] Y. Shao, M. F. el-Kady, C. Lin et al., "3D Freeze-casting of cellular graphene films for ultrahigh-power-density supercapacitors," *Advanced Materials*, vol. 28, no. 31, pp. 6719–6726, 2016.

[110] J. Kuang, L. Liu, Y. Gao et al., "A hierarchically structured graphene foam and its potential as a large-scale strain-gauge sensor," *Nanoscale*, vol. 5, no. 24, p. 12171, 2013.

[111] W. Li, K. Lu, and J. Walz, "Freeze casting of porous materials: review of critical factors in microstructure evolution," *International Materials Review*, vol. 57, pp. 37–60, 2012.

[112] J. Wang and M. Ellsworth, "Graphene aerogels," *ECS Meeting Abstracts.*, vol. 19, p. 5, 2009.

[113] H. Bai, C. Li, X. Wang, and G. Shi, "On the gelation of graphene oxide," *Journal of Physical Chemistry C*, vol. 115, pp. 5545–5551, 2011.

[114] H. Geng, X. Liu, G. Shi et al., "Graphene oxide restricts growth and recrystallization of ice crystals," *Angewandte Chemie, International Edition*, vol. 56, no. 4, pp. 997–1001, 2017.

[115] C. Wang, X. Chen, B. Wang et al., "Freeze-casting produces a graphene oxide aerogel with a radial and centrosymmetric structure," *ACS Nano*, vol. 12, no. 6, pp. 5816–5825, 2018.

[116] X. Xu, Q. Zhang, Y. Yu, W. Chen, H. Hu, and H. Li, "Naturally dried graphene aerogels with superelasticity and tunable Poisson's ratio," *Advanced Materials*, vol. 28, pp. 9223–9230, 2016.

[117] X. Xie, Y. Zhou, H. Bi, K. Yin, S. Wan, and L. Sun, "Large-range control of the microstructures and properties of three-dimensional porous graphene," *Scientific Reports*, vol. 3, p. 2177, 2013.

[118] H. Bai, Y. Chen, B. Delattre, A. Tomsia, and R. Ritchie, "Bioinspired large-scale aligned porous materials assembled with dual temperature gradients," *Science Advances*, vol. 1, article e1500849, 2015.

[119] M. Yang, N. Zhao, Y. Cui et al., "Biomimetic architectured graphene aerogel with exceptional strength and resilience," *ACS Nano*, vol. 11, no. 7, pp. 6817–6824, 2017.

[120] Y. Lin, F. Liu, G. Casano, R. Bhavsar, I. Kinloch, and B. Derby, "Pristine graphene aerogels by room-temperature freeze gelation," *Advanced Materials*, vol. 28, pp. 7993–8000, 2016.

[121] C. Zhu, T. Han, E. Duoss et al., "Highly compressible 3D periodic graphene aerogel microlattices," *Nature Communications*, vol. 6, no. 1, pp. 1–8, 2015.

[122] E. García-Tuñon, S. Barg, J. Franco et al., "Printing in three dimensions with graphene," *Advanced Materials*, vol. 27, no. 10, pp. 1688–1693, 2015.

[123] R. Hensleigh, H. Cui, J. Oakdale et al., "Additive manufacturing of complex micro-architected graphene aerogels," *Materials Horizons*, vol. 5, no. 6, pp. 1035–1041, 2018.

[124] J. Lewis, "Direct ink writing of 3D functional materials," *Advanced Functional Materials*, vol. 16, pp. 2193–2204, 2006.

[125] J. Kim, W. Chang, D. Kim et al., "3D printing of reduced graphene oxide nanowires," *Advanced Materials*, vol. 27, no. 1, pp. 157–161, 2015.

[126] K. Fu, Y. Yao, J. Dai, and L. Hu, "Progress in 3D printing of carbon materials for energy-related applications," *Advanced Materials*, vol. 29, p. 1603486, 2016.

[127] J. Smay, J. Cesarano, and J. Lewis, "Colloidal inks for directed assembly of 3-D periodic structures," *Langmuir*, vol. 18, pp. 5429–5437, 2002.

[128] C. Bao, H. Zhang, C. Wilkie et al., "On the dispersion systems of graphene-like two-dimensional materials: from fundamental laws to engineering guidelines," *Carbon*, vol. 107, pp. 774–782, 2016.

[129] J. Ma, P. Wang, L. Dong, Y. Ruan, and H. Lu, "Highly conductive, mechanically strong graphene monolith assembled by three-dimensional printing of large graphene oxide," *Journal of Colloid and Interface Science*, vol. 534, pp. 12–19, 2019.

[130] Y. Yao, K. Fu, C. Yan et al., "Three-dimensional printable high-temperature and high-rate heaters," *ACS Nano*, vol. 10, no. 5, pp. 5272–5279, 2016.

[131] C. Zhu, T. Liu, F. Qian et al., "Supercapacitors based on three-dimensional hierarchical graphene aerogels with periodic macropores," *Nano Letters*, vol. 16, no. 6, pp. 3448–3456, 2016.

[132] Y. Jiang, Z. Xu, T. Huang et al., "Direct 3D Printing of ultralight graphene oxide aerogel microlattices," *Advanced Functional Materials*, vol. 28, no. 16, p. 1707024, 2018.

[133] X. Tang, H. Zhou, Z. Cai et al., "Generalized 3D printing of graphene-based mixed-dimensional hybrid aerogels," *ACS Nano*, vol. 12, no. 4, pp. 3502–3511, 2018.

[134] Q. Zhang, F. Zhang, S. Medarametla, H. Li, C. Zhou, and D. Lin, "3D Printing of graphene aerogels," *Small*, vol. 12, pp. 1702–1708, 2016.

[135] Z. Xu, Y. Zhang, P. Li, and C. Gao, "Strong, conductive, lightweight, neat graphene aerogel fibers with aligned pores," *ACS Nano*, vol. 6, pp. 7103–7113, 2012.

[136] H. Cong, X. Ren, P. Wang, and S. Yu, "Wet-spinning assembly of continuous, neat and macroscopic graphene fibers," *Scientific Reports*, vol. 2, p. 613, 2012.

[137] Y. Zhao, C. Jiang, C. Hu et al., "Large-scale spinning assembly of neat, morphology-defined, graphene-based hollow fibers," *ACS Nano*, vol. 7, no. 3, pp. 2406–2412, 2013.

[138] Z. Xu and C. Gao, "Graphene chiral liquid crystals and macroscopic assembled fibres," *Nature Communications*, vol. 2, p. 571, 2011.

[139] L. Kou, Z. Liu, T. Huang et al., "Wet-spun, porous, orientational graphene hydrogel films for high-performance supercapacitor electrodes," *Nanoscale*, vol. 7, no. 9, pp. 4080–4087, 2015.

[140] X. Zhao, W. Yao, W. Gao, H. Chen, and C. Gao, "Wet-spun superelastic graphene aerogel millispheres with group effect," *Advanced Materials*, vol. 29, p. 1701482, 2017.

[141] S. Peurifoy, E. Castro, F. Liu et al., "Three-dimensional graphene nanostructures," *Journal of the American Chemical Society*, vol. 140, no. 30, pp. 9341–9345, 2018.

[142] Y. Yoon, K. Lee, C. Baik et al., "Anti-solvent derived non-stacked reduced graphene oxide for high performance supercapacitors," *Advanced Materials*, vol. 25, no. 32, pp. 4437–4444, 2013.

[143] H. Chen, C. Chen, Y. Liu et al., "High-quality graphene microflower design for high-performance Li-S and Al-Ion batteries," *Advanced Energy Materials*, vol. 7, no. 17, p. 1700051, 2017.

[144] K. Wu, K. Du, and G. Hu, "A novel design concept for fabricating 3D graphene with the assistant of anti-solvent precipitated sulphates and its Li-ion storage properties," *Journal of Materials Chemistry A*, vol. 6, pp. 3444–3453, 2018.

[145] J. Luo, H. Jang, and J. Huang, "Effect of sheet morphology on the scalability of graphene-based ultracapacitors," *ACS Nano*, vol. 7, pp. 1464–1471, 2013.

[146] X. Ma, M. Zachariah, and C. Zangmeister, "Crumpled nanopaper from graphene oxide," *Nano Letters*, vol. 12, pp. 486–489, 2011.

[147] A. Sakhaee-Pour, M. Ahmadian, and A. Vafai, "Potential application of single-layered graphene sheet as strain sensor," *Solid State Communications*, vol. 147, pp. 336–340, 2008.

[148] J. Wassei and R. Kaner, "Graphene, a promising transparent conductor," *Materials Today*, vol. 13, pp. 52–59, 2010.

[149] G. Divyapriya, P. Thangadurai, and I. Nambi, "Green approach to produce a graphene thin film on a conductive LCD matrix for the oxidative transformation of ciprofloxacin," *ACS Sustainable Chemistry & Engineering*, vol. 6, pp. 3453–3462, 2018.

[150] Q. Sun, J. Liu, Y. Peng, A. Wang, Z. Wu, and M. Chen, "Effective heat dissipation of high-power LEDs through creation of three-dimensional ceramic substrate with kaolin/graphene suspension," *Journal Of Alloys And Compounds.*, vol. 817, p. 152779, 2020.

[151] Y. Zhong, Z. Zhen, and H. Zhu, "Graphene: fundamental research and potential applications," *Flatchem*, vol. 4, pp. 20–32, 2017.

[152] T. Wang, D. Huang, Z. Yang et al., "A review on graphene-based gas/vapor sensors with unique properties and potential applications," *Nano-Micro Letters.*, vol. 8, no. 2, pp. 95–119, 2016.

[153] R. Singh, N. Kaur, and M. Singh, "Bio-compatible bio-fuel cells for medical devices," *Materials Today: Proceedings.*, vol. 44, pp. 242–249, 2021.

[154] M. Cao, J. Su, S. Fan, H. Qiu, D. Su, and L. Li, "Wearable piezoresistive pressure sensors based on 3D graphene," *Chemical Engineering Journal*, vol. 406, p. 126777, 2021.

[155] W. Zhang, C. Xu, C. Ma et al., "Nitrogen-superdoped 3D graphene networks for high-performance supercapacitors," *Advanced Materials*, vol. 29, no. 36, p. 1701677, 2017.

[156] R. Singh, A. Altaee, and S. Gautam, "Nanomaterials in the advancement of hydrogen energy storage," *Heliyon.*, vol. 6, article e04487, 2020.

[157] V. Silva, W. Fernandes-Junior, D. Rocha et al., "3D-printed reduced graphene oxide/polylactic acid electrodes: a new prototyped platform for sensing and biosensing applications," *Biosensors And Bioelectronics.*, vol. 170, p. 112684, 2020.

[158] B. Guo, G. Liang, S. Yu, Y. Wang, C. Zhi, and J. Bai, "3D printing of reduced graphene oxide aerogels for energy storage devices: a paradigm from materials and technologies to applications," *Energy Storage Materials.*, vol. 39, pp. 146–165, 2021.

[159] D. Xu, C. Xuan, X. Li et al., "Novel helical carbon nanotubes-embedded reduced graphene oxide in three- dimensional architecture for high-performance flexible supercapacitors," *Electrochimica Acta*, vol. 339, p. 135912, 2020.

[160] A. Smith, A. LaChance, S. Zeng, B. Liu, and L. Sun, "Synthesis, properties, and applications of graphene oxide/reduced graphene oxide and their nanocomposites," *Nano Materials Science.*, vol. 1, pp. 31–47, 2019.

Hindawi
Journal of Nanomaterials
Volume 2022, Article ID 4598887, 13 pages
https://doi.org/10.1155/2022/4598887

Research Article

Bio-Based Graphene Sheet/Copolymer Composite as Supporting Material for Nanocatalysts towards Electrochemical Studies and Direct Alkaline Alcohol Fuel Cells

V. Selvaraj,[1] **R. ThamilMagal**,[1,2] **V. Andal**,[3] **K. Arunkumar**,[1] **and Sivaraj Murugan**[4]

[1]*Nanotech Research Lab, Department of Chemistry, University College of Engineering, Kakuppam, Villupuram, 605 103 Tamilnadu, India*
[2]*Department of Chemistry, University College of Engineering, Panikkankuppam, Panruti, Tamilnadu, India*
[3]*Department of Chemistry, KCG College, Karapakkam, Tamil Nadu, Chennai, Tamilnadu, India*
[4]*Department of Mechanical Engineering, Institute of Technology, Hawassa University, Hawassa, Ethiopia*

Correspondence should be addressed to V. Selvaraj; vaithilingamselvaraj@gmail.com
and Sivaraj Murugan; msivaraj2014@gmail.com

Received 13 August 2021; Revised 14 October 2021; Accepted 9 December 2021; Published 6 January 2022

Academic Editor: Raul Arenal

Copyright © 2022 V. Selvaraj et al. This is an open access article distributed under the Creative Commons Attribution License, which permits unrestricted use, distribution, and reproduction in any medium, provided the original work is properly cited.

In this work, graphene carbon sheets (BGS) were prepared from writing paper and lemon peel, and its polymer composite has a higher surface area compared with the existing Vulcan carbon. Further, the use of lead as a promoter for the oxidation of alcohol and CO on platinum-supported poly(amine-terminated cyclophosphazene-co-cyclophosphazene)-biobased graphene sheet (Poly(AFCP-co-CP)-BGS) composite was demonstrated. The size, phase morphology, and distribution of metal nanoparticles on Poly(AFCP-co-CP)-BGS composite as well as the formation of composite based catalysts were confirmed from TEM, XRD, and FTIR studies. The catalytic activity and stability of the prepared catalysts were tested and compared to methanol, ethylene glycol, glycerol, and CO in 0.5 M KOH solution. The results conclude that the lead-doped Pt/Poly(AFCP-co-CP)-BGS catalyst shows higher oxidation current with respect to onset potential and lower I_f/I_r ratio for alcohol as well as CO oxidation. In addition, Pt-Pb/Poly(AFCP-co-CP)-BGS catalyst was checked for direct alkaline fuel cells and proved as a potent anode catalyst in alkaline medium for real-time fuel battery applications. In addition, Poly(AFCP-co-CP)-BGS composite also promotes the catalytic reaction compared to Poly(AFCP-co-CP) and BGS supports as noticed from methanol oxidation in alkaline medium. The surface area of the prepared supporting material is 750.72 m^2g^{-1}, which is higher than the activated carbon (250.12m^2g^{-1}). So, the prepared Poly(AFCP-co-CP)-BGS composite is a potent support for metal deposition, electrooxidation, and single stack fuel cell constructions.

1. Introduction

The increasing population, development in technology, modern culture, and sophisticated modern appliances require large quantity of power and increase the demand of power day by day. Almost 70 to 80% demand of power is being fulfilled by fossil fuel. However, the depletion of fossil fuel, scarcity, and its high cost are tempting the scientists to search some new energy resources. In this aspect, alkaline direct alcohol fuel cells (ADAFCs) have received much attention as they have more advantageous properties like improved methanol oxidation kinetics in alkaline than that of the acidic media. Further, they have low permeability of alcohol from anode to cathode and low-cost membranes [1, 2].

The developments of anode and cathode catalysts with better bustle as well as with decreased poison effects are the emerging area of research. In most of the cases, platinum and platinum-based nanoalloys (e.g., Pt-Ru, Pt-Au, Pt-Sn, and Pt-Pd) are frequently used as electrocatalysts in ADMFCs because of their high activities and stabilities [3–8]. But the high cost, scarcity, and poisonous effect of platinum catalyst limit its usefulness in commercial applications. In order to

decrease the platinum loading and to increase electrochemical performance for alcohol and CO oxidation, the studies are being performed using non-platinum-based catalysts and platinum loaded with appropriate support materials [9, 10]. The catalyst's activity and stability of alcohol oxidation in alkaline medium depend not only on the presence of metal nanoparticles but also on the properties of support material and interactions between the metal particles and support materials. Generally, conductive polymers [11]; carbon-based materials like graphene, carbon nanotubes, carbon fibers, and mesoporous carbon [12–15]; metal sulfides [16]; and zeolites [17] are used as catalyst supports for various applications.

The mesoporous carbon, a relatively new type of carbon-based material has become popular as an electrocatalyst support because of its large surface area, exceptional thermal and chemical durability, and stupendous electrical conductivity [18, 19]. Various nitrogen-doped carbon materials have been prepared recently as supports to promote the electrocatalytic activities of platinum-based catalysts for alcohol oxidation reactions (AOR) and oxygen reduction reaction [20–25] to be used in the applications of fuel cells. Recently, biobased carbons are used in various applications such as polymer composites [26–28], dye degradations, electromagnetic studies [29, 30], 3D printing [31], sensors, and electrocatalysts [32, 33]. Further, preparation, morphology, and electrochemical characterization of electrodeposited nanocrystalline Ni-Co [34], Au/Pt nanoanode [35], and ultrafine PtPd bimetallic nanoparticles [36] are studied for alcohol fuel cell applications. Generally, it has been found that the most frequently used methods for the preparation of nitrogen-doped carbon-based nanomaterials are pyrolysis and chemical vapour deposition (CVD). Alternatively, the nitrogen-containing pioneers like poly(indole), poly(pyrrole), and poly(aniline) have also been doped with carbon based materials via in situ polymerization procedure [37–41]. Advantages like uncomplicated preparation technique, producing more anchoring sites, and resulting improved conductivity can be derived from this procedure.

Having these points in mind, the present work has been initiated to prepare a composite-based hybrid supporting material containing both phosphorous and nitrogen along with biobased graphene carbon sheet. Moreover, lead nanoparticles have been doped on Pt/Poly(AFCP-co-CP)-BGS material to promote the catalytic activity of alcohol and CO oxidation in alkaline medium.

Typically, poly(amine-terminated cyclophosphazene-co-cyclophosphazene)-biobased graphene carbon sheet (Poly(-AFCP-co-CP)-BGS) composite was prepared through an in situ sonochemical method. To check the performance and promotion of catalytic activity of the prepared Poly(AFCP-co-CP)-BG composite, platinum nanocatalyst was coated on BGS, Poly(AFCP-co-CP), and Poly(AFCP-co-CP)-BGS. Various analytical methods such as X-ray diffraction (XRD), energy dispersive X-ray analysis (EDX), transmission emission spectroscopy (TEM), and Fourier Transform Infrared Spectroscopy (FTIR) were employed to characterized the metal nanoparticle-deposited Poly(AFCP-co-CP)-BGS composite catalysts. It was concluded from the electrochemical studies that the lead-doped Pt/Poly(AFCP-co-CP)-BG composite promotes both alcohol and CO oxidation reactions. To add further, Poly(AFCP-co-CP)-BGS composite also promotes the alcohol oxidation when compared with Poly(AFCP-co-CP) and BGS supports. It is suggested by the above results that both doping of lead as second metal and Poly(AFCP-co-CP)-BGS composite as support material promote the catalytic activity for alcohol and CO oxidation in fuel cell applications.

2. Materials and Methods

2.1. Materials. Hexachloroplatinic acid hexahydrate ($H_2PtCl_6.6H_2O$), lead(II)acetate trihydrate ($Pb(OAc)_2{\cdot}3H_2O$), formaldehyde, resorcinol, N,N′dimethyl sulfoxide, HCl, H_2SO_4, ethanol, methanol, ethylene glycol, glycerol, sodium hydroxide (NaOH), and triethylamine were purchased from SRL Chemicals, India. Hexachlorocyclotriphosphazene was purchased from Alfa Aesar, India. All the solvents were analytical grade and used as obtained from the chemical industries.

2.2. Preparation of Biobased Graphene Carbon Sheets. Using a modified reported procedure [42], biobased graphene carbon sheets (BGS) were prepared. BGS was prepared via a hydrothermal method by carbonization of waste materials such as waste writing paper (60%) and lemon peel (30 wt.%) using 50% dilute H_2SO_4 (170 mL) at 448 K. Typically, 6gm waste writing paper and 4 g of waste lemon peel materials was heated at 448 K with 50% dilute H_2SO_4 (170 mL) for 24 hours in an autoclave. When the hydrothermal reaction was completed, the autoclave was cooled and resulted product was filtered, washed with distilled water to remove excess acid. The washing was repeated until the filtrate became neutral. Finally, the resulted product was redispersed in the double distilled water and centrifuged to remove the ash material floating on the water if formed during the hydrothermal process. Finally, the filtered product was dried in a hot air oven. The dried product was ground into powder, and the resulted fine powder was immersed in KOH solution, which was then heated at 1093 K for 3 h in an inert atmosphere. The resultant biobased graphene powder was also washed with 20% HCl (*v*/*v*) to remove the inorganic impurities and then washed down with distilled water until the washed liquid became neutral pH. The biobased graphene carbon powder was dried in an oven at 70°C.

2.3. Preparation of Amine-Terminated Cyclotriphosphazene. The amine-terminated cyclotriphosphazene monomer was prepared as explained in our previous report [43, 44]. For this preparation, 4-acetamido phenol (15.65 g, 0.1035 mol) and K_2CO_3 (21.09 g, 0.15824 mol) were dispersed in dry acetone (200 mL) and effectively stirred at an ambient temperature for 45 minutes. To this mixture, hexachlorocyclotriphosphazene (5 g, 0.0143 mol) was added and refluxed at 60-65°C for 4 days. The product obtained as the result of the chemical reaction was cooled naturally to room temperature and filtered. The impure resulted sample (CPAC) was further purified using hexane and dried at 60°C for 3 h. It gave a yield of 63.8% and m.p. 253-256°C. The reaction mixture of hexa(acetamidophenyl)cyclotriphosphazene (9.0 g), methanol (180 mL), and sulfuric acid (108 mL) was taken in the

round bottom flask and refluxed for 4 h at 80-85°C. Then, the resultant reaction mixture was cooled to 25°C and then poured in to ice-cold water. To this, aqueous ammonia solution was added drop by drop until to reach pH = 8. The resulted solid product was filtered, washed with water, and dried at 60°C for 48 h.

2.4. Preparation of Poly(AFCP-co-CP)-BGS Composite. Poly(amine-terminated cyclophosphazene-co-cyclophosphazene)-biobased graphene carbon sheet (Poly(AFCP-co-CP)-BGS) composite-based support material was prepared using the modified procedure reported elsewhere [45]. For this copolymer-biobased graphene carbon sheet composite preparation, 58 mg of amine-terminated cyclophosphazene, and 116 mg cyclophosphazene were dissolved in 100 mL of N,N′-dimethyl sulfoxide (DMSO) solvent. With this reaction mixture, 10 mg of biobased graphene carbon sheet was added and dispersed utilizing ultrasonicator for 10 minutes. Finally, 4 mL of triethylamine was added to the above reaction mixture to start polymerization over graphene carbon sheet carbon, and the reaction was continued for another 12 hours under sonication (100 W, 40 kHz) at 30°C. The final resulted product was centrifuged, and the obtained Poly(AFCP-co-CP)-BGS composite was washed with ethanol followed by double distilled water and then dried at 50-60°C for 12 hours.

2.5. Preparation of Pt and Pt-Pb Nanoparticle-Deposited Poly(AFCP-co-CP)-Biobased Graphene Carbon Sheet Composites. Platinum-lead nanoparticle-deposited Poly(-AFCP-co-CP)-BGS catalyst (Pt-Pb/Poly(AFCP-co-CP)-BGS) was prepared by the formaldehyde reduction method [45]. For catalyst preparation, 70 mg Poly(AFCP-co-CP)-BGS composite was dispersed in 10 mL distilled water using an ultrasonic process for 30 minutes. 54 mg $H_2PtCl_6.6H_2O$ and 38 mg $Pb(OAc)_2$ $3H_2O$ dissolved in 40 mL of distilled water as a bimetallic catalyst precursor solution were added to the above suspension in drop by drop method and then pH was adjusted to 11 with 2.5 M NaOH solution. Stirring after about 30 minutes, 4 mL formaldehyde (37%) was added to the above solution at 85°C. The reduction reaction was continued for another five hours to dope platinum-lead nanoparticles on Poly(AFCP-co-CP)-BGS composite through an in situ codeposition method. The resulted Pt-Pb/Poly(AFCP-co-CP)-BGS solid was filtered, washed with distilled water, and then dried at 60°C for 8 hrs. Similarly, the platinum nanoparticles were deposited on Poly(AFCP-co-CP)-BGS composite (30 mg) by the HCHO (2 mL) reduction method with 54 mg of $H_2PtCl_6.6H_2O$ precursor to form Pt/Poly(AFCP-co-CP)-BGS catalyst by following same experimental procedure. To compare the efficiency of Poly(AFCP-co-CP)-BGS composite, the platinum nanoparticles were also deposited on Poly(AFCP-co-CP), biobased graphene carbon sheet (BGS) by following same experimental condition.

2.6. Fabrication of Working Electrodes. For the fabrication of working electrode, 5 mg of Pt-Pb/Poly(AFCP-co-CP)-BGS catalyst was dispersed in a mixture of 100 μL of 0.05% of Nafion solution and isopropanol (1 : 1) solution. A measured volume of 25 μL of this suspension was dropped on the top surface of the graphite electrode by using micropipette. The modified electrodes were used as working electrode for the electrooxidation of alcohol in alkaline medium. Similarly, the other catalysts Pt/Poly(AFCP-co-CP)-BGS, Pt/Poly(AFCP-co-CP), and Pt/BGS were also prepared by following the same procedure.

2.7. Characterization Techniques. To record the FT-IR spectra of the prepared samples, Perkin Elmer 6X FT-IR spectrometer was used. About 100 mg of optical grade KBr was grounded with sufficient quantity of the sample for making KBr pellets. Wide-angle X-ray spectra of the prepared samples were obtained using a Rich Seifert (Model 3000) diffractometer with CuKĮ radiation ($\theta = 0.15418$ nm), and the spectra were recorded from 0° to 80° at 2θ value. To characterize the size and phase morphology of the prepared catalyst, the AJEOLJEM-3010 analytical transmission electron microscope was used, which was operated at 300 kV with a measured point-to-point resolution of 0.23 nm. The HRTEM samples were prepared by dispersing the prepared catalyst in ethanol mounted on carbon coated copper grids and dried for 24 h at 25°C. A standard three-electrode glass cell equipped with prepared catalyst coated on graphite electrode was considered working, saturated calomel electrode was taken as reference, and platinum wire was used as counter electrode for the present investigation. Further, the electrocatalytic activity of alcohol oxidation was investigated in 0.5 M KOH and 0.5 M alcohol solution with a potential window of -1.0 to 0.3 V.

3. Results and Discussions

3.1. Fourier Transform Infrared Analysis of Poly(AFCP-co-CP) and Poly(AFCP-co-CP)-BGS Composite. Figure 1 shows the FT-IR spectra of Poly(AFCP-co-CP) and Poly(AFCP-co-CP)-BGS composite. The two bands observed at 3438 and 3338 cm^{-1} are corresponding to -NH stretching vibrations; in fact, they also ascertain the presence of AFCP material in Poly(AFCP-co-CP) copolymer (Figure 1). The peak noticed at 3043 cm^{-1} is assigned to ring C-H stretching vibration. The aromatic C-C stretching vibrations appear at 1507 and 1621 cm^{-1}. The typical stretching vibrations of P-O-Ph, P-N-P, and P-O-C appear at 1256, 1178, and 952 cm^{-1}, respectively. The aromatic C-H bending vibrations are visualized at 832 and 695 cm^{-1}.

Peaks with similar patterns are noticed for poly(amine-terminated cyclophosphazene-co-cyclophosphazene)-graphene carbon sheet composite. Further, it is noticed with a small shift in the wave number, which is due to the coating behavior of poly(amine-terminated cyclophosphazene-co-cyclophosphazene) copolymer on a biobased graphene carbon sheet.

3.2. BET Surface Analysis of the Prepared Poly(AFCP-co-CP)-BGS Supporting Materials. The surface area of biobased graphene carbon sheet-conductive copolymer (Poly(AFCP-co-CP)-BGS) was analyzed using the BET method. Figure 2 shows the N_2 adsorption-desorption measurements of the newly prepared biobased graphene carbon sheet-conductive

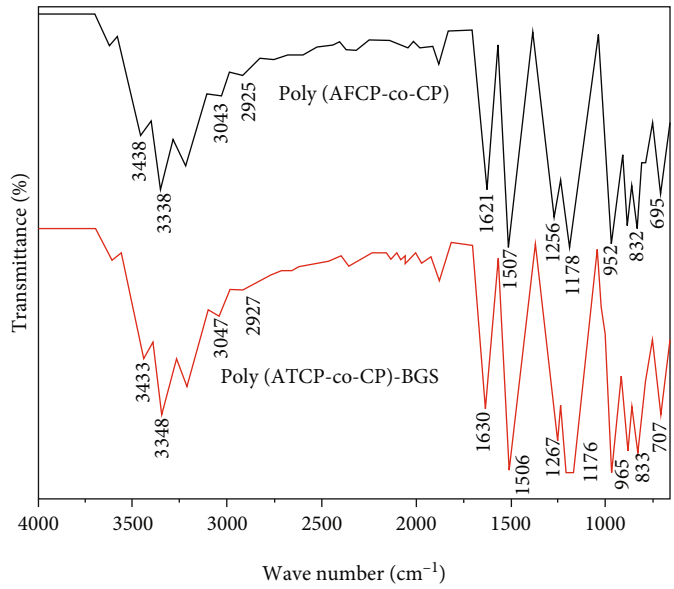

Figure 1: FTIR spectra of Poly(AFCP-co-CP) copolymer and Poly(AFCP-co-CP)-BGS composite.

copolymer composite. The adsorption-desorption curve in Figure 2 reveals a linear increase at low P/P_0 below 0.4. A hysteresis loop between $P/Po = 0.5$-0.9 is observed, which indicates the presence of graphene carbon sheet. The specific surface area of the BGS is determined to be 750.72 m^2 g^{-1} with a total pore volume of 0.318 cm^3 g^{-1} and an average pore diameter of 6.6592 nm.

According to a previous report [42], the specific surface area of Vulcan carbon black was determined to be 250.12 m^2 g^{-1} with a total pore volume of 2.31 cm^3 g^{-1}. The Poly(AFCP-co-CP)-BGS composite surface area was about three times larger that of the Vulcan carbon black. The high surface area determined by the BET method is correlated with improved catalytic activity. Therefore, the present study predicts that the catalytic activity of biobased Poly(AFCP-co-CP)-BGS composite should be superior to that of the Vulcan carbon blacks.

3.3. X-Ray Diffraction Analysis. XRD pattern of platinum nanoparticle-deposited Poly(AFCP-co-CP)-BGS composite shows three diffraction peaks at 2θ values of 39.25°, 45.25°, and 66.84° (Figure 3), which are matching to (111), (200), and (220) faces of the *fcc* platinum. The same type of pattern is noticed for Pt-Pb bimetallic nanoparticle-deposited Poly(-AFCP-co-CP)-BGS composite with the miniature shift to lower 2θ values with respect to Pt/Poly(AFCP-co-CP)-BGS composite. This is the atomic level displacement formation of bimetal Pt-Pb catalyst, and no other diffraction peaks that correspond to lead oxide/hydroxide are observed. Thus, XRD results obviously demonstrate that Pt-Pb nanoparticles are bimetallic and displacement in the crystalline structure is in the atomic level [43, 44].

3.4. Transmission Electron Microscope Analysis. TEM images of the platinum and platinum-lead nanoparticle-doped Poly(AFCP-co-CP)-BGS composites are shown in Figure 4. The prepared metal (Pt and Pt-Pb) nanoparticles have been well deposited as black dots on Poly(AFCP-co-CP)-BGS composite sheet without any aggregations. The presence of these homogeneously distributed nitrogen species on the surfaces of Poly(AFCP-co-CP)-BGS composite sheet could effectively provide good anchoring sites for the deposition of metal nanoparticles during the reduction process of their respective precursor metal salts, which favors small metal (Pt and Pt-Pb) nanoparticle formation with enhanced active surface area.

3.5. Cyclic Voltammetry Analysis. Cyclic voltammograms of platinum and platinum-lead nanoparticle-deposited Poly(AFCP-co-CP)-BGS electrodes have been carried out in 0.5 M KOH, 0.5 M KOH + 0.5 M methanol, 0.5 M KOH + 0.5 M ethylene glycol, and 0.5 M KOH + 0.5 glycerol solution at 50 mV s^{-1} (Figure 5).

From Figure 5(a), no change in the electroactive surface area of both Pt/Poly(AFCP-co-CP)-BGS and Pt-Pb/Poly(AFCP-co-CP)-BGS catalysts is noticed and they are nearly the same. Before entering into the detailed studies, it is essential to prove that Poly(AFCP-co-CP)-BGS support is better than the other support Poly(AFCP-co-CP) and BGS. To check the performances of the prepared Poly(AFCP-co-CP)-BGS support, platinum nanoparticle-deposited Poly(AFCP-co-CP)-BGS, Poly(AFCP-co-CP), and BGS catalysts have been subjected to the electrooxidation of methanol in alkaline medium.

Figure 5(b) shows the cyclic voltammograms of methanol in alkaline medium on platinum-deposited Poly(AFCP-co-CP)-BGS, Poly(AFCP-co-CP) and BGS catalysts. From Figure 5(b), it is found that the methanol oxidation peak current of Pt/Poly(AFCP-co-CP)-BGS catalyst is higher than that of the Pt/Poly(AFCP-co-CP) and Pt/BGS (Table 1). In addition, the Pt/Poly(AFCP-co-CP)-BGS exhibits lower onset potential than the Pt/Poly(AFCP-co-CP) and Pt/BGS catalysts. It has been concluded from this result that the Poly(-AFCP-co-CP)-BGS is a potent support than the Poly(AFCP-co-CP) and BGS. It is because of the integrated properties

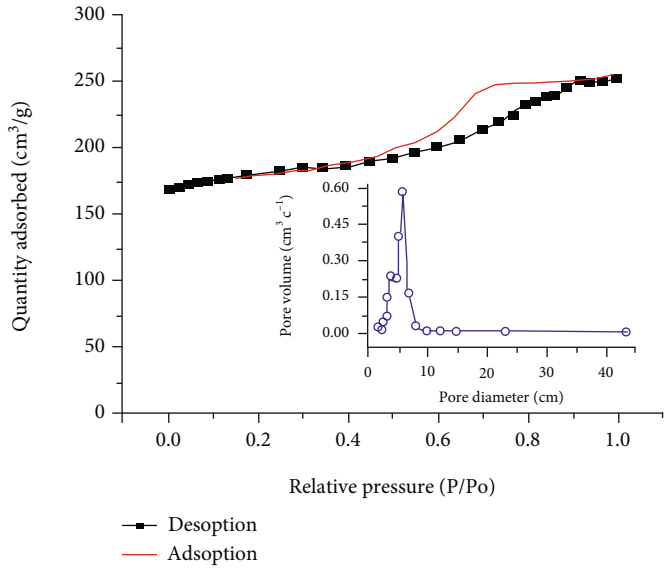

Figure 2: BET surface analysis of Poly(AFCP-co-CP)-BGS composite through nitrogen adsorption-desorption curves.

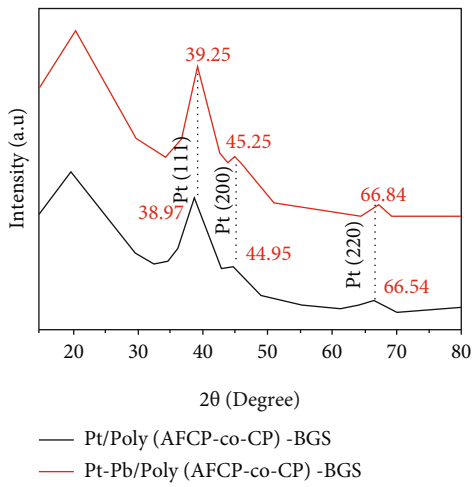

Figure 3: XRD patterns of Pt- and Pt-Pb-deposited Poly(AFCP-co-CP)-BGS composites.

resulted from noncovalent interaction between the BGS and Poly(AFCP-co-CP) in Poly(AFCP-co-CP)-BGS composite and the multifunctional groups (-NH, -O, and -P) present on Poly(AFCP-co-CP)-BGS acts as a better anchoring site for the uniform distribution of metal nanoparticles.

To promote the catalytic activity and to decrease the onset potential, the second metal lead (Pb) is added with Pt/Poly(AFCP-co-CP)-BGS catalyst. Hence, the prepared bimetal Pt-Pb/Poly(AFCP-co-CP)-BGS catalyst is analyzed for electrooxidation of methanol (Figure 5(b)). It has been noticed from the cyclic voltammetry results of lead particle-doped Pt/Poly(AFCP-co-CP)-BGS catalyst that both improved oxidation peak current and reduced onset potential values exist. The current density and onset potential of the prepared catalysts are given in Table 1. The improved performance of Pt-Pb/Poly(AFCP-co-PC)-BGS catalyst is because of the bifunctional mechanism of metal catalyst, electronic effect, and competitive adsorption of OH^- on lead nanoparticles surface. Further, Pb-OH is easily available near Pt-CO_{ads}/Pt-OOCH rather than Pt-OH, which can oxidize CO poison, $HCOO^-$, etc., at lower potential range or level and results in more platinum free active surface for further adsorption of alcohol and oxidation.

So, this work has been extended to the electrooxidation of ethylene glycol and glycerol in an alkaline medium on the prepared Pt/Poly(AFCP-co-CP)-BGS and Pt-Pb/Poly(-AFCP-co-CP)-BGS catalysts (Figures 5(c) and 5(d)). The electrochemical results confirm that Pt-Pb/Poly(AFCP-co-CP)-BGS catalyst exhibits higher oxidation current and lower onset potential for both ethylene glycol and glycerol in alkaline medium compared to Pt/Poly(AFCP-co-CP)-BGS catalyst (Table 1). Moreover, the oxidation current observed for ethylene glycol is higher than that of the oxidation current of methanol and glycerol. From the cyclic voltammetry analysis results, it has been concluded that the prepared Poly(AFCP-co-CP)-BGS composite is a good supporting material for metal catalysts.

In addition, the prepared Pt-Pb/Poly(AFCP-co-CP)-BGS catalyst shows better oxidation current for all the alcohols like methanol, ethylene glycol and glycerol, which may be due to the (i) electronic effect, (ii) interaction between metal nanoparticles and Poly(AFCP-co-CP)-BGS composite, (iii) ligand effect, (iv) low onset potential, (v) structural change of platinum in Pt-Pb/Poly(AFCP-co-CP)-BGS catalyst, and (vi) synergic interaction between the metal particles (Pt and Pb) [46]. Table 2 gives the comparative information of catalytic activity of the prepared catalysts and the literature reports, which highlights the novelty and superiority of the prepared composite electrodes.

3.5.1. Mechanism. Hand in hand with the previous literature reports, the enhancement due to the bimetallic system can be explained based on the byproduct formed during the

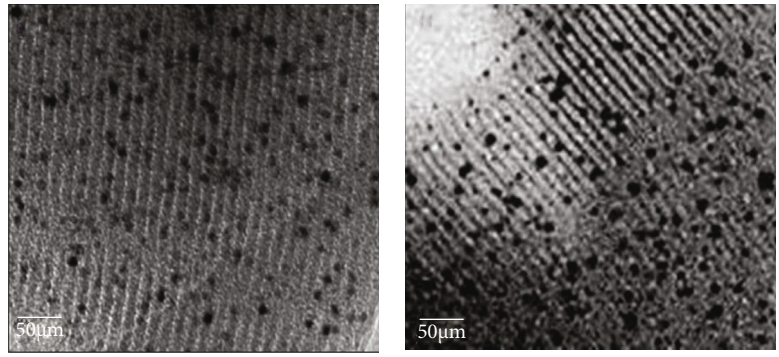

(a) (b)

Figure 4: HRTEM images of (a) Pt/Poly(AFCP-co-CP)-BGS and (b) Pt-Pb/Poly(AFCP-co-CP)-BGS composites.

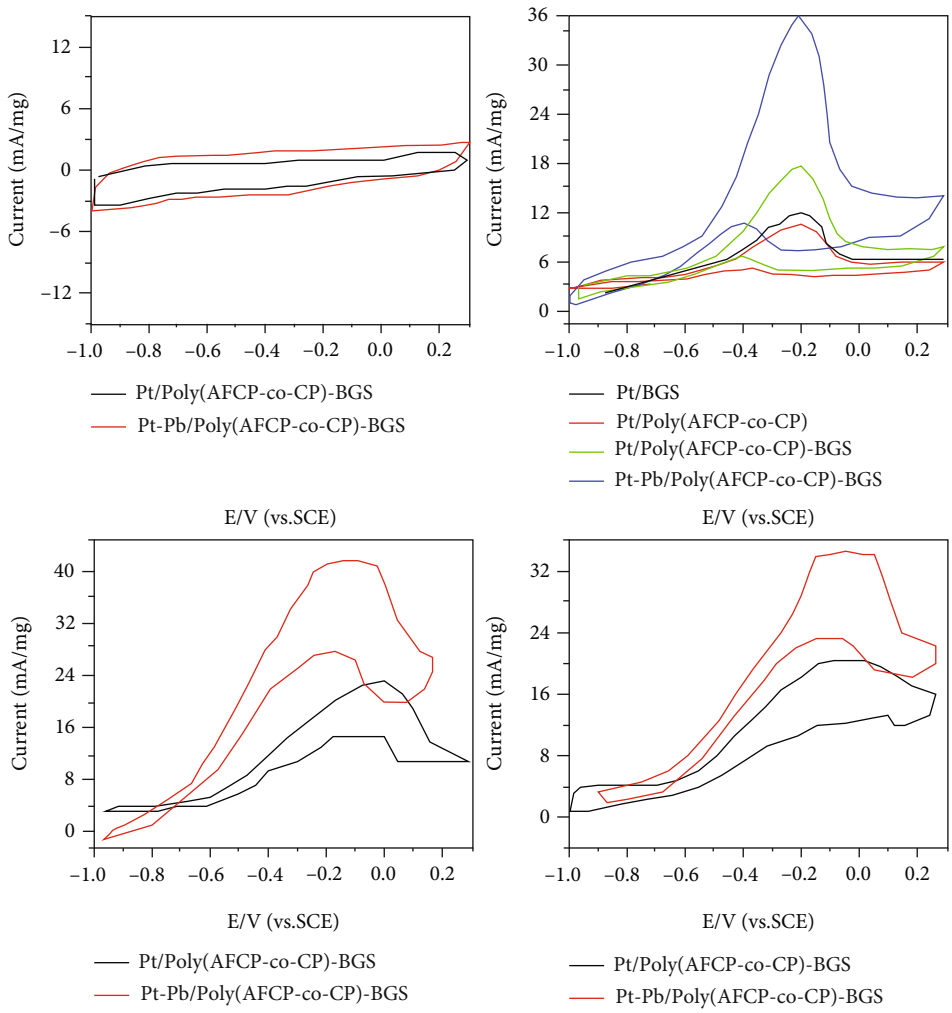

Figure 5: Cyclic voltammograms of Pt- and Pt-Pb-deposited Poly(AFCP-co-CP)-BGS electrodes in (a) 0.5 M KOH, (b) 0.5 M KOH + 0.5 M methanol, (c) 0.5 M KOH + 0.5 M ethylene glycol, and (d) 0.5 M KOH + 0.5 glycerol solution at 50 mV s^{-1}.

electrooxidation of alcohols. According to previous reports [54–56], the formic acid is the major by-product formed during the electrooxidation of methanol, ethylene glycol, and glycerol (Scheme 1).

The obtained formic acid and CO during the electrooxidation of methanol, ethylene glycol and glycerol on the surface of the metal nanoparticles can further undergo oxidation in the presence of oxygen rich species such as Pt-OH or Pb-OH as

Table 1: Oxidation peak current and onset potential of alcohol on various catalysts.

Catalysts	Methanol		Ethylene glycol		Glycerol	
	Current ($mAmg^{-1}$)	Onset potential (V)	Current ($mAmg^{-1}$)	Onset potential (V)	Current ($mAmg^{-1}$)	Onset potential (V)
Pt/BGS	6.58	-0.49	—	—	—	—
Pt/Poly(AFCP-co-CP)	8.62	-0.54	—	—	—	—
Pt/Poly(AFCP-co-CP)-BGS	15.14	-0.62	17.08	-0.83	14.63	-0.90
Pt-Pb/Poly(AFCP-co-CP)-BGS	36.72	-0.80	38.80	-0.95	30.83	-0.92

Table 2: Comparative studies of the present catalysts with the previous reports, which are carried out under similar experimental conditions.

S. no.	Catalysts	Current density (mA/cm^2)	Reference
1.	Pt/3D graphene	1.6	[47]
2.	Pt/PDDA/graphene	2.53	[48]
3.	Pt/3D graphene	2.5	[49]
4.	Pt/PDDA/GO	3.82	[50]
5.	Pt/CNT/graphene	11.1	[51]
6.	PtFe/graphene	3.55	[52]
7.	PtSn/graphene	16.21	[53]
8.	Pt/Poly(AFCP-co-CP)-BGS	15.14	Present work
9.	Pt-Pb/Poly(AFCP-co-CP)-BGS	36.72	Present work

given in the following equations (equations (1)–(4)), in accordance with the previous report [49]:

$$\mathrm{HCOO - Pt} \xrightarrow{\mathrm{Pt-OH}} \mathrm{CO_2 + H_2O} \quad (1)$$

$$\mathrm{HCOO - Pt} \underset{\mathrm{Pt/Pb-OH}}{\longrightarrow} \mathrm{CO_2 + H_2O + 2e^-} \quad (2)$$

$$\mathrm{Pt + OH^- \longrightarrow Pt - OH_{ads}} \xrightarrow{\mathrm{Pt-CO}} \mathrm{2\,Pt + H_2O + CO_2} \quad (3)$$

$$\mathrm{Pb + OH^- \longrightarrow Pb - OH_{ads}} \xrightarrow{\mathrm{Pt-CO}} \mathrm{Pb + Pt + H_2O + CO_2} \quad (4)$$

Here, the rate of oxidation is higher than in the case of bimetallic system (equations (2) and (4)) compared with monometallic system (equations (1) and (2)). This might be due to the easy formation of Pb-OH at lower potential and reduction of competition OH^- on platinum surface as in the case of bimetallic system. These two processes are expected to enhance the availability of oxygen near to a Pt-CO/Pt-OOCH species and make more number of free active surface area of platinum nanoparticles that are essential for adsorption and oxidation of further alcohol molecules [53].

3.6. Effect of Scan Rates. The diffusion property of alcohol and OH^{-1} ions during the electrooxidation process was checked for Pt- and Pt-Pb-deposited Poly(AFCP-co-CP)-BGS catalysts (Figure 6). From Figure 6, it has been visualized that the anodic oxidation current increases with the increase in the scan rates without changing the onset potential. The insert image in Figure 6 shows a linear relationship for anodic oxidation current obtained from forward CV scans with respect to the square root of different sweep rate, which means that the rate of electrooxidation of methanol, ethylene glycol, and glycerol on Pt/Poly(AFCP-co-CP)-BGS and Pt-Pb/Poly(AFCP-co-CP)-BGS catalysts are controlled by a diffusion process [56].

3.7. Chronoamperometric Analysis. In addition to the above electrochemical analysis, chronoamperometric analysis has also been carried out to test the electrocatalytic activity and stability of Pt and Pt-Pb nanoparticle-deposited Poly(-AFCP-co-CP)-BGS catalysts (Figure 7). From chronoamperometric results, it has been noticed that the steady-state oxidation currents have been observed within a few seconds for methanol, ethylene glycol, and glycerol in alkaline medium on both the electrodes. These results indicate that the metal nanoparticle-deposited Poly(AFCP-co-CP)-BGS composite shows good catalytic performance and stability, which are due to the uniform distribution of metal nanoparticles and chemical interaction between metal nanoparticles and Poly(AFCP-co-CP)-BGS composite.

3.8. CO Oxidation on Pt-Pb/Poly(AFCP-co-CP)-BGS and Pt/Poly(AFCP-co-CP)-BGS Catalysts. Further, CO oxidation has also been carried out in alkaline solution, which can be used to check the catalytic activity and CO resistance abilities of the prepared lead nanoparticle-doped Pt/Poly(AFCP-co-CP)-BGS catalyst at room temperature [57–60]. Figure 8 shows the CO electrooxidation on Pt-Pb/Poly(AFCP-co-CP)-BGS and Pt/Poly(AFCP-co-CP)-BGS catalysts. The lead nanoparticles doped Pt/Poly(AFCP-co-CP)-BGS catalyst shows enhanced CO electrooxidation current along with condensed onset potential than that of the Pt/Poly(AFCP-co-CP)-BGS catalyst. This observation substantiates that Pt-Pb/

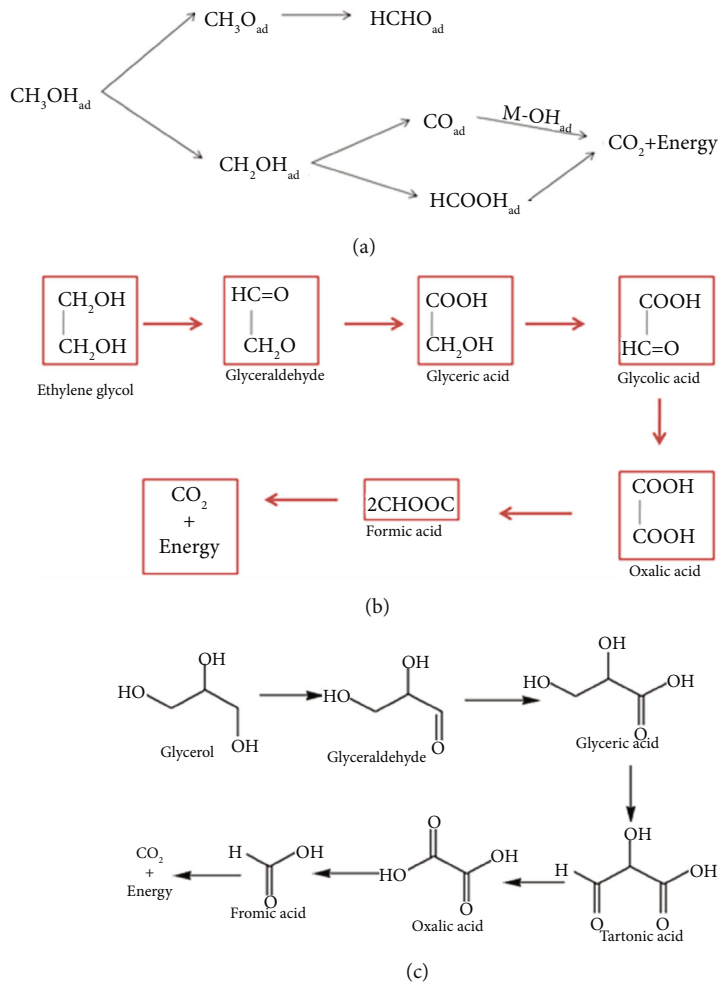

Scheme 1: Proposed mechanism for the cleavage of (a) methanol, (b) ethylene glycol, and (c) glycerol during the electrooxidation on the catalyst surface.

Poly(AFCP-co-CP)-BGS catalyst has more 'CO' tolerance. This result of carbon monoxide oxidation in alkaline medium also validate that the high catalytic activity and reduced poisonous effect of the Pt-Pb/Poly(AFCP-co-CP)-BGS catalyst compared to the Pt/Poly(AFCP-co-CP)-BGS catalyst.

3.9. Long-Term Stability and Storage Properties of the Prepared Catalysts. For the practical point of view, long-term stability of the prepared electrode materials is very important. The long-term stability of the prepared Pt/Poly(-AFCP-co-CP)-BGS and Pt-Pb/Poly(AFCP-co-CP)-BGS electrodes was examined in 0.5 M Methanol and 0.5 M NaOH solution (Figure 9) at a scan rate of 50 eV/s. It was observed that the oxidation peak current remains constant with the increase of the scan number at the initial stage. In the case of Pt/Poly(AFCP-co-CP)-BGS catalyst, the oxidation peak current starts decreasing (very small) after 100 numbers of scans.

The peak current density of the 500th scan is about 98.2% for Pt/Poly(AFCP-co-CP)-BGS catalyst than that of the first scan. In general, the small loss of the catalytic activity after successive number of scans may result from the consumption of methanol during the CV scan. It also may be due to poisoning effect and the structure change of the platinum nanoparticles as a consequence of the perturbation of the potentials during the scanning in aqueous solutions, particularly in the existence of methanol or any other organic fuel compounds [45, 61, 62]. Another characteristic might be due to the dispersion process happening between the surface of the electrode and the bulk solution.

With magnification of scan number, methanol disseminates gradually from the bulk solution to the surface of the electrode materials. In Pt-Pb/Poly(AFCP-co-CP)-BGS electrode, a sufficient enhancement was noticed, and the oxidation peak current decreased (very small) only after 250 numbers of scans. In Pt/Poly(AFCP-co-CP)-BGS, still, the electrode gets accumulated by COads poison, and hence, the anodic oxidation current decreases after the 100th scan itself showing a less stability. After the long-term electrocatalytic oxidation experiments, the Pt-Pb/Poly(AFCP-co-CP)-BGS and Pt/Poly(AFCP-co-CP)-BGS electrodes were stored in double distilled water for a week and electrooxidation of methanol was carried out. The excellent catalytic activities for the alcohol oxidations are still observed, which

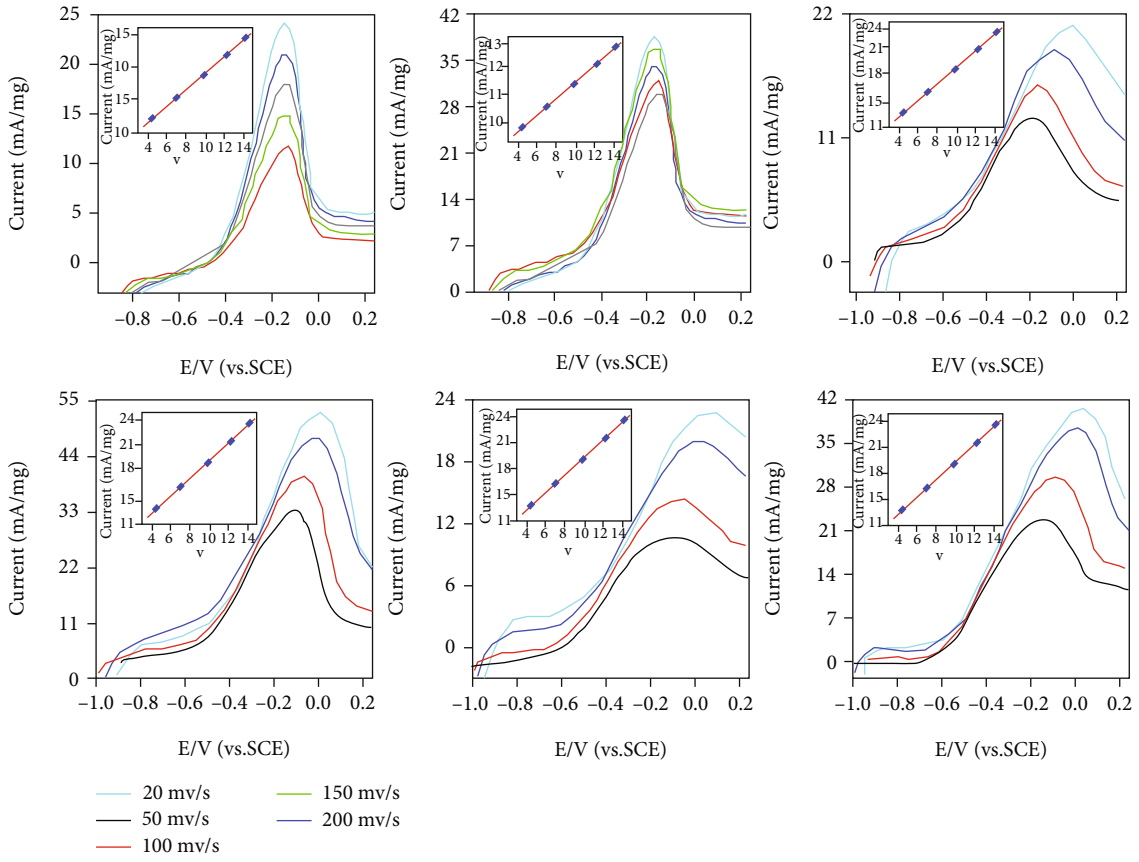

Figure 6: Effect of scan rate on Pt- and Pt-Pb-deposited Poly(AFCP-co-CP)-BGS catalysts for (i) 0.5 M methanol (a, b), (ii) 0.5 M ethylene glycol (c, d), and (iii) 0.5 M glycerol (e, f) in 0.5 M KOH solution. The inset graphs show the dependence of the anodic oxidation current with respect to the square root of scan rates.

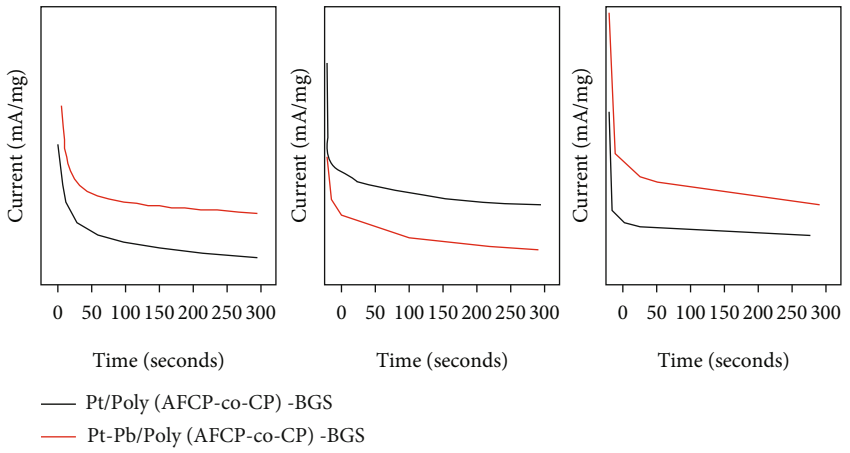

Figure 7: Chronoamperometric curves of Pt/Poly(AFCP-co-CP)-BGS and Pt-Pb/Poly(AFCP-co-CP)-BGS catalysts for (a) 0.5 M methanol, (b) 0.5 M ethylene glycol, and (c) 0.5 M glycerol in 0.5 M KOH solution.

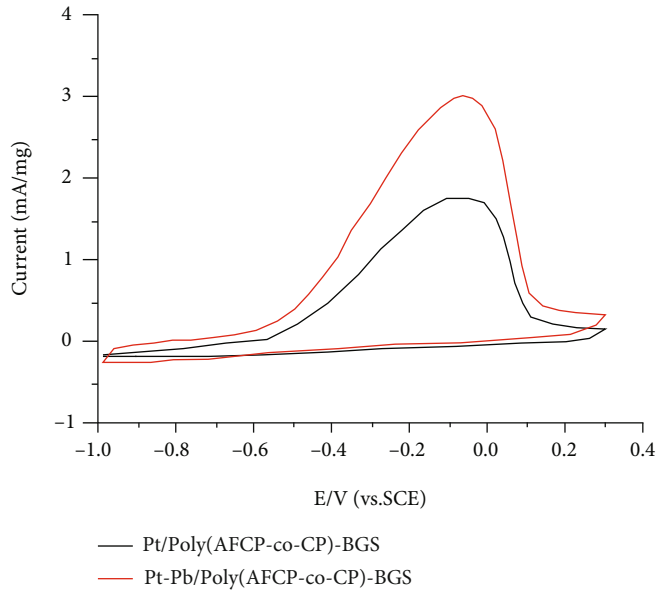

Figure 8: The electrooxidation of CO on the newly prepared Pt/Poly(AFCP-co-CP)-BGS and Pt-Pb/Poly(AFCP-co-CP)-BGS catalysts.

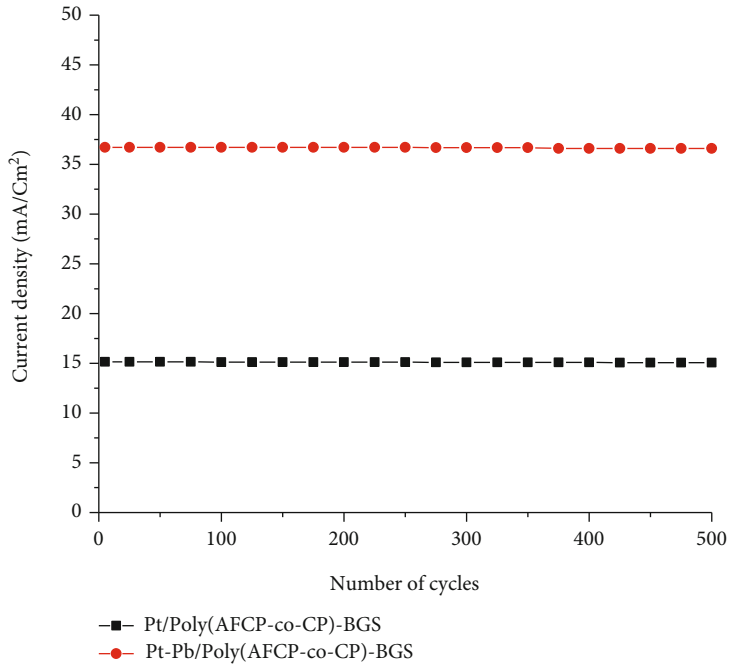

Figure 9: Long-term stability of the prepared Pt/Poly(AFCP-co-CP)-BGS and Pt-Pb/Poly(AFCP-co-CP)-BGS electrodes in 0.5 M methanol and 0.5 M NaOH solution at a scan rate of 50 eV/s.

indicate that the Pt/Poly(AFCP-co-CP)-BGS and Pt-Pb/Poly(AFCP-co-CP)-BGS composites prepared in the present experiment have good long-term stability and storage properties.

3.10. Direct Alkaline Alcohol Fuel Cell Studies. The single stack direct alkaline alcohol test fuel cell has been constructed to find out polarization and power density curve using Pt-Pb/Poly(AFCP-co-CP)-BGS catalyst as an anode in accordance with our previous report [61]. According to our previous studies [45, 61–63], polarization and power density have been measured at an optimum fuel concentration of 2.0 M in 1.0 M NaOH and at an optimum temperature of 70°C and their results are shown in Figure 10. The experimental results concluded that the direct alkaline ethylene glycol fuel cell has showed the maximum power density of 190 mW cm^{-2} at 70°C compared to methanol and glycerol, which has good agreement with cyclic voltammetric results.

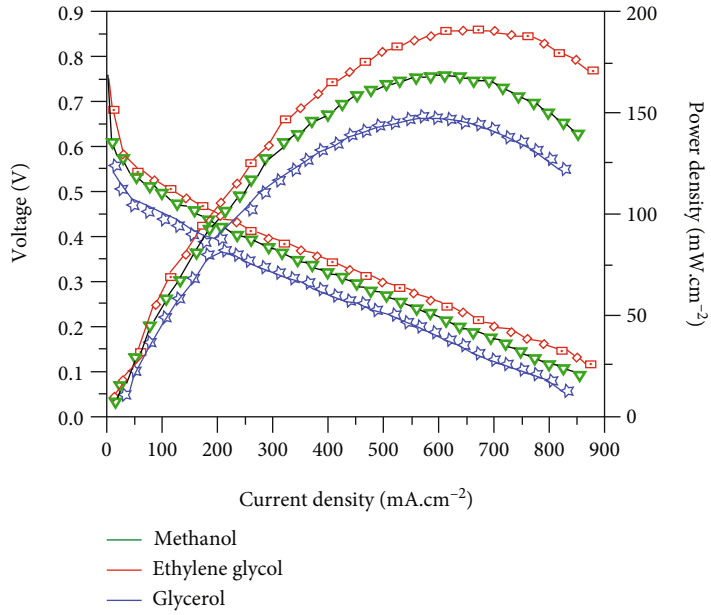

Figure 10: Polarization and current density curves of single stack fuel cell using Pt-Pb/Poly(AFCP-co-CP)-BGS as electrode material in (a) 1.0 M NaOH + 2.0 M CH_3OH, (b) 1.0 M NaOH + 2.0 M ethylene glycol, and (c) 1.0 M NaOH + 2.0 M glycerol at 70°C.

Hence, the prepared Pt-Pb/Poly(AFCP-co-CP)-BGS catalyst can be used to construct the alkaline alcohol fuel battery for commercial real-time practical applications.

4. Conclusion

Platinum-lead bimetallic nanoparticles have been loaded on Poly(AFCP-co-CP)-BGS composite through codeposition method to promote both electrooxidation of alcohol and CO oxidation, which are essential processes for fuel cell applications. Various characterizations have been carried out to determine the catalytic activity, particle size, shape, uniform distribution, and dispersion over the catalyst support. Pt-Pb/Poly(AFCP-co-CP)-BGS catalyst has shown enhanced oxidation current and lower onset potential for methanol, ethylene glycol, and glycerol oxidation in alkaline medium compared to Pt/Poly(AFCP-co-CP)-BGS catalyst. Moreover, Pt/Poly(-AFCP-co-CP)-BGS catalyst exhibits higher oxidation current for methanol compared with Pt/Poly(AFCP-co-CP) and Pt/BGS catalyst. It has been concluded from these results that the prepared Poly(AFCP-co-CP)-BGS support has been identified as a promising potent for electrocatalyst. Further, lead nanoparticle-deposited Pt/Poly(AFCP-co-CP)-BGS catalyst has been shown to improve CO oxidation and lower onset potential compared to Pt/Poly(AFCP-co-CP)-BGS catalyst. Hence, the above studies conclude that not only the Poly(-AFCP-co-CP)-BGS supporting material, but the introduction of lead also shows significant oxidation current for both alcohol and CO oxidation at a lower onset potential itself and thus reduces more CO catalytic poison effect.

Data Availability

All the data analyzed or used during this study are included within this article.

Conflicts of Interest

The authors declare that they have no conflicts of interest.

References

[1] S. Sen Gupta and J. Datta, "Electrode kinetics of ethanol oxidation on novel CuNi alloy supported catalysts synthesized from PTFE suspension," *Journal of Power Sources*, vol. 145, no. 2, pp. 124–132, 2005.

[2] Y. Xiong, Q. L. Liu, A. M. Zhu, S. M. Huang, and Q. H. Zeng, "Performance of organic-inorganic hybrid anion-exchange membranes for alkaline direct methanol fuel cells," *Journal of Power Sources*, vol. 186, no. 2, pp. 328–333, 2009.

[3] Y. Liu, H. Yang, X. Y. Li, and L. Q. Mao, "Pt nanoparticles supported on monodisperse carbon spheres for methanol oxidation in alkaline media," *Materials Letters*, vol. 106, pp. 287–289, 2013.

[4] C. W. Xu, L. Q. Cheng, P. K. Shen, and Y. L. Liu, "Methanol and ethanol electrooxidation on Pt and Pd supported on carbon microspheres in alkaline media," *Electrochemistry Communications*, vol. 9, no. 5, pp. 997–1001, 2007.

[5] Y. Hu, A. Zhu, C. Zhang, Q. Zhang, and Q. Liu, "Microwave-assisted synthesis of double-shell PtRu/TiO_2 catalyst towards methanol electro-oxidation," *International Journal of Hydrogen Energy*, vol. 40, no. 45, pp. 15652–15662, 2015.

[6] F. Ren, C. Zhai, M. Zhu et al., "Facile synthesis of PtAu nanoparticles supported on polydopamine reduced and modified graphene oxide as a highly active catalyst for methanol oxidation," *Electrochimica Acta*, vol. 153, pp. 175–183, 2015.

[7] G. Zhang, C. Huang, R. Qin et al., "Uniform Pd–Pt alloy nanoparticles supported on graphite nanoplatelets with high electrocatalytic activity towards methanol oxidation," *Journal of Materials Chemistry A*, vol. 3, no. 9, pp. 5204–5211, 2015.

[8] Y. Zhang, Y. Liu, W. Liu, X. Li, and L. Mao, "Synthesis of honeycomb-like mesoporous nitrogen-doped carbon

nanospheres as Pt catalyst supports for methanol oxidation in alkaline media," *Applied Surface Science*, vol. 407, pp. 64–71, 2017.

[9] P. K. Shen, Z. Yan, H. Meng et al., "Synthesis of Pd on porous hollow carbon spheres as an electrocatalyst for alcohol electrooxidation," *RSC Advances*, vol. 1, no. 2, pp. 191–198, 2011.

[10] C. Chen, Y. Li, and S. Liu, "Fabrication of macroporous platinum using monodisperse silica nanoparticle template and its application in methanol catalytic oxidation," *Journal of Electroanalytical Chemistry*, vol. 632, no. 1-2, pp. 14–19, 2009.

[11] V. Selvaraj, M. Alagar, and I. Hamerton, "Nanocatalysts impregnated polythiophene electrodes for the electrooxidation of formic acid," *Applied Catalysis B: Environmental*, vol. 73, no. 1-2, pp. 172–179, 2007.

[12] H. Liao, Z. Qiu, Q. Wan, Z. Wang, Y. Liu, and N. Yang, "Universal electrode Interface for Electrocatalytic oxidation of liquid fuels," *ACS Applied Materials & Interfaces*, vol. 6, no. 20, pp. 18055–18062, 2014.

[13] M. Liu, C. Peng, W. Yang et al., "Pd nanoparticles supported on three-dimensional graphene aerogels as highly efficient catalysts for methanol electrooxidation," *Electrochimica Acta*, vol. 178, pp. 838–846, 2015.

[14] P. Song, L. Zhu, X. Bo, A. Wang, G. Wang, and L. Guo, "Pt nanoparticles incorporated into phosphorus-doped ordered mesoporous carbons: enhanced catalytic activity for methanol electrooxidation," *Electrochimica Acta*, vol. 127, pp. 307–314, 2014.

[15] A. H. Lu, T. Sun, W. C. Li et al., "Synthesis of Discrete and dispersible hollow carbon nanospheres with high uniformity by Using Confined Nanospace pyrolysis," *Angewandte Chemie, International Edition*, vol. 50, no. 49, pp. 11765–11768, 2011.

[16] K. Kalpana and V. Selvaraj, "Development of ZnS/SnS/A-FA nanorods at ambient temperature: binary catalyst for the removal of Congo red dye and pathogenic bacteria from wastewater," *Journal of Industrial and Engineering Chemistry*, vol. 41, pp. 105–113, 2016.

[17] S. Durairaj and S. Vaithilingam, "Hydrothermal assisted synthesis of zeolite based nickel deposited poly(pyrrole-co-fluoro aniline)/CuS catalyst for methanol and sulphur fuel cell applications," *Journal of Electroanalytical Chemistry*, vol. 787, pp. 55–65, 2017.

[18] C. W. Zhang, L. B. Xu, N. N. Shan, T. T. Sun, J. F. Chen, and Y. S. Yan, "Enhanced electrocatalytic activity and durability of Pt particles supported on ordered mesoporous carbon spheres," *ACS Catalysis*, vol. 4, no. 6, pp. 1926–1930, 2014.

[19] S. Zhang, L. Chen, S. Zhou, D. Zhao, and L. Wu, "Facile synthesis of Hierarchically Ordered porous carbon viain SituSelf-Assembly of colloidal polymer and Silica Spheres and its use as a catalyst support," *Chemistry of Materials*, vol. 22, no. 11, pp. 3433–3440, 2010.

[20] H. W. Liang, X. Zhuang, S. Bruller, X. Feng, and K. Mullen, "Hierarchically porous carbons with optimized nitrogen doping as highly active electrocatalysts for oxygen reduction," *Nature Communications*, vol. 5, no. 1, p. 4973, 2014.

[21] Y. Liu, Y. M. Zhang, C. P. Zhai, X. Y. Li, and L. Q. Mao, "Nitrogen-doped porous carbons supported Pt nanoparticles for methanol oxidation in alkaline medium," *Materials Letters*, vol. 166, pp. 16–18, 2016.

[22] A. Navaee, A. Salimi, S. Soltanian, and P. Servati, "Facile one-pot synthesis of platinum nanoparticles decorated nitrogen-graphene with high electrocatalytic performance for oxygen reduction and anodic fuels oxidation," *Journal of Power Sources*, vol. 277, pp. 268–276, 2015.

[23] S. J. J. Jiang, L. Zhu, Y. W. Ma et al., "Direct immobilization of Pt-Ru alloy nanoparticles on nitrogen-dopedcarbon nanotubes with superior electrocatalytic performance," *Journal of Power Sources*, vol. 195, pp. 7578–7582, 2010.

[24] Y. Shao, J. Sui, G. Yin, and Y. Gao, "Nitrogen-doped carbon nanostructures and their composites as catalytic materials for proton exchange membrane fuel cell," *Applied Catalysis B, Environmental*, vol. 79, no. 1, pp. 89–99, 2008.

[25] L. M. Zhang, Z. B. Wang, J. J. Zhang, X. L. Sui, L. Zhao, and D. M. Gu, "Honeycomb-like mesoporous nitrogen-doped carbon supported Pt catalyst for methanol electrooxidation," *Carbon*, vol. 93, pp. 1050–1058, 2015.

[26] V. Selvaraj and T. R. Raghavarshini, "Development of high-performance hybrid sustainable bio-composites from biobased carbon reinforcement and cardanol-benzoxazine matrix," *Polymer Bulletin*, vol. 78, no. 8, pp. 4129–4148, 2021.

[27] V. Selvaraj, T. R. Raghavarshini, and M. Alagar, "Design and development of bio-carbon reinforced hetero structured biophenolics polybenzoxazine-epoxy hybrid composites for high performance applications," *Journal of Polymer Research*, vol. 28, no. 5, 2021.

[28] V. Selvaraj and T. R. Raghavarshini, "Building up of Prosopis juliflora carbon incorporated cardanol based polybenzoxazine composites with intensification of mechanical and corrosion resistance properties for adaptable applications," *Polymer Bulletin*, vol. 77, no. 12, pp. 6449–6466, 2020.

[29] X. Huang, B. Dai, Y. Ren, X. Jing, and P. Zhu, "Preparation and study of electromagnetic interference shielding materials comprised of Ni-Co coated on web-like biocarbon nanofibers via electroless deposition," *Journal of Nanomaterials*, vol. 2015, Article ID 320306, 7 pages, 2015.

[30] P. Bijesh, V. Selvaraj, and V. Andal, "A review on synthesis and applications of nano metal oxide/porous carbon composite," *Materials Today: Proceedings*, 2021.

[31] E. G. Ertane, A. Dorner-Reisel, O. Baran, T. Welzel, V. Matner, and S. Svoboda, "Processing and wear behaviour of 3D printed PLA reinforced with biogenic carbon," *Advances in Tribology*, vol. 2018, Article ID 1763182, 11 pages, 2018.

[32] K. Arunkumar and V. Selvaraj, "Development of livestock poultry waste based Ni-Co/S green nanocomposite catalysts: a facile one-pot in situ solvothermal method for alkaline methanol oxidation and super capacitor applications," *Ionics*, vol. 27, no. 8, pp. 3587–3603, 2021.

[33] S. Vaithilingam and T. M. Ramanujam, "Development of rice straw black liquor based porous carbon-poly (aniline-co-methoxy aniline) as supporting for electrochemical performances of alcohol oxidations," *Ionics*, vol. 24, no. 12, pp. 3923–3935, 2018.

[34] R. Abdel-Karim, M. Ramadan, and S. M. El-Raghy, "Morphology and electrochemical characterization of electrodeposited nanocrystalline Ni-Co electrodes for methanol fuel cells," *Journal of Nanomaterials*, vol. 2018, Article ID 9870732, 13 pages, 2018.

[35] I. M. Al-Akraa, Y. M. Asal, and A. M. Mohammad, "Facile synthesis of a tailored-designed Au/Pt nanoanode for enhanced formic acid, methanol, and ethylene glycol electrooxidation," *Journal of Nanomaterials*, vol. 2019, Article ID 2784708, 9 pages, 2019.

[36] T. Xia, H. Shen, G. Chang et al., "Facile and rapid synthesis of ultrafine PtPd bimetallic nanoparticles and their high

performance toward methanol electro-oxidation," *Journal of Nanomaterials*, vol. 2014, Article ID 496249, 7 pages, 2014.

[37] S. Chao, Q. Cui, Z. Bai, K. Wang, and L. Yang, "Template-free synthesis of hierarchical peanut-like Co and N codoped porous carbon with highly efficient catalytic activity for oxygen reduction reaction," *Electrochimica Acta*, vol. 177, pp. 79–85, 2015.

[38] M. Sevilla, L. Yu, T. Fellinger, A. Fuertes, and M. M. Titirici, "Polypyrrole-derived mesoporous nitrogen-doped carbons with intrinsic catalytic activity in the oxygen reduction reaction," *RSC Advances*, vol. 3, no. 25, pp. 9904–9910, 2013.

[39] G. Wang, Y. Sun, D. Li et al., "Controlled Synthesis of N-doped carbon nanospheres with tailored Mesopores through Self-Assembly of colloidal silica," *Angewandte Chemie, International Edition*, vol. 54, no. 50, pp. 15191–15196, 2015.

[40] K. Gong, F. Du, Z. Xia, M. Durstock, and L. Dai, "Nitrogen-doped carbon Nanotube Arrays with high electrocatalytic activity for oxygen reduction," *Science*, vol. 323, no. 5915, pp. 760–764, 2009.

[41] Y. Xue, B. Wu, L. Jiang et al., "Low temperature growth of highly nitrogen-doped single crystal Graphene arrays by chemical vapor deposition," *Journal of the American Chemical Society*, vol. 134, no. 27, pp. 11060–11063, 2012.

[42] K. Kim, M. P. Kim, and W.-G. Lee, "Preparation and evaluation of mesoporous carbon derived from waste materials for hybrid-type Li-air batteries," *New Journal of Chemistry*, vol. 41, no. 17, pp. 8864–8869, 2017.

[43] K. Krishnadevi and V. Selvaraj, "Development of halogen-free flame retardant phosphazene and rice husk ash incorporated benzoxazine blended epoxy composites for microelectronic applications," *New Journal of Chemistry*, vol. 39, no. 8, pp. 6555–6567, 2015.

[44] K. Krishnadevi, V. Selvaraj, and D. Prasanna, "Thermal, mechanical and antibacterial properties of cyclophosphazene incorporated benzoxazine blended bismaleimide composites," *RSC Advances*, vol. 5, no. 2, pp. 913–921, 2015.

[45] D. Prasanna and V. Selvaraj, "Development of ternary hexafluoroisopropylidenedianiline/cyclophosphazene/benzidine-disulfonic acid- carbon nanotubes (HFPA/CP/BZD-CNT) composite as a catalyst support for high performance alcohol fuel cell applications," *Electrochimica Acta*, vol. 190, pp. 668–677, 2016.

[46] M. Gong, F. Li, Z. Yao et al., "Highly active and durable platinum-lead bimetallic alloy nanoflowers for formic acid electrooxidation," *Nanoscale*, vol. 7, no. 11, pp. 4894–4899, 2015.

[47] X. D. ThandavarayanMaiyalagan, P. Chen, and X. Wang, "Electrodeposited Pt on three-dimensional interconnected grapheneasa free-standing electrode for fuel cell application," *Journal of Materials Chemistry*, vol. 22, pp. 5286–5290, 2012.

[48] J.-D. Qiu, G.-C. Wang, R.-P. Liang, X.-H. Xia, and H. W. Yu, "Controllable deposition of platinum nanoparticles on graphene as an electrocatalyst for direct methanol fuel cells," *Journal of Physical Chemistry C*, vol. 115, no. 31, pp. 15639–15645, 2011.

[49] H. Qiu, X. Dong, B. Sana et al., "Ferritin-templated synthesis and self-assembly of Pt Nanoparticles on a monolithic porous graphene network for Electrocatalysis in Fuel cells," *ACS Applied Materials & Interfaces*, vol. 5, no. 3, pp. 782–787, 2013.

[50] J. Y. Park and S. Kim, "Preparation and electroactivity of polymer-functionalized graphene oxide- supported platinum nanoparticles catalysts," *International Journal of Hydrogen Energy*, vol. 38, no. 14, pp. 6275–6282, 2013.

[51] J.-Y. Jhan, Y.-W. Huang, C.-H. Hsu, H. Teng, D. Kuo, and P.-L. Kuo, "Three-dimensional network of graphene grown with carbon nanotubes as carbon support for fuel cells," *Energy*, vol. 53, pp. 282–287, 2013.

[52] X. Y. BaominLuo, J. Chen, S. Xu, and Q. Xue, "PtFe nanotubes/graphene hybrid: facile synthesisand its electrochemical properties," *International Journal of Hydrogen*, vol. 38, pp. 13011–13016, 2013.

[53] F. Han, X. Wang, J. Lian, and Y. Wang, "The effect of Sn content on the electrocatalytic properties of Pt-Sn nanoparticles dispersed on graphene nanosheets for the methanol oxidation reaction," *Carbon*, vol. 50, no. 15, pp. 5498–5504, 2012.

[54] R. Nagao, D. A. Cantane, F. H. B. Lima, and H. Varela, "The dual pathway in action: decoupling parallel routes for CO_2 production during the oscillatory electro-oxidation of methanol," *Physical Chemistry Chemical Physics*, vol. 14, no. 23, pp. 8294–8298, 2012.

[55] H. Yue, Y. Zhao, X. Ma, and J. Gong, "Ethylene glycol: properties, synthesis, and applications," *Chemical Society Reviews*, vol. 41, no. 11, pp. 4218–4244, 2012.

[56] Z. Zhang, L. Xin, J. Qi, Z. Wang, and W. Li, "Selective electroconversion of glycerol to glycolate on carbon nanotube supported gold catalyst," *Green Chemistry*, vol. 14, no. 8, pp. 2150–2152, 2012.

[57] E. A. Baranova, M. A. Padilla, B. Halevi, T. Amir, K. Artyushkova, and P. Atanassov, "Electrooxidation of ethanol on PtSn nanoparticles in alkaline solution: correlation between structure and catalytic properties," *Electrochimica Acta*, vol. 80, pp. 377–382, 2012.

[58] E. Antolini and E. R. Gonzalez, "The electro-oxidation of carbon monoxide, hydrogen/carbon monoxide and methanol in acid medium on Pt-Sn catalysts for low-temperature fuel cells: a comparative review of the effect of Pt-Sn structural characteristics," *Electrochimica Acta*, vol. 56, no. 1, pp. 1–14, 2010.

[59] Y. Sun, C. Du, M. An et al., "Boron-doped graphene as promising support for platinum catalyst with superior activity towards the methanol electrooxidation reaction," *Journal of Power Sources*, vol. 300, pp. 245–253, 2015.

[60] J. Sun, J. Shi, J. Xu, X. Chen, Z. Zhang, and Z. Peng, "Enhanced methanol electro-oxidation and oxygen reduction reaction performance of ultrafine nanoporous platinum–copper alloy: Experiment and density functional theory calculation," *Journal of Power Sources*, vol. 279, pp. 334–344, 2015.

[61] P. Dakshinamoorthy and S. Vaithilingam, "Platinum–copper doped poly(sulfonyldiphenol/cyclophosphazene/benzidine)–graphene oxide composite as an electrode material for single stack direct alcohol alkaline fuel cells," *RSC Advances*, vol. 7, no. 56, pp. 34922–34932, 2017.

[62] D. Prasanna and V. Selvaraj, "Cyclophosphazene based conductive polymer-carbon nanotube composite as novel supporting material for methanol fuel cell applications," *Journal of Colloid and Interface Science*, vol. 472, no. 15, pp. 116–125, 2016.

[63] D. Saranya and V. Selvaraj, "Double metal oxide based nickel hybrid nanocatalyst for electrooxidation and alkaline fuel cell device fabrication," *International Journal of Hydrogen Energy*, vol. 43, no. 29, pp. 13450–13461, 2018.

Hindawi
Journal of Nanomaterials
Volume 2021, Article ID 7739359, 9 pages
https://doi.org/10.1155/2021/7739359

Research Article

Influence of Process Parameter on Carbon Nanotube Field Effect Transistor Using Response Surface Methodology

Mohana SundaramK,[1] **P. Prakash**,[2] **S. Angalaeswari**,[3] **T. Deepa**,[3] **L. Natrayan**,[4] **and Prabhu Paramasivam**[5]

[1]*Department of EEE, KPR Institute of Engineering and Technology, Coimbatore 641402, India*
[2]*-Department of ECE, Madha Engineering College, 600070, Chennai, India*
[3]*School of Electrical Engineering, Vellore Institute of Technology, Chennai, India*
[4]*-Department of Mechanical Engineering, Saveetha School of Engineering, SIMATS, Chennai, 602105 Tamil Nadu, India*
[5]*Department of Mechanical Engineering, College of Engineering and Technology, Mettu University, Ethiopia -318*

Correspondence should be addressed to P. Prakash; mp.prakash09@gmail.com, L. Natrayan; natrayanphd@gmail.com, and Prabhu Paramasivam; prabhuparamasivam21@gmail.com

Received 8 September 2021; Revised 25 October 2021; Accepted 29 November 2021; Published 15 December 2021

Academic Editor: Lakshmipathy R

Copyright © 2021 Mohana SundaramK et al. This is an open access article distributed under the Creative Commons Attribution License, which permits unrestricted use, distribution, and reproduction in any medium, provided the original work is properly cited.

Carbon nanotube field-effect transistor (CNTFET) is a good option to replace silicon for low power consumption application. Recent research shows that CN-FET thermal and electrical properties alter with length, diameter, and gate parameters. Optimization of CNTFET design parameters helps control some of the factors. Double gate and cylindrical gate layouts are introduced to overcome these facts. Carbon nanotubes have an intercapacitance between them that increases as their diameter increases. Total capacitance and inductance of CNTFETs increase with nanotube count. In order to reduce the voltage drop between semiconducting and metallic terminals, the diameter and pitch must be raised. This study employs response surface methodology and ANOVA technique that were used to optimize CNTFET process parameters. Thickness, voltage, delay, and power were all considered. The most affecting parameter was investigated.

1. Introduction

CNTFETs have been proposed as CMOS device changeover. It only needs to be combined with high-k dielectric CMOS technology to have other device characteristics. CNTFET is a three-terminal device made up of semiconducting nanotubes that connect the source and drain and act as a carrier channel. It can be electrostatically connected via the third contact (gate). Ding et al. investigated an FDSOI nMOSFET manufactured using a similar technique under the same irradiation environment and bias during irradiation comparison. They also explained how to compare experimental and simulated curves for a fresh TFET with a simulated curve for a TFET irradiated [1]. Sanchez Esqueda et al. demonstrated the development of radiation-induced oxide trapped charge and the production of interface traps in bulk MOSFETs, SOI MOSFETs, and SOI MOSFETs. They also brilliantly explained that the minimum data retention voltage (DRV) as a function of PMOS stress-induced trap building got results from simulations before and after including total ionizing dose (TID) effects as edge leakage in NMOS devices [2]. Ning and Zhang compared the off-state leakage current for I/O FB and TB devices under ON and OFF bias settings. They also looked at the back-gate threshold voltage shift for core FB and TB devices when the bias was turned off. For the core FB and TB devices, they specifically indicated simulated body potential with the channel length (horizontal direction) at the middle depth of the body area and simulated electric field strength (EY) along with the depth (vertical direction) at the middle depth of the BOX under OFF bias condition [3].

Table 1: Design of experiments for CNTFET.

Thickness (nm)	Voltage (V)
32	0.2
32	0.4
32	0.6
22	0.2
22	0.4
22	0.6
10	0.2
10	0.4
10	0.6

Table 2: Design of experiment of CNTFET with outputs.

Thickness (nm)	Voltage (V)	Delay (Ns)	Power (Nw)
32	0.2	1.25	4.789
32	0.4	1.29	4.6
32	0.6	1.34	4.897
22	0.2	1.27	4.9
22	0.4	1.28	4.91
22	0.6	1.97	4.9
10	0.2	1.87	4.91
10	0.4	2.4	4.92
10	0.6	2.15	4.9

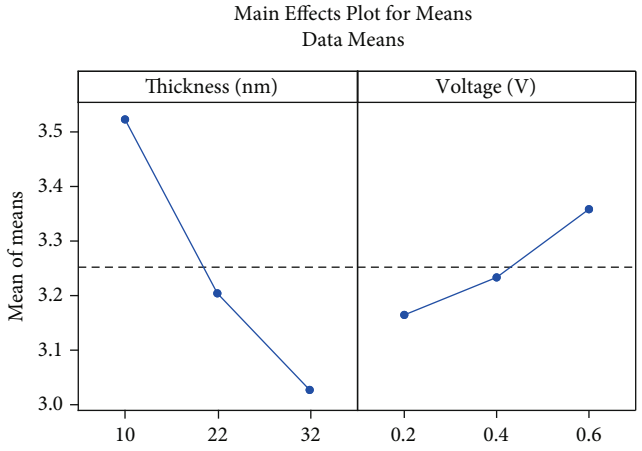

Figure 1: Main effect plot for means.

Cress et al. described ionizing dose-hardened CNT transistors with silicon oxynitride gate dielectrics. The irradiation impact causes substantial error operation in the CNTFET integrated circuit. The threshold voltage shift also appears to confirm the device structure in a radiation environment [4]. A CNT network between the source and drain electrodes was irradiated with gamma rays. They exhibited the device's I-V characteristics before and after 50 kGy irradiation, with VGS ranging from -20 to +20 V at VDS = −1 V and the averaged Vth dose-dependence. The averaged N (difference between before and 10 hours after irradiation) dose-dependency ranges from 5 to 50 kGy [5]. It was clearly stated by Avouris et al. Carbon electronics has been identified as a promising candidate for the next generation of electronics and nanodevices [6]. Tang et al. demonstrated that nanotube-based dosimeters could detect ionizing radiation like 6 MV therapeutic X-rays with greater sensitivity than MOSFET devices. They concluded that the gadget retained its form and functionality after radiation exposure and that the nanotubes were not damaged [7].

Schrimpf et al. convincingly demonstrated graphs of gate voltage vs. drain current for various relationships and concluded that total-ionizing-dose effects were, on average, less severe for substantially scalable technologies as opposed to preceding methods [8]. Cress et al. distinguished the transfer properties of a back-gated graphene-FET with incremental total ionizing radiation, the same device after 15 minutes of air exposure, and the same device with an additional total ionizing dose (TID). They also highlighted field-effect mobility as a function of TID for a graphene-FET irradiated in vacuum and air and the least amount conductivity for transfer characteristics estimated in a vacuum. The graph drain current vs. gate voltage also clearly demonstrated graphene transistors exposed to varied total ionizing doses [9]. Zhang et al. precisely described how CNTFET devices respond to electrical stress and cycling. They also demonstrated the current drain ID as a function of gate voltage VG for a variety of total doses using an irradiation gate bias of +10 V, as well as the postirradiation annealing time following irradiation to a whole dosage of 1 Mrad (SiO2), likewise with a functional gate bias of +10 V [10].

Baligidada et al. undoubtedly investigated the effects of restrictions such as the thickness of layer, power derived from the heater, and heater supply rate on properties like storage modulus and loss modulus of several test samples. They also recommended using CCD-RSM to optimize process settings for better mechanical qualities of polyamide parts [11]. Yang and Tarng used orthogonal array, signal-to-noise ratio, and ANOVA to optimize cutting parameters for turning operations and concluded that rotating improved tool life and surface roughness. Tool life and surface roughness were about 225% ideal cutting parameters [12]. Lipin and Govindan briefly described Taguchi methods for designing experiments and investigating records for optimizing processing conditions utilizing orthogonal arrays. They showed the influence of factors on MRR and surface roughness. They concluded that the Taguchi approach could improve tool life, surface roughness, cutting force, and overall productivity [13].

dos Santos et al. demonstrated that the independent variables' uncoded and coded levels were related to synthesis. The independent variables and experimental values of response variables for the central composite also demonstrated that design was connected to synthesis. They stated that they performed ANOVA on the degree of the variable response of quarterization, intrinsic viscosity, and reaction yield correlated to the synthesis of N-(2-hydroxy)-propyl-3-trimethylammonium chitosan chloride, as well as on the temperatures and corresponding weight losses related to the thermal degradation of chitosan and samples, among other things [14]. Tsao and colleagues described the primary

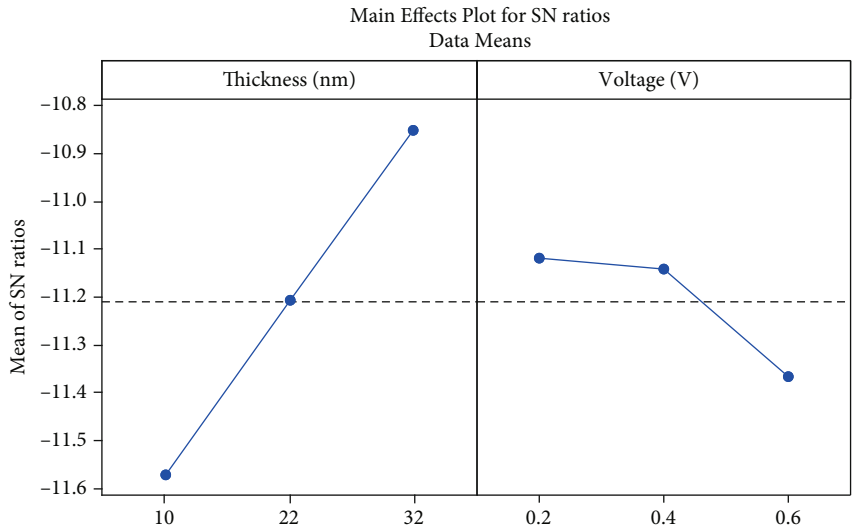

Figure 2: Primary effect plot for SN ratios.

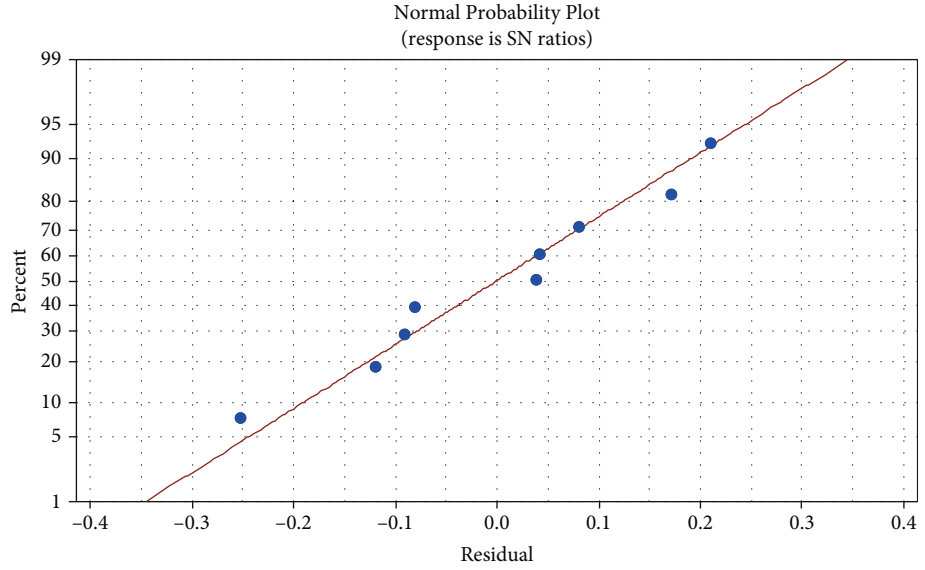

Figure 3: Normal plot of residuals for SN ratios.

elements experimentally impacting hole quality in drilling, such as cutting speed, temperature, feed rate, and geometrical parameters, and the influence of manipulating the cutting conditions and temperature on the tool life [15].

2. Methods and Methodology

Response surface methodology (RSM) is a collection of mathematics and arithmetic tools for assembling experimental representations. The goal of a suspicious proposal of experiments is to maximize a response such as an output variable subjective by numerous self-governing variables such as input variables. A series of tests are conducted in which the input variables are changed to identify the motivation for changes in the output response. In this configuration, the input parameters were thickness and voltage, whereas the desired output parameters were delay and power. Table 1 displays the various thickness and voltage input parameter ranges. The related delay and power values of thickness and voltage for CNTFETs are shown in Table 2.

3. Result and Discussion

The findings of the experiment were analysed for CNTFET based on the design of the experiment. Figure 1 depicts the main effect plot for means, highlighting the relationship between the mean of the mean and the thickness of the CNTFET and the link between the mean of the mean and the voltage utilized for the same. The mean was directly proportional to voltage and inversely proportional to thickness

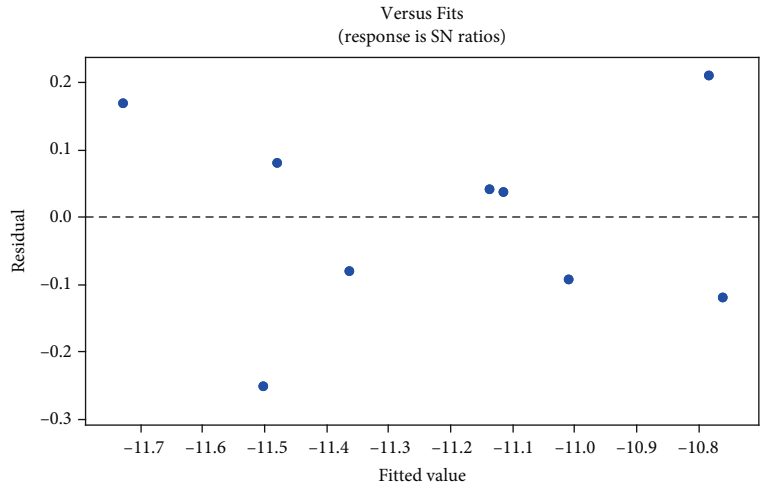

Figure 4: Residuals vs. fits for SN ratios.

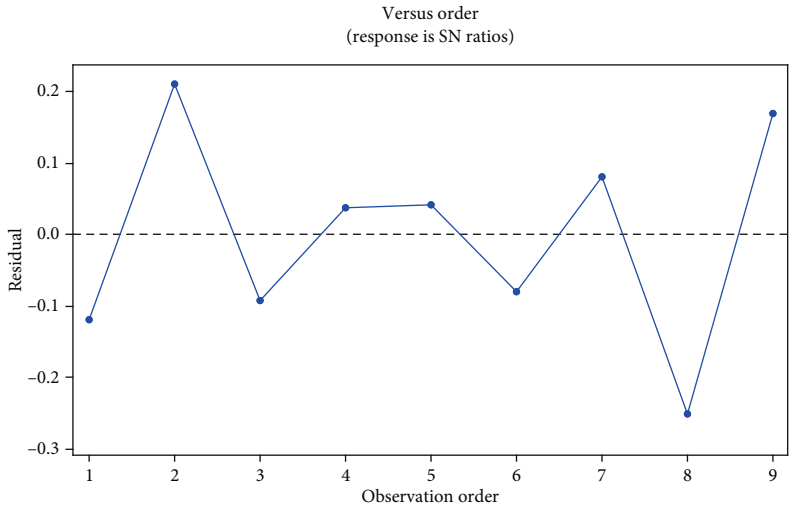

Figure 5: Residuals vs. order for SN ratios.

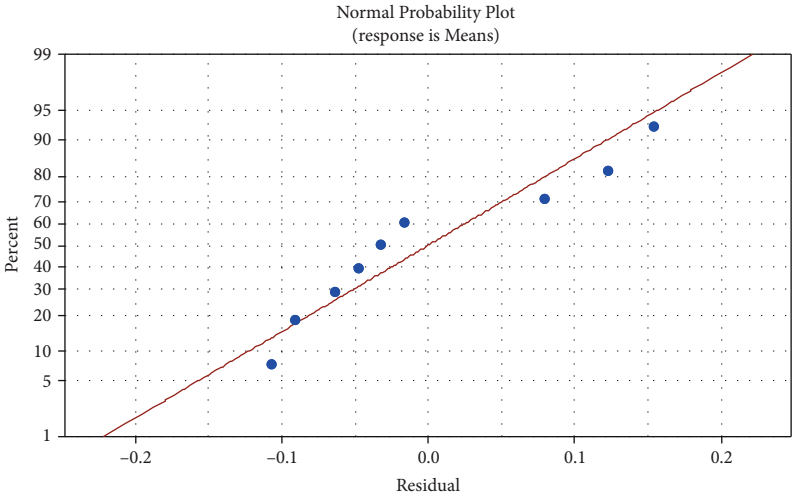

Figure 6: Normal plot of residuals for means.

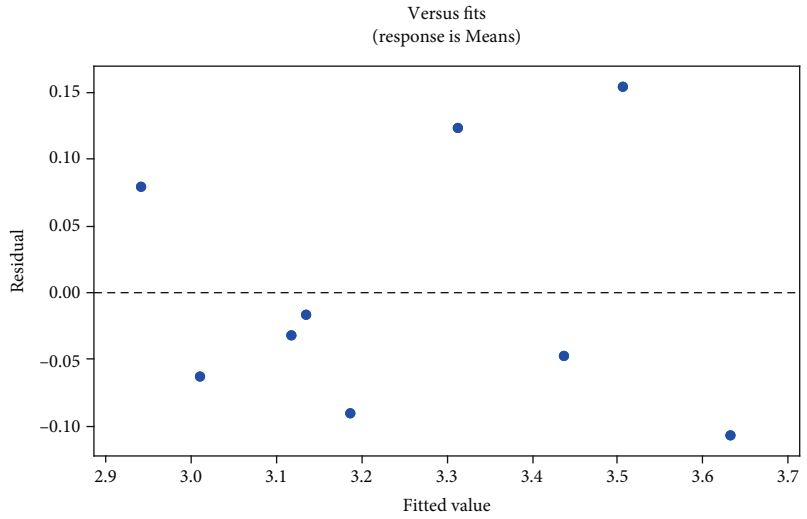

Figure 7: Residuals vs. fits for means.

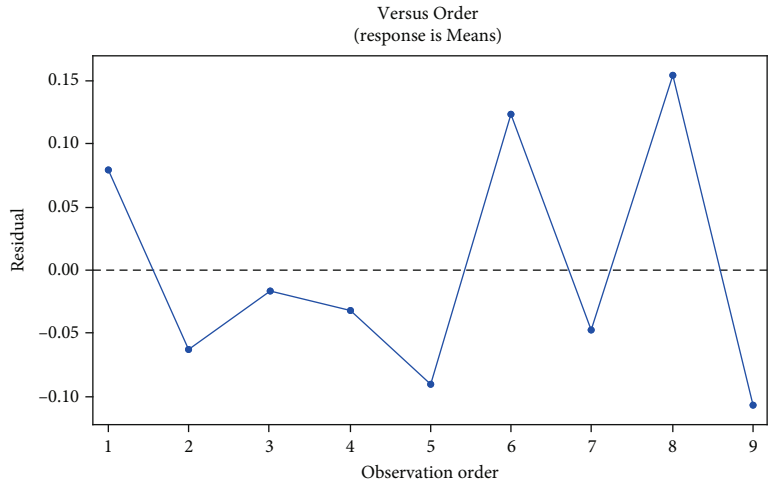

Figure 8: Residuals vs. order for means.

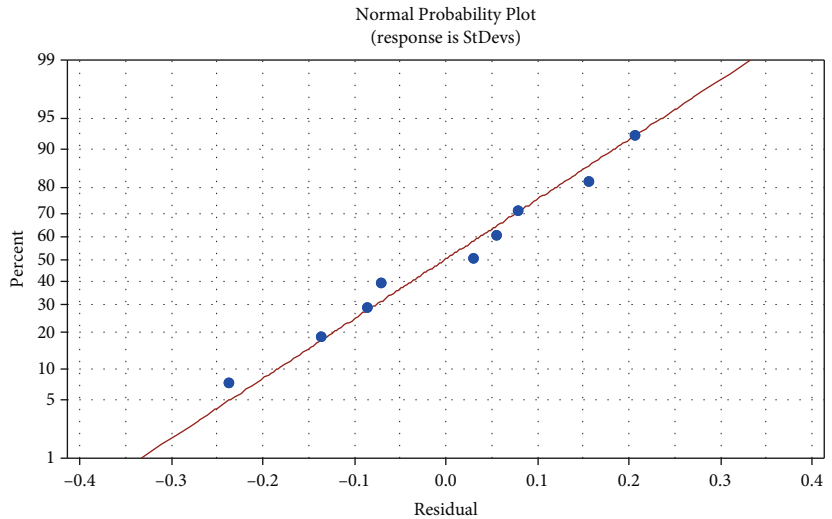

Figure 9: Normal plot of residuals for standard deviations.

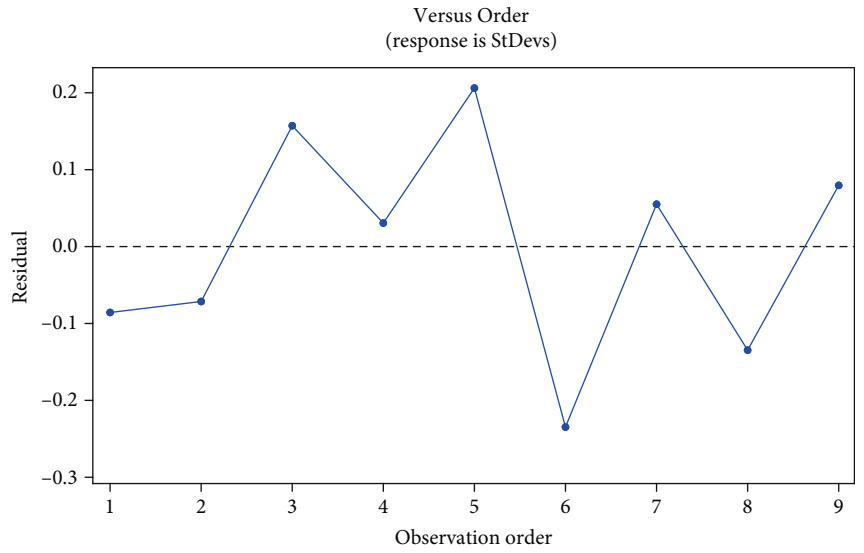

Figure 10: Residuals vs. fits for standard deviations.

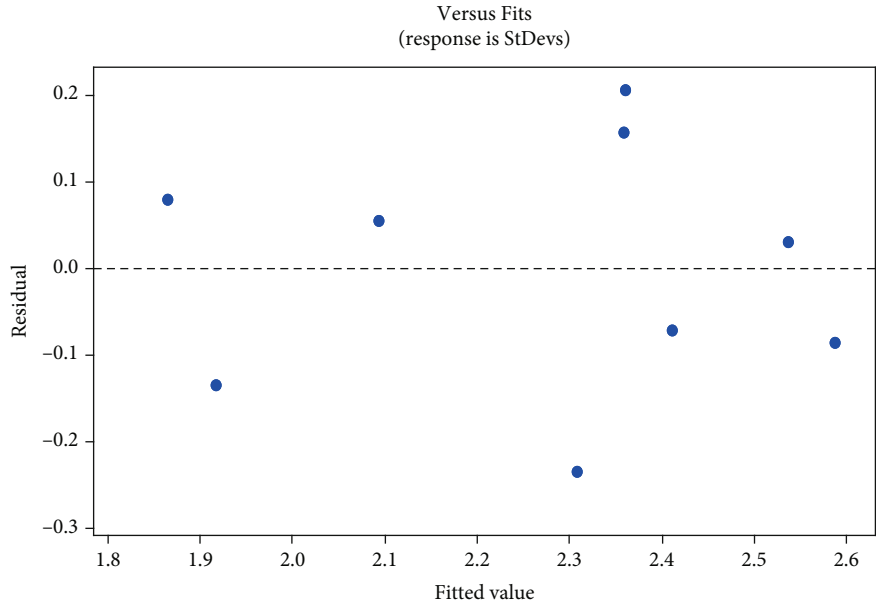

Figure 11: Residuals vs. order for standard deviations.

based on this indication [16]. The preferred thickness and voltage for the mean are 22 nm and 0.4 V, respectively, for the mean. Figure 2 shows the SN ratio's primary effects plot about thickness and voltage for the SN ratio. According to this graphical representation, the mean of the SN ratio fell in response to an increase in voltage. The SN ratio values, on the other hand, grow as the thickness of the CNTFET is raised. As a result, the almost optimal thickness and voltage were 20 nm and 0.6 V, respectively, when measured in the SN ratio.

Figure 3 depicts the responses of the SN ratio and residual values. Residual values gradually increase from negative to positive. According to the graph, the response for this configuration was close to the SN ratio in percentage terms. The solid colour line displayed the average value.

The graphical representation of residuals and fits for SN ratios is shown in Figure 4. The fitted values were listed horizontally, whereas the residual values were listed vertically. In response to SN ratios, residual values are arranged between -0.3 and 0.2, and fitted values are in the negative range.

Figure 5 shows various observation order for the residual values. There were less than 50% of the values in this graphical representation that was negative indicators, and more than 50% of the values in this graphical representation were positive indications. The options of rising and fall were accessible; however, the residuals were almost identical in the intermediate observation.

The normal probability plot about the residuals is depicted in Figure 6. The block line represented the average

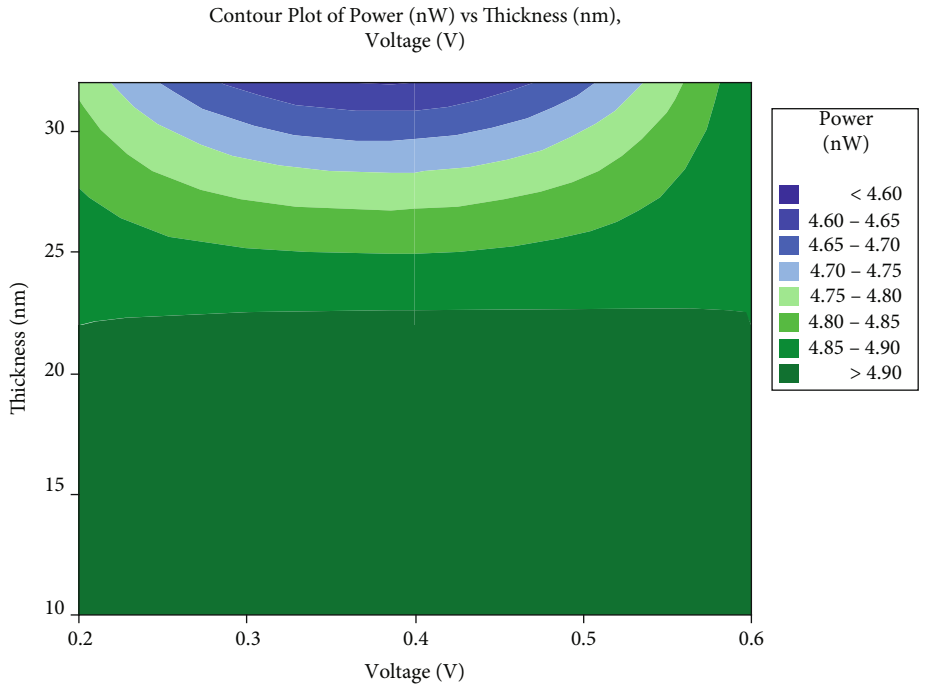

Figure 12: Contour plot of power vs. thickness and voltage.

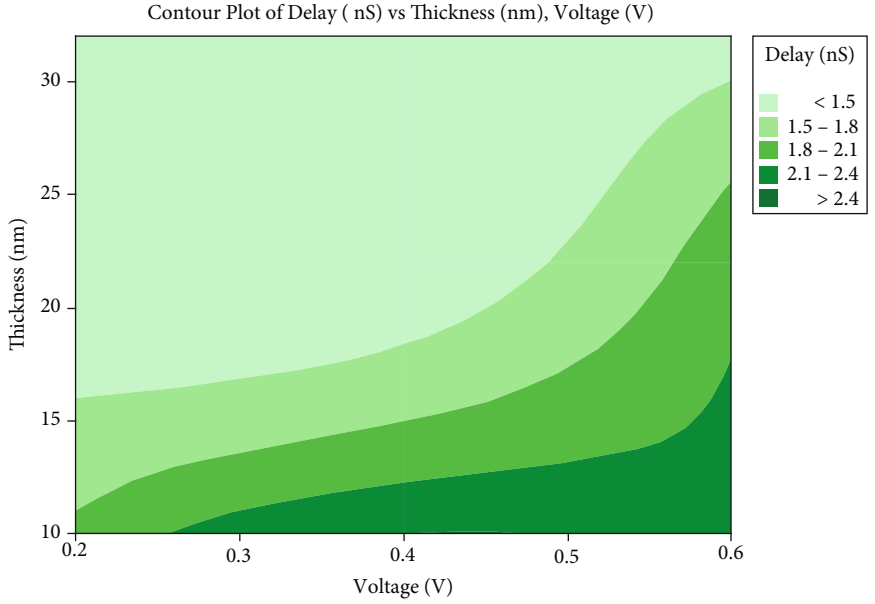

Figure 13: Contour plot of delay vs. thickness and voltage.

value, and the residual values were roughly equal to the average values depicted in the image.

The residual values to the fitted values with matching mean values are shown in Figure 7. The residual was in the range of -0.10 to 0.15. The majority of the fitted values were negative, accounting for almost 65% of the total, with the remaining positive replies.

An illustration of the residual about an order for means is depicted in Figure 8 in graphical form. There were residual values that were predominantly negative, accounting for roughly sixty-five percent of the total. However, the remaining thirty-five percent of respondents gave a positive reaction.

Figure 9 depicts the relationship between residuals for standard deviations and probability. This approach yielded results such as all values being quite close to the average. Figure 10 also depicts the responses of standard deviations concerning residuals in the range of -0.25 to 0.21.

Similarly, Figure 10 depicts residuals versus fits for standard deviations. 65% of respondents gave a good answer, while the remaining 35% gave a negative response.

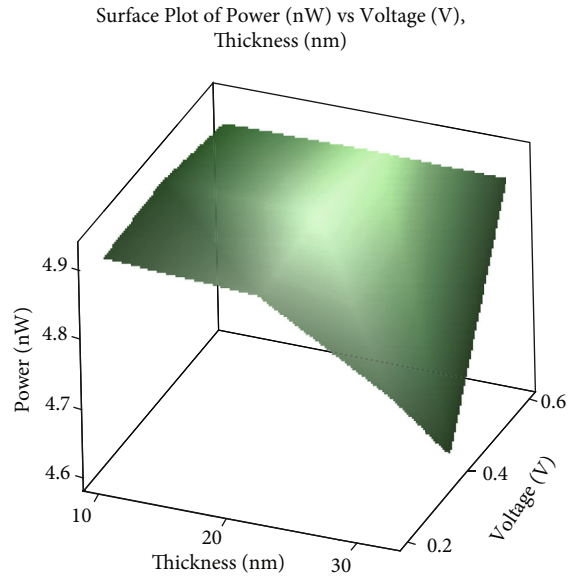

Figure 14: Surface plot of power vs. thickness and voltage.

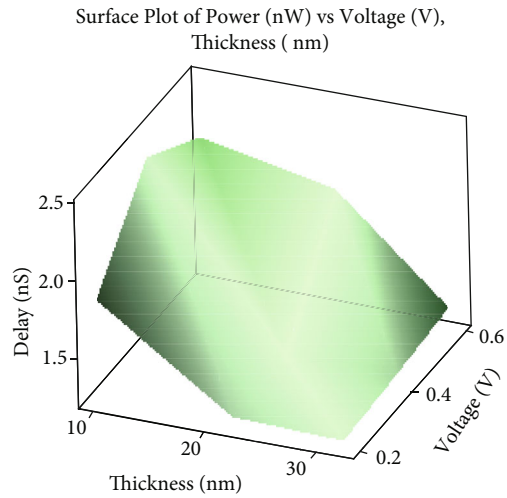

Figure 15: Surface plot of delay vs. thickness and voltage.

Standard deviations concerning residuals were in the range of -0.25 to 0.2.

Figure 11 depicts residual values about fitted values related to standard deviations. According to this graphical representation, the residual values ranged from -0.25 to 0.2, and the fitted values ranged from 1.85 to 2.6. Figure 12 depicts a contour plot of power vs. thickness and voltage, with significant colour changes. When the thickness is greater than 30 nm, the voltage exceeds 0.3 V, and power increases.

Figure 13 depicts the contour plot of delay vs. thickness and voltage using various colour differences. When the thickness value is increased (more than 17 nm) and the minimum voltage is close to 0.2 to 0.3, the delay decreases. Figure 14 shows a surface plot of power vs. thickness and voltage in three dimensions. Thickness was mentioned in the X-axis, power in the Y-axis, and voltage in the Z-axis. Powers increase in response to a decrease in thickness as well as an increase in voltage. Figure 15 depicts a surface plot representation of delay vs. thickness and voltage. Thickness was mentioned in the X-axis, latency in the Y-axis, and voltage in the Z-axis. With the increasing thickness and decreasing voltage, the delay decreased.

4. Conclusion

An examination of all of the parameters used in CNTFET optimization has been performed. The mean of the SN ratio fell in response to an increase in voltage. Optimal thickness and voltage were measured as 20 nm and 0.6 V. Standard deviations were observed in the range of -0.25 to 0.21. The thickness of the CNTFET is the most influential parameter to improve the results. The ideal thickness and voltage are 22 nm and 0.4 V resulting in the maximum power and lowest delay.

Data Availability

The data used to support the findings of this study are included in the article. Should further data or information be required, these are available from the corresponding author upon request.

Disclosure

The work was performed as a part of the Employment of Mettu University, Ethiopia.

Conflicts of Interest

The authors declare that there are no conflicts of interest regarding the publication of this paper.

Acknowledgments

The authors thank KPR Institute of Engineering and Technology and Vellore Institute of Technology, Chennai, for the technical assistance. The authors appreciate the supports from Mettu University, Ethiopia.

References

[1] L. Ding, E. Gnani, S. Gerardin et al., "Total ionizing dose effects in Si-based tunnel FETs," *IEEE Transactions on Nuclear Science*, vol. 61, no. 6, pp. 2874–2880, 2014.

[2] I. Sanchez Esqueda, H. J. Barnaby, and M. P. King, "Compact modeling of total ionizing dose and aging effects in MOS technologies," *IEEE Transactions On Nuclear Science*, vol. 62, no. 4, pp. 1501–1515, 2015.

[3] B. Ning and Z. Zhang, "Comparison of total ionizing dose effects for floating and tied body SOI nMOSFETs," *International Journal of Electronics and Electrical Engineering*, vol. 1, no. 1, pp. 31–33, 2013.

[4] C. D. Cress, J. J. McMorrow, J. T. Robinson et al., "Total ionizing dose-hardened carbon nanotube thin-film transistors with silicon oxynitride gate dielectrics," *Mrs Communications*, vol. 1, no. 1, pp. 27–31, 2011.

[5] S. Ishii, D. Yabe, S. Enomoto, S. Koshio, T. Hirao, and T. H. TeruakiKonishi, "Total ionizing dose effects in carbon

nanotube network transistors," in *2015 15th European Conference on Radiation and Its Effects on Components and Systems (RADECS)*, Moscow, Russia, 2015.

[6] P. Avouris, Z. Chen, and V. Perebeinos, "Carbon-based electronics," *Nature Nanotechnology*, vol. 2, no. 10, pp. 605–615, 2007.

[7] X.-W. Tang, Y. Yang, W. Kim et al., "Measurement of ionizing radiation using carbon nanotube field effect transistor," *Physics in Medicine and Biology*, vol. 50, no. 3, pp. N23–N31, 2005.

[8] R. D. Schrimpf, D. M. Fleetwood, M. L. Alles, R. A. Reed, G. Lucovsky, and S. T. Pantelides, "Radiation effects in new materials for nano-devices," *Microelectronic Engineering*, vol. 88, no. 7, pp. 1259–1264, 2011.

[9] C. D. Cress, J. J. McMorrow, J. T. Robinson, B. J. Landi, S. M. Hubbard, and S. R. Messenger, "Radiation effects in carbon nanoelectronics," *Electronics*, vol. 1, no. 1, pp. 23–31, 2012.

[10] C. X. Zhang, E. X. Zhang, D. M. Fleetwood et al., "Total-ionizing-dose effects and reliability of carbon nanotube FET devices," *Microelectronics Reliability*, vol. 54, no. 11, pp. 2355–2359, 2014.

[11] S. M. Baligidada, U. Chandrasekharb, K. Elangovanc, and S. Shankar, "RSM optimization of parameters influencing mechanical propertiesin selective inhibition sintering," *Materials Today: Proceedings*, vol. 5, pp. 4903–4910, 2018.

[12] W. H. Yang and Y. S. Tarng, "Design optimization of cutting parameters for turning operations based on the Taguchi method," *Journal of Materials Processing Technology*, vol. 84, no. 1-3, pp. 122–129, 1998.

[13] K. Lipin and P. Govindan, "A review on multi objective optimization of drilling parameters using Taguchi methods," *AKGEC International Journal of Technology*, vol. 4, no. 1, pp. 11–21, 2013.

[14] D. M. dos Santos, A. d. L. Bukzem, and S. P. Campana-Filho, "Response surface methodology applied to the study of the microwave-assisted synthesis of quaternized chitosan," *Carbohydrate Polymers*, vol. 138, pp. 317–326, 2016.

[15] C. C. Tsao and H. Hocheng, "Evaluation of thrust force and surface roughness in drilling composite material using Taguchi analysis and neural network," *Journal of Materials Processing Technology*, vol. 203, no. 1-3, pp. 342–348, 2008.

[16] S. Yogeshwaran, L. Natrayan, S. Rajaraman, S. Parthasarathi, and S. Nestro, "Experimental investigation on mechanical properties of epoxy/graphene/fish scale and fermented spinach hybrid biocomposite by hand lay-up technique," *Materials Today: Proceedings*, vol. 37, no. 2, pp. 1578–1583, 2021.

Hindawi
Journal of Nanomaterials
Volume 2021, Article ID 7323885, 7 pages
https://doi.org/10.1155/2021/7323885

Research Article

Processing and Characterization of Carbon Nanofibre Composites for Automotive Applications

L. Natrayan,[1] **Anjibabu Merneedi**,[2] **G. Bharathiraja**,[1] **S. Kaliappan**,[3] **Dhinakaran Veeman**,[4] **and P. Murugan**[5]

[1]*Department of Mechanical Engineering, Saveetha School of Engineering, SIMATS, Chennai, Tamil Nadu 602105, India*
[2]*Department of Mechanical Engineering, Aditya College of Engineering, Surampalem, 533437 Andhra Pradesh, India*
[3]*Department of Mechanical Engineering, Velammal Institute of Technology, Chennai, 601204 Tamil Nadu, India*
[4]*Centre for Additive Manufacturing, Chennai Institute of Technology, Chennai 600069, India*
[5]*Faculty of Mechanical Engineering, Jimma Institute of Technology, Jimma University, Jimma, Ethiopia*

Correspondence should be addressed to L. Natrayan; natrayanphd@gmail.com and P. Murugan; murugan.ponnusamy@ju.edu.et

Received 9 August 2021; Accepted 8 November 2021; Published 22 November 2021

Academic Editor: Lakshmipathy R

Copyright © 2021 L. Natrayan et al. This is an open access article distributed under the Creative Commons Attribution License, which permits unrestricted use, distribution, and reproduction in any medium, provided the original work is properly cited.

Currently, numerous studies have shown that carbon nanofibres have mechanical properties that are replaced by other widely used fibres. The high tensile strength of the carbon fibres makes them ideal to use in polymer matrix composites. The high-strength fibres can be used in short form in a composite and mass-produced to meet the high demands of automotive applications. These composites are capable of addressing the strength requirement of nonstructural and structural components of the automotive industry. Due to these composite lightweight and high-strength weight ratios, the applications can be widely varying. The research for these materials is a never-ending process, as researchers and design engineers are yet to tap its full potential. This study fabricated phenolic resin with different wt% of carbon nanofibre (CNF). The percentage of the CNF as a filler material is varied from 1 to 4 wt%. Mechanical properties such as hardness, tensile strength, and XRD were investigated. Phenolic resin with 4 wt% of carbon nanofibre (CNF) exhibits maximum tensile strength and hardness of 43.8 MPa and 37.8 HV.

1. Introduction

Nanocomposites provide a new class of material having combined properties of matrix and filler [1]. Nanocomposites using different fillers such as carbon nanotubes, nanofibres, silicates, clays, and metal nanoparticles can be prepared and applied in different fields like biomedical engineering, environmental applications, surface science, and the pharmaceutical field [2]. High-performance engineering materials with innovative properties were prepared through nanocomposite fabrication [3]. From the past few decades, the potential of carbon nanofibres (CNFs) and carbon nanotube (CNT) has been expanding [4]. Researchers around the globe are working to utilise the superior properties that these nanocomponents possess for various applications. The applications range from biosensors to new-age batteries [5]. The high surface area with less volume of CNF is suitable to suppress the defects that can be raised [6]. For micromechanical interlocking, the CNTs should exhibit some surface defects. This may include bonds in the CNT structure due to nonhexagonal defects and variation in diameter [7]. This kind of adhesion is very poor in CNT reinforced polymer composites because CNTs possess an almost smooth surface [8]. Chemical bonding includes ionic or covalent bonding capable of making changes in the smooth surface structure of CNTs. This helps to improve the effective stress transfer between the filler and matrix [9].

Depending on the carbon atom layer orientation in the CNF, the properties have varied. Carbon sp^2 filaments are stacked, and the CNFs are formed [10]. Depending on the stacking of the graphite planes, the CNF has different shapes [11]. Magesh et al. developed MWCNT incorporated

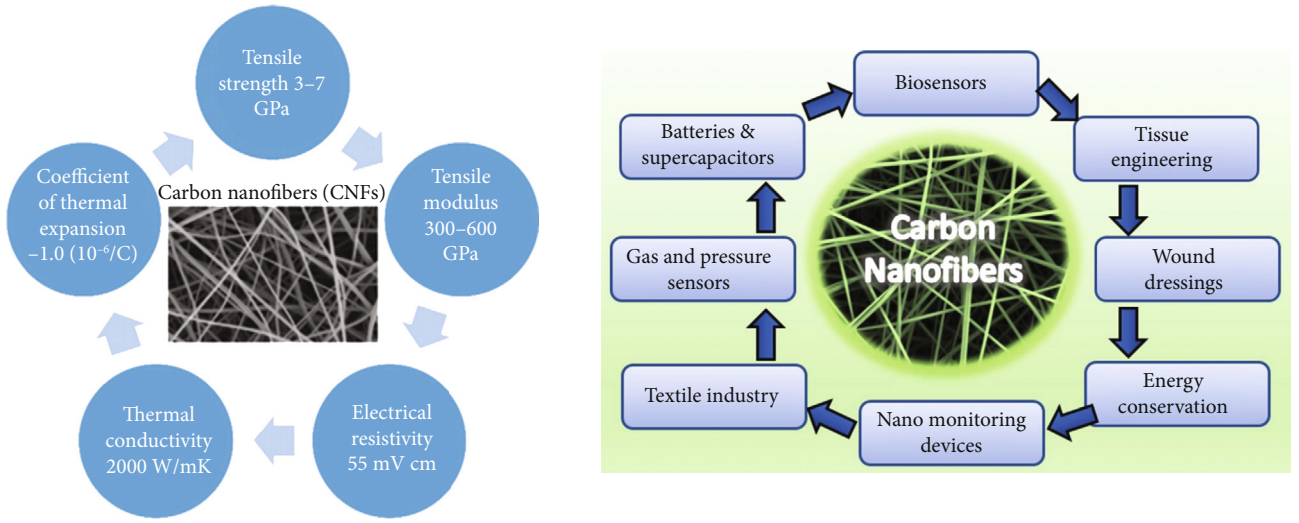

Figure 1: Overview of properties and applications of CNF.

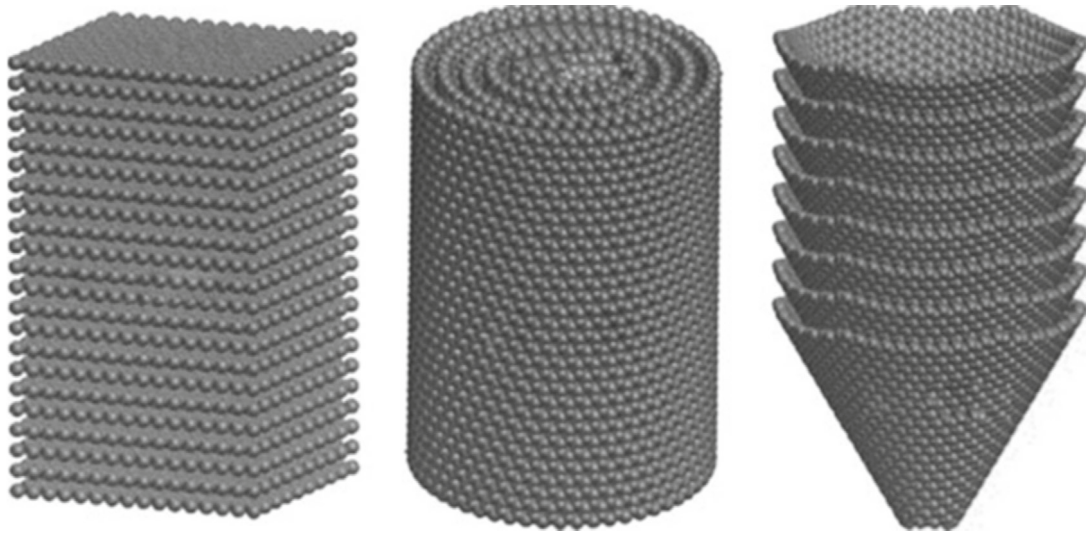

(a) (b) (c)

Figure 2: (a) Platelet type CNF; (b) tubular type CNF; (c) fishbone type CNF.

semitransparent composites from PVDF and studied its electrical properties [12]. The distinctive arrangements of the graphene layers depend on the geometric aspects of the metallic nanoparticle catalyst and the feedstock of the gaseous carbon (CO or hydrocarbon gas) introduced during the synthesis processing [13]. For the manufacturing of VGCFNs, catalytic chemical vapour deposition (CVD) in combination with heat- and plasma-assisted vapour deposition is the most often utilised approach. CNFs are grown via chemical vapour deposition using gaseous hydrocarbon precursors and metal catalysts at high temperatures [14]. CNF can be made using a mix of organic polymer electrospinning and thermal aftertreatment in an inert environment [15]. Merneedi et al. studied the effect of MWCNT/graphite nanoplate in polystyrene. The developed nanocomposite which has application in the EMI shielding area showed graphite nanoplate-MWCNT-graphite nanoplate networking [16]. The creation of electrospun polymer nanofibres is usually the first stage in the electrospinning process, followed by stabilisation and carbonization treatments, the latter of which is done in an inert atmosphere [17]. Avinash et al. developed epoxy/MWCNT composites. They studied the effect of the change in diameter, aspect ratio, and X-band microwave absorption using three different commercially available MWCNTs [18]. CNF features the intrinsic qualities of traditional carbon fibres and huge surface-to-volume ratios, making them particularly suited for applications involving environmental contact [19]. Surface features of multifunctional CNFs must be changed depending on the application [20]. The excellent intrinsic properties and high aspect ratio make MWCNT favourable in the research and industrial field [21]. The π-π interaction between MWCNT and PTT makes the importance of MWCNT-based PTT nanocomposites in the engineering application field [22].

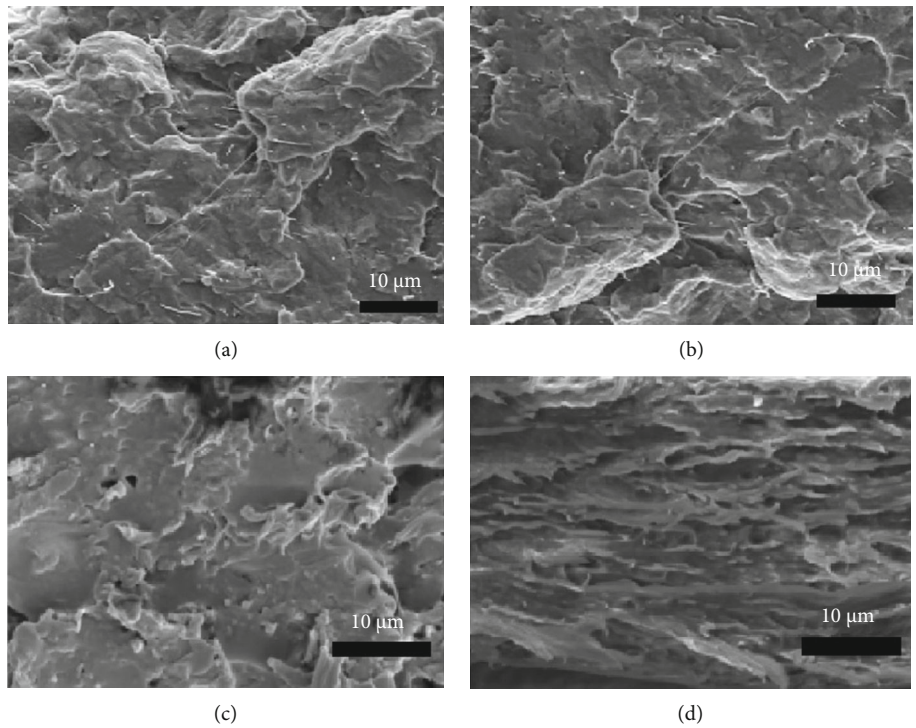

Figure 3: SEM micrographs of (a) 1% CNF, (b) 2% CNF, (c) 3% CNF, and (d) 4% CNF composites.

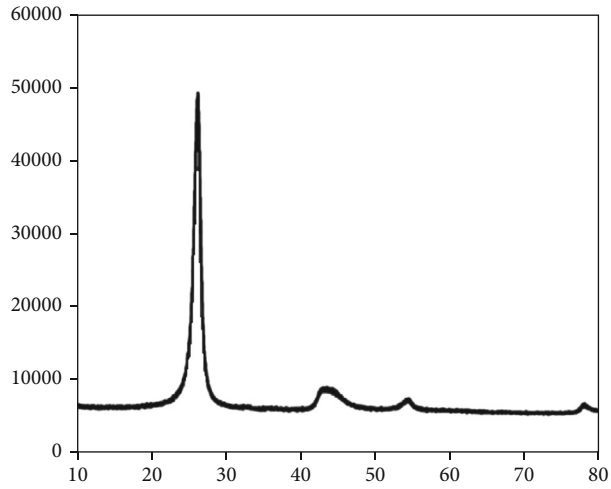

Figure 4: XRD of CNF composites (JCPDS card no. 96-101-106).

Based on the assumption that this extended π-π interaction will greatly influence the electrical properties and EMI shielding capability of PTT/MWCNT nanocomposites, a suitable mixing method was opted to prepare PTT/MWCNT nanocomposites [23].

The present study is aimed at determining the best percentage of the CNF in the CNF-based epoxy composites for obtaining optimal mechanical properties. The content of CNF in the composite is varied from 1 to 4% concerning the weight of the phenolic resin. The developed samples are then tested for their tensile strength and toughness, and micrographs are obtained using SEM.

Table 1: Microhardness (HV) of CNF composites.

Sample	Trial 1	Trial 2	Trial 3
CNF 1%	27.6	29.1	25.4
CNF 2%	31.5	30.1	31.2
CNF 3%	35.2	36.1	35.7
CNF 4%	36.2	37.8	36.6

2. Methodology

In this study, billets of CNF composites with phenolic resin are prepared with dimensions 5 mm diameter and 10 mm length [24]. CNF is procured with diameter dimensions of 10 nm and a length of 100 nm [25]. CNFs with large aspect ratios (length/diameter (L/D) ratios) agglomerate easily in general [26]. An overview of the properties of CNF and applications is shown in Figure 1.

Their aggregation decreases as the aspect ratios decrease. Vibration milling was employed to dissolve the agglomeration of CNFs and disseminate them uniformly in the matrix [27]. The different shapes such as platelet type CNF, tubular type CNF, and fishbone CNF type are shown in Figures 2(a)–2(c). The CNFs were milled to lower their aspect ratios throughout this operation [28]. The vibration-milled CNFs were agitated using ultrasonication in distilled water with polycarbon acid amine as a surfactant to improve their dispersion [29].

The distributed CNFs were sensitised and activated in $SnCl_2$ and $PdCl_2$ solutions at room temperature, respectively [30]. The pretreated CNFs were then filtered and thoroughly washed in distilled water [31]. CNF powder was combined

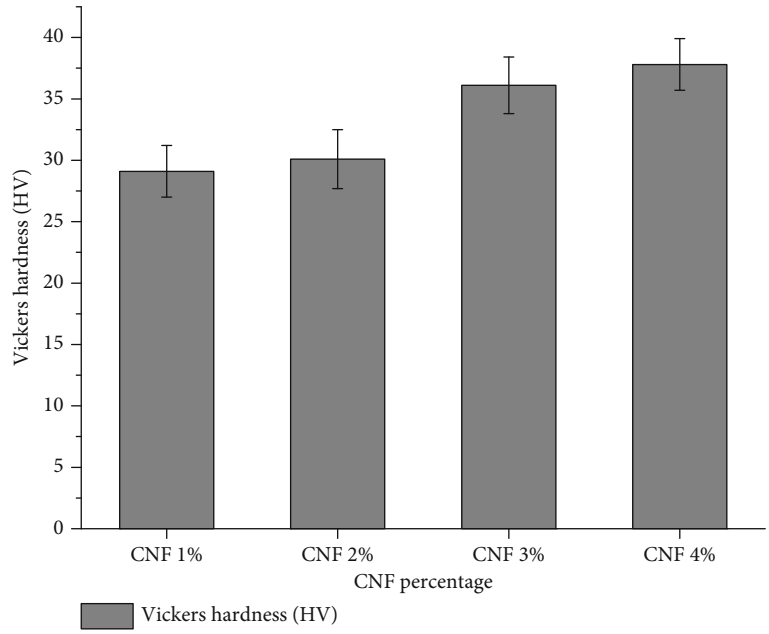

Figure 5: Hardness results of CNF composite.

Table 2: Tensile strength (MPa) of CNF composites.

Sample	Trial 1	Trial 2	Trial 3
CNF 1%	31.5	30.8	32.6
CNF 2%	35.5	37.8	35.3
CNF 3%	39.2	39.8	41.3
CNF 4%	40.5	42.3	45.8

with polyglycol-dissolved phenolic resin before making the CNF composite [32]. The phenolic resin was a thermosetting polymer made from phenol and formaldehyde with ammonia as a catalyst [33]. The billets are prepared such that the weight ratio of CNF varies between 1%, 2%, 3%, and 4%. For each percentage of CNF, multiple billets are prepared without changing the parameters. The mixed CNF and phenolic resin are then cured in an oven at 160°C to obtain the solidified billet sample [34]. For the developed samples, microhardness is tested with microindenter, tensile strength is calculated using UTM, and SEM micrographs are obtained by FE-SEM [35]. The chemical analysis of the CNF is done by using XRD analysis.

3. Results and Discussion

3.1. SEM Micrographs. The developed CNF composites are tested under the FE-SEM setup for identifying the distribution of CNF in the composite. The developed SEM micrographs are given below. It indicates that the CNF have been dispersed uniformly in the matrix. All the CNF content percentages are dissolved uniformly in the composite due to ultrasonic mixing before adding the resin [36]. The CNF ratio has been reduced by milling before the mixing with resin and improved the wettability of the fibres. No agglomeration of CNF in the matrix has been found for any of the developed composites. The four samples analysed for the SEM micrographs are given in Figure 3 and have no voids or crack defects, and also, agglomeration of fibres is absent.

3.2. XRD Analysis. Figure 4 exposes the peaks of graphitic-like carbon which can be seen in the CNF composite XRD diffraction pattern conforming JCPDS card no. 96-101-106. In terms of XRD patterns, the CNF composite closely mimics CNFs, implying that the graphite-like structure is preserved after the CNF powder is formed with polymer binder by pressing and then carbonized at high temperatures [37]. In the XRD diffraction spectrum, the contribution of polymer-derived carbon in the composite is undetectable. This could be caused by the surface graphitization of thermosetting resin during carbonization, resulting in a graphite-like coating that is distinct from the bulk glassy carbon. Therefore, it can be said that the composite is unaffected by any other contaminant or the curing medium or gasses. And the properties obtained by further investigation give the values of the CNF composite [38].

3.3. Mechanical Properties

3.3.1. Hardness. When a load is applied on a softer material, the substrates elastically deform, and the hardness measured is underreported. As a result, the results achieved in this case are the matrix and CNF collective hardness, which considerably reduced the composite attributes. Every sample has been subjected to many trials, with an average hardness value derived. The hardness of the composite is tested with the microindenter with a 100 g load for each indentation. Vickers indentation by Shimadzu has been used for the assessment. The hardness of the composites is increasing with an increase in the percentage of CNF in the composite.

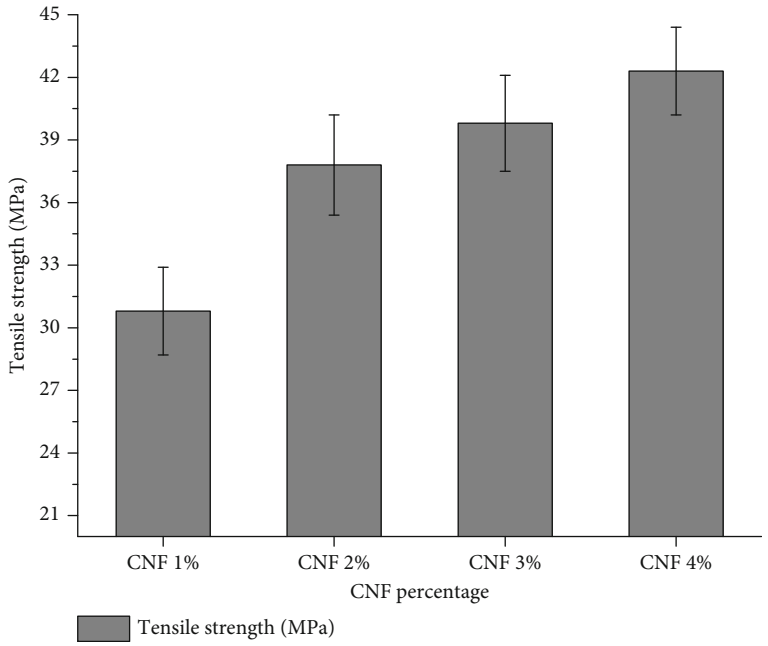

Figure 6: Tensile strength results for CNF composite.

1% CNF composite has a lesser hardness, and 4% has a higher hardness than the other composites. The values of the hardness obtained for each sample are given in Table 1. All values are recorded for an indentation period of 15 seconds. Figure 5 shows the hardness of CNF composites. The variation in the hardness values can be explained as the distribution of CNF at the surface layers of the composite for the higher CNF percentage composites is high; hardness is higher for the 4% CNF composites and gradually reduced for the lesser CNF percentage composites.

3.3.2. Tensile Strength. The tensile strength of the composites measured by UTM is given in Table 2. The composite with higher CNF content has a higher tensile strength value compared to other fabricated composites. The higher CNF in the composite absorbs the load as the bonding between matrix and CNF is sufficient without any voids. Figure 6 shows the tensile strength of CNF composites. There is a 48% increment in tensile strength for the composite when the CNF content is increased from 1% to 4% in the composite composition. The increment percentage is 22% when CNF is increased from 1 to 2% in the composite [39]. The percentage is reduced to 5% for tensile strength increment when CNF is bumped up to 3% from 2%. And from 3% CNF to 4% CNF, the tensile strength is even lesser than 5%. This shows that the increment in CNF content increases the tensile strength, but the increment level reduces gradually.

4. Conclusion

Phenolic resin with different wt% of carbon nanofibre composites was fabricated successfully. Among the composites, the one with higher CNF content has superior properties in terms of mechanical properties. The superior mechanical properties of CNF have influenced greatly testing composites.

(1) The XRD analysis revealed that there are no contaminants and other elements in the composite sample. XRD peaks obtained that CNF and resin

(2) The increment in CNF content increases the tensile strength, but the level of increment reduces gradually

(3) CNFs with 4 wt% composite tensile strength results were increased 48% compared to 1% of CNF composite

(4) The gradual increase in the CNF content in the composite will increase the strength of the composite and hence is useful in the automotive industry

Data Availability

The data used to support the findings of this study are included within the article. Should further data or information be required, these are available from the corresponding author upon request.

Disclosure

The study was performed as part of the employment of Jimma Institute of Technology, Jimma University, Ethiopia.

Conflicts of Interest

The authors declare that there are no conflicts of interest regarding the publication of this paper.

Acknowledgments

The authors thank Saveetha School of Engineering, SIMATS, Chennai, for providing characterization support to complete this research work.

References

[1] S. Yogeshwaran, L. Natrayan, G. Udhayakumar, G. Godwin, and L. Yuvaraj, "Effect of waste tyre particles reinforcement on mechanical properties of jute and abaca fiber- epoxy hybrid composites with pre-treatment," *Mater. Today Proc.*, vol. 37, no. 2, pp. 1377–1380, 2021.

[2] L. Natrayan, P. S. S. Sundaram, and J. Elumalai, "Analyzing the uterine physiological with mmg signals using svm," *International journal of pharmaceutical research*, vol. 11, no. 2, 2019.

[3] L. Natrayan and A. Merneedi, "Experimental investigation on wear behaviour of bio-waste reinforced fusion fiber composite laminate under various conditions," *Mater. Today Proc.*, vol. 37, no. 2, pp. 1486–1490, 2021.

[4] M. R. Taha and J. M. A. Alsharef, "Performance of soil stabilized with carbon nanomaterials," *Chemical Engineering Transactions*, vol. 63, pp. 757–762, 2018.

[5] P. Samaddar, Y. S. Ok, K. H. Kim, E. E. Kwon, and D. C. W. Tsang, "Synthesis of nanomaterials from various wastes and their new age applications," *Journal of Cleaner Production*, vol. 197, pp. 1190–1209, 2018.

[6] J. Wang, Y. Huyan, Z. Yang, A. Zhang, Q. Zhang, and B. Zhang, "Tubular carbon nanofibers: synthesis, characterization and applications in microwave absorption," *Carbon N. Y.*, vol. 152, pp. 255–266, 2019.

[7] K. Hemalatha, C. James, L. Natrayan, and V. Swamynadh, "Analysis of RCC T-beam and prestressed concrete box girder bridges super structure under different span conditions," *Mater. Today Proc.*, vol. 37, no. 2, pp. 1507–1516, 2021.

[8] N. D. K. R. Chukka, L. Natrayan, and W. D. Mammo, "Seismic fragility and life cycle cost analysis of reinforced concrete structures with a hybrid damper," *Advances in Civil Engineering*, vol. 2021, Article ID 4195161, 17 pages, 2021.

[9] L. Natrayan and M. S. Kumar, "Optimization of tribological behaviour on squeeze cast Al6061/Al_2O_3/SiC/Gr hmmcs based on Taguchi methodandartificial neural network," *J. Adv. Res. Dyn. Control Syst.*, vol. 11, no. 7, pp. 493–500, 2019.

[10] H. Varela-Rizo, I. Rodriguez-Pastor, C. Merino, and I. Martin-Gullon, "Highly crystalline graphene oxide nano-platelets produced from helical-ribbon carbon nanofibers," *Carbon N. Y.*, vol. 48, no. 12, pp. 3640–3643, 2010.

[11] M. J. Ledoux and C. Pham-Huu, "Carbon nanostructures with macroscopic shaping for catalytic applications," *Catalysis Today*, vol. 102-103, pp. 2–14, 2005.

[12] S. Magesh, V. R. Niveditha, P. S. Rajakumar, and L. Natrayan, "Pervasive computing in the context of COVID-19 prediction with AI-based algorithms," *Int. J. Pervasive Comput. Commun.*, vol. 16, no. 5, pp. 477–487, 2020.

[13] S. C. Tjong, "Recent progress in the development and properties of novel metal matrix nanocomposites reinforced with carbon nanotubes and graphene nanosheets," *Materials Science & Engineering R: Reports*, vol. 74, no. 10, pp. 281–350, 2013.

[14] C. S. Cojocaru and F. Le Normand, "On the role of activation mode in the plasma- and hot filaments-enhanced catalytic chemical vapour deposition of vertically aligned carbon nanotubes," *Thin Solid Films*, vol. 515, no. 1, pp. 53–58, 2006.

[15] A. Kumar and S. Sinha-Ray, "A review on biopolymer-based fibers via electrospinning and solution blowing and their applications," *Fibers*, vol. 6, no. 3, pp. 45–53, 2018.

[16] A. Merneedi, M. RaoNalluri, and V. V. S. Rao, "Free vibration analysis of a thin rectangular plate with multiple circular and rectangular cut-outs," *Journal of Mechanical Science and Technology*, vol. 31, no. 11, pp. 5185–5202, 2017.

[17] X. Wang, I. C. Um, D. Fang, A. Okamoto, B. S. Hsiao, and B. Chu, "Formation of water-resistant hyaluronic acid nanofibers by blowing-assisted electro-spinning and non-toxic post treatments," *Polymer (Guildf).*, vol. 46, no. 13, pp. 4853–4867, 2005.

[18] A. S. Avinash, "Evaluation on mechanical properties of basalt fiber-E glass reinforced polymer composite," *Test Eng. Manag.*, vol. 83, pp. 14222–14227, 2020.

[19] J. B. Kim, S. K. Lee, and C. G. Kim, "Comparison study on the effect of carbon nano materials for single-layer microwave absorbers in X-band," *Composites Science and Technology*, vol. 68, no. 14, pp. 2909–2916, 2008.

[20] C. Bavatharani, E. Muthusankar, S. M. Wabaidur et al., "Electrospinning technique for production of polyaniline nanocomposites/nanofibres for multi-functional applications: a review," *Synthetic Metals*, vol. 271, no. 2020, p. 116609, 2021.

[21] A. Merneedi, M. R. Nalluri, and V. S. R. Vissakodeti, "Free vibration analysis of an elliptical plate with cut-out," *J VIBROENG*, vol. 19, no. 4, pp. 2341–2353, 2017.

[22] S. L. K. Konuru, V. Umasankar, B. Sarkar, and A. Sarma, "Microstructure and mechanical properties of tungsten and tungsten-tantalum thin film deposited RAFM steel," *Materials Research Innovations*, vol. 24, no. 2, pp. 97–103, 2020.

[23] L. Natrayan and M. Senthil Kumar, "A novel feeding technique in squeeze casting to improve reinforcement mixing ratio," *Mater. Today Proc.*, vol. 46, pp. 1335–1340, 2021.

[24] C. S. S. Anupama, L. Natrayan, E. Laxmi Lydia et al., "Deep learning with backtracking search optimization based skin lesion diagnosis model," *Computers, Materials & Continua*, vol. 70, no. 1, pp. 1297–1313, 2022.

[25] N. J. Parizek, B. R. Steines, E. Haque et al., "Acute _in vivo_ pulmonary toxicity assessment of occupationally relevant particulate matter from a cellulose nanofiber board," *NanoImpact*, vol. 17, p. 100210, 2020.

[26] J. Y. Lim, S. Il Oh, Y. C. Kim, K. K. Jee, Y. M. Sung, and J. H. Han, "Effects of CNF dispersion on mechanical properties of CNF reinforced A7xxx nanocomposites," *Materials Science and Engineering A*, vol. 556, pp. 337–342, 2012.

[27] W. A. D. M. Jayathilaka, A. Chinnappan, and S. Ramakrishna, "A review of properties influencing the conductivity of CNT/Cu composites and their applications in wearable/flexible electronics," *Journal of Materials Chemistry C*, vol. 5, no. 36, pp. 9209–9237, 2017.

[28] P. Hvizdoš, V. Puchý, A. Duszová, J. Dusza, and C. Balázsi, "Tribological and electrical properties of ceramic matrix composites with carbon nanotubes," *Ceramics International*, vol. 38, no. 7, pp. 5669–5676, 2012.

[29] A. Czaikoski, R. Lopes, and F. C. Menegalli, "Rheological behavior of cellulose nano fi bers from cassava peel obtained by combination of chemical and physical processes," *Carbohydrate Polymers*, vol. 248, p. 116744, 2020.

[30] X. Wu, Z. Liu, Y. Jiang, J. Zeng, and S. Liao, "Randomly oriented Ni–P/nanofiber/nanotube composite prepared by electrolessly plated nickel–phosphorus alloys for fuel cell applications," *Journal of Materials Science*, vol. 52, no. 14, pp. 8432–8443, 2017.

[31] S. Oh, J. Y. Lim, Y. C. Kim et al., "Fabrication of carbon nanofiber reinforced aluminum alloy nanocomposites by a liquid process," *Journal of Alloys and Compounds*, vol. 542, pp. 111–117, 2012.

[32] J. K. Chinthaginjala, K. Seshan, and L. Lefferts, "Preparation and application of carbon-nanofiber based microstructured materials as catalyst supports," *Industrial and Engineering Chemistry Research*, vol. 46, no. 12, pp. 3968–3978, 2007.

[33] D. Wang, G. Chang, and Y. Chen, "Preparation and thermal stability of boron-containing phenolic resin/clay nanocomposites," *Polymer Degradation and Stability*, vol. 93, no. 1, pp. 125–133, 2008.

[34] D. Veeman, M. S. Sai, P. Sureshkumar et al., "Additive manufacturing of biopolymers for tissue engineering and regenerative medicine: an overview, potential applications, advancements, and trends," *Int. J. Polym. Sci.*, vol. 2021, pp. 1–20, 2021.

[35] M. S. K. Sharma, S. Singh, P. Singh Thind et al., "A Systematic Review on the Performance Characteristics of Sustainable, Unfired Admixed Soil Blocks for Agricultural and Industrial Waste Management," *Advances in Materials Science and Engineering*, vol. 2021, 9 pages, 2021.

[36] V. Paranthaman, K. S. Sundaram, and L. Natrayan, "Influence of SiC particles on mechanical and microstructural properties of modified interlock friction stir weld lap joint for automotive grade aluminium alloy," *SILICON*, vol. 1, pp. 1–11, 2021.

[37] R. Suryanarayanan, V. G. Sridhar, L. Natrayan et al., "Improvement on mechanical properties of submerged friction stir joining of dissimilar tailor welded aluminum blanks," *Advances in Materials Science and Engineering*, vol. 2021, 6 pages, 2021.

[38] L. Natrayan and M. Senthil Kumar, "An integrated artificial neural network and Taguchi approach to optimize the squeeze cast process parameters of AA6061/Al2O3/SiC/Gr hybrid composites prepared by novel encapsulation feeding technique," *Materials Today Communications*, vol. 25, p. 101586, 2020.

[39] S. L. K. Konuru, V. Umasankar, and A. K. Sarma, "Development and characterisation of W and W-25% Ta composite coatings on steel material," *Journal of Surface Science and Technology*, vol. 36, no. 3-4, pp. 103–108, 2020.

Hindawi
Journal of Nanomaterials
Volume 2021, Article ID 4043196, 14 pages
https://doi.org/10.1155/2021/4043196

Research Article

Influence of Nanographite on Dry Sliding Wear Behaviour of Novel Encapsulated Squeeze Cast Al-Cu-Mg Metal Matrix Composite Using Artificial Neural Network

L. Natrayan,[1] **M. Ravichandran**,[2] **Dhinakaran Veeman**,[3] **P. Sureshkumar**,[4] **T. Jagadeesha**,[5] **and Wubishet Degife Mammo**[6]

[1]*Department of Mechanical Engineering, Saveetha School of Engineering, SIMATS, Chennai, 602105 Tamil Nadu, India*
[2]*Department of Mechanical Engineering, K.Ramakrishnan College of Engineering, Samayapuram, 621112 Tamil Nadu, India*
[3]*Centre for Additive Manufacturing and Computational Mechanics, Chennai Institute of Technology, Chennai, 600069 Tamil Nadu, India*
[4]*Department of Mechanical Engineering, Ramco Institute of Technology, Virudhunagar, 626125 Tamil Nadu, India*
[5]*Department of Mechanical Engineering, National Institute of Technology, Calicut, 673601 Kerala, India*
[6]*Mechanical Engineering Department, Wollo University, Kombolcha Institute of Technology, Kombolcha, South Wollo, 208 Amhara, Ethiopia*

Correspondence should be addressed to L. Natrayan; natrayanphd@gmail.com,
Dhinakaran Veeman; dhinakaranv@citchennai.net, and Wubishet Degife Mammo; wubishetdegife7@gmail.com

Received 8 September 2021; Revised 20 October 2021; Accepted 1 November 2021; Published 19 November 2021

Academic Editor: Lakshmipathy R

Copyright © 2021 L. Natrayan et al. This is an open access article distributed under the Creative Commons Attribution License, which permits unrestricted use, distribution, and reproduction in any medium, provided the original work is properly cited.

This paper investigates the dry sliding wear behaviour of squeeze cast Al-Cu-Mg reinforced with nanographite metal matrix composites. The experimental study employed the Taguchi method. The Taguchi method plays a significant role in analyzing aluminium matrix composite sliding tribological behaviour. Specifically, this method was found to be efficient, systematic, and simple relative to the optimization of wear and friction test parameters such as load (10, 20, and 30), velocity (0.75, 1.5, and 2.25 m/s), and nanographite (1, 3, and 5 wt%). The optimization and results were compared with the artificial neural network. An orthogonal array L27 was employed for the experimental design. Analysis of variance was carried out to understand the impact of individual factors and interactions on the specific wear rate and the coefficient of friction. The wear mechanism, surface morphologies, and composition of the composites have been investigated using scanning electron microscopy with energy-dispersive X-ray spectroscopy. Results indicated that wt% addition of nanographite and increase of sliding speed led to a decrease in the coefficient of friction and wear rate of tested composites. Furthermore, individual parameter interactions revealed a smaller impact. The interactions involved wt% of nano-Gr and sliding speed, sliding speed and normal load, and wt% of nano-Gr and normal load. This inference was informed by the similarity between the results obtained ANN, ANOVA, and the experimental data.

1. Introduction

In modern society, there is an increasing demand for new hybrid composites. Particularly, the demand emphasizes lightweight alloys. Most previous studies indicate that this demand trend comes from construction price decrease, mass construction reduction, and working life increase [1]. One of the examples of the demand concerns the use of aluminium and its associated alloys to substitute steel and materials similar to the latter. Notably, the demand for aluminium alloys has arisen from the affirmation that the alloys exhibit good mechanical properties [2, 3]. However, some studies caution that the alloys have poor tribological characteristics. Imperative to highlight is that tribological characteristics concern wear, lubrication, and friction of interacting surfaces, especially those found to be in relative motion [4].

The demerit of poor tribological characteristics of aluminium alloy, although lightweight materials, has paved the way for improvements. Related composite materials have been developed in a quest to steer improvements to the material tribological characteristics [3, 4]. An example of composite materials is a case of Al-Si alloy (A356). Some scholarly investigations have also analyzed the information obtained from referent literature reviews concerning composite material exploitation [5]. For these studies, findings avow that the addition of specific reinforcements tends to improve the aluminium alloy mechanical characteristics [6]. Some of the reinforcements that have gained application in the quest to improve the aluminium alloy mechanical characteristics include Al_2O_3 and SiC.

Imperatively adding some volume amounts or masses of reinforcements to the aluminium alloys has led to a problem concerning the composite material mechanical treatment [7]. To solve this problem, nanographite has been proposed as an ideal material that could be added at a certain quantity. For investigations that have examined the latter process, most of the results concur that the resultant composite's tribological characteristics, due to nanographite addition, tend to improve [6, 7]. When two or more reinforcements are used to develop composite materials, the latter is translated into hybrid composite materials [8]. Some of the areas that have received attention relative to aluminium alloys and the hybrid composite tribological behaviour include electronic industry, aircraft, and automobiles. Currently, composite material production usage and annual growth lie at 6%, with the aluminium base on focus [9]. Different methods have been applied to steer the development of hybrid aluminium matrix composites (HMMC), which are mostly achieved by combining soft graphite particles and hard ceramic. Some of these methods include full factorial and response surface, analysis of covariance (ANOVA), and Taguchi [10–14]. The role of these methods has been to provide information regarding the possible impact of different parameters, assuming hierarchical rank orders. The methods mentioned above have tested the specific parameters: the impact of graphite or reinforcement weight percentage, the sliding speed and distance, and the normal load on hybrid AMCs' friction and wear properties [15, 16]. Most of the researchers have employed the ANOVA method and an orthogonal array. For these studies, findings suggest that in dry sliding conditions, the use of graphite particles proves effective in decreasing friction and increasing the wear resistance of AMCs [17].

For hybrid Al/SiC/Gr composite materials, the tribological behaviour has been investigated. For these investigations, graphite content with 2.5 and 8 wt% and SiC content with 10 wt% have been considered. The base used has been aluminium alloy Al 2024, with the semisolid powder densification method aiding in making composites [18]. Also, the metal matrix Al-Si7Mg composite's tribological behaviour has been investigated [16–19]. The reinforcement for the latter investigation has been achieved via 10% SiC and graphite particles without lubrication. With full factorial design gaining application, the central objective has been to unearth the impact of reinforcement content in terms of sliding distance, sliding speed, load, and percentage on the wear of Al alloy/SiC/graphite composite materials, Al alloys/SiC, and Al alloy/graphite. In the finding, these experimental studies suggest that hybrid composite material exhibits the best characteristics.

Imperative to note is that the decision to incorporate approaches such as factorial and surface response and Taguchi, which constitute the design of experiment (DOE) concepts, has been informed by the need to gain insights into the impact of different parameters, with the results obtained in terms of hierarchical rank order [20]. The techniques have also proved important by providing room for establishing correlation terms and the analysis of the parameters' combined effects [21]. Some investigations have focused on graphite (Gr) and silicon carbide (SiC) as reinforcements to understand the different behaviour of hybrid composites. For these studies, aluminium base Al 2219 has been used. The liquid metallurgy synthesis approach has been employed during the making of the hybrid composites [22]. With the Taguchi method embraced, a major focus has been to analyze the impact of reinforcement content in wt%, sliding distance, sliding speed, and normal load [20, 21]. For the latter investigations, findings indicate that in wt%, where reinforcement is done via the increase of graphite content, there is likely to be an increase in the hybrid composites' resistance to wear.

Imperatively, the aluminium bases used in most previous studies have been Al 2219 and Al 2024 [22]. Also, the majority of the studies have focused on hybrid AMCs or aluminium hybrid composites under dry sliding conditions [20–22]. It is also worth noting that from the critical review of the current literature, the majority of the investigations have used techniques such as Taguchi and ANOVA to establish hierarchical rank orders of test parameters independently [23]. Some of the test parameters considered include the weight percentage of graphite or reinforcements, the sliding speed and distance, and the normal load. As such, most of the experiments have not focused on the combined impact that the parameters pose on wear and friction. Therefore, the main aim of the current study is to find out the tribological behaviour of aluminium hybrid composites with Al-Cu-Mg reinforced nanographite. It is also imperative to highlight that the investigation employs the Taguchi method.

2. Experimental Details

2.1. Materials. In this study, Al-Cu-Mg is used as the base for metal matrix composite. The squeeze casting process is used to fabricate the composite specimens. Figure 1 shows the squeeze casting machine. The materials used in squeeze casting include nanographite with each stretching to 10 nm. The experiment also involved overheating and melting the matrix alloy to ensure that it was clean of slag. The overheating and melting procedure extended to 650°C. This process preceded the compocasting procedure. Homogenous mixing was done with nanographite powders. With the process conducted in the solid state, the preheating stage that followed extended to 150°C. The procedure followed involved the

Figure 1: Squeeze casting setup and novel encapsulated metal cap.

cooling of the alloy matrix, which was brought down to a range of 597°C–603°C. Imperative to note is that the latter temperature range was maintained for 10 minutes. With a semisolid melt obtained, a plate mixer was introduced, followed by a five-minute isothermal stirring procedure. This procedure was set at 500 rpm. Also, a squeeze casting procedure was conducted. The procedure lasted 15 seconds, and pressure was set at 90 MPa.

The nanographite particle was filled in the metal cap and melt in a squeeze casting furnace. The novel encapsulated metal cap is shown in Figure 1. The motivation to increase the temperature was informed by the need to promote the infiltration process with the secondary phase particle addition making the semisolid matrix increase in velocity. The temperature was also increased to 610°C in response to the increasing particle amount.

Figure 2 shows the Pin on Disc wear testing machine. On completing the infiltration procedure, the moving process that followed was in two stages. The initial stage lasted two minutes and was aimed at stabilizing the moving process. At this point, 1000 rpm was the rotation speed of the plate mixer. Similarly, this initial stage was marked by a restoration of temperature back to 600°C. The stage that followed was conducted in five minutes. Particularly, 1500 rpm was the rotation speed of the plate mixer, taking place in an isothermal context.

To ensure that the semisolid melts were cast successfully, the experiment employed a mold. This mold had been preheated to 500°C. Later, a special tool was set at 570°C and used to hot press the obtained castings. The hot pressing also involved a 100 MPa pressure. Particularly, commercial T6 heat treatment was the platform to which the experiment's specimens were subjected. Wear specimens are shown in Figure 3. Parameters of commercial T6 included artificial ageing and water quenching for 6 h and at 160°C, and the solution is heat-treated for 4 hr and at 540°C. Table 1 illustrates the chemical properties or composition of the Al-Cu-Mg used.

Figure 2: Pin on Disc wear testing machine.

2.2. The Case of Wear and Friction Tests. The wear and friction tests focused on material tribological behaviour. The ASTM G77 standard governed the investigation whereby block-on-disc contact geometry dominated the procedure. Also, TPD 93, a computer-aided tribometer, formed a platform for testing the tribological behaviour. As the experiment proceeded, the thickness of discs and blocks was 6.35 mm, which marked the initial contact. Ra = 0.2 μm

Figure 3: Wear samples.

Table 1: Chemical composition of Al-Cu-Mg.

Element	Al	Mg	Si	Fe	Cu	Mn	Cr	Zn	Ti
Weight %	97.81	0.95	0.54	0.22	0.17	0.13	0.09	0.08	0.01

Table 2: Dry sliding wear parameters and their levels.

Controllable factors	Level 1	Level 2	Level 3
Load (N)	10	20	30
Velocity (m/s)	0.75	1.5	2.25
Nanographite wt%	1	3	5

constituted the surface roughness of the tested composite materials, which formed the blocks.

On the other hand, Ra = 0.3 μm reflected the disc's surface roughness. Also, 90MnCrV8 steel was selected for the disc. The hardness of this disc stretched from 62 HRC to 64 HRC. The lubricant employed in this study involved ISO VG 46 hydraulic oil. The selection of this form of oil was informed by its recommended industrial application in situations involving high-pressure mechanical systems such as roller bearings, chain gears, and gearboxes. The submergence of the selected discs (into the oil) extended to 3 mm.

As the friction and wear tests progressed, the lubricated conditions involved five major sliding speeds. These speeds included 0.75, 1.5, and 2.25 m/s. Also, the normal loads embraced included 10, 20, and 30 N. Regarding the sliding distances, the study focused on nanographite such as 1, 3, and 5 wt% for the speeds and loads above, respectively. The choice of these ranges of normal load and sliding speed arose from their wide practical applications at roller bearings, chain gears, and gearboxes. The tribological behaviour of the selected materials have measured wear tracks, and the coefficient of friction was read continuously at the end of the respective tests. Dry sliding wear parameters and their levels are exposed in Table 2. Imperative to note is that each test or experiment was repeated thrice.

2.3. Experimental Design: Taguchi Method. The Taguchi method is employed in controlled settings, and its purpose is to analyze the impact that process variables are likely to have on other specific variables. The specific variables under investigation are usually unknown functions of process variables. After implementing the Taguchi method, the findings are used to inform industrial designs of improved and quality systems [24]. Practically, the Taguchi method has been applied by many previous researchers to understand aluminium metal matrix composites' sliding wear behaviour. Hence, the Taguchi method supports the creation of standard orthogonal arrays responsible for accommodating the influence of different variables on target values. To study the impact of parameters on the independent variables, ANOVA was used to analyze the results and make the Taguchi method meaningful [25].

When experimental results are established after applying the Taguchi method, they are usually converted into signal-to-noise (S/N) ratios. The Taguchi method incorporates statistical analyses of variance to predict optimal combinations that could be used based on the test parameters. As avowed by other studies, the latter procedure seeks to define or establish parameters that are deemed statistically significant and worth considering [26, 27].

With Taguchi giving the "smaller the better" characteristics relative to the wear rate ratio (S/N),

$$\mathrm{S/N} = -10\ \log\left(\frac{1}{n}\sum_{i=1}^{n}\frac{1}{y^2}\right)\ (\text{larger is better}). \tag{1}$$

In equation (1), n represent the number of observations made while $y_1, y_2, \cdots, y_n$ reflect sliding wear responses. Table 3 summarizes the average of characteristics associated with various levels of experimental factors.

3. Results and Discussion

This study sought to establish the most significant parameters and parameter combinations that are likely to exhibit the greatest impact on the coefficient of friction and the wear rate. By establishing these parameters, the experiment would then give an insight into how their values could be reduced to the minimum. The orthogonal array governed the tests to connect the impacts of nanographite wt%, sliding speed (S), and load (L). These parameters were also used due to their capacity to define the composite tribological behaviour and important influence on this process. Tables 4 and 5 show the signal-to-noise ratio for wear rate and coefficient of friction response.

3.1. ANOVA and the Resultant Impact of Factors or Parameters. The variance analysis (ANOVA) aided in analyzing the experimental results. ANOVA sought to give an insight into percentage factors that tend to influence the friction coefficient and wear intensity individually. Tables 6 and 7 highlight the ANOVA results. At $P < 0.05$, the results

Table 3: Experimental design using L27 (3^3) orthogonal array.

Sample Id	Load (N)	Velocity (m/s)	Nanographite wt%	Wear rate $\times 10^{-3}$ (mm^3/m)	COF	S/N ratio for wear rate	S/N ratio for COF	ANN wear rate	ANN COF
S1	10	0.75	1	0.323	0.4146	9.8159	7.6474	0.3230	0.4254
S2	10	0.75	3	0.3186	0.3162	9.9351	10.001	0.3200	0.3148
S3	10	0.75	5	0.3611	0.3651	8.8475	8.7518	0.3579	0.3598
S4	10	1.5	1	0.331	0.5477	9.6034	5.2291	0.3310	0.5582
S5	10	1.5	3	0.4166	0.3126	7.6056	10.1	0.4168	0.2980
S6	10	1.5	5	0.438	0.4955	7.1705	6.0991	0.4380	0.5019
S7	10	2.25	1	0.3568	0.5539	8.9515	5.1314	0.3568	0.5599
S8	10	2.25	3	0.3959	0.5168	8.0483	5.7335	0.3959	0.5347
S9	10	2.25	5	0.451	0.6258	6.9165	4.0713	0.4510	0.6460
S10	20	0.75	1	0.321	0.3256	9.8699	9.746	0.3214	0.3441
S11	20	0.75	3	0.2766	0.3569	11.163	8.9503	0.2766	0.3584
S12	20	0.75	5	0.4116	0.4038	7.7105	7.8767	0.4116	0.4218
S13	20	1.5	1	0.333	0.3904	9.5511	8.1698	0.3330	0.3966
S14	20	1.5	3	0.3016	0.3654	10.411	8.7446	0.3016	0.3598
S15	20	1.5	5	0.3766	0.4214	8.4824	7.5071	0.3754	0.4241
S16	20	2.25	1	0.358	0.4624	8.9223	6.6996	0.3571	0.4506
S17	20	2.25	3	0.3794	0.4915	8.4181	6.1695	0.3794	0.4972
S18	20	2.25	5	0.487	0.5125	6.2494	5.8061	0.5958	0.5306
S19	30	0.75	1	0.4023	0.4558	7.909	6.8245	0.4023	0.4329
S20	30	0.75	3	0.392	0.4262	8.1343	7.4077	0.3920	0.4222
S21	30	0.75	5	0.4327	0.5588	7.2763	5.0549	0.4327	0.5577
S22	30	1.5	1	0.4073	0.4351	7.8017	7.2282	0.4073	0.4191
S23	30	1.5	3	0.391	0.4195	8.1565	7.5454	0.3910	0.4247
S24	30	1.5	5	0.438	0.53	7.1705	5.5145	0.4380	0.5422
S25	30	2.25	1	0.4137	0.632	7.6663	3.9857	0.4137	0.6619
S26	30	2.25	3	0.396	0.6141	8.0461	4.2352	0.3960	0.5539
S27	30	2.25	5	0.4502	0.6545	6.9319	3.6818	0.4502	0.6542

Table 4: Signal-to-noise ratio for wear rate—smaller is better.

Level	Load (N)	Velocity (m/s)	Nanographite wt%
1	8.544	8.962	8.899
2	8.975	8.439	8.880
3	7.677	7.794	7.417
Delta	1.298	1.168	1.482
Rank	2	3	1

Table 5: Signal-to-noise ratio for coefficient of friction—smaller is better.

Level	Load (N)	Velocity (m/s)	Nanographite wt%
1	6.974	8.029	6.740
2	7.741	7.349	7.654
3	5.720	5.057	6.040
Delta	2.021	2.972	1.614
Rank	2	1	3

suggest that the interactions of the experimental factors pose a statistically significant impact on the performance measures examined. Tables 6 and 7 illustrate both the percentage influence of individual factors and the role they play in shaping the overall outcome.

The values were also converted to the S/N ratio to determine the quality of characteristics. Also, the S/N ratio was established after determining the process' control factors' role on the friction and wear rate coefficient. From Tables 4 and 5, nanographite addition forms the main parameter influencing the wear rate. Those that follow include normal load and sliding speed. Similarly, nanographite addition is the main factor influencing the coefficient of friction, but sliding speed and normal load follow, respectively. The last two parameters are different from the case of the wear rate in which normal load precedes sliding speed. Hence, Tables 6 and 7 illustrate the ANOVA results relative to the composites tested, giving an insight into the friction and wear rate coefficient.

The analysis in Tables 6 and 7 shows the nanographite addition, which translates into the load and poses the

Table 6: Analysis of variance for the signal to noise for wear rate.

Source	DF	Seq SS	Adj SS	Adj MS	F value	P value	Contribution
Load (N)	2	0.013342	0.013342	0.006671	15.90	0.002	19.23%
Velocity (m/s)	2	0.011273	0.011273	0.005637	13.43	0.003	16.25%
Nanographite wt%	2	0.025750	0.025750	0.012875	30.69	0.001	37.11%
Load (N) ∗ velocity (m/s)	4	0.007357	0.007357	0.001839	4.38	0.036	10.60%
Load (N) ∗ Gr wt%	4	0.006542	0.006542	0.001635	3.90	0.048	9.43%
Velocity (m/s) ∗ Gr wt%	4	0.001762	0.001762	0.000441	1.05	0.440	2.54%
Residual error	8	0.003356	0.003356	0.000420			4.84%
Total	26	0.069383					100.00%

Table 7: Analysis of variance for signal to noise for coefficient of friction.

Source	DF	Seq SS	Adj SS	Adj MS	F value	P value	Contribution
A	2	0.055604	0.055604	0.027802	19.31	0.001	21.32%
B	2	0.128709	0.128709	0.064354	44.71	0.001	49.34%
C	2	0.031144	0.031144	0.015572	10.82	0.005	11.94%
$A * B$	4	0.011470	0.011470	0.002867	1.99	0.189	4.40%
$A * C$	4	0.016552	0.016552	0.004138	2.87	0.095	6.35%
$B * C$	4	0.005852	0.005852	0.001463	1.02	0.454	2.24%
Residual error	8	0.011516	0.011516	0.001439			4.41%
Total	26	0.260846					100.00%

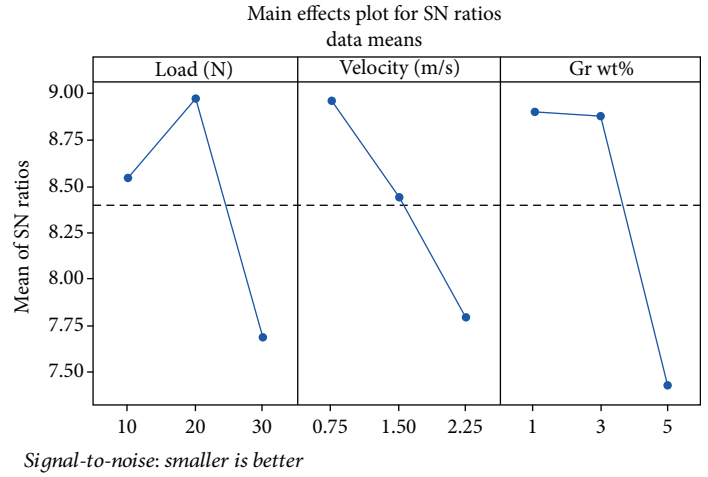

Figure 4: S/N plot for wear rate.

greatest impact on the wear rate ($F = 44.71$). The other two factors affect the wear rate in terms of load ($F = 19.31$) and sliding speed or velocity ($F = 10.82$). The implication is that the need to pay more attention to this factor cannot be overemphasized.

3.2. Focusing on the Impact of the Test Parameters on the Coefficient of Friction and Wear Rate. Figures 4 and 5 illustrate the impact of different parameters on the coefficient of friction and wear rate. In situations where a given parameter's line was closer to horizontal, it was inferred that it did not exhibit a significant impact. On the other hand, in situations where lines for certain parameters showed the highest degree of inclination, it was inferred that the effect was the most significant. Indeed, nanographite addition depicted the strongest impact on the rate of wear. Therefore, it was established that an increase in normal load tends to increase the wear rate. However, nanographite addition accompanied

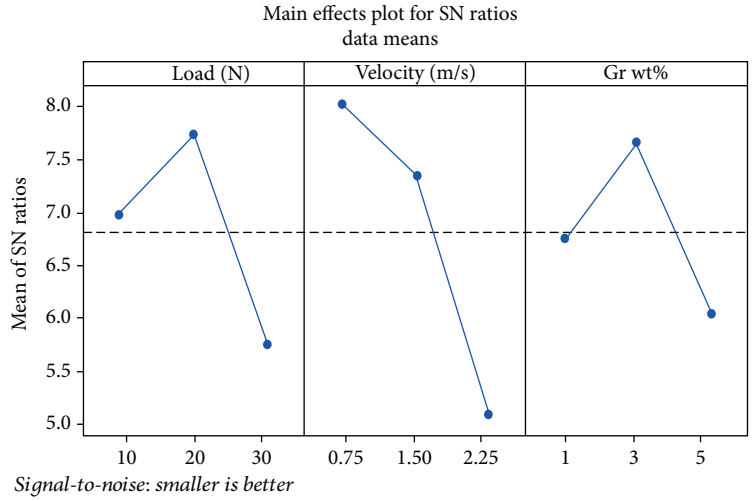

Figure 5: S/N plot for COF.

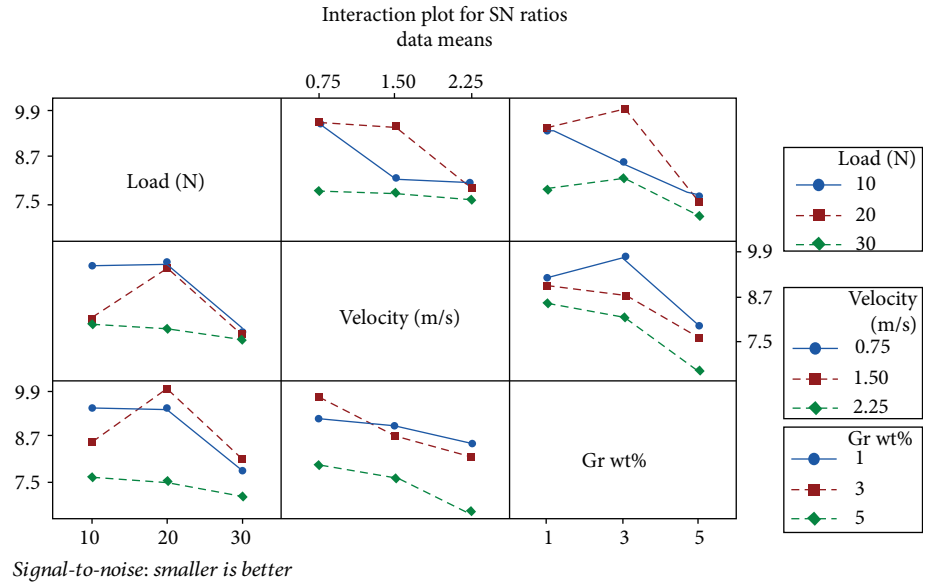

Figure 6: Interaction plot for S/N ratio wear rate.

by increased sliding speed depicted a decrease in wear rate. At the highest sliding speed, nanographite addition, and the lowest normal load, the wear rate was the lowest.

From Figures 4 and 5, it was also evident that for the curve of nanographite addition, the largest slope was the most significant factor affecting the coefficient of friction. With a decrease in sliding speed and nanographite addition, the coefficient of friction was found to decrease. As the normal load increased, the coefficient of friction also increased. The interactions between the analyzed parameters and their impact on the friction and wear rate coefficient are illustrated in Figures 6 and 7.

3.3. Multiple Linear Regressions. MINITAB 18 software was used to establish a multiple linear regression model with the experiment's linear dependence occurring between values of nanographite addition, sliding speed, and normal load. ANOVA analysis led to the establishment of the linear regression equation, setting the nanographite addition, sliding speed, and normal load values:

$$\text{Wear rate} = 0.1807 + 0.00641A + 0.0539B + 0.0201C - 0.00187AB + 0.00559BC - 0.000590CA. \quad (2)$$

For the coefficient of friction (COF), the regression equation was

$$\text{COF} = 0.232 + 0.00243A + 0.1359B - 0.0122\,C - 0.00156\,AB + 0.0007\,BC + 0.00104\,CA. \quad (3)$$

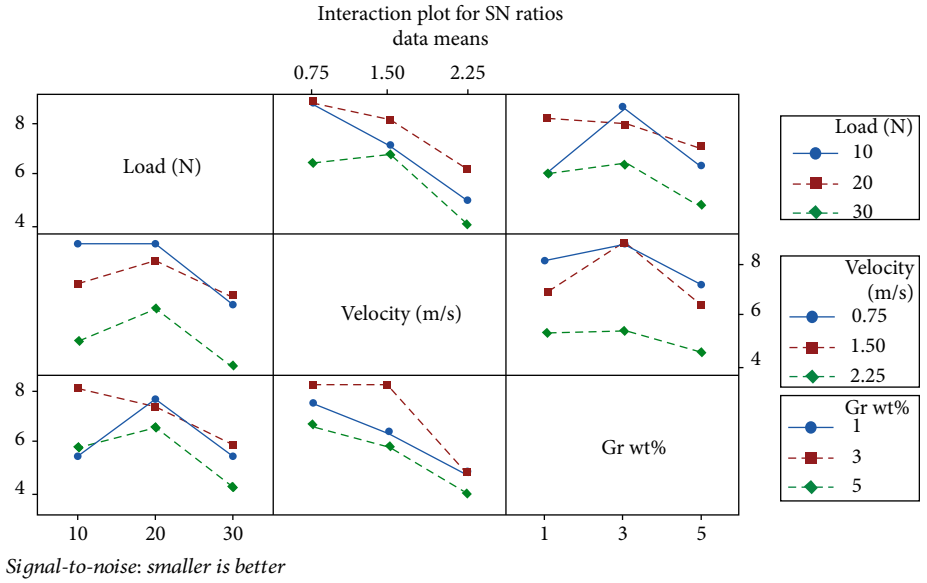

Figure 7: Interaction plot for S/N ratio COF.

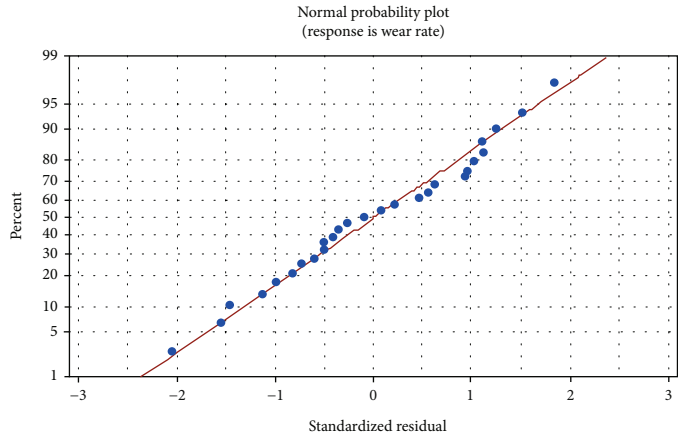

Figure 8: Normal probability plots of residuals for wear rate.

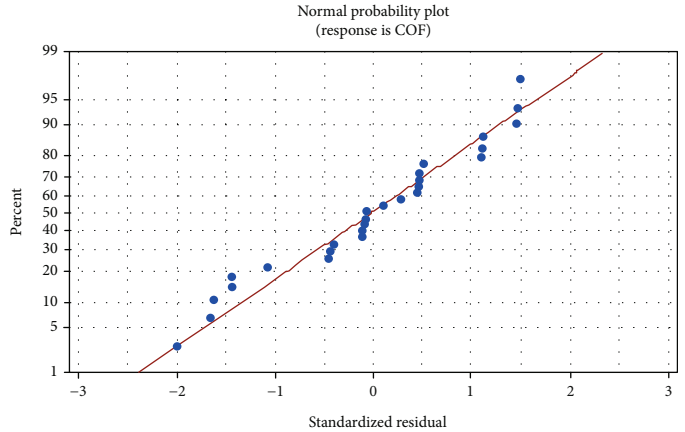

Figure 9: Normal probability plots of residuals for COF.

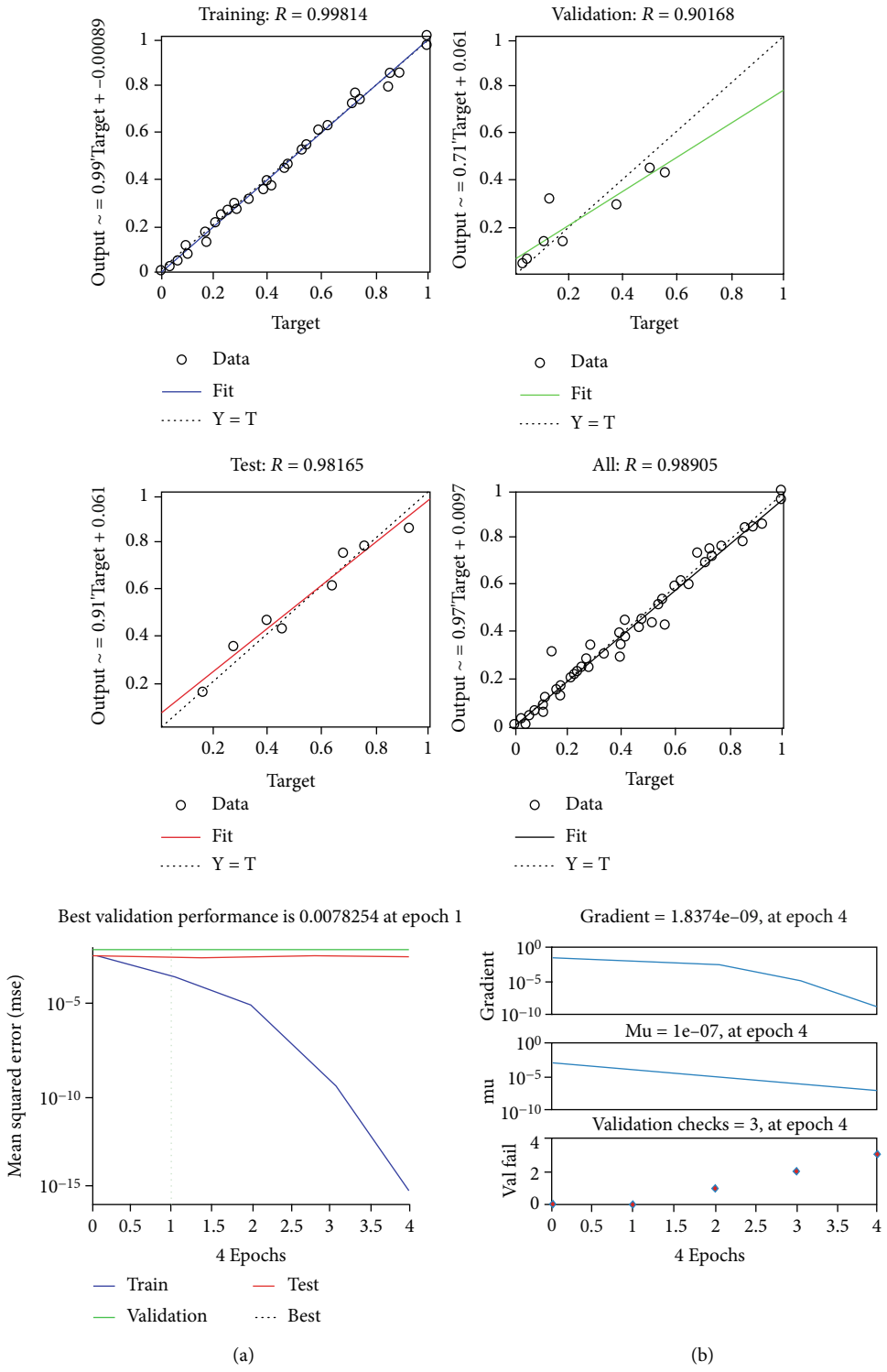

Figure 10: ANN mean square error and training state plot.

From the coefficients obtained in equations (2) and (3) above, the study established that when each factor was considered individually, the impact posed on the coefficient of friction and wear rate of the composites under examination differed. As the normal load increased, the coefficient of friction and wear rate increased. However, the friction and wear rate coefficient decreased with an increase in nanographite content and sliding speed. The eventuality is that the models developed to predict the coefficient of friction and wear rate relative to the composites that were tested proved adequate,

as shown in equations (2) and (3), with the points in Figures 8 and 9 confirming this result because they lie closer to the estimated line perceived to exhibit small disintegration.

3.4. Experimental Confirmation. Focus on the eventual impact of the control parameters examined. In this case, the role of experimental confirmation is to verify the results accruing from the Taguchi method. The experimental confirmation is also used to ensure that the quality characteristics are tested. Also, the optimal impact factor levels are used to establish values of the optimal friction coefficient and wear rate. Total error losses are considered to estimate the optimal levels. ANN mean square error and training state plot are shown in Figure 10.

Equation (4) was used to predict the optimal rate of wear rate and considered individual effects of nanographite (R), sliding speed (S), and load (L). The equation was

$$\mathrm{Wr} = T_w + (L1 - T_W) + (S3 - T_W) + (R3 - T_W). \quad (4)$$

Levels of the factors under examination were used to predict the optimal coefficient of friction. With personal effects of the respective factors governing the predicted optimal friction coefficient development, equation (5) was used:

$$\mu = T_\mu + \left(L1 - T_\mu\right) + \left(S3 - T_\mu\right) + \left(R3 - T_\mu\right). \quad (5)$$

3.5. The Case of Artificial Neural Network (ANN). In this experiment, ANN training and testing were achieved via MATLAB R2016a. From the results, this study established that a reasonably good performance arises from the trained ANN. The inference was informed by the similarity between the test and validation curves. It is also worth highlighting that the ANN training would extend to the 4^{th} epoch, but epoch 1 formed the point associated with optimal or the best validation performance. At this point (epoch 1), a value of 0.0078254 was obtained.

On the other hand, a value of 1.8374×10^{-9} was obtained for the case of epoch 4, illustrating a value closer to zero. Another notable trend was that as the number of epochs increased, the gradient value decreased. Table 8 summarizes the results of the confirmation experiments for the wear rate and coefficient of friction.

The regression equation was obtained upon employing the ANN output of training and ANOVA analysis before comparing the findings with experimental data. Figure 11 shows the findings after comparing the study's coefficient of friction and wear rate with the experimental data. Indeed, the analysis of the data obtained revealed that the two methods are highly reliable. Particularly, there was a close similarity between the findings established by ANN training and the experimental data. As such, the ANN was highly efficient relative to the prediction of the coefficient of friction and wear rate.

3.6. Analysis of the Worn Surface. Energy-dispersive spectroscopy (EDS) and scanning electron microscopy aided in testing and analyzing the tested composites' worn surfaces.

Table 8: Results of the confirmation experiments for wear rate and coefficient of friction.

	Prediction	Experimental	ANN
Wear rate 10^{-5} (mm^3/m) $L1, S3, R3$	0.118	0.195	0.125
S/N ratio (db)	18.56	17.12	17.56
Coefficient of friction $L1, S3, R3$	0.062	0.058	0.060
S/N ratio (db)	24.15	24.731	24.315

In most of the composites, the main mechanism of wear was similar. This dominant mechanism involves combinations of light abrasion and wiping or light adhesion identified in Figures 12(a)–12(d). Also, the backscattered electron image (BEC) aided in illustrating the morphology of the alloy, while the secondary electron image (SEI) aided in presenting the worn surface. Imperative to highlight is that the EDS analysis revealed the presence of nanographite particles.

Over the worn surface, the particles were randomly distributed. Hence, they were avowed to account for relatively high values of the coefficient of friction. It was also observed that silicon carbide is more brittle compared to the rest of the composite matrix. The EDS analysis also confirmed that all composite contact surfaces experienced counterbody material transfer. Notably, the majorities of counterbody materials transferred were in front of and around the nanographite particles (Figure 12(b)).

Figure 13 shows the worn surface of hybrid composite (sample S11) SEM with corresponding EDS analysis results. From the observations about the EDS analysis that focused on transferred material, it was established that counterbody material, oxides, and nanographite constituted the mixture in the transferred material, reflecting a mechanically mixed layer similar to that which is mostly observed in AMCs that have been examined under experimental settings with dry sliding conditions [22]. In the AMCs, the layer exists as a thin lubricant film occurring between the disc surface and the counterpart block. Effects of this layer include reductions in the coefficient of friction, wear, and heat generation because of the friction [20, 21]. Nanographite has also been found on the worn surfaces of hybrid composites. During the compocasting or composite preparation process, nanographite particles were fragmented to form small and fine particles. As such, they could not be detected in the form of large particles.

4. Conclusion

The Taguchi method plays a significant role in analyzing aluminium matrix composites' sliding tribological behaviour. The Taguchi method offers an efficient, systematic, and simple methodology for optimizing wear and friction test parameters. This study established that wt% addition of nanographite and an increase of sliding speed tend to decrease the coefficient of friction and wear rate of tested

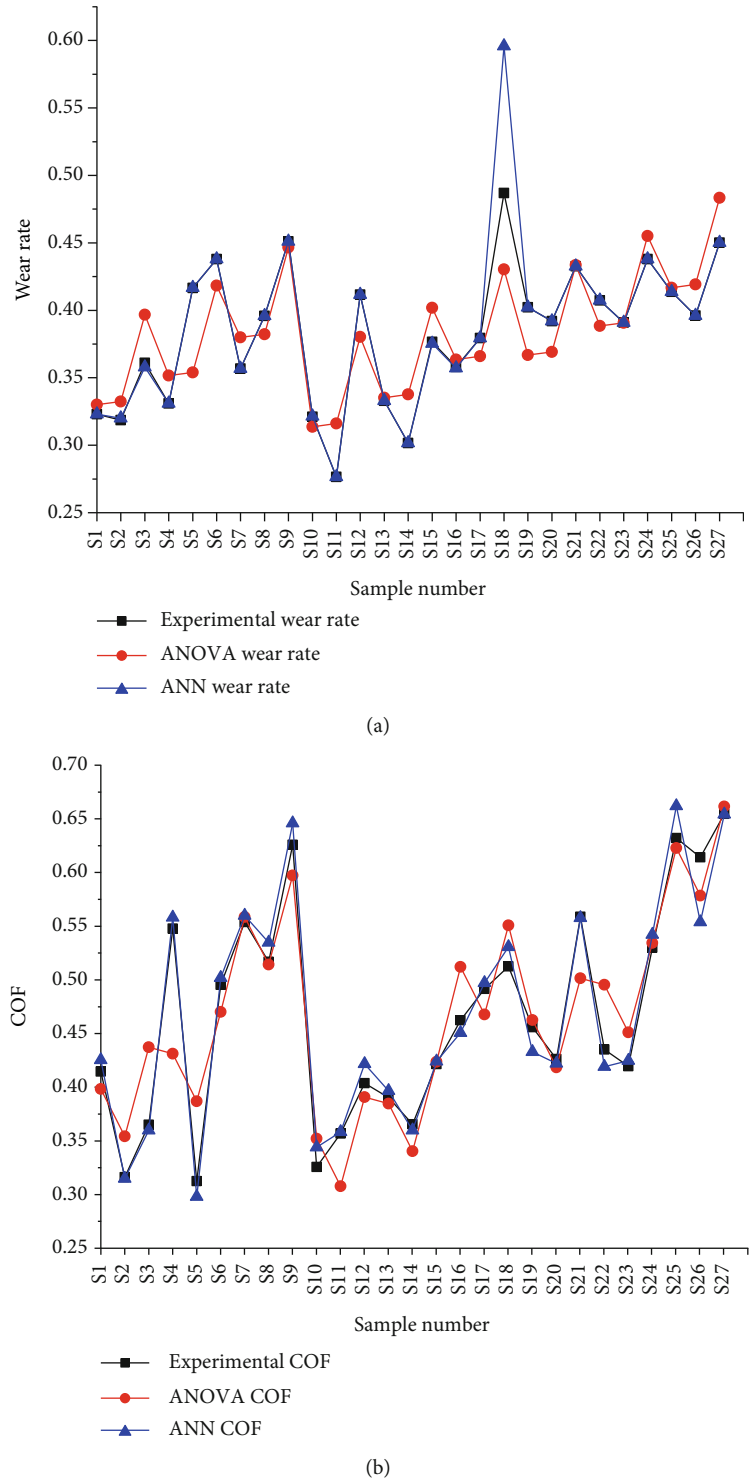

Figure 11: Comparison of results for (a) wear rate and (b) coefficient of friction.

composite tends. On the other hand, findings suggested that the increase of normal load leads to an increase in friction and wear rate coefficient. In the hybrid composites, minimal friction coefficient and wear rate were observed to be at maximal sliding speed and minimal load for the case of nanographite. The study concluded that sliding speed and normal load factors exhibit the lowest effect on wear rate while wt% of nanographite exhibits the largest effect. Also, individual parameter interactions revealed a smaller impact (interactions involving wt% of nanographite and sliding speed, sliding speed and normal load, and wt% of nanographite and normal load). From the results of MATLAB R2018

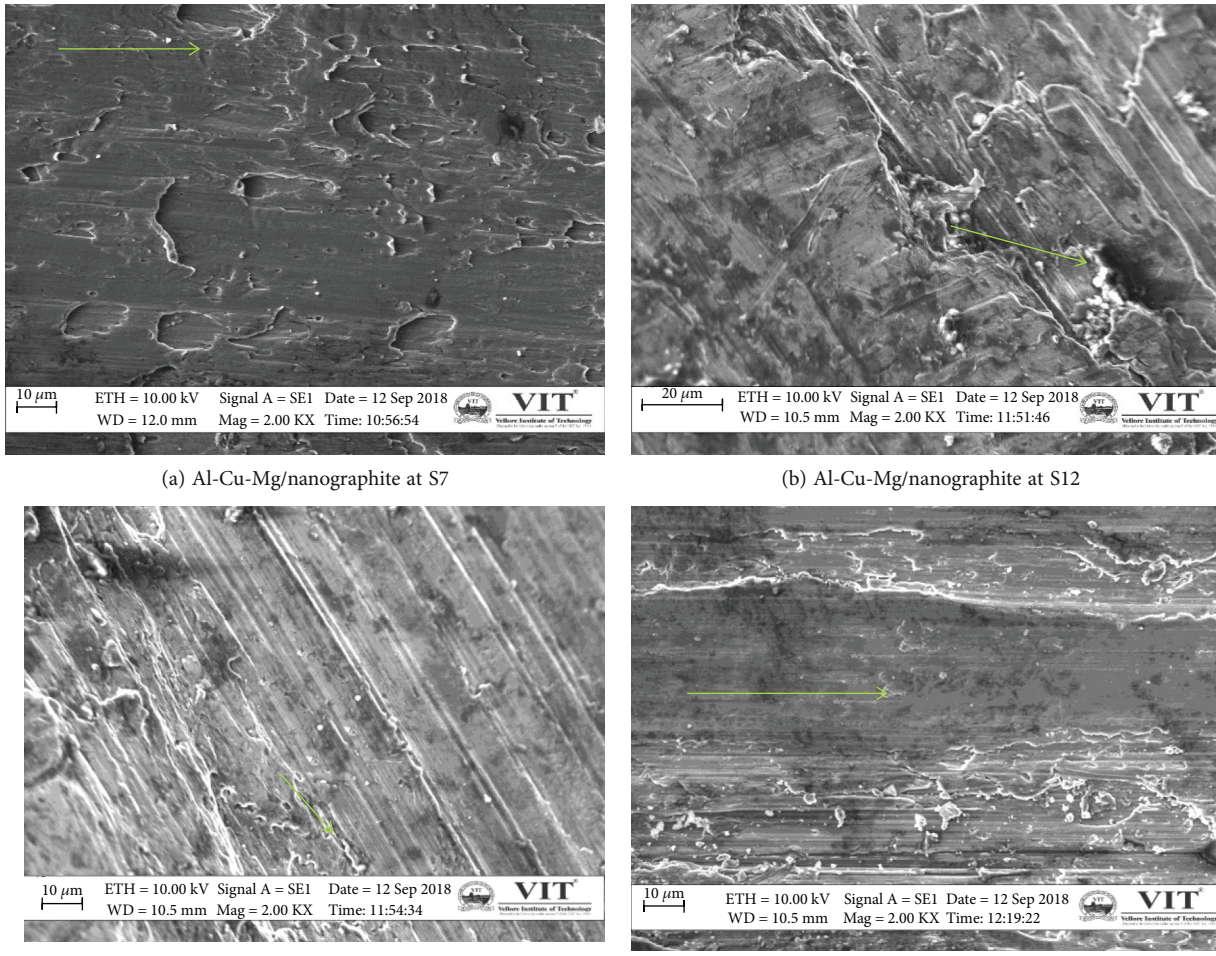

(a) Al-Cu-Mg/nanographite at S7

(b) Al-Cu-Mg/nanographite at S12

(c) Al-Cu-Mg/nanographite at S11

(d) Al-Cu-Mg/nanographite at S19

Figure 12: Worn surface of hybrid composite.

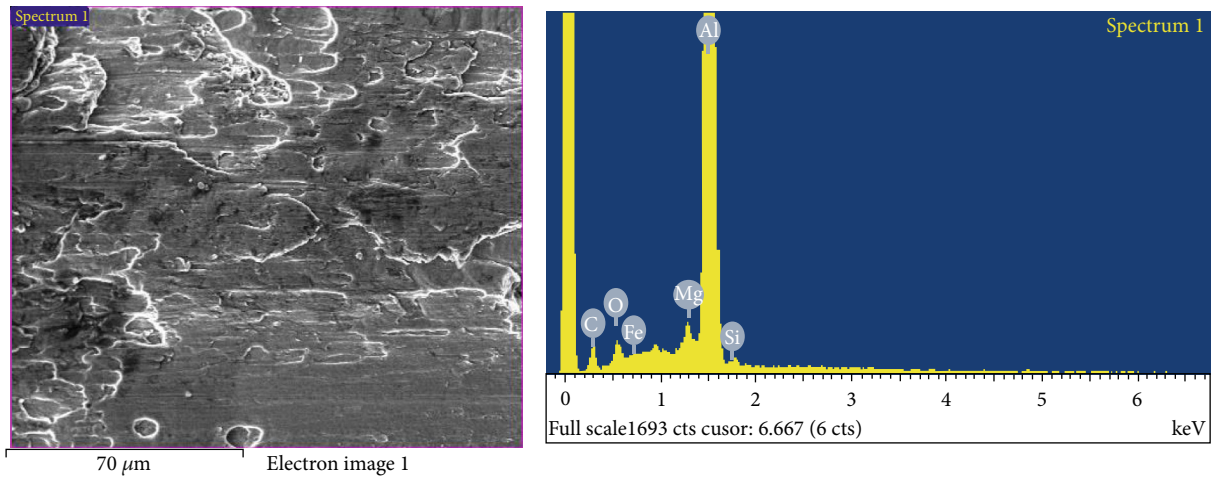

Figure 13: Worn surface of hybrid composite (sample S11) SEM and corresponding EDS analysis results.

software, ANN proved efficient in predicting the coefficient of friction and wear rate because the results obtained by ANN and ANOVA were similar to the experimental data.

Data Availability

The data used to support the findings of this study are included within the article. Should further data or information be required, these are available from the corresponding author upon request.

Disclosure

This research and publication was performed as part of the employment at the Kombolcha Institute of Technology, Wollo University, Kombolcha, Amhara, Ethiopia.

Conflicts of Interest

The authors declare that there are no conflicts of interest regarding the publication of this paper.

Acknowledgments

The authors thank Saveetha School of Engineering, SIMATS, Chennai, and Vellore Institute of Technology, Chennai, for providing characterization support to complete this research work.

References

[1] A. K. F. Hassan and S. Mohammed, "Artificial neural network model for estimation of wear and temperature in pin-disc contact," *Universal Journal of Mechanical Engineering*, vol. 4, no. 2, pp. 39–49, 2016.

[2] A. Vencl, I. Bobic, S. Arostegui, B. Bobic, A. Marinkovic, and M. Babic, "Structural, mechanical and tribological properties of A356 aluminium alloy reinforced with Al_2O_3, SiC and SiC + graphite particles," *Journal of alloys and compounds*, vol. 506, no. 2, pp. 631–639, 2010.

[3] B. Stojanović and J. Glišović, "Automotive engine materials," in *Saleem Hashmi (editorin-chief), Reference Module in Materials Science and Materials Engineering*, pp. 1–9, Elsevier, Oxford, 2016.

[4] L. Natrayan and M. Senthil Kumar, "An integrated artificial neural network and Taguchi approach to optimize the squeeze cast process parameters of AA6061/Al_2O_3/SiC/Gr hybrid composites prepared by novel encapsulation feeding technique," *Materials Today Communications*, vol. 25, article 101586, 2020.

[5] R. Ambigai and S. Prabhu, "Optimization of friction and wear behaviour of Al- Si_3N_4 nano composite and Al-Gr- Si_3N_4 hybrid composite under dry sliding conditions," *Transactions of Nonferrous Metals Society of China*, vol. 27, no. 5, pp. 986–997, 2017.

[6] B. Stojanović, M. Babić, S. Mitrović, A. Vencl, N. Miloradović, and M. Pantić, "Tribological characteristics of aluminium hybrid composites reinforced with silicon carbide and graphite. A review," *Journal of the Balkan Tribological Association*, vol. 19, no. 1, p. 83, 2013.

[7] A. K. Mondal and S. Kumar, "Dry sliding wear behaviour of magnesium alloy based hybrid composites in the longitudinal direction," *Wear*, vol. 267, no. 1-4, pp. 458–466, 2009.

[8] A. Kumar and M. Kumar, "Mechanical and dry sliding wear behaviour of B4C and rice husk ash reinfroced Al 7075 alloy hybrid composite for armors application by using Taguchi techniques," *Materials Today: Proceedings*, vol. 27, pp. 2617–2625, 2020.

[9] D. B. Miracle, "Metal matrix composites - From science to technological significance," *Composites science and technology*, vol. 65, no. 15–16, pp. 2526–2540, 2005.

[10] D. C. Montgomery, *Design and Analysis of Experiments*, John Wiley & Sons, 2012.

[11] A. Çiçek, T. Kivak, and G. Samtaş, "Application of Taguchi method for surface roughness and roundness error in drilling of AISI 316 stainless steel," *Strojniški vestnik-Journal of Mechanical Engineering*, vol. 58, no. 3, p. 165, 2012.

[12] K. R. Roy, *A Primer on the Taguchi Method*, Van Nostrand Reinhold, New York, 1990.

[13] Y. Sahin, "The prediction of wear resistance model for the metal matrix composites," *Wear*, vol. 258, no. 11-12, p. 1717, 2005.

[14] M. Babic, A. Vencl, S. Mitrović, and I. Bobić, "Influence of T4 heat treatment on tribological Behavior of Za27 alloy under lubricated sliding condition," *Tribology Letters*, vol. 36, no. 2, pp. 125–134, 2009.

[15] M. Babić, B. Stojanović, S. Mitrović et al., "Wear properties of A356/10SiC/1Gr hybrid composites in lubricated sliding conditions," *Tribology in industry*, vol. 35, no. 2, p. 148, 2013.

[16] M. L. Ted Guo and C. Y. A. Tsao, "Tribological behavior of self-lubricating aluminium/SiC/graphite hybrid composites synthesized by the semi-solid powder-densification method," *Composites science and technology*, vol. 60, no. 1, pp. 65–74, 2000.

[17] M. Sarikaya, H. Dilipak, and A. Gezginet, "Optimization of the process parameters for surface roughness," *Mat tehnol*, vol. 49, no. 1, p. 139, 2015.

[18] N. Chawla and K. K. Chawla, "Metal-matrix composites in ground transportation," *JoM*, vol. 58, no. 11, p. 67, 2006.

[19] S. Basavarajappa and G. Chandramohan, "Wear studies on metal matrix compositeTaguchi approach," *Journal of Materials Science and Technology*, vol. 21, no. 6, p. 845, 2005.

[20] S. Suresha and B. K. Sridhara, "Effect of silicon carbide particulates on wear resistance of graphitic aluminium matrix composites," *Materials & Design*, vol. 31, no. 9, pp. 4470–4477, 2010.

[21] A. Vencl, F. Vučetić, B. Bobić, J. Pitel, and I. Bobić, "Tribological characterisation in dry sliding conditions of compocasted hybrid A356/SiCp/Grp composites with graphite macroparticles," *The International Journal of Advanced Manufacturing Technology*, vol. 100, no. 9-12, pp. 2135–2146, 2019.

[22] S. V. Prasad and R. Asthana, "Aluminum Metal–Matrix Composites for Automotive Applications: Tribological Considerations," *Tribology letters*, vol. 17, no. 3, pp. 445–453, 2004.

[23] T. Kivak, "Optimization of surface roughness and flank wear using the Taguchi method in milling of Hadfield steel with PVD and CVD coated inserts," *Measurement*, vol. 50, pp. 19–28, 2014.

[24] U. Soy, F. Ficici, and A. Demir, "Evaluation of the Taguchi method for wear behavior of Al/Sic/B4c composites," *Journal of Composite Materials*, vol. 46, no. 7, pp. 851–859, 2012.

[25] Y. Kayali, B. Gokce, E. Mertgenc, F. Colak, and R. Kara, "Analysis of wear behavior of borided AISI 52100 steel with the Taguchi method," *The Journal of the Balkan Tribological Association*, vol. 19, no. 3, p. 365, 2013.

[26] M. O. Bodunrin, K. K. Alaneme, and L. H. Chown, "Aluminium matrix hybrid composites: a review of reinforcement philosophies; mechanical, corrosion and tribological characteristics," *Journal of Materials Research and Technology*, vol. 4, no. 4, pp. 434–445, 2015.

[27] B. Stojanović and S. Milojević, "Characterization, manufacturing and application of metal matrix composites," in *Advances in Materials Science Research*, M. C. Wythers, Ed., vol. 30, pp. 83–113, Nova Science Publishers, New York, 2017.

Hindawi
Journal of Nanomaterials
Volume 2021, Article ID 9096838, 6 pages
https://doi.org/10.1155/2021/9096838

Research Article

Antimicrobial Activity and Characterization of Pomegranate Peel-Based Carbon Dots

Waseem Akhtar Qureshi,[1] **B. Vivekanandan**,[2] **J. Altrin Jayaprasath**,[3] **Daoud Ali**,[4] **Saud Alarifi**,[4] **and Kalim Deshmukh**[5]

[1]*Cholistan Institute of Desert Studies, Baghdad–ul–Jadeed Campus, The Islamia University of Bahawalpur, Pakistan*
[2]*Department of Chemical Engineering, Hindustan Institute of Technology and Science, 603103, Chennai, Tamil Nadu, India*
[3]*Department of Botany, Voorhees College, 632001, Vellore, Tamil Nadu, India*
[4]*Department of Zoology, College of Science, King Saud University, PO Box 2455, Riyadh 11451, Saudi Arabia*
[5]*New Technologies - Research Center, University of West Bohemia, Plzeň 30100, Czech Republic*

Correspondence should be addressed to Daoud Ali; daoudali08@yahoo.com

Received 9 September 2021; Accepted 4 October 2021; Published 11 November 2021

Academic Editor: Lakshmipathy R

Copyright © 2021 Waseem Akhtar Qureshi et al. This is an open access article distributed under the Creative Commons Attribution License, which permits unrestricted use, distribution, and reproduction in any medium, provided the original work is properly cited.

This investigation reports the use of agrowaste pomegranate peels as an economical source for the production of fluorescent carbon dots (C-dots) and their potential application as an antimicrobial agent. The carbon dots were prepared through low-temperature carbonization at 200°C for 120 min. The obtained C-dots were found to be small in size and exhibited blue luminescence at 350 nm. Further, the synthesized C-dots were characterized with the help of analytical instruments such as DLS, UV-visible, FT-IR, TEM, and fluorescence spectrophotometer. Antimicrobial activity of the C-dot PP was estimated by the agar diffusion method and MIC. *S. aureus* and *K. pneumoniae* are showing susceptibility towards C-dot PP when compared to the standard and showing a moderate activity against *P. aeruginosa* and resistance towards *E. coli*. The obtained C dot PPs were found to be around 5-9 nm in size confirmed from DLS analysis and supported by TEM. The synthesized C-dots were investigated to understand their microbial efficiency against pathogens and found to have antimicrobial efficiency. These results suggest that pomegranate peels are a potential source of carbon dots with antimicrobial efficiency.

1. Introduction

Nanoparticles (NPs) have become indispensable in biological research due to long-term fluorescence imaging and identification of their properties. Photobleaching resistance, improved signal brightness, larger absorption coefficients, light emission, and simultaneous stimulation of multiple fluorescence colours are just a few of the unique properties of QDs that make them indispensable [1]. Guan et al. created bright C-dots by using folic acid molecules as both nitrogen and carbon donors [2].

Carbon dots are promising oxygenous carbon nanoparticles that exhibit photoluminescence properties. These dots can replace quantum dots in semiconductor devices and some future nanodevices because of their high water solubility, tiny size (<10 nm), intense brightness, high photostability, lesser cytotoxicity, and biocompatibility [3, 4]. The applications of carbon dots are diverse and found to be prolific in nature starting from pollutant detection to battery electrodes and markers [5–8]. However, the production of carbon dots involves tedious processes that are detrimental to the environment and ecosystems. The previously reported methods have many drawbacks such as the use of chemicals, high temperature, and low product yield. Researchers are always in search of new and better ways of producing C-dots [9]. In a growing number of publications, plant by-products such as exotic fruit by-products as a source of food additives, fruit by-product extracts as antioxidants

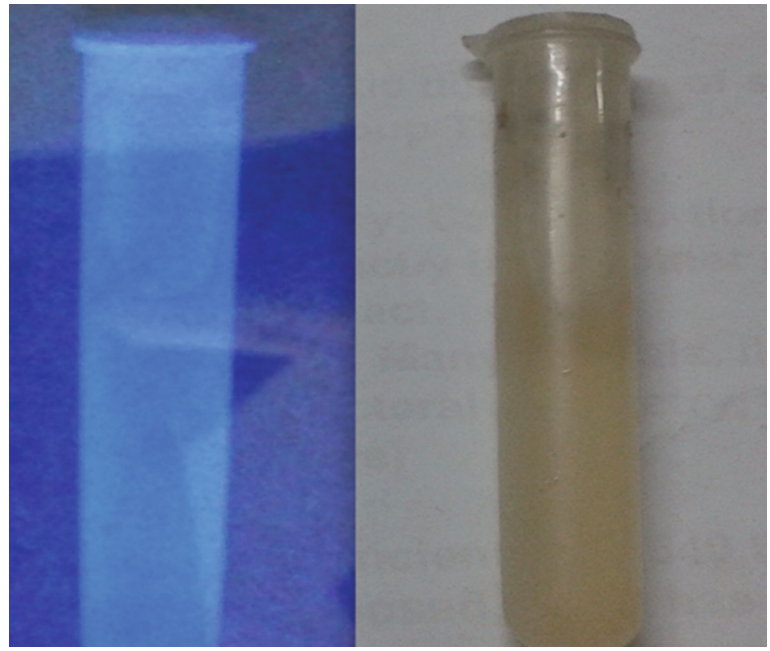

Figure 1: Fluorescence exhibited at 350 nm by carbon dots.

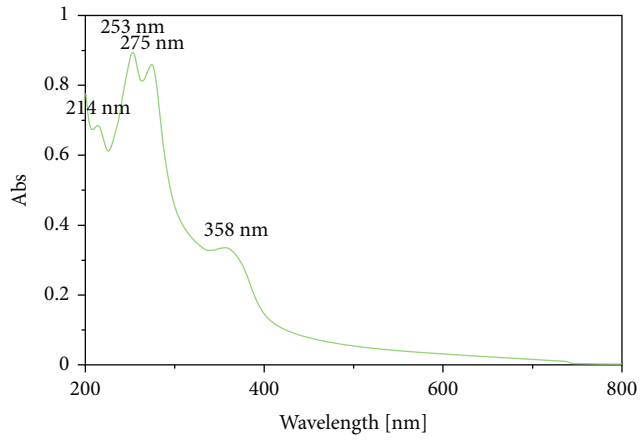

Figure 2: UV-visible absorption spectrum of C-dots prepared from pomegranate peels.

and antibacterial [10]. Plant wastes are appealing starting materials for CQDs because of their biocompatibility, low cost, and low toxicity [11].

Agrowastes are one of the potential sources for the production of carbon dots, and many fruit wastes are explored for this purpose [12–15]. Since the fruit wastes are easily available, low-cost, and eco-friendly, they have gained significance in the synthesis of carbon dots [14]. In continuation of the above, here, we report a new agrowaste fruit peel-based material (pomegranate peel) for the synthesis of carbon dots. Pomegranate is a delicious fruit with hard outer cover that is carbonaceous in nature. The peels are usually discarded, and this carbonaceous material can be a great precursor for the carbon dots.

The aim of this investigation is to produce C-dots from pomegranate peels through a low-temperature carbonization and filtration process. This method is extremely environment-friendly, and it does not involve any toxic or harmful chemical. The materials used for the synthesis are cheap and easily available and biowaste. The obtained C-dots are water soluble and highly fluorescent and have been investigated for antimicrobial activity.

2. Experiment

2.1. Synthesis of Fluorescent C-Dots. The fresh pomegranate peels sourced from local fruit vendors were cut into tiny pieces and dried in the sunlight to remove the moisture contents. The sun dried samples were then carbonized at 200°C for 2 hours. One gram of carbonized pomegranate peels was weighed and dispersed in 100 ml ultrapure water and sonicated for 15 minutes. The sonicated solution was later filtered with the help of a filter paper to obtain the supernatant solution containing carbon dots. Then, the superannuated solution was centrifuged, and the resultant supernate containing luminescent C-dots was analysed by various analytical methods.

2.2. Characterization

2.2.1. UV-Vis Spectral Analysis. The experimental absorption spectrum of compounds in the 200–700 nm regions in unpolarised light was obtained by using a JASCO V-670 UV-visible spectrophotometer. The estimated and observed absorption spectra demonstrate the accuracy of the derived model calculations.

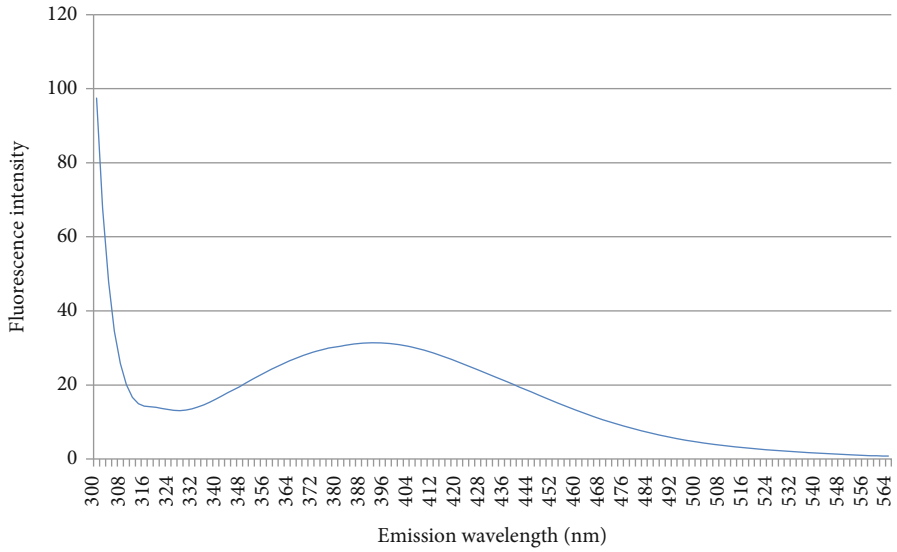

Figure 3: Emission spectra of C-dots prepared from pomegranate peels.

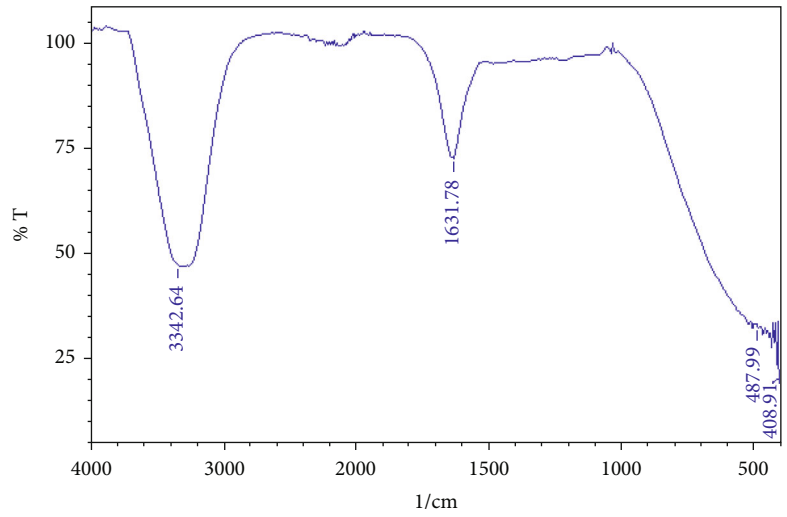

Figure 4: FT-IR spectrum of C-dots prepared from pomegranate peels.

2.2.2. Fluorescence Spectroscopy. A Hitachi F-7000 fluorescence spectrometer was equipped to obtain the fluorescence spectra as it has a high sensitivity measurement due to a design that prohibits fluorescence detecting along the flow channel.

2.2.3. FT-IR Analysis. FT-IR spectroscopy has proven to be a worldwide, sensitive, and highly repeatable physicochemical analytical approach that uses infrared absorption to identify the functional groups. FT-IR spectrum was obtained with an IR Affinity-1 (Shimadzu) between 400 and 4000 cm^{-1}. The samples were recorded on a KBr disc prepared freshly.

2.2.4. Particle Size and Zeta Potential. Using a Malvern Zetasizer Nano ZS (Malvern Instruments, Ltd., Malvern, Worcestershire, UK) equipped with a Ne-He laser, particle size was determined by dynamic light scattering (633 nm). According to the equipment specifications, measurements were taken at a fixed angle of 173° from 0.6 nm to 6 m. PC samples (5 mg ml^{-1}) were diluted to 1 : 100 in Milli-Q water and placed in disposable polaroid containers.

2.2.5. TEM (Transmission Electron Microscope). TEM was recorded with a JEOL JEM 2100F instrument operated at 200 kV. The diluted solution was placed over carbon-coated copper grids and dried outside. A total of ten sites on the TEM grid were examined.

2.2.6. Antimicrobial Activity. Four isolates such as *Staphylococcus aureus*, *Klebsiella pneumoniae*, *Pseudomonas*

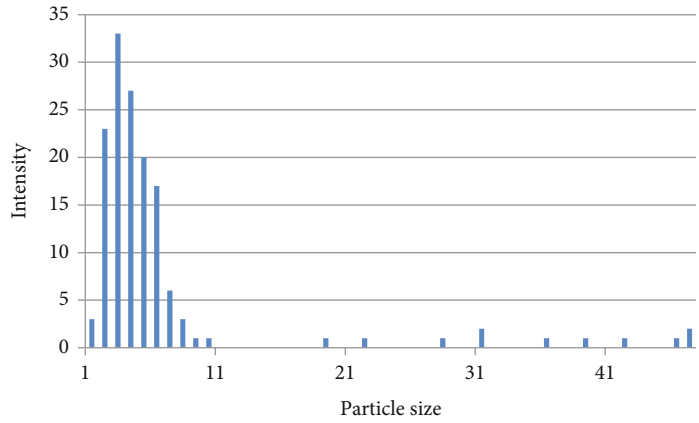

Figure 5: DLS pattern of C-dots prepared from pomegranate peels.

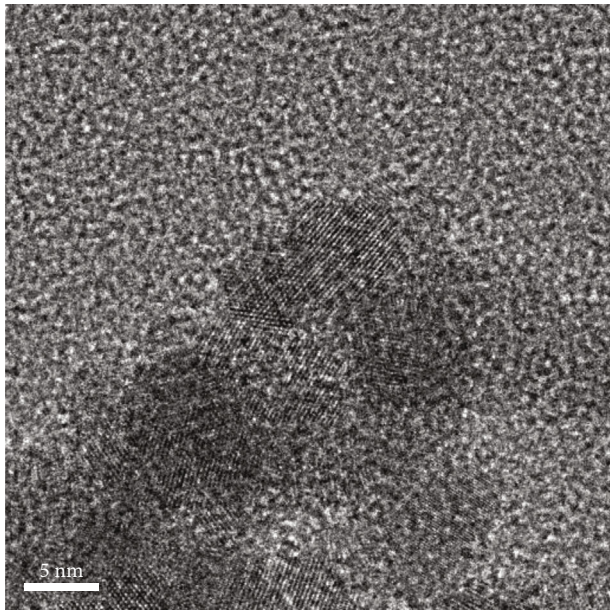

Figure 6: TEM image of C-dots prepared from pomegranate peels.

aeruginosa, and *Escherichia coli* were collected from the Department of Microbiology and Pathology, VIT, Tamil Nadu, India. The collected isolates were stocked and stored at -20°C in glycerol.

2.2.7. Agar Diffusion Method. Agar well diffusion on Mueller Hinton Agar, a popular method for antimicrobial screening, was adopted for pathogenic strains [15]. The incubation of isolates was carried out at 37°C for 24 hours in a nutrient broth with turbidity 0.5 adjusted with a spectrophotometer. The MHA plates were selected for the investigations, and wells were made with a sterilized gel borer and bacterial isolates of Actinobacteria were inoculated with the help of cotton. The solvent and carbon dot solution were tested against a test pathogen by adding 100 μl of test solutions into each well and ampicillin (30 μg/ml) as the standard. After incubation, the zone of inhibition developed around the wells in all the plates was examined [15].

2.2.8. Minimum Inhibitory Concentration (MIC). A tube dilution method was adopted to understand the MIC of the potent Actinobacteria. Carbon dot solution was diluted in 10% DMSO to obtain various concentrations ranging from 5 to 100 μg/ml of test solutions. Inoculation of 0.05 ml of bacterial culture was done by the addition of 5 ml of sterile Mueller Hinton Broth. To all the test tubes, 1 ml of C-dot PP solution was added and incubated for 24 h in order to observe any development of turbidity. The minimal concentration that could inhibit complete growth is considered MIC [16].

3. Results and Discussion

Carbon quantum dots (CQDs) have received a lot of attention in recent years because of their outstanding physical and optical properties. There are numerous types of carbon sources used in various fields, but CQDs used in the food industry must meet tighter safety standards. As a result, using 24 natural resources to prepare CQDs without involving humans is the best alternative [17]. Quantum dots, which range in size from 1 to 10 nanometers, are luminous semiconductor nanocrystals with complicated surface chemistry and unique optical properties (QDs). C-dots have optical features that allow them to reflect hits from particles of varying sizes in the sample [1].

The successfully synthesized C-dots from pomegranate peels were characterized for it properties with various analytical techniques. Preliminary investigations were made to confirm the formation of carbon dots with the help of the UV chamber. The samples were placed in the UV chamber, and UV light (354 nm) was passed on the tube containing carbon dot solution. A blue fluorescence was noticed at 354 nm which confirmed the presence of carbon dots. In the absence of UV light, ordinary solution was observed to have no fluorescence (Figure 1). Further, UV-vis analysis was carried out to observe the absorption spectra. An absorption peak at 214, 253, 275, and 358 nm was observed for the carbon dot solution; the peaks at 214 and 253 nm confirm the presence of carbon dots and light absorption due to sigma-sigma transitions (Figure 2). The absorption peak at 358 nm observed could be due to the presence of

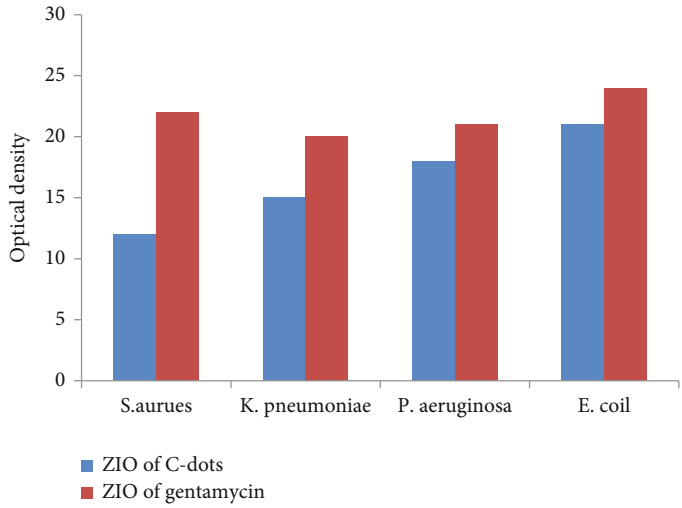

Figure 7: Zone of inhibition of microbial isolates.

Table 1: MIC test results of bacterial strains tested.

Microorganisms	MIC (μg/ml)
S. aureus	67
K. pneumoniae	72
P. aeruginosa	84
E. coli	89

C=O n-π^* transition. The result showed consistency with previous reports on the synthesis of C-dots [18, 19]. Further, the emission characteristics of C-dots obtained from the pomegranate peel were investigated with a photoluminescence spectrophotometer with excitation at 300 nm, and C-dots exhibited a fluorescence emission band at 390 nm (Figure 3). These observations are in accordance with the results reported in literature [20]. The stability of the carbon dots at various pH was also investigated to understand the application potential of carbon dots, and it was observed to be stable in acidic pH and an emission band constantly observed at 390 nm for the carbon dots in the 2-7 pH range. However, the emission bands disappear or diminish with the increase in pH in the base medium. These could be due to protonation and deprotonation of hydronium ions from the surface of the carbon dots. These findings help in the detection of pH and as biomarkers in acidic medium.

FT-IR spectroscopy was used for the identification of functional groups present on the C-dots. C-dots obtained from the pomegranate peel showed absorption peeks at 3342.64 and 1650 cm^{-1} (Figure 4). These two peaks are due to the hydroxyl groups of the water molecule, and there were no any other major peaks observed in the spectra. This confirms that the solution contains only carbon dots and no other impurities are present in the solution. The particle size was obtained from DLS which showed a range of 5-9 nm (Figure 5). This confirms that C-dots were present in nanoform. The size distribution of carbon dots was seen to be from 1 nm to 50 nm; however, the higher quantity of carbon dots was found to be between 5 and 9 nm in scale. These small-sized carbon dots are very much helpful in applications of carbon dots as biomarkers.

The transmission electron microscope was equipped to estimate and understand the size and shape of the carbon dots. It is observed that the carbon dots were found to be less than 10 nm in scale and shapes of the carbon dots were seen as spherical in nature (Figure 6). The size obtained through the TEM images supports the size confirmed through DLS. These results are in accordance with the production of carbon dots reported in literature [14, 21].

Microbial contamination of products from the farm to the table is a major source of concern in agriculture, as it costs producers money and puts the health of the final consumer at risk. Various investigations on the antibacterial effects of nanoparticles are currently being conducted [22].

The synthesized C-dots from pomegranate peels were investigated for their antimicrobial efficiency towards 4 pathogenic bacterial strains. The C-dot PP exhibits potent activity against selected isolates as shown in Figure 7, showing susceptibility towards *S. aureus* and *K. pneumonia*e, whereas it has moderate effect towards *P. aeruginosa* and resistance to *E.coli* when compared to ampicillin. MIC test results are represented in Table 1. The MIC was found to be high at 1000 μg/ml. The extracts were efficient towards three isolates such as *S. aureus* (MIC-67 μg/ml), *K. pneumoniae* (MIC-72 μg/ml), and *P. Aeruginosa* (MIC-84 μg/ml). However, it did not show any efficacy towards *E. coli*. These results suggest that C-dots have efficacy as antimicrobial agents towards certain pathogens. The main processes implicated in C-dots' antibacterial effects are likely associated with the generation of reactive oxygen species, according to available data (ROS). Reactive oxygen species (ROS) are produced by C-dots and have been found to kill or inhibit bacteria [23]. The mechanism of action includes C-dot adhesion to the bacterial surface, photoinduced production of ROS, disruption and penetration of the bacterial cell wall/membrane, induction of oxidative stress with DNA/RNA damage, which leads to changes or inhibitions of important gene expressions, and induction of oxidative damage to proteins [24].

4. Conclusion

This study reported the effective utilisation of the agrowaste pomegranate peel as a prolific precursor for the production of carbon dots. The production of C-dots was investigated via a low-temperature method and was characterized with various analytical techniques. The synthesized C-dots were found to be around 5-9 nm in size which is of great advantage. The synthesized C-dots were investigated for their antimicrobial efficiency against pathogenic bacteria and found to have very strong activity. These results confirm that pomegranate peels are capable of producing C-dots for antimicrobial activity.

Data Availability

The data used to support the findings of this study are included within the article.

Conflicts of Interest

The authors declare no conflicts of interest.

Acknowledgments

This work was funded by King Saud University (Researchers Supporting Project number RSP-2021/27), Riyadh, Saudi Arabia.

References

[1] I. Singh, R. Arora, H. Dhiman, and R. Pahwa, "Carbon quantum dots: synthesis, characterization and biomedical applications," *The Turkish Journal of Pharmaceutical Sciences*, vol. 15, no. 2, pp. 219–230, 2018.

[2] M. Xue, W. Guan, W. Gu et al., "Microwave-assisted polyol synthesis of carbon nitride dots from folic acid for cell imaging," *International Journal of Nanomedicine*, vol. 9, pp. 5071–5078, 2014.

[3] A. Prasannan and T. Imae, "One-pot synthesis of fluorescent carbon dots from orange waste peels," *Industrial & Engineering Chemistry Research*, vol. 52, no. 44, pp. 15673–15678, 2013.

[4] P. Y. Lin, C. W. Hsieh, M. L. Kung et al., "Eco-friendly synthesis of shrimp egg-derived carbon dots for fluorescent bioimaging," *Journal of Biotechnology*, vol. 189, pp. 114–119, 2014.

[5] H. Yi, Y. Huang, Z. C. Sha, X. H. Zhu, Q. Y. Xia, and H. Xia, "Facile synthesis of Mo_2N quantum dots embedded N-doped carbon nanosheets composite as advanced anode materials for lithium-ion batteries," *Materials Letters*, vol. 276, article 128205, 2020.

[6] J. Singh, S. Kaur, J. Lee et al., "Highly fluorescent carbon dots derived from _Mangifera indica_ leaves for selective detection of metal ions," *Science of The Total Environment*, vol. 720, article 137604, 2020.

[7] Y. Liang, L. X. Xu, K. Tang et al., "Nitrogen-doped carbon dots used as an "on-off-on" fluorescent sensor for Fe^{3+} and glutathione detection," *Dyes and Pigments*, vol. 178, article 108358, 2020.

[8] N. K. R. Bogireddy, J. Lara, L. R. Fragoso, and V. Agarwal, "One-step hydrothermal preparation of highly stable N doped oxidized carbon dots for toxic organic pollutants sensing and bioimaging," *Chemical Engineering Journal*, vol. 401, article 126097, 2020.

[9] C. H. Ding, Z. Q. Deng, J. C. Chen, and Y. Z. Jin, "One-step microwave synthesis of N,S co-doped carbon dots from 1,6-hexanediamine dihydrochloride for cell imaging and ion detection," *Colloids and Surfaces B: Biointerfaces*, vol. 189, article 110838, 2020.

[10] G. Ferrentino, M. D. Asaduzzaman, and M. M. Scampicchio, "Current technologies and new insights for the recovery of high valuable compounds from fruits by-products," *Critical Reviews in Food Science and Nutrition*, vol. 58, no. 3, pp. 1–19, 2016.

[11] R. Das, R. Bandyopadhyay, and P. Pramanik, "Carbon quantum dots from natural resource: a review," *Materials Today Chemistry*, vol. 8, pp. 96–109, 2018.

[12] R. Atchudan, T. N. J. I. Edison, S. Perumal, N. Muthuchamy, and Y. R. Lee, "Hydrophilic nitrogen-doped carbon dots from biowaste using dwarf banana peel for environmental and biological applications," *Fuel*, vol. 275, article 117821, 2020.

[13] Z. X. Hu, X. Y. Jiao, and L. Xu, "The N,S co-doped carbon dots with excellent luminescent properties from green tea leaf residue and its sensing of gefitinib," *Microchemical Journal*, vol. 154, article 104588, 2020.

[14] J. Zhou, Z. Sheng, H. Han, M. Zou, and C. Li, "Facile synthesis of fluorescent carbon dots using watermelon peel as a carbon source," *Materials Letters*, vol. 66, no. 1, pp. 222–224, 2012.

[15] S. Kumar and K. Kannabiran, "Activite antifongique de *Streptomyces VITSVK5* sp. sur des isolats d' *Aspergillus* mutir esistants isoles de patients atteints de tuberculose pulmonaire," *Journal de Mycologie Médicale*, vol. 20, no. 2, pp. 101–107, 2010.

[16] C. O. Okunji, C. N. Okeke, H. C. Gugnani, and M. M. Iwu, "An antifungal Spirostanol saponin from fruit pulp of Dracaena mannii," *International Journal of Crude Drug Research*, vol. 28, no. 3, pp. 193–199, 1990.

[17] H. Fan, M. Zhang, B. Bhandari, and C. H. Yang, "Food waste as a carbon source in carbon quantum dots technology and their applications in food safety detection," *Trends in Food Science & Technology*, vol. 95, pp. 86–96, 2020.

[18] X. W. Tan, A. N. B. Romainor, S. F. Chin, and S. M. Ng, "Carbon dots production via pyrolysis of sago waste as potential probe for metal ions sensing," *Journal of Analytical and Applied Pyrolysis*, vol. 105, pp. 157–165, 2014.

[19] X.-Y. Jiao, L.-s. Li, S. Qin, Y. Zhang, K. Huang, and L. Xu, "The synthesis of fluorescent carbon dots from mango peel and their multiple applications," *Colloids and Surfaces A: Physicochemical and Engineering Aspects*, vol. 577, pp. 306–314, 2019.

[20] D. Kukreja, J. Mathew, R. Lakshmipathy, and N. C. Sarada, "Synthesis of fluorescent carbon dots from mango peels," *International Journal of ChemTech Research*, vol. 8, no. 5, pp. 61–64, 2015.

[21] R.-J. Fan, Q. Sun, L. Zhang, Y. Zhang, and A.-H. Lu, "Photoluminescent carbon dots directly derived from polyethylene glycol and their application for cellular imaging," *Carbon*, vol. 71, pp. 87–93, 2014.

[22] D. G. Panpatte and Y. K. Jhala, Eds., *Nanotechnology for Agriculture: Crop Production & Protection*, Springer Nature, 2019.

[23] X. Dong, W. Liang, M. J. Meziani, Y. P. Sun, and L. Yang, "Carbon dots as potent antimicrobial agents," *Theranostics*, vol. 10, no. 2, pp. 671–686, 2020.

[24] M. M. Al Awak, P. Wang, S. Wang, Y. Tang, Y. P. Sun, and L. Yang, "Correlation of carbon dots' light-activated antimicrobial activities and fluorescence quantum yield," *RSC Advances*, vol. 7, no. 48, pp. 30177–30184, 2017.

Hindawi
Journal of Nanomaterials
Volume 2021, Article ID 4937059, 7 pages
https://doi.org/10.1155/2021/4937059

Research Article

Experimental Investigation on Mechanical Properties of Carbon Nanotube-Reinforced Epoxy Composites for Automobile Application

Anjibabu Merneedi,[1] **L. Natrayan**,[2] **S. Kaliappan**,[3] **Dhinakaran Veeman**,[4] **S. Angalaeswari**,[5] **Chidurala Srinivas**,[6] **and Prabhu Paramasivam**[7]

[1]*Department of Mechanical Engineering, Aditya College of Engineering, Surampalem, 533437 Andhra Pradesh, India*
[2]*Department of Mechanical Engineering, Saveetha School of Engineering, SIMATS, Chennai, Tamil Nadu 602105, India*
[3]*Department of Mechanical Engineering, Velammal Institute of Technology, Tamil Nnadu, Chennai 601204, India*
[4]*Centre for Additive Manufacturing, Chennai Institute of Technology, 600069, Chennai, India*
[5]*School of Electrical Engineering, Vellore Institute of Technology, 600127, 600 127 Chennai, Tamil Nadu, India*
[6]*Department of Mechanical Engineering, Vaageswari College of Engineering, Karimnagar, Telangana 505527, India*
[7]*Department of Mechanical Engineering, College of Engineering and Technology, Mettu University, 318, Ethiopia*

Correspondence should be addressed to L. Natrayan; natrayanphd@gmail.com, S. Angalaeswari; angalaeswari.s@vit.ac.in, and Prabhu Paramasivam; prabhuparamasivam21@gmail.com

Received 5 September 2021; Revised 14 October 2021; Accepted 27 October 2021; Published 10 November 2021

Academic Editor: Lakshmipathy R

Copyright © 2021 Anjibabu Merneedi et al. This is an open access article distributed under the Creative Commons Attribution License, which permits unrestricted use, distribution, and reproduction in any medium, provided the original work is properly cited.

Carbon nanotubes are established as a superior form of carbon. These have superior characteristics in terms of mechanical and chemical properties when compared to the other fibres available. High-strength fibres can be employed in a composite in a short form and mass-produced to fulfil high demands in composite applications. These composites can meet the strength requirements of nonstructural and structural components in a wide range of industries. Because of their light weight and excellent strength-to-weight ratio, these composites can be used in a wide range of applications. With Young's modulus as high as 1 TPa and tensile strength up to 63 GPa, they are among the stiffest and strongest fibres. There is currently a lot of interest in using carbon nanotubes in a matrix to take advantage of these features. There have been a variety of polymer matrices used, and nanotube/ceramic and nanotube/metal composites are gaining popularity. The study of these materials is an ongoing process, as researchers and design engineers have yet to realize their full potential. Carbon nanotubes (CNTs) are used in this study to create the composite with the resin. The percentage of CNT used as a filler material in the composite is varied from 1 to 4 percent, with the best percentage chosen for optimal mechanical properties.

1. Introduction

Carbon nanofibres (CNF) and carbon nanotubes (CNT) have had increasing potential in recent decades. Researchers from all around the world are attempting to apply the better qualities of these nanocomponents to a variety of applications [1]. The application range between biosensors and batteries of the new age CNTs has outstanding mechanical properties due to the two-dimensional arrangement of carbon atoms in a graphene sheet [2]. Due to this, massive out-of-plane distortions will happen while the strength of carbon-carbon in-plane bonds keeps the graphene sheet extremely strong against any in-plane distortion or fracture [3]. CNTs have a high aspect ratio and excellent electrical

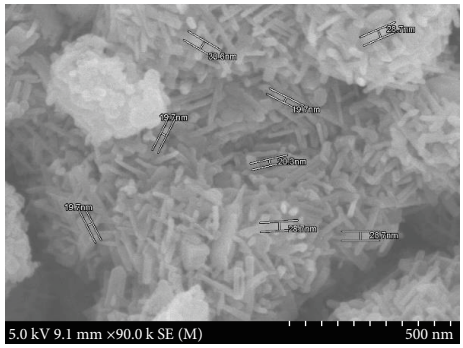

Figure 1: SEM of MWCNT.

and physical properties [4]. CNTs also have a high aspect ratio [5], as well as good electrical and physical properties [6]. Because of its unique characteristics, carbon nanotubes have been used in nanoscale electron devices namely field emission displays [7], atomic force microscope tips, and hydrogen storage cells [8]. According to both experimental and theoretical research, CNTs (both single walled and multiwalled) have remarkable mechanical properties, such as a high aspect ratio, lightweight [9], high thermal properties [10], excellent waviness characteristics, high melting point, low density, good electrical conductivity [11], larger surface area, remarkable biological properties, excellent hydrogen storage, and higher corrosion resistance [12]. Because of its symmetric structure, a typical CNT has a hexagonal arrangement of carbon atoms in the shape of tubes and offers extraordinary features [13]. Their performance is fully determined by their helical nature, and as a result, they operate as either a semiconductor or a metal [14].

Delogu et al. observed that a hybrid composite material can be formed by compression moulding of advanced sheet metal (ASMC) and unidirectional (UD) prepregs [15]. Ma et al. investigated the impact of nylon6 on cure behavior and mechanical properties of CF-nylon6 epoxy composites, produced by the hand lay-up process [16]. Kupski et al. manufactured two distinct configurations of the carbon/epoxy system; tests are carried out under quasistatic tension and it was found that mechanical properties vary with the thickness and length of the overlapping ply blocks [17]. Fotouhi et al. observed that in the case of UD all-carbon epoxy hybrid composites, delamination occurs from the outer high strength carbon layers subjected to uniaxial tensile loading [18]. Yogeshwaran et al. prepared a laminated CF-reinforced epoxy composite by hand lay-up and autoclave process, and the residual stresses are calculated using the incremental slitting method [19]. Based upon the build-up of the nanotubes, these are classified as two types [20], the single-walled carbon nanotube and the multiwalled carbon nanotube [21]. The single-walled carbon nanotube has one layer of carbon atoms as the wall of the tube, whereas in the multiwalled carbon nanotube, there are multiple layers of carbon as walls of the nanotube [22]. These multiwalled nanotubes can be considered as single-walled nanotubes inserted in one another [23]. Depending on the number of layers and the shape of the carbon tubes, the properties of the nanotubes vary [24]. There are numerous research publications on the synthesis of CNTs using diverse methodologies [25]. Currently, a wide range of carbon precursors, catalyst nanoparticles, carrier gases, and substrates may be used to produce CNTs in various crystallographic configurations [26].

CNTs have been used as extremely strong nanoreinforcements for composites, which possess extremely high strength with low weight and moderate electrostatic discharge properties [27]. Due to its highly adhesive, low weight, and good chemical resistance, epoxy-based composites are increasingly used in aerospace and car manufacturing as structural components [28]. The relatively weak mechanical characteristics of epoxy have however prevented its application in components which require high mechanical stability [29]. Recently, the use of MWNT as the polymer matrix filler has attracted considerable concern due to its mechanical, thermal, and electrical characteristics. Epoxy composite nanotubes were manufactured through different processes of purification and dispersion [30]. The amount of carbon nanotubes (CNT) in the present study composite varies from 1 to 4% of the total weight of the phenolic resin. This research is aimed at carrying out the fraction of CNT to use in CNT-based epoxy composites to get the greatest mechanical performance. The tensile strength and toughness of the prepared samples are then tested, and SEM micrographs are obtained to study the characteristics of CNT composites.

2. Methodology

Multiwalled CNTs have been procured from Iljin Nanotech Co. The chemical vapour deposition process synthesizes this MWCNT. The procured MWCNT have an average diameter of 25 nm, and the size is 10 microns. The SEM micrograph of MWCNT is shown in Figure 1. These MWCNT are cleaned for removing carbon particles, graphite, and other particles. A solution of 65% H_2SO_4/HNO_3 with 3 : 1 ratio is used for 30 min at 100°C to purify CNT.

CNTs with a large L/D ratio are bound to agglomerate together and make it difficult to disperse uniformly in a polymer matrix. The properties of the composite cannot be enhanced as the CNTs are not uniformly distributed, and on top of that, the agglomerated CNT acts as a defect and initiates a crack in the composite. $SnCl_2$ and $PdCl_2$ solutions were used to sensitize and activate the dispersed CNTs at room temperature. The CNTs were then filtered and thoroughly washed in distilled water after being pretreated. Before creating the CNT composite, CNT powder was mixed with polyglycol-dissolved phenolic resin. The phenolic resin was a thermosetting polymer created from phenol and formaldehyde with a catalyst of ammonia. The CNT weight ratio in the billets varies between 1 percent, 2 percent, 3 percent, and 4 percent. Multiple billets are prepared for each % of CNT without modifying the specifications. To obtain a solidified billet sample, the combined CNT and phenolic resin is cured in an oven at 160°C. Microhardness is determined using a microindenter, tensile strength is computed using UTM, and SEM micrographs are generated using a

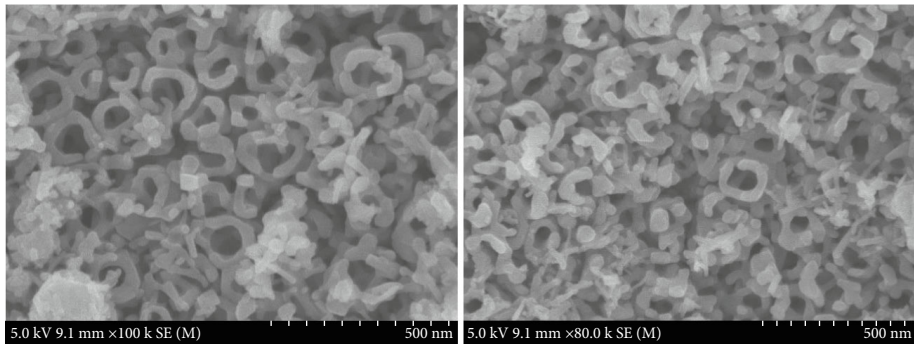

Figure 2: SEM micrograph of CNT composite.

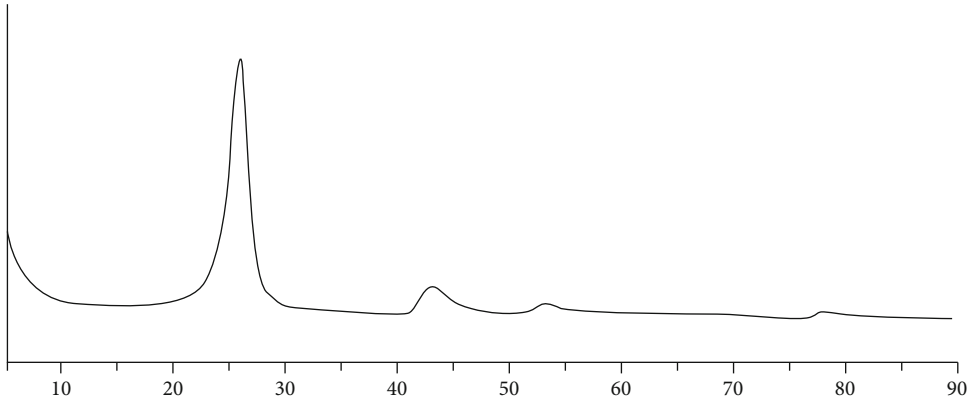

Figure 3: XRD graph of the CNT composite.

Table 1: Microhardness (HV) of CNT composites.

Sample	Trial 1	Trial 2	Trial 3
CNF 1%	29.5	25.2	25.4
CNF 2%	33.4	34.5	29.9
CNF 3%	34.6	36.4	36.6
CNF 4%	38.4	38.8	40.1

FE-SEM. XRD analysis is used to analyse the chemical composition of the CNT composite.

3. Results and Discussion

3.1. Micrographs. To determine the CNT dispersion in the composite, the generated CNT composites are examined using a FE-SEM apparatus. The SEM micrographs that have been developed are shown below. It signifies that the CNTs have been evenly distributed across the matrix. Due to ultrasonic mixing before adding the CNTs to the resin, all of the CNT content percentages are dissolved uniformly in the composite. Milling before combining with resin dropped the CNT ratio and enhanced the wettability of the fibres [31]. For any of the produced composites, no aggregation of CNT in the matrix has been discovered. There is no fracture of the matrix at the interface of the CNT and matrix in the composite. The CNTs have a good bond with the matrix, and there is no slipping of the fibre with the matrix.

The SEM micrographs of the all the composites have shown the same pattern without any significant difference to observe. The section that has been sliced for the composites has shown CNT at the cross-section and has a similar tendency of interaction between CNT and the matrix. Hence, a single micrograph is presented for all the four grades of the composites tested in Figure 2. The matrix is also uniform throughout the composite without any air bubbles trapped or any cracks detected. There is no slippage between CNT and the matrix. As the ultrasonic mixing is employed in the mixing of CNT, there is no agglomeration of CNT detected in the composite, and hence, the CNT is uniformly distributed. This gives the composite fine strength.

3.2. XRD Analysis. The graphitic-like carbon peaks can be seen in the CNT composite XRD diffraction pattern in Figure 3. The CNT composite closely resembles CNTs in terms of XRD patterns, implying that the graphite-like structure is conserved after the CNT powder is produced with a polymer binder and then carbonized at high temperatures. The contribution of polymer-derived carbon in the composite is undetectable in the XRD diffraction spectrum. Due to the surface graphitization of thermosetting resin during carbonization results in a graphite-like layer separate from the

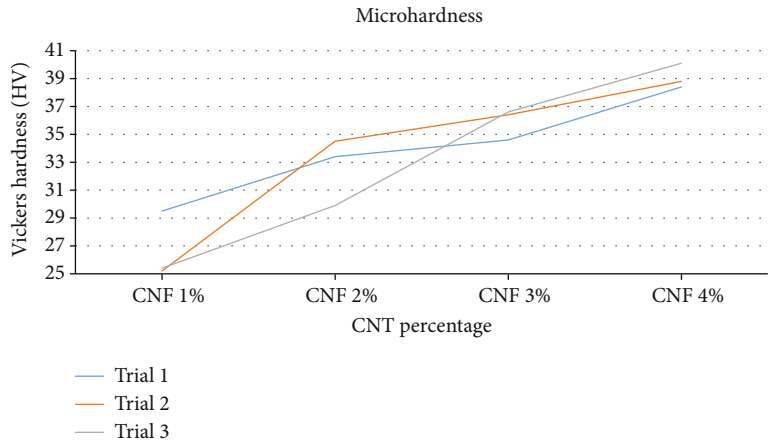

Figure 4: Hardness for CNT composites.

Table 2: Tensile strength (MPa) of CNF composites.

Sample	Trial 1	Trial 2	Trial 3
CNF 1%	47.2	45.2	46.3
CNF 2%	53.5	54.1	54.0
CNF 3%	58.4	57.9	58.2
CNF 4%	60.1	60.3	60.8

bulk glassy carbon. There is no mix-up of CNT and matrix polymer during curing, and no unwanted material has been observed. The XRD diffraction graphs obtained for the all samples developed gave the similar pattern and have no significant difference to be discussed individually, and hence, only one graph is provided for all the samples. The peak is consistent for all the samples, and no peak of the secondary carbon is detected consistently for all the samples detected.

3.3. Mechanical Properties

3.3.1. Hardness. When a load is applied to a softer material, the substrates deform elastically, resulting in an underreporting of hardness. As a result, the matrix and CNT collective hardness was obtained in this situation, significantly reducing the composite characteristics. Every sample has been put through a series of tests, yielding an average hardness value. The composite hardness is determined using a microindenter and a 100 g force for each indentation. Shimadzu's Vickers indentation was employed for the evaluation. The hardness of the composites increases as the percentage of CNT in the composite increases. The hardness of the 1% CNT composite is lower than the other composites, whereas the hardness of the 4% CNT composite is higher. The hardness values obtained for each sample are listed in Table 1. For a 15-second indentation time, all values are recorded. The hardness of CNT composites is seen in Figure 4. The variation in hardness values can be explained by the fact that the distribution of CNT at the surface layers of the composite is high for composites with a higher CNT percentage; hardness is higher for composites with a 4-percent CNT percentage and gradually decreases for composites with a lower CNT percentage.

3.3.2. Tensile Strength. Table 2 shows the tensile strength of the composites assessed by UTM. Compared to other produced composites, the composite with a higher CNT concentration has a higher tensile strength value. Because the connection between matrix and CNT is sufficient and there are no vacancies, the higher CNT in the composite absorbs the load. The tensile strength of CNT composites is shown in Figure 5. When the CNT concentration in the composite is increased from 1% to 4%, the tensile strength of the composite increases by 27%. When CNT is increased from 1% to 2% in the composite, the percentage increase is 13 percent. When CNT is increased to 3 percent from 2 percent, the percentage for tensile strength increment is reduced to 9%. This indicates that increasing CNT content enhances tensile strength, but the increment level decreases over time. Figure 6 shows the graphical presentation of the tensile strength of the CNT composites developed.

3.3.3. Elastic Modulus. The elastic modulus of the samples has been determined while testing for the tensile strength of the samples on UTM. While the tensile strength has increased almost linearly after addition of MWCNT, at the same time, it has reduced the elastic modulus of the composite. The least modulus has been registered for the 4% CNT composite while the highest modulus is registered for the 1% CNT composite. The total measurements of the modulus for the samples are given in Table 3 below. The highest modulus registered is for 1% of CNT at 1025 MPa and the lowest recorded for 4% CNT is 952 MPa. There is a total of 7% reduction in Young's modulus when CNT is increased from 1% to 4%. The graphical presentation of elastic modulus is given Figure 5.

4. Conclusions

Phenolic resin with different wt% of multiwalled carbon nanotube composite was fabricated successfully. Among the composites, the one with higher CNT content has

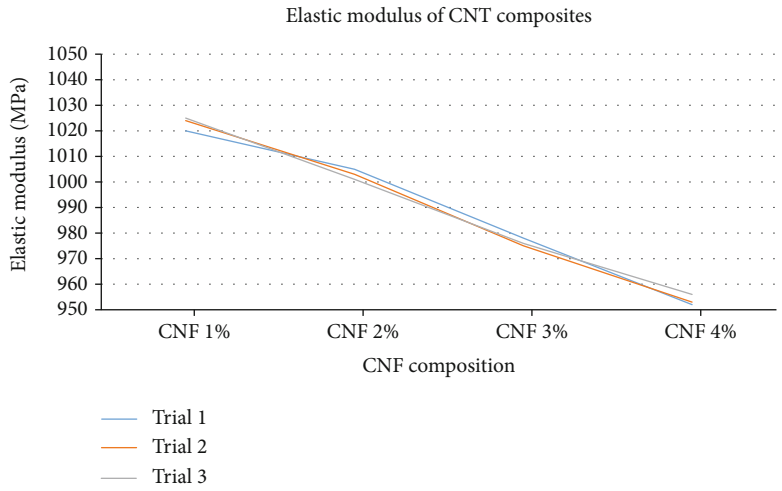

Figure 5: Graphical representation of elastic modulus of CNT composites.

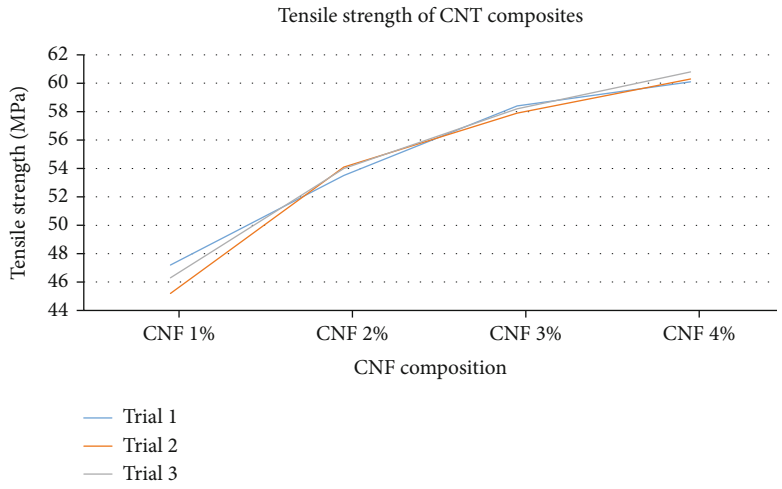

Figure 6: Tensile strength of CNT composites.

Table 3: Elastic modulus (MPa) of CNT composites.

Sample	Trial 1	Trial 2	Trial 3
CNF 1%	1020	1024	1025
CNF 2%	1005	1003	1001
CNF 3%	978	975	976
CNF 4%	952	953	956

superior properties in terms of mechanical properties. The superior mechanical properties of CNT have influenced greatly testing composites.

(i) The XRD examination confirmed that the composites sample contains no impurities or other materials. CNT and resin produced XRD peaks

(ii) The tensile strength increases as the CNT concentration increases, but the rate of increase decreases over time. CNT with 4 wt% composite tensile strength results were increased 27% compared to 1% of CNF composite

(iii) The hardness of the composite is increased when the CNT content is increased from 1% to 4%

(iv) The elastic modulus of the composite is reduced from 1% CNT to 4% CNT by over 7%

(v) The gradual increase in the CNT content in the composite will increase the strength of the composite and hence is useful in the automotive industry

Data Availability

The data used to support the findings of this study are included in the article. Should further data or information be required, these are available from the corresponding author upon request.

Disclosure

This study was performed as a part of the Employment of Mettu University, Ethiopia.

Conflicts of Interest

The authors declare that there are no conflicts of interest regarding the publication of this paper.

Acknowledgments

The authors thank Saveetha School of Engineering, SIMATS, Chennai, for the technical assistance. The authors appreciate the support from Mettu University, Ethiopia.

References

[1] S. Sahani and Y. C. Sharma, "Advancements in applications of nanotechnology in global food industry," *Food Chemistry*, vol. 342, article 128318, 2020.

[2] S. Sharif, K. S. Ahmad, F. Rehman, Z. Bhatti, and K. H. Thebo, "Two-dimensional graphene oxide based membranes for ionic and molecular separation: current status and challenges," *Journal of Environmental Chemical Engineering*, vol. 9, no. 4, article 105605, 2021.

[3] A. Baby, L. Trovato, and C. Di Valentin, "Single atom catalysts (SAC) trapped in defective and nitrogen-doped graphene supported on metal substrates," *Carbon N. Y.*, vol. 174, pp. 772–788, 2021.

[4] A. Ivanets, V. Prozorovich, M. Roshchina et al., "Heterogeneous Fenton oxidation using magnesium ferrite nanoparticles for ibuprofen removal from wastewater: optimization and kinetics studies," *Journal of Nanomaterials*, vol. 2020, Article ID 8159628, 2020.

[5] F. Sabir, M. I. Asad, M. Qindeel et al., "Polymeric nanogels as versatile nanoplatforms for biomedical applications," *Journal of Nanomaterials*, vol. 2019, Article ID 1526186, 2019.

[6] T. A. Dontsova, S. V. Nahirniak, and I. M. Astrelin, "Metaloxide nanomaterials and nanocomposites of ecological purpose," *Journal of Nanomaterials*, vol. 2019, 2019.

[7] F. Houdellier, A. Masseboeuf, M. Monthioux, and M. J. Hÿtch, "New carbon cone nanotip for use in a highly coherent cold field emission electron microscope," *Carbon*, vol. 50, no. 5, pp. 2037–2044, 2012.

[8] A. G. Mamalis, L. O. G. Vogtländer, and A. Markopoulos, "Nanotechnology and nanostructured materials: trends in carbon nanotubes," *Precision Engineering*, vol. 28, no. 1, pp. 16–30, 2004.

[9] Y. Saito and S. Uemura, "Field emission from carbon nanotubes and its application to electron sources," *Carbon*, vol. 38, no. 2, pp. 169–182, 2000.

[10] Z. Chen, A. Zhang, X. Wang et al., "The advances of carbon nanotubes in cancer diagnostics and therapeutics," *Journal of Nanomaterials*, vol. 2017, Article ID 3418932, 2017.

[11] E. Pazos-Ortiz, J. H. Roque-Ruiz, E. A. Hinojos-Márquez et al., "Dose-dependent antimicrobial activity of silver nanoparticles on polycaprolactone fibers against Gram-positive and Gram-negative bacteria," *Journal of Nanomaterials*, vol. 2017, Article ID 4752314, 2017.

[12] E. Baltazar-Encarnación, C. E. Escárcega-González, X. G. Vasto-Anzaldo, M. E. Cantú-Cárdenas, and J. R. Morones-Ramírez, "Silver nanoparticles synthesized through green methods using Escherichia coli top 10 (Ec-Ts) growth culture medium exhibit antimicrobial properties against nongrowing bacterial strains," *Journal of Nanomaterials*, vol. 2019, Article ID 4637325, 2019.

[13] Y. Zare, "Modeling of tensile modulus in polymer/carbon nanotubes (CNT) nanocomposites," *Synthetic Metals*, vol. 202, pp. 68–72, 2015.

[14] T. Sathish, K. Palani, L. Natrayan, A. Merneedi, M. V. de Poures, and D. K. Singaravelu, "Synthesis and characterization of polypropylene/ramie fiber with hemp fiber and coir fiber natural biopolymer composite for biomedical application," *International Journal of Polymer Science*, vol. 2021, 2021.

[15] M. Delogu, L. Zanchi, C. A. Dattilo, and M. Pierini, "Innovative composites and hybrid materials for electric vehicles lightweight design in a sustainability perspective," *Materials Today Communications*, vol. 13, pp. 192–209, 2017.

[16] Y. Ma, M. Ueda, T. Yokozeki, T. Sugahara, and Y. Yang, "Investigation of the flexural properties and failure behavior of unidirectional CF/nylon 6 and CF/epoxy composites," *Journal of Composite Materials*, vol. 7, no. 4, pp. 227–249, 2017.

[17] J. Kupski, D. Zarouchas, and S. T. De Freitas, "Thin-plies in adhesively bonded carbon fiber reinforced polymers," *Composites: Part B*, vol. 184, article 107627, 2020.

[18] M. Fotouhi, M. Jalalvand, and M. R. Wisnom, "High performance quasi-isotropic thin-ply carbon/glass hybrid composites with pseudo-ductile behaviour in all fibre orientations," *Composites Science and Technology*, vol. 152, pp. 101–110, 2017.

[19] S. Yogeshwaran, L. Natrayan, G. Udhayakumar, G. Godwin, and L. Yuvaraj, "Effect of waste tyre particles reinforcement on mechanical properties of jute and abaca fiber - epoxy hybrid composites with pre-treatment," *Materials Today: Proceedings*, vol. 37, Part 2, pp. 1377–1380, 2021.

[20] H. C. A. Murthy, T. Desalegn, M. Kassa, B. Abebe, and T. Assefa, "Synthesis of green copper nanoparticles using medicinal plant Hagenia abyssinica (Brace) JF. Gmel. Leaf extract: antimicrobial properties," *Journal of Nanomaterials*, vol. 2020, Article ID 3924081, 2020.

[21] R. Reshmy, E. Philip, S. A. Paul et al., "Nanocellulose-based products for sustainable applications-recent trends and possibilities," *Reviews in Environmental Science and Biotechnology*, vol. 19, no. 4, pp. 779–806, 2020.

[22] T. T. Vo, T. T. N. Nguyen, T. T. T. Huynh et al., "Biosynthesis of silver and gold nanoparticles using aqueous extract from crinum latifolium leaf and their applications forward antibacterial effect and wastewater treatment," *Journal of Nanomaterials*, vol. 2019, Article ID 8385935, 2019.

[23] E. D. M. Isa, H. Ahmad, and M. B. A. Rahman, "Optimization of synthesis parameters of mesoporous silica nanoparticles based on ionic liquid by experimental design and its application as a drug delivery agent," *Journal of Nanomaterials*, vol. 2019, Article ID 4982054, 2019.

[24] A. Shahzad, H. Saeed, M. Iqtedar et al., "Size-controlled production of silver nanoparticles by Aspergillus fumigatus BTCB10: likely antibacterial and cytotoxic effects," *Journal of Nanomaterials*, vol. 2019, Article ID 5168698, 2019.

[25] A. Shahsavar, A. A. A. A. Al-Rashed, S. Entezari, and P. T. Sardari, "Melting and solidification characteristics of a double-pipe latent heat storage system with sinusoidal wavy channels

embedded in a porous medium," *Energy*, vol. 171, pp. 751–769, 2019.

[26] E. Vélez, G. Campillo, G. Morales, C. Hincapié, J. Osorio, and O. Arnache, "Silver nanoparticles obtained by aqueous or ethanolic aloe vera extracts: an assessment of the antibacterial activity and mercury removal capability," *Journal of Nanomaterials*, vol. 2018, Article ID 7215210, 2018.

[27] G. O. Akalin and M. Pulat, "Preparation and characterization of nanoporous sodium carboxymethyl cellulose hydrogel beads," *Journal of Nanomaterials*, vol. 2018, Article ID 9676949, 2018.

[28] Z. H. Tang, Y. Q. Li, P. Huang, Y. Q. Fu, N. Hu, and S. Y. Fu, "A new analytical model for predicting the electrical conductivity of carbon nanotube nanocomposites," *Composites Communications*, vol. 23, article 100577, 2021.

[29] L. Meng, J. Zhang, H. Li, W. Zhao, and T. Zhao, "Preparation and progress in application of gold nanorods," *Journal of Nanomaterials*, vol. 2019, Article ID 4925702, 2019.

[30] H. Che, A. C. Liberati, X. Chu et al., "Metallization of polymers by cold spraying with low melting point powders," *Surface and Coatings Technology*, vol. 418, article 127229, 2021.

[31] L. Natrayan and A. Merneedi, "Experimental investigation on wear behaviour of bio-waste reinforced fusion fiber composite laminate under various conditions," *Materials Today: Proceedings*, vol. 37, Part 2, pp. 1486–1490, 2020.

Hindawi
Journal of Nanomaterials
Volume 2021, Article ID 6244874, 13 pages
https://doi.org/10.1155/2021/6244874

Research Article

Design, Simulation, and Analysis of Micro/Nanoelectromechanical System Rotational Devices

A. R. Kalaiarasi,[1] T. Deepa,[2] S. Angalaeswari,[2] D. Subbulekshmi,[2] and Raja Kathiravan[3]

[1]*Department of Electronics and Instrumentation, Saveetha Engineering College, Chennai, India*
[2]*School of Electrical Engineering, Vellore Institute of Technology, Chennai, India*
[3]*School of Mechanical Engineering, Bahir Dar University, Bahir Dar, Ethiopia 6000*

Correspondence should be addressed to T. Deepa; deepa.t@vit.ac.in, S. Angalaeswari; angalaeswari.s@vit.ac.in, and Raja Kathiravan; kathirrk3000@gmail.com

Received 8 September 2021; Revised 29 September 2021; Accepted 21 October 2021; Published 9 November 2021

Academic Editor: Lakshmipathy R

Copyright © 2021 A. R. Kalaiarasi et al. This is an open access article distributed under the Creative Commons Attribution License, which permits unrestricted use, distribution, and reproduction in any medium, provided the original work is properly cited.

This work is focused on design and simulation of microelectromechanical system (MEMS)/nanoelectromechanical system (NEMS) rotational devices such as micro/nanothermal rotary actuator and micro/nanogear. MEMS/NEMS technologies have allowed the development of advanced miniaturized rotational devices. MEMS/NEMS-based thermal actuator is a scaled version of movable device which will produce amplified motion when it is subjected to thermal forces. One of the applications of such thermal micro/nanoactuator is integrating it into micro/nanomotor that makes a thermal actuated micro/nanomotor. In this work, design and simulation of micro/nanothermal rotary actuator are done using MEMS/NEMS technology. Stress, current density, and temperature analysis are done for microthermal rotary actuator. The performance of the device is observed by varying the dimensions and materials such as silicon and polysilicon. Stress analysis is used to calculate the yield strength of the material. Current density is used to calculate the safer limit of the material. Temperature analysis is used to calculate the melting point of the material. Also, in this work, design and simulation of microgear have been done. Micro/nanogears are devices that can be used to improve motion performance. The essential is that it transmits rotational motion to a different axis.

1. Introduction

MEMS technology is a representation of microscopic implementations of sensors and actuators which are fabricated using microfabrication techniques. MEMS/NEMS devices generally fall in the range between 1 and 1000 nanometers in size. MEMS/NEMS technologies are developed for the fabrication of integrated circuits (IC). MEMS/NEMS devices can be categorized in to sensors and actuators in μ scale, which can be further used in macroworld. They have wide applications in the fields as diverse as microsatellites, automotive, aerospace, telecommunication, biomedical, wind tunnel instrumentation etc. MEMS/NEMS has strong multidisciplinary character. MEMS/NEMS devices have the following advantages like less power consumption, small size, improved performance, increasing reliability, lesser weight, and less cost than devices which are working on similar fundamental principle in macrosize. MEMS/NEMS-based devices are fabricated using IC fabrication techniques along with special techniques to fabricate three dimensional (3D) structures. It has high precision and high aspect ratio. It scales the size of the device without changing the property of the materials.

MEMS-based thermal actuator is an electromechanically actuated device which works based on Joules' law of electrothermal heating. Amplification of thermal force may be done in design of thermal actuator. Electrothermal actuator fabricated using single crystal silicon or polysilicon as a compliance structure. Atre and Boedo [1] analyzed the variation of tip deflection of actuator with respect to the applied

voltage. The thermal behavior of the polysilicon material and its relationship in the calculation of deflection by analytical methods are studied. The experimental and simulation results of six different actuator designs are compared. At high voltages, the finite element model overestimates experimentally determined values. Thermal conductivity of polysilicon plays an important role in predicting actuator deflection. Geisberger et al. [2] discussed about the influence of dopant concentration in electrical and thermal conductivity. Investigating the static and transient response of the thermal actuator at different excitation frequency and voltage, the simulated and measured data are compared. Relatively poor fit of simulation data using constant conductivities explains the importance of thermal properties of the material. Heo and Kim [3, 4] designed a robust to maximize the actuator deflection with respect to applied voltage and baseline design by the topology optimization method. Optimize the thermal actuator design, which is robust to noise factors.

Heo and Kim [5] described the optimal design to maximize the rotation angle of the actuator for fixed input power. Element connectivity parameterization formulation method is used to eradicate numerical instabilities. Haefner et al. [6] evaluated the lifetime evaluation of microgears, which depend on the geometry shape deviations (tooth deformation) and finite element model-based prognostic method. Islam and Islam [7] analyzed the finite element method of stress, contact stress, and bending stress for spur gears, used in the hybrid vehicle power transmission system. Arefin et al. [8] implemented both PV module and wind turbine in internal combustion engine-based vehicle. Wind turbine blade design was simulated using ANSYS CFD. Jin et al. [9] designed impact of upstream deflector parameters (rotor distance influence, width influence, distance influence, and height influence) in vertical axis wind turbines. Compare with the simulated and experimental results with and without deflector, Deflector reduces negative torque and increases efficiency of wind turbine.

Arefin and Islam [10] studied about noise characteristics and emission characteristics of micro gas turbine, which is used as range extender for electric truck. Suitable temperature of operating the micro gas turbine for maximum power is studied. Noise reduction methods are proposed at higher speed, output power is increased, and vibration (noise) and CO emission are reduced. Karbosi et al. [11] compared the properties of two microactuators such as distribution of temperature, power consumed, and actuation of two microactuators. Analysis of two designs is like design a—different beam lengths and design B—different beam sections and flexure part, to produce maximum deflection. GA Optimal design produces 70% increase in tip deflection. Lo et al. [12] modeled the electrothermal-mechanical system into a combination of electrical, thermal, and mechanical model using the lumped model technique. Deflection and frequency bandwidth are analyzed to attain and determine static gain.

Dhinakaran et al. [13] demonstrated the combination of electrothermal and electrostatic actuation mechanisms. It gives pull-in behavior at low voltage and makes hybrid actuator and hybrid bidirectional actuator perfect for switching

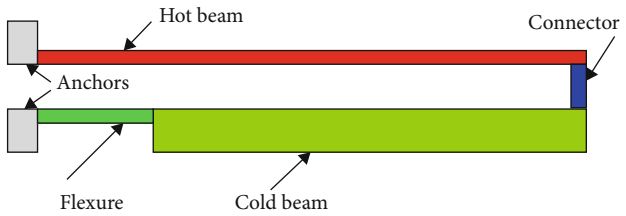

Figure 1: A-symmetric (bimorph).

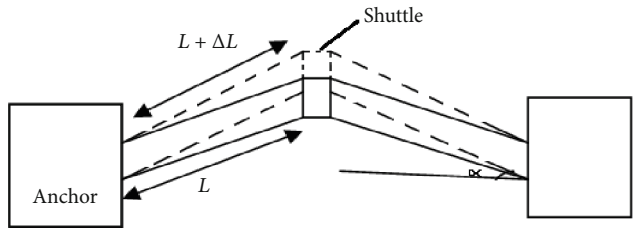

Figure 2: Chevron single beam actuator.

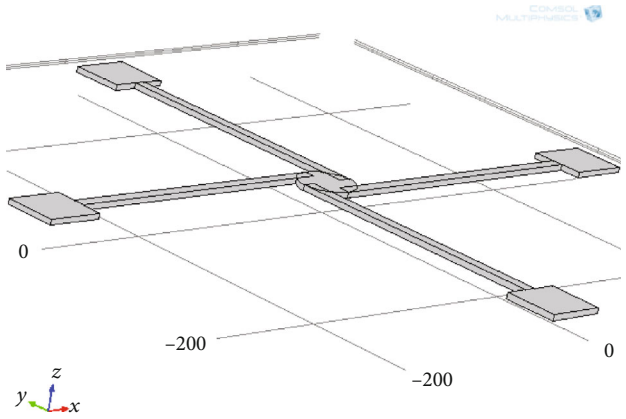

Figure 3: Microthermal rotary actuator structure.

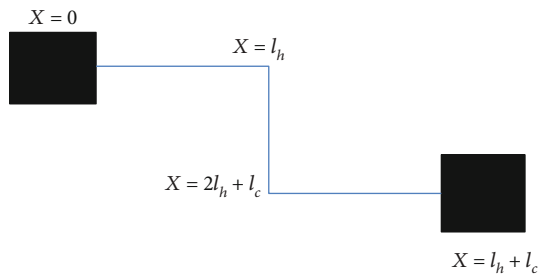

Figure 4: 1D of actuator.

applications. Chiorean et al. [14] analyzed the effect of geometrical parameters on the output force of Chevron actuators. The authors also considered the effect of thermal expansion of substrate. It studies about the impact of substrate silicon deformation due to forces in anchors and thermal expansion of substrate silicon or effect of central shaft expansion in actuator displacement. Suocheng et al. [15] studied bimetal film thermal expansion-based microthermal actuator variation of actuator displacement at

Table 1: Parameters used.

Sl. No.	Parameters	Values
1.	Coefficient of thermal expansion of polysilicon (α)	2.7×10^{-6} K^{-1}
2.	Electrical specific resistance of polysilicon at room temperature (ρ_0)	2×10^{-3} Ω – cm
3.	Thermal conductivity of polysilicon (k_p)	32 W-m^{-1}-K^{-1}
4.	Thermal conductivity of air (k_a)	0.006 W-m^{-1}-K^{-1}
5.	Thermal conductivity of silicon(k_n)	2.25 W-m^{-1}-K^{-1}
6.	Thickness of polysilicon (t_p)	2000 nm
7.	Thickness of air (t_a)	2000 nm
8.	Thickness (t_{p0})	2000 nm
9.	Thickness of silicon (t_n)	2000 nm

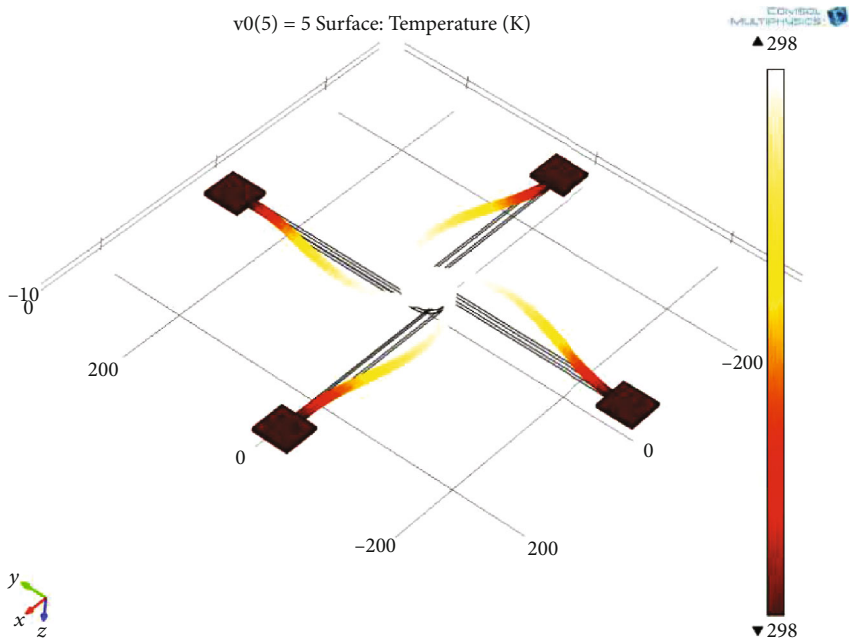

Figure 5: Temperature analysis of silicon (circular disc 5 μm).

different voltage values and temperature ranges. Time taken to achieve maximum displacement (response time) at different voltage levels is also investigated. Potekhina and Wang [16] designed hot and cold arm type actuators where differential thermal expansion is achieved by various geometrical shapes like changing beam shape, modifying electrical parameters like selective doping, modified resistance, or topological parameter changes like multimode or bidirectional operation. Sun et al. [17] explained about the single walled carbon nanotube (SWCNT) electrothermal actuators thermal expansion that is based on the following parameters such as amount of joule heating and coefficient of thermal expansion, induced stress relaxation mechanism and post-secondary curing. Li et al. [18] studied the application of series of V-beam thermal actuator amplification for MEMS applications in specific areas like safety and arming. Yogeshwaran et al. [19] discussed about the temperature distribution dynamics and displacement and its impact on the device dimensions and properties of material and applied

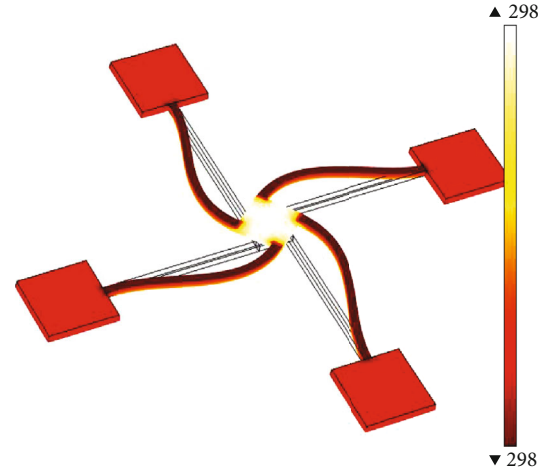

Figure 6: Temperature analysis of silicon (square arm 10 μm).

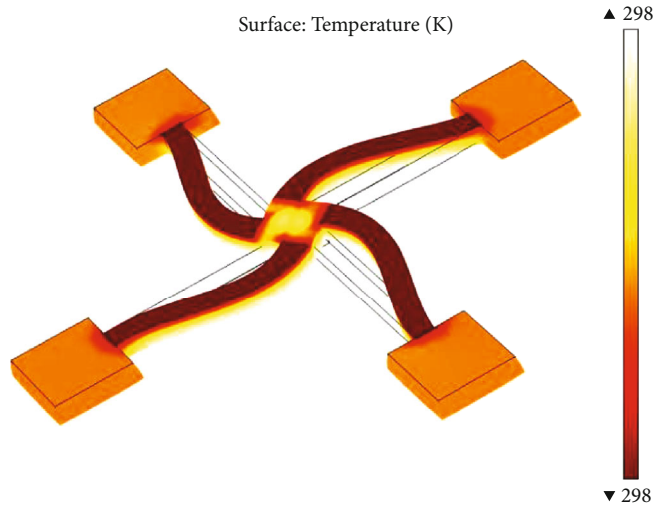

Figure 7: Temperature analysis of silicon (square arm 25 μm).

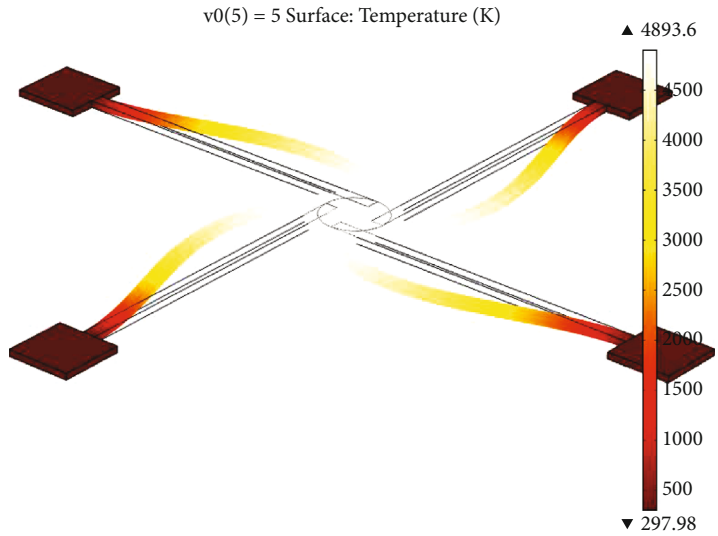

Figure 8: Temperature analysis of polysilicon (circular disc 5 μm).

voltage. Kim et al. [20] designed and fabricated the multilayered structure with platinum heater. Ni-Co-based flexible substrate as thermal bimorph actuators and thermal insulation (isolation) layers are also employed. Ulkir [21] designed bidirectional electrothermal actuator which displaces in two directions. Authors compared the fabrication process of 2 photon polymerization (2PP) and digital light processing (DLP) methods, which are 3D printing techniques. Steiner et al. [22] studied the relation between actuator area and deflection distance based on V-shaped Chevron type beams.

Duzng [23] modeled the V-shaped thermal actuator using ordinary differential equations. Author studied about the thermal inertia of the system, if the applied voltage is in the form of square pulse, the output is in form of concave trapezium. Li et al. [24] discussed the application of thermal actuator in testing the fracture strength of thin films. Voltage is applied to thermal actuator, which creates the thermal expansion; due to thermal expansion force that is created which is used to fracture the test structure. Suryanarayanan et al. [25] compared experimental results, and simulation results are correlated using back propagation neural network. Simulation results fitted with neural network provide a cost-effective model for V-shaped thermal actuator. Gong et al. [26] studied the relation between length of flexure and thermal deflection of bimorph thermal actuator. The author proposes that the length of flexure would not increase the stress on the arm length, and it also increases the lifetime of actuator. López-Walle et al. [27] discussed heat transfer characteristics that are important in improving the performance of thermal actuator. Kim et al. [28] discussed the application of bimorph thermal actuators in rotation control of micromirrors. Two bimorph actuators produce vertical displacement of 25 μm at 10 V, which rotates micromirror by 20°.

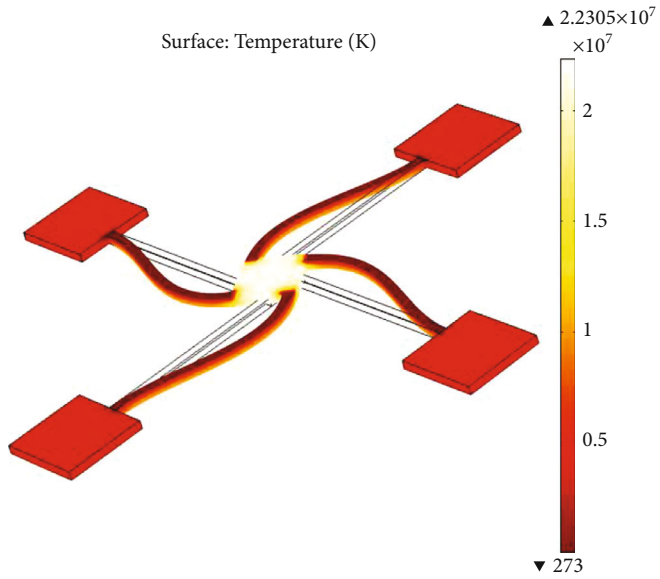

Figure 9: Temperature analysis of polysilicon (square arm 10 μm).

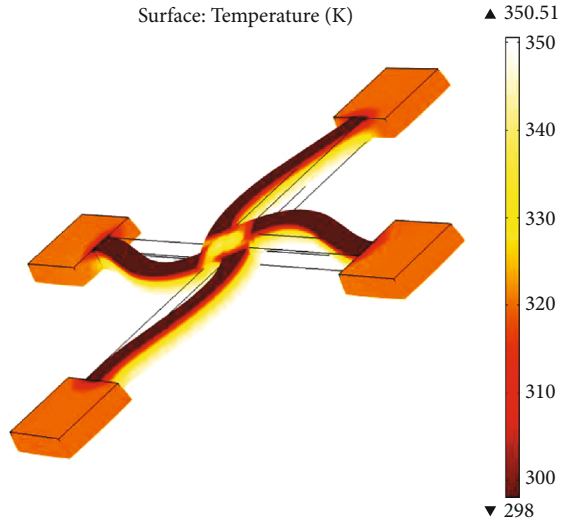

Figure 10: Temperature analysis of polysilicon (square arm 25 μm).

2. Importance of Microthermal Rotary Actuator

Electrostatic actuation and thermal actuation are methods to obtain actuation in MEMS. This method of actuations is very popular since this actuation provides simplicity, fast actuation rates, and low power consumption, and it uses silicon as its material. This type of actuation method is a common method of driving MEMS devices because it is compatible with microfabrication.

Thermal microactuators have the following advantages like higher force, lesser operating voltages, and less susceptibility to adhesion failures compared to electrostatic actuators. Microthermal actuators do require more power, and their switching speeds are limited by cooling times. It produces higher displacement and higher force than electrostatic actuators.

3. Types of Microthermal Rotary Actuator

3.1. A-Symmetric (Bimorph). A bimorph is a microcantilever based thermal actuator used as an actuator or sensor which consists of two metal layers. In some applications, it also has a passive layer between the two active layers. The term bimorph is most commonly used with thermal bimorphs. The first theory about the bending of thermally actuated bimorph was given by Stoney. In Figure 1, schematic diagram of A-symmetric (bimorph) is shown. It has generally a single material. The deflection is produced here due to asymmetry in the shape. This type of thermal actuator is also called as hot-cold beam actuator.

3.2. Symmetric (Bent Beam, Chevron). Chevron-shaped actuators are one of the most popular actuators in the MEMS

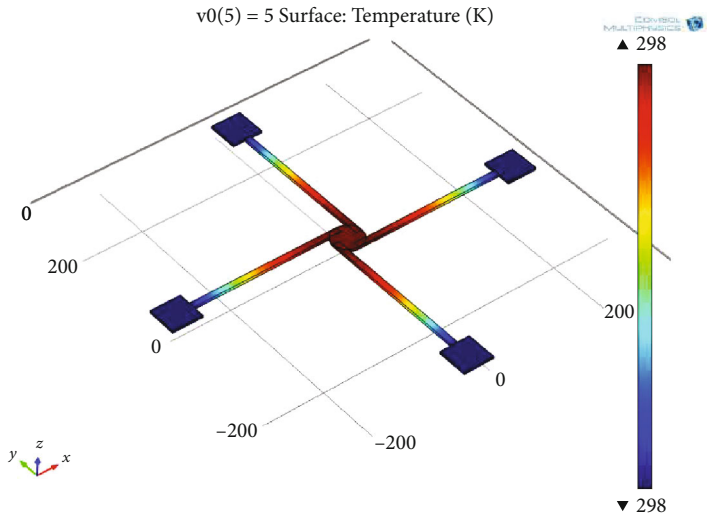

Figure 11: Current density analysis of silicon (circular disc 5 μm).

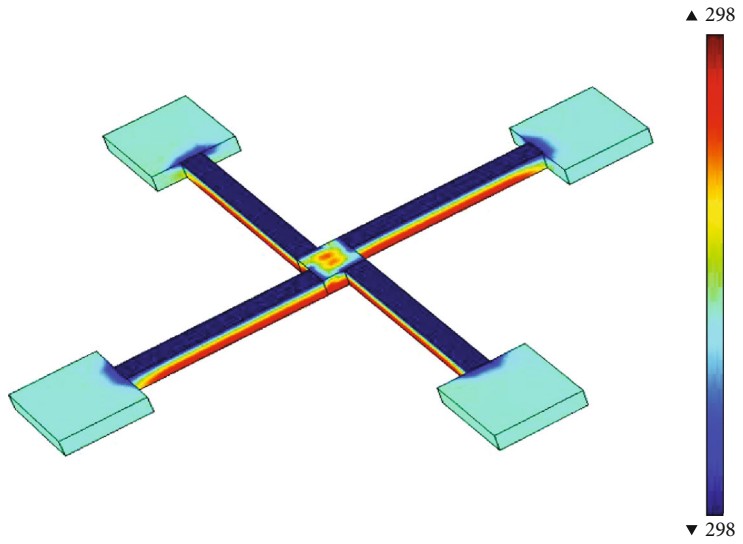

Figure 12: Current density analysis of silicon (square arm 10 μm).

community (also called V-beam thermal actuator). Its principle is based on the thermal expansion of a single material to generate the motion, which is amplified using different geometric constraints. The V-beam thermal actuators are capable of producing high output force for low operating voltage. The output force (displacement) depends on the inclination of the beam. In Figure 2, Chevron beam actuator is shown.

3.3. Designing of Microthermal Rotary Actuator. Designing of microthermal rotary actuator is done using structural mechanics. For designing the microthermal rotary actuator, the important parameters used are materials and dimensions. Finite element method (FEM) software used to design the thermal actuator. Here, COMSOL is used for simulation. The actuator's operation involves three coupled physics phenomena: electric current conduction, heat conduction with heat generation, and structural stresses and strains due to thermal expansion. In COMSOL, the joule heating model uses the heat equation given in equation as the mathematical model for heat transfer in solids.

3.3.1. Dimensions. Microthermal rotary actuator is done using structural differ from varying its length and shape of the cold disc. Length of the hot arm is varies from 500 nm to 2500 nm. Height of the cold beam is 500 nm, and the diameter of the cold beam is 200 nm. Figure 3 shows the microthermal rotary actuator structure.

3.3.2. Materials. Materials used for designing of microthermal rotary actuator are silicon and poly silicon. Each material has a unique property which makes them to use in designing the microthermal rotary actuator.

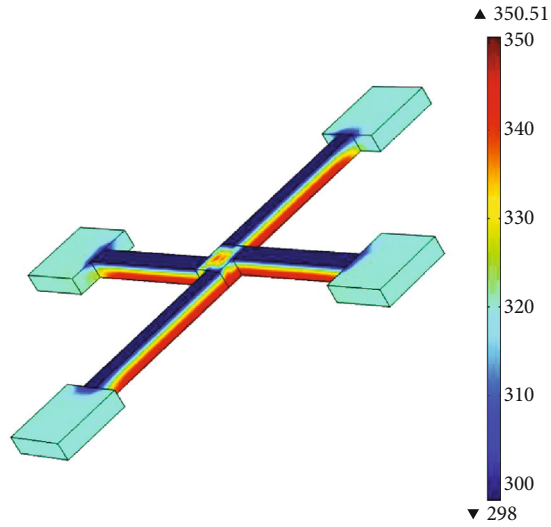

Figure 13: Current density analysis of silicon (square arm 25 μm).

3.4. Theoretical Analysis

3.4.1. Electrothermal Analysis. The above Figure 4 shows the 1D of actuator. According to joule's heating,

rate of heat input = rate of heat going out

$$Q_{\text{in}} + Q_{\text{joule}} = Q_{\text{out,arm}} + Q_{\text{out,sub.}} \tag{1}$$

Since

$$Q_{\text{in}} = -k_p w t_p \left[\frac{dT}{dx}\right]_x ; Q_{\text{joule}} = J^2 \rho w t_p dx,$$
$$Q_{\text{out,arm}} = -k_p w t_p \left[\frac{dT}{dx}\right]_{x+dx} ; Q_{\text{out,sub}} = Sdxw\frac{T - T_{\text{sub}}}{R_T}, \tag{2}$$

where T is the temperature at any given location of the actuator. T_{sub} is the substrate temperature. ρ is the resistivity of material. k_p is the thermal conductivity of material. J is the current density of hot arm or cold disc. S is the shape factor. R_T is the thermal resistance between the device and the substrate.

Substitute above values in Equation (1), and we get

$$-k_p w t_p \left[\frac{dT}{dx}\right]_x + J^2 \rho w t_p dx = -k_p w t_p \left[\frac{dT}{dx}\right]_{x+dx} + Sdxw\frac{T - T_{\text{sub}}}{R_T} \tag{3}$$

Thermal resistance between the device and the substrate is given by

$$R_t = \frac{t_a}{k_a} + \frac{t_{p0}}{k_{p0}} + \frac{t_n}{k_n}, \tag{4}$$

where t_a, $t_{p0,}$ and t_n are the thickness of the element above the polysilicon layer, thickness of polysilayer, and thickness of silicon layer. k_a, k_{p0}, and k_n are the thermal conductivity values of air, polysilicon and silicon, respectively.

Substitute the needed values to Equation (4) from Table 1. After calculating thermal resistance obtained, it is$R_t = 7.7205 \times 10^{-5}$.

Current density is the amount of current by unit area. The current density of hot arm and cold disc is calculated from

$$J_h = \frac{I}{w_p t_p}, \tag{5}$$

$J_c = .$

Using the above equation, the calculated current density value is $J_h = 7.5 \times 10^{11}$ and $J_c = 15 \times 10^{11}$. The calculated values almost match with the values obtained from simulation; so, the device can be able to fabricate.

Shape factor of the hot arm is given by

$$S = \frac{t_p}{w_h}\left[\frac{2t_a}{t_p} + 1\right] + 1. \tag{6}$$

The obtained shape factor is $S = 1.6\,\mu$m.

Resistivity is calculated by using the Van der paw method:

$$\rho = \left(2.971 \times 10^{-2}\right)T + 20.858. \tag{7}$$

At room temperature, the resistivity is $\rho = 21.5\,\mu\Omega$.

Simplifying the Equation (3), we get

$$\frac{d^2T(x)}{dx^2} = \frac{S(T(x) - T_{sub})}{k_p t_p R_T} - \frac{J^2\rho}{k_p}. \tag{8}$$

3.4.2. Rotational Analysis.

$$\Delta \text{Lh} = R\delta. \tag{9}$$

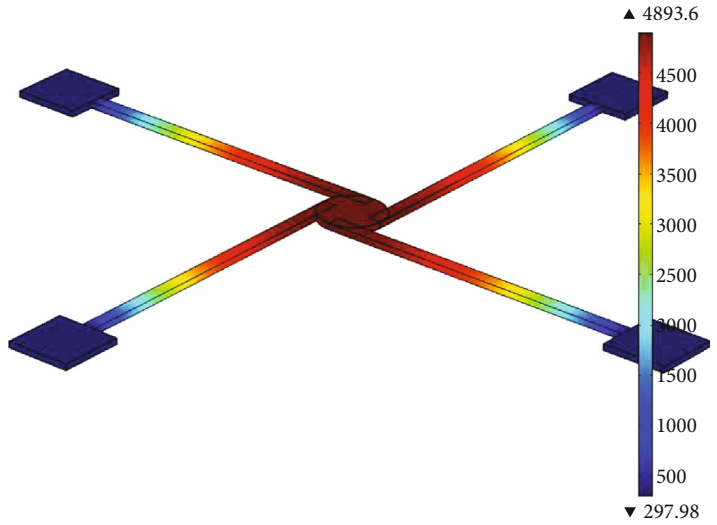

Figure 14: Current density analysis of polysilicon (circular disc 5 μm).

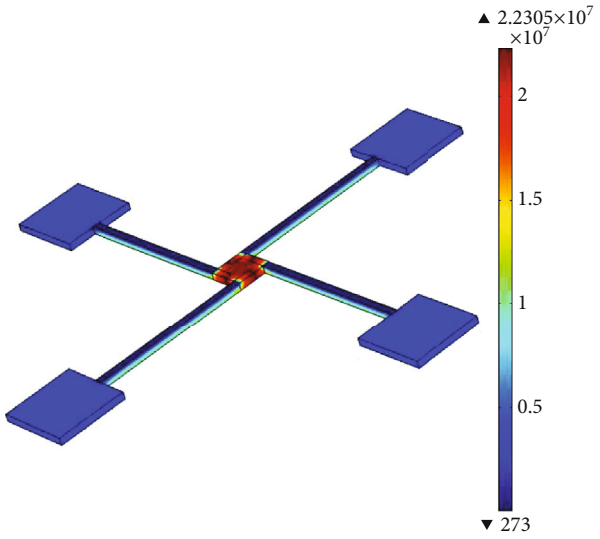

Figure 15: Current density analysis of polysilicon (square arm 10 μm).

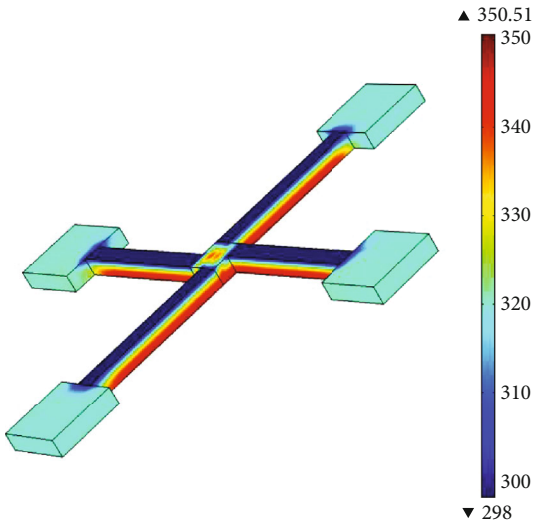

Figure 16: Current density analysis of polysilicon (square arm 25 μm).

where R is the radius of the disc. ΔLh is the total expansion of the free end. δ is the angle of rotation.

Here, taking R as 10 and the angle of rotation as 3.90, then ΔLh = 3900 nm.

4. Results and Discussion

4.1. Stress Analysis. Stress analysis is conducted to find the deformation of microthermal rotary actuator for the given pressure. Normal pressure for the stress analysis is about 7 GPa which is the yield strength of the silicon material and 8.4 GPa for poly silicon.

4.2. Von Mises Stress Analysis. This analysis is used in microthermal rotary actuator. So, when the stress is given, the material starts to yield after the critical value of yield strength which depends on von Mises stress.

4.3. Current Density Analysis. Current density is defined as the amount of charge per unit time that flows through a unit area of a chosen cross-section. Here, expected current density of a MEMS/NEMS thermal rotary actuator should be less than the electric field for fabrication.

4.4. Temperature Analysis. Temperature is a physical property of matter that quantitatively defines hot and cold. It is the indication of thermal energy present in all matter, which is the source of occurrence of heat, which is a flow of energy, when a body is in contact with another one which is cooler. The obtained temperature plot should be less than melting point of the material used there, and the devices is simulated under room temperature 298 K.

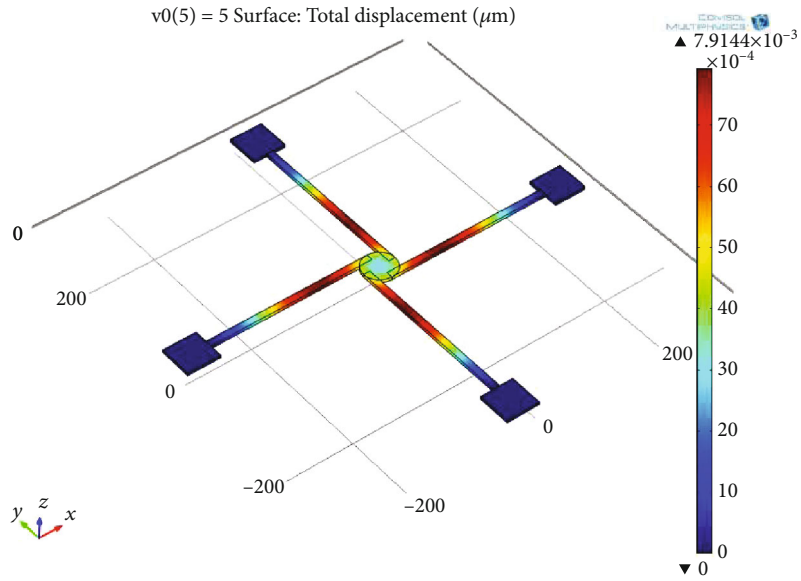

Figure 17: Von Mises stress of silicon (circular disc 5 μm).

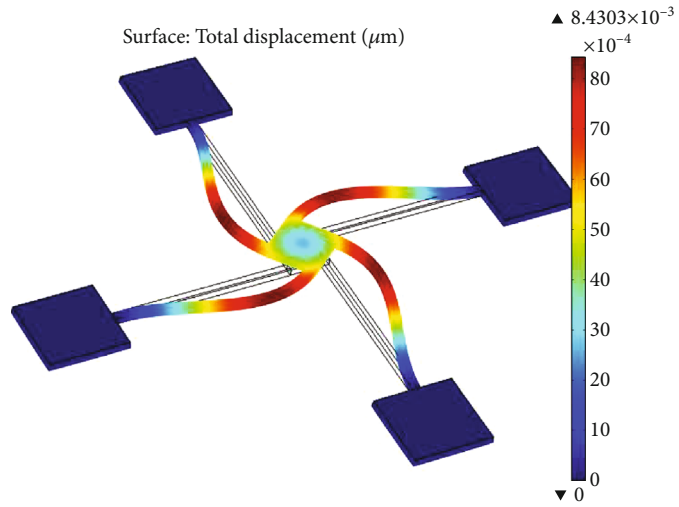

Figure 18: Von Mises stress of silicon (square arm 10 μm).

4.4.1. Temperature Analysis. Figure 5 shows the temperature plot of silicon actuator at room temperature. Here, center arm experiences high heat because the current value is high. Figure 6 shows the temperature of silicon actuator at room temperature.. If the area of the centre arm is increased, temperature is high but less compared to previous square arm of 10 μm. Figure 7 shows the temperature of silicon actuator. The obtained value is 298 K. Polysilicon and silicon are behaving similar in temperature analysis. If the square arm size is 5 μm, temperature developed is so high. Figure 8 shows the temperature of polysilicon actuator. The obtained value varies from 297.98 K to 4893.6 K. As discussed in silicon-based rotary actuator, here, also, if size of arm is increase, then temperature rise is reduced.

Figure 9 shows the temperature of polysilicon actuator. The obtained value varies from 273 K to 2.2305×10^7. Figure 10 shows the temperature of polysilicon actuator. Here, the thickness is increased; hence, heat developed is decreased. The obtained value varies from 298 K to 350.51 K.

4.4.2. Current Density Analysis. Figure 11 shows the current density of silicon actuator. The obtained value is 298. Figure 12 shows the current density of Silicon actuator. The value of bending is 298. Figure 13 shows the current density of silicon actuator. The value of bending varies from 298 to 350.51. Figure 14 shows the current density of poly Si actuator. The value of bending varies from 297.98 to 4893.6. Figure 15 shows the current density of poly silicon actuator.

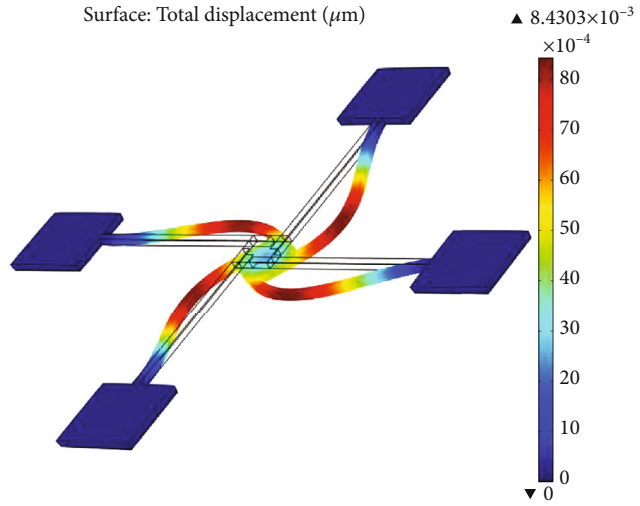

Figure 19: Von Mises stress of silicon (square arm 25 μm).

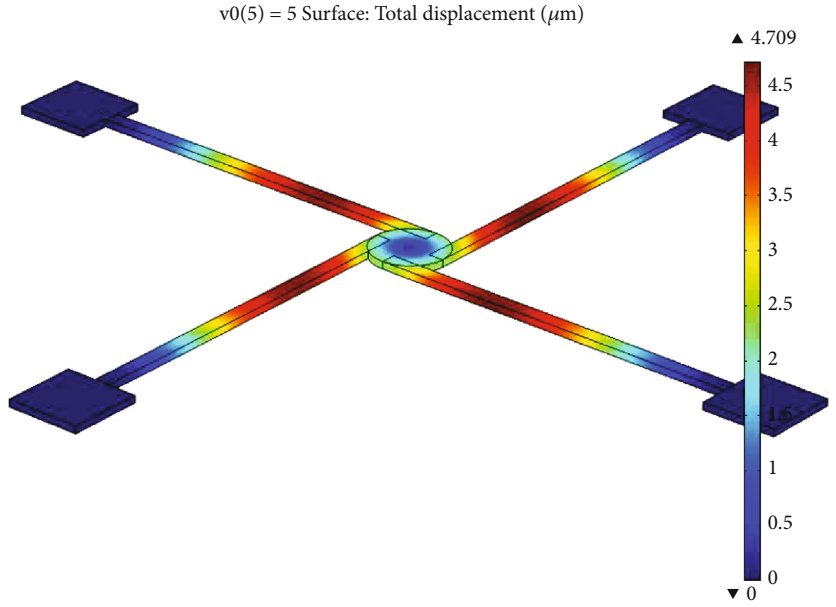

Figure 20: Von Mises stress of polysilicon (circular disc 5 μm).

The value of bending varies from 272 to 2.2307×10^7. Figure 16 shows the current density of poly silicon actuator. The value of bending varies from 272 to 350.

4.4.3. Stress Analysis. Figure 17 shows the von Mises stress of silicon-based actuator. Its range varies from 0 to 7.9144×10^{-9}. Figure 18 shows the von Mises stress of silicon-based actuator. Its range varies from 0 to 8.403×10^{-9}. Figure 19 shows the von Mises stress of silicon-based actuator. Its range varies from 0 to 8.4303×10^{-8}. Figure 20 shows the von Mises stress of polysilicon actuator. The value of bending varies from 0 to 4.709. Figure 21 shows the von Mises stress of silicon-based actuator. Its range varies from 0 to 1.3664×10^4. Figure 22 shows the von Mises stress of silicon-based actuator. Its range varies from 8.0636×10^5 to 4.7792×10^7. Thermal rotary microactuators are a favorable solution to the need for large displacement, low-power MEMS actuators. It is confirmed to be a robust actuation method in surface micromachined devices. Such devices have been used in variety of different applications like

(i) Micromechanical switches

(ii) Micromotors

(iii) Microscale tensile testing

4.4.4. Micro/Nanogear. A micro/NEMS gear is a part of rotating machine which is having cut teeth or, in the case of a cog wheel, it is having inserted teeth (called cogs), which wire with another toothed part which is used to transmit

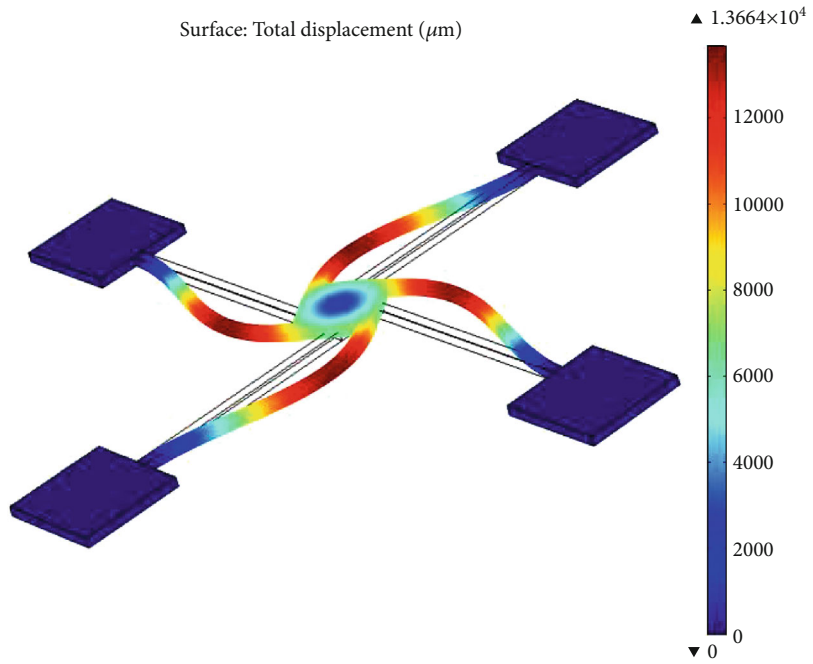

Figure 21: Von Mises stress of polysilicon (square arm 10 μm).

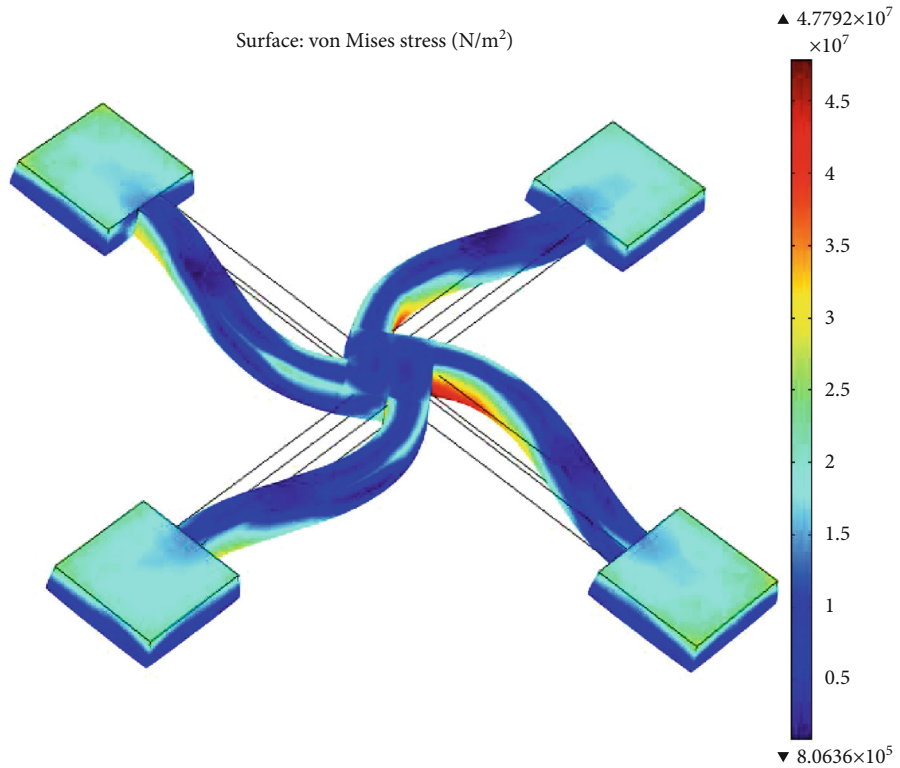

Figure 22: Von Mises stress of polysilicon (square arm 25 μm).

torque. Geared devices can change the speed, torque, and direction of a power source. Gears always used to change torque, through their gear ratio, and they are considered as a simple machine. The teeth on the two interlocked gears have the same shape. Two or more meshing gears, working in a sequence, are called a gear train or a transmission. A gear can mesh with a linear toothed part, called a rack, producing translation instead of rotation.

4.5. Dimension. Microgear design has been done in Figure 23 using the parameters such as inner dimension that is 171 μm and outer dimensions that are 40 μm. The number of teeth is

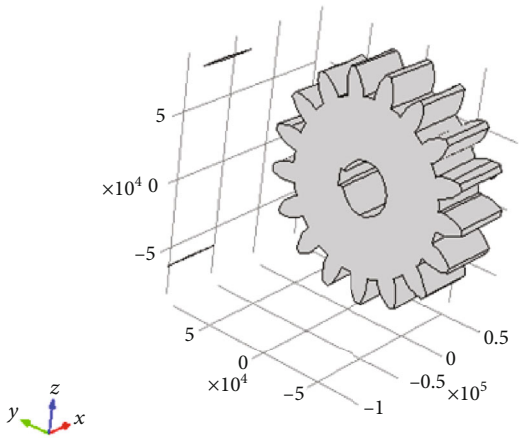

Figure 23: Structure of single microgear.

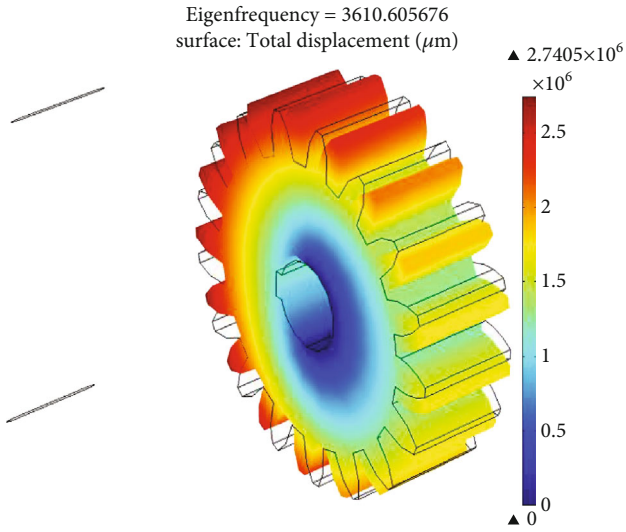

Figure 24: Eigen frequency analysis of micro gear.

17 μm, its width is about 14 μm, and the width is about 50 μm. This design is done by using material called cast iron.

4.6. Eigen Frequency Analysis. When the gear is vibrating at eigen frequency, the gear structure deforms into a corresponding shape which is called eigen mode. An eigen frequency analysis of Figure 24 can only provide the shape of the mode, not the amplitude of the physical vibration. Eigen analysis is done to find the structural behavior of the rotary actuator. If the structure deformation is less, then it is concluded that the designed device will work safely.

5. Conclusion

This work presents the out of plane microthermal rotary actuator with different structures and different dimensions. Stress analysis of microthermal rotary actuator shows its stress bearing capacity for different structures that are different. Current density and temperature analysis show that the safer limit and melting point of the actuator are the same at the every point in the actuator. Also, in microgear eigen frequency analysis is done, it shows that the total displacement of the microgear is same as every point of the design.

Data Availability

The data used to support the findings of this study are included in the article. Should further data or information be required, these are available from the corresponding author upon request.

Conflicts of Interest

The authors declare that there are no conflicts of interest regarding the publication of this paper.

Acknowledgments

The authors appreciate the supports from Bahir Dar Institute of Technology, Bahir Dar University, Ethiopia. The authors thank Saveetha School of Engineering and Vellore Institute of Technology, Chennai, for the technical assistance to support this study.

References

[1] A. Atre and S. Boedo, "Effect of Thermophysical property variations on surface micromachined polysilicon beam flexure actuator," *NSTI-Nanotech*, vol. 2, pp. 263–266, 2004.

[2] A. A. Geisberger, N. Sarkar, M. Ellis, and G. D. Skidmore, "Electrothermal properties and modeling of polysilicon microthermal actuators," *Journal of Microelectromechanical Systems*, vol. 12, no. 4, pp. 513–523, 2003.

[3] S. Heo, G. H. Yoon, and Y. Y. Kim, "The robust design for micro electro-thermal actuators," in *Smart Structures and Materials 2004: Smart Electronics, MEMS, BioMEMS, and Nanotechnology (Vol. 5389, pp. 241-247)*, International Society for Optics and Photonics, 2004.

[4] Q.-A. Huang and N. K. S. Lee, "Analysis and design of polysilicon thermal flexure actuator," *Journal of Micromechanics and Microengineering*, vol. 9, no. 1, pp. 64–70, 1999.

[5] S. Heo and Y. Y. Kim, "Optimal design and fabrication of MEMS rotary thermal actuators," *Journal of Micromechanics and Microengineering*, vol. 17, no. 11, pp. 2241–2247, 2007.

[6] B. Haefner, M. Quiring, J. Gullasch, G. Glaser, T. Dmytruk, and G. Lanza, "Finite element simulation for quality dependent lifetime analysis of micro gears," *Science Direct*, vol. 31, pp. 41–46, 2015.

[7] A. Islam and M. M. Islam, "Stress on spur gear and simulation for micro hybrid systems by Ansys workbench," *Journal of Mechanical and Energy Engineering*, vol. 3, no. 1, pp. 25–30, 2019.

[8] M. A. Arefin, A. Mallik, and M. Asfaquzzaman, "Renewable energy–assisted hybrid three-wheeler: a numerical investigation," *Advances in Mechanical Engineering*, vol. 10, no. 12, Article ID 168781401881437, 2018.

[9] X. Jin, Y. Wang, W. Ju, J. He, and S. Xie, "Investigation into parameter influence of upstream deflector on vertical axis wind turbines output power via three-dimensional CFD simulation," *Renewable Energy*, vol. 115, pp. 41–53, 2018.

[10] A. Arefin and R. Islam, "Investigation of different validation parameters of micro gas turbine for range extender electric

truck," *International Journal of Engineering*, vol. 31, no. 10, pp. 1782–1788, 2018.

[11] S. M. Karbosi, M. Shamshrisar, M. Naraghi, and M. Manoufi, "Optimal design analysis of electrothermally driven microactuators," *Microsystem Technologies*, vol. 16, no. 7, pp. 1065–1071, 2010.

[12] C. Lo, M. Lin, and C. Hwan, "Modeling and analysis of electrothermal microactuators," *Journal of the Chinese Institute of Engineer*, vol. 32, no. 3, pp. 351–360, 2009.

[13] D. Veeman, M. S. Sai, P. Sureshkumar et al., "Additive manufacturing of biopolymers for tissue engineering and regenerative medicine: an overview, potential applications, advancements, and trends," *International Journal of Polymer Science*, vol. 2021, Article ID 4907027, 20 pages, 2021.

[14] R. S. Chiorean, M. C. Dudescu, and M. Pustan, "Analytical and numerical study on the maximum force developed by a V-beam thermal actuator," *Procedia Technology*, vol. 12, pp. 359–363, 2014.

[15] S. Wang, Y. Hao, and S. Liu, "The design and analysis of a MEMS electrothermal actuator," *Journal of Semiconductors*, vol. 36, no. 4, p. 044012, 2015.

[16] A. Potekhina and C. Wang, "Review of Electrothermal Actuators and Applications," *MDPI Actuators*, vol. 8, no. 4, 2019.

[17] Y. Sun, B. D. Leaker, J. E. Lee, R. Nam, and H. E. Naguib, "Shape programming of polymeric based electrothermal actuator (ETA) via artificially induced stress relaxation," *Scientific Reports*, vol. 9, no. 1, article 11445, 2019.

[18] X. Li, Y. Zhao, T. Hu et al., "Design of a large displacement thermal actuator with a cascaded V-beam amplification for MEMS safety-and-arming devices," *Microsystem Technologies*, vol. 21, no. 11, pp. 2367–2374, 2015.

[19] S. Yogeshwaran, L. Natrayan, S. Rajaraman, S. Parthasarathi, and S. Nestro, "Experimental investigation on mechanical properties of epoxy/graphene/fish scale and fermented spinach hybrid bio composite by hand lay-up technique," *Materials Today: Proceedings*, vol. 37, no. 2, pp. 1578–1583, 2021.

[20] S. Kim, W. Kim, and Y. Kim, "Design and performance evaluation of thin-film actuators based on flexible Ni-Co substrates," *Micro and Nano Systems Letters*, vol. 8, no. 1, 2020.

[21] O. Ulkir, "Design and fabrication of an electrothermal MEMS micro-actuator with 3D printing technology," *Materials Research Express*, vol. 7, no. 7, 2020.

[22] H. Steiner, F. Keplinger, J. Schalko, W. Hortschitz, and M. Stifter, "Highly efficient passive thermal micro-actuator," *Journal of Microelectromechanical Systems*, vol. 24, no. 6, pp. 1981–1988, 2015.

[23] N. T. Duzng, "Modeling and simulation of V-shaped thermal actuator," *American Journal of Engineering Research*, vol. 7, no. 4, pp. 222–227, 2018.

[24] M. Li, Z. Zhou, L. Yi, X. Wang, and S. Adnan, "Design of a test structure based on chevron-shaped thermal actuator for in-situ measurement of the fracture strength of MEMS thin films," *Nanotechnology and Precision Engineering*, vol. 2, no. 4, pp. 163–168, 2019.

[25] R. Suryanarayanan, V. G. Sridhar, L. Natrayan et al., "Improvement on mechanical properties of submerged friction stir joining of dissimilar tailor welded aluminum blanks," *Advances in Materials Science and Engineering*, vol. 2021, Article ID 3355692, 6 pages, 2021.

[26] Y. J. Gong, F. Zhao, H. Y. Xiang, and L. Zhang, "Thermal analysis and simulation of MEMS thermal actuator for food industry," *Advanced Materials Research*, vol. 179-180, pp. 392–397, 2011.

[27] B. López-Walle, M. Gauthier, and N. Chaillet, "Dynamic modelling for thermal micro-actuators using thermal networks," *International Journal of Thermal Sciences*, vol. 49, no. 11, pp. 2108–2116, 2010.

[28] D. H. Kim, K. S. Oh, and S. Park, "Design and analysis of a twisting-type thermal actuator for micromirrors," *Journal of Mechanical Science and Technology*, vol. 23, no. 6, pp. 1536–1543, 2009.

Hindawi
Journal of Nanomaterials
Volume 2021, Article ID 1754325, 11 pages
https://doi.org/10.1155/2021/1754325

Research Article

Flexural Behavior Performance of Reinforced Concrete Slabs Mixed with Nano- and Microsilica

Rakesh Kancharla,[1] Venkata Rao Maddumala,[2] T. V. N. Prasanna,[2] Lokaiah Pullagura,[3] Ratna Raju Mukiri,[4] and M. Viju Prakash[5]

[1]*Department of CSE, Sasi Institute of Technology and Engineering, Tadepalligudem, Andhra Pradesh, India*
[2]*Vignan's Nirula Institute of Technology & Science for Women, Guntur, Andhra Pradesh, India*
[3]*Department of CSE, Vignan's Foundation for Science, Technology & Research, Vadlamudi, Guntur, Andhra Pradesh, India*
[4]*St. Ann's College of Engineering and Technology, Chirala, Andhra Pradesh, India*
[5]*Department of Computer Science, Kombolcha Institute of Technology, Wollo University, P.O. Box 208, Ethiopia*

Correspondence should be addressed to Venkata Rao Maddumala; venkatmaddumala@gmail.com
and M. Viju Prakash; vijuprakash@kiot.edu.et

Received 27 August 2021; Revised 2 October 2021; Accepted 19 October 2021; Published 8 November 2021

Academic Editor: Lakshmipathy R

Copyright © 2021 Rakesh Kancharla et al. This is an open access article distributed under the Creative Commons Attribution License, which permits unrestricted use, distribution, and reproduction in any medium, provided the original work is properly cited.

Present technology has been evaluated greatly over the past decades, where new particles are being designed and fabricated to fulfill specific needs. The field of nano- and micromaterials has prospered in many disciplines. It has been recently used in reinforced concrete in the production of high-strength, high-performance concrete. Microsilica (MS) and nanosilica (NS) particles have proven to be highly profitable to the concrete mix. Concrete has become denser with considerable improvement in their mechanical characteristics, particularly compressive strength. This proposed method includes a comparative study of the flexural bending behavior of conventional reinforced concrete (without MS or NS) slabs with other slabs. Each has various mixes of MS and NS particles incorporated into the concrete mix. The material content utilized in the slabs is kept constant by replacing a portion of the cement with an equivalent amount of either NS or MS particles or both. MS particles are altered from 0, 5, and 10% while NS particles are altered from 0, 0.5, and 1.0%. It cracks the widths and has higher final load-bearing capacity.

1. Introduction

Present-day modern concrete mixes now not satisfy the growing desires for advanced strengths and outstanding durability. Constructions have invaded severe exposure conditions such as those in arid, coastal, and marine environments, where sizable deterioration of systems has been recorded. The need for highly priced restoration and rehabilitation measures has boomed to hold structures to function successfully, at some stages inside the live carrier lives. An evolving need for denser and higher electricity concrete is to be fulfilled nicely by using new contemporary materials that are probably designed and fabricated on a micro- and nanoscale. Material advances have superior micro- and nanosilica that have been efficiently followed to reap immoderate and extremely high-energy concrete that displays exceptional sturdiness characteristics. Cement is the most used advent commodity in some unspecified time in the future of the world. Still, its production consequences in excessive gasoline consumption levels and sizable tiers of surroundings' pollutants are alarming that many European countries have banned its manufacturing [1].

In addition, when emitted into the environment, microsilica (a by-product of industry) leads to high levels of air pollution. The essential strategy is to rid the environment of microsilica emission and reduce cement consumption, hence obtaining superior concrete mixes that are more durable and denser and provide much higher mechanical

Table 1: Chemical analysis of used OPC.

Oxides	Al_2O_3	SiO_2	Fe_2O_3	CaO	MgO	SO_3	L.O.I	Insoluble residue
%	4.78	20.38	3.93	62.85	1.95	2.18	2.68	0.69

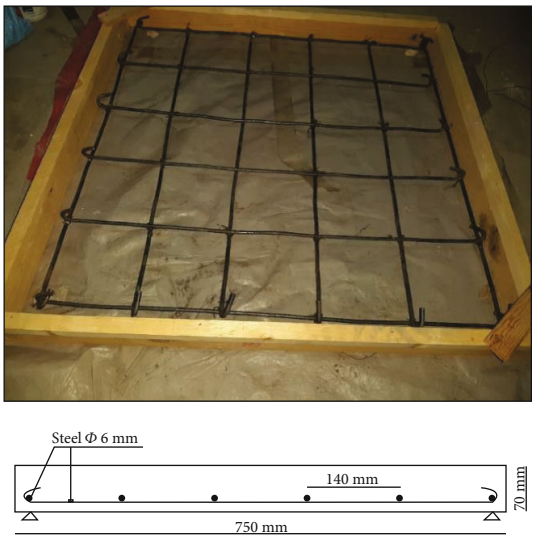

Figure 1: Slab mold and reinforcement details.

strength [2]. Silica fume is collected, refined, and used in concrete mixes in the form of microsilica or nanosilica as a partial substitute for cement, effective on both levels, reducing cement consumption and reducing environmental pollution [3]. Silica fume either nano- or microparticles is pozzolanic in nature. Microsilica (MS) is a polymorph (amorphous) silicon dioxide, but nanosilica (NS) is made up of an amorphous silica (SiO_2) core with a hydroxyl surface [4].

The amorphous structure of nanomaterials such as nanosilica physically affects the hydrate products. Still, the pozzolan material reacts with the carbon hydroxide (CH) generated from the reaction of water with both dicalcium silicate (2CaO). SiO_2 and tricalcium silicate ($3CaO{\cdot}SiO_2$). In this process, nanosilica (NS) with particle sizes ranging from 1 to 500 nm is amorphous silicon dioxide, which can accelerate the wetting rate of bonding materials due to their high surface area and amorphous nature [5]. In addition, NS has a relatively high pozzolanic activity, which aids in additional CSH gel formation, as working NS is intended to be a site for CSH gel growth and speeds up the hydration of fly ash and cement [6]. Also, NS particles are smaller than cement and fly ash particles, improving particle packing and purification of porous structures [7–9]. Ultrahigh strength concrete is achieved with minimal pores as the hydrates work to harden between the cement paste and the aggregate particles [10]. It is worth noting that incorporating the methods of nanosilica (NS) in the mix, either by addition or replacement, and the method of its mixing in its either wet or dry condition, both have considerable influence on the mechanical properties of concrete [11]. Effective dispersion of nanosilica particles in concrete mixtures leads to better mechanical and durable properties, resulting in high-strength concrete [12, 13]. Much recent research has been done on the use of nanomaterials in concrete. Still, only a few studies have examined the use of a mixture of nanosilica and microsilica in concrete [14].

Table 2: Physical properties of microsilica and nanosilica.

Property	Microsilica	Nanosilica
Surface area (cm^2/gm)	170000	240000
Particle size	1.0 μm (1×10^{-6} m)	5 to 20 nm (5 to 20×10^{-9} m)
Specific gravity	2.20	2.40
Unit weight (kg/m^3)	345	505
Colour	Grey	White

The disadvantages of using micro- and nanoparticles in concrete include the high specific surface area of the binding material. The specific surface area for microsilica is 17 m^2/g (70 times greater than OPC), while that for nanosilica is 25 m^2/g (100 times greater than OPC). The introduction of nanosilica particles (finer than microsilica) increases the surface area of the mixture's reactive powders, which causes a further decrease in the consistency and operability of the mixture [15]. Consequently, using an effective high-range water reducer is inevitable to maintain consistency and workability of the mix and elevate strength to ultrahigh levels [16, 17]. On the mortar level, micro- and nanosilica cement mortars are highly superior to traditional cement mortars when mixed and cured under high temperatures [18, 19]. Ultrasonic technology under high temperatures is a very effective dispersion technique used in mixing nanosilica particles. Mortar analysis indicates better homogeneity of the mix and superior mechanical strength and superb durability resulting in ultra-high-strength and ultra-high-performance concrete [20–22]. Also, previous researchers mentioned a decrease in porosity and permeability of the slurry as nanomaterials [23] replaced the cement. The study focused on the partial replacement of cement by NS, MS, and a combination of both and their effect on the flexural behaviour of supported one-panel slabs subjected to uniformly distributed loads.

2. Experimental Program

Detailed descriptions of materials used by this investigation, particularly cement, aggregates, steel bar, microsilica, nanosilica, water, and chemical admixtures, are given in this section.

2.1. Material Properties

2.1.1. Cement. Ordinary Portland Cement (OPC) (CEM I 52.5 N) was produced by Beni Suef Cement Factory. The chemical analysis of the used cement supplied by the

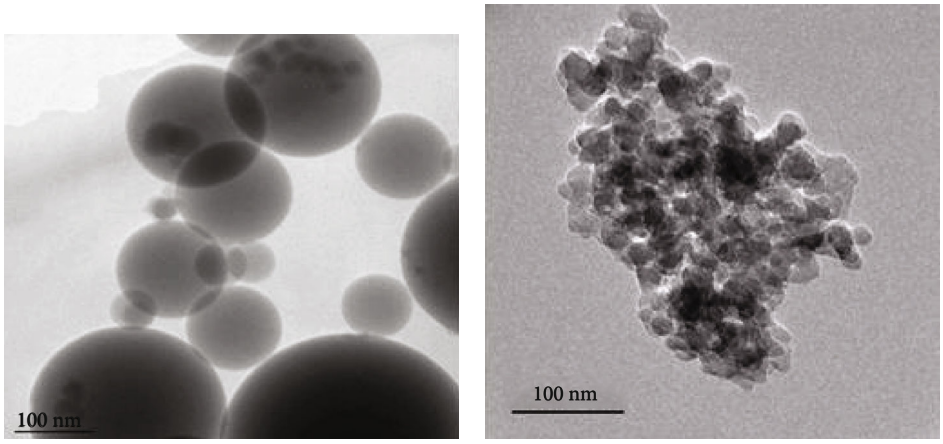

(a) (b)

Figure 2: Transmission electron microscope (TEM) images of micro- and nanosilica.

Table 3: Chemical analysis of microsilica and nanosilica.

Oxides	Microsilica Result (%)	Nanosilica Result (%)
Al_2O_3	1.10	7.39
SiO_2	96%	92.5
Fe_2O_3	1.45	0.08
CaO	1.2	0.06
MgO	0.18	0.21
SO_3	0.25	0.20
Na_2O	0.45	0.02
K_2O	1.20	0.04
L.O.I	—	0.15
H_2O	0.85	—

manufacturer and the limits according to the Egyptian Standard Specification (ESS) (4756-1/2009) are presented in Table 1.

2.1.2. Aggregates. The coarse aggregate used is crushed dolomite with a specific gravity of 2.6 and a water absorption of 0.95% with a maximum nominal size 10 mm. The fine aggregate is siliceous sand with a specific gravity of 2.57, a fineness modulus of 3.11, and a dry unit weight of 1.78 t/m^3 according to the Egyptian Standard Specification—ESS 1109(2002). All aggregates used in this research are locally available from quarries in Andhra Pradesh, India.

2.1.3. Reinforcement Bars. Reinforcement steel rods were used with a nominal diameter of 6 mm and having a yield stress of 269 MPa and ultimate tensile strength of 386 MPa (Figure 1).

2.2. Mineral Admixtures (Pozzolans)

2.2.1. Microsilica. The microsilica used in this research as a mineral admixture is imported from Sisco Research Laboratories (SRL)—Chennai. The manufacture data sheet contains the physical composition, properties, and shape (Table 2 and Figure 2(a)). The chemical composition of microsilica depends strongly on raw materials and the production process parameters. According to the international standard ASTM 1240-01, pr EN 13263-1 is shown in Table 3).

2.2.2. Nanosilica. The used nanosilica consisting of silicon dioxide with a purity of 99.9% is a product of Sisco Research Laboratories (SRL)—Chennai. The physical properties and shape are obtained from the manufacture data sheet (Table 2 and Figure 2(b)). The chemical analysis of NS used supplied by the manufacturing company is shown in Table 3.

2.2.3. Superplasticizer. The high-performance plasticine mixture Sikament NN was used in this work, which is a third-generation upper plasticizer for homogeneous concrete with a density of 1.185 kg/L and pH value of 8. It meets superior requirements of plasticizers according to ASTMC-494 Types A and F and EN934-2:2001. By using this kind of superplasticizer, we can get very high percentage of water reduction resulting in high density and strength. It also improves shrinkage, creep behavior, and water permeability. The dose used of the superstable plasticizer was maintained at 2.5% by weight of cement for all mixtures.

2.2.4. Test Specimens. Several blends were examined in order to achieve target properties. The pilot program included nine mixtures, all of which were engineered based on the absolute volume of the components in a saturated dry surface condition. All slabs are $750 \times 750 \times 70$ mm in dimensions, reinforced with 6 mm diameter steel bars distributed at 140 mm spacing which was maintained (Figure 1). The mixes (M0N0) include a control mix without any mineral admixture additives. Two other mixes (M5N0 and M10N0) consist of cement replaced by 5% and 10% of microsilica, respectively. Another two mixes (M0N0.5 and M0N1.0) consist of cement replaced by 0.5% and 1.0% of nanosilica, respectively. These previous mixes illustrate the effect of replacing cement by either micro- or nanosilica alone without their combined effect. Another four mixes include

Table 4: Test program and contents of mixtures.

Slab no.	Cement (kg/m^3)	Coarse aggregates (kg/m^3)	Fine aggregates (kg/m^3)	Microsilica (kg/m^3)	Nanosilica (kg/m^3)	Water (kg/m^3)	Superplasticizer (kg/m^3)	Notes
M0N0	450	1176	588	0	0	180	11.25	Control
M0N0.5	447.75	1176	588	0	2.25	180	11.25	0.5% NS
M0N1.0	445.5	1176	588	0	4.5	180	11.25	1.0% NS
M5N0	427.5	1176	588	22.5	0	180	11.25	5% MS
M5N0.5	425.25	1176	588	22.5	2.25	180	11.25	5%MS + 0.5%NS
M5N1.0	423	1176	588	22.5	4.5	180	11.25	5%MS + 1.0%NS
M10N0	405	1176	588	45	0	180	11.25	10% MS
M10N0.5	402.75	1176	588	45	2.25	180	11.25	10%MS + 0.5%NS
M10N1.0	400.5	1176	588	45	4.5	180	11.25	10%MS + 1.0%NS

Figure 3: Slabs before testing.

Figure 4: Ultrasonic device for mixing nanoparticles.

different combinations (M5N0.5, M5N1.0, M10N0.5, and M10N1.0). The first consists of 5% microsilica and 0.5% nanosilica, the second consists of 5% microsilica and 1.0% nanosilica, the third consists of 10% microsilica and 0.5% nanosilica, and the fourth consists of 10% microsilica and 1.0% nanosilica. These four mixes illustrate the combined effect of replacing the cement with a combination of both micro- and nanosilica. The cementitious content of all high-strength concrete mixes is kept constant at $450\,kg/m^3$ (Table 4); then, twelve cubes with dimensions ($100 \times 100 \times 100$ mm) are casted and tested throughout this study to reach the target compressive strength. A constant dose of 2.5% high-range water reducer (superplasticizer) by weight of cementitious materials along with a fixed water/cementitious ratio of 0.4 is maintained for all mixes.

2.2.5. Mixing Procedure. All concrete components were mixed using a horizontal mixer. For mixes without nanosilica, coarse and fine aggregates and cementitious materials (cement and microsilica) were added into the mixer in their dry state and mixed for 2 minutes. The mixing water and superplasticizer were added gradually and mixed for another 3 minutes to get uniform and homogeneous mix consistency and texture. The fresh concrete properties were measured immediately after mixing, and the concrete was removed from the mixer and placed in the slab formwork with the rebar rods distributed correctly and with reasonable cover. Concrete slabs and cube samples were kept in molds for 24 h in air and then removed from the formwork and cured daily by wetting with fresh water for 28 days (Figure 3). For mixes with nanosilica, coarse aggregate, fine aggregate, and cement materials (cement and microsilica) were loaded into the mixer and mixed dry for 2 minutes. Three-fourth of the water content is gradually to dry mix and mix it more for another 1 minute. The superplasticizer dose is added to the remaining quarter of the water content; then, the required amount of nanosilica is added to the water and the superplasticizer and mixed well in an ultrasonic device (Figure 4) for a duration of ten minutes at a temperature of 40°C for achieving the best possible dispersion of nanoparticles in solution and preventing the possibility of any agglomeration. Then, it is added to the wet mixture and then mixed for another four minutes until a homogeneous concrete mixture is obtained.

2.2.6. Setup and Testing. The compressive strength test was conducted on the cured cube specimens ($100 \times 100 \times 100$ mm) at ages 28 and 56 days. All cubes exhibited a typical failure mode of a cube (Figure 5) which indicates proper loading of the cube specimens.

The bending test of all panels is performed with a hydraulic jack mounted on the frame of the testing machine. A load cell is placed beneath the jack drum which is connected to a data logger that records readings of simultaneous load and deflection measured with variable linear differential

Figure 5: Hydraulic machine used in a compressive test and mode of a crushed cube.

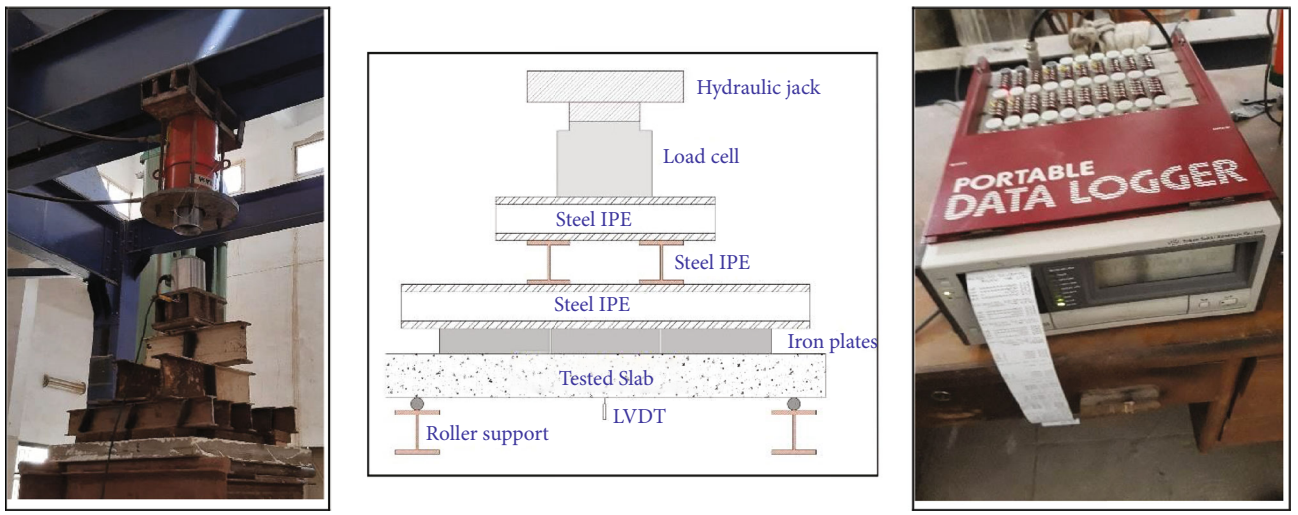

Figure 6: Test preparation and instrumentation.

transformers (VLDTs) located at the center of the slab. A series of I-shaped beams and slabs are stacked in a pyramid shape to transfer the concentrated drum load to a uniformly distributed load on the upper face of the slab (Figure 6).

3. Experimental Results and Discussion

3.1. Compressive Strength. The compression test was conducted on all ratios, the comparison was made between the lowest value of compressive strength M0N0 (control specimen) and the highest value of compressive strength that has the high proportions of the replacement ratio M10N1.0 (10%MS + 1.0%NS) at ages 7 and 28 days. Values of compressive strength are recorded, and the average of three specimens is calculated and values are 27.5 MPa and 30.6 MPa for M0N0 and M10N1.0 at 7 days and 36.6 MPa and 40.7 MPa at 28 days, respectively. Early strength improvement effect of nanosilica-modified concrete is more obvious, which was due to the higher pozzolan activity of nanosilica particles [24, 25].

3.2. Flexural Strength. Samples M0N0, M0N0.5, and M0N1.0 all contain 0% microsilica, with a binder content of 450 kg/m^3, a water-cement ratio of 0.4, and a superplasticizer dose of 2.5% cement weight, with 0, 0.5, and 1.0% nanosilica, respectively. The bending strength at the load causing the initial cracking increased significantly from M0N0 by 7.8% and 15.7% for nanosilica 0.5% and 1.0%, respectively, indicating some resistance to initial cracking of the concrete (Figure 7(a)), whereas the final failure strength has slight increment from M0N0 by 0.42% and 1.26% for 0.5% and 1.0% nanosilica, respectively. This slight improvement in early bending resistance results from simple replacement of cement with nanosilica (Figure 7(b)).

Specimens M0N0, M5N0, and M10N0 that all possessed 0% nanosilica and water-cement ratio 0.4, and the plasticizer superdose is 2.5% by weight of cement, with 0, 5, and 10% of microsilica, respectively.

According to the literature, the microsilica improves the packing properties of the matrix and thus have a noticeable effect on the bending strength. Flexural strength at the initial cracking load increased significantly by 58.6% and 88.0% for 5% and 10% microsilica, respectively, indicating great resistance to initial cracking of the concrete (Figure 7(c)), whereas the final failure strength has increased marginally by 2.1% for 5% microsilica and 4.2% for 10% microsilica (Figure 7(d)). Other researchers note this apparent improvement in the early bending strength of concrete; at 28 days, the microsilica content increases from 5% to 10% [26]. The addition of mineral admixtures results in an increase in all

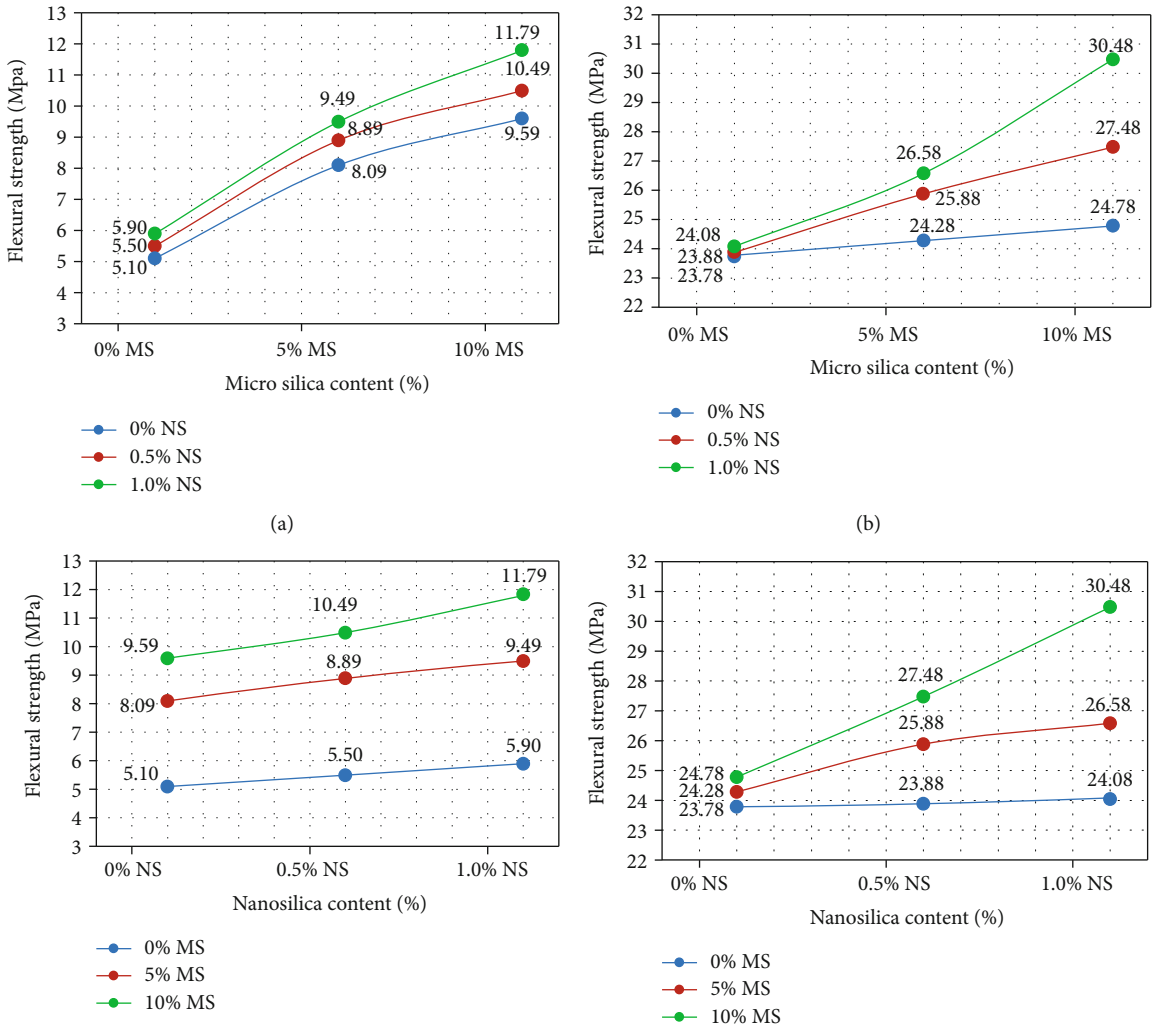

Figure 7: Nano- and microsilica effect on flexural strength of RC slabs.

concrete strengths including compressive, split-tensile, and flexure [27].

A comparison was made between the flexural strength for mixes M5N0, M5N0.5, and M5N1.0 at cracking and failure states, respectively. The cement content in mixes was 450 kg/m^3, the silica fume content was 5%, and the content of nanosilica was 0, 0.5, and 1.0%, respectively. The data in figures clearly show a remarkable increase in flexural strength at both cracking and failure states due to a marginal implementation of nanosilica [28]. The flexural strength at cracking increased by 9.9 and17.3% for nanosilica contents 0.5 and 1.0%, respectively (Figure 7(a)), while the flexural strength at failure increased by 6.6 and 9.5% for nanosilica contents 0.5 and 1.0%, respectively (Figure 7(b)). Similar results are recorded for the specimens M10N0, M10N0.5, and M10N1.0 which have the same aggregate, *w*/*c* ratio, silica fume content, and curing conditions [29]. The data in figures clearly show an improvement in bending strength as a result of adding nanosilica by 0.5 and 1.0%, where the strength at cracking was increased by about 9.4 and 22.9% (Figure 7(a)), while the strength at failure was increased by about 10.9 and 23.0% for M10N0.5 and M10N1.0, respectively (Figure 7(b)).

Apparently, the results of implementing nanosilica in the combination or presence of microsilica indicate extra improvement and much higher flexural strengths as compared to nanosilica specimens with no microsilica added [30]. In this study, specimen with 10% microsilica and 1.0% of nanosilica replacement of cement show a superior performance, where the flexural strength of the slab increased by about 131.2% at the cracking state and 28.2% at the failure state as compared to that of the control slab [31].

3.3. Load Deflection Behavior. Incorporation of microsilica alone showed a better pattern of load deflection (Figure 8(a)), compared to incorporating nanosilica alone (Figure 8(b)). As higher loads are achieved with lower deflection values, this may be attributed to the fact that the microparticles together with the cement particles result in better packing characteristics than the nanoparticles with the cement particle [32]. This conclusion is better reinforced

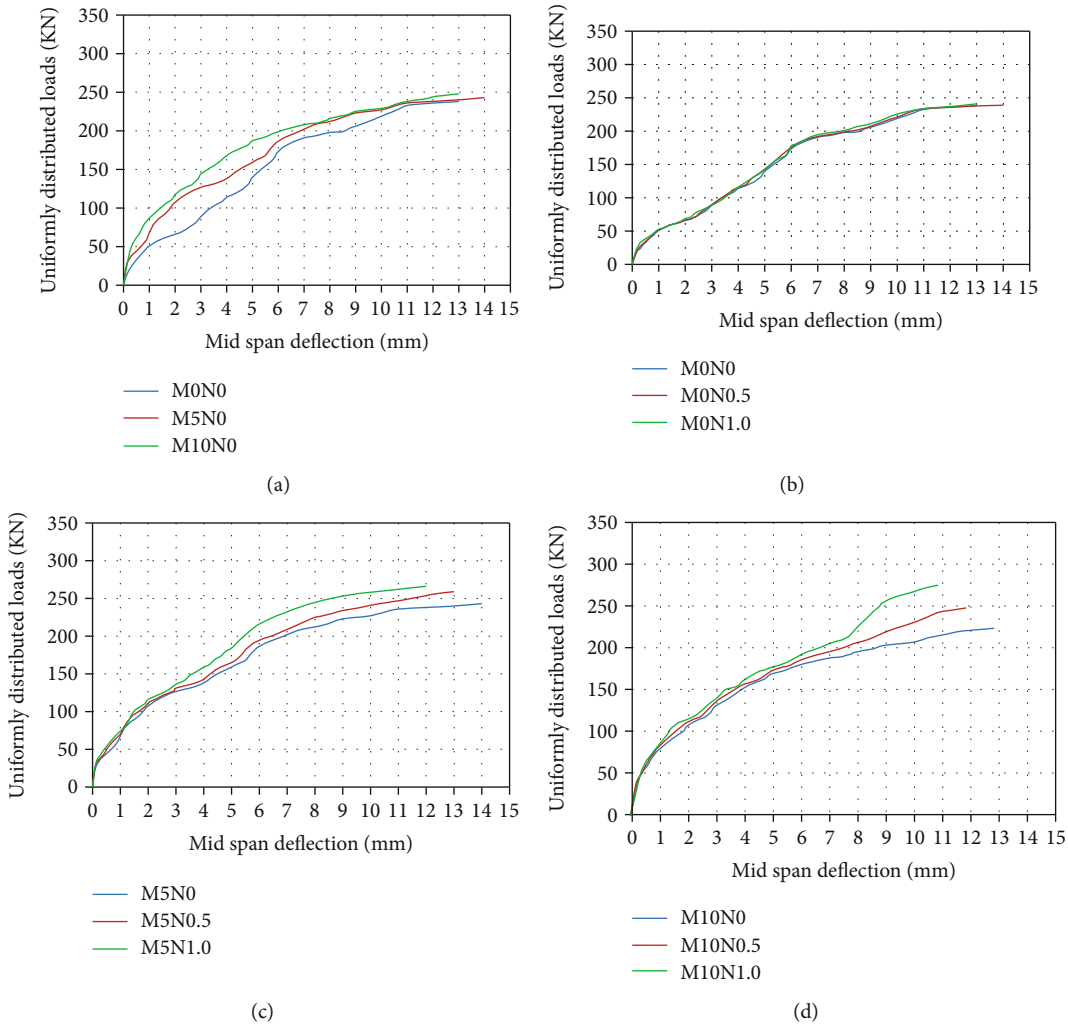

Figure 8: Effect of nanosilica and microsilica on the values of deflection.

when a blend of both nano- and microsilica is used with the cement particle where a better grading of the binding materials is available; hence, a more improved packing result is achieved (Figures 7(d) and 8(c)). Results of the specimen that incorporates 10% microsilica in addition to 1.0% of nanosilica show a superior load deflection curve where higher loads are achieved at lower deflections [33].

This indicates the improved strength of the concrete matrix which is able to resist more compression above the neutral axis of the slab hence considerably affecting its flexural capacity. This improvement can be attributed to the effect of nanosilica and microsilica fillings that have a large surface area which improves chemical reaction because of pozzolanic activity. Hence, additional C-S-H gel was formed for generating more force resulting in less deflection [34].

3.4. Crack Patterns. The reference slab specimen M0N0 exhibited initial cracking at much lower loads, with wider intervals and small width (Figure 9(a)). These cracks extended in length due to the load propagation till the slab failed in flexure at a lower failure load due to the compression failure of the concrete in the top fibers of the slab [35–38]. In addition to silica cement replacing mineral admixtures either nano- or microparticles, it is realized that the initial cracks occur much later at much higher loads indicating better concrete resistance to cracking (Figures 9(b)–9(i)). These cracks are few in number and wider, which is noticeable when the plate fails, which occurs at a much higher load due to the better performance of the concrete compression area [39–41]. Accordingly, the bending ability of the slab is greatly improved. Similar results have been reported [42] whereas the presence of nanocrystal line silica greatly changes the hardness.

Properties of C-S-H calcium silicate hydrate of the concrete matrix thus improve the bending ability of the reinforced slabs. All previous research has indicated that nanoparticles can improve fresh and hardened-state properties [43].

4. Conclusions

In this research, the experimental program was implemented for studying the effect of using microsilica as well as nanosilica on properties of reinforced concrete slabs. Based on the results obtained, the following main conclusions can be drawn:

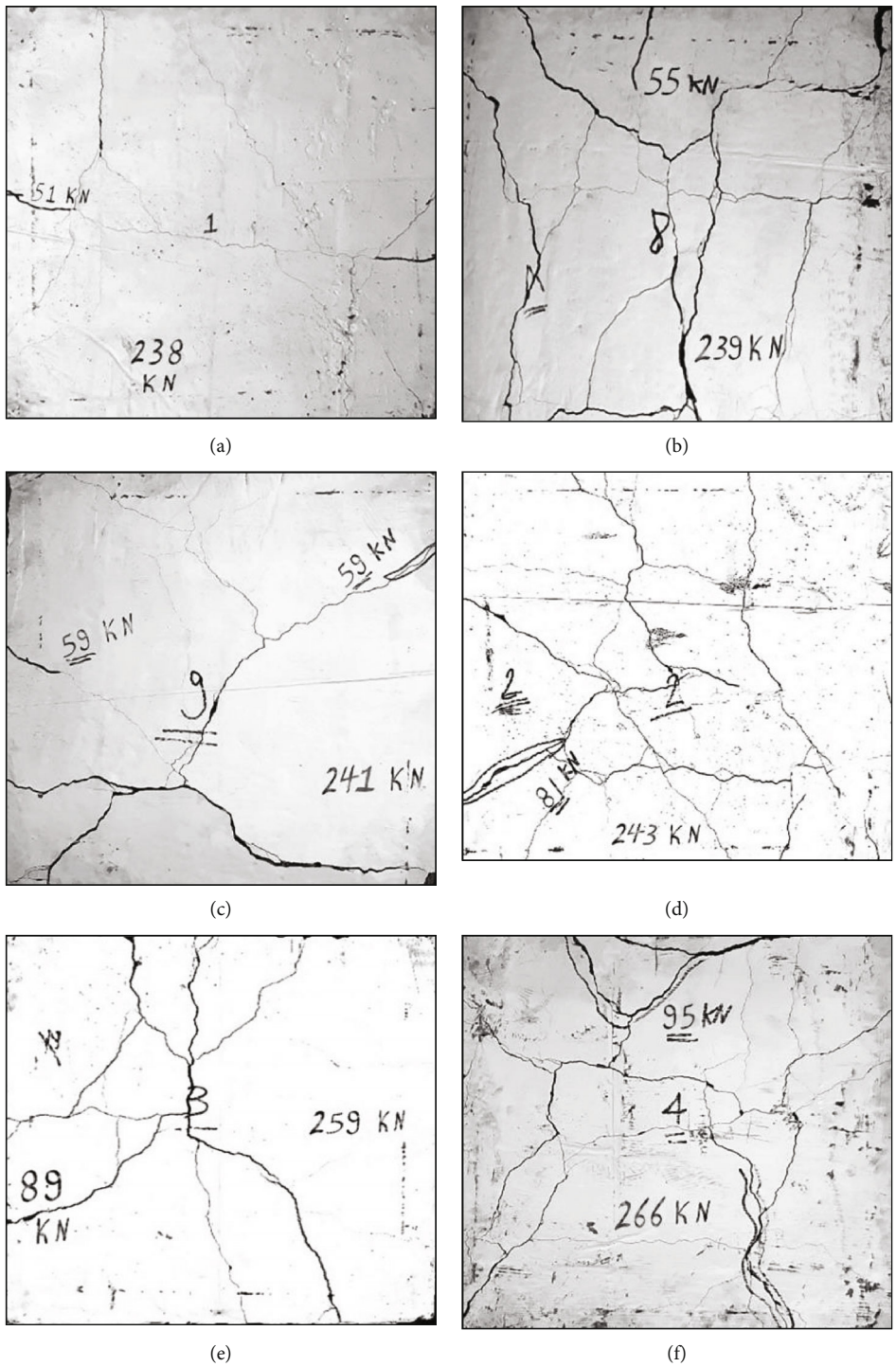

Figure 9: Continued.

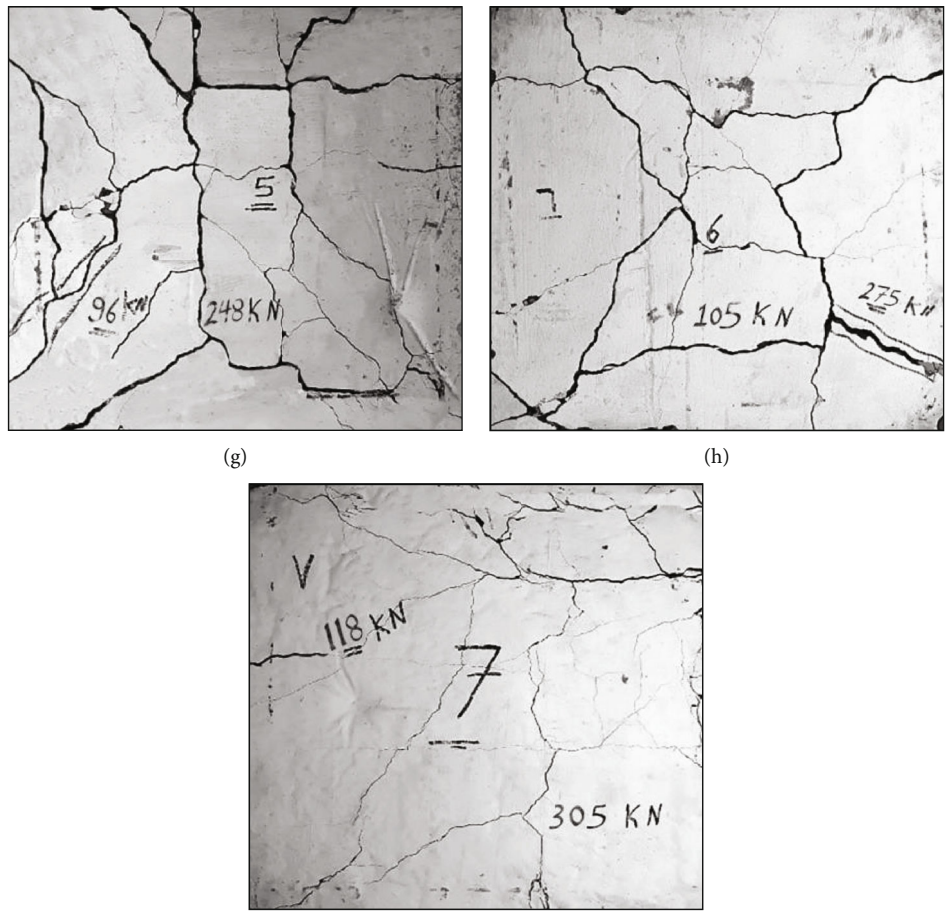

(g) (h)

(i)

Figure 9: Crack patterns for all test specimens.

(i) Substituting 5% and 10% of cement with microsilica significantly increases bending resistance in both the cracking and failure phases

(ii) Substituting 0.5% and 1.0% cement with nanosilica (in the absence of microsilica) shows good improvement in bending strength of 7.8 and 15.7% in the crushing stage and slight improvement in bending strength of 0.42 and 1.26% in the failure stage, respectively

(iii) Replacing a portion of cement by a combination of nanosilica and 5% microsilica reveals an enhanced improvement in flexural strength of 9.9 and 17.3% at the cracking state and 6.6 and 9.5% at the failure state of 0.5% and 1.0% nanosilica, respectively

(iv) Replacing a portion of cement by a combination of nanosilica and 10% microsilica reveals an enhanced improvement in flexural strength of 9.4 and 22.9% at the cracking state and 10.9 and 23.0% at the failure state of 0.5% and 1.0% nanosilica, respectively

(v) Reinforced slabs with 10% microsilica and 1.0% of nanosilica replacement of cement show a superior performance indicated by the load deflection curve where higher loads are achieved at lower deflections. Hence, the concrete matrix can resist higher compressive strength above the neutral axis by 30.6 MPa and 40.7 MPa at 7 and 28 days, respectively, which considerably affects its flexural capacity, where the flexural strength of the slab increased by 131.2% at the cracking state and 28.2% at the failure state as compared to that of the control slab

(vi) Addition of mineral admixtures of either micro- or nanosilica or a combination of both affects the crack pattern of the slab where cracks are less in number and get wider at failure which occurs at a much higher load due to the better performance of the concrete compression zone

Data Availability

The data used to support the findings of this study are included within the article. Should further data or information be required, these are available from the corresponding author upon request.

Disclosure

It was performed as a part of the employment in Kombolcha Institute of Technology, Wollo University, Kombolcha, Amhara, Ethiopia.

Conflicts of Interest

The authors declare that there are no conflicts of interest regarding the publication of this paper.

Acknowledgments

The authors thank Vignan's Nirula Institute of Technology and Science for Women for providing characterization support to complete this research work.

References

[1] T. Ji, "Preliminary study on the water permeability and microstructure of concrete incorporating nano-SiO_2," *Cement and Concrete Research*, vol. 35, no. 10, pp. 1943–1947, 2005.

[2] N. D. K. R. Chukka, L. Natrayan, and W. D. Mammo, "Seismic fragility and life cycle cost analysis of reinforced concrete structures with a hybrid damper," *Advances in Civil Engineering*, vol. 2021, Article ID 4195161, 17 pages, 2021.

[3] A. Nazari, S. Riahi, S. Riahi, F. Shamekhi, and A. Khademno, "Embedded ZrO2 nanoparticles mechanical properties monitoring in cementitious composites," *Journal of American Science*, vol. 6, pp. 86–89, 2010.

[4] M. Aly, M. S. J. Hashmi, A. G. Olabi, M. Messeiry, E. F. Abadir, and A. I. Hussain, "Effect of colloidal nano-silica on the mechanical and physical behaviour of waste-glass cement mortar," *Materials and Design*, vol. 33, pp. 127–135, 2012.

[5] V. Paranthaman, K. Shanmuga Sundaram, and L. Natrayan, "Effect of silica content on mechanical and microstructure behaviour of resistance spot welded advanced automotive TRIP steels," *Silicon*, vol. 1, pp. 1–10, 2021.

[6] P. Hou, K. Wang, J. Qian, S. Kawashima, D. Kong, and S. P. Shah, "Effects of colloidal nanoSiO_2 on fly ash hydration," *Cement and Concrete Composites*, vol. 34, no. 10, pp. 1095–1103, 2012.

[7] Z. Rong, W. Sun, H. Xiao, and G. Jiang, "Effects of nano-SiO_2 particles on the mechanical and microstructural properties of ultra-high performance cementitious composites," *Cement and Concrete Composites*, vol. 56, pp. 25–31, 2015.

[8] L. P. Singh, S. R. Karade, S. K. Bhattacharyya, M. M. Yousuf, and S. Ahalawat, "Beneficial role of nanosilica in cement based materials - a review," *Construction and Building Materials*, vol. 47, pp. 1069–1077, 2013.

[9] R. Suryanarayanan, V. G. Sridhar, L. Natrayan et al., "Improvement on mechanical properties of submerged friction stir joining of dissimilar tailor welded aluminum blanks," *Advances in Materials Science and Engineering*, vol. 2021, Article ID 3355692, 6 pages, 2021.

[10] G. Quercia and H. J. H. Brouwers, *Application of nano silica (NS) in concrete mixtures*, The 8th Fib PhD Symposium in Kgs, Lyngby, Denmark, 2010.

[11] A. M. Mohamed, "Influence of nano materials on flexural behavior and compressive strength of concrete," *HBRC Journal*, vol. 12, no. 2, pp. 212–225, 2016.

[12] A. Nazari, S. Riahi, S. Riahi, S. F. Shamekhi, and A. Khademno, "Improvement of the mechanical properties of the cementitious composites by using TiO_2 nanoparticles," *Journal of American Science*, vol. 6, pp. 98–101, 2010.

[13] A. Nazari, S. Riahi, S. Riahi, F. Shamekhi, and A. Khademno, "Mechanical properties of cement mortar with Al_2O_3 nanoparticles," *Journal of American Science*, vol. 6, pp. 94–97, 2010.

[14] A. Naji Givi, S. Abdul Rashid, F. N. A. Aziz, and M. A. M. Salleh, "Experimental investigation of the size effects of SiO_2 nano-particles on the mechanical properties of binary blended concrete," *Composites B*, vol. 41, no. 8, pp. 673–677, 2010.

[15] M. Berra, F. Carassiti, T. Mangialardi, A. E. Paolini, and M. Sebastiani, "Effects of nanosilica addition on workability and compressive strength of Portland cement pastes," *Construction and Building Materials*, vol. 35, pp. 666–675, 2012.

[16] K. L. Lin, W. C. Chang, D. F. Lin, H. L. Luo, and M. C. Tsai, "Effects of nano-SiO_2 and different ash particle sizes on sludge ash-cement mortar," *Journal of Environmental Management*, vol. 88, no. 4, pp. 708–714, 2008.

[17] L. Senff, J. A. Labrincha, V. M. Ferreira, D. Hotza, and W. L. Repette, "Effect of nano-silica on rheology and fresh properties of cement pastes and mortars," *Construction and Building Materials*, vol. 23, no. 7, pp. 2487–2491, 2009.

[18] A. M. Said, M. S. Zeidan, M. T. Bassuoni, and Y. Tian, "Properties of concrete incorporating nano-silica," *Construction and Building Materials*, vol. 36, pp. 838–844, 2012.

[19] N. Chahal and R. Siddique, "Permeation properties of concrete made with fly ash and silica fume: influence of ureolytic bacteria," *Construction and Building Materials*, vol. 49, pp. 161–174, 2013.

[20] A. A. I.-M. Shakir, A. M. Ibraham, and Z. H. Naji, "The effect of nano metakaolin materials on some properties of concrete," *Diyala Journal of Engineering Sciences*, vol. 6, pp. 50–61, 2013.

[21] G. Dhinakaran, A. Rajasekharareddy, B. Kartikeyan, K. Sumanth, and G. Harshavardhan, "Microstructure analysis and strength properties of concrete with nano SiO2," *International Journal of ChemTech Research*, vol. 6, pp. 3004–3013, 2014.

[22] M. Gesoglu, E. Güneyisi, D. S. Asaad, and G. F. Muhyaddin, "Properties of low binder ultra-high performance cementitious composites: comparison of nanosilica and microsilica," *Construction and Building Materials*, vol. 102, pp. 706–713, 2016.

[23] M. Jung, Y. S. Lee, and S. G. Hong, "Study on improvement in electromagnetic interference shielding effectiveness of ultra-high-performance concrete (UHPC)/carbon nanotube (CNT) composites," *Journal of the Korea Concrete Institute*, vol. 31, no. 1, pp. 69–77, 2019.

[24] M. Jalal, A. Pouladkhan, O. F. Harandi, and D. Jafari, "RETRACTED: Comparative study on effects of Class F fly ash, nano silica and silica fume on properties of high performance self compacting concrete," *Construction and Building Materials*, vol. 94, pp. 90–104, 2015.

[25] K. Hemalatha, C. James, L. Natrayan, and V. Swamynadh, "Analysis of RCC T-beam and prestressed concrete box girder bridges super structure under different span conditions," *Materials Today: Proceedings*, vol. 37, no. 2, pp. 1507–1516, 2021.

[26] K. M. Lakshmi, M. K. M. V. Ratnam, and U. Rangaraju, "Experimental study on light weight aggregate concrete with pumice stone, silica fume and fly ash as a partial replacement of coarse aggregate," *International Journal of Innovative Research in Science, Engineering and Technology*, vol. 3, no. 12, 2014An ISO 3297: 2007 CertifiedOrganization.

[27] K. Anusha and S. Kesavan, "A study on behavior of ultra-high strength concrete at elevated temperatures," *International*

Journal of Engineering Sciences & Emerging Technologies, vol. 7, no. 5, pp. 761–765, 2015.

[28] N. Atmaca, M. L. Abbas, and A. Atmaca, "Effects of nano-silica on the gas permeability, durability and mechanical properties of high-strength lightweight concrete," *Construction and Building Materials*, vol. 147, pp. 17–26, 2017.

[29] D. HajizadehAsl, "Application of nano-silica in concrete to improve its mechanical properties and durability: a review," *International Journal of Recent Scientific Research*, vol. 7, pp. 12251–12254, 2016.

[30] R. A. Narender and T. Meena, "Study on effect of colloidal nanosilica blended concrete under compression," *International Journal of Engineering & Technology*, vol. 7, pp. 210–213, 2018.

[31] S. Yogeshwaran, L. Natrayan, S. Rajaraman, S. Parthasarathi, and S. Nestro, "Experimental investigation on mechanical properties of epoxy/graphene/fish scale and fermented spinach hybrid bio composite by hand lay-up technique," *Materials Today: Proceedings*, vol. 37, no. 2, pp. 1578–1583, 2021.

[32] R. A. Narender and T. Meena, "A Comprehensive Overview on Performance of Nano Silica Concrete," *International Journal of pharmacy &Technology*, vol. 9, pp. 5518–5529, 2017.

[33] M. Sandeep Kauthsa Sharma, S. Umadevi, Y. Sai Sampath et al., "Mechanical behavior of silica fume concrete filled with steel tubular composite column," *Advances in Materials Science and Engineering*, vol. 2021, Article ID 3632991, 9 pages, 2021.

[34] R. A. Narender and T. Meena, "A study on compressive behavior of ternary blended concrete," *Materials Today: Proceedings*, vol. 5, pp. 11356–11363, 2018.

[35] Z. Wu, C. Shi, K. H. Khayat, and S. Wan, "Effects of different nanomaterials on hardening and performance of ultra-high strength concrete (UHSC)," *Cement and Concrete Composites*, vol. 70, pp. 24–34, 2016.

[36] L. P. Singh, S. K. Bhattacharyya, S. P. Shah, G. Mishra, S. Ahalawat, and U. Sharma, "Studies on early stage hydration of tricalcium silicate incorporating silica nanoparticles: part I," *Construction and Building Materials*, vol. 74, pp. 278–286, 2015.

[37] S. Yogeshwaran, L. Natrayan, G. Udhayakumar, G. Godwin, and L. Yuvaraj, "Effect of waste tyre particles reinforcement on mechanical properties of jute and abaca fiber-epoxy hybrid composites with pre-treatment," *Materials Today: Proceedings*, vol. 37, no. 2, pp. 1377–1380, 2021.

[38] J. Björnström, A. Martinelli, L. Matic, and I. P. Börjesson, "Accelerating effects of colloidal nano-silica for beneficial calcium-silicate-hydrate formation in cement," *Chemical Physics Letters*, vol. 392, no. 1-3, pp. 242–248, 2004.

[39] Y. Qing, Z. Zenan, K. Deyu, and C. Rongshen, "Influence of nano-SiO_2 addition on properties of hardened cement paste as compared with silica fume," *Construction and Building Materials*, vol. 21, no. 3, pp. 539–545, 2007.

[40] M. Collepardi, J. J. O. Olagot, and U. Skarp, "Influence of amorphous colloidal silica on the properties of self-compacting concretes," in *Proceedings of the International Conference in Concrete Constructions–Innovations and Developments in Concrete Materials and Constructions*, pp. 473–483, Scotland, UK, 2002.

[41] H. Li, M. H. Zhang, and J. P. Ou, "Abrasion resistance of concrete containing nano-particles for pavement," *Wear*, vol. 260, no. 11-12, pp. 1262–1266, 2006.

[42] B. W. Jo, C. H. Kim, G. H. Tae, and J. B. Park, "Characteristics of cement mortar with nano-SiO_2 particles," *Construction and Building Materials*, vol. 21, no. 6, pp. 1351–1355, 2007.

[43] G. Li, "Properties of high-volume fly ash concrete incorporating nano- SiO_2," *Cement & Concrete Research*, vol. 34, no. 6, pp. 1043–1049, 2004.

Hindawi
Journal of Nanomaterials
Volume 2021, Article ID 8428822, 7 pages
https://doi.org/10.1155/2021/8428822

Research Article

Evaluating the Mechanical and Tribological Properties of DLC Nanocoated Aluminium 5051 Using RF Sputtering

L. Natrayan,[1] **Anjibabu Merneedi**,[2] **Dhinakaran Veeman**,[3] **S. Kaliappan**,[4] **P. Satyanarayana Raju**,[5] **Ram Subbiah**,[6] **and S. Venkatesh Kumar**[7]

[1]*Department of Mechanical Engineering, Saveetha School of Engineering, SIMATS, Chennai, Tamil Nadu 602105, India*
[2]*Department of Mechanical Engineering, Aditya College of Engineering, Surampalem, 533437 Andhra Pradesh, India*
[3]*Centre for Additive Manufacturing, Chennai Institute of Technology, 600069, Chennai, India*
[4]*Department of Mechanical Engineering, Velammal Institute of Technology, Chennai, 601204 Tamil Nadu, India*
[5]*Department of Mechanical Engineering, Vardhaman College of Engineering, Kacharam, Shamshabad, Hyderabad, 501218 Telangana, India*
[6]*Department of Mechanical Engineering, Gokaraju Rangaraju Institute of Engineering and Technology, Hyderabad, India*
[7]*Department of Mechanical Engineering, College of Engineering and Technology, Mettu University, Ethiopia P.O. Box: 318*

Correspondence should be addressed to L. Natrayan; natrayanphd@gmail.com
and S. Venkatesh Kumar; s.venkateshkumar@meu.edu.et

Received 3 September 2021; Revised 15 October 2021; Accepted 28 October 2021; Published 8 November 2021

Academic Editor: Lakshmipathy R

Copyright © 2021 L. Natrayan et al. This is an open access article distributed under the Creative Commons Attribution License, which permits unrestricted use, distribution, and reproduction in any medium, provided the original work is properly cited.

The diamond-like carbon- (DLC-) coating technique is used in the sliding parts of automotive engines, among other applications, to reduce friction and wear. In this work, DLC has been coated on the Aluminium 5051 sample to assess the mechanical and tribological properties. A sputtering deposition mechanism is used, and the DLC is coated using a graphite target. The developed DLC coatings are tested for adhesion strength, hardness, chemical composition using XRD, and wear behaviour. The developed DLC thin films have considerably increased the wear behaviour of the Aluminium 5051 sample and have fulfilled the objective of this study. The XRD data indicated the presence of amorphous carbon in the coating with a threefold increase to the hardness of the naked aluminium. This study provides insight into improving the aluminium wear resistance by developing a considerably hard coating.

1. Introduction

In today's machinery sector, surface engineering is critical. Hard coatings extend the service life of tools and moulds, yet hard coatings are difficult to apply to machine parts built of soft materials such as aluminium [1]. Thin films with high hardness can bear higher loads, but as the substrate is a soft material, the substrate fails the coating and the thin film too shall fail [2]. Surfaces take up a very little area in a matter when compared to the bulk. Still, they are extremely difficult to investigate [3] due to the very asymmetric nature of the forces acting on the surfaces. Pristine surfaces are highly susceptible to impurities and flaws. When two extremely pure surfaces come into contact, adhesive force is created, and energy is used to separate those surfaces [4]. Adhesion energy is the energy exerted by atoms on the outer surfaces of nearby atoms when they come into contact with each other [5]. A simple van der Waal, covalent, ionic, or electrostatic force can be used as adhesive forces [6]. Cohesive forces hold atoms together in bulk materials. Atoms are held together by a cohesive force, and it takes a lot of force to rip a substance in half [7]. The breaking of cohesive links between atoms causes the metal to tear. The atoms with broken cohesive bonds on the new surfaces generated after breaking the parent material will be readily attracted to the new atoms [8]. Surface energy is the excess free energy per unit area on a crystal's surface. It is denoted by and plays a crucial role in thin-film adherence to the substrate. Surface tension

values of liquid metals can be extrapolated to absolute zero, or crystal cleavage can be used to compute this [9]. Other than the actual approaches, there are several theoretical ways to calculate surface energy. There are disparities between practical and theoretical values, and no theoretical value equates to a practical value. The presence of numerous faults and impurities in a chosen crystal is the primary source of this mismatch, and obtaining a crystal-free of defects or impurities is difficult [10]. Bazan et al. concluded that the CF-reinforced epoxy composites exhibit 14% reduction in ILSS, when the samples are aged hydrothermally at 60°C and at 95% humidity for 1200 hours, and this is due to the crack initiation at the interface which is caused by thermal stress [11]. Shrivastava and Singh concluded that the UD and BD CF-reinforced epoxy composites exhibit 20%and 75% increase in flexural strength, respectively, due to the growth of CNTs on the surface thereby resulting in good adhesion with the matrix [12]. An et al. found that the CF-reinforced epoxy composites with CNTs grown by an aerosol-assisted CVD process exhibit 94% increase in IFSS and 210% increase in surface area because of the formation of the 3D structure on the surface of the fiber, and also, the fiber diameter is increased from 7 micrometres to 20 micrometres [13].

In general, adhesion can be attributed to the sticking of two surfaces with each other. Technically, adhesion is defined as the transfer of mechanical energy in shear between two surfaces without any damage to the surfaces or the interface by a slip or inelastic displacement [14]. The most difficult aspect of thin-film adhesion is determining the strength of the adhesion between the thin film and the substrate. Even though numerous approaches have been created, it is critical to select the appropriate process based on the nature of the coating, substrate, and type of bonding between the two [15]. There is a wealth of information for thin-film adhesion on the many types and adhesion measurement methods. Simple pull tests, scratch tests, X-ray spectroscopy, nanoindentation scratch, and laser spallation are among the methods used. According to Tamtögl et al., theoretical approaches measure theoretical forces at the atomic level [16]. The observations include the nucleation rate, island density measurement, critical condensation, and residence time of depositing atoms. Adhesion between substrate and coating can be viewed on an atomic scale as adsorption energy between substrate surface atoms and coating atoms. Breaking the links between these atoms suffices to remove the coating from the substrate [17]. So, by measuring the total adsorption energy between atoms and relating it to all atoms, these approaches measure the total adsorption energy present between atoms to break the bond. A smooth round stylus is drawn on a hard-coated sample in a scratch test by gradually increasing the load. When the coating breaks and peels away from the substrate, the stylus is halted and the critical load recorded [18]. Even though it appears like a simple compression force applied by the stylus and the substrate is separating the coating, many complex forces are at work in this test. The load causes plastic deformation of the substrate, while the stylus penetrates the coating and causes shear strain. This process increases thermomechanical reactions with the viscoelastic flow, interfacial failure, and bulk fracture [19]. Scratch tests are difficult to test to study as a result of this. A direct tensile force is imparted to the film by pulling it off the substrate with a pin or rod attached in the usual direction. This approach can be used to attach thin films, as well as other sticky surfaces and objects. The failure that occurs at the substrate-thin-film contact is referred to as adhesion force [20].

Butler invented the toppling test by modifying the direct pulling method. Instead of using the conventional force, he used a brass rod with two legs to impart force laterally to the thin sheet. When a load is applied, one leg applies compressive force while the other exerts tensile force, causing the film to peel. Karapappas et al. observed that the CF-reinforced epoxy composites incorporated with 0.1% CNT exhibit reduced mechanical properties and 1% incorporation of CNT leads to enhancement of fracture energy by 45 to 75% [21]. Konuru et al. reported that the CF-reinforced epoxy composites exhibit incremental IFSS by 70 to 200%, depending on CNT deposition time on the CF surface [22]. Yogeshwaran et al. found that the CF-reinforced epoxy composites with CNTs grown on the surface possess 150 to 300% increased toughness due to different aspect ratios of the CNT [23]. Surface modification of many metals is done with DLC (diamond-like carbon) thin film. These thin films have good wear resistance along with corrosion resistance and hardness. DLC films are amorphous carbon materials containing sp^3 and sp^2 bonds that are metastable. DLC films have received much attention among all surface treatment materials because of their exceptional tribological properties. The DLC film is increasingly being used as a protective layer. It is associated with the percentage of sp3 bonds in the films, and for example, it has a low coefficient of friction and good wear resistance. On the other hand, it is critical to reducing the friction and wear of the inner wall surface of many industrial components with undetectable holes, such as dies, bushings, and pipes, as a type of industrial application. DLC has high mechanical properties like high wear resistance and low friction, which are highly desirable for industrial applications. DLC nanocoated Aluminium 5051 is mainly used to reduce the sliding friction of moving parts.

Novel in the research work is that DLC has been coated on the Aluminium 5051 sample to assess the mechanical and tribological properties. A sputtering deposition mechanism technique is used in this research work. The developed DLC coatings were tested for adhesion strength, hardness, chemical composition using XRD, and wear behaviour.

2. Methodology

The RF sputtering procedure was used to place graphite targets on aluminium. Graphite targets with a purity of 99.99%, a diameter of 50 mm, and a thickness of 3.0 mm were procured from Testbourne and utilized for the current study. Figure 1 depicts a schematic design of the experimental system. The magnetron on which the target material to be coated is placed is connected to the RF power supply through an impedance matching network. The magnetron serves as an electrode, and the entire chamber is grounded.

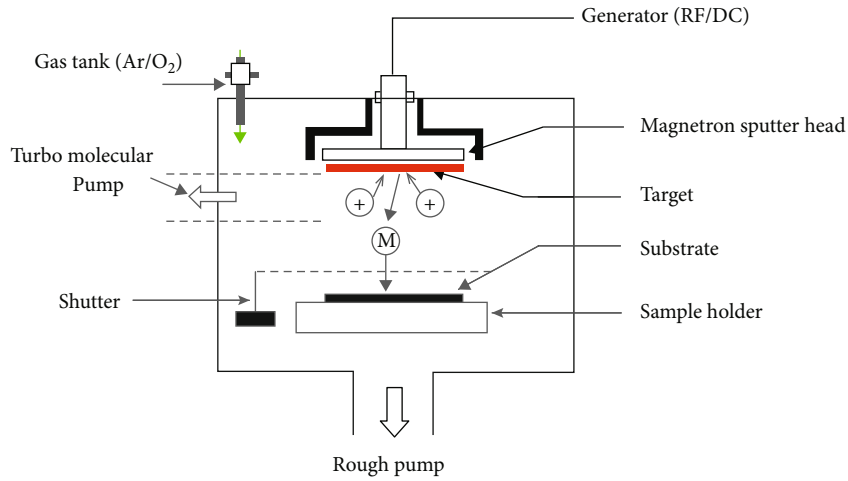

Figure 1: Schematic representation of sputtering machine.

Figure 2: Aluminium 5051 plate ($10 \times 20 \times 3$ mm).

Table 1: Measured hardness values of samples deposited at room temperature along with modulus values.

Sample	100 W	200 W	300 W	400 W
Hardness (GPa)	10.6	13.5	18.2	12.3
Modulus (GPa)	51.3	70.2	120	68.1

Table 2: Measured hardness values of samples deposited at 500 degrees along with modulus values.

Sample	100 W	200 W	300 W	400 W
Hardness (GPa)	15.1	20.8	22.5	20.1
Modulus (GPa)	76.2	111.2	130.5	100.6

In this experiment, the sputtering power was changed in stages of 100 W from 100 to 400 W.

Aluminium is cut into $10 \times 20 \times 3$ mm substrates and ground to a high level of precision of order 0.5 m using various grades of abrasive papers and diamond polish. Aluminium 5051 plates are shown in Figure 2. With acetone solution, aluminium samples are cleaned and etched in Ar plasma for 10 minutes before sputtering. Working pressure is maintained at 10^{-2} bar in the vacuum chamber and used for the turbopump. The temperature of the substrate is monitored and can be adjusted manually by the substrate holder. For the temperature-dependent adhesion qualities, two different substrate temperatures were used: room temperature and 500 degrees. A total thickness of the film 1200 nm is achieved for the DLC thin films.

The nanoindentation procedure is used to measure the hardness and elastic modulus. At a specified temperature and working pressure, samples are mounted on resin for stabilization. The nanoindentation machine with model G200 from Agilent Technologies is utilized for Berkovich indenter indentations in nanoindentation operations. A scratch test is done on the samples for estimating the adhesion of the developed DLC coatings. The same machine used for nanoindentation is used for the scratch analysis with the Berkovich indenter. Load is gradually increased to identify the critical load at which the DLC coating peels off. This load is taken as the ultimate load and is considered as adhesion strength of the film.

The pin on disk is carried out to find the wear and friction of the samples; the pin is the aluminium sample without any coating, and the disk is aluminium coated with DLC. XRD analysis is done on the DLC samples to find the chemical composition of the coating. A load of 100 gm is used for the test, and a total of 500 is carried out.

3. Results and Discussion

3.1. Hardness. Tables 1 and 2 show the hardness and modulus values of the developed thin films measured by nanoindentation by the load vs. deflection method. The Berkovich indenter was used to apply a load in the micronewton range.

The hardness of the coated hard thin films is hard to measure as the soft substrate takes away all the load, so an underreported value is measured. It is difficult to detect the hardness and elastic modulus of the coating using regular indentation. The substrate effect is unavoidable in this scenario, regardless of whether the 10% thickness criterion is implemented. The soft substrate cushioned the rigid thin-film coating. The DLC coating is extremely rigid, and it directly applies the load to the substrate. When a load is applied, elastic deformation occurs on the substrate, and the hardness under the load is measured. As a result, the

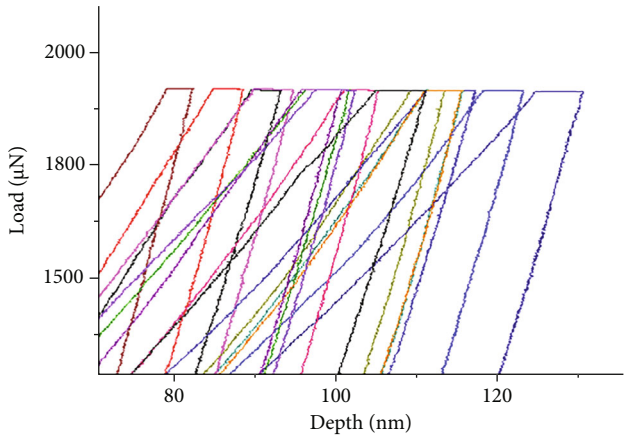

Figure 3: Load vs. displacement curves developed by nanoindentation data.

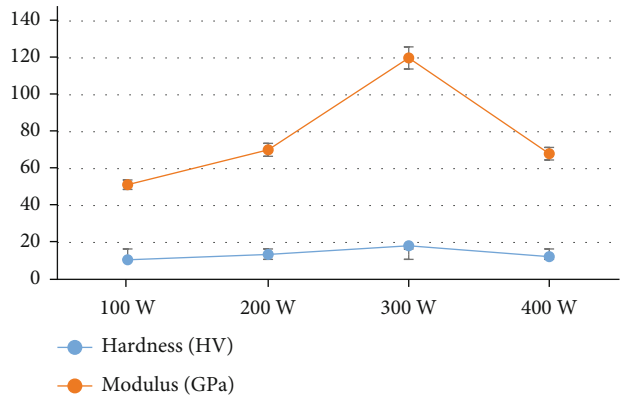

Figure 4: Hardness and modulus values of samples deposited at room temperature.

findings achieved in this situation are the coating and substrate's combined hardness, which considerably reduced the coating's ensuing qualities. On each sample, many trials were conducted, and the average hardness and modulus of elasticity were computed. The area is calculated when the load is withdrawn to identify the sample's exact hardness. At the maximum load, all trials were assigned a holding time of 15.0 seconds.

The hardness of the samples is calculated, and the highest hardness is measured for samples deposited at higher substrate temperature conditions. For the samples deposited at room temperature conditions, the hardness is less compared to other samples. As the deposition power increases from 100 W to 400 W, the hardness increases up to 300 W. It decreases for 400 W. This trend is observed for both room temperature and high-temperature deposition conditions [24]. The highest hardness increment found for the room temperature deposition condition is 71%, as the sputtering power is increased from 100 W to 300 W. In contrast, the hardness increment is 42% when the deposition power is increased from 100 W to 300 W. Figure 3 shows the load vs. displacement diagram achieved using nanoindentation data. Figures 4 and 5 represent hardness and modulus data of samples in graphical form.

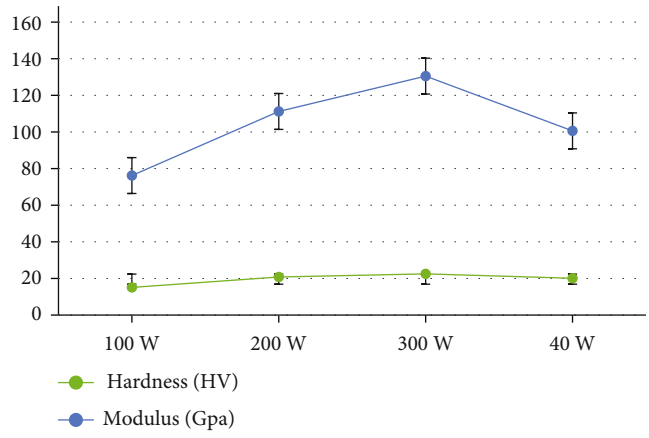

Figure 5: Hardness and modulus values of samples deposited at 500 degrees.

Table 3: Adhesion strength of DLC films.

Sample	Room temperature	500-degree heat
100 W	35.2	41.2
200 W	38.9	45.6
300 W	42.3	49.1
400 W	32.1	33.5

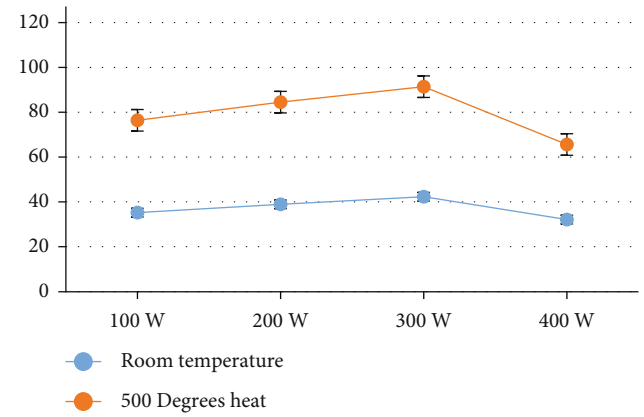

Figure 6: Adhesion strength of DLC films.

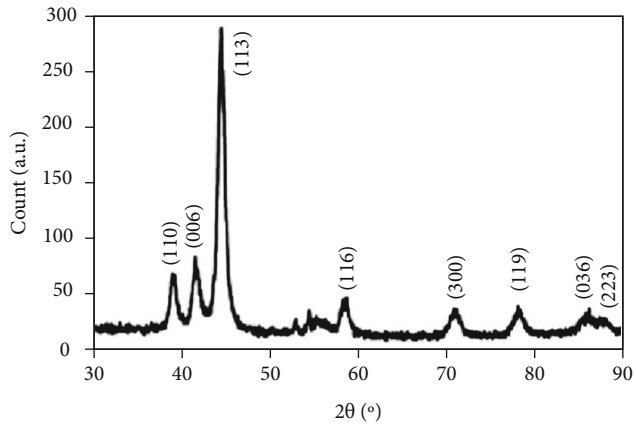

Figure 7: XRD graph of DLC coating.

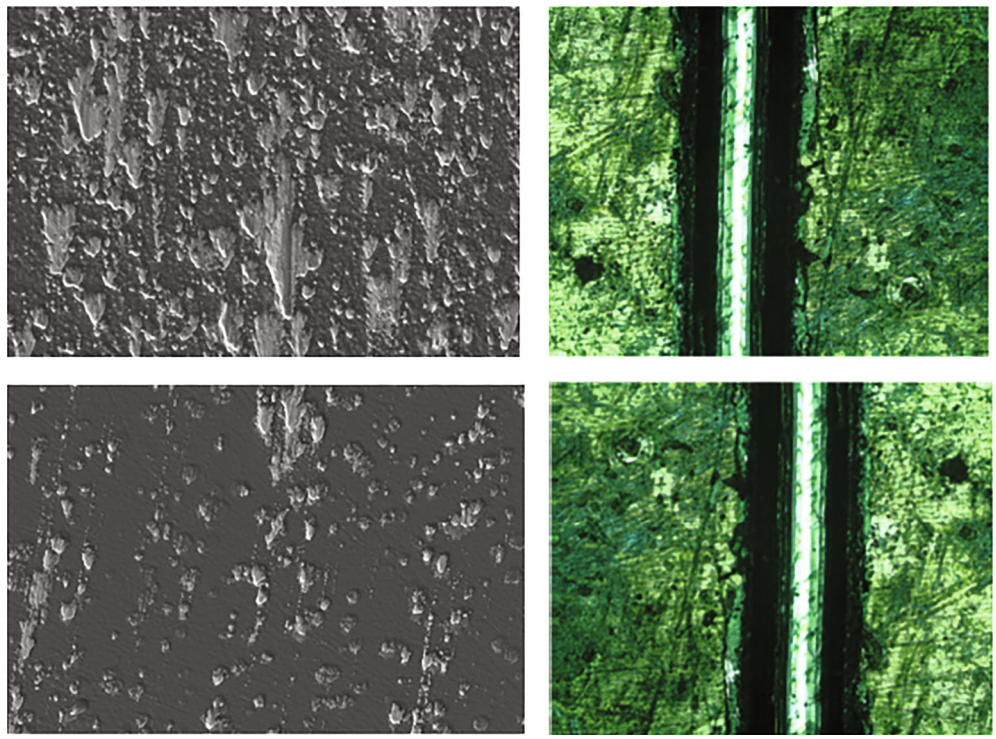

Figure 8: Wear track of DLC coating.

3.2. Adhesion Strength. The adhesion strength of the DLC films is measured by using a nanoscratch test. The values of the results obtained are given in Table 3. The adhesion strength of the samples increases with the increment in the substrate power up to 300 W. From 300 W to 400 W, the adhesion strength is found to decrease drastically [25]. This trend is observed for both room temperature deposited and high temperature deposited samples. The decrement in the adhesion can be attributed to the high stresses developed in the film deposition process when the sputtering power increases.

As the power increases, the depositing atoms come with higher energy and strikes the depositing material; this causes stress at the atom strike site. Before these stresses dissipate, other atoms get deposited on top of it causing stress concentration [26]. The adhesion strength is higher for the samples deposited at higher temperatures than the room temperature deposition samples. The reason for the higher adhesion is the stress-relieving phenomena taking place during the substrate heating process [27]. The substrate temperature acts as annealing during the deposition process and relieves stress, thus increasing the adhesion strength. The graphical representation of the adhesion strength is given in Figure 6.

3.3. XRD Analysis. The XRD analysis shows the presence of amorphous carbon in the DLC coating. The XRD graph is presented in Figure 7. The sample is kept in an XRD machine and swept from 20° to 90° angles for analysis [28]. There are no other peaks other than carbon, and the detected carbon is in amorphous graphite without crystalline diamond form. It indicates there are sp^2 bonds in the developed films but not sp^3, which helps in a further increase in the hardness of the film [29].

3.4. Wear Test. The coating samples were put through a dry wear test in a pin-on-disk mode with an aluminium pin as the counter body. Figure 8 shows the wear track of the DLC coating. The samples' coefficients of friction (COF) range from 0.10 to 0.15. The COF of the high temperature-DLC sample is marginally greater than the COF of the room temperature-DLC sample at the same test load [30]. The COF curves of the SNC-DLC sample have some variations. During the test, it appears that this sample suffers from abrasion wear. Despite this, the COF for both coating samples (COF0.15) is very low [31].

3.5. Raman Spectroscopy. Raman spectroscopy is a common technique for identifying diamonds, graphite, and other carbon-based materials. The Raman spectra have two large peaks for amorphous carbon: 1200–1450 cm^{-1} for the D mode and 1500–1700 cm^{-1} for the G mode. The G band is attributed to sp^2 graphite-like microdomain graphite-like layers, whereas the D band is attributed to the bond-angle disorder in the sp^2 graphite-like microdomains.

The tested sample which is used for XRD has been tested for the Raman spectroscopy. The sample showed the presence of sp^2 bonds majorly in the DLC and the traces of sp^3. The Raman spectra in Figure 9 shows two broad peaks centred around 1348 cm^{-1} (D-line) and 1600 cm^{-1} (G-line). The peak about 1600 cm^{-1} could be noticeably different from the crystalline graphite's characteristic sharp peak around 1580 cm^{-1}. It demonstrates that the film is a normal DLC film with a combination of sp^2 and sp^3 carbon structures.

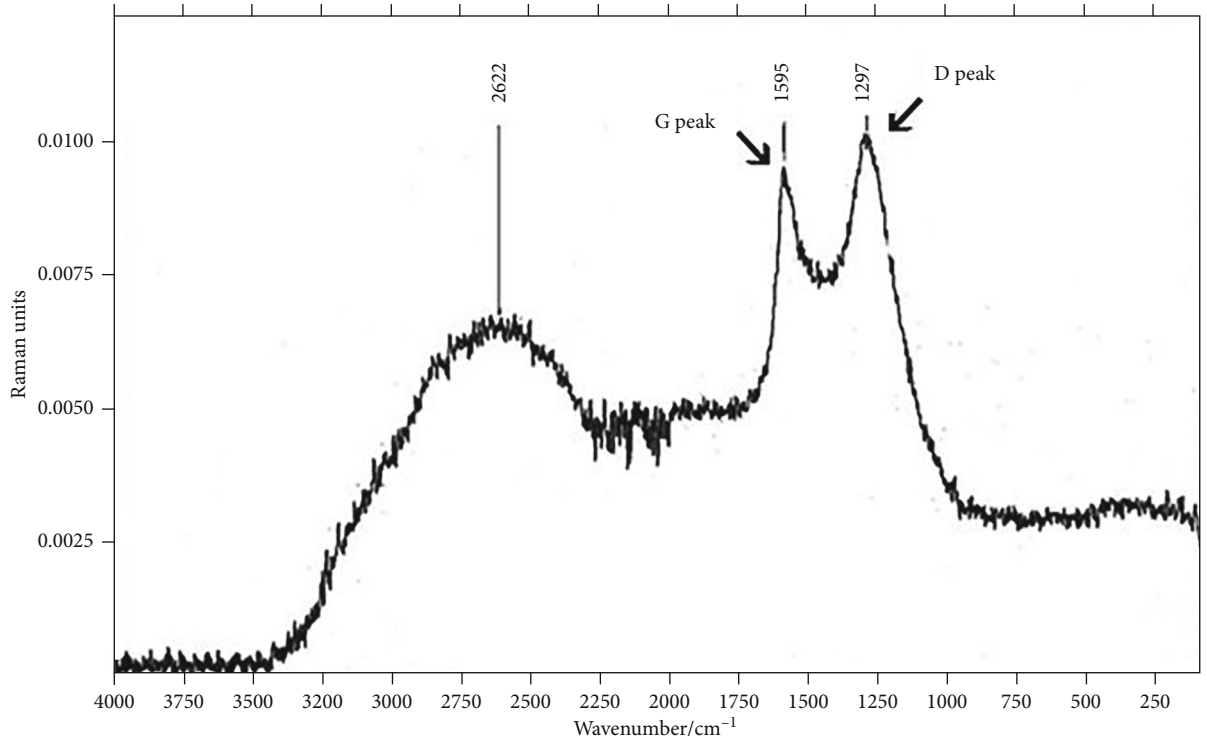

Figure 9: Raman spectra of DLC film.

4. Conclusion

The DLC thin films have been successfully developed on the Aluminium 5051 samples by the sputtering deposition method. The substrate heating during the deposition process plays a crucial role in the adhesion of the film and its hardness. By changing the sputtering deposition power, the films' hardness and adhesion can be tailor-made. A total hardness increment of 71% can be achieved by changing the sputtering power in the deposition. By incorporating substrate heat and 300 W power, the highest hardness can be achieved for the given aluminium DLC thin film. The adhesion is also influenced by the substrate temperature as well as power, and the highest adhesion strength can be achieved for substrate heating and 300 W power DLC thin film. XRD and Raman spectroscopy indicated the presence of amorphous graphite in the DLC films rather than the crystal diamond form and is mainly due to the formation of sp^2 bonds in the DLC rather than sp^3 bonds.

Data Availability

The data used to support the findings of this study are included in the article. Should further data or information be required, these are available from the corresponding author upon request.

Disclosure

This study was performed as a part of the Employment of the College of Engineering and Technology, Mettu University, Ethiopia.

Conflicts of Interest

The authors declare that there are no conflicts of interest regarding the publication of this paper.

Acknowledgments

The authors thank Saveetha School of Engineering, SIMATS, Chennai, for providing characterization support to complete this research work.

References

[1] M. Aamir, K. Giasin, M. Tolouei-Rad, and A. Vafadar, "A review: drilling performance and hole quality of aluminium alloys for aerospace applications," *Journal of Materials Research and Technology*, vol. 9, no. 6, pp. 12484–12500, 2020.

[2] L. Patnaik, S. R. Maity, and S. Kumar, "Mechanical and tribological assessment of composite AlCrN or a-C:Ag-based thin films for implant application," *Ceramics International*, vol. 47, no. 5, pp. 6736–6752, 2021.

[3] L. H. Hu and Y. K. Wang, "Silicon carbonitride ceramic surface-modified nanoporous aluminum alloy by preceramic polysilazane precursor for surface strengthening," *Materials Science and Engineering: B*, vol. 267, article 115113, 2021.

[4] I. Suresh Kannan and A. Ghosh, "Anti-friction and wetting behavior of a new polymer composite coating towards aluminium and dry machining of AA2024 alloy by coated end mills," *Journal of Materials Processing Technology*, vol. 252, pp. 280–293, 2018.

[5] G. S. Goindi and P. Sarkar, "Dry machining: A step towards sustainable machining - Challenges and future directions," *Journal of Cleaner Production*, vol. 165, pp. 1557–1571, 2017.

[6] X. Wang, B. Zhang, Y. Qiao, and F. Sun, "Chemo-mechanical abrasive flow machining (CM-AFM): a novel high-efficient technique for polishing diamond thin coatings on inner hole surfaces," *Journal of Manufacturing Processes*, vol. 69, pp. 152–164, 2021.

[7] C. S. S. Anupama, L. Natrayan, E. Laxmi Lydia et al., "Deep learning with backtracking search optimization based skin lesion diagnosis model," *Computers, Materials & Continua*, vol. 70, no. 1, pp. 1297–1313, 2022.

[8] F. S. F. Ribeiro, J. C. Lopes, E. C. Bianchi, and L. E. de Angelo Sanchez, "Applications of texturization techniques on cutting tools surfaces—a survey," *International Journal of Advanced Manufacturing Technology*, vol. 109, no. 3–4, pp. 1117–1135, 2020.

[9] N. M. El Basiony, E. E. Badr, S. A. Baker, and A. S. El-Tabei, "Experimental and theoretical (DFT&MC) studies for the adsorption of the synthesized Gemini cationic surfactant based on hydrazide moiety as X-65 steel acid corrosion inhibitor," *Applied Surface Science*, vol. 539, article 148246, 2021.

[10] P. Sesták, M. Friák, D. Holec, M. Všianská, and M. Sob, "Strength and brittleness of interfaces in Fe-Al superalloy nanocomposites under multiaxial loading: an Ab initio and atomistic study," *Nanomaterials*, vol. 8, no. 11, p. 873, 2018.

[11] P. Bazan, P. Nosal, A. Wierzbicka-Miernik, and S. Kuciel, "A novel hybrid composites based on biopolyamide 10.10 with basalt/aramid fibers: mechanical and thermal investigation," *Composites Part B: Engineering*, vol. 223, p. 109125, 2021.

[12] R. Shrivastava and K. K. Singh, "Interlaminar fracture toughness characterization of laminated composites: a review," *Polymer Reviews*, vol. 60, no. 3, pp. 542–593, 2020.

[13] F. An, C. Lu, Y. Li et al., "Preparation and characterization of carbon nanotube-hybridized carbon fiber to reinforce epoxy composite," *Materials and Design*, vol. 33, no. 1, pp. 197–202, 2012.

[14] R. Chatzimichail, A. Christogerou, S. Bebelis, and P. Nikolopoulos, "Surface and grain boundary energies as well as surface mass transport in polycrystalline MgO," *Journal of Materials Engineering and Performance*, 2021.

[15] M. M. Shaban, A. M. Eid, R. K. Farag, N. A. Negm, A. A. Fadda, and M. A. Migahed, "Novel trimeric cationic pyrdinium surfactants as bi-functional corrosion inhibitors and antiscalants for API 5L X70 carbon steel against oilfield formation water," *Journal of Molecular Liquids*, vol. 305, article 112817, 2020.

[16] A. Tamtögl, E. Bahn, M. Sacchi et al., "Motion of water monomers reveals a kinetic barrier to ice nucleation on graphene," *Nature Communications*, vol. 12, no. 1, pp. 4–11, 2021.

[17] L. Natrayan and A. Merneedi, "Experimental investigation on wear behaviour of bio-waste reinforced fusion fiber composite laminate under various conditions," *Mater. Today Proc.*, vol. 37, Part 2, pp. 1486–1490, 2021.

[18] A. S. Mitko, D. R. Streltsov, P. V. Dmitryakov, A. A. Nesmelov, A. I. Buzin, and S. N. Chvalun, "Evolution of morphology in the process of growth of island poly(p-xylylene) films obtained by vapor deposition polymerization," *Polymer Science, Series A*, vol. 61, no. 5, pp. 555–564, 2019.

[19] B. von Boehn, C. Penschke, X. Li et al., "Reaction dynamics of metal/oxide catalysts: methanol oxidation at vanadium oxide films on Rh(1 1 1) from UHV to 10^{-2} mbar," *Journal of Catalysis*, vol. 385, pp. 255–264, 2020.

[20] M. Yang, Y. Liu, T. Fan, and D. Zhang, "Metal-graphene interfaces in epitaxial and bulk systems: a review," *Progress in Materials Science*, vol. 110, article 100652, 2020.

[21] P. Karapappas, A. Vavouliotis, P. Tsotra, V. Kostopoulos, and A. Paipetis, "Enhanced fracture properties of carbon reinforced composites by the addition of multi-wall carbon nanotubes," *Journal of Composite Materials*, vol. 43, no. 9, pp. 977–985, 2009.

[22] S. L. K. Konuru, V. Umasankar, B. Sarkar, and A. Sarma, "Microstructure and mechanical properties of tungsten and tungsten-tantalum thin film deposited RAFM steel," *Materials Research Innovations*, vol. 24, no. 2, pp. 97–103, 2020.

[23] S. Yogeshwaran, L. Natrayan, G. Udhayakumar, G. Godwin, and L. Yuvaraj, "Effect of waste tyre particles reinforcement on mechanical properties of jute and abaca fiber- epoxy hybrid composites with pre-treatment," *Materials Today: Proceedings*, vol. 37, Part 2, pp. 1377–1380, 2021.

[24] A. Salman, D. Catur, I. Made Septayana, and M. Dani Masterawan, "Tensile strength and bending analysis in producing composites by using vacuum resin infusion (VARI) method for high-voltage insulator application," in *2018 2nd International Conference on Applied Electromagnetic Technology (AEMT)*, pp. 39–43, Lombok, Indonesia, 2018.

[25] M. Wang, Z. Wang, X. Gong, and Z. Guo, "The intensification technologies to water electrolysis for hydrogen production - a review," *Renewable and Sustainable Energy Reviews*, vol. 29, pp. 573–588, 2014.

[26] M. B. Ali, R. Saidur, and M. S. Hossain, "A review on emission analysis in cement industries," *Renewable and Sustainable Energy Reviews*, vol. 15, no. 5, pp. 2252–2261, 2011.

[27] K. Aarthi and K. Arunachalam, "Durability studies on fibre reinforced self compacting concrete with sustainable wastes," *Journal of Cleaner Production*, vol. 174, pp. 247–255, 2018.

[28] Z. Yuan, F. Tao, J. Wen, and Y. Tu, "The dependence of microstructural evolution and corrosion resistance of a sandwich multi-layers brazing sheets on the homogenization annealing," *IEEE Access*, vol. 7, pp. 121388–121394, 2019.

[29] C. W. Tan, Z. G. Jiang, L. Q. Li, Y. B. Chen, and X. Y. Chen, "Microstructural evolution and mechanical properties of dissimilar Al-Cu joints produced by friction stir welding," *Materials and Design*, vol. 51, pp. 466–473, 2013.

[30] D. D. Gorhe, K. S. Raja, S. A. Namjoshi, V. Radmilovic, A. Tolly, and D. A. Jones, "Electrochemical methods to detect susceptibility of Ni-Cr-Mo-W alloy 22 to intergranular corrosion," *Metallurgical and Materials Transactions A, Physical Metallurgy and Materials Science*, vol. 36, no. 5, pp. 1153–1167, 2005.

[31] Q. Lin, W. Dong, Z. Wang, and D. Xue, "Research on galling behavior in square cup drawing of high tensile strength steel," in *2010 International Conference on Digital Manufacturing & Automation*, pp. 212–215, Changcha, China, 2010.

Hindawi
Journal of Nanomaterials
Volume 2021, Article ID 3383146, 8 pages
https://doi.org/10.1155/2021/3383146

Research Article

Nanotechnology-Based Sensitive Biosensors for COVID-19 Prediction Using Fuzzy Logic Control

Vikas Maheshwari,[1] Md Rashid Mahmood,[1] Sumukham Sravanthi,[2] N. Arivazhagan,[3] A. ParimalaGandhi,[4] K. Srihari,[5] R. Sagayaraj,[6] E. Udayakumar,[4] Yuvaraj Natarajan,[7] Prashant Bachanna,[8] and Venkatesa Prabhu Sundramurthy[9]

[1]*Dept. of ECE, Guru Nanak Institutions Technical Campus, Ibrahimpatnam, Dist R.R., Hyderabad Telangana State 501506, India*
[2]*Dept. of CSE, Kakatiya Institute of Technology and Science, Warangal, India*
[3]*Department of Computational Intelligence, SRM Institute of Science and Technology, SRM Nagar, Kattankulathur 603203, India*
[4]*Dept. of ECE, KIT-Kalaignarkarunanidhi Institute of Technology, Coimbatore, India*
[5]*CSE, SNSCT, India*
[6]*Department of EEE, Muthayammal Engineering College, Namakkal, India*
[7]*Research and Development, ICT Academy, 600096, Chennai, India*
[8]*Dept. of ECE, Bharat Institute of Engineering and Technology, Hyderabad, Telangan 501510, India*
[9]*Department of Chemical Engineering, Addis Abada Science and Technology University, Ethiopia*

Correspondence should be addressed to Venkatesa Prabhu Sundramurthy; venkatesa.prabhu@aastu.edu.et

Received 4 September 2021; Revised 22 September 2021; Accepted 7 October 2021; Published 3 November 2021

Academic Editor: Lakshmipathy R

Copyright © 2021 Vikas Maheshwari et al. This is an open access article distributed under the Creative Commons Attribution License, which permits unrestricted use, distribution, and reproduction in any medium, provided the original work is properly cited.

Increasing the growth of big data, particularly in healthcare-Internet of Things (IoT) and biomedical classes, tends to help patients by identifying the disease early through methods for the analysis of medical data. Hence, nanotechnology-based IOT biosensors play a significant role in the medical field. *Problem*. However, the consistency continues to decrease where missing data occurs in such medical data from nanotechnology-based IOT biosensors. Furthermore, each region has its own special features, which further lowers the accuracy of prediction. The proposed model initially reconstructs lost or partial data in order to address the challenge of handling the medical data structures with incomplete data. *Methods*. An adaptive architecture is proposed to enhance the computing capabilities to predict the disease automatically. The medical databases are managed by unpredictable environments. This optimized paradigm for diagnosis produces the fuzzy, genetically categorized decision tree algorithm. This work uses a normalized classifier namely fuzzy-based decision tree (FDT) algorithm for classifying the data collected via nanotechnology-based IOT biosensors, and this helps in the identification of nondeterministic instances from unstructured datasets relating to the medical diagnosis. The FDT algorithm is further enhanced by using genetic algorithms for effective classification of instances. Finally, the proposed system uses two larger datasets to verify the predictive precision. In order to describe a fuzzy decision tree algorithm based upon the fitness function value, a modified decision classification rule is used. The structure and unstructured databases are configured for processing. *Results and Conclusions*. This evaluation of test patterns helps to track the efficiency of FDT with optimized rules during the training and testing stages. The proposed method is validated against nanotechnology-based IOT biosensors data in terms of accuracy, sensitivity, specificity, and *F*-measure. The results of the simulation show that the proposed method achieves a higher rate of accuracy than the other methods. Other metrics relating to the model with and without feature selection show an improved sensitivity, specificity, and *F*-measure rate than the existing methods.

1. Introduction

As medical knowledge grows, the electronic health record (EHR) subsequently grows dramatically. The COVID-19 prediction has become a major factor in big data analytics as data increases in size. Classification algorithms were developed to improve medical diagnosis accuracy [1]. The classification method in big data analysis leads to the classification of datasets according to the diagnostic application with machine learning algorithms.

Efficient techniques are employed in large data analytics to find insights, correlations, and cached patterns from input data collected from the nanotechnology-based IoT biosensors. The data analytics provides improved decision-making, cost reductions, and development of new items to meet the customer requirements. Hence, it addresses the challenges of various applications, such as health care, plants, and bioinformatics, with wide advantages [2]. The problems are addressed via machine learning strategies that include rule-based and decision-making. Most classification algorithms only take structured data into account. In the processing of unstructured data, structured and unstructured information is generally combined [3, 4] to reduce the disease-prediction risk. The combination of the information eases the cost of processing and reduces the redundant information.

Artificial Intelligence (AI) is a troublesome technology used as smarter technology on wide varied applications, ranging from automobile industry to healthcare industry. AI was additionally used to track the virus spread, to identify the patients with high risk areas and antiviral drug in controlling the pandemic in real-time environment. AI predicts the risk of mortality rate by analyzing the patient datasets. This application of AI can help in screening the population, notification, medical help, and suggestion on infection control. It further assists in treatment, planning, and prediction of disease spread and outcomes of patients using AI evidence-based tool.

AI is a powerful intelligence method in the fighting the pandemic, and it has scrambled the AI on healthcare analytics. AI with predefined datasets can predict and track the infectious spread on timely manner across various regions. The challenges include problems associated with forecasting the pandemic over unbiased and historical data for training the AI. It includes panic activities among humans and the statistics difference from existing pandemics (Spanish flu, H1N1 influenza, and AIDS). The lack of proper datasets and big data is considered problematic in finding the infectious spread.

Therefore, the classification of unstructured data using classification algorithms is important to classify separately. The risk of disease prediction based on qualified classifiers is reduced in this manner. Structured data treatment method is proposed in the [5] for unstructured medical image data. Integrated structure systems [6] for medical text documents are structured using a Bayesian classifier for extracting the attributes. In addition, k-means identifies the data and ensures optimum data classification. The search method [7, 8] is used to classify the connections through which unstructured medical data is organized. This proposed technique produces improved accuracy results than the other techniques based on the SVM [9–13]. Some of the methods are listed in Table 1.

Table 1: List of AI-based classification.

Classification model	Dataset	Accuracy
3D CNN model	498 CT scans	70.02
Desenet201	1260 images	96.21
3D CNN	413 CT images	93.01
ResNet-50	60,457 CT images	98.81
RF and SVM	626 CT images	83.77
DL model	219 images	86.72

The above-mentioned methodology cannot identify medical datasets through a rule-based system. The processing of datasets from the input nanotechnology IoT sensitive biosensors [14–16] was done using a rule-based method to minimize redundant data. The rule-based framework with its rule base and systems unregulated data removes redundant data. In order to improve the risk of accuracy in classification, the rule set is needed.

In this paper, we propose a fuzzy decision tree (FDT) method for classification, thereby enhancing the novelty using the genetic algorithm (GA) to improve decision-making on a rule-based basis in broad unstructured datasets from nanotechnology-based IoT biosensors.

The main contribution of the paper is as follows:

(i) The work uses a normalized classifier namely the fuzzy-based decision tree (FDT) algorithm to identify the nondetermined instances relating to the medical diagnosis due to the unstructured nature of the datasets from nanotechnology-based IoT biosensors

(ii) The genetic algorithm(GA) is used to improve the FDT algorithm's classification rule collection

(iii) The evaluation of test patterns helps to track the efficiency of FDT with optimized rules during the training and testing stages

(iv) Finally, the proposed system uses two larger datasets to verify the likelihood of predictive precision.

In this proposed work, Section 2 provides the concept of the article. Section 3 discusses the FDT with GA to design the predictive problem. Section 4 validates the entire work. Section 5 concludes the paper with possible directions of future scope.

2. Basic Concept

This section provides the basics of the hesitant fuzzy algorithm (HFA) that eliminates the hesitations associated with fuzzy set assignment and membership degree to process the data from nanotechnology-based IoT biosensors. The following provides the HFA preliminaries:

For a fuzzy set D with reference set (Y) is generally represented in terms of a function $hD(y)$, where Y produces a subset $[0, 1]$, when D is applied over the Y:

$$D = \{\langle y, h(y)\rangle | y \in Y\} \text{where } y \in \mathbf{Y}, \tag{1}$$

where the membership degree of $y \longrightarrow A$ is defined as different values set $hD(y)$. Hence, for simplicity, the $h(y)$ is generally referred to as a fuzzy set element.

3. Fuzzy Decision Tree (FDT)

In this section, we provide FDT details and how the genetic algorithm provides the optimized rule for FDT as illustrated in Figure 1.

3.1. Data Balancing. Unbalanced datasets collected from nanotechnology-based IoT biosensors. The former model tends to reduce the high-dimensional samples and do not take useful information from the account. Samples for the small class can be oversized by the latter procedure. At first, k-means collects the samples from several classes in various clusters. A number of pseudoclasses were marked or numerated for the classes of balanced dataset collected from nanotechnology-based IoT biosensors.

3.2. Construction of FDT. Instances with differential membership are permitted to use FDT from $[0, 1]$ to multiple branches. Using fuzzy rules, the node conditions of a branch are specified. The cases are degraded by different membership levels as they fall at different nodes. If the information or noise is incomplete, the downfall of the cases is considered beneficial. However, FDT is slow to use, but the ranking is better than an ordinary tree.

The FDT consists of construction of tree and nodes for optimal decision-making. FDT is a fuzzy logic algorithm, which uses language terms to change the attributes of the data on medical training. The knowledge gained is used for attribute evaluation on the connected node. It also uses a fuzzy dataset that includes membership, input, and target attributes. The child node set includes all instances of parent nodes that delete branch attributes. Furthermore, in all cases, the main distinction occurs in the fuzzy membership.

Consider an input preprocessed dataset (S) collected from collected from nanotechnology-based IoT biosensors with an attribute (A_i), where the study uses $\{F_i^{(1)}, \cdots, F_i^{(r_i)}\}$. The membership degree of is given by

$$\mu_{S\left[F_i^{(j)}\right]}(\mathrm{X}_e) = \mu_{F_i^{(j)}}\left(x_e^{(i)}\right) \times \mu_S(\mathrm{X}_e), \tag{2}$$

where $\mu_S(\mathrm{X}_e)$ is defined as the membership degree of X_e, $\mu_{F_i^{(j)}}(x_e^{(i)})$ is defined as the membership degree of $x_e^{(i)}$ with a fuzzy term $F_i^{(j)}$, and $S[F_i^{(j)}]$ is defined as the child node.

The algorithm takes the branch attribute into consideration, based on Figure 2, based on the maximum data gain fuzzy value indicating the fuzzy entropy.

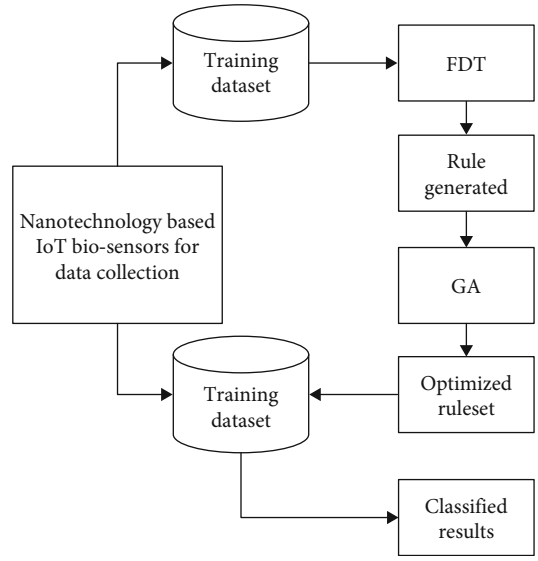

Figure 1: Proposed classification framework.

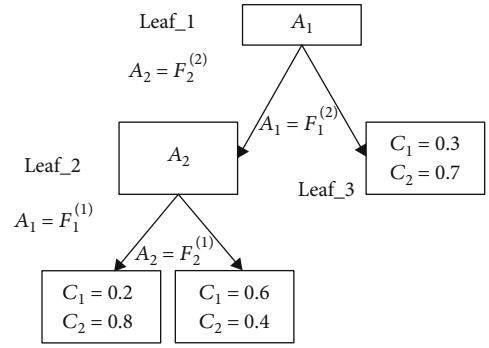

Figure 2: Fuzzy decision tree.

$$E(S) = \sum_{i=1}^{m} - \frac{\left|S_{y=c_i}\right|}{|S|} \log_2 \frac{\left|S_{y=c_i}\right|}{|S|}. \tag{3}$$

Information gain is given by

$$I_G(A_i, S) = E(S) - \sum_{j=1}^{r_i} w_j E\left(S\left[F_i^{(j)}\right]\right), \tag{4}$$

where $E(S)$ is defined as the entropy function of S, $E(S[F_i^{(j)}])$ is defined as the child node (j) entropy, and w_j is defined as the child node (j) instances and it is given as follows:

$$w_j = \frac{\left|S\left[F_i^{(j)}\right]\right|}{\sum_{j=1}^{r_i}\left|S\left[F_i^{(k)}\right]\right|}. \tag{5}$$

The above algorithm illustrates the FDT implementation process. The implementation of the FDT uses a stopping criterion. The standardised maximum I_G [28] method is used as a stopover criterion.

Inputs: membership function, training data, threshold value.
Membership function is set as unity.
Generate root node using fuzzy set.
For a node (N).
Check if the end criteria is reached,
Assume the existence of a leaf N.
Mark the record N belongs to a class is labelled.
Else if end criteria is not reached, then,
Estimate the I_G.
Estimate maximum I_G.
Find child nodes.
End.
End

Algorithm 1: FDT algorithm.

The FDT builds the decision tree using discrete procedure in which a fuzzy system is specified for a certain attribute A_i:

$$B = \{\langle A_i, e_B(A_i)\rangle | A_i \in A\}. \quad (6)$$

Finally, the HI_G over an attribute A_i on a dataset (S) is given by

$$HI_G(A_i, S) = 0.2\left(I_G\left(f_{uf}(A_i, S)\right)^2 + I_G(f_{\text{in}}(A_i, S))^2\right). \quad (7)$$

Here, Equation (7) is computed using two energy values: (i) merging and (ii) uniform discretization.

$$e_B(A_i) = \left\{I_G\left(f_{uf}(A_i, S)\right), I_G(f_{\text{in}}(A_i, S))\right\} \quad (8)$$

$F(A_i, S)$ is defined as the predicted drop of entropy due to an attribute A_i.

$f_{\text{in}}(A_i, S)$ is defined as the predicted drop in entropy (discretization merge) due to an attribute A_i.

$f_{uf}(A_i, S)$ is defined as the predicted drop in entropy due to an attribute A_i (uniform frequency).

The generated intervals of parameter n are considered the same and represent a controlled process. In this node, the fuzzy discretization method based on the information gain is selected using discrete methods.

3.3. FDT Inference Engine. The decision tree is considered a rule in the form of leaves. This condition contributes to the combined history and is classified as a leaf. The rule set is regarded as consistent when a single classification is performed between the leaves. The main significant for a rule is also known as consistent training information and a set of appropriate characteristics. However, when the fuzzy set is inconsistent, the nonnull membership function results from its fuzzy value over a single fuzzy set.

The FDT is then transformed into a fuzzy decision trees in Figure 2. The fuzzy rule fits every leaf. The approximate reasoning operates under four different categories that include (i) firing strength, (ii) compatibility degree, (iii) certainty degree, and (iv) overall output.

3.4. Membership Function Generation. In this paper, two discretizing methods are used for the cutting points and triangular membership functions. The SD membership feature transforms the left/right functions into trapezoidal ones, where the left and right median values are the same. Finally, both discretization functions generate and build up a membership function.

4. Rule Optimization Using GA

The decision-making with fuzzy cannot change the membership rules in order to obtain maximal results. As a result, the genetic algorithm is used as a primary factor to optimize rules using FDT output optimization.

The FDT will be used first in this article to generate classification rules. The GA builds the fitness function based on the advantages of classification and precision. The rule will be optimized if the genetic value is greater and vice versa. To optimize fitness with the crossover and mutation function, the fitness function is modified. With this change, the rules get simplified.

4.1. Coding for the Rule. GA uses the binary code, which is a fixed-long bitcode used in strings with the $\{0, 1\}$ symbol as the human symbol. The encoding length is determined by the attributes value which affects the various GA bitcodes. If k-means values in an attribute, they are distributed into k bits having a value. The chromosomes are long and easier to convert in GA.

The key disadvantage of the FDT tree is the absence of discrete and numerical characteristics. A number of secondary steps must therefore be taken in conjunction with the binary code. The chromosome is set by the law of classification of instances. As the problem can be resolved by some chromosomes, its consistency would determine the rule set. If the rule set recognises a new sample, the GA selects the best rule, and GA selects next rule if the rules set does not recognise a new sample. Hence, if the rules do not recognise the new model, then the GA classifies this instance as a

default situation. There are a number of regulations based on its genetic priority; the chromosome is competitive with other chromosomes.

The proposed model provides the details of the genes in terms of fixed length and chromosomes:

(i) *Weight*. Boolean variable of an attribute

(ii) *Value*. Attribute value: continuous or discrete

(iii) *Operator*. Genes conjunction: continuous or discrete

(iv) *Gain ratio*. Information gain (I_G).

The rules are thus obtained with the four characteristic with a fixed and variable length of chromosome.

4.2. FDT Optimization Using GA. When rules are created by FDT over a subset with few rules on attaining a higher classification rate, the optimization process is applied. The aim is, therefore, to improve the accuracy of FDT by reducing the fitness function. The fitness function at GA tests the rule consistency. The fitness function is divided into four classes based on the rules established:

(i) Class_A predicts true value as true and false value as true

(ii) Class_B predicts true value as true and false value as fault

(iii) Class_C predicts true value as fault and false value as true

(iv) Class_D predicts true value as fault and false value as fault.

Therefore, the accuracy defines the fitness function:

$$\text{Accuracy or } A = \frac{Class\_A + Class\_D}{T + F}, \tag{9}$$

where T is defined as the true data sample and F is defined as the fault data sample.

The precision is capable of producing the correct results for classification:

$$\text{Support or } S = \frac{Class\_A + Class\_C}{T + F}. \tag{10}$$

The rule is larger if the value of the support is higher in dataset and the fitness is estimated as

$$\text{fitness or } f = \frac{N_{att} + n_{r\_att}}{N_{att}}, \tag{11}$$

where N_{att} is defined as the total attributes and n_{r_att} is defined as the total attributes in a rule.

The rule is easy to understand if the individual fitness is high. Finally, it is calculated by the maximum function as well:

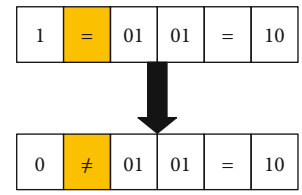

Figure 3: Operator mutation.

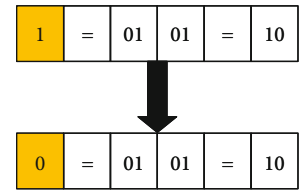

Figure 4: Weight mutation.

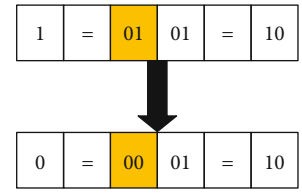

Figure 5: Value mutation.

$$fitness_{\max} = x \times f + y \times s + w \times a + z \times I_{\_G}, \tag{12}$$

where x, y, w, and z are defined as the variable weights lying in $[0, 1]$ and

$$x + y + w + z = 1. \tag{13}$$

4.2.1. Crossover and Mutation Operations. The sample dataset collected from nanotechnology-based IoT biosensors is coded using code rules, creating new successful individuals. Search space will then be reduced significantly, and processing speed will be increased.

This paper uses a 2-point crossover and generates an interval of random numbers $[0, 1]$. The parents are selected randomly for crossover operation if the chance of a crossover exceeds the random number. In the same way, a random number is generated by an interval $[0, 1]$, resulting in a mutation that exceeds a random number.

The genes consist of four components that must be effectively designed. It is a three-way transmission and one operator benefit ratio, which is shown in Figures 3–5, which is as follows:

(i) *Operator mutation*. If the original gene attributes are changed, the gene will mutate into the gene and vice versa

(ii) *Weight mutation*. Count the weight of the new gene to be zero, and vice versa. The gene attribute does not occur in this article if the weight changes from one to zero

Table 2: Evaluation of accuracy with and without feature selection (FS).

Algorithms	With FS	Without FS
Proposed	0.99543	0.982747
SVM-AIRF	0.995378	0.981016
SVM-GA	0.996133	0.981992
SVM-Fuzzy	0.996146	0.96138
BC	0.996901	0.963646
LDA	0.996901	0.96293
LR	0.981094	0.966107
DMDA	0.98082	0.964219
NLP	0.982174	0.965951

Table 3: Evaluation of *F*-measure.

Algorithms	With FS	Without FS
Proposed	0.881778	0.822648
SVM-AIRF	0.880592	0.802064
SVM-GA	0.901165	0.819711
SVM-Fuzzy	0.90153	0.604428
BC	0.915121	0.625737
LDA	0.915121	0.622364
LR	0.796866	0.645609
DMDA	0.795615	0.630347
NLP	0.812901	0.647051

(iii) *Value mutation*. In the case of a different attribute, the initial gene replaces the gene value. Likewise, when a decimal value is created at random, the decimal value will be changed to + or - in the event of continuing attributes.

5. Experimental Results and Discussion

This section presents the validation of FDT used to collect data from nanotechnology-based IoT biosensors, where the sensors are supplied with the data from cord-19 dataset (available at https://www.kaggle.com/allen-institute-for-ai/CORD-19-research-challenge). Performance metrics of the proposed method are evaluated as accuracy, sensitivity, specificity, and *F*-measure. In other classifiers, such as SVM or Bayes, the performance is measured. Parameters are chosen based on the fuzzy model setup. It means that the algorithm, while learning, optimizes these coefficients (according to a given optimization strategy) and returns an array of parameters which reduces the error.

The proposed model is evaluated using an Artificial Immune Recognition System based on support vector machine, SVM-genetic algorithm, SVM-Fuzzy, Latent Dirichlet allocation, Bayesian classifier, dictionary-based linguistic rules decision models, and natural language processing, as shown in Tables 2–7.

The results show that the FDT (Table 8) is more accurate than conventional methods. The principal reason for the

Table 4: Evaluation of precision.

Algorithms	With FS	Without FS
Proposed	0.826911	0.998376
SVM-AIRF	0.825347	0.998985
SVM-GA	0.869621	0.996198
SVM-Fuzzy	0.869147	0.544712
BC	0.903521	0.568991
LDA	0.903521	0.569417
LR	0.972014	0.58184
DMDA	0.986919	0.574265
NLP	0.986401	0.589668

Table 5: Evaluation of sensitivity.

Algorithms	With FS	Without FS
Proposed	0.944444	0.699522
SVM-AIRF	0.943764	0.669993
SVM-GA	0.935083	0.696346
SVM-Fuzzy	0.93642	0.67885
BC	0.927023	0.695057
LDA	0.927023	0.686166
LR	0.675202	0.725076
DMDA	0.666434	0.698569
NLP	0.691306	0.716806

Table 6: Evaluation of specificity.

Algorithms	With FS	Without FS
Proposed	0.996367	0.999931
SVM-AIRF	0.996327	0.999959
SVM-GA	0.997306	0.999834
SVM-Fuzzy	0.997293	0.974218
BC	0.998183	0.975927
LDA	0.998183	0.975825
LR	0.99887	0.976826
DMDA	0.999476	0.97635
NLP	0.999434	0.977293

Table 7: Validation of infections developing in a patient w.r.t risk factors (RF).

Patient	Unchangeable RF	Changeable RF	Controllable RF	Likelihood of infection
1	0.6438	0.6071	0.5946	0.6124
2	0.3241	0.4017	0.3339	0.3439
3	0.5096	0.6256	0.6842	0.6399
4	0.4389	0.3392	0.5057	0.451
5	0.696	0.6609	0.7347	0.6908
6	0.6408	0.6396	0.6725	0.6513

Table 8: Notations.

$\{A_1, \cdots, A_k, Y\}$	Dataset attributes
Y	Target attribute
k	Total attributes
A_i	i^{th} instance of an attribute A
$\{A_1, \cdots, A_k\}$	Set of attributes
y_i	Value of Y
m	Total number of classes
$\mathrm{Y} \in \{c_1, \cdots, c_m\}$	Class labels
$\mu_s(\mathrm{X}_i)$	Membership degree
$S = \{(\mathrm{X}_1, \mu_s(\mathrm{X}_1)), \cdots, (\mathrm{X}_n, \mu_s(\mathrm{X}_n))\}$	Fuzzy input dataset structure
n	Total number of instances
$\left\{F_i^{(1)}, \cdots, F_i^{(r_i)}\right\}$	Fuzzy term
r_i	Total fuzzy terms
$\left[x_i^{(1)}, \cdots, x_i^{(k)}, y_i\right]^T$	Attribute values
$\lvert S\rvert = \sum_{i=1}^{n} \mu_s(\mathrm{X}_i)$	Total instances
$\mu_{F_i}(j)$	Fuzzy membership function
$F_i^{(j)}$	Fuzzy term
$S\left[F_i^{(j)}\right]$	Child node
$S_{y=c_i}$	Instance

improvement is that the genetic algorithm is present to optimize the rules for structuring the large dataset collected from nanotechnology-based IoT biosensors. In the testing and training phase, the proposed method manages incomplete data. The FDT-classifier effectively manages the missing data during the preprocessing operation, which produces better results and outweighs conventional classifiers. This method also reduces the disparity in classification decisions based on their respective decision-making treaties. A new record is effectively classified on the basis of HDFT. In prediction, the presence of the feature selection method is significant in comparison with the standard methods. As the information gain is selected by its entropy values for the corresponding data, consequently, the results are increased and correctly diagnosed.

6. Conclusion

In this paper, we propose technique to improve the risk prediction for COVID-19 new classification technique incorporating FDT in genetic algorithms for rule optimization. The proposed solution is much more likely to be diagnosed by physicians compared to traditional prediction algorithms. Moreover, by using metaheuristic methods, the proposed work can be strengthened to refine the rule set of the decision tree.

Future methods can rely on finding the confirmation of real-time data over polymerase chain reaction of a viral agent. AI-based ML/DL/RIL methods can be used for finding the polymerase chain reaction in finding the viral medicine. The studies can be developed on collection of datasets that can provide a balance between public health and data privacy with AI interactions. The privacy of the data using blockchain technology can enable secured transactions of healthcare data and embedding AI for data analytics to predict the future of infectious spread.

Data Availability

The data used to support the findings of this study are available from the corresponding author upon request.

Conflicts of Interest

None of the authors have any conflicts of interest.

References

[1] B. Qian, X. Wang, N. Cao, H. Li, and Y. G. Jiang, "A relative similarity based method for interactive patient risk prediction," *Data Mining and Knowledge Discovery*, vol. 29, no. 4, pp. 1070–1093, 2015.

[2] J. Ranjan and C. Foropon, "Big data analytics in building the competitive intelligence of organizations," *International Journal of Information Management*, vol. 56, p. 102231, 2021.

[3] G. Ryu, A. Nasridinov, H. Rah, and K. H. Yoo, "Forecasts of the amount purchase pork meat by using structured and unstructured big data," *Agriculture*, vol. 10, no. 1, p. 21, 2020.

[4] Z. Xu, J. Chou, X. S. Zhang et al., "Identifying sub-phenotypes of acute kidney injury using structured and unstructured electronic health record data with memory networks," *Journal of Biomedical Informatics*, vol. 102, p. 103361, 2020.

[5] S. Singh and G. Jagdev, "Execution of structured and unstructured mining in automotive industry using Hortonworks sandbox," *SN Computer Science*, vol. 2, no. 4, pp. 1–25, 2021.

[6] N. S. Spillane, M. R. Schick, K. T. Kirk-Provencher, D. C. Hill, J. Wyatt, and K. M. Jackson, "Structured and unstructured activities and alcohol and marijuana use in middle school: the role of availability and engagement," *Substance Use & Misuse*, vol. 55, no. 11, pp. 1765–1773, 2020.

[7] Q. Zhu, X. Rui, Y. Li, Y. You, X. L. Sheng, and B. Lei, "Identification of four novel variants and determination of genotype–phenotype correlations for ABCA4 variants associated with inherited retinal degenerations," *Frontiers in cell and developmental biology*, vol. 9, 2021.

[8] S. I. Ayon, M. M. Islam, and M. R. Hossain, "Coronary artery heart disease prediction: a comparative study of computational intelligence techniques," *IETE Journal of Research*, vol. 66, pp. 1–20, 2020.

[9] Z. Song and S. Ren, "Product market competition and R&D investment: evidence from textual analysis on annual report of China's listed firms," *Asian Economics Letters*, vol. 1, no. 4, p. 17663, 2020.

[10] J. V. Freitas-Jesus, L. Rodrigues, and F. G. Surita, "The experience of women infected by the COVID-19 during pregnancy in Brazil: a qualitative study protocol," *Reproductive Health*, vol. 17, no. 1, pp. 1–7, 2020.

[11] S. N. Kasthurirathne, Y. A. Ho, and B. E. Dixon, "Public Health Analytics and Big Data," in *Public Health Informatics and Information Systems*, pp. 203–219, Springer, Cham, 2020.

[12] A. Y. Odisho, B. Park, N. Altieri et al., "Natural language processing systems for pathology parsing in limited data environments with uncertainty estimation," *JAMIA open*, vol. 3, no. 3, pp. 431–438, 2020.

[13] M. Petic, A. Gorea, and I. Ciobanu, "Important aspects in assessing the credibility of unstructured information," in *International Conference on Intelligent Information Systems*, pp. 151–156, 2020.

[14] S. Talebian, G. G. Wallace, A. Schroeder, F. Stellacci, and J. Conde, "Nanotechnology-based disinfectants and sensors for SARS-CoV-2," *Nature Nanotechnology*, vol. 15, no. 8, pp. 618–621, 2020.

[15] C. Weiss, M. Carriere, L. Fusco et al., "Toward nanotechnology-enabled approaches against the COVID-19 pandemic," *ACS Nano*, vol. 14, no. 6, pp. 6383–6406, 2020.

[16] M. Vaculovicova, P. Michalek, S. Krizkova, M. Macka, and V. Adam, "Nanotechnology-based analytical approaches for detection of viruses," *Analytical Methods*, vol. 9, no. 16, pp. 2375–2391, 2017.

Hindawi
Journal of Nanomaterials
Volume 2021, Article ID 5943486, 7 pages
https://doi.org/10.1155/2021/5943486

Research Article

Experimental Investigation on Mechanical Properties of TiAlN Thin Films Deposited by RF Magnetron Sputtering

L. Natrayan,[1] **S. Balaji**,[2] **G. Bharathiraja**,[1] **S. Kaliappan**,[3] **Dhinakaran Veeman**,[4] **and Wubishet Degife Mammo**[5]

[1]*Department of Mechanical Engineering, Saveetha School of Engineering, SIMATS, Chennai, Tamil Nadu 602105, India*
[2]*Department of Mechanical Engineering, SRM Institute of Science and Technology, 603203, Chennai, India*
[3]*Department of Mechanical Engineering, Velammal Institute of Technology, Tamil Nadu, 601204, Chennai, India*
[4]*Centre for Additive Manufacturing, Chennai Institute of Technology, 600069, Chennai, India*
[5]*Mechanical Engineering Department, Wollo University, Kombolcha Institute of Technology, Kombolcha, South Wollo-, 208 Amhara, Ethiopia*

Correspondence should be addressed to L. Natrayan; natrayanphd@gmail.com
and Wubishet Degife Mammo; wubishetdegife7@gmail.com

Received 6 September 2021; Revised 17 October 2021; Accepted 25 October 2021; Published 1 November 2021

Academic Editor: Lakshmipathy R

Copyright © 2021 L. Natrayan et al. This is an open access article distributed under the Creative Commons Attribution License, which permits unrestricted use, distribution, and reproduction in any medium, provided the original work is properly cited.

The mechanical properties of TiAlN deposited on the steel are explained in this study. Thin films are deposited by RF magnetron sputtering on the steel substrates to improve the wear resistance and hardness of the samples. Due to their improved microstructure and nanograins, the nanofilms have improved the mechanical properties of the steel substrate surface. The thin film deposited has improved the wear resistance by 80% and has improved the hardness by 95%. The deposited thin films are tested for hardness by nanoindentation and wear test by the pin-on-disk test. SEM has tested films for their microstructure and adhesion by nanoscratch test.

1. Introduction

Titanium aluminium nitride (TiAlN) films have grown due to several notable mechanical characteristics, such as exceptional hardness, wear resistance, and corrosion resistance [1]. TiAlN films have several other advantages as well [2]. TiAlN also has a low thermal expansion coefficient and a high conductivity coefficient [3]. These coatings are used in various industries, including the semiconductor device business, where they serve as an electrode barrier to protect semiconductor devices from damage [4]. TiAlN films are also being used in bioapplications as coatings for bioimplants [5]. Titanium-based implants made using DMLS (direct metal laser sintered) technology are relatively new to the biomedical profession [6]. Even though cobalt-based and nickel-based alloys are still in use in the medical profession [7], titanium and its alloys are becoming increasingly popular in the field [8].

PVD coatings are responsible for both the gradient diffusion layer's thickness and the layer's adherence to the substrate [9]. Utilizing PVD methods for nitride layer formation to improve the properties of biomaterials or machining tools is a fairly popular method of improving performance [10]. This metal nitride is extremely resistant to oxidation due to the formation of a sublayer of titanium dioxide (TiO_2) and protective aluminium oxide (Al_2O_3) protective film [11]. TiAlN thin film has already been applied using a variety of deposition techniques, including physical vapour deposition (PVD), thermogradient reactive deposition process (TRD), and magnetron sputtering [12]. Other deposition techniques, such as physical vapour deposition (PVD), thermogradient reactive deposition process (TRD), and magnetron sputtering process, are used [13]. Faults, such as interstitial faults, emptiness, and point defects, can occur in the design process [14]. When a coating is applied, residual stress and other defects impact the coating's

Figure 1: Sputtering machine.

Figure 2: Agilent G200 nanoindenter and nanoscratch device.

Table 1: Hardness values of TiAlN thin films.

Sample	100 W-TiAlN	150 W-TiAlN	200 W-TiAlN	250 W-TiAlN
Hardness (HV)	28.1	30.5	32.1	30.2

Table 2: Elastic modulus values of TiAlN thin films.

Sample	100 W-TiAlN	150 W-TiAlN	200 W-TiAlN	250 W-TiAlN
Modulus (GPa)	510	545	555	530

Figure 3: TiAlN thin film on steel.

performance [15]. Kishi et al. investigated and found that the adhesion between polystyrene and CF reinforced epoxy ply should be improved for better flexural properties [16]. Cho et al. observed that incorporation of GO in to CF reinforced epoxy composites improves the interfacial strength between matrix and reinforcement due to hydrogen bonding and mechanical interlocking [17]. Kumar et al. found that the carbon black modified CFs possess better surface energy, due to the topology of the CFs than the untreated CFs and also observed that carbon black modified CF epoxy composites have better interfacial adhesion due to the wettability between matrix and CF [18]. Yogeshwaran et al. investigated and found that carbon fabric reinforced epoxy composite exhibits better shear response than UDCF reinforced epoxy composites because of the energy absorption capacity of fabric at ultimate levels of stress and strain [19].

AISI 304 is one of the most widely used modern structural materials [20]. These properties allow it to be welded, making it highly corrosion resistant and capable of withstanding mechanical stress [21]. However, only wear and cavitation erosion resistance is protected by this cap (CER) [22]. To strengthen the wear resistance of SS, apply several types of hard coatings, such as TiN, CrN, TiAlN, AlTiN, or AlCrN. As a result of advances in TiAlN or AlTiN technology, current TiAlN or AlTiN hard films are now extensively used to manufacture machine tools or machine components to reduce tribochemical and adhesive wear or to enhance their resilience to extreme heat conditions [23]. Therefore, if metal components undergo severe wear processes, their overall wear resistance can be enhanced by utilizing AlTiN and TiAlN coatings, with various Al/(Ti + Al) ratios. Another benefit of TiAlN or AlTiN-based universal ternary coating systems is their ability to significantly improve tribological properties, as well as resistance to cavitation erosion [24].

TiN and CrN hard thin film coatings have a higher CER on their steel substrates than steel substrates that have not been coated with hard thin films. When it comes to mechanical properties, ternary film systems are often preferable to binary coating processes in most cases. Furthermore, according to the literature, for CER and PVD coatings, film characteristics and substrate mechanical properties are critical considerations. In addition to this, research is looking into using an aluminium alloy coated with a thin TiAlN layer as a structural component [25]. The constant evolution of the metal machining industry has resulted in the introduction of continuous cutting and interrupted cutting methods of cutting. When milling is interrupted during cutting, the mechanical impact and heat induce mechanically and comb cracks to form in the material. Damage resistance and adhesion are critical for a successful application. Because coated milling tools are subjected to fractures that

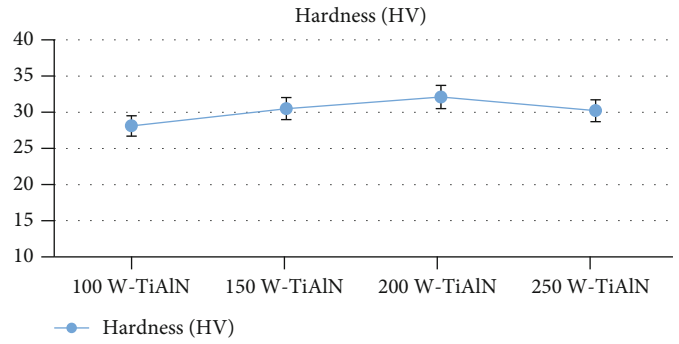

Figure 4: Hardness variation in samples.

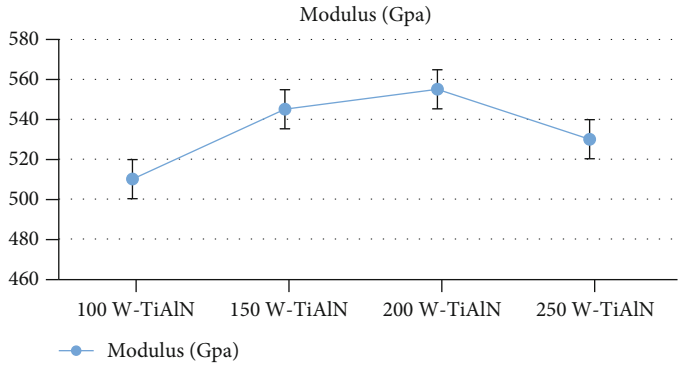

Figure 5: Modulus variation in samples.

originate and propagate throughout the milling process, their cutting capabilities are severely limited. When the tool's surface layers are alternately extended and contracted when the tool is being used, this is a highly common source of cracks in the tool. Since the tool coating promotes numerous comb cracks and the fact that the multilayered TiN/TaN combination allows the tools to interact with each other, stainless steel that is milled using cemented carbide tools coated with multilayered TiN/TaN and single-layered TiN and TaN tends to suffer from higher rates of failure when milled with tools with these coating combinations [26]. Cutting tools with high hardness, high toughness, high oxidation resistance, and high hot hardness are ideal for interrupting processes in the manufacturing process.

In this study, HSS steel of grade M35 is selected for the study and is coated by TiAlN by using RF sputtering deposition process. Samples were tested for their hardness, microstructure, wear resistance, and adhesion. Coatings are tested with nanoindentation, SEM, pin-on-disk, and nanoscratch test that were evaluated.

2. Materials and Methods

The RF sputtering procedure was used to coat TiAlN targets on steel to get a uniform coating. This material, which has a purity of 99.99%, a diameter of 50 mm, and a thickness of 3 mm were obtained and used in the current study. The experimental system is depicted in Figure 1. A magnetron is connected to the power source through an impedance matching network to hold the target material in place. In order to serve as an electrode, the chamber is connected to the ground, resulting in a fully functional circuit. Sputtering power is varied from 100 W to 250 W in steps of 50 W.

Steel is cut into $10 \times 10 \times 1$ mm substrates and ground down to a degree of precision of order 0.2 m by utilizing several grades of abrasive papers and diamond polish to achieve this precision level. Steel samples that have been cleaned and etched are submerged in an acetone solution for ten minutes, after which they are sputter-etched in oxygen plasma for the remaining ten minutes [27]. Turbo pumps are used to keep the operating pressure in the vacuum chamber constant at 10-12 bar at all times. The total thickness of TiAlN films is 1000 nm. The nanoindentation procedure is used to investigate the mechanical behaviour of thin films (hardness, elastic modulus). Temperature and pressure are always maintained as constant. Figure 2 shows the nanoindentation instrument, which is used for both hardness and adhesion tests [28].

The scratch test is performed on the samples to determine the adhesion of the DLC coatings that have been developed. Furthermore, the scratch analysis of the film is carried out using the nanoindentation machine with Berkovich indenter. The critical load of coating peels offload gradually increased over a period of time. This load is considered the adhesion strength of the film, and it is considered the maximum load [29].

The scanning electron microscope (SEM) is used in the examination of the thin film microstructure. Pin-on-disk

method is used for the wear resistance measurement. Pin made of uncoated steel samples is used to measure wear and friction in the laboratory. For the test, 100 gm of the load is utilized, and 5000 revolutions are completed.

3. Results and Discussions

Tables 1 and 2 exhibit the developed thin film modulus and hardness values, determined using nanoindentation testing with a load vs. deflection measurement method [30]. A micro-Newton load was applied using the Berkovich indenter. Figure 3 shows the TiAlN thin film on a steel substrate.

As the soft substrate takes away all the load, the underreported value is difficult to measure. It has hard to discern the hardness and elastic modulus of the coating with ordinary indentation. The soft substrate cushioned the rigid thin film coating. The DLC coating is extremely rigid, and it directly applies the load to the substrate [31]. When a load is applied, elastic deformation occurs to the substrate, and the hardness under load is measured. When a load is applied, the substrate exhibits elastic deformation, and the load-hardness relationship is examined. These findings resulted in the combined hardness of the coating and substrate, which degraded the quality of the coating. Many trials were performed on each sample, and the average hardness and elasticity modulus were determined. The exact hardness of the sample area is determined under the condition of unplugging the load. When the maximum load was reached, each trial was held for 15 seconds [32].

The hardness values of the thin films calculated are presented in Table 1. The highest hardness has been measured for the sample, which is coated at 200 W substrate power. The highest hardness is 14% higher than the least hardness measured. Although the nanohardness of the TiAlN sample is measured, there are high chances of getting defective measurements due to the presence of defects under the subsurfaces of the surface [33].

Due to these defects, the nanoindentation method is not suitable for bulk materials. However, the modulus of the materials can be compared. The modulus of M35 steel is 207 GPa, whereas the highest measured modulus in this study is 555 GPa. TiAlN is 168% higher than the M35 steel. Figures 4 and 5 expose graphical representations of hardness and modulus values of thin films deposited. It indicates that the TiAlN thin film has considerably increased the hardness and modulus of the substrate [34].

4. Microstructure

SEM micrograph of the TiAlN sample deposited at 200 W sputtering power is shown in Figure 6. The deposited thin film has a microstructure of size 5-6 nm. The microstructure is uniform in nature and has very few pinholes and defects. The nature of the film as it has nano-sized grains is responsible for the increase in hardness. The structure is similar to all the samples [35]. The remaining samples have the same microstructure but with higher defects. Due to these defects, it can be said that the hardness has been reduced for the other samples. The TiAlN particles are evenly distributed in the thin film. The defects present in the thin film are generated due to the stresses developed during the deposition process. As the incoming atoms come with high energy, the impact of the particles causes stresses in the film. There is no stress-relieving mechanism employed during the deposition like annealing. There is no film peel off that has been observed indicating the good affinity of the film with

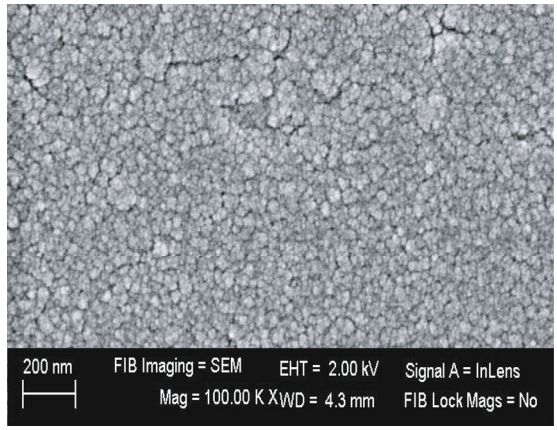

Figure 6: SEM micrograph of TiAlN thin film.

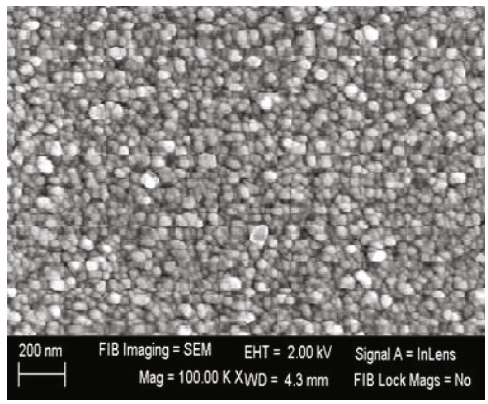

Figure 7: TiAlN deposited at 100 W power.

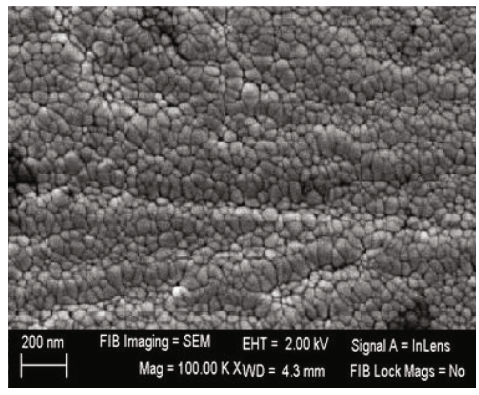

Figure 8: TiAlN deposited at 150 W power.

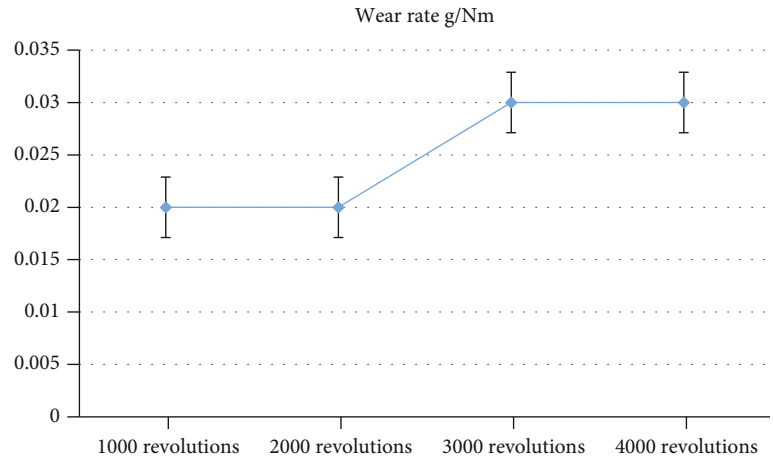

Figure 9: Wear rate of TiAlN thin film.

Table 3: Elastic modulus values of TiAlN thin films.

Sample	100 W-TiAlN	150 W-TiAlN	200 W-TiAlN	250 W-TiAlN
Adhesion strength (GPa)	32.1	38.6	41.3	34.3

the sample [36]. For comparison purposes, the SEM micrographs of films deposited at 100 and 150 are given in Figures 7 and 8.

4.1. Wear Test. The coating samples were tested using pin-on-disk wear testing after being placed on a steel pin and subjected to wear. Wear values in the samples ranged between 0.02 and 0.04. There are some differences in the COF curves of the two samples. It means that the sample was subjected to abrasion wear during the testing process. Despite low COF concentrations, it is still possible to detect them. Figure 9 gives the wear rate behaviour of the sample tested.

All coating samples exhibited no signs of film chipping or peeling, indicating that the TiAlN coating adhered to the substrates effectively under the conditions used in the current test.

4.2. Adhesion Test. The nanoscratch test is used to determine the adhesion strength of TiAlN films. The values that are included in the results are shown in Table 3. The samples' adhesive strength increases in direct proportion to the increase in substrate power up to 20 W. When the power output is increased from 200 W to 250 W, the adhesion strength decreases significantly. When the amount of sputtering energy supplied to an atom increases, so does the amount of energy transferred from that atom to the impact point, causing increased stress. Following the nondissipation of this stress, additional atoms are deposited on top of it, resulting in a stress build-up. The stress in the film increases as the sputtering power increases, resulting in a loss of adhesion between the film and the substrate.

5. Conclusion

TiAlN thin films are successfully deposited onto the H35 steel substrate. The TiAlN thin films have remarkably improved the hardness and the modulus of the substrate. The modulus has increased by 168% compared to the substrate by the thin film application. The thin film generated has a microstructure of order less than 10 nm with a uniform surface. Further study is needed to make the film error-free with pinholes and cracks. The adhesion of the film is better when the sputtering power is maintained at 200 W. Overall, to obtain better adhesion and hardness along with wear resistance suggested maintaining sputtering power at 200 W.

Data Availability

The data used to support the findings of this study are included within the article. Should further data or information be required, these are available from the corresponding author upon request.

Disclosure

It was performed as a part of the Employment of Kombolcha Institute of Technology, Wollo University, Kombolcha, Amhara, Ethiopia.

Conflicts of Interest

The authors declare that there are no conflicts of interest regarding the publication of this paper.

Acknowledgments

The authors thank Saveetha School of Engineering, SIMATS, Chennai, for providing characterization supports to complete this research work.

References

[1] B. Gao, X. Du, Y. Li, S. Wei, X. Zhu, and Z. Song, "Effect of deposition temperature on hydrophobic CrN/AlTiN nanolaminate composites deposited by multi-arc-Ion plating," *Journal of Alloys and Compounds*, vol. 797, pp. 1–9, 2019.

[2] H. Ma, Q. Miao, G. Zhang et al., "The influence of multilayer structure on mechanical behavior of TiN/TiAlSiN multilayer coating," *Ceramics International*, vol. 47, no. 9, pp. 12583–12591, 2021.

[3] Z. R. Liu, L. Chen, Y. Du, and S. Zhang, "Influence of Ru-addition on thermal decomposition and oxidation resistance of TiAlN coatings," *Surface and Coatings Technology*, vol. 401, article 126234, 2020.

[4] M. Ghufran, G. M. Uddin, S. M. Arafat, M. Jawad, and A. Rehman, "Development and tribo-mechanical properties of functional ternary nitride coatings: applications-based comprehensive review," *Proceedings of the Institution of Mechanical Engineers, Part J: Journal of Engineering Tribology*, vol. 235, no. 1, pp. 196–232, 2021.

[5] M. Walczak, K. Pasierbiewicz, and M. Szala, "Adhesion and mechanical properties of TiAlN and AlTiN magnetron sputtered coatings deposited on the DMSL titanium alloy substrate," *Acta Physica Polonica, A*, vol. 136, no. 2, pp. 294–298, 2019.

[6] I. Pana, V. Braic, M. Dinu et al., "In vitro corrosion of titanium nitride and oxynitride-based biocompatible coatings deposited on stainless steel," *Coatings*, vol. 10, no. 8, 2020.

[7] R. Bahi, C. Nouveau, N. E. Beliardouh, C. E. Ramoul, S. Meddah, and O. Ghelloudj, "Surface performances of Ti-6Al-4V substrates coated PVD multilayered films in biological environments," *Surface and Coatings Technology*, vol. 385, article 125412, 2020.

[8] L. Patnaik, S. R. Maity, and S. Kumar, "Lubricated sliding of CFRPEEK/AlCrN film tribo-pair and its effect on the mechanical properties and structural integrity of the AlCrN film," *Materials Chemistry and Physics*, vol. 273, article 124980, 2021.

[9] W. Tillmann, A. Fehr, D. Stangier, and M. Dildrop, "Influences of substrate pretreatments and Ti/Cr interlayers on the adhesion and hardness of CrAlSiN and TiAlSiN films deposited on Al 2 O 3 and ZrO 2-8Y 2 O 3 thermal barrier coatings," *Results in Physics*, vol. 12, pp. 2206–2212, 2019.

[10] T. Borowski, K. Kulikowski, B. Adamczyk-Cieślak, K. Rożniatowski, M. Spychalski, and M. Tarnowski, "Influence of nitrided and nitrocarburised layers on the functional properties of nitrogen-doped soft carbon-based coatings deposited on 316L steel under DC glow-discharge conditions," *Surface and Coatings Technology*, vol. 392, 2020.

[11] D. Veeman, M. S. Sai, P. Sureshkumar et al., "Additive manufacturing of biopolymers for tissue engineering and regenerative medicine: an overview, potential applications, advancements, and trends," *International Journal of Polymer Science*, vol. 2021, Article ID 4907027, 20 pages, 2021.

[12] A. Moreno-Bárcenas, J. M. Alvarado-Orozco, J. M. G. Carmona, G. C. Mondragón-Rodríguez, J. González-Hernández, and A. García-García, "Synergistic effect of plasma nitriding and bias voltage on the adhesion of diamond-like carbon coatings on M2 steel by PECVD," *Surface and Coatings Technology*, vol. 374, pp. 327–337, 2019.

[13] B. Bakhit, J. Palisaitis, J. Thörnberg et al., "Improving the high-temperature oxidation resistance of TiB_2 thin films by alloying with Al," *Acta Materialia*, vol. 196, pp. 677–689, 2020.

[14] A. Y. Adesina, Z. M. Gasem, and A. Madhan Kumar, "Corrosion resistance behavior of single-layer cathodic arc PVD nitride-base coatings in 1M HCl and 3.5 pct NaCl solutions," *Metallurgical and Materials Transactions B: Process Metallurgy and Materials Processing Science*, vol. 48, no. 2, pp. 1321–1332, 2017.

[15] Z. Zhang, Q. Song, B. Jiang et al., "Electrochemically assisted carbonization of Nb in molten salt," *Surface and Coatings Technology*, vol. 358, pp. 865–872, 2019.

[16] H. Kishi, N. Nakao, S. Kuwashiro, and S. Matsuda, "Carbon fiber reinforced thermoplastic composites from acrylic polymer matrices: interfacial adhesion and physical properties," *Express Polymer Letters*, vol. 11, no. 4, pp. 334–342, 2017.

[17] B. G. Cho, J. E. Lee, S. H. Hwang, J. H. Han, H. G. Chae, and Y. Bin Park, "Enhancement in mechanical properties of polyamide 66-carbon fiber composites containing graphene oxide-carbon nanotube hybrid nanofillers synthesized through in situ interfacial polymerization," *Composites Part A: Applied Science and Manufacturing*, vol. 135, article 105938, 2020.

[18] A. Kumar, K. Sharma, and A. R. Dixit, "A review of the mechanical and thermal properties of graphene and its hybrid polymer nanocomposites for structural applications," *Journal of Materials Science*, vol. 54, no. 8, pp. 5992–6026, 2019.

[19] S. Yogeshwaran, L. Natrayan, G. Udhayakumar, G. Godwin, and L. Yuvaraj, "Effect of waste tyre particles reinforcement on mechanical properties of jute and abaca fiber - epoxy hybrid composites with pre-treatment," *Materials Today: Proceedings*, vol. 37, Part 2, pp. 1377–1380, 2021.

[20] P. Stoyanov, J. Schneider, M. Rinke et al., "Microstructure, mechanical properties and friction behavior of magnetron-sputtered V-C coatings," *Surface and Coatings Technology*, vol. 321, pp. 366–377, 2017.

[21] V. V. Çay, "Effects of abrasive particle type, load and sliding distance on micro-abrasion resistance of high speed steel coated with AlCrN or AlTiN," *Medziagotyra*, vol. 27, no. 1, pp. 50–56, 2021.

[22] Y. M. Durmaz and F. Yildiz, "The wear performance of carbide tools coated with TiAlSiN, AlCrN and TiAlN ceramic films in intelligent machining process," *Ceramics International*, vol. 45, no. 3, pp. 3839–3848, 2019.

[23] S. Kumar, S. R. Maity, and L. Patnaik, "Effect of tribological process parameters on the wear and frictional behaviour of Cr-(CrN/TiN) composite coating: an experimental and analytical study," *Ceramics International*, vol. 47, no. 11, pp. 16018–16028, 2021.

[24] P. Luo, C. Gong, Y. Li, X. Wang, and X. Tian, "Effect of auxiliary enhanced magnetic field on microstructure and mechanical behaviors of multilayered CrN/AlCrN films," *Journal of Materials Engineering and Performance*, 2021.

[25] A. Y. Adesina, Z. M. Gasem, and A. S. Mohammed, "Comparative investigation and characterization of the scratch and wear resistance behavior of TiN, CrN, AlTiN and AlCrN cathodic arc PVD coatings," *Arabian Journal for Science and Engineering*, vol. 44, no. 12, pp. 10355–10371, 2019.

[26] A. Krella, "Resistance of PVD coatings to erosive and wear processes: a review," *Coatings*, vol. 10, no. 10, 2020.

[27] H. Chen, J. Miao, J. Yan, Z. He, and H. Wu, "Improving organic solar cells efficiency through a two-step method consisting of solvent vapor annealing and thermal annealing," *IEEE Journal of Selected Topics in Quantum Electronics*, vol. 22, no. 1, pp. 66–72, 2016.

[28] K. Takahashi, H. Fujishiro, T. Naito, Y. Yanagi, Y. Itoh, and T. Nakamura, "Numerical simulation of electromagnetic and thermal stress in REBaCuO superconducting ring and disk bulks reinforced by stainless steel ring with various widths during field-cooled magnetization," *IEEE Transactions on Applied Superconductivity*, vol. 28, no. 3, 2018.

[29] Z. Zhang, H. Zhao, H. Zhang et al., "Effect of isothermal aging on the pitting corrosion resistance of UNS S82441 duplex stainless steel based on electrochemical detection," *Corrosion Science*, vol. 93, pp. 120–125, 2015.

[30] M. R. Shaner, H. A. Atwater, N. S. Lewis, and E. W. McFarland, "A comparative technoeconomic analysis of renewable hydrogen production using solar energy," *Energy & Environmental Science*, vol. 9, no. 7, pp. 2354–2371, 2016.

[31] N. J. Parizek, B. R. Steines, E. Haque et al., "Acute _in vivo_ pulmonary toxicity assessment of occupationally relevant particulate matter from a cellulose nanofiber board," *NanoImpact*, vol. 17, article 100210, 2020.

[32] A. Shahzad, H. Saeed, M. Iqtedar et al., "Size-controlled production of silver nanoparticles by Aspergillus fumigatus BTCB10: likely antibacterial and cytotoxic effects," *Journal of Nanomaterials*, vol. 2019, Article ID 5168698, 2019.

[33] D. Kumar Rajak, D. D. Pagar, P. L. Menezes, and A. Eyvazian, "Friction-based welding processes: friction welding and friction stir welding," *Journal of Adhesion Science and Technology*, vol. 34, no. 24, pp. 2613–2637, 2020.

[34] J. F. Guo, H. C. Chen, C. N. Sun, G. Bi, Z. Sun, and J. Wei, "Friction stir welding of dissimilar materials between AA6061 and AA7075 Al alloys effects of process parameters," *Materials and Design*, vol. 56, pp. 185–192, 2014.

[35] L. Natrayan, P. S. S. Sundaram, and J. Elumalai, "Analyzing the uterine physiological with MMG signals using SVM," *International Journal of Pharmaceutical Research*, vol. 11, no. 2, pp. 165–170, 2019.

[36] A. S. Mitko, D. R. Streltsov, P. V. Dmitryakov, A. A. Nesmelov, A. I. Buzin, and S. N. Chvalun, "Evolution of morphology in the process of growth of island poly(p-xylylene) films obtained by vapor deposition polymerization," *Polymer Science, Series A*, vol. 61, no. 5, pp. 555–564, 2019.

Hindawi
Journal of Nanomaterials
Volume 2021, Article ID 6946540, 6 pages
https://doi.org/10.1155/2021/6946540

Research Article

An Experimental Performance on Solar Photovoltaic Thermal Collector with Nanofluids for Sustainable Development

Srinivasulu Gundala,[1] **M. Mahaboob Basha**,[2] **V. Madhurima**,[3] **N. Praveena**,[4] **and S. Venkatesh Kumar**[5]

[1]*Department of Electronics and Communication Engineering, Lakireddy Bali Reddy College of Engineering (Autonomous), Andhra Pradesh, India*
[2]*Department of Electronics and Communication Engineering, Sreenidhi Institute of Science and Technology, Hyderabad, India*
[3]*Department of Electronics and Communication Engineering, SV Engineering College, Tirupati, India*
[4]*Department of Information Technology, Velagapudi Ramakrishna Siddhartha Engineering College, Vijayawada, India*
[5]*Department of Mechanical Engineering, College of Engineering and Technology, Mettu University, Ethiopia Po Box: 318*

Correspondence should be addressed to Srinivasulu Gundala; srinivasulugundala46@gmail.com
and S. Venkatesh Kumar; s.venkateshkumar@meu.edu.et

Received 24 August 2021; Revised 29 September 2021; Accepted 11 October 2021; Published 31 October 2021

Academic Editor: Lakshmipathy R

Copyright © 2021 Srinivasulu Gundala et al. This is an open access article distributed under the Creative Commons Attribution License, which permits unrestricted use, distribution, and reproduction in any medium, provided the original work is properly cited.

In this article, the photovoltaic thermal collector (PVT) have designed and fabricated using nanoparticle nanofluid. The cause of this is to check out the effect of using water and water-based totally graphene nanoplatelets at an awareness of 0.05 wt% on the performance of PVT structures. Outdoor assessments have been performed at quantity along with the float prices of 0.5 L/min and 1.0 L/min for the aforementioned nanofluids, respectively, using water as a reference fluid. The results that have been analyzed from an active angle confirmed and determined that, graphene water nanofluid achieved higher in phrases of photovoltaic active conversion, than water that might generate the first-class thermal performance sooner or later of the peak period of sun radiation and high mobile temperature. The inclusion of water in the PVT collector increases average daily electrical efficiency by 7.8%, and 8.5%at flow rates of 0.5 LPM and 1.0 LPM, respectively. Furthermore, using water in the PVT collector increases average daily thermal efficiency by 24.9%, and 26.3%at flow rates of 0.5 LPM and 1.0 LPM, respectively.

1. Introduction

Renewable energy such as solar, wind, hydro, biogas, tidal, and waves plays a vital role all over the world. Solar energy is one of the eminent renewable power resources that offer future technology properly [1]. The critical software of solar strength can be labeled into two kinds: sun thermal device, which renovates sun electricity to thermal energy, and photovoltaic (PV) device, which transfigures solar electricity to electric power [2]. Usually, the structures are used after the opportunity [3]. The combined shape of sun thermal and photovoltaic (PV) is thought to be a photovoltaic thermal (PVT) system [4]. A noteworthy study which works on PVT structures has been completed in the past 50 years [5, 6]. Increasing the temperature of a solar panel by way of one degree Celsius has been shown to result as zero [7, 8], five percent lower in electric performance for silicon cells [9]. As an end result, solar panels can be cooled using an expansion of coolants, along with water and nanofluids. The following arethe number of most trendy research that have been tested in this literature. Wolf [10] provided an idea of PV/T creditors for the first time and large observation has been carried out at the general performance of the module using experimental and theoretical techniques, with water-cooled flat-panel PV/T lenders, being frequently used .

Natrayan and Merneedi [11] pioneered the use of water or air as a fluid medium in a sun thermal collector. Sardarabadi et al. [12] performed a test in PVT systems using

water, due to the fact that bottom fluid and Sio_2 nanofluid at adaquate concentrations. They observed that, standard overall performance come to be 3.6 percent for 1 wt percentage and 7.9 percent for 3 wt percentage whilst in evaluation to PVT water. Ghadiri et al. [13] tested diverse portions of water and ferro fluid (Fe_3O_4/water) in an indoor PVT device. In comparison to a PV gadget, the overall modified performance is proven to be 45 percent. Sardarabadi and Passandideh-Fard [14] combined three types of nanodebris (Al_2O_3, TiO_2, and ZnO) with deionized water at an attention of 0-2 wt%. The authors concluded that TiO_2 and ZnO had higher electrical performance, and ZnO had higher thermal performance.

Al-Shamani et al. [15] investigated with the glide prices on diverse nanofluids together with SiO_2, TiO_2, SiC, and water as a base fluid. According to the results, SiC had the very fantastic electric-powered performance around thirteen, fifty percent and usual performance of 81.73 percent. Soltani et al. [16] accomplished experimental research in a PVT device using a Fe_3O_4/water nanofluid. It was concluded that preferred typical performance and electricity technology had been advanced by using the use of 13% and 52%, respectively. The authors additionally confirmed that, using SiO2 stepped forward trendy, overall performance and electricity output is 3.35 percent and 54.29 percent, respectively.

Al-Waeli et al. [17] experimentally studied 3 varieties of water-based totally nanofluids consisting of Al_2O_3, CuO, and SiC on photovoltaic thermal creditors. It ends up locating that SiC had better thermal conductivity than the alternative nanofluids. Natrayan et al. [18] achieved an experiment having an observation on the silica/water nanofluid and its overall performance in a PVT system. It is determined that overall performance and exergy might be stepped forward by way of 7.9% and 24.3%, respectively. For lengthy-term stability, Ag/water nanofluid turn out to be dealt with through electric-powered explosion of wire [19, 20] and the device modified into evaluated the usage of thermodynamics, specifically power and energy performance.

This test turned into carried out with varied concentrations and glide regimes. The intention of this check is to draw interest to the use of carbon nanomaterials in improving the general performance of PVT systems. To the greatness of the author's understanding, graphene nanoplatelet nanofluid grows to be experimentally explored in this paper for nonconcentrating PVT tool and evaluates its typical overall performance. The authors examined in contrast the electric and thermal efficiency of water and the use of nanofluids on a PVT collector.

2. Analytical Methodology

Two kinds of energy analysis were carried out in this study such as electrical and thermal performance of PVT collector [21] as given below.

2.1. Electrical Energy Analysis. The electrical efficiency of a PV/T system is typically used to decide its electric overall performance [22]. The most viable performance at a given solar intensity is received, through dividing the maximum

Table 1: Technical specification of PV panel.

Specification	Values
P_p	260 W
V_{mp}	30.18 V
I_{mp}	7.96A
V_{oc}	36.72 V
I_{sc}	8.99A
T_{lc}	0.045%K^{-1}
Single-cell dimension	156 mm × 156 mm
Single-module dimension	1640 mm × 992 mm × 35 mm

Figure 1: Photographic view of experimental setup.

appropriate electric-powered energy output of the PV module, with the useful resource of the sun intensity accomplishing the PV module's glazing surface [23].

$$\eta_{elec} = \frac{P_{max}}{Q_s}, \tag{1}$$

where P_{max} is the maximum electrical energy output from the PV module and may be calculated using Equation (2). The rate of solar energy received by the panel, which can be calculated using Equation (3).

$$P_{max} = I_{mp} V_{mp}, \tag{2}$$

where I_{mp} denotes the maximum current (amps) and maximum voltage (volts) of the panel.

$$Q_s = A_{col} I_G, \tag{3}$$

where A_{col} is the area of the collector (m^2) and IG is the solar intensity (W/m^2).

2.2. Thermal Energy Analysis. The term thermal efficiency is commonly used to describe the thermal performance of a

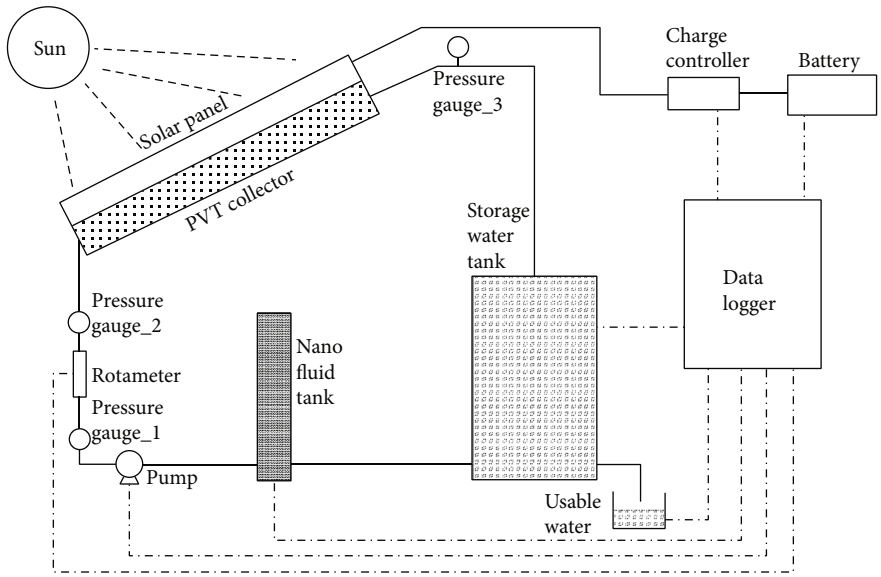

Figure 2: Schematic view of experimental setup.

Figure 3: Preparation of nanoparticle and nanofluid during the laboratory.

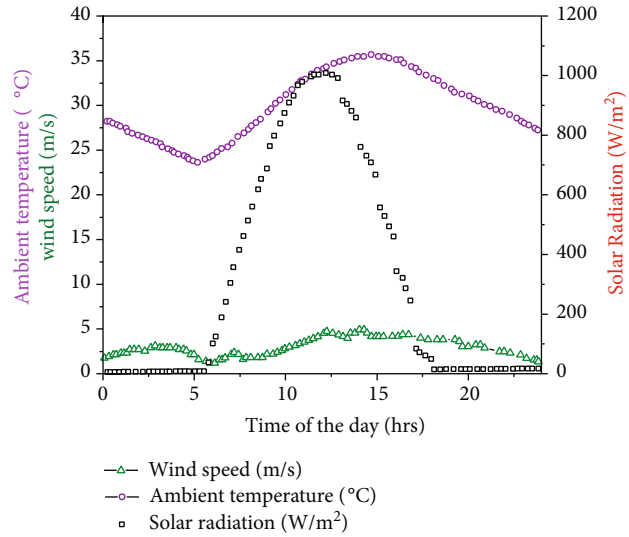

Figure 4: Average results of the solar radiation, ambient temperature, and wind speed at the experimental set up.

PV/T_{system} [24]. The low temperature heat is created from the rear side of the solar panel (as shown by the equation below).

$$\eta_{\text{ther}} = \frac{Q_u}{Q_s}, \tag{4}$$

where Q_u is the rate of useful low temperature heat attained by the solar panel, which can be drawn from

$$Q_u = mC_p\Delta T = mC_p(T_o - T_i), \tag{5}$$

where m is mass flow rate of the fluid (Kg/s), C_p is specific heat capacity of the fluid (kJ/kg K), ΔT is difference in temperature (K), T_o is the outlet fluid temperature (K), and T_i is the inlet fluid temperature (K) [25].

2.3. Experimental Methodology. A photovoltaic thermal sun collector is made from a storage tank, a nanofluid tank, a water pump, a temperature gauge, and a pressure gauge [26]. The outdoor dimensions of the PV/STSC tool are 1640 mm in period, 992 mm in width, and 35 mm in peak, with serpentine copper tube diameter and top of 6.35 mm and 1600 mm, respectively [27]. The technical characteristics of the PV panel evaluated in these studies are confirmed in Table 1. A storage tank with an indoor diameter of 300 mm and a top of 500 mm becomes built out of chrome steel [28].

Glass wool insulation with a thickness of 0.07 m was put around the storage tank's perimeter and associated pipes. The flow rate of the HTF, as well as the system's intake and outlet pressure differential, was monitored with a rotameter and a pressure gauge. The temperature of the heat transfer fluid, as well as the system's current and voltage, was measured every 30 minutes. The experimental testing facilities are depicted in Figure 1.

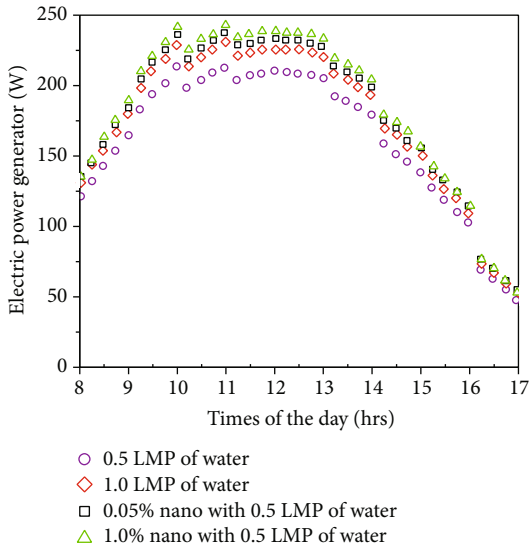

Figure 5: Electrical power generation of the water and nanofluid with different flow rates.

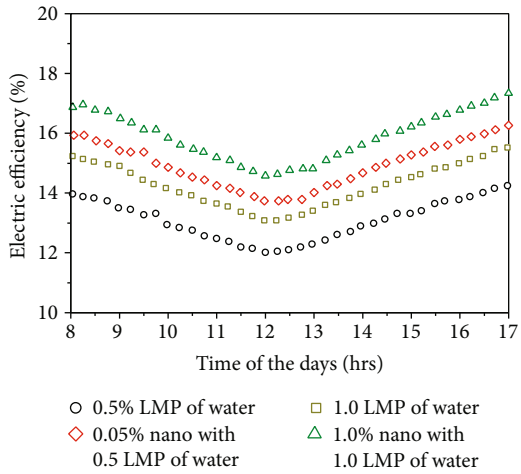

Figure 6: Electrical efficiency of the water and nanofluid with different flow rates.

The experiment was carried out from June to August 2020, with the system-oriented East-West. The photographic view of experimental setup is shown in Figure 1. Schematic view of the architectural design details is displayed in Figure 2. Preparation of nanofluid and its related things are depicted in Figure 3.

3. Results and Discussion

The collected data is averaged and provided for further computations and examination at every 15 seconds. The trial days' climatic parameters, solar intensity, and ambient temperature have been accumulated and displayed in Figure 4. The distribution of sun radiation for the duration is a bell form, with the highest rate at 12:00 pm being 1017.07 W/m^2 and the lowest values being 307.18 W/m^2 at 7:00 am and 229.29 W/m^2 at 17:00 pm, in step with this

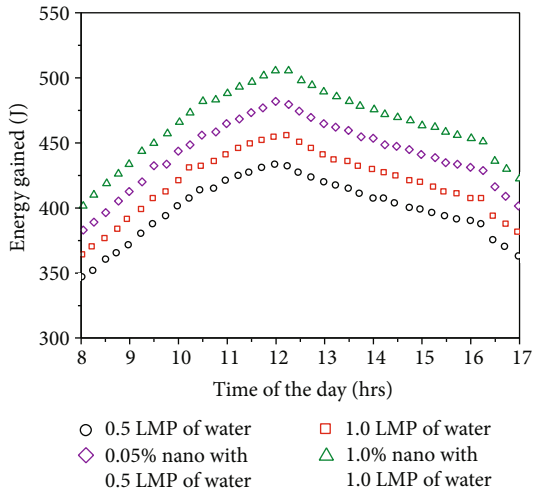

Figure 7: Heat energy gained of the water and nanofluid with different flow rates.

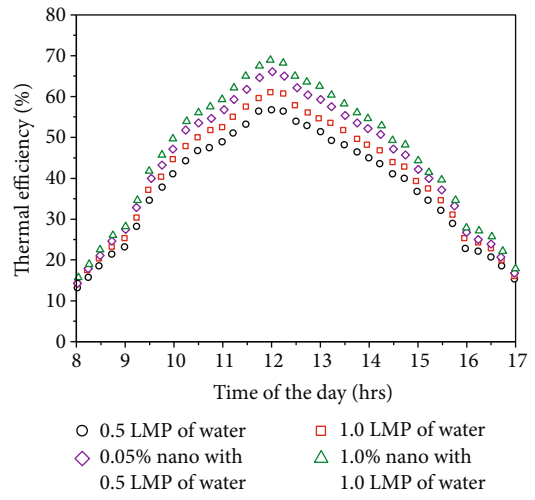

Figure 8: Thermal efficiency of the water and nanofluid with different flow rates.

graph. The day-by-day common place ambient temperature climbs from 29.36°C at 09:00 A.M. to 34.23°C at 17:00 P.M. The consequences of electrical energy on water and nanofluid waft charges of 0.5 and 1.0 litres in line with minute are shown in Figure 5. Electrical energy grew with time until 12 pm because of developing solar intensity, however, then declined. The common electrical electricity for water is with glide quotes of 0. 5 LPM and 1.0 LPM have become around 46.43 W and 50.34 W, respectively. Similarly, the common electric-powered electricity for water primarily based graphene nanofluids with 0.05 percent concentrations of 0.5 and 1. Zero LPM becomes 51.81 W and 53.28 W, respectively. The electrical power of PV panels grew in proportion to the flow rate [21, 22].

Figure 6 depicts the impact of electrical efficiency on water and nanofluid flow rates of 0.5 and 1.0 liters per minute. Electrical power decreases with time until 12 p.m. due to increased solar intensity, then increases. The average

electrical efficiency for water flow rates of 0.5 and 1.0 LPM was around 13.03 percent and 14.19 percent, respectively. Additionally, the average electrical efficiency of water-based graphene nanofluids with 0.05 percent concentrations of 0.5 and 1.0 LPM was 14.92%, and 15.93%, respectively. Electrical efficiency, like electrical power, and coolent flow rate increased [29]. Figure 7 exposed that, the heat energy gained of the water and nanofluid with different flow rates.

Thermal overall performance of PVT collector with water primarily based on nanofluids has been located at particular drift charges. As seen from Figure 8, maximum thermal overall performance for water at 0.5 LPM turn out to be 56.7%, and 61.2%, respectively. Similarly, a bent had been found for 1.0 LPM for water-based totally graphene nanofluids with 0.05% attention modified into determined to be 66.3% and 69 and 5%, respectively. Thermal normal performance of PVT device changed into more first-class through increasing flow charge due to the reality at higher glide fee temperature distinction among inlet and outlet of PV/T device becomes extra due to excessive warmth absorption of nanofluid from tool [29].

4. Conclusion

The overall performance of a PVT collector accomplished through water and graphene nanoplatelets-water nanofluid with a concentration of 0.5 wt% has acheved in this experimental studies. It changed into tested from the factor of view of the first regulation of thermodynamics at regular coolant together with the flow prices of 0.5 L/m and 1.0 L/m, which may be compared. The use of water in the PVT collector complements not unusual each day electric-powered performance with the aid of 8.5%, while using water-based totally graphene nanofluids inside the PVT collector boosts common each day thermal overall performance thru manner of 26.3%.

Data Availability

The data used to support the findings of this study are included within the article. Should further data or information be required, these are available from the corresponding author upon request.

Disclosure

This research was performed as a part of the Employment of College of Engineering and Technology, Mettu University, Ethiopia.

Conflicts of Interest

The authors declare that there are no conflicts of interest regarding the publication of this paper.

Acknowledgments

The authors thank the Management of Lakireddy Bali Reddy College of Engineering, Sreenidhi Institute of Science and Technology, SV Engineering College, VR Siddhartha Engineering College, and College of Engineering and Technology Mettu University for providing research supports to complete this research work.

References

[1] B. J. Brinkworth, B. M. Cross, R. H. Marshall, and H. Yang, "Thermal regulation of photovoltaic cladding," *Solar Energy*, vol. 61, pp. 169–178, 1997.

[2] S. Yogeshwaran, L. Natrayan, S. Rajaraman, S. Parthasarathi, and S. Nestro, "Experimental investigation on mechanical properties of Epoxy/graphene/fish scale and fermented spinach hybrid bio composite by hand lay-up technique," *Materials Today: Proceedings*, vol. 37, pp. 1578–1583, 2021.

[3] J. Ji, J. Han, T. Chow et al., "Effect of fluid flow and packing factor on energy performance of a wall-mounted hybrid photovoltaic/water-heating collector system," *Energy and Buildings*, vol. 38, pp. 1380–1387, 2006.

[4] K. Hemalatha, C. James, L. Natrayan, and V. Swamynadh, "Analysis of RCC T-beam and prestressed concrete box girder bridges super structure under different span conditions," *Materials Today: Proceedings*, vol. 37, pp. 1507–1516, 2021.

[5] H. M. Bahaidarah, A. A. Baloch, and P. Gandhidasan, "Uniform cooling of photovoltaic panels: a review," *Renewable and Sustainable Energy Reviews*, vol. 57, pp. 1520–1544, 2016.

[6] M. Sandeep Kauthsa Sharma, S. Umadevi, Y. Sai Sampath et al., "Mechanical behavior of silica fume concrete filled with steel tubular composite column," *Advances in Materials Science and Engineering*, vol. 2021, 9 pages, 2021.

[7] A. Chauhan, V. V. Tyagi, and S. Anand, "Futuristic approach for thermal management in solar PV/thermal systems with possible applications," *Energy Conversion and Management*, vol. 163, pp. 314–354, 2018.

[8] R. Suryanarayanan, V. G. Sridhar, L. Natrayan et al., "Improvement on mechanical properties of submerged friction stir joining of dissimilar tailor welded aluminum blanks," *Advances in Materials Science and Engineering*, vol. 2021, 6 pages, 2021.

[9] A. Merneedi, N. Mohan Rao, L. Natrayan, L. Yuvaraj, and P. Paramasivam, "Free vibration analysis of thick rectangular and elliptical plates with concentric cut-out," *Advances in Materials Science and Engineering*, vol. 2021, article 7212075, pp. 1–14, 2021.

[10] M. Wolf, "Performance analyses of combined heating and photovoltaic power systems for residences," *Energy Convers*, vol. 16, pp. 79–90, 1976.

[11] L. Natrayan and A. Merneedi, "Experimental investigation on wear behaviour of bio-waste reinforced fusion fiber composite laminate under various conditions," *Materials today: proceedings*, vol. 37, no. 2, pp. 1486–1490, 2021.

[12] M. Sardarabadi, M. Passandideh-Fard, and S. Z. Heris, "Experimental investigation of the effects of silica/water nano fluid on PV/T (photovoltaic thermal units)," *Energy*, vol. 66, pp. 264–272, 2014.

[13] M. Ghadiri, M. Sardarabadi, M. Passandideh-fard, and A. J. Moghadam, "Experimental investigation of a PVT system performance using nano ferrofluids," *Energy Conversion and Management*, vol. 103, pp. 468–476, 2015.

[14] M. Sardarabadi and M. Passandideh-Fard, "Experimental and numerical study of metal oxides/water nanofluids as coolant in photovoltaic thermal systems (PVT)," *Solar Energy Materials and Solar Cells*, vol. 157, pp. 533–542, 2016.

[15] A. N. Al-Shamani, K. Sopian, S. Mat, H. A. Hasan, A. M. Abed, and M. H. Ruslan, "Experimental studies of rectangular tube absorber photovoltaic thermal collector with various types of nano fluids under the tropical climate conditions," *Energy Conversion and Management*, vol. 124, pp. 528–542, 2016.

[16] S. Soltani, A. Kasaeian, H. Sarrafha, and D. Wen, "An experimental investigation of a hybrid photovoltaic/thermoelectric system with nanofluid application," *Solar Energy*, vol. 155, pp. 1033–1043, 2017.

[17] A. H. Al-Waeli, M. T. Chaichan, H. A. Kazem, and K. Sopian, "Comparative study to use nano-(Al2O3, CuO, and SiC) with water to enhance photovoltaic thermal PV/T collectors," *Energy Conversion and Management*, vol. 148, pp. 963–973, 2017.

[18] V. Paranthaman, K. Shanmuga Sundaram, and L. Natrayan, "Influence of SiC particles on mechanical and microstructural properties of modified interlock friction stir weld lap joint for automotive grade aluminium alloy," *SILICON*, pp. 1–11, 2021.

[19] S. Aberoumand and A. Jafarimoghaddam, "Mixed convection heat transfer of nanofluids inside curved tubes: An experimental study," *Applied Thermal Engineering.*, vol. 108, pp. 967–979, 2016.

[20] D. Veeman, M. V. Shree, P. Sureshkumar et al., "Sustainable development of carbon nanocomposites: synthesis and classification for environmental remediation," *Journal of Nanomaterials*, vol. 2021, 2021.

[21] B. Srimanickam and A. Saranya, "Thermal performance of single glazing flat plate photovoltaic thermal hybrid system with various air channels," *Journal of Testing and Evaluation*, vol. 49, no. 3, pp. 2119–2150, 2019.

[22] B. Srimanickam, M. M. Vijayalakshmi, and E. Natarajan, "Energy and exergy efficiency of flat plate PVT collector with forced convection," *Journal of Testing and Evaluation*, vol. 46, no. 2, pp. 783–797, 2017.

[23] D. Veeman, M. S. Sai, P. Sureshkumar et al., "Additive manufacturing of biopolymers for tissue engineering and regenerative medicine: an overview, potential applications, advancements, and trends," *International Journal of Polymer Science*, vol. 2021, 20 pages, 2021.

[24] M. R. Salem, M. M. Elsayed, A. A. Abd-Elaziz, and K. M. Elshazly, "Performance enhancement of the photovoltaic cells using Al2O3/PCM mixture and/or water cooling-techniques," *Renewable Energy*, vol. 138, pp. 876–890, 2019.

[25] A. H. Al-Waeli, K. Sopian, M. T. Chaichan, H. A. Kazem, H. A. Hasan, and A. N. Al-Shamani, "An experimental investigation of SiC nanofluid as a base-fluid for a photovoltaic thermal PV/T system," *Energy Conversion and Management*, vol. 142, pp. 547–558, 2017.

[26] N. E. Hjerrild, S. Mesgari, F. Crisostomo, J. A. Scott, and R. Amal, "Hybrid PV/T enhancement using selectively absorbing Ag–SiO2/carbon nanofluids," *Solar Energy Materials & Solar Cells*, vol. 147, pp. 281–287, 2016.

[27] V. Paranthaman, K. Shanmuga Sundaram, and L. Natrayan, "Effect of silica content on mechanical and microstructure behaviour of resistance spot welded advanced automotive TRIP steels," *Silicon*, vol. 1, pp. 1–10, 2021.

[28] A. H. Al-Waeli, H. A. Kazem, J. H. Yousif, M. T. Chaichan, and K. Sopian, "Mathematical and neural network modeling for predicting and analyzing of nanofluid-nano PCM photovoltaic thermal systems performance," *Renewable Energy*, vol. 145, pp. 963–980, 2020.

[29] A. Hassan, A. Wahab, M. A. Qasim et al., "Thermal management and uniform temperature regulation of photovoltaic modules using hybrid phase change materials-nanofluids system," *RenewableEnergy*, vol. 145, pp. 282–293, 2020.

Hindawi
Journal of Nanomaterials
Volume 2021, Article ID 7024032, 12 pages
https://doi.org/10.1155/2021/7024032

Research Article

Improved Carbon Nanotube Field Effect Transistor for Designing a Hearing Aid Filtering Application

K. Mohana Sundaram,[1] **P. Prakash**,[2] **D. Karthikeyan**,[3] **and Wubishet Degife Mammo**[4]

[1]*Department of EEE, KPR Institute of Engineering and Technology, Coimbatore 641402, India*
[2]*Department of ECE, Madha Engineering College, Chennai 600070, India*
[3]*Department of EEE, SRM Institute of Science and Technology, Kattankulathur, Chennai 603203, India*
[4]*Mechanical Engineering Department, Wollo University, Kombolcha Institute of Technology, Kombolcha, South Wollo, 208 Amhara, Ethiopia*

Correspondence should be addressed to K. Mohana Sundaram; mohanasundaram.k@kpriet.ac.in
and Wubishet Degife Mammo; wubishetdegife7@gmail.com

Received 8 September 2021; Revised 9 October 2021; Accepted 18 October 2021; Published 31 October 2021

Academic Editor: Lakshmipathy R

Copyright © 2021 K. Mohana Sundaram et al. This is an open access article distributed under the Creative Commons Attribution License, which permits unrestricted use, distribution, and reproduction in any medium, provided the original work is properly cited.

Designing a hearing aid device is one of the challenging applications recently, since it is useful for the people with hearing loss. For this purpose, various circuit designing procedures such as MOSFET and carbon nanotube field effect transistor (CNTFET) are introduced in the existing works. But it mainly lacks the following drawbacks: increased leakage current, not highly efficient, and increased area and power consumption. In order to mitigate these issues, this paper is aimed at designing an improved CNTFET (ECNFET) for hearing aid filtering application. The major objectives of the proposed work are leakage current minimization and the improvements in transconductance and mobility. At first, the layout is designed with 10 layers based on the specific dimensionalities, and different materials are placed in each and every layer. It includes gold, silicon, silicon dioxide, bismuth telluride, and carbon tube. Then, the parameters such as band gap, electron concentration, hole concentration, electron mobility, hole mobility, and insulator breakage voltage are verified to determine the efficiency of the layout. If all the parameters are satisfied, the characteristics such as voltage current, leakage current, mobility, and transconductance are validated. If all measures are satisfied, the library is created for the designed ECNFET layout by using the Comsol tool. Furthermore, the operational amplifier is designed based on the generated library function. After amplification, the hearing aid filter is designed with the use of the proposed ECNFET layout. The experimental validation of the proposed work and comparison with the existing method based on the measures of area consumption, power consumption, speed, and frequency range confirm the effectiveness of ECNTFET in filtering applications.

1. Introduction

In today's world, approximately 10% of people suffer due to the hearing loss in which a small amount people use hearing aid devices. The result of wearing this device is highly efficient with minimum noise and distortion. Moreover, a variety of digital signal processing algorithms is required to design the hearing aid device. Traditionally, some of the existing research works are aimed at developing a hearing aid filter by using the VLSI circuit designing technology. But it poses several challenges like increased power and area consumption, when compared to other portable devices. So, the layouts such as MOSFET and CNTFET [1] are developed to design this filtering application. The MOSFET is an integrated circuit that is capable of both voltage gain and signal power gain, in which the MOS capacitor is the main part, and then, the application of gate voltages changes the semiconductor operation from p-type to n-type. Furthermore, it functions based on the deflection mode and the enhancement mode [2]. But it has the major constraints such as process variations, short channel effect, and high leakage current issues. Thus, a CNTFET [3] is developed that is the next

generation of MOSFET [4], which uses the carbon nanotube between the source and drain. The major reasons for designing CNTFET are reduced size, high-performance channel material, and mobility enhancement. Normally, the CNT is considered as a rolled-up sheet of graphene, in which the electrical properties are dependent on the chirality of the distortion direction [5]. In CNTFET, the core of integrated circuit is implemented in a single chip that contains four terminal units, namely, source, drain, gate, and body as shown in Figure 1. A CNTFET relates to a FET that uses single or multiple carbon nanotubes as channel being a substitute for bulk silicon found in the conventional MOSFET [6]. Here, the power supply is provided to the source and drain; then the triggering is enabled for the gate. If it is high, the layout goes to on state; otherwise, it goes to off state.

1.1. Problem Definition. The procedure of CNTFET [7, 8] is the same as that of MOSFET, in which the source terminal supplies the electrons and it is collected by the drain terminal. The CNTFET is the most widely used technology for the past decades [9]. The dimensional criticality in the silicon material reduced the utilization level for the transistor fabrication [10]. Hence, the research studies focused on the identification of alternatives to improve the density and recital of electronic information system [11]. The gate terminal controls the current intensity [12]. If the transistor is in off stage, there is no gate voltage is supplied [13]. However, it also has some major limitations [14] such as increased area consumption and power consumption, reduced speed and frequency range, and increased leakage current [15]. So, it is highly important to determine whether the hearing aid device is good for the hearing loss patients [16]. To mitigate the issues, this article explores the development of a novel hearing aid filtering application by implementing the CNTFET layout.

1.2. Objectives. The objectives modelled from the problem identification are listed as follows:

(i) To reduce the leakage current

(ii) To increase the transconductance

(iii) To increase the electron mobility

(iv) For these objectives, an enhanced CNTFET (ECNFET) layout is designed and implemented in the hearing aid filtering application

(v) The novelty behind the proposed work lies in following cases:

(i) The design of CNTFET-based hearing aid filter in 2 nm technology with the thickness of 0.6 m

(ii) The minimization in layer thickness and the design technology reduce the leakage current compared to the existing models

(iii) The reduction of thickness of the layering initiates the thin material design and increases the operational speed simultaneously

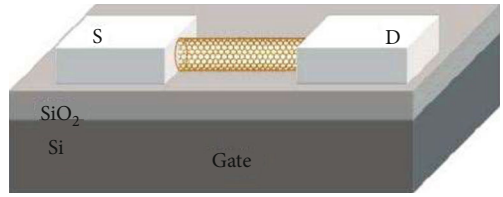

Figure 1: Source, drain, and gate of ECNFET layout.

1.3. Organization. The article is structured as follows: the existing filtering applications and field effect transistor layouts with its advantages and disadvantages are surveyed in Section 2. The detailed description about the proposed ECNFET-hearing aid filtering application is presented in Section 3. The measured results of both available and proposed filtering applications are evaluated in Section 4. Section 5 provides the overall summary and the future enhancement.

2. Associated Works

The existing available FET layout designs used for hearing aid filters are surveyed with their advantages and disadvantages here. The compensation of hearing loss utilizes the device, namely, hearing-aid system, which contains several processes such as amplification, noise removal, suppressing the feedback, and automatic program switching. The amplification of sounds and transferring such sounds to the human ear are the major operations of hearing-aid system. The adjustments of speech signals were performed through the filter bank-based algorithms. Wei and Wang [17] proposed an adjustable filter bank to achieve wave composition based on hearing loss. The changes in 4-bit control signal provide the adjustments in number of subbands and their location. The size optimizing of filter used in hearing-aid system turned the research studies to make the fast-efficient filter with low-power consumption. Kotha et al. [18] discussed the 4 : 2 compressors for finite impulse response (FIR) design. The realization gate level-17 order filter was illustrated by using Hardware Description Language (HDL). The UMC-90 technology was used to implement the architectures with the integration of Cadence compiler. Recently, the revolution in wireless communications systems changes the people lifestyle and leads to the numerous smart device utilization. Based on the application areas such as environmental monitoring and healthcare monitoring, the frequency ranges were defined. Trivedi et al. [19] pointed out the maximum frequency range for the hearing aid is 6 kHz. Under different biasing conditions, the power dissipation among the components was investigated with the subthreshold operation. In some cases, the degree of hearing loss was worse against the time variations. For the severe hearing loss, the acoustic-based amplification was insufficient to restore the satisfactory result [20]. Based on these operational constraints, the design of hearing aid filter was the next stage of research FET-based models which was employed to design several models. Under the temperature variations, power and delay consumed by the operating

phases were high and hence, the reduction mechanisms were required.

Nguyen et al. [21] developed a new sensing system, namely, Low cost In-ear Bioelectrical Sensing (LIBS) for providing a solution to healthcare applications. It automatically captured the signal from the ear canal based on the process of data acquisition and signal separation. Also, a Nonnegative Matrix Factorization (NMF) method was introduced to decompose the signal for separation. Yogeshwaran et al. [22] investigated the drain current and delay of the hearing aid device. Here, the relationship between these measures was validated based on the features of ON and OFF. Kuo et al. [23] implemented an ANSI S1.11 filter for designing a digital hearing aid device. The intention of this application was to cancel the echo, reduce the noise, and enhance the speech. The stages involved in this design were filter bank architecture formation, low power optimization, computation reordering, clock gating, and operand isolation. Guo et al. [24] implemented an acoustic feedback cancellation approach for eliminating the probe noise in a hearing aid filter. The intention of this paper was to reduce the convergence rate with the use of probe noise enhancement filters. Here, two different probe noise-based approaches were evaluated for analyzing the suitable approach with increased convergence rate and reduced steady-state error. However, this design strategy failed to reduce the computational complexity.

Kalathil and Elias [25] designed a nonuniform cosine-modulated filter, and the aim of this application was to fulfill the requirements of hearing-impaired people with the use of uniform filter and transition filter. The merits observed from this paper were increased flexibility, reduced complexity, and improved performance. Pandey and Matthews [26] implemented a Spectral Gain Shaping Method (SGSM) for hearing loss compensation with dynamic range compression and noise suppression. Also, the unwanted effects of the long and broadband path delays were reduced with the use of hearing aid signal processing algorithms. Moreover, the spectral gain shaping capability of the hearing aid system was analyzed for reducing the delay. Ngo et al. [27] designed an improved prediction error filter for modelling the acoustic feedback and estimating the feedback signal in a hearing aid system. Here, the correlation between the near-end signal and loudspeaker signal was identified with the use of Prediction Error Method (PEM). Moreover, an energy-based voiced and unvoiced detection was performed by using the Zero Crossing Rate (ZCR) feature. Pandey and Mathews [28] employed an adaptive filtering technique to enhance the sound quality of hearing aid device. The aim of this paper was to increase the hearing aid gain and to reduce the perceptual distortion. Here, the amplification process was controlled and the frequency components were automatically identified. The use of CNTFET sensors in biomedical applications is growing at a rapid pace [29–31].

3. Suggested Method

The clear description about the proposed hearing aid filtering application using ECNFET layout is provided here. The design of a hearing aid filter with an enhanced CNTFET layout is the major objective of this paper. In this design, the single-walled nanotube is used for providing high current conductivity. It mainly focused to reduce the leakage current and increase the transconductance and electron mobility. For these purposes, an ECNFET layout is designed based on the dimensionalities of length, width, height, CNT thickness, CNT length, and CNT diameter. After designing the circuit, the required materials such as gold, silicon, silicon oxide, bismuth telluride, and carbon are used. Then, the parameters such as band gap, electron concentration, hole concentration, electron mobility, hole mobility, and insulator breakage voltage are considered.

After verifying these parameters, the characteristics such as voltage current, mobility, leakage current, and transconductance of the layout are validated. If the characteristics are satisfied, the library is created by using the Comsol tool. Furthermore, the operation amplifier is designed by using the ECNFET layout for increasing the efficiency of filtering application. Finally, the hearing aid filter is designed by implementing this ECNFET layout. To demonstrate the superiority of the suggested application, the evaluation parameters such as area, power, frequency, and speed are considered during the evaluation. ECNFET flow is shown in Figure 2.

3.1. Physical Design Based on the Dimensionality Analysis. At first, the ECNFET layout is designed based on the specific dimension of each layer. It contains 10 layers, in which different materials are placed in each layer. Layers 1 and 3 are termed as intralayers, and layer 2 is termed as interlayer. Then, layer 5 acts as a source, layer 8 acts as gate, and layer 10 acts as a drain. Also, layers 4, 7, and 9 act as either p-substrates or n-substrates; finally, the CNT is placed in layer 6. The layout design is represented in Figure 3, in which the dimensionalities are determined based on rules of circuit designing. The rules specified that the entire layout should contain the minimum width of 2λ and height of 1.5λ, if the layout design does not follow these rules, it is termed as a worst case design. In the proposed design, the height of the ECNFET is 1λ and the width is 2λ. Also, each and every layer should follow some dimensionalities for a good design. The intralayers (i.e., D1 and D3) have the height of 0.2 nm and width of 2 nm, because these dimensions provide an increased doping concentration. Also, it has a minimum opening for allowing the current conductance from electrons to holes and holes to electrons. Then, the inter layer (i.e., D2) has the height of 0.2 nm and width of 2 nm, because it offers an increased conductance and peak doping concentration. The p-type and n-type substrates (i.e., D4, D9, and D7) have the height of 0.2 nm and width of 0.7 nm, because it controls the materials based on the resistance. Moreover, the source, drain, and gate layers (i.e., D5, D8, and D10) have the height of 0.1 nm and width of 0.4 nm, because they offer a high-level implant and energy. Finally, the CNT that is placed in D6 has the height of 0.1 nm, width of 0.6 nm, and diameter of 0.6 nm, which is placed between the source and drain for increasing the conductivity.

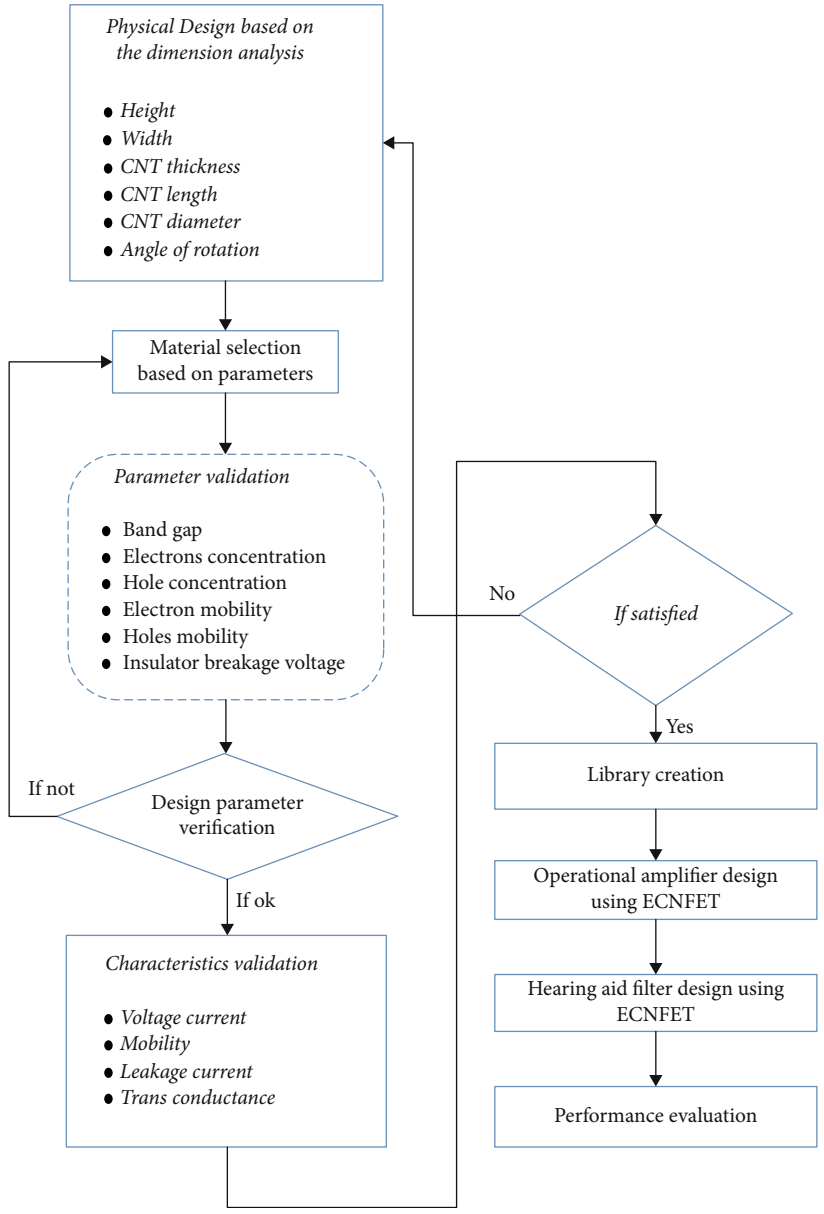

Figure 2: Flow of the ECNFET-based hearing aid filtering.

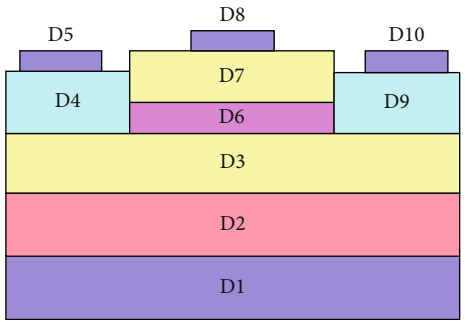

Figure 3: Layout design with different materials.

3.2. Material Selection. After designing the layout, different materials are placed in each and every layer, which includes gold, silicon, quartz, bismuth telluride, and carbon nanotube. The main reasons of using gold are it increases the conductivity of semiconductor and accuracy and improves the movement of electrons to holes and holes to electrons. This material is placed in the layers of D1, D5, D8, and D10. The silicon is considered the second-best material that is placed in D2, which provides little flow electricity when it acts as a semiconductor. Then, the silicon dioxide is placed in D3 and D7, which provides an increased dielectric strength and acts as an excellent insulator. Also, it can function even in high temperature. Bismuth telluride is placed in D4 and D9, which provides low lattice thermal conductivity. Moreover, it acts as a power generation device and is used in both p-type and n-type substrates. Finally, the single-walled thin

CNT is placed in D6, which reduces the diameter size by using the single graphite sheet. Due to this, the size of transistor component is reduced to 2 nm.

3.3. Parameter Verification. After selecting the materials, the parameters such as band gap, electron concentration, hole concentration, electron mobility, hole mobility, and insulator breakage voltage are validated [32]. As for band gap, the energy band gap of the circuit is highly depending on the materials that are used for circuit designing.

The materials or insulators having the energy gap of 1 eV are termed as semiconductors. It is calculated as follows:

$$E_g = E_c - E_v, \tag{1}$$

$$E_g = 1.210 - 3.60 \times 10^{-4} \times T \text{ eV}, \tag{2}$$

where T indicates the temperature, eV indicates the electron volts, E_g represents the energy band gap, E_c is the conductance band, and E_v is the valence band.

3.3.1. Electron Concentration. The electron concentration is defined as the concentration of electrons in the conduction band. Here, the intrinsic concentration is calculated for both n-type and p-type transistors, which is shown below:

$$n_i = N_c e^{((E_F - E_c)/kT)}, \tag{3}$$

where $N_c = (2\pi m_e kT/h^2)^{3/2}$.

3.3.2. Hole Concentration. The hole concentration is defined as the concentration of electrons in the valence band, which is calculated as follows:

$$p_i = N_v e^{((E_v - E_F)/kT)}, \tag{4}$$

where$N_v = 2(2\pi m_h kT/h^2)^{3/2}$, where$N_c$is effective density of states in the conduction band, N_v is effective densities of states in the valence band, k is Boltzmann constant, T is temperature, E_F is Fermi energy, E_v is valence band level, E_c is conduction band level, m_h is effective mass of a hole, m_e is effective mass of an electron, and h is Planck constant 6.624×10^{-34} Js.

3.3.3. Electron Mobility. The movement of electrons through a semiconductor or metal is characterized by using the electron mobility. It is estimated as follows:

$$v_d = \mu E. \tag{5}$$

3.3.4. Hole Mobility. Typically, there is an analogous quantity for holes in a semiconductor, which is generally lower than the electron mobility. It is estimated as follows:

$$v_d = \mu H, \tag{6}$$

where μ represents the mobility, E is the electric field, H represents the holes, and v_d is the drift velocity.

3.3.5. Insulator Breakage Voltage. This should be minimum, because it causes some portion of an insulator as an electrically conductive. It is calculated as follows:

$$V_{\text{breakdown}} = B \times p \times \frac{d}{(C + \text{In}(p \times d))}, \tag{7}$$

where p is pressure of the gas, d represents the distance between two conducting plats, and B and C are the constants that are determined based on the experiments. Based on these parameters, the effectiveness of the layout is determined; if these measures are fully satisfied, the characteristics of the layout are validated.

3.4. Characteristic Validation. After verifying the measures, the major characteristics of the layout is validated; this includes voltage current, mobility, leakage current, and transconductance. The controlling of voltage and flow of current between the source and drain through the proposed ECNFET model reduced leakage current [33].

3.4.1. Voltage Current. It is defined as the amount of current taken for the movement of electrons to holes and holes to electrons. It is calculated as follows:

$$I = \mu W c_i \times \frac{(V_{GS} - V_T)V}{L}, \tag{8}$$

where μ is the mobility and I indicate the current.

3.4.2. Transconductance. The transconductance is also called as mutual conductance, in which the electrical characteristics are related to the output current through the device and the input voltage across the device. Also, the conductance is represented as the reciprocal of the resistance.

$$g_m = \frac{dI_d}{dV_{GS}}\bigg|V_{DS}, \tag{9}$$

where g_m is transconductance, I_d is drain current, V_{GS} is gate source voltage, and V_{DS} is drain source voltage.

3.4.3. Leakage Current. It is an important conduction of PN junction diode, in which the width of the depletion region is increased, when a diode is reverse biased. This condition is required to restrict the current carrier accumulation. The depletion region acts as an insulator, if the majority of current carriers are primarily negated. It is calculated as follows:

$$I = I_0 e^{-Ee/2kT}. \tag{10}$$

I_0 is the initial current, E defines the electrons, and e is the permittivity. Here and mainly, the leakage current reduction is concentrated, because it leads to the band-to-band tunnelling leakage.

3.5. ECNFET Layout Design and Library Creation. After triggering, the transistors are enabled by using the analytic doping model, in which the P, N, and P are substrates in the P-type transistor, and the N, P, and N are substrates in

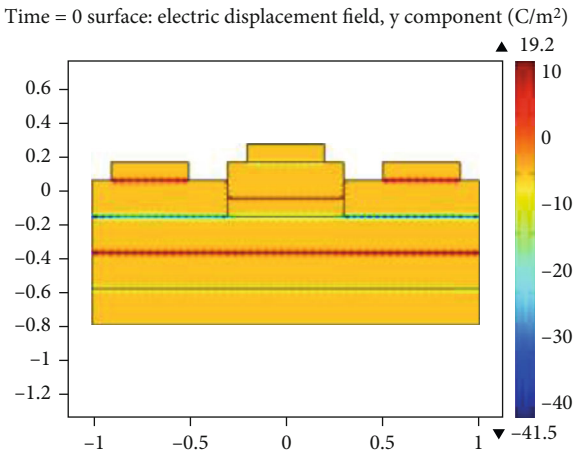

Figure 4: ECNFET layout design.

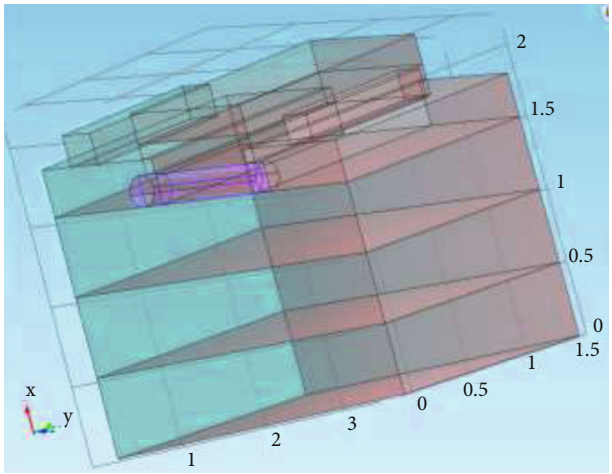

Figure 5: 3D representation of ECNFET.

the N-type transistor. In this layout, the semiconductor is placed in between the source and drain under the oxide layer domain. Furthermore, the application of positive and negative voltages on gate terminal switches the operation between n-type and n-type transistors. Here, the holes across the oxide layer are pushed downward to the substrate, when the positive gate voltage is applied. Then, the bound negative charges populate the deflection region with the acceptor atoms. The current flows freely once the voltage is applied between the drain and source; then, the electrons in the channel are controlled by the gate voltage. The hole channel is made under the oxide, when the negative voltage is supplied. The designed ECNFET layout is shown in Figure 4, and its 3D representation is shown in Figure 5. After that, the library is generated for both p-type and n-type transistors by using the Comsol tool. Then, the generated libraries are given to the input of filtering for noise removal.

3.6. Operational Amplifier Design. The ECNFET is a kind of semiconductor device that is mainly used to amplify the signals in the electronic devices. Figure 6 shows the operational amplifier [34] with the 7 ECNFETs which are used as a p-type transistor, and 5 ECNFETs are used as an n-type transistor. Also, one capacitor is used to avoid the current loss, which is 0.1 μf. This layout gets the low-level frequency as input and provides an improved frequency as output. In this design, the V_d is taken as 10 mw and V_g is taken as 2 v.

The op-amp design using the proposed ECNFET operates at the constant common mode voltage close to source voltage. The input to the op-amp stage is simplified with the Miller-compensated simplified voltage supply. The proposed op-amp comprises the cascaded Miller-compensated stage and output stage to minimize the power intake. The input and output waveforms with frequency variations are illustrated in Figure 7.

With the linear increase of frequencies from 2 kHz to 10 kHz, the voltage variations are graphically depicted in Figure 7. The stable operating point for the voltage and current is observed after the frequency range 2 kHz.

The major benefits of the ECNFET-hearing aid filter shown in Figure 8 are as follows:

It helps to increase the speed of transistor.

It avoids the current loss by designing the capacitor with 0.1 μf.

It efficiently reduces the noise by designing the hearing aid using the ECNFET layout.

The output voltage waveform variations with respect to the time period clearly demonstrate the operation of filter design using the ECNFET model. It is shown in Figure 9.

For the minimum time period (50 ns), the output voltage is in maximum state. When the simulation period is linearly increased from the minimum to maximum value (500 ns), the voltage value is decreased to low value due to the reduction in drain current under the constant drain-to-source voltage.

4. Performance Analysis

The results of both existing and proposed hearing aid filtering applications are measured and equated depending on the measures of leakage current, mobility, transconductance, voltage current, voltage current, area consumption, power consumption, speed, and frequency. The software tools used to implement the proposed work are Comsol 5.0, Electric 9.07, and H-spice J2014. The operating phases of the proposed CNTFET-based hearing aid filter design are layout design, library creation for electric properties, and the performance evaluation. Initially, Comsol 5.0 is used to design the layout with the material specification. In general, there are five materials employed to design the CNTFET such as gold, silicon, graphite, carbon, and SiO_2. But, gold and SiO_2 are used for our proposed work. Then, the electrical properties are defined as the library which is performed by the software electric tool. The layout is considered as the base for the electric property's declaration. Once the layout and electric properties are completed, the numerical variations of current, voltage, and the mobility for the design are investigated to state the effectiveness of the proposed work. This is achieved

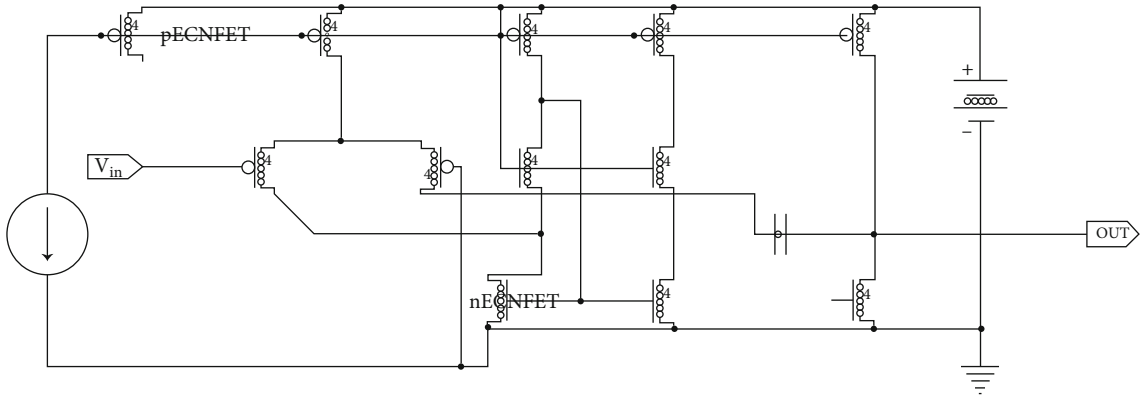

Figure 6: Design of operational amplifier.

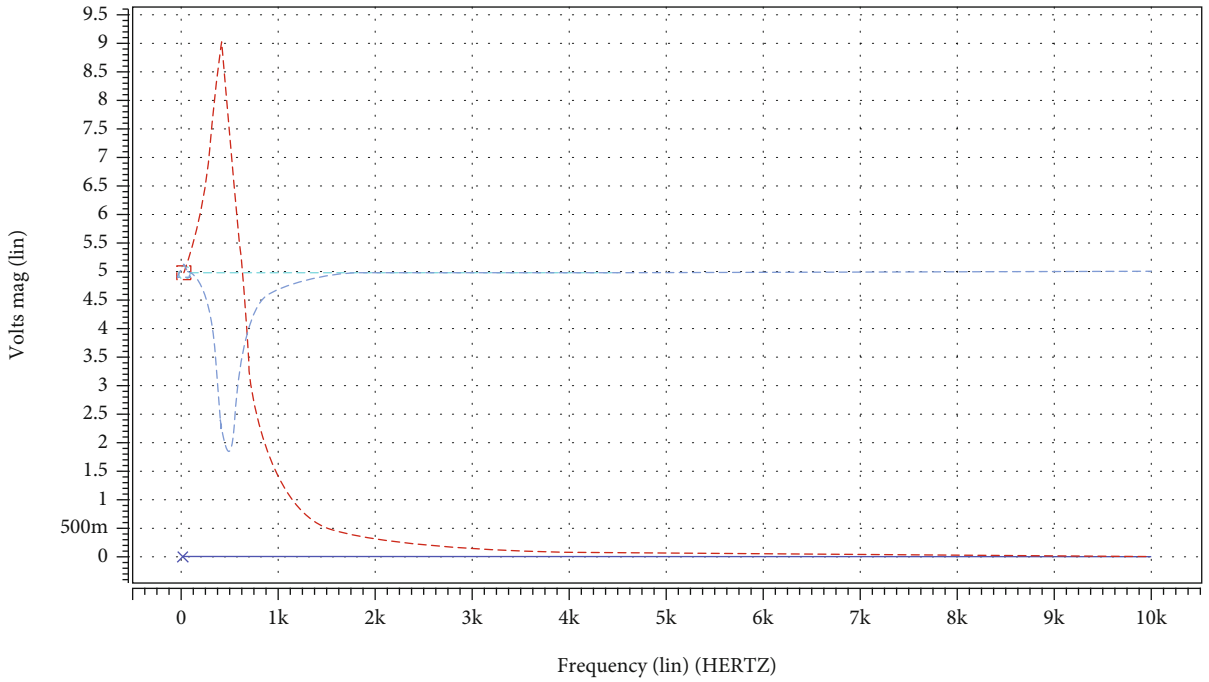

Figure 7: Output voltage analysis.

by using the H-spice simulation tool. Hence, the integration of three software tools is the major requirement for our proposed work.

4.1. Leakage Current. Figure 10 graphically illustrates the leakage current of the proposed ECNFET design with respect to the gate voltage. The leakage current can flow between the source and drain, which is linearly increased with the increase of the gate voltage by minimum leakage current in nanoamps (nA) [33]. In the proposed application, the overall leakage current is reduced to 0.02 nA by using the ECNFET layout.

Figure 11 represents the drain current variations for the proposed ECNFET. With respect to gate-to-source voltage, there is a linear increase of gate-to-source voltage. The graphical variations of drain current show that it increased to 1.65 mA by using the ECNFET layout. On the basis of the threshold and saturation, the overall peak value of the current is estimated.

4.2. Mobility. The mobility defines the movement of electrons and holes from n-substrate to p-substrate, in which the electron conductivity and electron charge carrier are increased, when compared to the holes. The mobility of the proposed ECNFET layout is shown in Figure 12. The linear increase in gate voltage from 0 to 2 V increases the mobility values linearly.

4.3. Transconductance. Typically, the transconductance of ECNFET is based on the current of output device and the voltage of input device. Figure 13 shows the transconductance of the ECNFET design. From the evaluation, it is observed that the transconductance is improved with respect to the varying gate source voltage and is evaluated in terms of V_{GS}.

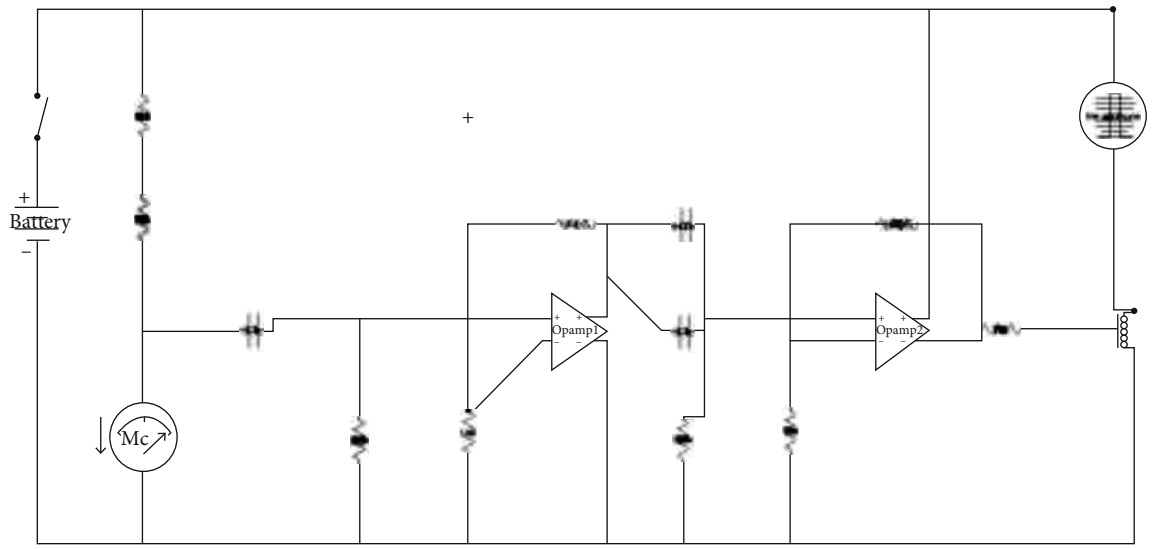

Figure 8: Hearing and filtering application.

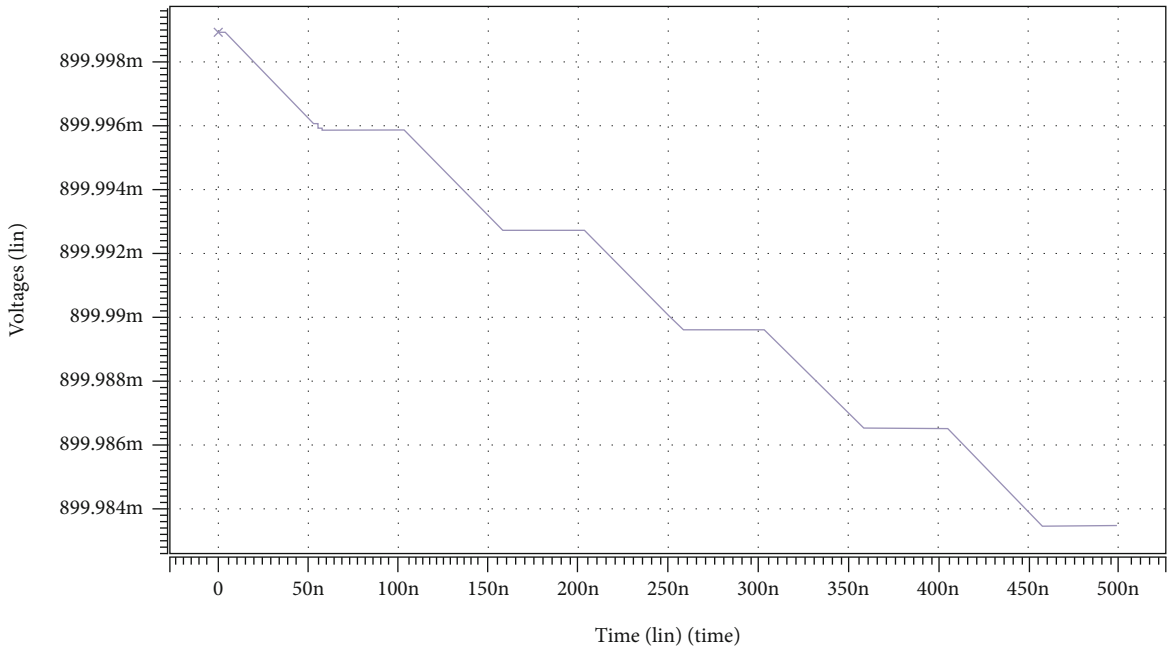

Figure 9: Filter output.

4.4. Area, Power, Frequency, and Speed. Table 1 provides the area consumption, power intake, frequency, and speed of both the existing CNTFET-based filtering design and the proposed ECNFET layout-based filtering design. Here, the amount of area and power required to design the layout is drastically reduced with the increase in the frequency range and speed. In this design, the best materials are used in this circuit design, which reduces the area and power consumption. Also, the operational amplifier improves the frequency range by amplifying the ECNFET layout. Moreover, the hearing aid filter improves the overall efficiency and speed of the system. Based upon the results, it is found that the suggested ECNFET-based hearing aid filtering design provides the better performance, in comparison to the available filtering design.

4.5. Comparative Analysis. Table 2 shows the threshold voltage of existing CNTFET and proposed ECNFET layouts based on varying temperatures. Due to the less heat dissipation mechanism, the heating effect of ECNFET is lower than that of CNTFET, in which the highest value appears in both source and drain, because the heat is nonuniformly distributed. Here, the threshold voltage is calculated with respect to various temperature values, which evaluates the optimized

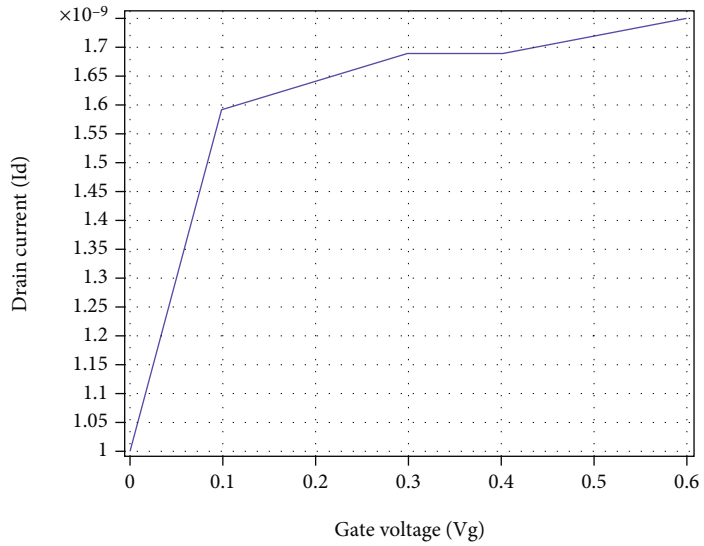

Figure 10: Leakage current.

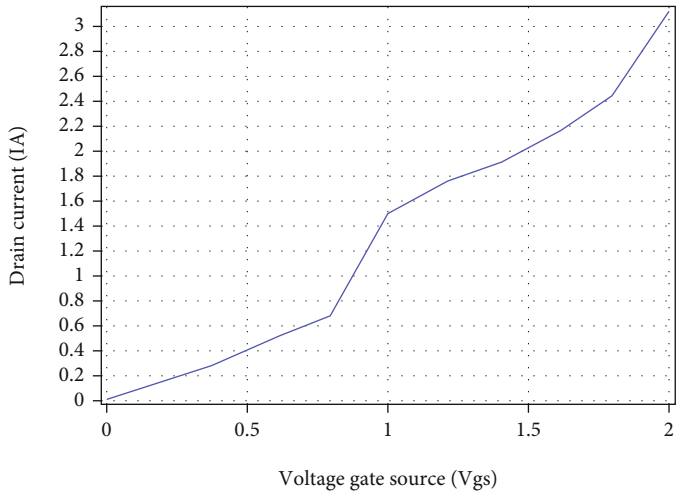

Figure 11: Voltage current.

usage of voltage by the proposed layout. Moreover, different temperatures from 27°C to 227°C are taken to analyze the threshold voltage. For minimum temperature values (27°C), the threshold voltage values for CNTFET and ECNFET are 0.210 and 0.205 V, respectively. Similarly, they are 0.164 and 0.160 V for maximum temperature values 227°C, respectively. The comparative analysis between the proposed ECNFET with the CNTFET shows that the proposed model reduces the threshold voltage values by 2.38 and 2.44%, respectively.

Table 3 compares the threshold voltage of CNTFET and ECNFET with respect to gold and silicon dioxide materials. The threshold voltage variations on CNTFET and ECNFET corresponding to gold and SiO_2 are illustrated in Table 3. In this analysis, various materials are used for estimating the threshold voltage, because each layer has separate voltage. So, selecting an appropriate material for each layer is an

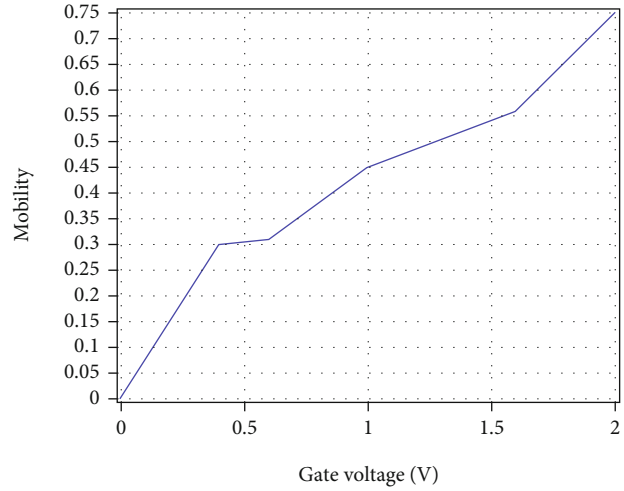

Figure 12: Mobility graph.

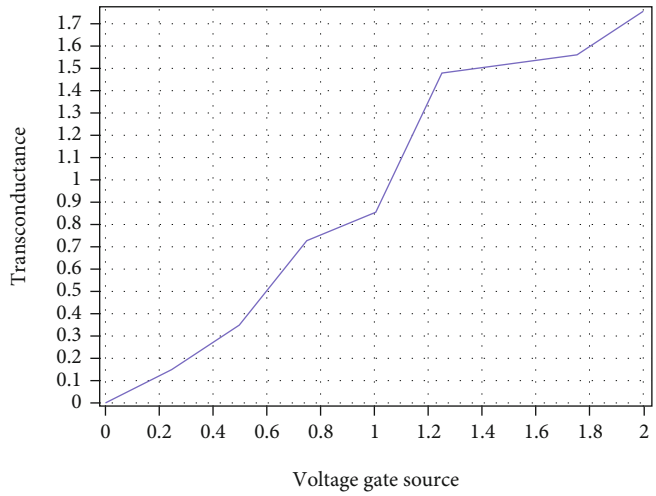

Figure 13: Transconductance analysis.

Table 1: Performance analysis of ECNFET.

Measures	Existing CNTFET filter	Proposed ECNFET hearing aid filter
Area [35]	151 components	134 components
Power [36]	58.96 μw	26.03 μw
Frequency	1.9×10^3 Hz	2×10^3 Hz
Speed [37]	2.8×10^9 m/s	4×10^{11} m/s
Delay [37]	$7.4e^{-12}$	$6.63e^{-14}$

Table 2: Threshold voltage with respect to temperature.

Temperature (°C)	Threshold voltage (V)	
	CNTFET	ECNFET
27	0.210	0.205
47	0.210	0.205
67	0.210	0.204
87	0.210	0.204
107	0.202	0.198
127	0.198	0.197
147	0.194	0.193
167	0.191	0.186
187	0.187	0.182
207	0.180	0.174
227	0.164	0.160

Table 3: Threshold voltage with respect to different materials.

Materials	Threshold voltage (V)	
	CNTFET	ECNFET
Gold	0.210	0.205
Silicon dioxide (SiO_2)	0.240	0.235

important process. For gold material, the threshold voltage values for CNTFET and ECNFET are 0.210 and 0.205 V, respectively. Similarly, they are 0.240 and 0.230 V for SiO_2. The proposed design reduces the voltage values by 2.38 and 4.17%, respectively.

Table 4 compares the drain voltage of the existing CNFET and proposed ECNFET with respect to varying dielectric constants and drain current. The necessity of the drain voltage is decreased for a specific drain current in an ECNFET device. Here, the electric constant is varied for estimating the current value; based on this, the current consumption of the proposed ECNFET layout is calculated. Also, the voltage consumption is highly depending on the current consumption or resistance, so the current consumption must be reduced. Here, the current consumption is reduced with the increase of electric constant.

The reduction of gate layer thickness of 0.6 nm in the proposed layout design reduces the drain voltage further compared to CNTFET models. For the high value of drain current (80 μA) and dielectric constant (19), the drain voltage for CNTFET and ECNFET is 0.40 and 0.39 V, respectively. The comparative analysis between the proposed ECNFET with the existing CNTFET models shows that the proposed ECNFET provides the 2.5% reduction compared to the CNTFET model, respectively.

4.5.1. Limitations of CNTFET

(i) When modelling CNTFETs, a consistent model that is suitable for both analogue and digital applications and capable of mass production must be developed

(ii) The fault tolerance of CNTFET circuits should be investigated

(iii) Scalability of CNTFETs should be thoroughly investigated

(iv) It is necessary to discover new materials for the synthesis and integration of CNTFETs

Table 4: Comparative analysis based on dielectric constant and drain voltage.

Dielectric constant	Drain current							
	20 (μA)		40 (μA)		60 (μA)		80 (μA)	
	CNTFET	ECNFET	CNTFET	ECNFET	CNTFET	ECNFET	CNTFET	ECNFET
3.9	0.30	0.29	0.56	0.54	0.84	0.83	—	0.74
9.0	0.15	0.14	0.28	0.28	0.44	0.40	0.56	0.53
15.6	0.11	0.10	0.22	0.20	0.33	0.31	0.44	0.41
19.0	0.12	0.11	0.18	0.17	0.30	0.27	0.40	0.39

5. Conclusions

This paper designs a new hearing aid filtering application by using an ECNFET layout. Here, five different materials such as gold, silicon, silicon dioxide, bismuth telluride, and single-walled carbon nanotube are placed in the layers, which are selected based on their specific advantages. After selecting these materials, the parameters such as band gap, electron concentration, hole concentration, electron mobility, hole mobility, and insulator breakage voltage are validated. If all the parameters are satisfied, the characteristics of the layout are validated for proving the effectiveness of the proposed design. It includes voltage current, transconductance, mobility, and leakage current, which are all satisfied; the library is created for the corresponding ECNFET layout by using the Comsol tool. After that, the operational amplifier is designed based on the generated library function, which is used to improve the level of frequency. Finally, the hearing aid filter is implemented with the use of ECNFET layout that improves the accuracy of filter by efficiently reducing the noise. The experimental results evaluate the performance of this application based on different performance measures such as area consumption, power consumption, frequency range, and speed. The proposed ECNFET-hearing aid filter provides the better performance in drain voltage, current, threshold voltage, and mobility compared to the existing layout designs.

The proposed ECNFET layout can been used to some other applications such as head phone, telephone, and biomedical devices in the future. The parameter estimation of CNTFET could be investigated further using other cutting-edge intelligent optimization algorithms. The most recent materials may be incorporated into the design of a CNTFET in order to identify the one that will yield the longest life of the CNTFET as well as the best performance.

Data Availability

The data used to support the findings of this study are included within the article. Should further data or information be required, these are available from the corresponding author upon request.

Disclosure

This study was performed as a part of the Employment of Kombolcha Institute of Technology, Wollo University, Kombolcha, Amhara, Ethiopia.

Conflicts of Interest

The authors declare that there are no conflicts of interest regarding the publication of this paper.

Acknowledgments

The authors thank the KPR Institute of Engineering and Technology, Coimbatore, for providing characterization supports to complete this research work.

References

[1] H. Gautam and P. Bindra, "Structure and a detailed analysis of various simulation results of CNTFET: a review," *International Journal of Scientific Engineering and Technology*, vol. 4, no. 2, pp. 32–35, 2015.

[2] S. Yogeshwaran, L. Natrayan, S. Rajaraman, S. Parthasarathi, and S. Nestro, "Experimental investigation on mechanical properties of epoxy/graphene/fish scale and fermented spinach hybrid bio composite by hand lay-up technique," *Materials Today: Proceedings*, vol. 37, no. 2, pp. 1578–1583, 2021.

[3] A. G. N. Raeini, Z. Kordrostami, and M. Javaheri, "High on/off current ratio in SB-CNTFET based on tuning the gate insulator parameters for different ambient temperatures," in *Nano/-Micro Engineered and Molecular Systems (NEMS), 2015 IEEE 10th International Conference on, 2015*, pp. 630–634, Xi'an, China, 2015.

[4] S. K. Sinha and S. Chaudhury, "Impact of oxide thickness on gate capacitance—a comprehensive analysis on MOSFET, nanowire FET, and CNTFET devices," *IEEE Transactions on Nanotechnology*, vol. 12, no. 6, pp. 958–964, 2013.

[5] M. S. Ansari and S. Tripathi, "Carbon nanotubes as FET channel: analog design optimization considering CNT parameter variability," in *IOP Conference Series: Materials Science and Engineering*, p. 012167, India, 2017.

[6] P. Prakash, K. Mohana Sundaram, and M. Anto Bennet, "A review on carbon nanotube field effect transistors (CNTFETs) for ultra-low power applications," *Renewable and Sustainable Energy Reviews*, vol. 89, pp. 194–203, 2018.

[7] B. N. Kumar, A. K. Singh, C. Prabhu, C. Venkataseshaiah, and G. C. Sheng, "Compact analytical model for one dimensional carbon nanotube field effect transistor (CNTFET)," *ECS Solid State Letters*, vol. 4, no. 6, pp. M12–M14, 2015.

[8] K. Hemalatha, C. James, L. Natrayan, and V. Swamynadh, "Analysis of RCC T-beam and prestressed concrete box girder bridges super structure under different span conditions," *Materials Today: Proceedings*, vol. 37, no. 2, pp. 1507–1516, 2021.

[9] S. G. Shirazi and S. Mirzakuchaki, "High on/off current ratio in ballistic CNTFETs based on tuning the gate insulator parameters for different ambient temperatures," *Applied Physics A*, vol. 113, no. 2, pp. 447–457, 2013.

[10] N. Ghaderi and M. Alidadi-Shamsabadi, "A novel ultra high speed and low power phase detector using carbon nanotube field effect transistors," in *Electrical and Electronics Engineering (ELECO), 2017 10th International Conference on*, pp. 467–471, Bursa, Turkey, 2017.

[11] W. Makni, I. Barrage, H. Samet, M. Masmoudi, and M. Najari, "Low noise high frequency CNTFET amplifier," in *Design & Technology of Integrated Systems in Nanoscale Era (DTIS), 2013 8th International Conference on*, pp. 45–49, Abu Dhabi, United Arab, 2013.

[12] M. Moghaddam, M. H. Moaiyeri, and M. Eshghi, "Design and evaluation of an efficient Schmitt trigger-based hardened latch in CNTFET technology," *IEEE Transactions on Device and Materials Reliability*, vol. 17, no. 1, pp. 267–277, 2017.

[13] S.-A. Imam, N. Kalam, and S. Abdullah, "Comparative analysis of control coefficients on the performance of CNTFET under different parameters," *International Journal of Nanoscience*, vol. 15, no. 3, p. 1640005, 2016.

[14] S. K. Sinha and S. Chaudhury, "Comparative study of leakage power in CNTFET over MOSFET device," *Journal of Semiconductors*, vol. 35, no. 11, p. 114002, 2014.

[15] A. K. Dadori, K. Khare, T. Gupta, and R. Singh, "Leakage power reduction technique by using multigate FinFET in DSM technology," in *Proceedings of International Conference on Communication and Networks, 2017*, pp. 233–244, Ahmedabad, India, 2017.

[16] M. Sandeep Kauthsa Sharma, S. Umadevi, Y. Sai Sampath et al., "Mechanical behavior of silica fume concrete filled with steel tubular composite column," *Advances in Materials Science and Engineering*, vol. 2021, Article ID 3632991, 9 pages, 2021.

[17] Y. Wei and Y. Wang, "Design of low complexity adjustable filter bank for personalized hearing aid solutions," *IEEE/ACM Trans Audio Speech Lang Process*, vol. 23, no. 5, pp. 923–931, 2015.

[18] S. R. Kotha, D. Bilaye, U. Jain, and S. S. Kumar, "An approach for efficient FIR filter design for hearing aid application," in *VLSI Design and Test, 18th International Symposium on, 2014*, pp. 1–5, IEEE, 2014.

[19] A. R. Trivedi, S. Carlo, and S. Mukhopadhyay, "Exploring tunnel-FET for ultra low power analog applications: a case study on operational transconductance amplifier," *Proceedings of the 50th annual design automation conference, 2013*, , IEEE, p. 109, 2013.

[20] V. Paranthaman, K. Shanmuga Sundaram, and L. Natrayan, "Influence of SiC particles on mechanical and microstructural properties of modified interlock friction stir weld lap joint for automotive grade aluminium alloy," *Silicon*, vol. 4, pp. 1–11, 2021.

[21] A. Nguyen, Z. Raghebi, F. Banaei-kashani, A. C. Halbower, and T. Vu, "LIBS: a low-cost in-ear bioelectrical sensing solution for healthcare applications," in *Proceedings of the Eighth Wireless of the Students, by the Students, and for the Students Workshop*, pp. 33–35, New York, NY, USA, 2016.

[22] S. Yogeshwaran, L. Natrayan, G. Udhayakumar, G. Godwin, and L. Yuvaraj, "Effect of waste tyre particles reinforcement on mechanical properties of jute and abaca fiber- epoxy hybrid composites with pre-treatment," *Materials Today: Proceedings*, vol. 37, no. 2, pp. 1377–1380, 2021.

[23] Y.-T. Kuo, T.-J. Lin, Y.-T. Li, and C.-W. Liu, "Design and implementation of low-power ANSI S1. 11 filter bank for digital hearing aids," *IEEE Transactions on Circuits and Systems I: Regular Papers*, vol. 57, pp. 1684–1696, 2010.

[24] M. Guo, S. H. Jensen, and J. Jensen, "Novel acoustic feedback cancellation approaches in hearing aid applications using probe noise and probe noise enhancement," *IEEE Transactions on Audio, Speech and Language Processing*, vol. 20, no. 9, pp. 2549–2563, 2012.

[25] S. Kalathil and E. Elias, "Efficient design of non-uniform cosine modulated filter banks for digital hearing aids," *AEU International Journal of Electronics and Communications*, vol. 69, no. 9, pp. 1314–1320, 2015.

[26] A. Pandey and V. J. Mathews, "Low-delay signal processing for digital hearing aids," *IEEE Transactions on Audio, Speech and Language Processing*, vol. 19, no. 4, pp. 699–710, 2011.

[27] K. Ngo, T. Van Waterschoot, M. G. Christensen, M. Moonen, and S. H. Jensen, "Improved prediction error filters for adaptive feedback cancellation in hearing aids," *Signal Processing*, vol. 93, no. 11, pp. 3062–3075, 2013.

[28] A. Pandey and V. J. Mathews, "Improving adaptive feedback cancellation in digital hearing aids through offending frequency suppression," in *Acoustics Speech and Signal Processing (ICASSP), 2010 IEEE International Conference on, 2010*, pp. 173–176, Dallas, TX, USA, 2010.

[29] S. S. Alabsi, A. Y. Ahmed, J. O. Dennis, M. H. M. Khir, and A. S. Algamili, "A review of carbon nanotubes field effect-based biosensors," *IEEE Access*, vol. 8, pp. 69509–69521, 2020.

[30] V. D. Bezzon, T. L. Montanheiro, B. R. de Menezes et al., "Carbon nanostructure-based sensors: a brief review on recent advances," *Advances in Materials Science and Engineering*, vol. 2019, 21 pages, 2019.

[31] B. K. Santhoshi, K. Mohanasundaram, and L. A. Kumar, "ANN-based dynamic control and energy management of inverter and battery in a grid-tied hybrid renewable power system fed through switched Z-source converter," *Electrical Engineering*, vol. 103, pp. 2285–2301, 2021.

[32] W. Shockley, "Electrons and holes in semiconductors," vol. 471, p. 237, 1952.

[33] Q. Gong, *Fabrication and Characterization of Carbon Nanotube Random Network Transistors*, Universität München, 2015.

[34] L. Marques, C. Galup-Montoro, and M. Schneider, "A switched-MOSFET filter for application in hearing aid devices," in *Circuits and Systems, 2001. ISCAS 2001. The 2001 IEEE International Symposium on*, pp. 77–80, Sydney, NSW, Australia, 2001.

[35] M. Bahadori, M. Kamal, A. Afzali-Kusha, and M. Pedram, "High-speed and energy-efficient carry skip adder operating under a wide range of supply voltage levels," *IEEE Transactions on Very Large Scale Integration (VLSI) Systems*, vol. 24, no. 2, pp. 421–433, 2016.

[36] P. Bhattacharyya, B. Kundu, S. Ghosh, V. Kumar, and A. Dandapat, "Performance analysis of a low-power high-speed hybrid 1-bit full adder circuit," *IEEE Transactions on Very Large Scale Integration (VLSI) Systems*, vol. 23, no. 10, pp. 2001–2008, 2015.

[37] R. P. Somineni, B. Madhavi, and K. L. Kishore, "Low leakage CNTFET SRAM cells," *Procedia Computer Science*, vol. 57, pp. 1049–1056, 2015.

Hindawi
Journal of Nanomaterials
Volume 2021, Article ID 3199949, 6 pages
https://doi.org/10.1155/2021/3199949

Research Article

Synthesis and Characterization of the Chitosan Silver Nanoparticle-Reinforced *Borassus flabellifer* Trichome- and *Prosopis juliflora* Wood-Based Nanocomposite for Environmental Application

Ch. Nanda Krishna,[1] **Madhavi Katamaneni**,[1] **Kalyan Chakravarti Yelavarti**,[1] **B. Sobhan Babu**,[2] **B. Ravi Kumar**,[3] **and M. Viju Prakash**[4]

[1]*Department of Information Technology, VR Siddhartha Engineering College, Kanuru, Vijayawada, Andhra Pradesh 520007, India*
[2]*Department of Information Technology, Gudlavalleru Engineering College, Gudlavaleru, Andhra Pradesh 521356, India*
[3]*Department of ECE, Institute of Aeronautical Engineering, Dundigal, 500043 Telangana, India*
[4]*Department of Computer Science, Kombolcha Institute of Technology, Wollo University, P.O. Box 208, Ethiopia*

Correspondence should be addressed to Ch. Nanda Krishna; nkcherukuri@gmail.com
and M. Viju Prakash; vijuprakash@kiot.edu.et

Received 18 August 2021; Revised 24 September 2021; Accepted 4 October 2021; Published 22 October 2021

Academic Editor: Lakshmipathy R

Copyright © 2021 Ch. Nanda Krishna et al. This is an open access article distributed under the Creative Commons Attribution License, which permits unrestricted use, distribution, and reproduction in any medium, provided the original work is properly cited.

Wood is a wide flexible material appreciated extremely for its cost-effectiveness, great quantity, and biocompatibility. In addition, naturally existing materials possess prominent biomedical applications, and they can withstand efficiently when compared to other materials like glass, steel, and plastics. The present study revealed the prepared chitosan, silver nanoparticles incorporated with *Borassus flabellifer* trichome, and fabrication of *Prosopis juliflora* wood-based biomaterial. A characterization study was done by UV-visible spectroscopic analysis, FTIR analysis, and SEM analysis expressing and confirming a significant characteristic and morphological property of the prepared biomaterial.

1. Introduction

Wood is a wide natural reusable material which is important in different industries making the researchers to work on it [1]. The naturally existing porous wood acts as a good carrier to build a functional composite that is still rarely used. Nanotechnology is a promising area to enhance the efficiency and effectiveness towards different bioremediation processes. Its improved reactivity and increased surface area to volume ratio had great impact when compared with those bulk materials [2]. The physical characteristic of chitosan is its flexibility, and studies regarding its properties have been performed and the outcome is very positive [3]. This latest material has its durability, biodegradability, biocompatibility, nontoxicity, and adsorption in pharmaceuticals, agriculture, forestry, skincare products, and food and water treatment applications. Still, it is emerging as an innovator in textiles, health care and pharmaceuticals [4].

In India, the palmyra tree is the official tree of Tamil Nadu. In tradition, it is called askarpaha, a celestial tree, nudged and extremely cherished by the people, and considered a god [5]. Borassus flabellifer includes innumerable essential constituents, gums, fats, albuminoids, carbohydrates were investigated [6]. Silver nanoparticles are considered to have a strong and wide range of therapeutic applications, and even low concentration of silver nanoparticles has been found, in some cases, to possess strong potential to treat a variety of diseases [7]. A nanocomposite is one of the unusual composite materials that are shown to possess a capability of being used as a biometric sensor as well as in numerous treatment protocols. Silver nanoparticle (AgNP) incorporation has a great impact on the water purification

process due to its stability, chemical catalytic ability, low toxicity to humans, and effective antimicrobial property [8].

The present investigation strongly focused on the preparation and characterization of the *Borassus flabellifer* trichome and *Prosopis juliflora* wood, silver nanoparticles (AgNPs), and chitosan with different proportions by UV-visible spectroscopic analysis, FTIR analysis, and SEM analysis.

2. Materials and Methodology

2.1. Chemicals and Samples. From Sigma-Aldrich Chemical Company, USA, the required fine chemicals like silver nitrate were purchased and all other requirements are of first-class analytical grade.

2.2. Preparation of Chitosan Solution (Ch). The purified chitosan was significantly obtained by performing alkaline deacetylation of chitin from crab shells. The mixture was obtained by dissolving 1 gram of chitosan in 100 ml of 0.25 N hydrochloric acid.

2.3. Preparation of the Borassus flabellifer Trichome-Chitosan Biocomposite (TC-Ch). In 50 ml double distilled water, 1 g of *Borassus flabellifer* trichome and 1% chitosan (Ch) were mixed to this solution [9]. The pH of the solutions was adjusted to 7.0, and the resultant materials were used for further use. It was denoted as TC-Ch [10].

2.4. Preparation of Silver Nanoparticle (AgNP) Solution. Silver nanoparticles were prepared by using a modified method of Turkevich. In brief, 30 ml of 1 mM silver nitrate solution was boiled and kept in a magnetic stirrer. Once it starts to boil, add 3 ml of 10 mM trisodium citrate in the ratio of one drop per second and wait till it change into brown color. Finally, it is denoted as AgNPs [11].

2.5. Preparation of the Wood Sample (W). The wood pieces were collected from *Prosopis juliflora*, and the hardwood of the plant was finely powdered. The obtained finely powdered wood sample was collected, and it is denoted as W [12].

2.6. Incorporation of AgNPs and W into the TC-Ch Biocomposites (TC-Ch-AgNPs-W). The prepared TC-Ch biocomposite was soaked in solution having 0.01% of AgNPs and wood sample for about 24 hrs. Silver nanoparticle- (AgNP-) and wood-integrated TC-Ch was taken and dried at 37°C [13]. The obtained material was expressed as TC-Ch-Ag-W.

2.7. Characterization Studies. The characterization studies were performed for *Prosopis juliflora* wood (W), *Borassus flabellifer* trichome- (TC-) prepared AgNPs, Ch, TC-AgNPs, TC-W, TC-Ch, TC-Ch-AgNPs, and TC-Ch-AgNPs-W [14].

2.8. UV-Visible Spectrometric Analysis. A UV-visible spectrum was obtained for different samples observed using a UV-visible spectrophotometry analysis for authentication of availability of the desired/formed molecule. The deionized water was used as a blank.

2.9. FTIR Analysis. IR provides significant data on the rotational and vibrational motion of the specific molecules, and it improves the effective identification and characterizations of the obtained composite interactions evaluated under FTIR to observe structural conformation [15]. All the required measurements were carried out in the range of 400 to 4000 cm^{-1}.

2.10. Morphology Observation. The morphological experiment was performed for TC-Ch-AgNPs and TC-Ch-AgNPs-W by using a JEOL JSM-7401F scanning electron microscope.

3. Result and Discussion

From the present investigation, *Prosopis juliflora* wood (W), *Borassus flabellifer* trichome (TC), silver nanoparticles (AgNPs), and chitosan (Ch) with incorporation of TC-AgNP, TC-W, TC-Ch, TC-Ch-AgNP, and TC-Ch-AgNP-W composites have been prepared by a modified method of the available literature and were systematically partially characterized by UV spectroscopy, FTIR spectroscopy, and SEM analysis, and the obtained results were interpreted with the available literature.

3.1. UV-Visible Spectroscopic Analysis. The optical properties of TC, AgNPs, Ch, W, TC-AgNPs, TC-W, TC-Ch, TC-Ch-AgNPs, and TC-Ch-AGNPs-W were experimented by using UV-visible spectroscopy, and the obtained results are shown in Figures 1–3. The obtained spectrum broad absorption band intensity was compared with that of different proportions like TC, AgNPs, Ch, W, TC-AgNPs, TC-W, TC-Ch, TC-Ch-AgNPs, and TC-Ch-AGNPs-W [16].

The UV-visible spectroscopy analysis for TC, W, Ch, and AgNPs is represented in Figure 1 with the absorptive peak at 282 nm, 285 nm, 320 nm, and 400 nm in the UV region.

The UV-visible spectroscopy analysis was performed for TC-W, TC-Ch, and TC-AgNPs and is represented in Figure 2. Here, *Borassus flabellifer* trichomes (TC) act as a base for Ch, W, and AgNPs. From the obtained results, the absorptive peak was observed at 280 nmin all three different compositions [17].

The biocomposites TC-Ch-AgNPs and TC-Ch-AGNPs-W were subjected to UV-visible spectroscopy analysis to determine the optical property which is represented in Figure 3. It indicated that TC-Ch-AgNPs is not showing any absorptive peak and TC-Ch-AGNPs-W exhibits a peak at 300 nm [18].

From Figure 3, it represents that when four different components (TC, Ch, AgNPs, and W) were mixed, the interaction between one and other molecules with the 1 : 1 ratio has been successfully achieved to form a single bionanomaterial [19]. From the above results, the absorptive peak confirmed that TC acts as a base for the incorporation of Ch, AgNPs, and W.

3.2. FTIR Spectroscopic Analysis. The significant vibrational patterns acquired from FTIR spectroscopic analysis offer the existing functional groups such as nitrogen, carbon,

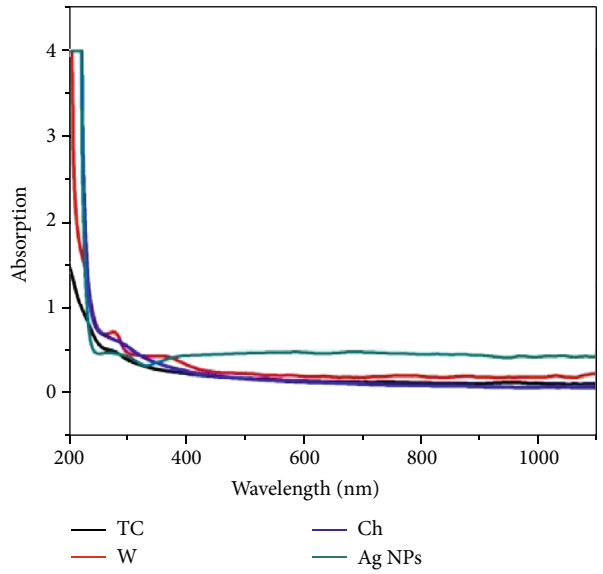

Figure 1: UV-visible spectroscopy analysis for TC, W, Ch, and AgNPs.

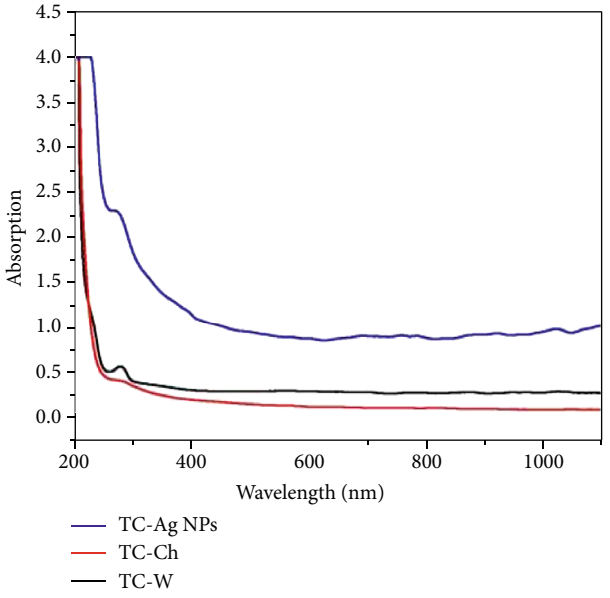

Figure 2: UV-visible spectroscopy analysis for TC-W, TC-Ch, and TC-AgNPs.

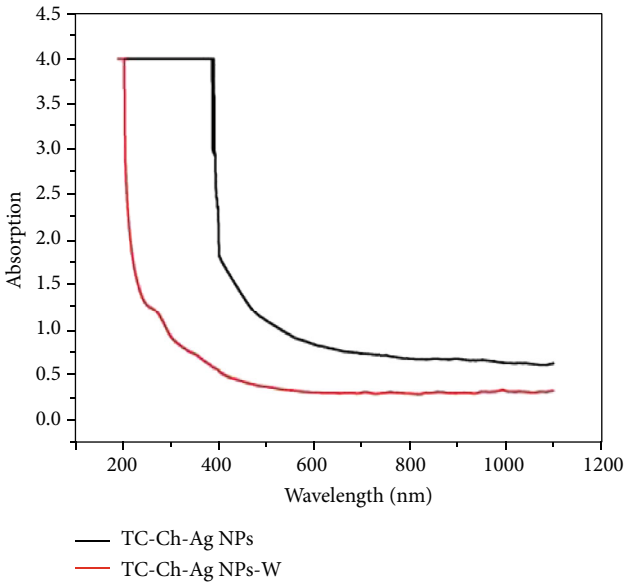

Figure 3: UV-visible spectroscopy analysis for TC-Ch-AgNPs and TC-Ch-AGNPs-W.

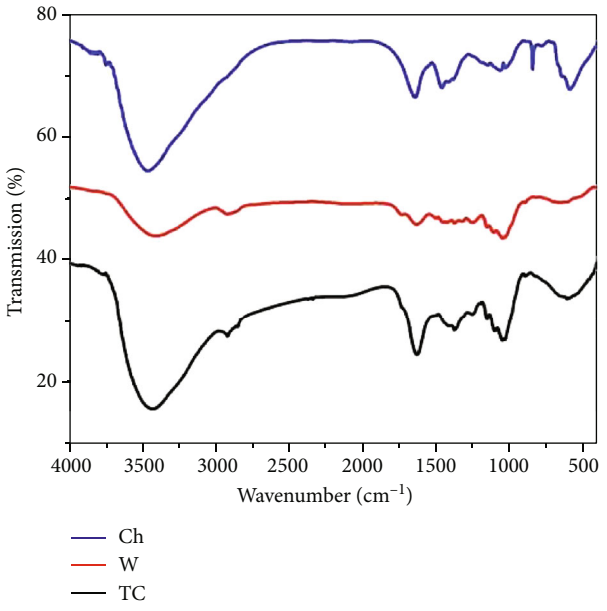

Figure 4: FTIR spectroscopy analysis for TC, W, Ch, and AgNPs.

and oxygen in different samples (TC, Ch, W, TC-AgNPs, TC-W, TC-Ch, TC-Ch-AgNPs, and TC-Ch-AGNPs-W). The FTIR spectroscopic analysis was performed, and the characteristic peak was obtained in the range between 4000 and 500 cm^{-1}. The obtained results are presented in Figures 4–6, and they were interpreted with the available literature [20].

For the chief functional groups for chitosan, a characteristic peak was obtained at 3500 to 3300 cm^{-1} and was attributed to the O-H group of vibrational spreads. Figure 4 shows the FTIR spectroscopy analysis for TC, W, Ch, and AgNPs. The C-H bending vibration of the alkyl group and the N-H bending vibration of the protonated amino ($-NH_2$) group are attributed to absorption peaks at 1630 cm and 1531 cm^{-1}. The peaks at 1059 and 886 cm^{-1} by the glucopyranose ring of the chitosan matrix and antisymmetric detention vibration of C-O-C-bridges are allocated.

The FTIR analysis (Figure 5) for W has shown O-H vibrations with approximately 3200-3600 cm^{-1}. Carboxylic acids of the O-H stretch occur at 290836 cm^{-1} of the *P. juliflora* and 173845 cm^{-1} of the C=O stretch. The 1373 cm^{-1} peak is designed for W with an aromatic amino group of strong C-N stretches. Populations were collected in the C-N alcohol stretch at 1158 cm^{-1}, 1111 cm^{-1}, and 1053 cm^{-1}

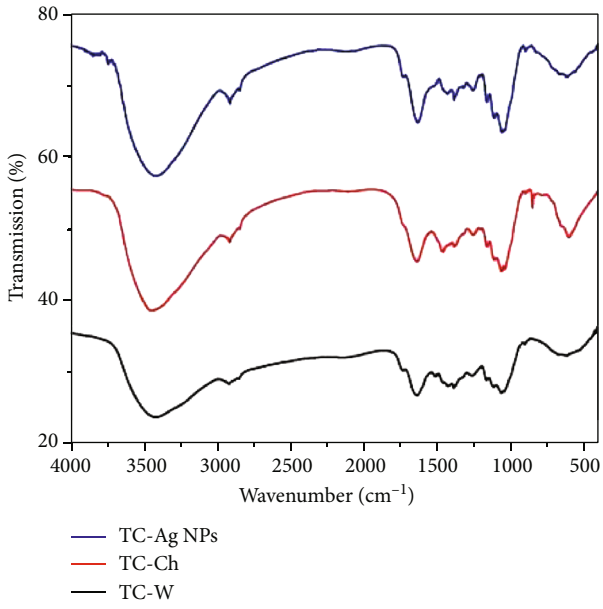

Figure 5: FTIR spectroscopy analysis for TC-W, TC-Ch, and TC-AgNPs.

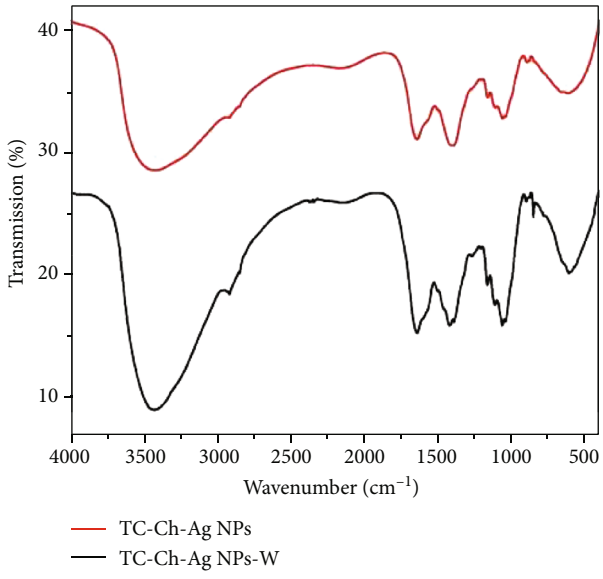

Figure 6: FTIR spectroscopy analysis for TC-Ch-AgNPs and TC-Ch-AGNPs-W.

[21]. The 1400-600 cm^{-1} area has a peculiar pattern of absorption in this region, which is often called a region of fingerprinting because the fingerprints of an individual are unique. Carboxylic acids, amines, and compounds are responsible for hydroxy replacements.

The characteristic FTIR analysis exhibits the TC peak as the parameter went up in 3500 cm^{-1}, the chitosan molecule shifted to 3000 cm^{-1}, and a simple O-H stretching vibration was observed, attributable to the NH stretching of the main functional group. Figure 5 shows the FTIR spectroscopy analysis for TC-W, TC-Ch, and TC-AgNPs. The presence of absorption peaks at 1750 to 1.5 to 3.5H to 15.5 cm^{-1} was triggered by the stretching of the N-protonated amino group

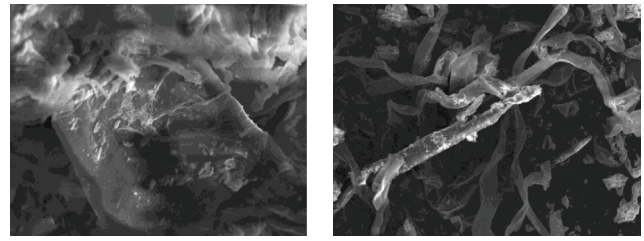

Figure 7: SEM images of (a) TC-Ch-AgNP and (b) TC-Ch-AgNP-W biocomposites.

and alkyl-group bending from 17.5 to 18.5 cm to 19.5 ppm. When the remaining amide groups have a bond stretching intensity of intermolecular bonds, the groups have an N-H vibration at a frequency of 1663.5 cm^{-1}, and when intermolecular bonds are involved, it is at 1500 cm^{-1}. The amide I peak at 1429.9 cm^{-1}, IH2N deformation, 1451.1 cm^{-1}, and 14.2 cm^{-1} NH_2 is given a lifetime of 79 μs which is long [22]. The absorption peak occurs at 1405-680 cm^{-1} due to the asymmetric vibration of the C-O-C bonds in the chitosan matrix and is interpreted as a glucosyl group due to the glucose rings.

For all three samples, TC-AgNPs, TC-W, and TC-Ch, the characteristic FTIR analysis shows the most similar peak with minor alteration. The three peaks at 3500 to 3000 cm^{-1} were expressed having the main functional group of chitosan, which are due to the O-H group of stretching vibrations. The N-H bending vibration of the protonated amino group and C-H bending express the alkyl groups that are responsible for the peaks at 1750 to 1500 cm^{-1}. At 1663.5 cm^{-1} and 1500 cm^{-1} and 1659.5 cm^{-1}, respectively, the existing amide frequencies consist of the remaining acetamido groups' -C-O bond stretch and the N-H bending vibrations of the -NH_2 groups. -NH_2 deformation is responsible for the peaks at 1429.9 cm^{-1}, 1451.1 cm^{-1}, 1418.2 cm^{-1}, and 1419.1 cm^{-1}.

The characteristic FTIR analysis (Figure 6) shows that TC-Ch-AgNPs and TC-Ch-AGNPs-W show most similar peaks with slight modification. The changes were observed that TC-Ch-AgNPs peak was sharp compared then TC-Ch-AgNPs peak, and it was expressed that there was a formation of strong peak with a précised functional group at the peak which represented the above proportions.

3.3. SEM Analysis. SEM investigation gives strong impact to visualize the significant size and shape of the prepared biomaterial with the composition of TC-Ch-AgNPs and TC-Ch-AgNPs-W. The SEM images of these two composites are shown in Figures 7(a) and 7(b).

Figures 7(a) and 7(b) show the improved surface morphology of the prepared biomaterials TC-Ch-AgNPs and TC-Ch-AgNPs-W.

From Figures 7(a) and 7(b), one can clearly see the fibrous nature of chitin with the crumbles, as well as the silver particles and woody texture of the cuticle, particularly under a microscope. The trichome size ranges from 10 to 20 m particles that make up the vast majority of the surface

having a spherical shape, while some particles on the surface appear as single units, but the majority of the rest appears to be aggregated. At the lowest concentrations, silver particles are just about 45 nanometers in size, and the average size of the aggregated particles is about 64 nanometers. The wood sample size is around 55.54 nm, and the chitosan size is around 85.4 nm. SEM images clearly depict the presence of different molecules in the incorporated biomaterial.

4. Conclusion

The present investigation of UV and FTIR characteristic peaks was obtained for TC, Ch, W, TC-AgNPs, TC-W, TC-Ch, TC-Ch-AgNPs, and TC-Ch-AGNPs-W. The UV spectroscopic results expressed a significant peak confirming the presence of molecules. From the FTIR graph, the different functional groups were observed, and it was confirmed that the improved and strong peak was in TC-Ch-AGNPs-W. The SEM images for TC-Ch-AgNPs and TC-Ch-AGNPs-W improved the surface area scanning electron microscopic investigation. It shows the incorporation of Ch and AgNPs to W and TC. The morphograph exhibits fibrous nature with an improved surface area. From the prepared materials, it may have a great impact on the different applications. In addition, it also may offer different bioremediation processes with ecofriendly nature.

Data Availability

The data used to support the findings of this study are included within the article. Should further data or information be required, these are available from the corresponding author upon request.

Disclosure

The study was performed as a part of the employment in Kombolcha Institute of Technology, Wollo University, Kombolcha, Amhara, Ethiopia.

Conflicts of Interest

The authors declare that there are no conflicts of interest regarding the publication of this paper.

Acknowledgments

The authors thank the VR Siddhartha Engineering College, Vijayawada, and Institute of Aeronautical Engineering, Dundigal, for providing characterization support to complete this research work.

References

[1] I. Hussain, N. B. Singh, A. Singh, H. Singh, and S. C. Singh, "Green synthesis of nanoparticles and its potential application," *Biotechnology Letters*, vol. 38, no. 4, pp. 545–560, 2016.

[2] S. Bhakya, S. Muthukrishnan, M. Sukumaran, and M. Muthukumar, "Biogenic synthesis of silver nanoparticles and their antioxidant and antibacterial activity," *Applied Nanoscience*, vol. 6, no. 5, pp. 755–766, 2016.

[3] M. Vidiella del Blanco, E. J. Fischer, and E. Cabane, "Underwater superoleophobic wood cross sections for efficient oil/water separation," *Advanced Materials Interfaces*, vol. 4, no. 21, pp. 170–184, 2017.

[4] J. J. Wang, Z. W. Zeng, R. Z. Xiao et al., "Recent advances of chitosan nanoparticles as drug carriers," *International Journal of Nanomedicine*, vol. 6, pp. 765–774, 2011.

[5] F. Chen, A. Gong, M. Zhu et al., "Mesoporous, three-dimensional wood membrane decorated with nanoparticles for highly efficient water treatment," *ACS Nano*, vol. 11, no. 4, pp. 4275–4282, 2017.

[6] J. Hai, F. Chen, J. Su, X. Fu, and B. Wang, "Porous wood members-based amplified colorimetric sensor for Hg2+ detection through Hg2+-triggered methylene blue reduction reactions," *Analytical chemistry*, vol. 90, no. 7, pp. 4909–4915, 2018.

[7] L. Cabrales, N. Abidi, and F. Manciu, "Characterization of developing cotton fibers by confocal Raman microscopy," *Fibers*, vol. 2, no. 4, pp. 285–294, 2014.

[8] F. Jiang, T. Li, Y. Li et al., "Wood-based nanotechnologies toward sustainability," *Advanced Materials*, vol. 30, no. 1, pp. 17034–17053, 2018.

[9] M. I. Niyas Ahamed, N. Gomathi, V. Ragul et al., "Novel preparation of chitosan from crab shell using probe sonicator and its antibacterial activity," *Journal of Academia and Industrial Research*, vol. 6, no. 8, pp. 133–136, 2018.

[10] C. A. Mecha and V. L. Pillay, "Development and evaluation of woven fabric microfiltration membranes impregnated with silver nanoparticles for potable water treatment," *Journal of membrane science*, vol. 458, pp. 149–156, 2014.

[11] N. Supraja, S. Thiruchenduran, and T. Prasad, "Synthesis and characterization of chitosan nanoparticles and evaluation of antimicrobial activity antioxidant activity," *Advancements in Bioequivalence & Bioavailability*, vol. 2, no. 1, pp. 88–94, 2018.

[12] S. Yogeshwaran, L. Natrayan, G. Udhayakumar, G. Godwin, and L. Yuvaraj, "Effect of waste tyre particles reinforcement on mechanical properties of jute and abaca fiber-epoxy hybrid composites with pre-treatment," *Materials Today: Proceedings*, vol. 37, no. 2, pp. 1377–1380, 2021.

[13] M. I. Niyas Ahamed, S. Sankar, P. Mohammed Kashif, S. K. Hayath Basha, and T. P. Sastry, "Evaluation of biomaterial containing regenerated cellulose and chitosan incorporated with silver nanoparticles," *International Journal of Biological Macromolecules*, vol. 72, pp. 680–686, 2015.

[14] H. M. Ericsson and J. C. Sherris, "Acta Pathologica," *Microbiologica Scandinavica*, vol. 217, 1971.

[15] L. H. Reddy, J. L. Arias, J. Nicolas, and P. Couvreur, "Magnetic nanoparticles: design and characterization, toxicity and biocompatibility, pharmaceutical and biomedical applications," *Chemical Reviews*, vol. 112, no. 11, pp. 5818–5878, 2012.

[16] P. Kumar, M. Govindaraju, S. Senthamilselvi, and K. Premkumar, "Photocatalytic degradation of methyl orange dye using silver (Ag) nanoparticles synthesized from *Ulva lactuca*," *Colloids and Surfaces, B: Biointerfaces*, vol. 103, pp. 658–661, 2013.

[17] M. Goudarzi, N. Mir, and M. Mousavi-Kamazani, "Biosynthesis and characterization of silver nanoparticles prepared from two novel natural precursors by facile thermal decomposition methods," *Scientific Reports*, vol. 6, no. 1, pp. 325–339, 2016.

[18] A. Soroush, W. Ma, Y. Silvino, and M. S. Rahaman, "Surface modification of thin film composite forward osmosis membrane by silver-decorated graphene-oxide nanosheets," *Nano*, vol. 2, no. 4, pp. 395–405, 2015.

[19] R. Suryanarayanan, V. G. Sridhar, L. Natrayan et al., "Improvement on mechanical properties of submerged friction stir joining of dissimilar tailor welded aluminum blanks," *Advances in Materials Science and Engineering*, vol. 2021, Article ID 3355692, 6 pages, 2021.

[20] R. Xing, H. Yu, S. Liu, Q. Zhang, Z. Li, and P. Li, "Preparation of low-molecular-weight and high-sulfate-content chitosans under microwave radiation and their potential antioxidant activity in vitro," *Carbohydrate research*, vol. 339, no. 15, pp. 2515–2519, 2004.

[21] S. Yogeshwaran, L. Natrayan, S. Rajaraman, S. Parthasarathi, and S. Nestro, "Experimental investigation on mechanical properties of epoxy/graphene/fish scale and fermented spinach hybrid bio composite by hand lay-up technique," *Materials Today: Proceedings*, vol. 37, no. 2, pp. 1578–1583, 2021.

[22] D. J. Goodwin, S. Sepassi, and S. M. King, "Characterization of polymer adsorption onto drug nanoparticles using depletion measurements and small-angle neutron scattering," *Molecular Pharmacology*, vol. 10, no. 11, pp. 4146–4158, 2013.

Hindawi
Journal of Nanomaterials
Volume 2021, Article ID 7492532, 12 pages
https://doi.org/10.1155/2021/7492532

Research Article

Production of Nanocellulose Crystal Derived from Enset Fiber Using Acid Hydrolysis Coupled with Ultrasonication, Isolation, Statistical Modeling, Optimization, and Characterizations

Surafel Mustefa Beyan,[1] **Temesgen Abeto Amibo**,[1] **S. Venkatesa Prabhu**,[2] **and Abraham Getahun Ayalew**[3]

[1]*School of Chemical Engineering, Jimma Institute of Technology, Jimma University, Jimma, P.O. Box 387, Ethiopia*
[2]*Department of Chemical Engineering, College of Biological and Chemical Engineering, Addis Ababa Science and Technology University, Addis Ababa, P.O. Box 16417, Ethiopia*
[3]*Central Laboratory, Research and Technology Transfer, Addis Ababa Science and Technology University, Addis Ababa, P.O. Box 16417, Ethiopia*

Correspondence should be addressed to Surafel Mustefa Beyan; surafel.beyan@ju.edu.et

Received 31 August 2021; Accepted 16 September 2021; Published 7 October 2021

Academic Editor: Lakshmipathy R

Copyright © 2021 Surafel Mustefa Beyan et al. This is an open access article distributed under the Creative Commons Attribution License, which permits unrestricted use, distribution, and reproduction in any medium, provided the original work is properly cited.

Currently, many scholars are looking for renewable biomass sources for the isolation of nanomaterials that have a sustainable property and are ecofriendly. Thus, effectively synthesize and characterization enset fiber nanocellulose using acid hydrolysis with sonication is focus of study. Additionally, process optimization for isolation of nanocellulose (CNCs) from raw enset fiber using RSM-CCD and characterizations of obtained CNCs was explored. The quadratic model was selected, and optimized values for CNCs yield (77.69%) that were acquired to be H_2SO_4: 51.6 wt. %, reaction temperature: 47°C, and time: 66.5 min. Chemical composition analysis, XRD, FTIR, PSA, SEM, and TGA were used for characterizing CNCs. The particle size distribution of CNCs is 66 nm. It has a crystalline index of 80.91% and excellent thermal stability. FTIR and chemical composition result indicated the reduction and removal of lignin and hemicellulose components that are usually available in the raw enset fibers. The SEM analysis reveals the structure and arrangement of the fiber bundles inside the raw material to nanocellulose. This property shows its endowing as a possibly consistent load-bearing material. This study could be given a noteworthy thought for designing and emerging CNC isolation, optimization, and industrial application.

1. Introduction

Recently, many scholars are searching for renewable biomass sources for the production material which is an ecoenvironmentally friend and most of all sustainability. In this context, biomasses containing lignocellulosic compounds are the largest access as they are capable of being renewable raw materials for the synthesis of biobased cellulosic nanomaterials, and more than a few researchers have discovered the potential lignocellulosic biomass for supersede fossil-based feedstocks [1–5]. Plants have plenty of cellulose which is the renewable raw material for most biopolymers, and this sight availability of cellulosic material is very abundant as such wood to agricultural waste can be used [6–8]. Ethiopia is one of the fewest countries which are blessed with having more than enough cellulosic-rich materials such as agricultural products, byproducts, and wastes.

Currently, rising attention is being seen in the field of nanotechnology synthesis from potential green-based raw materials which have sustainability [3, 7, 8]. Thus, cellulose nanocrystals (CNCs) synthesized from the plant have wide practical use in various areas due to their physical characteristics, namely, aspect ratio, strength, rheology, lightweight, low density, opticality modification, modification rich hydroxyl group, inexhaustibility, and environmentally friend [9]. Other extraordinary properties of CNCs are their

simplicity for modification and dissolvability in water. The surface of CNCs can be improved with numerous chemical treatments in the direction of any anticipated surface adjustment owing to the profuse hydroxyl groups on the surface of CNCs which provide them reactive. This can successfully make the CNSs ultra practicable and facilitate the integration and dispersion of CNCs into various matrices of polymer. CNCs show great potential in the various applications including a barrier in the separation process of hazardous waste, biomedical products, electronic sensors, paints, and coatings, as the thickener in cosmetics, biodegradable package, and CO_2 adsorbent, as filler of special textiles, food wraps, and texturing agent which replace the nonbiodegradable plastics, and as fillers and rheology modifiers in different fields like foams, aerogels, and polymer electrolytes [9]. It can also be used as nanocomposite materials in polymer science to improve the mechanical, thermal, and ionic conductivity properties of the polymer [4, 8]. For this interesting material, lignocellulosic biomass from different sources has become the most potential renewable and promising feedstock [8, 10]. The cell wall structure of lignocellulosic biomasses mainly consists of components such as cellulose, hemicellulose, lignin, and additionally some extractable components. Agricultural residues, forest residues, and energy crops have been used as raw materials for CNCs. Some of the raw materials for the isolation of cellulose are sugar cane bagasse [11], wheat straw [12], pineapple leaf [3], corn cob [4], arecanut husk fiber [1], water hyacinth [5], and other plants [8]. Among other plants, Enset ventricosum (E. ventricosum) of the steam fiber major components is cellulose (69.51%) and the small quantity of lignin (5.7%) contents while the leaf has cellulose (37.96%) and a high quantity of lignin (18.93%) content [13]. The chemical method has been used for the isolation of fibrotic nanocellulose material from agricultural residues by removing their hemicellulose and lignin components [1, 2, 4, 5, 14]. Commonly, the isolated nanocellulose is a colloidal suspension with transparent optical property [5].

To obtain a fiber with nanosize, several studies have evaluated the use of mechanical treatment for instance sonication, high-speed blender, high-pressure homogenization, ultrafine grinder, and ball mill [3, 5, 11]. Nevertheless, this treatment by itself is not efficient to separate hemicellulose, cellulose, and lignin. The combination of sonication and chemical treatment can yield pure CNCs. Among the different mechanical treatments, the sonication method has been proved to be the simplest technique to produce pure Cs fibers in combined with chemical treatments [5].

Enset ventricosum, commonly known as enset, is *a monocarpic* perennial flowering plant native to Ethiopia. It is a drought-resistant plant that is cultivated in more than 200,000 hectares in a wider range of altitude 1100-3000 m of central, southern, and southwestern parts of Ethiopia. It is harvested as food in most of Ethiopia especially in the southern part where it is utilized as nutritional food [13]. As they prepared it for food, a large amount of biomass residues is generated in the process mainly from the enset steam, (i.e., many bundles of fiber are obtained from the leaf sheath and the steam after being scrapped to produce *Bula* and *Kocho* which are starchy food) and stack of inflorescence. According to the report by Berhanu et al., 2021, about 150,000 tons of fiber bundles residue are produced annually from enset in Ethiopia. Thus, this enormous quantity of fibers residue could be used to produce CNC products. Several studies have evaluated responses to enset in growing cattle and horses, and its potential has been proven on the production of different products, namely, pulp and paper, food, and medicinal application [15–17]. To date, beyond these studies, no work has been carried out concerning enset fiber-based cellulosic nanomaterial. Keeping the view on the significance of CNCs, there is an immense need for researches on CNC production from an economical source which involves extracting fiber and process optimization for improved production of cellulose nanocrystal. Consequently, enset fiber, lignocellulosic biomass, is the largest reservoir of renewable cellulose source in Ethiopia, and cellulose nanocrystal can be isolated from it.

Up to date, no significant study has been done on the production of cellulose nanocrystal from enset fiber (E. Ventricosum). Thus, the focuses of this study are as follows: (I) novel synthesis of cellulose nanocrystal form enset fiber using chemical hydrolysis technique coupled with sonication, (II) the investigation of the chosen prosses parameters, namely, acid concentration reaction time, and reaction temperature, on the significant of hydrolysis on the yield of cellulose nanocrystal, and (III) the interaction effect of the designated factors was designed with five-level response surface central composite design approach (RSM-CCD); further, the obtained nanocellulose was characterized using different techniques.

2. Materials and Methods

2.1. Materials. Enset ventricosum plant was obtained from enset harvesting area located at Kefa, southwest, Ethiopia. Bundles of enset fiber (EF) are obtained from the stem and leaf sheath after the enset has been scrapped. Sodium chloride (NaCl-99%), toluene (C_7H_8-99%), ethanol (C_2H_5OH-98%), sodium hydroxide (NaOH), sodium hypochlorite (NaOCl), acetic acid (CH_3CH_2OOH), sulfuric acid (H_2SO_4), and distilled water were used in EF preparation. The chemical reagent used in this study was analytical grade, and they were obtained from the Department of Material Engineering, Jimma Institute of Technology, Jimma University, Jimma, Ethiopia.

2.2. Preparation of Enset fiber. As described in the material section, the fiber is isolated from the enset, and it was dried under the sun for five days. The dried fiber was chopped, grounded, and sieved through a mesh size of 60 (250 μm). Finally, the acquired fiber powder was put in a polyethylene bag and stored in a desiccator till further experimental work. The dewaxing process was carried out, 2 : 1 v/v mixture ratio of toluene and ethanol and in sox-let apparatus at 120°C using oil bath for 5 h to get rid of extractive components such as wax, debris, pectin, and oils. The dewaxed fiber was rinsed with distilled water and ethanol frequently and

finally, it was filtered using a 45 μm sieve to remove solvents and at last, it was dried in the oven at 45°C for overnight.

2.3. Alkaline Pretreatments of Enset fiber. To remove lignin and hemicellulose from EF, alkaline treatment was carried out accordingly. The dewaxed EF was treated with 15% NaOH solution in the ratio of 1 : 20 in a high-pressure autoclave at 4 bars for 6 hr and 130°C under steady agitation of 500 rpm. The treated EF was excessively washed with distilled water till the pH is neutral and dried under the sunlight for three days till it has constant weight.

2.4. Bleaching of Enset fiber. The dried EF was bleached by soaking it in a 4 : 1 v/v ratio mixture of acetic acid and 6% sodium hypochlorite solution under a pH of 4 for 2 hr and 60°C. Throughout the process of bleaching, the color of EF changed to clear white. The processed fiber came to neutralize by rinsing it with distilled water successively. Lastly, cellulose was put in a deep freezer to obtain powder cellulose. The powder cellulose was sealed in a polyethylene bag and kept in a desiccator till further experimental work. Bleaching was done to remove the remaining hemicellulose and lignin completely from the EF.

2.5. Cellulose Nanocrystal Isolation from Enset fiber Using RSM. The bleached cellulose was hydrolyzed in different concentrations of H_2SO_4 with a 1 : 15 v/w ratio of acid, and the reaction time and temperature were also varied according to the central composited design experiment set up (Table S.1) and the bleached cellulose, under a controlled condition and continuous agitation at 500 rpm. The reaction was quenched by adding ice to the mixture to halt the reaction, and the resulting mixture was then cooled to room temperature [18]. The hydrolyzed cellulose was washed frequently with distilled water till the pH is neutral. Furthermore, the hydrolyzed cellulose was dialyzed against deionized water via a cellulose membrane for five days to neutralize and fully remove the remaining acid and other unwanted chemicals. Subsequently, the dialysis suspension of CNCs was sonicated at 20 kHz of frequency and 600 W power supply for 1 hr in an ultrasonic crusher to get aqueous homogenized dispersion, and the resulting nano cellulose was labeled as the CNCs suspension.

For the hydrolysis process, three parameters (Table S.1) were selected after the survey of previous related works from different works of literature [14, 19, 20]. For the RSM study, the experiment set up of chosen parameters was determined using CCD. This statistical tool technique guarantees that each factor and its relations are systematically studied [21].

Using CCD and experimental data, a polynomial Eq. (1) as a process model can be fitted. The statistical analyses of the experimental data can be performed by using Design Expert 12.0, Stat-Ease, Inc., Minneapolis, MN.

$$Y = \beta_0 + \sum_{j=1}^{k} \beta_j X_j + \sum_{j=1}^{k} \beta_{jj} X_j^2 + \sum_{i} \sum_{<j=2}^{k} \beta_{ji} X_i X_j + e_i, \quad (1)$$

where Y is the yield of CNCs $[(W_1/W_2) \times 100\%)]$. W_1 and W_2 refer to the dry weight of bleached fiber after and before hydrolysis sonication, respectively; X_i and X_j represent parameters (i and j ranging from 1 to k). β_0 represents the intercept coefficient. β_j, β_{jj}, and β_{ij} are known interaction coefficients for the corresponding terms, k is the number of selected independent variables ($k = 3$ in this study), and e_i is an error term [22].

Moreover, the constraints were optimized using numerical optimization to maximize the yield. Analysis of variance (ANOVA) was accustomed to check the competence of the model for the experimental response. It is a statistical tool applied for analyzing any variation in the average performances of tested constraints [23]. The optimal values of the selected constraints were reached through analyzing the equation of regression. Effects of interaction between the parameters were examined through developing response surfaces [24]. The developed model was validated through prediction using the feature of prediction point of the Design-Expert software, and experimental runs were carried out in triplicate.

2.6. Characterizations of Enset fiber and Cellulose Nanocrystal

2.6.1. Chemical Composition. The enset fiber was characterized in terms of its physiochemical properties. American Society for Testing and Materials (ASTM International) standard methods and Technical Association of the Pulp and Paper Industry (TAPPI) were used for characterization of the enset fiber. Three grams of the prepared dried material was used for testing each sample according to the standard test.

2.6.2. Particle Size Determination of CNCs. The particle size of CNCs which is diluted in distilled water was determined using dynamic light scattering (DNS) by the Malvern Zeta Nano (ZE3600) system. This method is also described as photon correction spectroscopy in that sample's particle size that is analyzed by measuring arbitrary variations in scattered light intensity from a solution. The measurement was carried out at 25°C with a calibration time of 60 sec. The obtained data were then processed by using Malvern Zeta sizer software.

2.6.3. Scanning Electron Microscope (SEM). SEM (FEI, INSPCT-F50, Germany) was utilized to investigate the surface image of EF, bleached cellulose, and CNC samples. This operation was done under a vacuum at an accelerating voltage of 2 kV.

2.6.4. X-Ray Diffraction (XRD). The alteration in crystallinity of the samples from EF to cellulose nanocrystals was determined by X-ray diffraction ((XRD – BTX, inXitu, inc, USA) patterns. The powder of EF, bleached cellulose and CNCs samples were scanned at room temperature with an angle in the range of 5° to 80° and a step size of 0.03°. The crystallinity percentage area (Eq. (2)), d-spacing (Eq. (3)) and average crystallite size (Eq. (4)) from XRD data were found by using the Scherrer equation (1). Origin Lab program (Origin Pro-2018) was used for processing peak

observed data.

$$\text{Crystallinity (CI) (\%)} = \frac{\text{Area ofcrystalline peaks}}{\text{Area of all peaks (Crystalline + Amorophous)}} \times 100, \quad (2)$$

$$d - \text{spacing}\left(\mathring{A}\right) = \frac{K\lambda}{\beta \cos\theta}, \quad (3)$$

$$D\,(\text{nm}) = \frac{k\lambda}{\beta \cos\theta}, \quad (4)$$

where D is the crystallite size in nm, K is 0.9 (Scherrer constant), λ is 0.15406 nm which is the wavelength of the X-ray sources, β is the full width of half maximum (FWHM) in radians, and θ is the peak position in radians.

2.6.5. Fourier Transform Infrared Spectroscopy (FTIR). FTIR (FTIR- iS50 ABX, Germany) analysis was carried out in order to investigate the functional groups of EF, bleached cellulose, and CNC samples. The samples were analyzed with a spectrum wavenumber range of 400 cm^{-1} to 4500 cm^{-1} and an average scanning rate of 250. KBr pellet technique was accustomed to accomplish FTIR analysis.

2.6.6. Thermographic Analysis (TGA). Thermogravimetric analysis (TGA) was used to analyze the thermal decomposition properties of enset fiber, bleached cellulose, and nanocellulose. Before the analysis, the fibers were dry for 24 h at 65°C and saved in a desiccator. These fibers are cut into fine parts and then analyzed by using an aluminum pan from 25°C to 600°C under the atmosphere of inert nitrogen through 100 ml/min of flow rate and 10°C/min of heating rate.

3. Result and Discussion

3.1. Isolation, Interaction Effect, and Parameter Optimization of CNCs via CCD-RSM. The interaction of factors with each other and the optimum operating conditions for the isolation of nanocellulose from raw enset fiber via using acid hydrolysis were examined using a central composite design. The observed and predicted results are presented in Table 1.

3.1.1. Model Fitting and Analysis of Variance. The weight of each factor for all models was assessed via analysis of variance (ANOVA). From the various choices of models, a quadratic model is selected after studying R^2 values, P values, and lack of fit, and the quadratic model of mathematical equations for the estimation of CNCs yield is given in Eq. (5).

$$\begin{aligned}\text{Yield (\%)} = {} & +77.04 + 3.96 \times A + 3.39 \times B + 2.56 \times C \\ & - 0.875AB - 2.03AC - 0.355BC - 11.24A^2 \\ & - 11.02B^2 - 17.46C^2.\end{aligned} \quad (5)$$

The summarized ANOVA is presented in Table S.2. The outcomes gotten in Section 3.1 are explored, coefficient determination (R-squared) for the yield of CNC response from the raw enset fiber weighed 0.9930, and this signified that 99.30% of the response was agreed upon and it could be described amid of the quadratic model. Better yet, the model has inconsistency predicting the response with only 0.70% of extent. Therefore, the higher R-square implied that the predicted value by the quadratic model and the actual response values were very close to one another [25], and this information is also supported by predicted vs. actual data (Figure S.1). Again, the model was very consistent to be promising in investigating the data since Adj R-square is 0.9877, and the pred R-square is 0.9579 proving that they were reasonably in agreement with one another since their difference is less than 0.2 [21].

The consequence of the constraints was examined using F-value and p-value. And, the lesser p-value and higher F-value indicated that the chosen model is extremely significant [21, 26]. Thus, the quadratic model has an F-value of 170.61 and a p-value of less than 0.0001. The terms of the model can be significant if the p-value is less than 0.05 [27]. Accordingly, the process parameters for the isolation of CNCs from raw enset fiber, A, B, C, AC, A^2, B^2, and C^2 were obtained to be quite significant. The lack of fit P value for isolation yield of CNCs was 0.0543 which was not noteworthy compared to the pure error. Signal-to-noise ratio was determined via Adeq precision, and its values were observed to be 34.9332 which indicated an adequate signal for the production of CNCs. it signifies the reputation of the quadratic model if the ratio was more than four. Thus, this model for CNC yield is capable of being considered to use for the navigation of design space. Besides, the coefficient variation (4.35) wants to be smaller since a lower value of it favors the precision with which the experiments were carried on [28].

The model accuracy can be tested by comparing and contrasting the actual value with the predicted value as shown in Figure S.1. It can fairly be inferred from the graph that both values, experimental and predicted data, are close enough to each other. Correspondingly, the smaller predicted residual sum of squares (PRESS) statistic indicates the wellness of data points fit the model [23]. Normal probability plots are too an appropriate graphical technique for analyzing the normality of the residuals [26]. A normal plot of residuals among the normal probability (%) and the internal student zed residuals was gotten to analyze how well the model satisfies the assumptions of ANOVA. The internally student zed residuals can also be used to measure the standard deviations separating the experimental and predicted values [23]. Figure S.1 illustrates the association between the normal probability (%) and the internal student zed residuals. The straight line specifies that neither any transformation of response is required nor outward problem with normality.

3.1.2. Analysis of Interaction Effects of the Parameters. Using the support of the RSM-CCD method, the significant effects of the process constraints, namely, reaction time, reaction temperature, and H_2SO_4 concentration, were investigated on the isolation yield of CNCs. By putting one variable

Table 1: CCD experimental design matrix of the three factors and corresponding response.

Run	Factor 1	Factor 2	Factor 3	Response: CNCS yield %	
	A: H_2SO_4 Conc (wt. %)	*B*: reaction temperature (°C)	*C*: reaction time (min)	Actual value (mean + SD)	Predicted value
1	60	60	90	45.18 ± 0.05	43.94
2	40	60	40	35.52 ± 0.05	33.39
3	60	60	40	45.08 ± 0.025	43.62
4	50	45	107	30.59 ± 0.033	31.96
5	50	45	65	77.68 ± 0.05	77.04
6	50	45	65	75.52 ± 0.05	77.04
7	50	45	65	78.65 ± 0.075	77.04
8	50	45	23	20.94 ± 0.05	23.36
9	40	30	40	25.61 ± 0.05	24.14
10	50	45	65	78.23 ± 0.0667	77.04
11	50	45	65	76.94 ± 0.0333	77.04
12	33	45	65	36.12 ± 0.667	38.58
13	40	30	90	35.12 ± 0.033	34.03
14	67	45	65	50.56 ± 0.05	51.89
15	50	45	65	75.85 ± 0.025	77.04
16	50	70	65	49.12 ± 0.033	51.57
17	60	30	40	39.05 ± 0.1	37.87
18	40	60	90	43.36 ± 0.1	41.86
19	60	30	90	40.19 ± 0.02135	39.64
20	50	20	35	38.82 ± 0.0333	40.16

SD: standard deviation.

constant, the interaction effect of two variables at a time on CNC yield was determined and presented as following using 3D response surface plots (Figure 1).

The interaction effect of acid concentration (H_2SO_4, wt. %) and reaction temperature (°C) is shown in Figure 1. Based on the plots obtained, it is seen that the yield increases as H_2SO_4 concentration is from 33.18 to 50 wt. % and reaction temperature 20 to 45°C, but the further increment of both parameters has a negative response to the CNC yield. As it is given from the response variable of the coded equation, the combined interaction effect of reaction time and the temperature has a negative effect on the yield of CNC isolation with the coefficient of -0.8750 (Eq. (5)). In another word, higher acid concentration and reaction temperature result in low isolation yield. The pick for isolation yield was obtained at 50 wt. % of H_2SO_4 and 45°C of reaction temperature.

The interaction effect of acid concentration (H_2SO_4, wt. %) and reaction time (min) on the isolation yield of CNCs is depicted in Figure 1. The efficiency of isolation became increased with increasing reaction time until it reaches 65 minutes for an acid concentration of 50 wt. %. Further increases in both resulted in low CNC yield. As it is presented from the quadratic equation of the response (Eq. (5)), the interaction effect of acid concentration and reaction time of raw enset fiber has a negative effect on isolation yield with a coefficient of -2.03. The maximum isolation yield is attained at a reaction time of 65 minutes and an acid concentration of 50 wt.%.

The interaction effect of reaction temperature (°C) and time (min) of enset raw fiber on CNC yield is shown in Figure 1. As it is illustrated through the 3D, it is well observed that the isolation yield of CNCs from the raw enset fiber increases with increasing the reaction temperature from 20 to 45°C and reaction time from 23 to 65 minutes. The combined interaction effect of reaction temperature and time affects the isolation yield negatively with the coefficient of – 0.3550 (Eq. (5)). The maximum isolation yield of CNCs is gotten at the reaction temperature of 45°C and a reaction time of 65 minutes.

H_2SO_4 concentration, reaction temperature, and time are the utmost significant parameters on the synthesis of CNCs during the acid hydrolysis isolation process. Reaction time affects various CNCs characterization such as crystallinity index, size, and most of all, the yield. This is due to as reaction time increases, some hydrolyze crystalline surfaces will, in turn, decrease the yield and as time is lower, the polymerization rate will be high due to undispersed fiber, and also the obtained nanocellulose will have an amorphous structure and larger diameter. According to different previous studied data, reaction time varies from 30 min to 4 hr [1, 14, 19, 20, 29]. The concentration of sulfuric acid has a potential effect on synthesizing of CNCs. H_2SO_4 concentration can range from 40 to 60 wt. %, and it has been widely

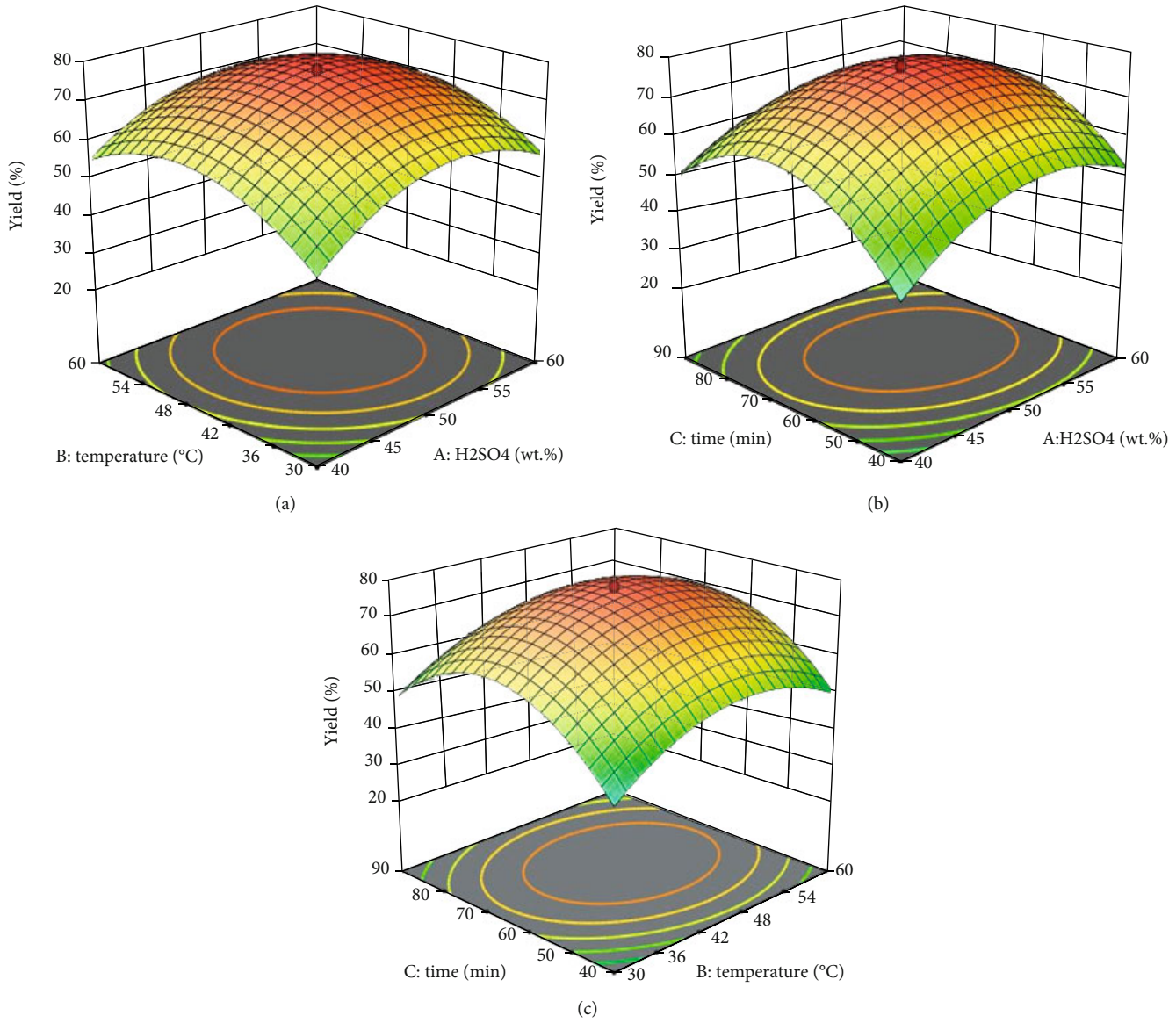

Figure 1: 3-D illustrations of response surface curve for the interaction of effect. (a) H_2SO_4 (wt. %) concentration and reaction temperature (°C). (b) H_2SO_4 concentration and reaction time (min). (c) Reaction temperature and reaction time on CNC production from EF.

used for the isolation of nanocellulose from residues of agriculture. The other parameter which has a significant role in the yield increment of nanocellulose is reaction temperature. At low temperatures, most of the process reactions takes a long time to get the desired yield and at high temperatures, the reaction is hard to control. The temperature can range from 25 to 70°C. Previous works on the isolation of nanocellulose via acid (H_2SO_4) hydrolysis are briefed in Table 2.

3.1.3. Optimized Condition for CNC Yield and Parameter Validation. The experiment has been performed, pretreatments, and interaction via the aid of RSM. The sole purpose of all of these is an examination for optimum operating conditions but nothing more. The isolation process of CNCs from raw enset fiber is governed by at least the three variables that were discussed in the above sections. The search for optimum numerical values of these variables on isolation yield was summarized in Table S.3.

Grounded on the criteria set in Table S.3, the optimum values of H_2SO_4 concentration, reaction temperature, and reaction time for isolation of CNCs from raw enset fiber come out to be 51.6 wt. %, 47°C, and 66.5 minutes, respectively, and with these parameters, the isolation yield of CNCs was 77.69% with a desirability of 0.983. Finally, to validate the parameters, a triplicate experimental run was conducted at optimum conditions and showed a good agreement with the predicted isolation yield (4.27% error).

3.2. Characterizations

3.2.1. Chemical Composition Analysis. The compositional characteristics of EF after each step of treatment are presented in Table 3. The raw enset fiber contains 32.68%

Table 2: Different works on the isolation of nanocellulose using acid hydrolysis.

Raw materials	H_2SO_4 concentration (wt. %)	Condition Reaction temperature (°C)	Reaction time (min)	Yield %	Crystalline index (%)	Particle size (nm)	References
Sugar cane bagasse	60	50	40	65	65.37	—	[30]
Sisal fiber	60	45	30	—	75	30.9	[20]
Laminaria japonica	51	30	70	52.3	69.4	—	[2]
Rice hulls	63.7	45	60	—	70	100	[19]
Corncob	62	44	90	23.5	79.3	70	[14]

Table 3: Chemical compositions of EF for each stage of processing.

Sample	Cellulose (%)	Hemicellulose (%)	Lignin (%)	MC (%)	AC (%)	VM (%)
Raw EF	40.09	32.68	10.53	15.76	4.15	8.46
Pretreated and bleached	51.37	22.26	5.8	—	—	—
Hydrolysis	80.91	14.53	2.91	—	—	—

hemicellulose, 40.09% cellulose, and 10.53% lignin. Before the treatment of EF, the content of lignin is very high due to the bonding between hemicellulose and lignin that is close. Most agriculturally based raw materials have similar cellulose content such as teff straw (36.7%) [31], arecanut husk fiber (34.18%) [1], coffee husk fiber (41.34%) [32], straw of wheat fiber (43.2%) [12], Laminaria japonica (42%) [2], and sisal fiber (50%) [20].

The purpose of alkaline pretreatment and digesting of EF is to break down the bond between hemicellulose and lignin and as a result, it decreases the proportion of hemicellulose and lignin content in the raw enset fiber [1, 33, 34]. The result after the treatments validates that the process effectively removed hemicellulose and lignin as has been established in works of literature. The results were also reinforced by FTIR and SEM characterization.

Alkaline pretreatments followed by digesting and hydrolysis coupled with sonication result in a higher increment of celluloses of the enset fiber from the raw enset fiber. This is due to the disintegration of hydrogen bond linkage among hemicellulose and cellulose chains and also hemicellulose decomposition [1, 35, 36]. This process has increased the crystallinity of the material. The XRD characterization and previous works are in agreement with these results [5, 20].

3.2.2. Particle Size Distribution. DLS is commonly accustomed for the measurement of particle size in colloids, suspensions, polymer, emulsions, etc. The lead of this system is it has a significant up to 1 nm in measuring the particle size. The particle size distribution of CNCs prepared by the process of acid hydrolysis coupled with sonication is presented in Figure 2. The result reveals that the fiber isolated from enset is in the range of nano (66 nm), and it has an intensity of 100%.

Britannica reported that the nanoparticle sizes can vary between 1 nm to 100 nm ranges [37]. [38, 39] reported that the nanocellulose size of 115 nm and 70 nm, respectively. [40] reported that the size distribution of nanocellulose is about 100 nm with a unimodal peak. Determining the distribution of particle size by laser diffraction produces the most promising results [41].

3.2.3. SEM Analysis. The dimension and the morphology of the enset fiber are affected by acid hydrolysis and sonication treatment. Figure 3 presents the SEM morphology of the enset fiber at different steps of treatments.

Figure 3(a) presents the SEM morphology of raw enset fiber. The untreated raw enset fiber surface is accredited to the existence of lignin, hemicellulose, wax, pectin, oil, etc. Succeeding treatment with alkali and bleaching of enset fibers produces surface morphology that confirms removal of lignin, hemicelluloses, and other extractives components (Figure 3(b)). The effect bleaching treatment with the mixture of acetic acid and sodium hypochlorite solution was manifest through the assessment of surface morphology in Figure 3(b). This phenomenon is also supported by physiochemical composition analysis. It is observed that the enset fiber separated into individual fibers and finally, the CNCs were isolated from it using acid hydrolysis and sonication of the fibers (Figure 3(c)). Further, it indicates that practically all of the components that attach the fibril bundle assembly of the enset fibers were eliminated under the strong chemical treatment and sonication.

The obtained result also demonstrates the effectiveness of the parameters used during hydrolysis and also validates that CNCs' aqueous suspensions contained individual nanocrystals. From these images (Figure 3(c)), it is also observed that the chemical treatment coupled with mechanical treatment affects the morphological structure of the fibers concerning the size.

3.2.4. XRD Analysis. The XRD intensity curve of raw enset fiber, encet fiber cellulose, and CNCs is presented in Figure 4. Peaks at $2\theta = 15.58$ and 22.13 have appeared in

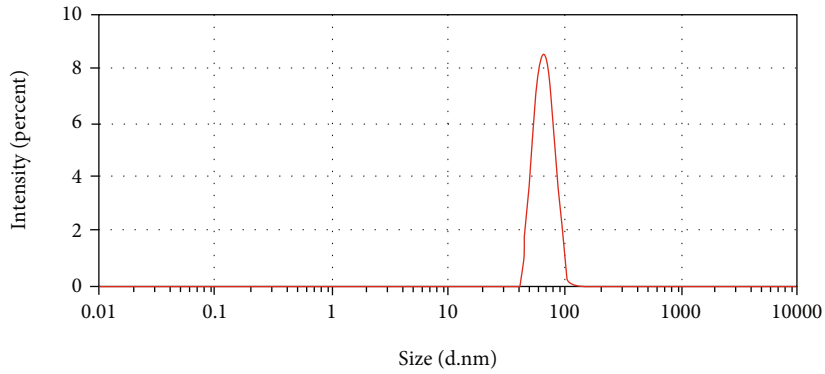

Figure 2: Size distribution of CNCs by the intensity.

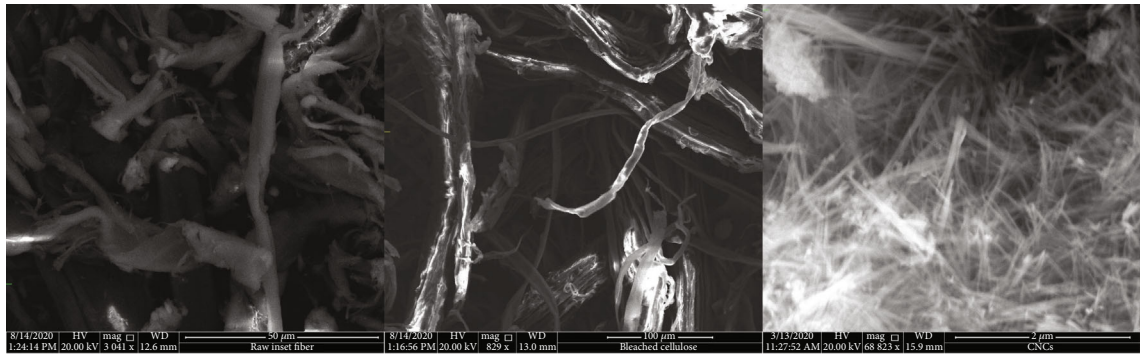

(a) (b) (c)

Figure 3: SEM morphology of (a) raw enset fibers, (b) bleached cellulose, and (c) CNCs.

Figure 4, which signifies the characteristics features of the crystalline region. This typicality is alike to cellulose type-I material. According to previous literature works, these crystallographic planes epitomize the CNC sample in structural category of cellulose Iβ [42]. There is a valuable difference in the intensity of peak between the three samples which indicates the difference in index of crystallinity. The crystallinity area of the raw enset fiber (Table 4) was much lower than that of the bleached and acid hydrolysis-treated enset fiber. This phenomenon is due to the removal of lignin and hemicelluloses components in alkaline, the bleaching treatment, and acid hydrolysis. This result was endured by chemical composition and FTIR analysis.

As presented in Table 4, the highest crystallinity percentage was obtained after the hydrolysis treatment. This is due to the amorphous components of enset fiber that was acid hydrolyzed; lignin and hemicellulose components were removed in turn increase the yield of cellulose nanocrystals [1, 33, 34]. The space between atoms' lattices was decreased after each treatment step. The obtained data was reinforced by the area value of the domain crystalline structure.

As seen from Table 4, the crystallinity index has a direct relationship between crystallites thickness. After hydrolysis reaction and sonication, the thickness of the crystals has increased that indicates the contact surface area increment of the crystalline structure. Different researchers who have worked on nanocellulose material isolated from agricultural residues reported similar results [1, 5].

3.2.5. FTIR Analysis. Amorphous hemicellulose, lignin, and crystalline cellulose are the main components of natural fiber, and with the aid of FTIR, their functional groups can be characterized [5, 18, 20]. Raw enset fiber, bleached enset fiber cellulose, and CNC FTIR spectra are given in Figure 5.

The FTIR spectrum acquired cellulose nanocrystal isolated from enset fiber corresponds to the characteristic spectrum of natural nanocellulose material (Figure 5). The typical broad peak in the province of 3330-3408 cm^{-1} confirms the existence of stretching motion hydrogen-bonded -O-H. The small peak in the zone of 2897 cm^{-1} corresponds to C-H stretching of the alkane group. Strong alkane compound (C-H stretching) functional group found in the region of 2911 cm^{-1}. These clusters of peaks signify that all of them have aliphatic saturated functional groups.

The detected peak around 1435 cm^{-1} in all samples indicates that the existence of -OH bending absorbed water. The raw enset fiber has lower transmittance than the bleached cellulose and cellulose nanocrystal. It also has a characteristics peak at 1250 cm^{-1} and 1527 cm^{-1} because of the presence of streaking C=O double bond. This reveals the existence of

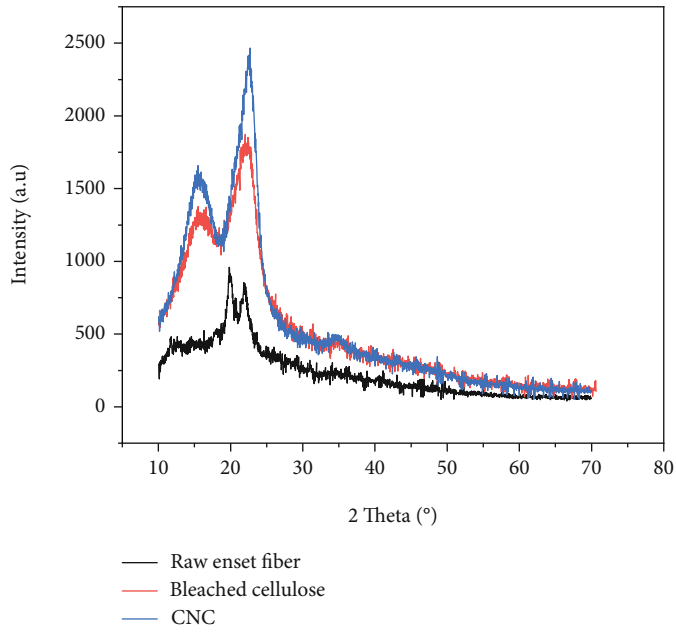

Figure 4: XRD pattern of samples after different treatment steps.

Table 4: Crystallinity percentage of enset fiber with different treatments.

Treatments	Index of crystallinity	Average crystalline size (nm)	d-spacing (Å)
Raw enset fiber	10.4264%	0.06437	4.2585
Bleached cellulose	63.9827%	0.23265	4.0186
CNCs	80.91%	1.56888	3.9734

lignin and hemicellulose in the untreated fiber [5]. This peak did not appear after pretreatment and acid hydrolysis of the enset fiber.

The characteristics peak at 1644 cm^{-1} shows the presence of the hemicellulose or the ester linkage of the carboxylic group of ferulic and p-coumaric acids of lignin and hemicelluloses [40]. This was disappeared after the treatment process.

The peak observed at 895 cm^{-1} shows the presence of β-glycosidic linkages in cellulose [43]. These results were confirmed by chemical composition investigation too.

3.2.6. Thermal Stability Analysis. The thermal stability behaviors of raw enset fibers, bleached cellulose, and CNC samples were analyzed using TGA. The results of TGA and DTG curves for each sample are presented in Figure 6. Previous literature works regarding fiber and fiber-based nanocellulose categorize the thermal degradation stages as two main parts [5].

The temperature range from 25 to 185°C covers the initial weight loss, and it is called stage I. In stage I, the weight loss of the samples is 7.1%, 7.15%, and 3.77% that corresponds to raw enset fiber, bleached cellulose, and CNCs, respectively (Figure 6(a)). The equivalent stages of the DTG graph also show a minor trough of about 102°C for a similar reason. As observed in DTG curves (Figure 6(b)), also, the raw enset fiber had a sharper V-shaped than the curves of bleached cellulose and CNCs. The maximum weight loss observed at stage I was 7.43% owing to a more swollen and less compact characteristic structure. The treated enset fiber with alkaline treatment, digesting, and acid hydrolyzed lost a few weight since the hemicellulose and lignin components have been eliminated as stated in different literature works [2, 5, 20].

The temperature from 190 to 395°C (active pyrolysis) is called stage II. At this stage, substantial weight losses are recorded. Previously studied data shows that lignin and hemicellulose degrade mainly in the temperature range of 200 to 315°C [5]. Stage II is further divided into two parts, (190-350°C) and (350–395°C). Raw enset fiber, about 279°C temperature of degradation, losses a large amount of its weight at starting of stage II or in the stage of pyrolysis than bleached cellulose and CNC.

4. Conclusions

In the present work, RSM was used to determine the optimum value of parameters that could maximize the yield of CNCs during the acid hydrolysis and sonication treatment. Accordingly, second-order polynomial predicts the yield of CNCs. The predicted and actual values are in respectable agreement with each other ($R^2 = 99.3\%$). ANOVA analysis showed the effects of process parameters, and their interactions influence significantly on the CNC yield. The values of optimum isolation (77.69% of CNCs) levels are H_2SO_4 concentration (51.6 wt. %), reaction temperature (47°C), and reaction time (65.5 min). The present study undoubtedly indicated that the isolation of CNCs from raw enset fiber can be ameliorated using optimized process parameters, and the obtained CNCs showed excellent properties

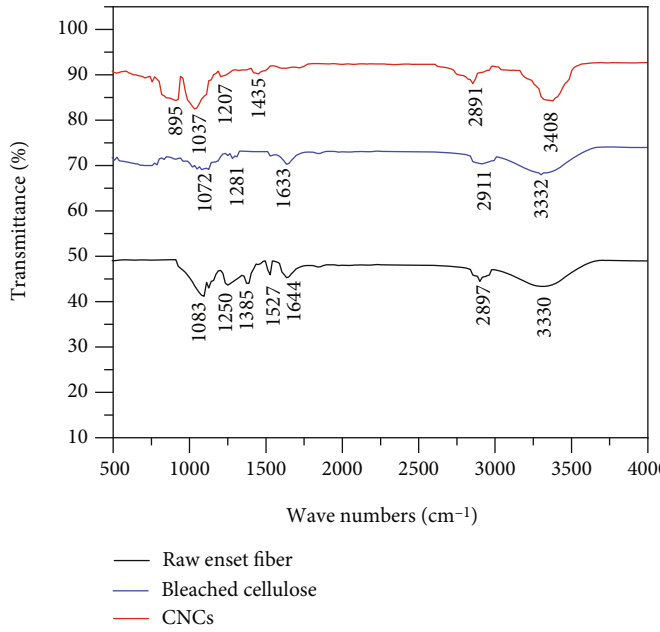

Figure 5: FTIR spectra of samples after different treatment steps.

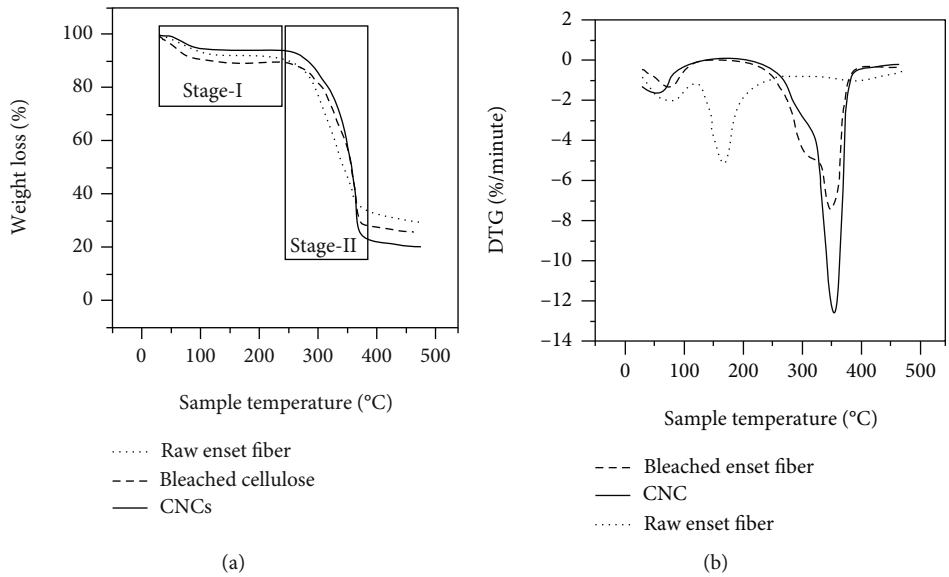

Figure 6: (a) TGA and (b) DTG curves of raw enset fiber, bleached cellulose, and CNCs.

regarding crystallinity index and crystallite domain and thermal stability. FTIR, XRD, TGA, PSA and chemical compositions investigation support the claims made in this study. The SEM morphology of CNCs reveals the structure and arrangement of the fiber bundle inside of enset. XRD study indicated that the crystallinity of yielded products had been improved after each successive treatment subjected to the treated fiber. The crystallinity index of bleached cellulose and CNCs was 63.98% and 80.91%, respectively. And the average crystalize size was obtained at 66 nm. FTIR spectrum indicated that the reduction and removal of lignin, hemicellulose, and other amorphous parts found in raw enset fibers. These remarkable findings of enset fiber nanocellulose indicate that CNCs could be utilized as striking reinforced material for a biobased film.

Data Availability

The data used to support the findings of this study are included within the article.

Disclosure

This research did not receive any specific grant from funding agencies in the public, commercial, or not-for-profit sectors.

Conflicts of Interest

The authors declare that they have no conflicts of interest.

Authors' Contributions

Corresponding author ensures that the descriptions are accurate and agreed by all authors. Surafel Mustefa Beyan (first author and corresponding author) contributed to the primary data collection and carried out experimental work, designed the experimental setup and do characterization of the samples, and contributed to draft formulating, draft checking, and manuscript writing and finalizing. Temesgen Abeto Amibo designed the experiment and provided necessary facilities. Venkatesa S. Prabhu edited the paper and assisted in writing papers and overall improved the manuscript. Abraham A. Getahun assisted in the characterization of the sample.

Acknowledgments

The authors would like to extend their sincere appreciation to the Department of Material Engineering at Jimma University for providing facilities and laboratories for this research.

Supplementary Materials

Table S.1: levels of the three independent variables studied. Table S.2: table ANOVA analysis for response surface quadratic model. Table S.3: summary of the optimization process. Figure S 1: predicted Vs actual velues (a) and normal plot residual (b) of response values. *(Supplementary Materials)*

References

[1] C. S. Julie Chandra, N. George, and S. K. Narayanankutty, "Isolation and characterization of cellulose nanofibrils from arecanut husk fibre," *Carbohydrate Polymers*, vol. 142, pp. 158–166, 2016.

[2] Z. Liu, X. Li, W. Xie, and H. Deng, "Extraction, isolation and characterization of nanocrystalline cellulose from industrial kelp (Laminaria japonica) waste," *Carbohydrate Polymers*, vol. 173, pp. 353–359, 2017.

[3] M. Mahardika, H. Abral, A. Kasim, S. Arief, and M. Asrofi, "Production of nanocellulose from pineapple leaf fibers via high-shear homogenization and ultrasonication," *Fibers.*, vol. 6, pp. 1–12, 2018.

[4] H. A. Silvério, W. P. Flauzino Neto, N. O. Dantas, and D. Pasquini, "Extraction and characterization of cellulose nanocrystals from corncob for application as reinforcing agent in nanocomposites," *Industrial Crops and Products*, vol. 44, pp. 427–436, 2013.

[5] M. Asrofi, H. Abral, A. Kasim et al., "Isolation of nanocellulose from water hyacinth fiber (WHF) produced via digester-sonication and its characterization," *Fibers and Polymers*, vol. 19, pp. 1618–1625, 2018.

[6] A. García, A. Gandini, J. Labidi, N. Belgacem, and J. Bras, "Industrial and crop wastes: a new source for nanocellulose biorefinery," *Industrial Crops and Products*, vol. 93, pp. 26–38, 2016.

[7] M. Rajinipriya, M. Nagalakshmaiah, M. Robert, and S. Elkoun, "Importance of agricultural and industrial waste in the field of nanocellulose and recent industrial developments of wood based nanocellulose: a review," *ACS Sustainable Chemistry & Engineering*, vol. 6, pp. 2807–2828, 2018.

[8] M. Alle, R. Bandi, S.-H. Lee, and J.-C. Kim, "Recent trends in isolation of cellulose nanocrystals and nanofibrils from various forest wood and nonwood products and their application," in *Nanomater*, Agric. For. Appl, H. Azama and J. Mohammad, Eds., pp. 41–80, Elsevier, 2020.

[9] A. Chakrabarty and Y. Teramoto, "Recent advances in nanocellulose composites with polymers: a guide for choosing partners and how to incorporate them," *Polymers*, vol. 10, no. 5, p. 517, 2018.

[10] H. V. Lee, S. B. A. Hamid, and S. K. Zain, "Conversion of lignocellulosic biomass to nanocellulose: structure and chemical process," *Scientific World Journal*, vol. 2014, article 631013, 20 pages, 2014.

[11] Y. Wang, X. Wei, J. Li et al., "Homogeneous isolation of nanocellulose from eucalyptus pulp by high pressure homogenization," *Industrial Crops and Products*, vol. 104, pp. 237–241, 2017.

[12] A. Alemdar and M. Sain, "Isolation and characterization of nanofibers from agricultural residues – wheat straw and soy hulls," *Bioresource Technology*, vol. 99, pp. 1664–1671, 2008.

[13] H. Berhanu, Z. Kiflie, I. Miranda et al., "Characterization of crop residues from false banana/ensete ventricosum/in Ethiopia in view of a full-resource valorization," *PLoS One*, vol. 13, pp. 1–21, 2018.

[14] F. I. Ditzel, E. Prestes, B. M. Carvalho, I. M. Demiate, and L. A. Pinheiro, "Nanocrystalline cellulose extracted from pine wood and corncob," *Carbohydrate Polymers*, vol. 157, pp. 1577–1585, 2017.

[15] H. Berhanu, D. Neiva, J. Gominho et al., "Bio-refinery potential of enset/ensete ventricosum/fiber bundle using non-catalyzed and alkali catalyzed hydrothermal pretreatment," *Waste and Biomass Valorization*, vol. 12, pp. 663–672, 2021.

[16] C. Mizera, D. Herak, P. Hrabe, M. Muller, and A. Kabutey, "Mechanical behavior of Ensete ventricosum fiber under tension loading," *Journal of Natural Fibers*, vol. 14, pp. 287–296, 2017.

[17] A. Bosha, A. L. Dalbato, T. Tana, W. Mohammed, B. Tesfaye, and L. M. Karlsson, "Nutritional and chemical propertie s of fermented food of wild and cultivated genotypes of enset (Ensete ventricosum)," *Food Research International*, vol. 89, pp. 806–811, 2016.

[18] H. Sadeghifar, I. Filpponen, S. P. Clarke, D. F. Brougham, and D. S. Argyropoulos, "Production of cellulose nanocrystals using hydrobromic acid and click reactions on their surface," *Journal of Materials Science*, vol. 46, pp. 7344–7355, 2011.

[19] P. Nascimento, R. Marim, G. Carvalho, and S. Mali, "Nanocellulose produced from rice hulls and its effect on the properties of biodegradable starch films," *Materials Research*, vol. 19, pp. 167–174, 2016.

[20] J. I. Morán, V. A. Alvarez, V. P. Cyras, and A. Vázquez, "Extraction of cellulose and preparation of nanocellulose from sisal fibers," *Cellulose*, vol. 15, pp. 149–159, 2008.

[21] S. M. Beyan, S. V. Prabhu, T. T. Sissay, and A. A. Getahun, "Sugarcane bagasse based activated carbon preparation and

its adsorption efficacy on removal of BOD and COD from textile effluents: RSM based modeling, optimization and kinetic aspects," *Bioresource Technology Reports*, vol. 14, p. 100664, 2021.

[22] P. S. Venkatesa, G. Girma, A. K. Gizachew, B. M. Surafel, and G. Ramesh, "Biosolubilization of Cr (VI) from tannery sludge: process modeling, optimization, rate kinetics and thermodynamics aspects," *International Journal of Recent Technology and Engineering*, vol. 8, no. 4, pp. 4808–4816, 2019.

[23] W. Kidus Tekleab, S. M. Beyan, S. Balakrishnan, and H. Admassu, "Chicken feathers based keratin extraction process data analysis using response surface-box-Behnken design method and characterization of keratin product," *Current Agricultural Science and Technology*, vol. 20, pp. 163–177, 2020.

[24] S. Mustefa Beyan, S. Venkatesa Prabhu, T. K. Mumecha, and M. T. Gemeda, "Production of alkaline proteases using Aspergillus sp. isolated from Injera: RSM-GA based process optimization and enzyme kinetics aspect," *Current Microbiology*, vol. 78, pp. 1823–1834, 2021.

[25] T. K. Mumecha, B. Surafel Mustefa, S. Venkatesa Prabhu, and F. T. Zewde, "Alkaline protease production using eggshells and membrane-based substrates: process modeling, optimization, and evaluation of detergent potency," *Engineering and Applied Science Research*, vol. 48, pp. 171–180, 2021.

[26] Y. Asrat, A. T. Adugna, M. Kamaraj, and S. M. Beyan, "Adsorption phenomenon of Arundinaria alpina stem-based activated carbon for the removal of lead from aqueous solution," *Journal of Chemistry*, vol. 2021, Article ID 5554353, 9 pages, 2021.

[27] R. Sathishkumar, G. Ananthan, and J. Arun, "Production, purification and characterization of alkaline protease by ascidian associated Bacillus subtilis GA CAS8 using agricultural wastes," *Biocatalysis and Agricultural Biotechnology*, vol. 4, pp. 214–220, 2015.

[28] E. K. Tetteh and S. Rathilal, "Application of response surface methodology (RSM) - reduction of industrial wastewater chemical oxygen demand," *CBU International Conference Proceedings*, vol. 5, pp. 1226–1232, 2017.

[29] L. K. Kian, M. Jawaid, H. Ariffin, and Z. Karim, "Isolation and characterization of nanocrystalline cellulose from roselle-derived microcrystalline cellulose," *International Journal of Biological Macromolecules*, vol. 114, pp. 54–63, 2018.

[30] M. Kacem, G. Simon, A. Elleuch, F. M. Ayadi, T. Boudawara, and A. Elfeki, "Protective effect of Ruta Chalepensis L. extract on oxidative stress and liver-kidney function induced by polymicrobial sepsis in rats," *Journal of Advances in Chemistry*, vol. 10, no. 1, pp. 2146–2161, 2014.

[31] A. Chufo, H. Yuan, D. Zou, Y. Pang, and X. Li, "Biomethane production and physicochemical characterization of anaerobically digested teff (Eragrostis tef) straw pretreated by sodium hydroxide," *Bioresource Technology*, vol. 181, pp. 214–219, 2015.

[32] L. Huang, B. Mu, X. Yi, S. Li, and Q. Wang, "Sustainable use of coffee husks for reinforcing polyethylene composites," *Journal of Polymers and the Environment*, vol. 26, pp. 48–58, 2018.

[33] E. Abraham, B. Deepa, L. A. Pothan et al., "Extraction of nanocellulose fibrils from lignocellulosic fibres: a novel approach," *Carbohydrate Polymers*, vol. 86, pp. 1468–1475, 2011.

[34] R. M. Sheltami, I. Abdullah, I. Ahmad, A. Dufresne, and H. Kargarzadeh, "Extraction of cellulose nanocrystals from mengkuang leaves (Pandanus tectorius)," *Carbohydrate Polymers*, vol. 88, pp. 772–779, 2012.

[35] B. Xiao, X. Sun, and R. Sun, "Chemical, structural, and thermal characterizations of alkali-soluble lignins and hemicelluloses, and cellulose from maize stems, rye straw, and rice straw," *Polymer Degradation and Stability*, vol. 74, pp. 307–319, 2001.

[36] B. Deepa, E. Abraham, B. M. Cherian et al., "Structure, morphology and thermal characteristics of banana nano fibers obtained by steam explosion," *Bioresource Technology*, vol. 102, pp. 1988–1997, 2011.

[37] S. King, P. Dobson, and H. Jarvie, "Nanoparticle," *Encyclopædia Britannica*, 2021, https://www.britannica.com/science/nanoparticle.

[38] Y. M. Zhou, S. Y. Fu, L. M. Zheng, and H. Y. Zhan, "Effect of nanocellulose isolation techniques on the formation of reinforced poly(vinyl alcohol) nanocomposite films," *Express Polymer Letters*, vol. 6, pp. 794–804, 2012.

[39] T. Fattahi Meyabadi, F. Dadashian, G. M. M. Sadeghi, and H. E. Z. Asl, "Spherical cellulose nanoparticles preparation from waste cotton using a green method," *Powder Technology*, vol. 261, pp. 232–240, 2014.

[40] M. R. K. Sofla, R. J. Brown, T. Tsuzuki, and T. J. Rainey, "A comparison of cellulose nanocrystals and cellulose nanofibres extracted from bagasse using acid and ball milling methods," *Advances in Natural Sciences: Nanoscience and Nanotechnology*, vol. 7, p. 035004, 2016.

[41] K. P. Y. Shak, Y. L. Pang, and S. K. Mah, "Nanocellulose: recent advances and its prospects in environmental remediation," *Beilstein Journal of Nanotechnology*, vol. 9, pp. 2479–2498, 2018.

[42] A. D. French, "Idealized powder diffraction patterns for cellulose polymorphs," *Cellulose*, vol. 21, pp. 885–896, 2014.

[43] F. A. Ahmad Kuthi, K. Haji Badri, and A. Mohmad Azman, "X-ray diffraction patterns of oil palm empty fruit bunch fibers with varying crystallinity," *Advances in Materials Research*, vol. 1087, pp. 321–328, 2015.

Hindawi
Journal of Nanomaterials
Volume 2021, Article ID 3484125, 10 pages
https://doi.org/10.1155/2021/3484125

Research Article

Antifungal Activity and Mechanism of Action of Different Parts of *Myrtus communis* Growing in Saudi Arabia against *Candida* Spp.

Abdullah A. Alyousef

Department of Clinical Laboratory Sciences, College of Applied Medical Sciences, King Saud University, P.O. Box 10219, Riyadh 11433, Saudi Arabia

Correspondence should be addressed to Abdullah A. Alyousef; abalyousef@ksu.edu.sa

Received 30 August 2021; Revised 13 September 2021; Accepted 15 September 2021; Published 7 October 2021

Academic Editor: Lakshmipathy R

Copyright © 2021 Abdullah A. Alyousef. This is an open access article distributed under the Creative Commons Attribution License, which permits unrestricted use, distribution, and reproduction in any medium, provided the original work is properly cited.

Discovering new antifungal drugs from natural products is a key target for the treatment of infections, such as candidiasis and other *Candida*-related infections. As current therapeutic drugs for the treatment of infections, such as candidiasis and other *Candida*-related infections, have adverse effects on human health, discovering new antifungal drugs from natural products is urgently needed. The objective of this study was to evaluate the antifungal activity of the methanolic and sodium phosphate buffer extracts derived from various parts of *Myrtus communis*, a plant that is traditionally used in Saudi Arabia, against *Candida albicans* (ATCC 10213), *Candida glabrata* (ATCC 2001), *Candida kefyr* (ATCC 66028), *Candida parapsilosis* (ATCC 22019), and *Candida tropicalis* (ATCC 750). A well diffusion assay was performed to assess the antifungal activity through the measurement of the zone of inhibition. Of the extracts, those extracted with methanol from the roots and leaves displayed strong inhibitory activity against *Candida glabrata* (23.5 ± 0.12 and 20.7 ± 0.22, respectively), at 50 mg/ml, with 5 mg/ml fluconazole administered as the standard control. The minimal inhibitory concentration (MIC) and minimum fungicidal concentration (MFC) values were 12.5 mg/ml and 25 mg/ml for the *M. communis* root extract and 25 mg/ml and 50 mg/ml for the *M. communis* leaf extract against *Candida glabrata*. The results were confirmed by scanning electron microscopy (SEM) imaging of the control and treated strains of *Candida glabrata*. Based on SEM, these extracts could alter the morphology and cause loss of cell integrity. The effect of *M. communis* root and leaf extracts on *Candida* cells was also determined by measuring the absorbance at 260 nm after treatment for 1 h at 37°C. Interestingly, the 260 nm absorbing material was higher in *Candida glabrata* than in the resistant strain, *Candida parapsilosis* (ATCC 22019). Based on our findings, the crude methanolic extract of *M. communis* roots and leaves exhibited good antifungal activity against the *Candida glabrata* strain. SEM results and estimation of the 260 nm absorbance material proved that the extract might act on the cell wall and cell membrane of *Candida* cells, further leading to cell death.

1. Introduction

Medicinal plants are employed as alternatives to Western medicine in developing countries to treat various health conditions. According to a survey by the World Health Organisation (WHO), 80% of the world's population uses natural remedies and traditional medicines [1, 2]. Plant extracts and their essential oils have shown exceptional biological activities against microorganisms. Globally, many countries, such as India, Jordan, and Mexico, have diverse flora and a rich tradition of using medicinal plants for antibacterial and antifungal applications [3, 4]. Screening of plant extracts against fungal strains has revealed that these plants contain active compounds with antimicrobial properties.

Invasive fungal infections are mainly caused by *Candida albicans* either locally or systemically [5]. These infections pose a serious threat to the public health sector economically and medically as they are associated with high

mortality rates and increased cost burden as well as hospital duration [6].

Some of the factors contributing to increased infections in immunocompromised patients include the use of intravenous catheters, invasive procedures, and total parenteral nutrition and the increasing use of broad-spectrum antibiotics, cytotoxic chemotherapies, and transplantation [7]. The virulence factors that lead to the pathogenicity of *Candida* species include their ability to evade host defences, adherence, promotion of hyphae, biofilm development (on host tissue and on medical devices), and the production of tissue-damaging hydrolytic enzymes, such as proteases, phospholipases, and haemolysin [8]. Abnormal hosts, such as immunocompromised persons or those with diabetes mellitus, are more prone to mucosal or systemic infections than healthy individuals [9].

Infections due to non-*albicans* species are rapidly increasing. In fact, *C. glabrata* is the second most common cause of candidiasis or vaginal candidiasis after *C. albicans* and *C. tropicalis*, which is the third most common species. In neonates, *C. parapsilosis* has become a dominant fungal pathogen in children and neonates in some centers [10].

Several antifungal agents have been discovered and are available for the treatment of invasive fungal infections, such as polyenes, pyrimidines, echinocandins, and triazoles. Fluconazole and voriconazole are the most commonly used antifungals. However, pathogenic microorganisms are constantly developing resistance to these agents [11, 12]. Antifungal drugs have undesirable side effects or are very toxic, induce drug-drug interactions, or lead to the development of resistance. Some drugs are also ineffective and have become less successful as therapeutic agents. Thus, searching for alternative antifungal drugs has been a major concern in recent years [13]. Natural products play an important role in drug development programs in the pharmaceutical industry [14]. As a result, several medicinal plants have been extensively studied in order to find safe, less toxic, and more effective drugs.

Myrtus communis L. (*M. communis*), also called myrtle (*Myrtaceae family*), is native to the Mediterranean basin and Arabian Peninsula. Since ancient times, different parts of myrtle, especially its leaves and fruit, have been used in food preparation and applied in traditional medicines as a general antiseptic, disinfectant, and therapy for many types of infectious diseases [15, 16]. Many previous studies on *Myrtus* demonstrated that different parts of this plant, such as leaves, branches, berries, and flowers, have different chemical compositions as well as pharmacological activities, such as antifungal, antibacterial, antiviral, anticancer, anti-inflammatory, analgesic, antioxidant, antidiabetic, and antimutagenic effects [17, 18]. Discovering more effective and less toxic novel antifungal agents is thus needed to overcome these disadvantages.

The objectives of this study were to determine the antifungal activity of different parts of the *M. communis* plant against known standard ATCC *Candida* strains using methanol and sodium phosphate buffer extraction methods and to investigate the mechanism of action of these extracts on the growth inhibition of different *Candida* species.

2. Materials and Methods

2.1. Fungal Strains. Five standard strains of *Candida* species were obtained from the Research Laboratory, Clinical Laboratory Sciences Department, College of Applied Medical Science, King Saud University: *Candida albicans* (ATCC 10213), *Candida glabrata* (ATCC 2001), *Candida kefyr* (ATCC 66028), *Candida parapsilosis* (ATCC 22019), and *Candida tropicalis* (ATCC 750). Each strain was subcultured on Sabouraud's dextrose agar (SDA) (Scharlau, Spain) medium and incubated at 37°C for 24 h to obtain inoculums for testing.

2.2. Sample Preparation. M. communis plants were procured from the Alfath nursery (Al-Qassim region, Saudi Arabia) in October 2019. Samples were transported to the Research Lab in a sterile bottle, washed with running tap water and later with distilled water, and air-dried under shade at room temperature. Subsequently, the samples were ground into a fine powder using an electric blender and stored in sterile 50 ml universal containers. Methanolic extraction was performed as described previously, with some modifications [15, 19, 20]. Briefly, a 25 g aliquot of each dried sample was extracted using 100 ml of methanol (95%) for 72 h at room temperature. Thereafter, the methanolic extracts were separated and filtered through Whatman filter paper No.1 and dried under pressure at 37°C with a rotator evaporator. The yield percentages were determined by dividing the weight of the extract by the weight of the sample multiplied by 100. The dried extracts were reconstituted in 1% dimethyl sulfoxide (DMSO; purity 99.7%) to prepare stock solutions, which were stored in a refrigerator at 4°C until the analysis.

Antimicrobial proteins and peptides were extracted as previously described [21, 22]. Briefly, a 25 g aliquot of each dried sample was soaked in sodium phosphate buffer (pH 6.5) at 30°C and left overnight. The next day, the extracts were filtered with Whatman filter paper No. 1 and subjected to 80% ammonium sulfate saturation. The collected saturated material was then separated by dialysis using a 3 kDa cut-off dialysis tubing (Sigma Aldrich, St. Louis, MO, USA), and the samples were subjected to spectrophotometric analysis at 280 nm to determine protein concentration.

2.3. Preparation of the Inoculum. Two to three colonies from 24 h old culture were used as the inoculum following suspension in 10 ml of 0.85% sodium chloride solution, which was autoclaved. The turbidity was adjusted to 0.5 McFarland standard units (i.e., 1.5×10^8 CFU/ml).

2.4. Antifungal Susceptibility Test. A well diffusion assay was used to determine the antifungal properties of medicinal plants, as described previously [20, 23, 24]. SDA was prepared according to the manufacturer's instructions and autoclaved. Medium (15-20 ml) was poured into sterile Petri dishes and allowed to solidify for 30 min. Thereafter, 0.2 ml of inoculum (fungal strain in saline) was spread on an agar plate, and the excess was removed via draining. The plates were then incubated at room temperature for 10 min. Using a sterile cork borer, 7 ditches of 4 mm were made in each plate. Methanolic plant extracts (50 mg/ml) were prepared

in dimethyl sulfoxide (DMSO). Each well was filled with either 50 μl of the methanolic extracts or 50 μl of crude protein; fluconazole (5 mg/ml) was used as a positive control while DMSO was used as a negative control. The plates were incubated at 37°C for 24 h. The zone of inhibition was measured in millimetres. The assay was repeated thrice for confirmation.

2.5. Determination of the Minimum Inhibitory Concentration (MIC) and Minimum Fungicidal Concentration (MFC). The minimal concentration of plant extracts that induced the inhibition of visible yeast growth or turbidity was referred to as the MIC. MIC was determined for the fungal strains that were sensitive to the extract in the well diffusion assay using the microdilution method and 2,3,5-triphenyltetrazohum chloride (TTC, tetrazolium red, purity min. 99%, SRL Pvt. Ltd. Mumbai, India) dye as a growth indicator, as described previously with some modifications [15, 25, 26].

Twofold serial dilutions of the extracts were prepared directly in a microtiter plate containing Sabouraud broth to obtain concentrations ranging from 100 to 1.56 mg/ml.

Thereafter, 100 μl of the strain inoculum, which was cultured overnight and adjusted to 0.5 McFarland units, was added to each well. The experiment was performed in triplicate. The culture plates were incubated overnight at 37°C for 24 h. The following controls, negative control (Sabouraud broth only) and positive controls (Sabouraud broth and microorganism), were tested to determine medium sterility and inoculum viability, respectively. The activity of fluconazole (5 mg/ml) was also compared with that of the extracts. To indicate fungal growth, 40 μl TTC (2 mg/ml) was added to each of the 96 wells in the plate. Thereafter, the plate was incubated for 30 min at 37°C. The lowest concentration at which there was no colour change was considered the MIC of the plant extract.

To determine the MFC, 20 μl of each of the wells with no turbidity or fungal growth was cultured on SDA. The plates were then incubated at 37°C for 24 h. The MFC was considered to be the lowest concentration cultivated in the plate that induced a fungicidal effect with no visible viable colonies on an agar plate.

2.6. Scanning Electron Microscopy (SEM). SEM was carried out to confirm the inhibitory effect of the plant extracts on sensitive strains using JSM-6380LA at an accelerating voltage of 10 kV. Two sets of samples were processed, control and treated. Overnight grown cultures of *Candida* spp. were inoculated in 10 ml Sabouraud dextrose broth (SDB) to derive the 0.5 McFarland standard. Suspensions of *Candida spp* were treated with 100 μl of the plant extracts at the MIC and incubated at 37°C for 24 h at 120 rpm; these samples were considered treated cultures. Suspensions of *Candida spp* that were not treated with the plant extracts were termed as the control cultures.

After incubation, the cultures were centrifuged at 1,500 $\times$ g for 5 min at room temperature to collect the pellet. Pellets were washed thrice with distilled water. A 200 μl volume of 2.5% glutaraldehyde was added to the Eppendorf tubes before sample preparation.

The sample pellets were fixed in buffer aldehyde (2.5% glutaraldehyde in phosphate buffer) solution for 3 h. After the removal of the glutaraldehyde solution, the samples were rinsed thrice in sodium cacodylate solution buffer for 5 min. Postfixation was performed using osmium tetroxide for 1 h, and the samples were rinsed in distilled water. Thereafter, the samples were dehydrated using a graded ethanol series of 25%, 50%, 75%, 90%, and twice with 100% ethanol for 10 min each. The sample was dried with a critical point dryer device, mounted on specimen stabs with gold coating, and viewed under an electron microscope.

2.7. Measurement of the Release of 260 nm Absorbing Cellular Materials. Spectrophotometer analysis of the 260 nm absorbing cellular materials was performed as described previously with some modifications [27, 28]. Briefly, an overnight grown culture of *Candida spp* was inoculated into fresh SDB to derive the 0.5 McFarland standard. Cells were harvested by centrifugation at 1,500 $\times$ g for 10 min at room temperature, and the pellet was resuspended in 10 ml phosphate buffer. Suspensions of *Candida spp* were treated with 100 μl of plant extracts at the MIC or the same volume of DMSO (control) and incubated at 37°C for 1 h. Samples were centrifuged at 12,000 $\times$ g for 1 min at 4°C, filtered through a 0.2 μm pore-size filter, and subjected to optical density measurement at 260 nm. Absorbance was estimated for the control and treated cells using a UV microplate reader (Bio-Tek), and the absorbance of DMSO control was subtracted.

2.8. Statistical Analysis. All studies were performed in triplicate. The data are presented as mean values. The difference between the control and treated samples was analysed using Student's *t*-test.

3. Results

3.1. Extraction Yields of the Plant Extract. The 25 g of dried plant material extracted with methanol (95%) yielded plant extract residues ranging from 0.7 to 2.4 g. The highest yield was obtained from *M. communis* leaves (2.4 g) followed by *M. communis* roots (1.53 g). The flowers had the lowest extract yield (Table 1).

As shown in Table 2, different concentrations of the protein extracts were successfully extracted from 25 g of dried plant materials. The flowers of *M. communis* had a low protein concentration of 50.1 μg/ml while the leaf extract had the highest protein concentration of 140.6 μg/ml when extracted with sodium phosphate buffer (pH 6.5).

3.2. Antifungal Activity of the Plant Extracts. An evaluation of the antifungal activity of different parts of the *M. communis* extracts against five standard *Candida* species was initially conducted using the well diffusion method. The *Candida* strains used in this study were *C. albicans* (ATCC 10213), *C. glabrata* (ATCC 2001), *C. keyfr* (ATCC 66028), *C. parapsilosis* (ATCC 22019), and *C. tropicalis* (ATCC 750). The effects of the extracts were compared with that of the standard antifungal agent, fluconazole (5 mg/ml), and the negative control, DMSO. The results for the

Table 1: Yield percentage of the methanolic extraction (%).

Plant parts	Extract yield (%)
Stems	4.2
Flowers	2.8
Leaves	9.6
Roots	6.12

Table 2: Protein concentration (μg/ml) in different parts of *Myrtus communis* extracted using sodium phosphate buffer.

Plant parts	Protein concentration (μg/ml)
Stems	76.2
Flowers	50.1
Leaves	140.6
Roots	109.8

antifungal activity of these extracts are presented in Table 3 and illustrated in Figure 1.

All *M. communis* extracts used in the study exhibited varying degrees of antifungal activity against the *Candida* strains. However, the methanolic extract of *M. communis roots* was the most effective among the extracts tested. In fact, this extract resulted in a zone of inhibition (ZOI) of 23.5 mm against *C. glabrata* compared with the standard antifungal, fluconazole (5 mg/ml). However, there was no significant activity against other *Candida* spp. The methanolic leaf extract resulted in a zone of inhibition of 20.7 mm against *Candida glabrata*; however, this extract did not exhibit any activity against other *Candida* spp.

C. parapsilosis and *C. keyfr* were found to be resistant to all methanolic extracts, whereas *C. albicans* showed very low sensitivity with zones of inhibition of 4 mm and 2 mm when treated with the methanolic extracts of roots and leaves, respectively. *C. tropicalis* showed very low sensitivity toward the methanolic root extract with a zone of inhibition of 5.2 mm.

Other methanolic extracts (stems and flowers) were not found to display antifungal activity against all tested strains.

The present study was conducted to investigate the efficacy of the crude extracts of antifungal proteins and peptides from different parts of *M. communis*. Extraction was carried out herein in sodium phosphate buffer at pH 6.5. The antifungal activities of these extracts were determined by the microbiological technique using the agar well diffusion assay.

The root extract displayed high activity against *C. glabrata* with a zone of inhibition of 14.5 mm and protein concentration of 109.8 μg/ml. The leaf extracts were found to be effective against *C. glabrata* and *C. albicans* with zones of inhibition of 13 mm and 6 mm, respectively.

C. glabrata showed very low sensitivity with a zone of inhibition of 4 mm when treated with the buffer extract of stems. Further, the extracts of stem and flowers had no activity against other *Candida* strains.

The antifungal activity of all the extracts suggested that all *Candida* strains were resistant to the methanolic and buffer extracts. The highest and most promising results against *C. glabrata* were obtained with the methanolic extract of *M. communis* roots and leaves. Hence, experiments were conducted to determine the MIC and MFC of this extract against *C. glabrata* (ATCC 2001), which were used for further characterization studies.

3.3. Determination of MIC and MFC. The effectiveness of the plant extracts in the standard *Candida* strains was confirmed by measuring the MIC and MFC. The MIC and MFC were only determined for organisms that had a zone of inhibition and were sensitive to the plant extracts in the previous antimicrobial assay carried out using the agar well diffusion method. In summary, the MIC and MFC values of the leaf extracts against *C. glabrata* (ATCC 2001) (MIC: 25 mg/ml, MFC: 50 mg/ml) were lower than those of the root extracts (MIC: 12.5, MFC: 25 mg/ml). *C. glabrata* (ATCC 2001) was found to be resistant to the other plant extracts.

3.4. SEM Analysis. SEM was performed to determine the morphology of the *C. glabrata* strain (ATCC 2001) after treatment with the *M. communis* roots and leaf extracts for 24 h. The cells that were not treated had normal *Candida* cell morphology, were oval-shaped, and had smooth outer surfaces. In contrast, the cells exposed to the MIC of the extracts showed considerable morphological alterations, including shrinkage, rough surface, and deformity, leading to the prominent loss of cell shape and integrity (Figure 2). This finding indicates that the *M. communis* root and leaf extracts might act on the cell wall and membrane of *C. glabrata*, which may be attributed to their high content of polyphenols and oxygenated monoterpenes [17], causing a loss in membrane integrity, leakage of cellular materials, and ultimately cell death.

3.5. Measurement of the Release of 260 nm Absorbing Cellular Materials. The effect of the methanolic extract of *M. communis* roots and leaves was also determined by confirming the leakage of 260 nm absorbing materials when *Candida* spp. were exposed to the MIC of the extracts (Figure 3). The OD of the sensitive strain, *C. glabrata* (ATCC 2001), significantly increased at 260 nm with the root extract and leaf extract relative to the control after 1 h, which may be attributed to leakage in the cytoplasmic membrane and release of cell materials, including nucleic acids, metabolites, and ions [29]. However, no changes in the optical density were observed for the resistance strain, *C. parapsilosis* (ATCC 22019), in this study.

4. Discussion

The treatment of *Candida* infections is currently challenging owing to the limited number of available drugs, increased resistance to these drugs, high costs, and toxicity [30]. Consequently, novel alternative molecules that are more effective than conventional antifungal agents are urgently needed to prevent the emergence of fungal resistance. Only a few studies have assessed the antifungal activity of plants found in various regions of Saudi Arabia using ethanol, methanol,

Table 3: In vitro antifungal activity (mm zone of inhibition) of the methanolic (M) and sodium phosphate buffer (P) extracts derived from various parts of *M. communis* against standard *Candida* spp.

Sample No.	Stems		Flowers		Leaves		Roots		Fluconazole (5 mg/ml)	DMSO
	P	M	P	M	P	M	P	M		
C. albicans ATCC 10213	0.0 ± 0.0	0.0 ± 0.0	0.0 ± 0.0	0.0 ± 0.0	6.0 ± 0.12	2.0 ± 0.21	0.0 ± 0.0	4.0 ± 0.6	22.5 ± 0.22	0.0 ± 0.0
C. glabrata ATCC 2001	4.0 ± 0.11	6.1 ± 0.5	0.0 ± 0.0	0.0 ± 0.0	13.1 ± 0.17	20.7 ± 0.22	14.5 ± 0.61	23.5 ± 0.12	29.5 ± 0.42	0.0 ± 0.0
C. keyfr ATCC 66028	0.0 ± 0.0	0.0 ± 0.0	0.0 ± 0.0	0.0 ± 0.0	0.0 ± 0.0	0.0 ± 0.0	0.0 ± 0.0	0.0 ± 0.0	19.8 ± 0.37	0.0 ± 0.0
C. parapsilosis ATCC 22019	0.0 ± 0.0	0.0 ± 0.0	0.0 ± 0.0	0.0 ± 0.0	0.0 ± 0.0	0.0 ± 0.0	0.0 ± 0.0	0.0 ± 0.0	30.8 ± 0.22	0.0 ± 0.0
C. tropicalis ATCC 750.	0.0 ± 0.0	0.0 ± 0.0	0.0 ± 0.0	0.0 ± 0.0	0.0 ± 0.0	0.0 ± 0.0	0.0 ± 0.0	5.2 ± 0.2	22.8 ± 0.31	0.0 ± 0.0

Data are means of three replicates ($n = 3$) ± standard error.

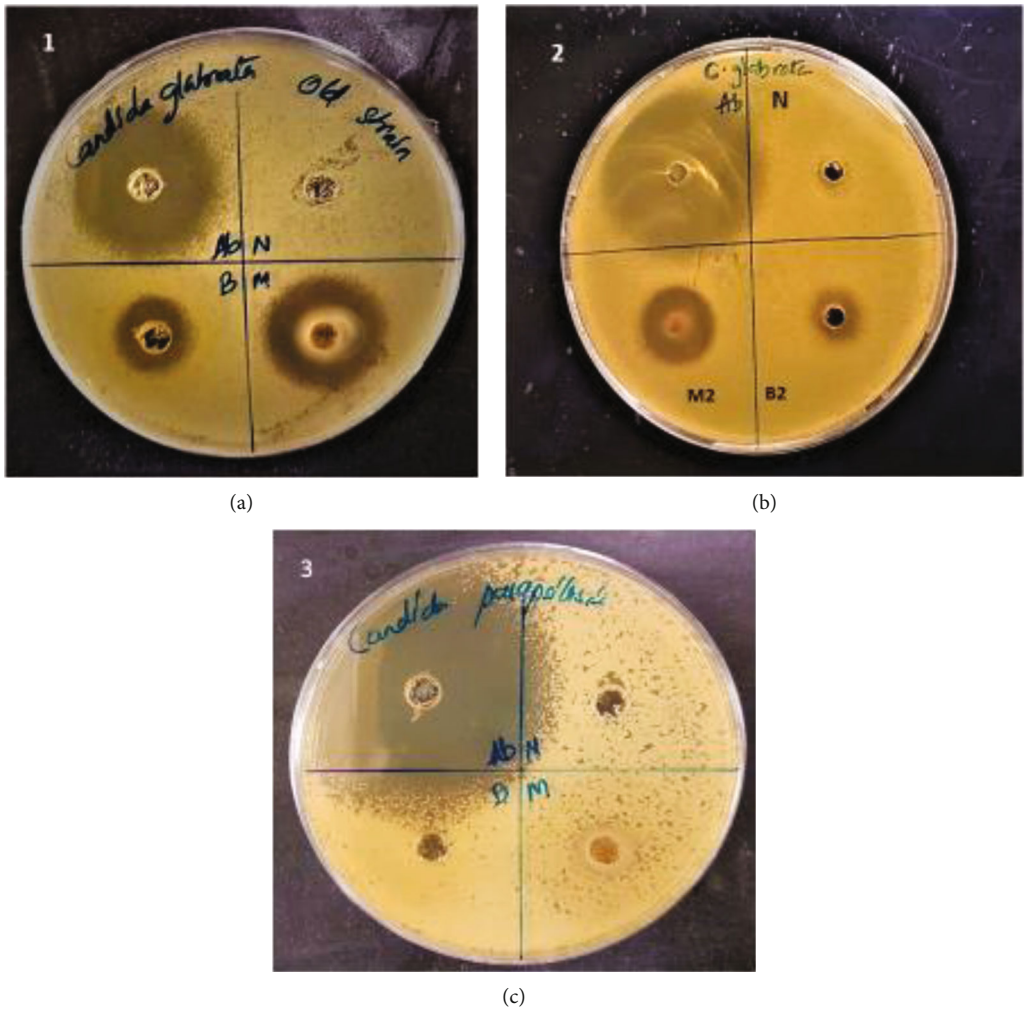

(a) (b)

(c)

Figure 1: Antifungal activity of the *Myrtus communis* extracts. The antifungal activity against the sensitive strain, *Candida glabrata* (ATCC 2001) (a, b), and the lack of antifungal activity of these extracts against *Candida parapsilosis* (ATCC22019) (c). M: methanolic root extract; B: buffer root extract; M2: methanolic leaf extract; B2: buffer leaf extract; Ab: fluconazole (5 mg/ml); N: DMSO (used as a negative control).

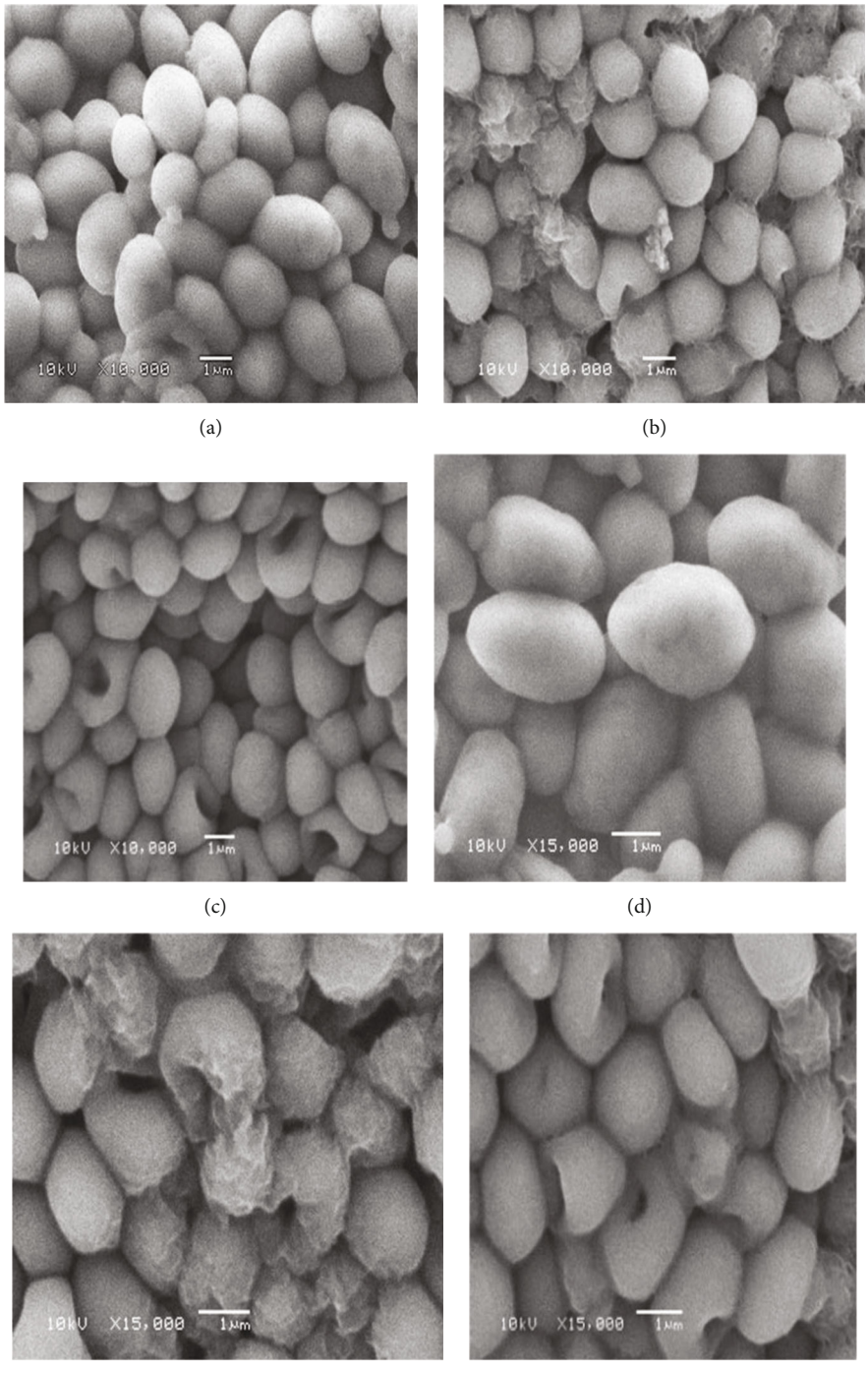

Figure 2: SEM analysis of the effects of plant extracts on the morphology of *Candida glabrata* (ATCC 2001). (a) Control cells (10,000x magnification); (b) morphological alterations in the cells, including shrinkage, rough surface, and deformity, when treated with the *Myrtus communis* root extracts (10,000x magnification); (c) morphological alterations in the cells, including shrinkage, rough surface, and deformity, when treated with the *Myrtus communis* leaf extracts (10,000x magnification); (d) control cells (15,000x magnification). Cell burst, rough surface, and deformity are indicated by arrows in cells treated with the *Myrtus communis* root (e) and leaf (f) extracts (15,000x magnification).

and other solvents to screen for alkaloids, terpenoids, and other antifungal agents.

Studies in the regions of Saudi Arabia, such as Abha, Dammam, Hail, Jeddah, and Najran, have revealed some significant results. A study carried out in Abha revealed that the antifungal activity of extracts from *Salvadora persica* and *Vigna fragrans* against *Aspergillus* sp. and *C. albicans* was higher than that of *Peganum harmala* and *Withania somnifera* extracts [31]. A study in Dhahran also revealed the antimicrobial activity of ethanol leaf extracts of *Catharanthus*

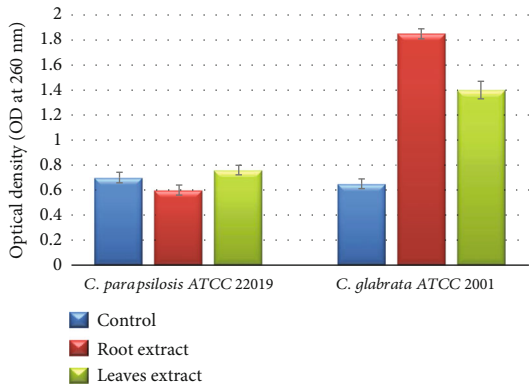

FIGURE 3: Absorbance of the cell material content of *C. glabrata* (ATCC 2001) and *C. parapsilosis* (ATCC 22019) at 260 nm following treatment with the MIC of the *M. communis* root and leaf extracts for 1 h. Values are expressed as the mean ± SD ($n = 3$).

roseus (Periwinkle) against *Staphylococcus aureus*, *Escherichia coli*, and *C. albicans* [32]. In another study, the antifungal activities of the aqueous and organic crude extracts of six medicinal plants collected from the markets of Jeddah, including *Azadirachta indica* (neem), *Zingiber officinale* (ginger), *Eucalyptus globulus*, *Lawsonia inermis*, *Lepidium sativum*, and *Rosmarinus officinalis*, were determined against different pathogenic fungi. The results revealed that some of the plant extracts had high antifungal activity against both *C. albicans* and *C. tropicalis* [33]. A study conducted by Bokhari revealed the remarkable antidermatophytic properties of the methanolic extracts of *Cymbopogon citratus* (lemon grass) and *Lantana camara* (lantana), which were collected from different localities of Jeddah city [34]. Further, a few studies have shown that different solvents (ethanol, ether, methanol, and chloroform) and aqueous extracts of *Commiphora myrrha* (myrrh), which is commonly used in Saudi Arabia, show broad-spectrum activity against pathogenic bacteria, moulds, and different *Candida* spp. [35, 36].

In a previous study, essential oils of *Ocimum basilicum* collected from the Jeddah region displayed antimicrobial activity against some bacteria and fungi [37]. Furthermore, the extract obtained from *Salvadora persica* (miswak) has been found to exhibit potent antifungal activity against all *Candida* strains. In this study, the plants were selected based on their traditional use among Middle Eastern communities for dental hygiene purposes and the prevention of tooth decay [38]. A review conducted in Najran, a city in Saudi Arabia, revealed the various therapeutic effects of *S. persica* on oral health, which can help elucidate the significance and importance of this indigenous oral hygiene tool [39].

In previous studies, the fruit (berry) extracts, leaf extracts, and essential oils of *M. communis* have been extensively analysed to determine their antimicrobial properties [17, 40]. However, only a few studies have reported the antifungal activities of these plant extracts. In a previous in-depth study that investigated the methanolic extracts of *M. communis* leaves, high antimicrobial activity was observed; the extraction procedures employed in this study included heat and a long incubation period of approximately 7 days [19, 41]. Previous studies have shown that methanolic extracts of the aerial parts of *M. communis* are highly active against three human pathogenic fungi, *C. albicans* (ATCC 10231), *C. tropicalis* (ATCC 13801), and *C. glabrata* (ATCC 28838) [42]. In another study, oil obtained from the leaves of myrtle exhibited strong antifungal activity against different *Candida* species [43]. Myrtle leaf oil has also shown significant antifungal activity against different strains of *C. albicans* when combined with the antifungal agent amphotericin B [44]. However, a study conducted by Mert et al. revealed that the n-hexane, ethanol, methanol, ethyl acetate, and aqueous extracts of the leaves of *M. communis* did not exhibit any antifungal activity against *C. albicans* (ATCC 10239) [45].

Many types of molecules with antimicrobial activity have been isolated from plants. Among these phytomolecules, proteins and peptides with antifungal activity have been recently reported [46]. The present study was conducted to investigate the efficacy of crude extracts of antifungal proteins and peptides from different parts of *M. communis*. The root extract displayed high antifungal activity only against *C. glabrata*, and the leaf extracts were found to be effective against *C. glabrata* and *C. albicans*. Furthermore, the stem and flower extracts displayed no activity against other *Candida* strains. However, our previous studies have revealed that the antibacterial activity of the crude protein extracted from leaves is highly active against methicillin-resistant *Staphylococcus aureus* (MRSA), *Acinetobacter baumannii*, and *S. aureus*. In addition, this extract has been found to be more active than standard antibiotics [22].

The MIC and MFC of these extracts against sensitive *Candida* strains were determined to quantify their activity. Methanolic root extracts showed MIC and MFC values of 12.5 mg/ml and 25 mg/ml, respectively, against *C. glabrata* (ATCC 2001). Methanolic leaf extracts showed MIC and MFC values of 25 mg/ml and 50 mg/ml, respectively, against *C. glabrata* (ATCC 2001). Therefore, the results of the present study indicate some of the advantages of *M. communis* root and leaf extracts that could be applied for the treatment of microbial infections.

To examine the antifungal mode of action of the studied extracts, it is important to estimate changes in fungal cell morphology, surface structure, and cell membrane permeability and integrity [29]. SEM analysis was performed to understand the effects of the extracts on *C. glabrata*. SEM images showed that the cells exposed to the MIC of the extracts displayed numerous morphological alterations, which caused a loss in membrane integrity, leakage of cellular materials, and ultimately cell death. This finding indicates that *M. communis* root and leaf extracts might disrupt the cell wall and membrane of *C. glabrata*, which may be attributed to their high content of polyphenols and oxygenated monoterpenes [17]. SEM was employed in previous studies to demonstrate that plant extracts can cause morphological changes in the tested organisms. In a recent study, SEM analysis was used to determine the effect of 150 μl/ml of the ethanolic extract of *Ziziphus spina-christi* leaves and *Phoenix dactylifera* seeds on *C. albicans*, and the results showed reduced cellular activity and shrinkage of the cell wall in the fungus [47]. SEM analysis was also

performed on bacteria to understand the effects of plant extracts on their cell morphology. Changes in cell morphology have been reported in some bacteria, such as *S. aureus*, *E. coli*, and *Salmonella*, after treatment with various plant extracts [29, 48]. The findings of the present study are consistent with those of previous studies.

Leakage of cellular materials was analysed by detecting 260 nm absorbing materials. In the present study, the OD of the sensitive strain, *C. glabrata* (ATCC 2001), significantly increased at the wavelength of 260 nm following a 1 h treatment with the root and leaf extracts compared with the control, suggesting damage to the cell wall and cytoplasmic membrane of the yeast cells. Similar results have also been reported for the essential oil of *Aloysia triphylla* and ethanolic extract of *Salvia miltiorrhiza* when tested against *C. albicans*, showing increased absorbance at a wavelength of 260 nm [13, 28]. Therefore, the absorbance of the material and proteins at 260 nm wavelength can be used as an indicator of damage to the cell wall and membrane, which causes leakage of the cellular materials into the surroundings [49].

5. Conclusion

Based on the results of our study, it can be concluded that the methanolic extracts of the roots and leaves of *M. communis* could serve as potential sources of herbal drug preparations against *C. glabrata*. Further studies are necessary to determine the antifungal activity of different parts of the *M. communis* plant using different extraction methods, solvents, and conditions as well as identify the chemical identity and toxicity of the bioactive compounds in *M. communis* root extracts that are responsible for the significant antifungal activity observed in this study.

Data Availability

Data used to support the findings of this study are included within the article.

Conflicts of Interest

The author declares that there are no conflicts of interest.

Acknowledgments

The author extends their appreciation and acknowledges the Deanship of Scientific Research, College of Applied Medical Sciences, at King Saud University, Riyadh, Kingdom of Saudi Arabia, for the financial support. The Deanship of Scientific Research at King Saud University funded this work.

References

[1] World Health Organisation (WHO), *Traditional Medicine Strategy: 2002–2005*, World Health Organisation (WHO), Geneva, 2001.

[2] World Health Organisation (WHO), *Traditional medicine. Fact sheet No 134*, World Health Organization, Geneva, 2003.

[3] M. J. Martínez, J. Betancourt, N. Alonso-González, and A. Jauregui, "Screening of some Cuban medicinal plants for antimicrobial activity," *Journal of Ethnopharmacology*, vol. 52, no. 3, pp. 171–174, 1996.

[4] V. L. G. Rehder, A. L. M. Machado, C. Delarmelina, A. Sartoratto, M. C. T. Duarte, and G. M. Figueira, "Composic¸ ˜ao qu'ımica e atividade antimicrobiana do ´oleo essencial de duas esp'ecies de Origanum," *Revista Brasileira de Plantas Medicinais*, vol. 6, pp. 67–71, 2004.

[5] D. L. Horn, D. Neofytos, E. J. Anaissie et al., "Epidemiology and outcomes of candidemia in 2019 patients: data from the prospective antifungal therapy alliance registry," *Clinical Infectious Diseases*, vol. 48, no. 12, pp. 1695–1703, 2009.

[6] C. C. Lai, C. Y. Wang, W. L. Liu, Y. T. Huang, and P. R. Hsueh, "Time to positivity of blood cultures of different *Candida* species causing fungaemia," *Journal of Medical Microbiology*, vol. 61, no. 5, pp. 701–704, 2012.

[7] M. Ortega, F. Marco, A. Soriano et al., "*Candida* species bloodstream infection: epidemiology and outcome in a single institution from 1991 to 2008," *The Journal of Hospital Infection*, vol. 77, no. 2, pp. 157–161, 2011.

[8] S. Silva, M. Negri, M. Henriques, R. Oliveira, D. W. Williams, and J. Azeredo, "*Candida glabrata*, *Candida parapsilosis* and *Candida tropicalis*: biology, epidemiology, pathogenicity and antifungal resistance," *FEMS Microbiology Reviews*, vol. 36, no. 2, pp. 288–305, 2012.

[9] M. A. Pfaller, D. J. Diekema, R. N. Jones et al., "International surveillance of bloodstream infections due to *Candida* species: frequency of occurrence and in vitro susceptibilities to fluconazole, ravuconazole, and voriconazole of isolates collected from 1997 through 1999 in the SENTRY Antimicrobial Surveillance Program," *Journal of Clinical Microbiology*, vol. 39, no. 9, pp. 3254–3259, 2001.

[10] B. D. Chow, J. R. Linden, and J. M. Bliss, "*Candida parapsilosis* and the neonate: epidemiology, virulence and host defense in a unique patient setting," *Expert Review of Anti-Infective Therapy*, vol. 10, no. 8, pp. 935–946, 2012.

[11] J. K. Oberoi, C. Wattal, N. Goel, R. Raveendran, S. Datta, and K. Prasad, "Non-albicans Candida species in blood stream infections in a tertiary care hospital at New Delhi, India," *The Indian journal of medical research*, vol. 136, no. 6, pp. 997–1003, 2012.

[12] D. Sanglard, "Emerging threats in antifungal-resistant fungal pathogens," *Frontiers in Medicine*, vol. 3, pp. 11–13, 2016.

[13] M. de las Mercedes Oliva, M. E. Carezzano, M. N. Gallucci, and M. S. Demo, "Antimycotic effect of the essential oil of *Aloysia Triphylla* against *Candida* Species obtained from human pathologies," *Natural Product Communications*, vol. 6, no. 7, pp. 1934578X1100600–1934578X1101043, 2011.

[14] J. T. Baker, R. P. Borris, B. Carté et al., "Natural product drug discovery and development: new Perspectives on international collaboration," *Journal of Natural Products*, vol. 58, no. 9, pp. 1325–1357, 1995.

[15] A. A. Alyousef, M. Arshad, R. AlAkeel, and A. Alqasim, "Biogenic silver nanoparticles by *Myrtus communis* plant extract: biosynthesis, characterization and antibacterial activity," *Biotechnology and Biotechnological Equipment*, vol. 33, no. 1, pp. 931–936, 2019.

[16] M. E. Mohamed, O. M. Mohafez, H. E. Khalil, and I. A. Alhaider, "Essential oil from myrtle leaves growing in the eastern part of Saudi Arabia: components, anti-inflammatory and cytotoxic activities," *Journal of Essential Oil-Bearing Plants*, vol. 22, no. 4, pp. 877–892, 2019.

[17] V. Aleksic and P. Knezevic, "Antimicrobial and antioxidative activity of extracts and essential oils of *Myrtus communis* L," *Microbiological research*, vol. 169, no. 4, pp. 240–254, 2014.

[18] A. Hennia, S. Nemmiche, S. Dandlen, and M. G. Miguel, "*Myrtus communis* essential oils: insecticidal, antioxidant and antimicrobial activities: a review," *Journal of Essential Oil Research*, vol. 31, no. 6, pp. 487–545, 2019.

[19] M. Amensour, S. Bouhdid, J. Fernández-López, M. Idaomar, N. S. Senhaji, and J. Abrini, "Antibacterial activity of extracts of *Myrtus communis* Against food-borne pathogenic and spoilage bacteria," *International Journal of Food Properties*, vol. 13, no. 6, pp. 1215–1224, 2010.

[20] S. Manandhar, S. Luitel, and R. K. Dahal, "In vitro antimicrobial activity of some medicinal plants against human pathogenic bacteria," *Journal of Tropical Medicine*, vol. 2019, Article ID 1895340, 5 pages, 2019.

[21] R. al Akeel, A. Mateen, R. Syed, A. A. Alyousef, and M. R. Shaik, "Screening, purification and characterization of anionic antimicrobial proteins from *Foeniculum vulgare*," *Molecules*, vol. 22, no. 4, p. 602, 2017.

[22] A. A. Alyousef, R. Al Akeel, A. Alqasim, A. Mohammed, A. Mateen, and R. Syed, "Evaluation of antibacterial activity of twenty-two medicinal plants traditionally used in Saudi Arabia against pathogenic bacteria," *EC Microbiology*, vol. 14, no. 3, pp. 108–112, 2018.

[23] K. A. Salih, "Synergistic effects of plant extracts and antifungal drugs on C. albicans," *Journal of Developing Drugs Open Access*, vol. 5, no. 3, p. 165, 2016.

[24] S. Magaldi, S. Mata-Essayag, C. Hartung de Capriles et al., "Well diffusion for antifungal susceptibility testing," *International Journal of Infectious Diseases*, vol. 8, no. 1, pp. 39–45, 2004.

[25] J. N. Eloff, "A sensitive and quick microplate method to determine the minimal inhibitory concentration of plant extracts for bacteria," *Planta Medica*, vol. 64, no. 8, pp. 711–713, 1998.

[26] W. A. Oliveira, F. O. Pereira, C. G. D. G. Luna et al., "Antifungal activity of Cymbopogon winterianus Jowitt ex Bor against Candida albicans," *Brazilian Journal of Microbiology*, vol. 42, no. 2, pp. 433–441, 2011.

[27] M. S. A. Khan, I. Ahmad, and S. S. Cameotra, "Phenyl aldehyde and propanoids exert multiple sites of action towards cell membrane and cell wall targeting ergosterol in *Candida albicans*," *AMB Express*, vol. 3, no. 1, p. 54, 2013.

[28] H. S. Lee and Y. Kim, "Antifungal activity of Salvia miltiorrhiza against Candida albicans is associated with the alteration of membrane permeability and (1,3)-β-D-glucan synthase activity," *Journal of Microbiology and Biotechnology*, vol. 26, no. 3, pp. 610–617, 2016.

[29] A. Musini and A. Giri, "Investigation of mode of action of Anti Bacterial activity of *Salacia oblonga* extract against drug resistant pathogen," *Brazilian Archives of Biology and Technology.*, vol. 62, article e19180051, 2019.

[30] Z. U. Khan, R. Chandy, and K. E. Metwali, "*Candida albicans* strain carriage in patients and nursing staff of an intensive care unit: a study of morphotypes and resistotypes," *Mycoses*, vol. 46, no. 11-12, pp. 479–486, 2003.

[31] A. M. A. Saadabi, "Antifungal activity of some Saudi plants used in traditional Medicine," *Asian journal of plant sciences*, vol. 5, no. 5, pp. 907–909, 2006.

[32] A. Khalil, "Antimicrobial activity of ethanol leaf extracts of *Catharanthus roseus from Saudi Arabia*," in *Second International Conference on Environment Science and Biotechnology*, vol. 48, Singapore, 2012.

[33] M. M. Aly and S. O. Bafeel, "Screening for antifungal activities of some medicinal plants used traditionally in Saudi Arabia," *Journal of Applied Animal Research*, vol. 38, no. 1, pp. 39–44, 2010.

[34] F. M. Bokhari, "Antifungal activity of some medicinal plants used in Jeddah, Saudi Arabia," *Mycopathologia*, vol. 7, pp. 51–57, 2009.

[35] S. A. Omer, S. E. I. Adam, and O. B. Mohammed, "Antimicrobial activity of Commiphora myrrha against some bacteria and Candida albicans isolated from gazelles at King Khalid Wildlife Research Centre," *Research Journal of Medicinal Plant*, vol. 5, no. 1, pp. 65–71, 2011.

[36] M. Alhussaini, A. M. Saadabi, M. I. Alghonaim, and K. E. Ibrahim, "An evaluation of the antimicrobial activity of *Commiphora myrrha* Nees (Engl.) oleo-gum resins from Saudi Arabia," *Journal of Medical Sciences (Faisalabad)*, vol. 15, no. 4, pp. 198–203, 2015.

[37] A. Ba-Hamdan, A. Hamdan, M. M. Aly, and S. O. Bafeel, "Antimicrobial activities and phytochemical analysis of the essential oil of Ocimum basilicum, collected from Jeddah region," *Saudi Arabia Journal Of Microbiology Research*, vol. 4, no. 6a, pp. 1–9, 2014.

[38] H. Balto, I. Al-Sanie, S. Al-Beshri, and A. Aldrees, "Effectiveness of *Salvadora persica* extracts against common oral pathogens," *The Saudi dental journal*, vol. 29, no. 1, pp. 1–6, 2017.

[39] M. M. Haque and S. A. Alsareii, "A review of the therapeutic effects of using miswak (*Salvadora Persica*) on oral health," *Saudi Medical Journal*, vol. 36, no. 5, pp. 530–543, 2015.

[40] F. Giampieri, D. Cianciosi, and T. Y. Forbes-Hernández, "Myrtle (*Myrtus communis* L.) berries, seeds, leaves, and essential oils: new undiscovered sources of natural compounds with promising health benefits," *Food Frontiers*, vol. 1, no. 3, pp. 276–295, 2020.

[41] S. Mansouri, A. Foroumadi, T. Ghaneie, and A. G. Najar, "Antibacterial activity of the crude extracts and fractionated constituents of Myrtus communis," *Pharmaceutical Biology*, vol. 39, no. 5, pp. 399–401, 2001.

[42] O. Gortzi, S. Lalas, I. Chinou, and J. Tsaknis, "Reevaluation of bioactivity and antioxidant activity of *Myrtus communis* extract before and after encapsulation in liposomes," *European Food Research and Technology*, vol. 226, no. 3, pp. 583–590, 2008.

[43] S. Cannas, P. Molicotti, M. Ruggeri et al., "Antimycotic activity of *Myrtus communis* L. towards Candida spp. from clinical isolates," *Journal of Infection in Developing Countries*, vol. 7, no. 3, pp. 295–298, 2013.

[44] M. Mahboubi and F. Ghazian Bidgoli, "*In vitro* synergistic efficacy of combination of amphotericin B with *Myrtus communis* essential oil against clinical isolates of *Candida albicans*," *Phitomedicine*, vol. 17, no. 10, pp. 771–774, 2010.

[45] T. Mert, T. Fafal, B. Kivcak, and H. T. Ozturk, "Antimicrobial and cytotoxic activities of *Myrtus communis* L," *Journal of Faculty of Pharmacy of Ankara University*, vol. 37, pp. 191–199, 2008.

[46] J. Jeenkeawpieam, S. Yodkeeree, A. Andrianopoulos, S. Roytrakul, and M. Pongpom, "Antifungal activity and molecular mechanisms of partial purified antifungal proteins from *Rhinacanthus nasutus* against *Talaromyces marneffei*," *Journal of Fungi*, vol. 6, no. 4, p. 333, 2020.

[47] S. al-Ali and A. al-Judaibi, "Biochemical and Molecular Effects of *Phoenix dactylifera* and *Ziziphus spina-christi* Extracts on *Candida albicans*," *Journal of Biosciences and Medicines*, vol. 7, no. 3, pp. 29–43, 2019.

[48] M. B. Sadiq, J. Tarning, T. Aye Cho, and A. Anal, "Antibacterial activities and possible modes of action of *Acacia nilotica* (L.) Del. against multidrug-resistant *Escherichia coli* and *Salmonella*," *Molecules*, vol. 22, no. 1, p. 47, 2017.

[49] J. Zhang, K. P. Ye, X. Zhang, D. D. Pan, Y. Y. Sun, and J. X. Cao, "Antibacterial activity and mechanism of action of black pepper essential oil on meat-borne *Escherichia coli*," *Frontiers in microbiology*, vol. 7, no. 7, p. 2094, 2017.

Hindawi
Journal of Nanomaterials
Volume 2021, Article ID 2555525, 10 pages
https://doi.org/10.1155/2021/2555525

Research Article

Enhancement of Mechanical Properties on Novel Friction Stir Welded Al-Mg-Zn Alloy Joints Reinforced with Nano-SiC Particles

L. Natrayan,[1] **M. Ravichandran**,[2] **Dhinakaran Veeman**,[3] **P. Sureshkumar**,[4] **T. Jagadeesha**,[5] **R. Suryanarayanan**,[6] **and Wubishet Degife Mammo**[7]

[1]*Department of Mechanical Engineering, Saveetha School of Engineering, SIMATS, Tamil Nadu, Chennai 602105, India*
[2]*Department of Mechanical Engineering, K. Ramakrishnan College of Engineering, Samayapuram, 621112, Tamil Nadu, India*
[3]*Centre for Additive Manufacturing, Chennai Institute of Technology, Chennai, Tamil Nadu 600069, India*
[4]*Department of Mechanical Engineering, Ramco Institute of Technology, Tamil Nadu, Virudhunagar 626125, India*
[5]*Department of Mechanical Engineering, National Institute of Technology, Calicut, 673601 Kerala, India*
[6]*School of Mechanical Engineering, Vellore Institute of Technology, Tamil Nadu, Chennai 600127, India*
[7]*Mechanical Engineering Department, Wollo University, Kombolcha Institute of Technology, Kombolcha, South Wollo, 208 Amhara, Ethiopia*

Correspondence should be addressed to L. Natrayan; natrayanphd@gmail.com,
Dhinakaran Veeman; dhinakaranv@citchennai.net, and Wubishet Degife Mammo; wubishetdegife7@gmail.com

Received 27 July 2021; Revised 11 September 2021; Accepted 15 September 2021; Published 5 October 2021

Academic Editor: Lakshmipathy R

Copyright © 2021 L. Natrayan et al. This is an open access article distributed under the Creative Commons Attribution License, which permits unrestricted use, distribution, and reproduction in any medium, provided the original work is properly cited.

Friction stir welding (FSW) is a solid-state technique used to join Al-Zn-Mg alloys effectively compared with other conventional welding methods. Al-Zn-Mg alloy was processed for welding because they significantly demanded various engineering applications. A novel method of this research work is to characterize the unique mechanical properties of Al-Zn-Mg alloy reinforced with 1 to 3 wt% of nano silicon carbide (nano-SiC) particles developed by novel interlock friction-stir welding. The process parameters chosen for welding are rotational tool speed 1100 rpm, weld speed 25 mm/min, and triangular pin profile. The weld joint properties such as tensile strength, yield strength, and hardness were tested per ASTM standard. The microstructure of weld joints was studied with XRD and optical and scanning electron microscopy. The existence of silica particles in the weld joints and uniformed and homogeneous distribution of the particulates in the weld was verified by EDS analysis and microstructure. Al-Zn-Mg reinforced with nano-SiC joints has better static properties due to intensive softening in the stir region. Al-Zn-Mg with 3 wt% nano-SiC exhibits maximum tensile strength, yield strength, and nugget hardness of 191 MPa, 165 MPa, and 171 HV. Weld microstructures showed a pinning mechanism because nano-SiC particles were used as reinforcement during friction stir welding.

1. Introduction

Welding is the most widely used fabrication technique in the manufacturing industry. Friction stir welding (FSW) was invented by Thomas WM at TWI UK in 1991 to overcome the fusion welding problems [1]. Kapil and Sharma investigated on few similar and dissimilar materials and identified some unsolved critical issues [2]. Few researchers extend the limits of FSW in welding of different materials such as Al-Mg [3], Cu-Al [4], Al-Cu [5], and plastics [6]. The material flow during the process was analytically studied [7]. Since its invention, the FSW process has been extensively used in various industrial applications, joining current and future advanced materials [8]. In this process, the shoulder/-workpiece interface causes the frictional heat to form plastic deformation [9]. Welding parameters impact the material

flow and heat generation, which affected the weld strength [10]. The surface roughness of the sample and the oxide layer presence were reported to influence the tensile shear force of the joint [11]. The rotational weld speeds of the tool and pin profile geometry affect the temperature and plastic flow field [12]. The filling stud is a single-stage process where the stud is placed onto the prefabricated hole in the joint. Weld joint strength was increased with an increase in TRS which was studied and reported in dissimilar AA7075-AA2024 Al-alloy FSW joints [13].

The weld quality was evaluated by the hardness of the joint; the relationship between peak temperature and hardness profile at the stir zone was investigated on AA6061-AA7075 Al-alloy joints [14]. The impact of weld speed on joint strength was studied in dissimilar AA6061-T6/AA7075-T6 Al-alloy joints. The welds were fabricated at different weld speeds of 80, 100, and 120 mm/min, where defect-free and superior strength joints were produced at 120 mm/min [15]. Employing lower plunge depth during FSSW produced weaker mechanical interlocking. The gradual rise in the plunge depth produced a stronger FSSW joint. However, a variation in the hook morphology was observed [16]. The noncircular tool profiles were reported to allow a smoother flow of plasticized material around the pin by breaking the oxide particles and producing fine grains at the stir zone [17]. The effects of the number of passes on microstructure and mechanical properties were discussed and reported with an increasing number of pass, the average grain size in the weld zone of aluminium 5083 decreases, and mechanical properties increased [18]. The effect of TRS on the stir zone of dissimilar AA6061/AA7050 Al-alloy joints revealed that the degree of material transfer was influenced by the rotational tool speed [19]. The study report on AA6061/AA5086 Al-alloy revealed that welds fabricated with threaded cylindrical pin profiles exhibit better mechanical properties than welds fabricated with other welds [20]. Dissimilar AA6061/AA5010 Al-alloy welds made with square pin profile exhibit superior strength compared to cylindrical pin profiles [21]. The hardness at the TMAZ-HAZ was observed to be low compared to the other weld regions, irrespective of the changes in the process parameters. The detailed analysis of the weld zone by TEM revealed that the size and shape of the strengthening precipitate influence the microstructure and the microhardness. The adherence of the plasticized material on the pin at the high dwell times [22]. The study reported on dissimilar AA6061/AA2014 revealed that joints fabricated by hybrid square pin profiles exhibit good material flow than other welds [23]. The thread profiles were observed to influence the material flow in the FSW process [24]. The increased upward material flow was observed with the right-hand threaded tool, which resulted in the tunnel defect formation. However, with left-hand threaded tools, excellent tensile properties were obtained due to the increased downward material flow, which resulted in defect-free weld joints with superior tensile strength [25].

Fabrication of different grade materials with FSW is challenging to the researchers and manufacturers. FSW of Al-Mg-Zn alloys was reported to produce stronger weld joints than conventional fusion welding methods by inhibiting the negative influence of intermetallic compound formation due to high heat input. Therefore, the present study was aimed at investigating the influence of nano-SiC particle reinforcement on mechanical and microstructural properties of 2 mm thick dissimilar Al-Mg-Zn alloy FSW interlock weldments. Al-Mg-Zn alloy has been widely employed to fabricate truck frames, aircraft structures, automotive parts, marine and shipbuilding, storage tanks, railroad cars, etc.

Table 1: Sample wt% combinations.

Sample No.	Combinations
Sample 1	Al-Mg-Zn/1.0 wt% nano-SiC
Sample 2	Al-Mg-Zn/1.5 wt% nano-SiC
Sample 3	Al-Mg-Zn/2.0 wt% nano-SiC
Sample 4	Al-Mg-Zn/2.5 wt% nano-SiC
Sample 5	Al-Mg-Zn/3.0 wt% nano-SiC

2. Experimental Procedure

Flat plates of Al-Mg-Zn alloy of 2 mm thick with various wt% of nanosilicon carbide particles (1 to 3 wt%) with 10 nm particle size were added in joint lap configuration. Sample numbers with reinforcement wt% are shown in Table 1. Initially, the specimens were chemically treated to remove grease and dirt particles at the weld site. Then, the process is carried out by a friction stir welding machine [26].

The interlock FSW of Al-Mg-Zn alloy was conducted at 1100 RPM, 25 mm/min triangular pin and varying wt% of nano-SiC particles from 1 to 3%. The base metal of $100 \times 100 \times 2$ mm thickness was milled to a depth of 1 mm and width of 35 mm along the longitudinal direction [27]. The aluminium sheet top surface was milled to 0.75 mm width, as shown in Figure 1. Nano-SiC reinforcements were filled in the top groove that intersects to produce a hybrid seal between the welds [28]. The nonconsumable tool material used for this experiment is AISI-H13 tool steel, shown in Figure 2. During the process, a shoulder diameter of 25 mm and a triangular profile pin of 3 mm inscribed in a circle of 8 mm diameter were employed [29]. The tool is plunged to a depth of 3 mm and traversed along the longitudinal direction to a distance of 85 mm to form a weld joint with assistance from frictional heat and plastic deformation [30].

FSW interlock weldments joined at varying wt% of nano-SiC samples are shown in Figure 3. The hardness was tested on a Vickers hardness testing machine with a working load of 110 kgf and a dwell period of 10 sec [31]. Tensile test was conducted as per ASTM E8 on the precision universal testing machine (SHIMADZU) which has a test load of 50 kN at a crosshead velocity of 0.5 mm/min [16]. Microstructure analysis was studied with optical scanning electron microscopy.

3. Results and Discussion

3.1. X-Ray Diffraction Test. Figure 4 shows the XRD pattern for FSW interlock samples in the heat-affected zone. The

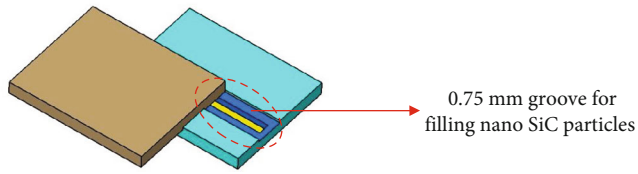

Figure 1: Groove in base metal.

weld cross section of the joint with the maximum tensile strength is analysed using XRD for different phases across the weld zone. In comparison to the normal diffraction data, the peaks were examined with the existence of various phases. 2θ reflections at 38.01, 52.5, and 75.6° correspond to the Al phase [32]. $MgZn_2$ and $MgSi_2$ phase is confirmed from the peaks at 21.45 and 24.32, respectively. The nano-SiC particle peak was observed at 62.03 and 88.6° confirmed with the JCPDS No. 29-1128. Peak intensity was found to vary with Si composition. It is observed that the peak shift was observed with increasing Si wt%.

3.2. Temperature Measurement. During the FSW process, heat was generated from tool-workpiece interaction and the plastic deformation of the Al-Mg-Zn alloy. The temperature profile during the process was measured with the help of an infrared thermometer. The heat generated in the process is responsible for softening the material at the weld region, reducing the thermomechanical stresses on the tool during the process [33].

In the FSW process, the contact area between the pin profile and the weld surfaces was responsible for generating the frictional heat [34].

$$Q_{\text{Tot}} = \frac{2\pi\mu P\tau}{3}\omega\left(R^3 - R_{\text{p}}^3\right) + 3R_{\text{p}}^2 P_{\text{l}}\Big). \quad (1)$$

Q_{Tot} is the total heat input, W; μ is the friction coefficient; P is the axial force, N; ω is the rotational speed; R is the shoulder radius, m; R_p is the pin radius, m; and P_l is the pin length. The heat input was primarily estimated by using equation 1 as

$$Q = \eta\frac{2\pi\omega T}{V}. \quad (2)$$

The estimated heat generated of 9546.24 W during the process was calculated by using the following equation. The heat generated during the process was measured in terms of temperature with the help of an IR thermometer. The temperature transferred from NZ to the ends of the weld plates was observed to vary due to the influence of the tool shown in Figure 5. The maximum temperatures were observed during welding to be maximum around the edge of the tool.

3.3. Microstructure. The weldments were cut across the weld joint to view the microstructure. The specimens were prepared by polishing till a scratch-free mirror-like image was

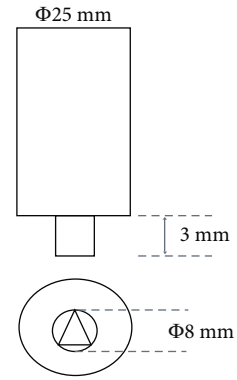

Figure 2: AISI-H13 tool steel dimensions.

obtained. Further, they are etched with Keller's reagent (95 ml of water, 2.5 ml of nitric acid, 1.5 ml of hydrofluoric acid, and 1 ml of hydrochloric acid). The microstructures of etched specimens were observed under an optical microscope. The microstructures captured at different samples are shown in Figures 6(a)–6(d).

In the FSW process, the plastically deformed material in the weld zone was experienced by the thermomechanical cycle. The weld zone cross section has a fine-grained structure. In dissimilar material welding, the analysis of microstructure is complex due to the heterogeneous properties of materials. The microstructure obtained shows grains, grain boundaries are shown in Figures 6(a)–6(d) with intermetallic particles, and some grains are elongated. The microstructure analysis has reported that TMAZ consists of coarser and elongated grains because of the heat produced by the tool shoulder during rotation. Uniform distribution is observed in Figures 6(a)–6(d).

3.4. SEM Analysis. SEM image of the interlock friction stir welded sample with different w.t% of nano-SiC is shown in Figures 7(a)–7(e). The microstructure at the weld zone was asymmetric due to different wt% of the composition of the silicon carbide particles (Figures 7(a) and 7(b)). The elements magnesium and silicon form the Mg_2Si compound shown as bright regions that do not dissolve in parent materials (Figures 7(c) and 7(d)). This leads to conclude that dark and bright lamellar originates from Al–Mg-Zn alloys. On the other hand, the welds processed with nano-SiC 3 wt% have uniform distribution and good mixing as shown in Figure 7(e).

EDAX analysis shown in Figures 8(a) and 8(b) addresses the secondary phase IMCs in the form of Mg_2Si, which

Figure 3: FSW interlock weldments joined at varying wt% of nano-SiC.

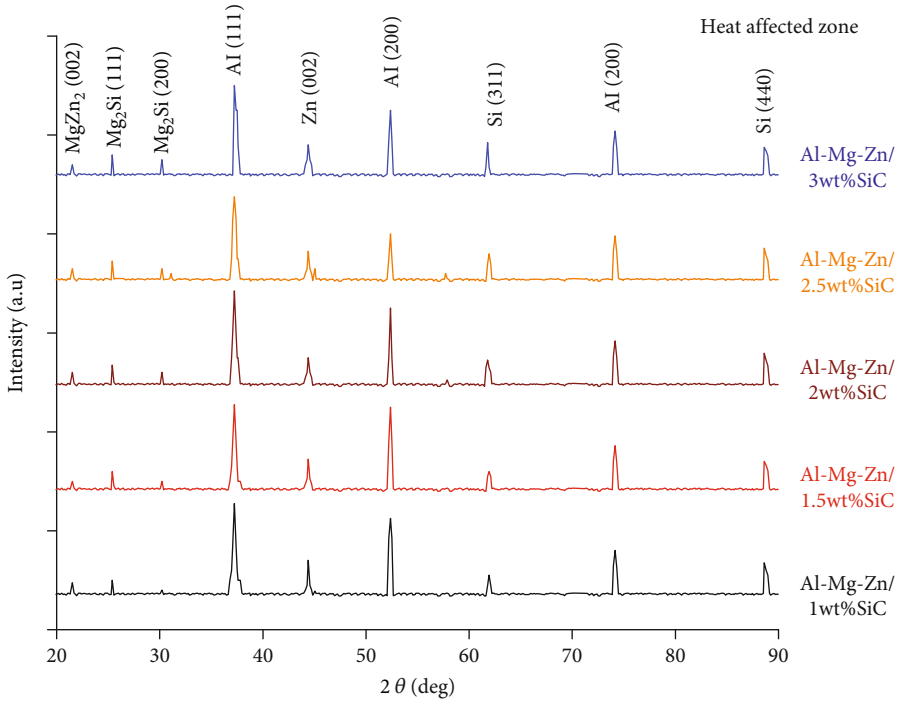

Figure 4: XRD pattern for FSW interlock samples (heat-affected zone).

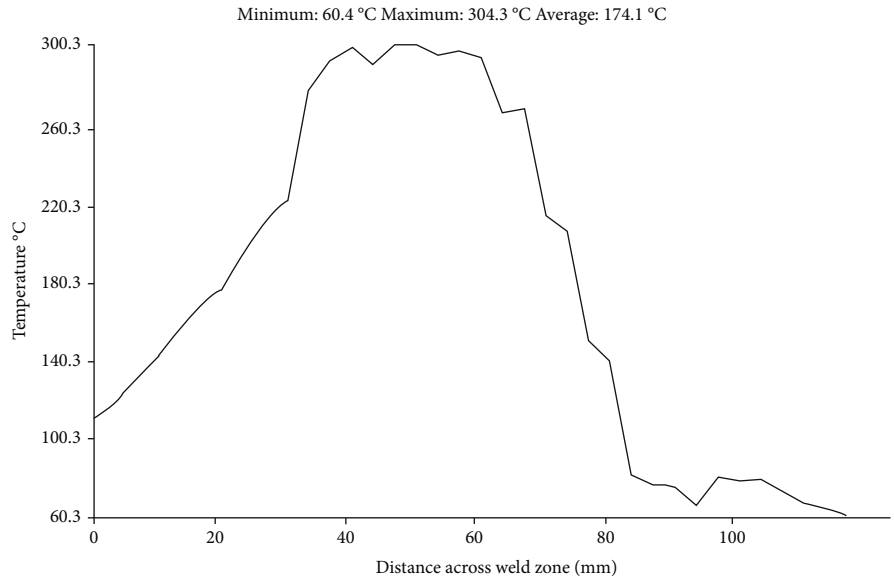

Figure 5: Temperature profile of weldment along the weld joint for sample 5.

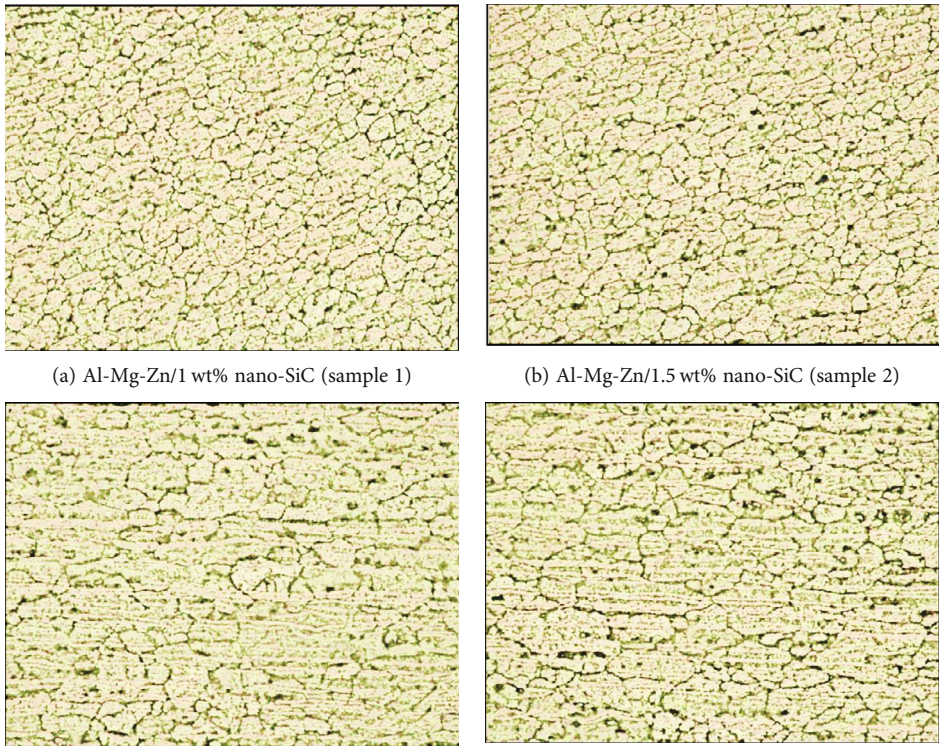

(a) Al-Mg-Zn/1 wt% nano-SiC (sample 1)

(b) Al-Mg-Zn/1.5 wt% nano-SiC (sample 2)

(c) Al-Mg-Zn/1 wt% nano-SiC (sample 4)

(d) Al-Mg-Zn/1 wt% nano-SiC (sample 5)

Figure 6: (a–d) Microstructures of modified interlock FSW welded samples with addition of nano-SiC.

consists at the nugget zone. In the NZ, an average composition close to that of the Al-Mg-Zn was found in EDAX. The EDAX confirmed the elemental composition of the welds at the nugget zone. EDAX profile showed that NZ has less Mg content than base materials. The compounds like Si, Zn, Mg, and CO_3 were present in the NZ.

3.5. Mechanical Properties. The microstructure variations in and around the weld zone can lead to a change in the tensile strength of the weldment. FSW interlock sample mechanical properties and joint efficiency are shown in Table 2. Base metal strength was observed as 285 MPa. The joint efficiency is the ratio of UTS of the weld and UTS of the parent metal.

$$\text{Joint efficiency\%} = \frac{\text{Weld joint strength}}{\text{Base metal strength}} \times 100. \quad (3)$$

3.6. Hardness. Hardness test was conducted on the transverse section of welded samples with a spacing of 5 mm and load of 110 kgf with a dwell period of 10 sec. Al-Mg-Zn with various wt% of nano-SiC samples interlocked with friction stir welding using triangular pin profiles processed at 1100 rpm exhibits differences in hardness along the weld line as shown in Figure 9.

The hardness of the weld joint was determined across the weld zone. The hardness variation across the weld zone was observed to possess a W profile, with hardness at nugget higher than thermomechanically affected zone (TMAZ), heat-affected zone (HAZ), and parent metal irrespective of changes in wt% of nano-SiC particles. The increased hardness at the nugget is credited to the grain refinement and nano-SiC particles. The intense stirring action during FSW and presence of nano-SiC particles resulted in severe plastic deformation resulting in increased hardness at the nugget. Moreover, nano-SiC particle addition resulted in grain boundary pinning [35]. The minimum hardness value was found at HAZ. The hardness at the HAZ is minimum due to precipitation phenomena [36]. The less hardness observed in the HAZ is due to the fact that IMCs may form Mg_2Si and less Si compound on the Al-Mg-Zn/1 wt% nano-SiC (sample 1). The maximum hardness values of sample 5 (Al-Mg-Zn/5wt% nano-SiC) observed were 88 to 171 HV from NZ to HAZ. The weld zone hardness varied between 125 and 171 HV.

3.7. Tensile Strength. Tensile test samples were prepared as per the standard of ASTM E8/ASTM B557. The test specimen shape was cut by wire EDM machine to get accurate dimensions shown in Figure 10. The test was conducted on the precision universal testing machine (SHIMADZU) at a test load of 50 kN and a crosshead velocity of 0.5 mm/min. The results observed from the experiment are tabulated in Table 2. The test results revealed that the interlock welded joints failed by tensile and shear mode of failure.

The tensile and yield strength was observed to increase with the wt% of nano-SiC particles. The increase in the

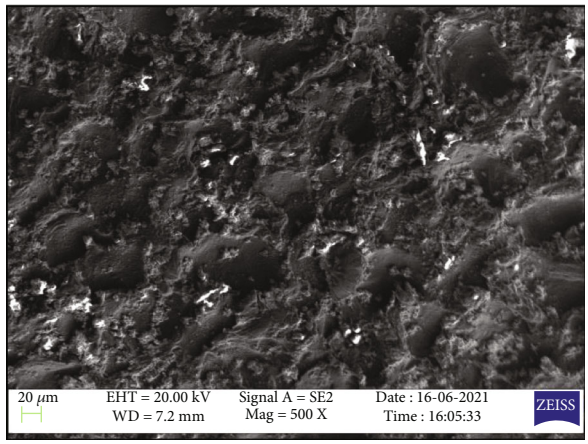

(a) SEM of Al-Mg-Zn/1 wt% nano-SiC (sample 1)

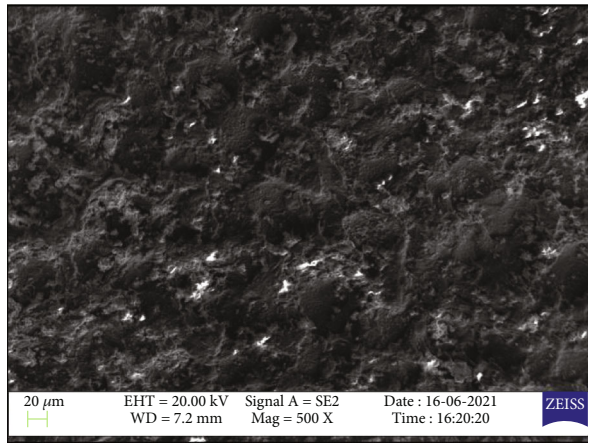

(b) SEM of Al-Mg-Zn/1.5 wt% nano-SiC (sample 2)

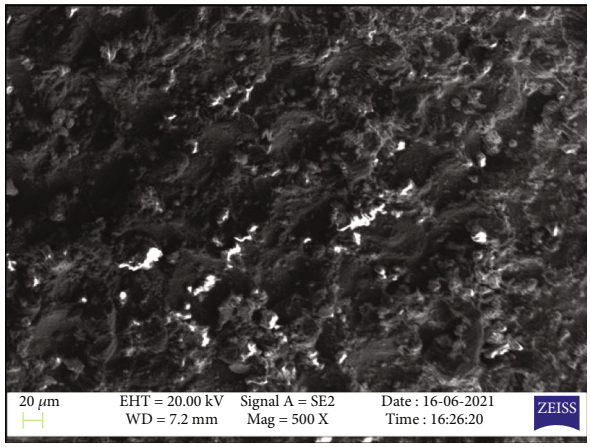

(c) SEM of Al-Mg-Zn/2 wt% nano-SiC (sample 3)

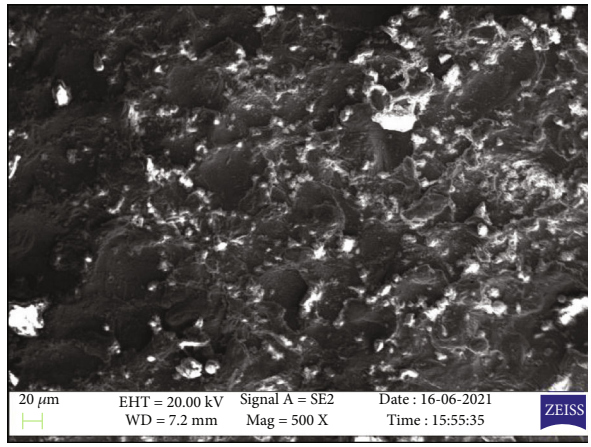

(d) SEM of Al-Mg-Zn/2.5 wt% nano-SiC (sample 4)

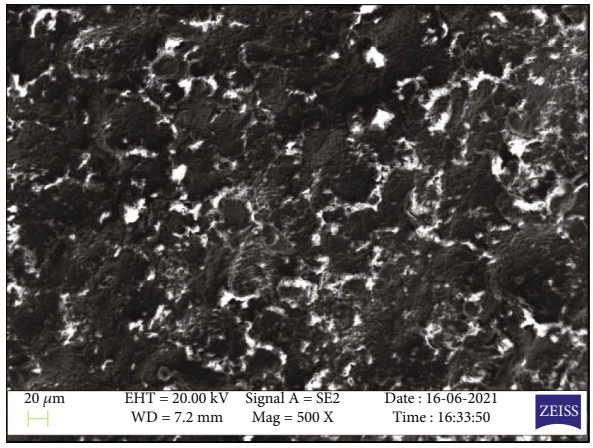

(e) SEM of Al-Mg-Zn/2.5 wt% nano-SiC (sample 5)

Figure 7: (a–e) SEM images of modified interlock FSW welded samples with addition of nano-SiC.

mechanical strength of the weld joint with the increase in the wt% of nano-SiC reinforcements is credited to the increased material mixing between the base metal and the reinforcement, which led to the accumulation of large amounts of reinforcement particles at the grain boundaries due to decreased dislocation during dynamic recrystallization [35]. The NZ was composed of equiaxed and fine grains, and TMAZ has coarse bent recovered grains. The fracture location is between WN and TMAZ on AS. Maximum UTS and YS values were recorded as 191 MPa and 170 MPa, respectively. As per AWS D17 specifications, the joint efficiency factor for aerospace applications is 0.6 to 0.7,

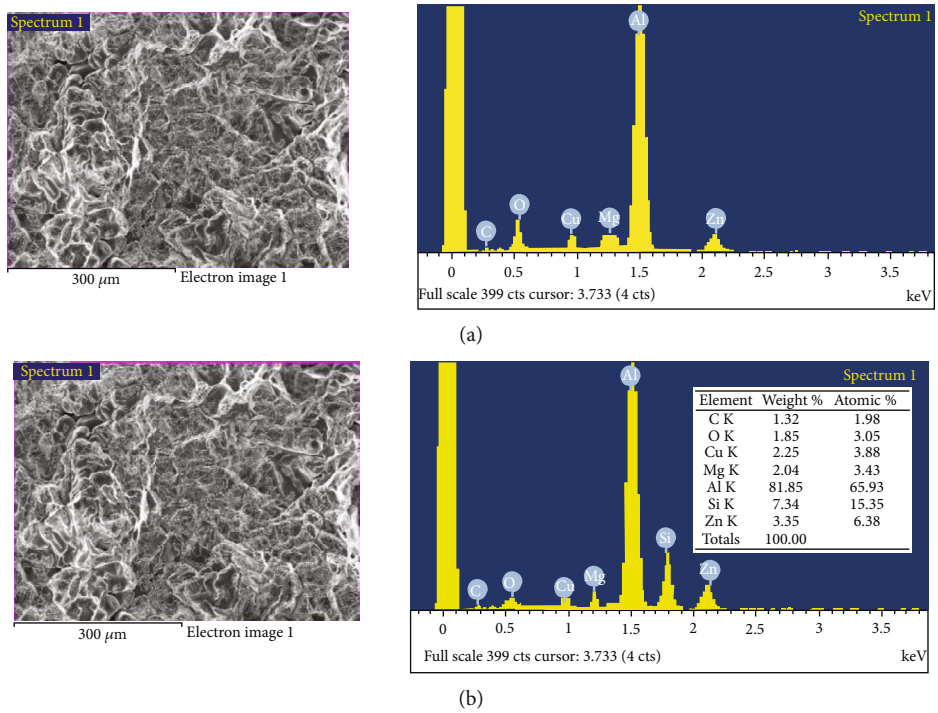

Figure 8: (a) EDAX analysis for Al-Mg-Zn/1 wt% nano-SiC (sample 1). (b) EDAX analyses for Al-Mg-Zn/3 wt% nano-SiC (sample 5).

Table 2: Mechanical properties of fabricated samples with joint efficiency.

Sample composition	Ultimate tensile strength (MPa)	Hardness (HV)	Yield strength (MPa)	Joint efficiency (%)
Al-Mg-Zn/1.0 wt% nano-SiC	125	137	94	0.43
Al-Mg-Zn/1.5 wt% nano-SiC	143	152	99	0.50
Al-Mg-Zn/2.0 wt% nano-SiC	157	163	107	0.55
Al-Mg-Zn/2.5 wt% nano-SiC	178	167	133	0.62
Al-Mg-Zn/3 wt% nano-SiC	191	171	165	0.67

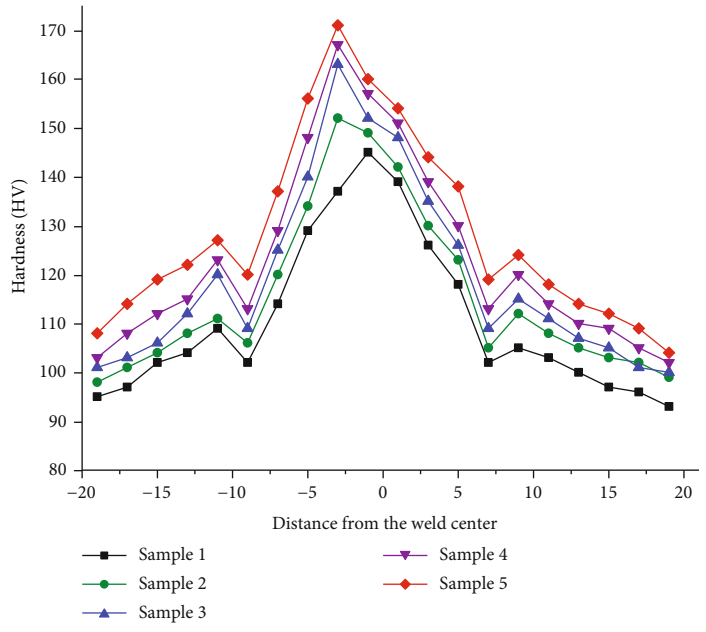

Figure 9: Hardness profile of weld joints processed at different wt% of nano-SiC.

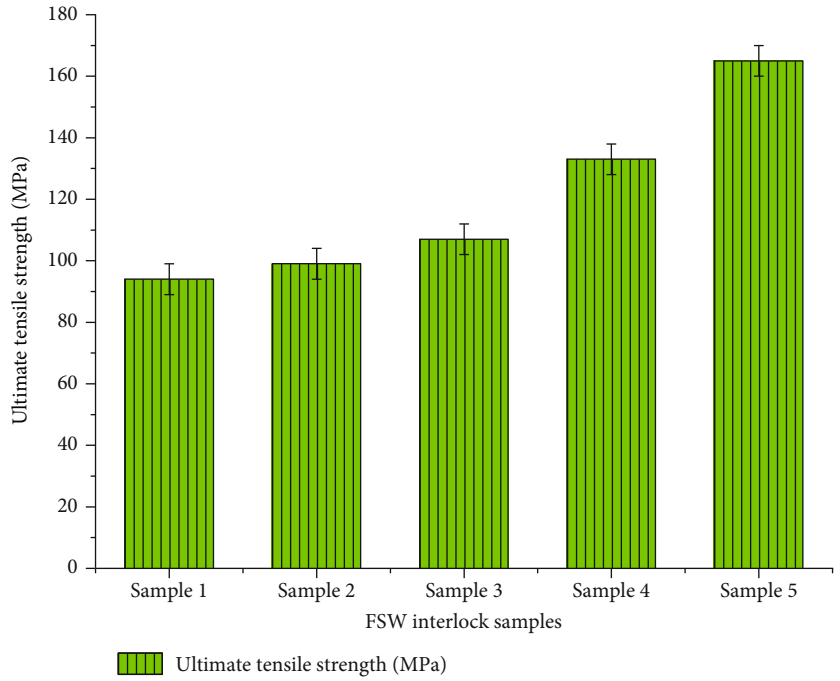

Figure 10: Tensile strength of weld joints processed at different wt% of nano-SiC.

achieved in this experiment sample 5. Hence, the fabricated joints were recommended for various structural applications where the above properties are required.

4. Conclusions

In this research, Al-Zn-Mg alloy added with 1 to 3 wt% of silicon carbide (nano-SiC) particles was successfully developed by novel interlock friction-stir welding methods. The process parameters chosen for welding are rotational tool speed 1100 rpm, weld speed 25 mm/min, and triangular pin profile. FSW interlock weld samples were characterized, and the following findings were drawn:

(i) Al-Zn-Mg/3 wt% nano-SiC (sample 5) shows better yield strength, tensile strength, and hardness

(ii) SEM microstructure showed that very fine grains and nano-SiC particles uniformly mix between the base materials

(iii) EDAX analysis confirmed the presence of silicon carbide particles in the interlock weld zone

(iv) AWSD17 requirement attained with a common efficiency factor of 0.67

(v) The highest tensile strength was reported as 191 MPa, and hardness was reported as 171 HV

Data Availability

The data used to support the findings of this study are included in the article. Should further data or information be required, these are available from the corresponding author upon request.

Disclosure

This research was performed as a part of the Employment of Kombolcha Institute of Technology, Wollo University, Kombolcha, Amhara, Ethiopia.

Conflicts of Interest

The authors declare that there are no conflicts of interest regarding the publication of this paper.

Acknowledgments

The authors thank Saveetha School of Engineering, SIMATS, Chennai and Vellore Institute of Technology, Chennai, for providing characterization support to complete this research work.

References

[1] D. Kumar Rajak, D. D. Pagar, P. L. Menezes, and A. Eyvazian, "Friction-based welding processes: friction welding and friction stir welding," *Journal of Adhesion Science and Technology*, vol. 34, no. 24, pp. 2613–2637, 2020.

[2] A. Kapil and A. Sharma, "Magnetic pulse welding: an efficient and environmentally friendly multi- material joining technique," *Journal of Cleaner Production*, vol. 100, pp. 35–58, 2015.

[3] V. Firouzdor and S. Kou, "Al-to-Mg friction stir welding: effect of positions of Al and Mg with respect to the welding tool," *Welding Journal*, vol. 88, 2009.

[4] X. Fei, Y. Ye, L. Jin, H. Wang, and S. Lv, "Special welding parameters study on Cu/Al joint in laser-heated friction stir welding," *Journal of Materials Processing Technology*, vol. 256, pp. 160–171, 2018.

[5] C. W. Tan, Z. G. Jiang, L. Q. Li, Y. B. Chen, and X. Y. Chen, "Microstructural evolution and mechanical properties of dissimilar Al-Cu joints produced by friction stir welding," *Materials and Design*, vol. 51, pp. 466–473, 2013.

[6] R. Nandan, G. G. Roy, T. J. Lienert, and T. Debroy, "Numerical modelling of 3D plastic flow and heat transfer during friction stir welding of stainless steel," *Science and Technology of Welding and Joining*, vol. 11, no. 5, pp. 526–537, 2006.

[7] A. K. Kadian and P. Biswas, "Effect of tool pin profile on the material flow characteristics of AA6061," *Journal of Manufacturing Processes*, vol. 26, pp. 382–392, 2017.

[8] V. Paranthaman, K. Shanmuga Sundaram, and L. Natrayan, "Effect of silica content on mechanical and microstructure behaviour of resistance spot welded advanced automotive TRIP steels," *SILICON*, vol. 1, pp. 1–10, 2021.

[9] A. R. Darvazi and M. Iranmanesh, "Prediction of asymmetric transient temperature and longitudinal residual stress in friction stir welding of 304L stainless steel," *Materials and Design*, vol. 55, pp. 812–820, 2014.

[10] R. Suryanarayanan and V. G. Sridhar, "Effect of process parameters in pinless friction stir spot welding of Al 5754-Al 6061 alloys," *Metallography, Microstructure, and Analysis*, vol. 9, no. 2, pp. 261–272, 2020.

[11] S. Yogeshwaran, L. Natrayan, S. Rajaraman, S. Parthasarathi, and S. Nestro, "Experimental investigation on mechanical properties of Epoxy/graphene/fish scale and fermented spinach hybrid bio composite by hand lay-up technique," *Materials Today: Proceedings*, vol. 37, pp. 1578–1583, 2021.

[12] A. S. Avinash, "Evaluation on mechanical properties of basalt fiber-E glass reinforced polymer composite," *Test Engineering and Management*, vol. 83, pp. 14222–14227, 2020.

[13] C. Zhang, G. Huang, Y. Cao, Y. Zhu, and Q. Liu, "On the microstructure and mechanical properties of similar and dissimilar AA7075 and AA2024 friction stir welding joints: effect of rotational speed," *Journal of Manufacturing Processes*, vol. 37, pp. 470–487, 2019.

[14] S. Magesh, V. R. Niveditha, P. S. Rajakumar, S. Radha RamMohan, and L. Natrayan, "Pervasive computing in the context of COVID-19 prediction with AI-based algorithms," *International Journal of Pervasive Computing and Communications*, vol. 16, no. 5, pp. 477–487, 2020.

[15] J. F. Guo, H. C. Chen, C. N. Sun, G. Bi, Z. Sun, and J. Wei, "Friction stir welding of dissimilar materials between AA6061 and AA7075 Al alloys effects of process parameters," *Materials and Design*, vol. 56, pp. 185–192, 2014.

[16] L. Natrayan and M. Senthil Kumar, "An integrated artificial neural network and Taguchi approach to optimize the squeeze cast process parameters of AA6061/Al_2O_3/SiC/Gr hybrid composites prepared by novel encapsulation feeding technique," *Materials Today Communications*, vol. 25, p. 101586, 2020.

[17] K. Hemalatha, C. James, L. Natrayan, and V. Swamynadh, "Analysis of RCC T-beam and prestressed concrete box girder bridges super structure under different span conditions," *Materials Today: Proceedings*, vol. 37, pp. 1507–1516, 2021.

[18] D. Veeman, M. S. Sai, P. Sureshkumar et al., "Additive manufacturing of biopolymers for tissue engineering and regenerative medicine: an overview, potential applications, advancements, and trends," *International Journal of Polymer Science*, vol. 2021, Article ID 4907027, 20 pages, 2021.

[19] R. I. Rodriguez, J. B. Jordon, P. G. Allison, T. Rushing, and L. Garcia, "Microstructure and mechanical properties of dissimilar friction stir welding of 6061-to-7050 aluminum alloys," *Materials and Design*, vol. 83, pp. 60–65, 2015.

[20] M. Sandeep Kauthsa Sharma, S. Umadevi, Y. Sai Sampath et al., "Mechanical behavior of silica fume concrete filled with steel tubular composite column," *Advances in Materials Science and Engineering*, vol. 2021, 9 pages, 2021.

[21] M. Ahmadnia, S. Shahraki, and M. A. Kamarposhti, "Experimental studies on optimized mechanical properties while dissimilar joining AA6061 and AA5010 in a friction stir welding process," *International Journal of Advanced Manufacturing Technology*, vol. 87, no. 5–8, pp. 2337–2352, 2016.

[22] L. Natrayan and A. Merneedi, "Experimental investigation on wear behaviour of bio-waste reinforced fusion fiber composite laminate under various conditions," *Materials Today: Proceedings*, vol. 37, pp. 1486–1490, 2021.

[23] M. Raturi, A. Garg, and A. Bhattacharya, "Tensile strength and failure of dissimilar friction stir welded joints between 6061-T6 and 2014-T6 aluminum alloys," *Procedia Structural Integrity*, vol. 17, pp. 495–502, 2019.

[24] S. Yogeshwaran, L. Natrayan, G. Udhayakumar, G. Godwin, and L. Yuvaraj, "Effect of waste tyre particles reinforcement on mechanical properties of jute and abaca fiber- epoxy hybrid composites with pre-treatment," *Materials Today: Proceedings*, vol. 37, pp. 1377–1380, 2021.

[25] R. Suryanarayanan, V. G. Sridhar, L. Natrayan et al., "Improvement on mechanical properties of submerged friction stir joining of dissimilar tailor welded aluminum blanks," *Advances in Materials Science and Engineering*, vol. 2021, 6 pages, 2021.

[26] L. Natrayan and M. S. Kumar, "Optimization of tribological behaviour on squeeze cast al6061/al2o3/sic/gr hmmcs based on taguchi methodandartificial neural network," *Journal of Advanced Research in Dynamical and Control Systems*, vol. 11, no. 7, pp. 493–500, 2019.

[27] L. Natrayan, P. S. S. Sundaram, and J. Elumalai, "Analyzing the uterine physiological with MMG signals using SVM," *International Journal of Pharmaceutical Research*, vol. 11, no. 2, 2019.

[28] V. Paranthaman, K. S. Sundaram, and L. Natrayan, "Influence of SiC particles on mechanical and microstructural properties of modified interlock friction stir weld lap joint for automotive grade aluminium alloy," *SILICON*, vol. 1, pp. 1–11, 2021.

[29] V. V. Patel, V. J. Badheka, and A. Kumar, "Influence of pin profile on the tool plunge stage in friction stir processing of Al–Zn–Mg–Cu alloy," *Transactions of the Indian Institute of Metals*, vol. 70, no. 4, pp. 1151–1158, 2017.

[30] L. Natrayan and M. Senthil Kumar, "A novel feeding technique in squeeze casting to improve reinforcement mixing ratio," *Materials Today: Proceedings*, vol. 46, pp. 1335–1340, 2021.

[31] G. Ghangas and S. Singhal, "Effect of tool pin profile and dimensions on mechanical properties and microstructure of friction stir welded armor alloy," *International Journal of Pharmaceutical Research*, vol. 5, no. 6, 2018.

[32] C. S. S. Anupama, L. Natrayan, E. Laxmi Lydia et al., "Deep learning with backtracking search optimization based skin lesion diagnosis model," *Computers, Materials & Continua*, vol. 70, no. 1, pp. 1297–1313, 2022.

[33] H. I. Dawood, K. S. Mohammed, A. Rahmat, and M. B. Uday, "Effect of small tool pin profiles on microstructures and mechanical properties of 6061 aluminum alloy by friction stir welding," *Transactions of Nonferrous Metals Society of China*, vol. 25, no. 9, pp. 2856–2865, 2015.

[34] H. Search, C. Journals, A. Contact, M. Iopscience, M. Simul, and I. P. Address, "A local model for the thermomechanical conditions in friction stir welding," *Modelling and Simulation in Materials Science and Engineering*, vol. 13, no. 1, pp. 77–93, 2005.

[35] H. A. Deore, J. Mishra, A. G. Rao, H. Mehtani, and V. D. Hiwarkar, "Effect of filler material and post process ageing treatment on microstructure, mechanical properties and wear behaviour of friction stir processed AA 7075 surface composites," *Surface and Coatings Technology*, vol. 374, pp. 52–64, 2019.

[36] R. Suryanarayanan and V. G. Sridhar, "Process parameter optimisation in pinless friction stir spot welding of dissimilar aluminium alloys using multi-start algorithm," *Proceedings of the Institution of Mechanical Engineers, Part C: Journal of Mechanical Engineering Science*, vol. 234, no. 20, pp. 4101–4115, 2020.

Hindawi
Journal of Nanomaterials
Volume 2021, Article ID 3175569, 13 pages
https://doi.org/10.1155/2021/3175569

Review Article

Evaluation of Prestrain Annealing Impact on Nanomaterial Sensitization

T. N. Suresh Kumar,[1] T. Deepa,[2] L. Natrayan,[3] Marabathina Maheedhar,[2] and Raja Kathiravan[4]

[1]*Department of Mechanical Engineering, Dhaanish Ahmed College of Engineering, Chennai, 601301 Tamil Nadu, India*
[2]*School of Electrical Engineering, VIT University, Chennai, 600 127 Tamil Nadu, India*
[3]*Department of Mechanical Engineering, Saveetha School of Engineering, SIMATS, Chennai, 602105 Tamil Nadu, India*
[4]*Department of Mechanical Engineering, Bahir Dar Institute of Technology, Bahir Dar University, Bahir Dar 6000, Ethiopia*

Correspondence should be addressed to T. Deepa; deepa.t@vit.ac.in, L. Natrayan; natrayanphd@gmail.com, and Raja Kathiravan; kathirrk3000@gmail.com

Received 25 July 2021; Revised 10 September 2021; Accepted 18 September 2021; Published 5 October 2021

Academic Editor: Lakshmipathy R

Copyright © 2021 T. N. Suresh Kumar et al. This is an open access article distributed under the Creative Commons Attribution License, which permits unrestricted use, distribution, and reproduction in any medium, provided the original work is properly cited.

Light metal alloys are extensively used in automotive, aerospace, aircraft, and military sectors since their lightweight leads to reduced energy consumption, increased fuel efficiency, and better environmental protection. In the present situation, nanomaterials are the potential candidate for weight saving in the structural application and can meet stringent government norms. Nanomaterial was heat-treated in the furnace to about a certain temperature and time and then normalized for strengthening. The heat-treated nanomaterial undergoes different forging processes, namely, hot forging and cold forging, using a certain capacity's hydraulic press. Hence, in this work, an extensive study on the influence of the prestrain annealing, the corrosion rate on differently treated samples, and the effect of sensitization heat treatment on the nanomaterial was done.

1. Introduction

Until cooling, the nanomaterial must be heated above its recrystallization temperature for a specified period. The cooling rate is determined by the metals being annealed [1]. Steel is typically permitted to cool to room temperature in still air, whereas copper, silver, and brass can be cooled slowly in the air or quenched quickly in water [2]. The heating process causes atoms in the crystal lattice to migrate, reducing the number of dislocations and altering the nanomaterial's ductility and hardness [3]; when the heat-treated nanomaterial cools, it recrystallizes. The crystal grain size and phase composition determined by the heating and cooling rates dictate the nanomaterial properties [4]. The silicon as the major alloy element in aluminum alloy improves the strength of the matrix. The Cu and Mg elements are secondary alloying elements in the aluminum matrix, Mg improves the uniform dispersion of the matrix elements, and Cu improves the matrix strength with a combination of Fe elements. Fe, Ni, Ti, Zn, and Cr are commonly used as minor addition in the aluminum matrix, and their composition varies dependent upon the applications. [5]. In the hot or cold working annealing process, the metal parts change the nanomaterial structure again so additional heat treatments can be needed to achieve the desired properties [6]. The key benefits of annealing are how it increases a nanomaterial's workability by improving durability, decreasing stiffness, and increasing machinability. Metal brittleness is reduced while their magnetic properties and electrical conductivity are improved by the heating and cooling process [7]. Feng et al. have prepared W-TaC alloys by hot pressing and high energy rate forging. For locating thermal surprise resistance of the as-solid samples, ELMS-like thermal surprise had been carried out [8]. The cracking formation of the developed

W-Tac was blocked due to the base temperature that increased to 100°C [9]. The W-Tac alloy density and hardness before and after HERF are shown in Table 1.

Lin et al. reported that galling happens at the die surface's boundary bottom point, in the center of the straight and corner edge. On the other hand, galling begins at the same boundaries' top as the die surface and spreads downward on the drawn cup as drawing cycles progress [10]. On both die and drawn cup surfaces, galling occurs clearly; the SLD nanomaterial shows good performance than SKD11 and ADI [11]. Figure 1 shows that the temperature was extremely high around the boundary between the straight and corner edges.

Sharma et al. focused on laser beam in-field vacuum oven annealing which is compared with CW-laser annealing. There was no loss of texture or surface roughness in this process for laser intensities. The laser annealing process is dependent on heat propagation through the thin-film system and into the substrate; significant changes were observed when the laser processed region was changed [12]. The ceramic particle size, distribution, quantity of reinforcement, and shape of the reinforcement are enhancing the mechanical, tribological, and corrosion properties of the metal matrix composites and also depend on the induced load which is transferred to the reinforcing phase [13]. Kim et al. [14] presented that after low-temperature annealing, it causes diminished leakage current. The thin Te layer is generated during the electroless deposition process, oxidized to TeO_2 or $CdTeO_3$ at low-temperature annealing. Effective resistance was increased when CZT connected with the thin oxidized layer in series. So, the leakage current is reduced. Zhao et al. investigated LDX 2404 DSS's corrosion behaviour which was presented at 700°C for various aging times. The sigma granular particles phase grows larger but less with aging time. The aged specimen's Ir/Ia current ratios increase with time, but when aging time is more than 16 hr, the change rates become alleviative [15]. As the holding time is extended to 48 hr, corrosion becomes more important, and corrosion form changes to general corrosion [16]. Eggleston et al. presented in this paper which generates higher Suns-V_{oc} voltage than the natural belt-furnace annealing process. The silicon or glass interface device attains a steady state at any point. During the process sequence, the substrate temperature reduces from 960°C to 620°C and a max sun voltage of 492 mV is generated. By the reduced processing temperature, cheaper substrates can be used, which reduces the manufacturing cost [17]. He et al. used high mechanical properties in aerospace, automobile, and shipbuilding forging production. This study concentrated on the conversion and consumption of thermal energy in heating and forging. The relationship between nanomaterial flow and energy flow is proportional, according to the study. To reduce heat loss, enterprises have to reduce heat loss and energy-carrying water emission and design a good heating furnace [18].

1.1. Variation of Metal Characteristics under Heat. Maysa Terada et al. [19], reported that the effect of known DIN 14970 steel precipitation conduct on intergranular erosion opposition was examined. $M_{23}C_6$ residues were found at the boundaries of the solution. By using X-ray diffraction, carbides were found, by the TTP curves; OM, SEM-EDS, and TEM were also listed. Temperatures between 873 and 1073 K display a low sensitivity to intergranular attack in aged specimens [20]. Kosec et al. find the austenite heat-resistant stainless steel transformation kinetics which were discussed. Long-annealed steel samples showed a heavy coarsening of precipitates, as well as a significant amount of phase particles in the form of a chain and network of plates [21]. The hardness of annealing at a temperature of 600°C started to increase after 48 hours, and the hardness increased in the temperature range of 700-900°C. The results concluded that after isothermal annealing, the microstructure steel consisted of austenite, carbide, and σ-phase [22]. Sahlaoui et al. discussed the phenomenological and analytical analysis which was carried out for the depleted chromium zone in Ni-Cr-Fe alloys caused by carbide precipitation during aging to predict the evolution of the chromium profile. Dechromization and rechromization are the two steps in the chromium concentration extraction process. For Inconel 690 heat-treated for various periods and temperatures, the proposed model constants were established. By using an approximate solution, an analytical calculation can correctly describe the dichotomization and rechromization [23]. Lv et al. investigated that at 600 degrees Celsius, the impact of refinement on latent movies outside of 2205 duplex tempered steel was considered. Passive film on the sensitized sample had less corrosion resistance than the solid solution at 0.6 V_{SCE} [24].

Table 1: W-Tac alloys' density and hardness before and after HERF [8].

	Density (g/cm^3)	Relative density	Hardness (HV)
AS-sintered	18.646	96.7%	395
AS-forged	19.091	99.05%	533

The doping focus in the sharpened example is higher than that in the strong arrangement tempered example, resulting in the former's poorer corrosion resistance in the borate buffer solution [25]. Zhang et al. specially considered the impact of isothermal maturing on the consumption conduct of UNS S82441 duplex hardened steel at different occasions utilizing both potentiodynamic polarization and potential static basic pitting temperature strategies. Utilizing morphological perception and electrochemical location, the microstructure advancement and pitting erosion conduct of UNS S82441 DSS matured at 700°C for different occasions were examined. By increasing, aging time corrosion resistance of the specimen decreased [26]. Polarization behaviour and localized corrosion morphology are strongly affected by artificial aging. Zhang and Frankel investigated various AA2024 pitting and intergranular corrosion behaviours in 1 M NaCl. In the arrangement of heat-treated and water extinguished states, the anodic polarization bends of AA2024 T3 and T3+ tempers uncovered two breakdown possibilities. At 190°C breakdown, the potential decreases with an increase in aging [27]. Gorhe et al. investigated alloy 22 as Ni-Cr-Mo-W alloy made for nuclear waste containers'

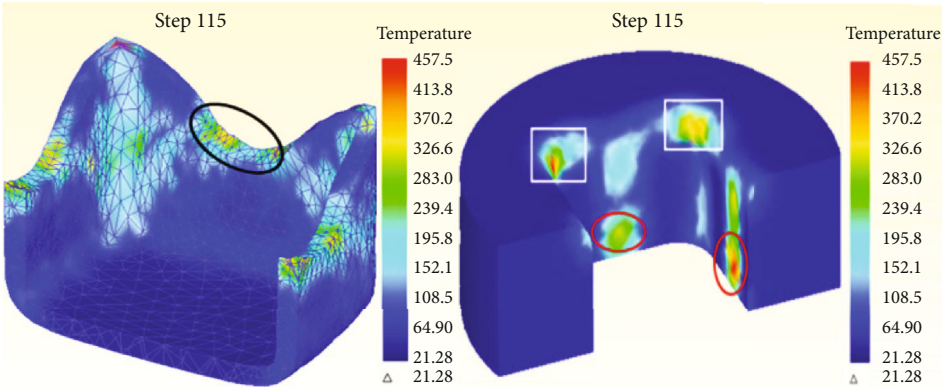

Figure 1: Workpiece and die temperature distribution at step 115 [10].

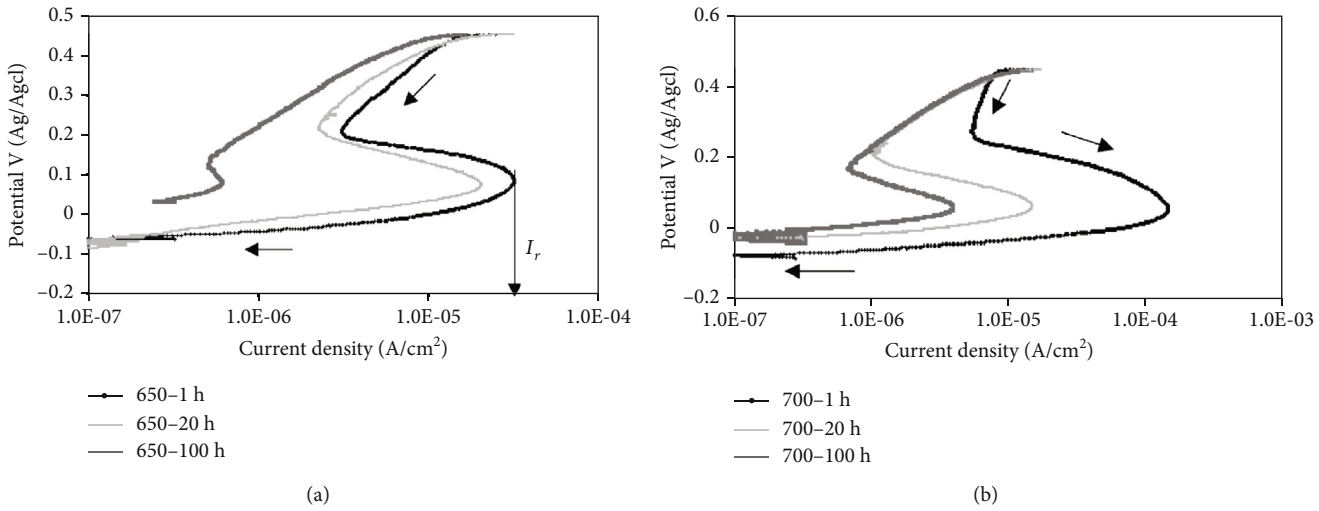

Figure 2: (a, b) SL-EPR test for alloy 22 aged at 650°C [28].

outer walls. This study used a variety of electrochemical experiments to confirm the microstructural changes caused by aging and welding. The EPR testing detected that the Cr depletion in 1 M H_2 SO_4 +0.5 M NaCl +0.01 M KSCN solution at 30°C for long-duration aging above 650°C replenishes the Cr depletion as reactivation of current peaks decreased [28]. The increase of aging time and reactivation peak current decrease is shown in Figure 2(a). Figure 2(b) shows the same results that are shown in Figure 2(a).

Takahashi et al. reported electromagnetic hoop stress numerical results, σ_θ^{FCM} during FCM from 20 T at 50 K, and thermal hoop stress, σ_θ^{cool} under cooling, in REBaCuO discs and ring bulks reinforced by SUS ring with various widths, were compared. The maximum of σ_θ^{total} at step 6 during FCM was reduced from +216 MPa without SUS ring reinforcement to -29 MPa for Wsus =20 mm, which is less than that if the disc bulb was used [29]. The wider SUS ring alleviated the tension concentration in the ring bulk, according to the numerical findings [30]. L. Dal Negro et al. [31] reactive RF magnetron sputtering and thermal annealing make Er.SRO samples. Optimizing a temperature range of 600-800°C for annealing temperatures, Er light emission was demonstrated. With full CMOS compatibility, these Er.SRO films can be used to fabricate compact waveguide optical amplifiers and integrated light sources [32].

1.2. Variation of Metal Characteristics under Different Surrounding and Working Conditions. Chen et al. reported that solvent vapour annealing (SVA) two-step method and thermal annealing (TA) can improve overall system performance, particularly by avoiding reduction in V_{oc}. The use of solvent vapour annealing can improve inefficiency. Unit performance parameters with different annealing treatments under 100 MW/cm^2 are shown in Table 2. Reduction of V_{oc} can be eliminated when the devices are treated with consequent TA [33].

Ma et al. reported that TMS-PCs of N80 and J55 oil tube steels show a substantial reduction in both uniform and pitting corrosion rates. Since TMS-PCs are hydrophobic, brine solution has a hard time contacting the steel matrix. The corrosion resistance of vacuum direct current plasma coatings (VDCPC) is more excellent than atmospheric direct current plasma coatings (ADCPC). In a brine solution, plasma chemical vapour deposition PCVD

Table 2: Unit performance parameters with different annealing treatments under 100 MW/cm^2 [33].

Treatment	V_{oc} (V)	Jsc (mA/cm^2)	FF (%)	PCE (%)
None	0.790	8.610	34.30	2.310
SVA	0.7691	14.81	65.41	7.481
SVA+Ta	0.801	15.20	67.70	8.220

Table 3: Computational performance comparison [37].

Control type	CPU time at case 1 (s)	CPU time at case 2 (s)
NN	214.50	117.161
Incremental LS-SVM	139.511	0.4830
ELM-based bootstrap	237.361	4.7180
Proposed method	2.44920	0.18721

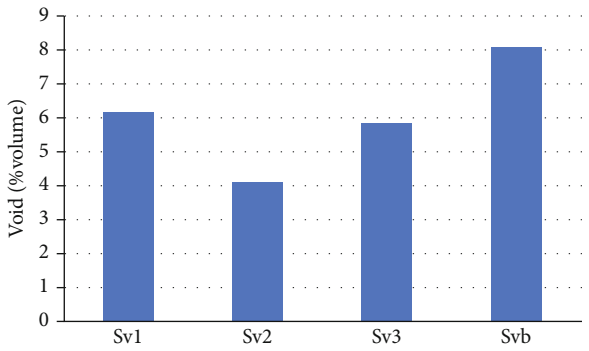

Figure 3: Void volume average values in every variation [39].

is a great way to improve tube steel corrosion and pitting resistance [34].

Bahrami and Taheri introduced the IGC of undeformed specimens increasing sensitization temperature and exposure time. A high deformation and low deformation reduce IGC and tend to increase IGC, respectively. On sensitizing condition, transition point concerning deformation is reliant. Grain boundaries were attacked at low levels of deformation, and uniform corrosion can be overcome at high deformation levels. Throughout the matrix, chromium depletion occurs concerning lower local depletion [35]. Chen et al. reported that Ag alloy bonding wires doped with PD and Au components were produced to replace traditional Au wire. By electrochemical polarization Ag alloy, the wire's corrosion behaviour is tested. Cu wire can be protected by a Pd film from corrosion. Under the potentiodynamic test, Au wire can be completely protected from corrosion [36]. Lu et al. proposed modeling complex batch forging process online probabilistic ELM. Based on the findings, it was determined that probabilistic ELM could accurately represent the distribution behaviour of the batch forging process [37]. Data collected from the new forging distribution model is updated effectively by the developed model update strategy. Table 3 refers to the computation performance [38].

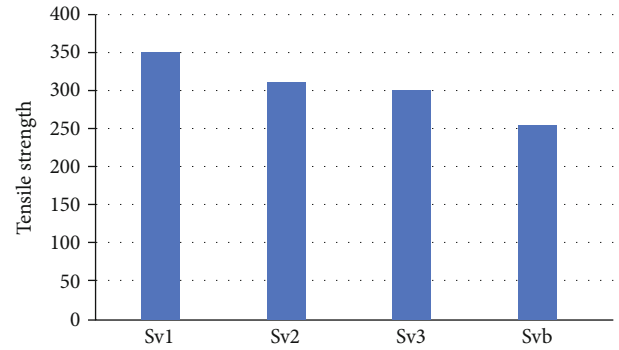

Figure 4: Average maximum of tensile stress at each variation [39].

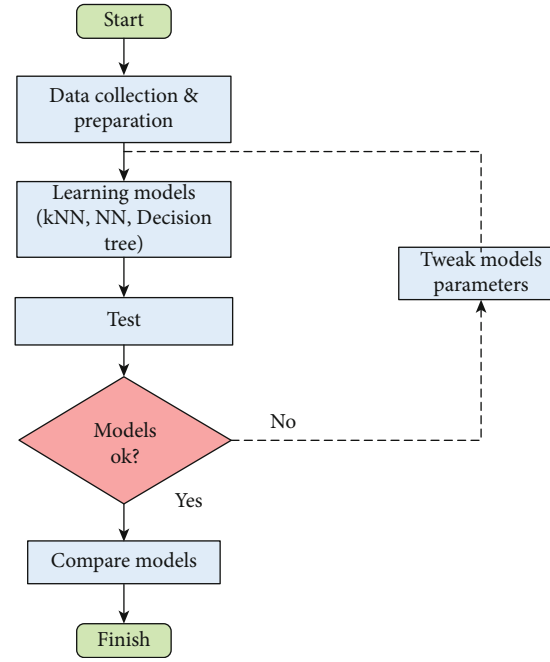

Figure 5: Methodology flow chart [42].

In Salman et al.'s study, using the VARI method, maximum tensile stress values were found, but the bending value is not smaller than the hand lay-up method. Figures 3 and 4 show that the smallest void volume average fraction was obtained at the second variety with a 4.2841% void volume average value. The highest void volume fraction was obtained at 8.141% and the highest tensile stress at every variation [39].

Li et al. investigated the effect of grain size on 316L SS intergranular corrosion. Both DLEPR tests and microstructure inspection indicate that 316L SS becomes less susceptible to intergranular corrosion as grain size increases. At long-duration high temperatures, the intergranular corrosion resistance of 316L is improved [40]. The current study indicates that raising the grain size to an optimal level effectively increases the intergranular corrosion resistance of 316L stainless steel [41]. Alhindawi and Altarazi reported that predicting the tensile strength of extrusion-blown HDPE film has been demonstrated by applying CART, KNN, and ANN. This algorithm can achieve the required

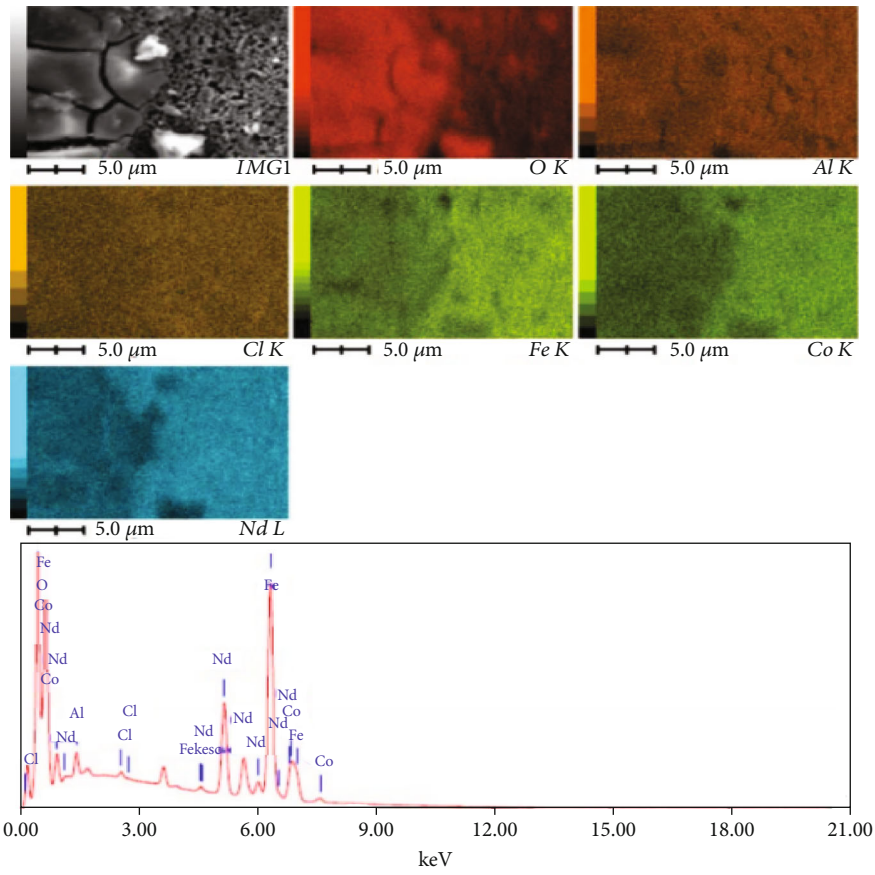

(a)

Figure 6: Continued.

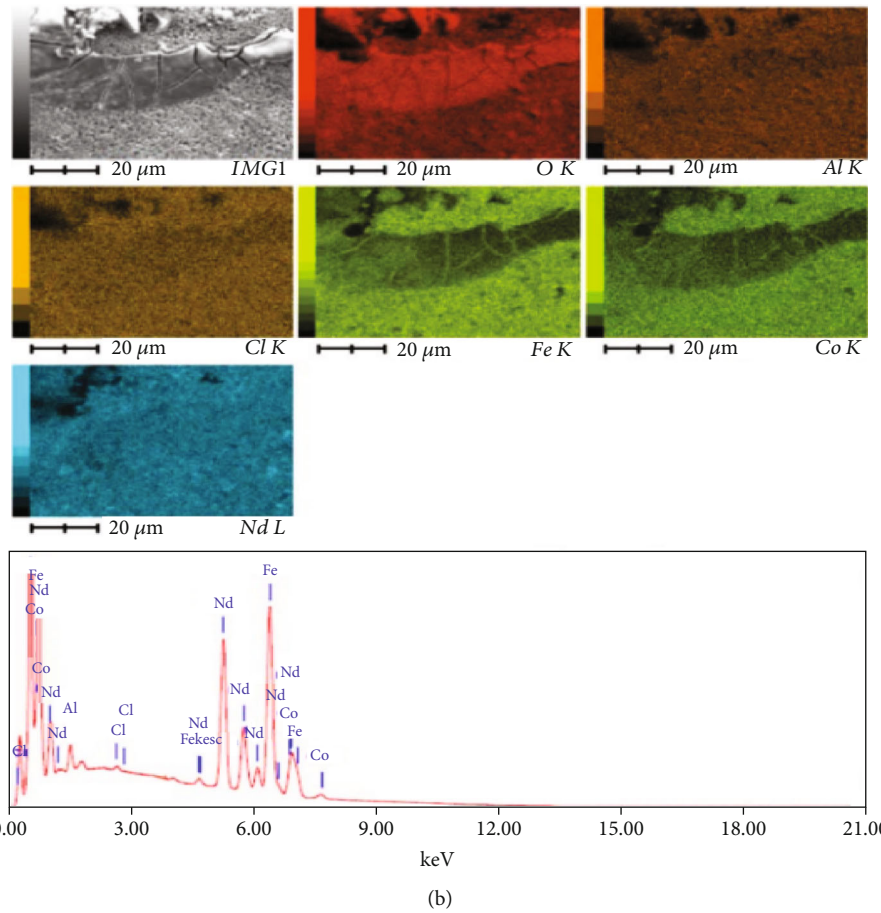

Figure 6: EDS and elemental mapping of corroded samples from a defined area: (a) ND15Al3 composition; (b) ND20Al3 composition [43].

tensile strength. Figure 5 shows the methodology flowchart [42].

Parmar et al. reported that alloy composition was made by microwave combustion, followed by a reduction diffusion process. Nd2(FeCo)14B hard magnet corrosion resistance increased by adding Al by 3% and again increased by replacing Fe by 5% Nd. 5% substitution of Nd improved both coercivity and corrosion resistance. The majority phase protects from corrosion but the minority phase dissolves. By Ni planting, both the Al and Nd substituted sample corrosion resistance improved. The Nd substitute's best potential corrosion values and current density appear by 10 μm thickness of Ni plating. SEM-EDS analyzed ND15A13 and ND20A13 corroded portions [43]. Figure 6(a) shows the oxide elements in the corroded part; the aluminum map is brighter; Figure 6(b) shows Nd and Al oxides as both elements available in the corroded part; map images are brighter.

Thanh Hung Nguyen et al. [44] presented some new results using low-frequency vibrations for the forging process improvement with different waveforms. Although load reduction is observed, it is critical to compare results found in the literature. Also, the forging process assisted by a PA was presented by using the EMR in low frequency. Both electrical and mechanical component investigations of energy loss are needed to estimate energy reduction [15]. Lee et al. studied the MAO process which was used to create an oxide film on ZK60 magnesium alloy; effect on corrosion resistance was determined. The impact of electrical parameters such as power mode and applied voltage is calculated. Characterization of the MAO-coated ZK60 Mg alloy and the bare ZK60 Mg alloy is shown in Table 4. The properties of the electrical source and properties of the coating are related [45].

Liu et al. reported that with AlGaN/GaN, the ohmic contact is obtained. This method is advantageous for fabricating GaN high electron mobility transistor HEMT and advantageous in integrating GaN devices with Si CMOS [46]. Lu et al. investigated the modeling complex forging process; a novel LS-SVM was developed. The entire working region can be divided into many local regions with prior knowledge of HPM. Figure 7 shows the novel LS-SVM modeling method. Local LS-SVM models can accurately show local dynamics. On a local and global scale, regularization is essential. Avoid overfitting each local LSSVM; consider the interaction between neighboring local regions [47].

Luo et al. reported that the corrosion and electrochemical actions of 304L SS at various levels of cold deformation were investigated using potentiodynamic polarization curves, EIS, EBSD, and XPS. With the increase in cold deformation, 304L stainless steel passive current density increases [48]. Yuji Gotoh et al. [49] prepared a specimen in large size; with maximum tensile strength and low permeability, conductivity of

Table 4: Characterization of the MAO-coated ZK60 Mg alloy and the bare ZK60 Mg alloy [45].

Sample	Roughness average (μm)	Mean pore diameter (μm)	Area percent of pores (% of total)	The thickness of the coating (μm)
Substrate	0.089	—	—	—
Dc				
250 V	0.190	0.82	5.54	4.8
Unipolar pulsed				
250 V	0.570	2.03	47.8	5.5
300 V	1.439	4.15	36.9	9.8
350 V	2.456	11.2	18.6	19.6
400 V	3.441	13.4	14.2	22.1
Bipolar pulsed				
250 V-20 V	0.193	0.48	28.5	5.5
300 V-20 V	1.950	3.73	18.3	13.2
350 V-20 V	2.844	11.5	9.77	23.5
400 V-20 V	3.017	7.42	5.94	24.3

the steel nanomaterial becomes large. An inspection method was proposed using alternating electromagnetic fields [18]. The results show that as lift-off and tensile strength increase, the flux density amplitude in the search coil decreases [50]. By the proposed inspection method, tensile strength inspection is possible in steel without influencing the lift-off [51]. The tensile strength becomes equal to 1 in a search coil exciting current and flux density B waveform shown in Figure 8.

Poh et al. investigated hybrid magnetic overcoat (Hy-MOC) magnetic properties and inhibition properties. Two types of Hy-MOC were investigated using various types of Co-based alloys. Reactive sputtering withN_2Hy-MOC($\propto$) used CoCrPt:SiO_2while Hy-MOC(β) used$CoCr_{22}$. Figure 9 shows the experimental setup used for the investigation. From the research, it was concluded that Hy-MOC(β) hard disk media has weaker magnetic properties than the Hy-MOC($\propto$), but Hy-MOC(β) is more corrosive resistant. The magnetic media can be protected by a new Hy-MOC system and also provides thermal stability [52].

Zhang et al. examined the influence of microstructure on corrosion behaviour by the laboratory rolling Ni-Fe-Cr alloy 028 which was subject to cold deformation in various degrees. This study involves improvement in various structures via cold rolling. After rolling in the corrosive environment, a significant improvement in corrosion is reported. ND/(111) orientation is reduced as cold reduction increases, resulting in texture described by ND/(110) orientation [53]. Despite the same misorientation between grains, the misorientation distribution inside differently oriented grains was different, as determined by EBSD analysis [54]. Zinno et al. presented an equal little standard subset calculation for the age of differential synthetic aperture radar interferometry distortion guides, and time arrangement appeared. The calculation was ported to the cloud. According to the findings, the P-SBAS cloud migration can process ENVISAT SAR image time series in a short amount of time and at a low cost. The performance of the P-SBAS is compared with the high-performance computing cluster, and the proposed cloud solution produces no overheat [55]. Kwon et al. arbitrary message signal was utilized to examine the impact of high-pressure deuterium and hydrogen strengthening on the commotion attributes of source adherent square (SF), SF, and line selector (SEL) semiconductors in CMOS picture sensor (CIS) dynamic pixel sensor (RTS). High-pressure D_2 annealing shows the great reduction in $\Delta I_D/I_D$ of SF block. After high-pressure deuterium and hydrogen annealing, $\Delta I_D/I_D$ for SF and SEL has reduced by 48%-52% compared with FG annealing [56]. Xi et al. frequency domain spectroscopy is commonly used for detecting and assessing the oil-paper insulation state, and it has many advantages. Insulation paper/pressboard is considered a direct reflection of mechanical output regarding the degree of polymerization and tensile strength. Table 5 shows the DP and TS values at different stages. Results show that with a decrease of DP and TS, the tan δ value varies in exponential form. The established mathematical relation under 0.001 Hz frequency fits best [57].

Yuan et al. reported that the effect of microstructure on aluminum sheet corrosion and mechanism was investigated. The homogenization annealing treatment causes copper segregation on the resolidified clad nanomaterial surface and improved Si diffusion depth during brazing. The fluidity of the brazing layer is stronger without homogenization. After brazing the affected area, Si concentration increases. During brazing in the diffusion zone, dense precipitates were formed, which improves the brazing sheet's corrosion resistance [20]. Li et al. present the feasible test for aluminum alloy bridge deck based on the experimental study on wearability and corrosion resistance. The wearability of the aluminum alloy bridge deck was calculated by a line friction test of standard specimens. To measure the corrosion rate and morphology characteristics of the specimen, electrochemical test was conducted. In nanomaterial science, a field wearability test is commonly used to obtain an accurate measurement. The corrosion resistance test was performed in an acid solution with a pH value of 4.0 to 6.0. Taking

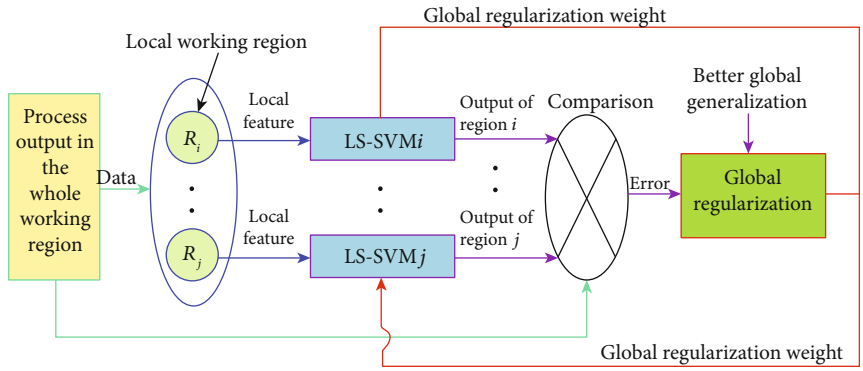

Figure 7: Novel LS-SVM method modeling [47].

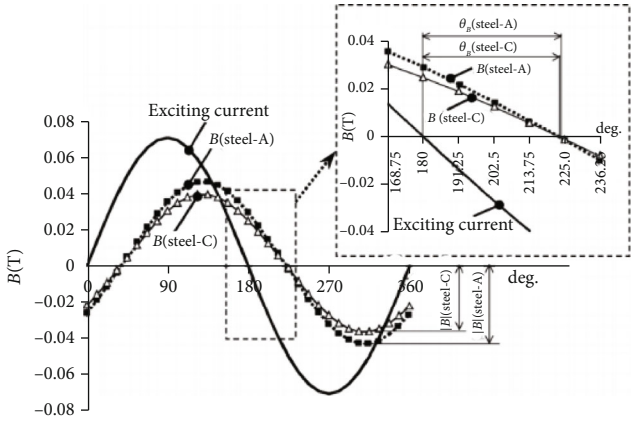

Figure 8: Waveforms of the exciting current and flux density in a search coil (calculated, 10 kHz, 100 AT, steel-A and -C, mm) [18].

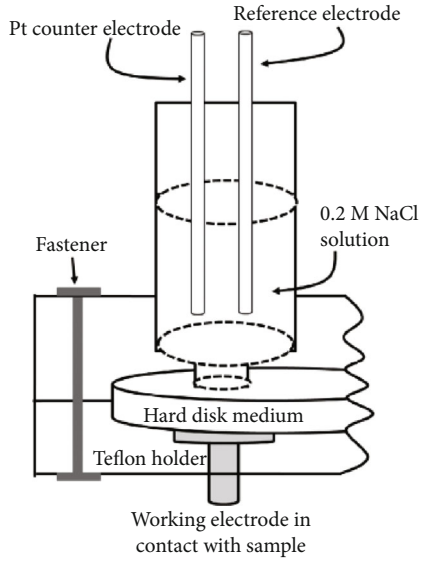

Figure 9: Schematic diagram of electrochemical setup used for the investigation [52].

maximum corrosion rate is 34 μm/a; it takes 30 years to corrode [58]. Seo et al. presented trends of science and engineering expertise in global industries. As the film progresses through the forging ahead phase, this study shows an increase in science and engineering activities. At last, this paper focuses on exploring the evolutionary patterns of latecomer firm. First, there is an aggregation issue in this report, which ignores the consideration of internal mechanisms and the contributions of universities and public research institutes. Further research that includes internal and external universities' motivations and roles are being investigated and public research institutes and examine the knowledge flow of inventions [59].

Barbi and Judd analyzed stainless steel austenitic intergranular by using transmission electron microscopy of the corroded thin film. To attack in the copper sulphate-sulphuric acid solution, the carbide particles are not susceptible but are subjected to assault in potassium dichromate-nitric acid solution. Exposing the sensitized nanomaterial in a potassium dichromate nitric oxide solution, carbide disappears from corroded grain boundaries. In a commercial annealed nanomaterial for nickel and chromium chemical composition, inhomogeneities were measured [60]. Yeganeh et al. investigate the nanostructured copper stores made with EB-PVD, just as a heartbeat plating procedure is proposed. Transmission electron microscopy was utilized to analyze the morphology of the stored film, and a DEKTAK profilometer was used to assess the roughness of the surface deposits. EB-PVD and pulse plating can be used to create the nanostructured nanomaterial. In this examination, the normal grain size of EB-PVD and heartbeat plated copper was 40 nm. Passivation behaviour was not shown in pulse-plated copper (Figure 10). However, pulse-plated copper in grain size is equal to EB-PVD copper [61].

Arutunow and Darowicki reported that the unique electrochemical impedance spectroscopy (DEIS) method was utilized to recognize rapid impedance changes versus reactivation potential for the AISI 304 hardened steel disintegration measure. During the dissolution of AISI 304 stainless steel, the DEIS technique can detect complex changes in impedance [62]. Arutunow and Darowicki research results into the dissolution of AISI 304 SS in the presence of IGC are presented. According to the experiments, variations in impedance observed during the IGC of AISI 304 SS at various reactivation possibilities were brought about by direct changes in the overall viable surface locale [63]. Iwai et al. made two-course curls out of a pile of four single hotcakes

Table 5: DP and TS values at various stages [57].

Day	Degree of polymerization (DP)	Tensile strength (TS)
0	906.9	96.1
10	675.0	79.9
20	508.1	58.1
30	424.9	39.0
35	359.0	34.9
40	286.1	24.0

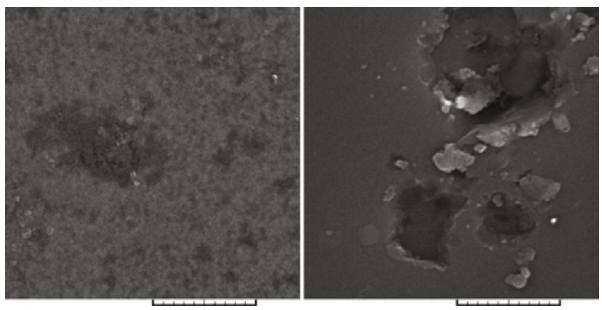

Figure 10: Surface morphology after potentiodynamic polarization tests in 0.5 M NaCl solution: (a) EB-PVD copper and (b) pulse-plated copper [61].

twisted with two various types of created REBCO tapes, with one of the REBCO loops in the hardened steel case cooled by implication through a warm obstruction layer. After the cryocooler stopped cooling, the temperature rose [64]. The test results were very close to the calculated values, showing that controlling the heat flow into the coil is very effective [65].

S. Xu et al. [66] fabricated a TGP with dimensions of 10 cm ∗ 5 cm ∗ 0.28 mm and tested it at various condenser temperatures. At an applied power of 7.9 W, the thermal resistance is estimated to be as low as 4.38 K/W, resulting in a good thermal conductivity of 1398 W/m-K. As the applied power was less than 6.0 W after 45 days, the reliability of TGP output degradation was negligible. At 7.0 W, the thermal resistance increased to 18% [67]. Due to improved evaporation heat transfer, thermal resistance is reduced by increasing the applied power shown in Figure 11(a). Due to partial dry-out condition, a jump in the evaporator temperature as the applied power increase is shown in Figure 11(b).

T. Li et al. [68] investigate the effects of prestrain; a specimen comprised of four types of polyethylene-terephthalate (PET)/Al-doped zinc oxide (AZO) was prepared. The start of pop-in activity is known as the inflexion point. The prestrain added to the PET substrate has an inverse relationship with the pop-in. The sheet resistance is shown to be inversely proportional to the carrier mobility. The magnitude of these defect parameters is inversely proportional to the electrical current calculated at the end of the loading step [69]. Balbola et al. reported that both tensile and compressive uniaxial transverse strains were generated locally using a new technique. This improvement in affectability of n-type-based 3-D sensors for pressure and out-of-plane typical pressure hits 82% for compressive strain and 21% for pressure. Besides, compressive crossover strains build the pressing factor coefficient of intensely doped n-type silicon up to 80% [70]. Zhang et al. investigated that architecture's two thickest component layers calculated the mechanical behaviour of a REBCO-coated conductor wire under uniaxial stress. The elastic modulus (E) yield stress ($\sigma_{0.2}$), critical stress (σ_c, 0.95), and irreversible stress (σ_{irr}, 0.99) of REBCO wires decreased with increasing copper thickness or copper thickness ratio Cu/(Cu+Sub), according to the experimental results. Critical strain (ε_c, 95) and irreversible strain (ε_{irr}, 0.99) were unaffected by copper thickness, with intrinsic values of 0.45 and 0.75%. The calculated results are consistent with the measured stress-strain curves, which can be well adapted using the Ramberg-Osgood equation and substrate [71].

Janecska et al. show that enraptured pressure imaging can distinguish lithography surrenders in the 70 nm FinFET gadget's development cycle stream. Running pressure investigation as a screening technique could help engraving and statement measure increase by eliminating probably the main imperfection sources in an extremely short circle on the sweeping wafers without the requirement for costly pattering. Stress imaging can identify process deviations that lead to high defect rates [72]. Daniel and Hubert have proposed ways to apply several equivalent stresses in the case of uniaxial and biaxial mechanical loading, and it has been verified experimentally. The effect of multiaxial stress on multiaxial activity has been contrasted using several numbers of stress-related criteria. The inability of these models to explain the effect of bicompression stress on magnetic activity is their key flaw [73]. Yang researched the impacts of mechanical pressure incited by the door line end (GLE) on gadget attributes for high-k/metal entryway FinFETs utilizing analyses and TCAD recreations. The framework with GLE =100 nm displays 6.3% and 5.7% drive current upgrade over the gadget with GLE =35 nm, separately, as far as n-FinFETs and p-FinFETs. In a TCAD reproduction, the normal channel pressure was diminished from 295 MPa to 168 MPa [74]. Yong et al. reported measurement wire bonding phase; piezoresistive sensors have been demonstrated. According to studies, the voltage output responses are comparable, allowing for proper sample alignment regulation. Various captured bond forces and bonding durations affect the resistors. US signals can be filtered using the FET technique. The stress sensors are found to be capable of capturing various impact forces, bond forces, bonding durations, and US strength [75].

Tingting et al. proposed a degradation model for products in a dynamic environment considering stress drift and shock damage. For some practical problems, the stress drift function may be complex or has a similar form as the shock damage function, making it difficult to separate the effect of the stress drift from that of shock damage. Second, only one type of stress is considered, and for many cases, products experience complex environmental conditions (stress and load) in their life cycle. Third, it is assumed that the stress

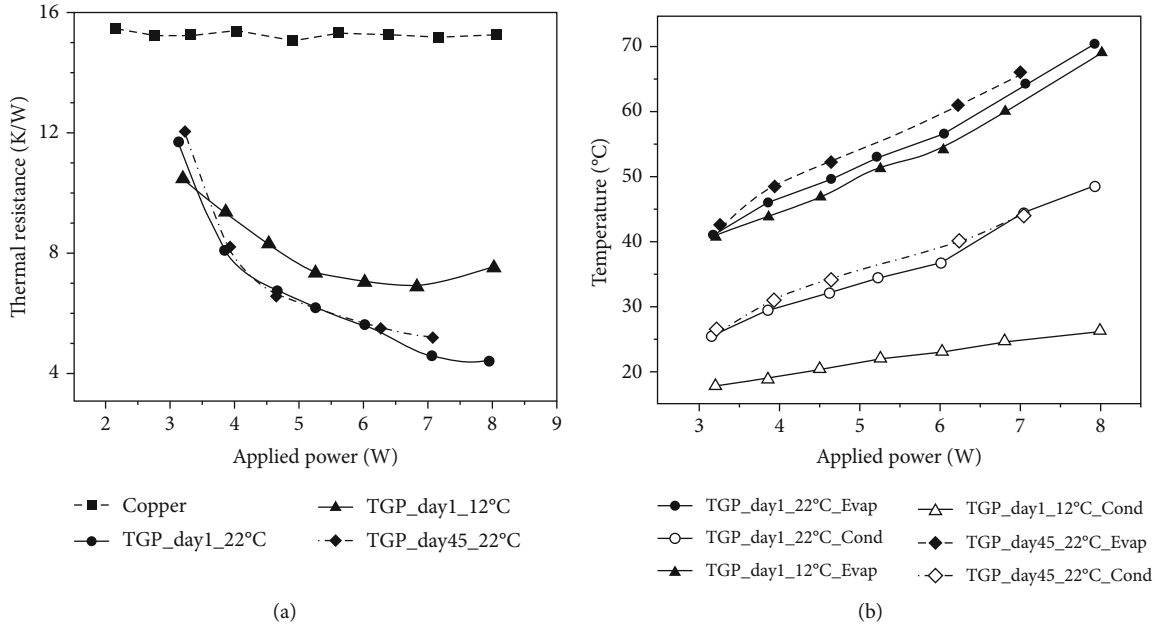

Figure 11: (a) Measured thermal resistance of TGP and copper [67]. (b) Measured evaporator and condenser temperature [67].

profile is deterministic and prespecified. The assumption can be relaxed in future research to consider a more complex case that the stress level changes randomly and the stress profile is unknown in advance. A simulation analysis is presented to illustrate the model's implementation, and a case study of miniature light bulbs is used to validate the proposed model's effectiveness [76]. Miyagi et al. utilizing finite element analysis examined the transient temperature appropriation and transient warm pressure circulation inside a covered conductor's loop while cooling with LN2 (FEA). The effect of the bobbin's actual property estimations on the temperature dissemination and transient warm pressure inside the curl was additionally exhibited. Furthermore, when bobbin nanomaterial with lower thermal conductivity is used, adequate precooling is needed to reduce transient thermal stress [77].

2. Conclusion

Austenitic stainless steel 316 finds extensive use as a structural nanomaterial for nuclear core components because of its good combination of strength, toughness, and resistance to uniform corrosion. Austenitic stainless steel 316 has FCC crystal structure and three major alloying elements—Fe, Cr, and Ni, with its composition as carbon 0.08%, silicon 1%, manganese 2%, chromium 16-18%, nickel 10-14%, and molybdenum 2-3%. Carbon was used as low as commercially feasible to obtain Cr 16-26% and Ni >8%. For austenitic steel, during sensitization, depletion of chromium in the grain boundary occurs. This results in susceptibility to intergranular corrosion. A higher sensitization rate means poor hot strength and mechanical properties at a higher temperature.

It was found that the effect of prestraining of nanomaterials on sensitization phenomena had a comparison. The different sensitization rates were calculated between samples with different degrees (percentage) and deformation modes (hot and cold). The comparative study gave us the best deformation mode and optimized percentage of deformation of the nanomaterial. It serves as a preprocessing mechanical method to decrease the corrosion reactivity and enhance its hot working properties. The metal forming of workpieces was done, and the percentage compression was taken care of like 3%, 6%, and 9%. For corrosion test, Huey test has been used according to ASTM A262 practice C. The corrosion rate is determined from the weight loss after boiling cycles. The analysis of microstructure is done. Microstructure provides a qualitative analysis of sensitization rate while the Huey test provides a quantitative study. The degree of deformation increases as intergranular corrosion decreases.

From the microstructure, it is shown that intergranular corrosion is less in the case of hot forming. Weight loss is more in cold pressing as compared to hot pressing. Hot forming serves as a better preprocessing measure if one needs high hot strength in the nanomaterial. As the deformation increases from more than 9%, the corrosion is very low. Hence, hot forming and a high degree of deformation are good measures to increase hot strength and reduce intergranular corrosion.

Data Availability

The data used to support the findings of this study are included in the article. Should further data or information be required, these are available from the corresponding author upon request.

Disclosure

This study was performed as a part of the Employment of Bahir Dar Institute of Technology, Bahir Dar University, Ethiopia.

Conflicts of Interest

The authors declare that there are no conflicts of interest regarding the publication of this paper.

Acknowledgments

The authors appreciate the supports from Bahir Dar Institute of Technology, Bahir Dar University, Ethiopia. The authors thank Vellore Institute of Technology, Chennai, and Saveetha School of Engineering Chennai for the technical assistance to carry this review work.

References

[1] H. Wang, L. Chen, B. Dovgyy et al., "Micro-cracking, microstructure and mechanical properties of Hastelloy-X alloy printed by laser powder bed fusion: as-built, annealed and hot-isostatic pressed," *Additive Manufacturing*, vol. 39, p. 101853, 2021.

[2] H. Tian, Z. Guo, J. Pan et al., "Comprehensive review on metallurgical recycling and cleaning of copper slag," *Resources, Conservation and Recycling*, vol. 168, p. 105366, 2021.

[3] M. K. Trivedi and R. M. Tallapragada, "A transcendental to changing metal powder characteristics," *Metal Powder Report*, vol. 63, no. 9, pp. 22–29, 2008.

[4] Q. Yin, Z. Liu, and B. Wang, "Machinability improvement of Inconel 718 through mechanochemical and heat transfer effects of coated surface-active thermal conductive mediums," *Journal of Alloys and Compounds*, vol. 876, p. 160186, 2021.

[5] P. Snopiński, M. Krol, T. Tański, and B. Krupińska, "Effect of cooling rate on microstructural development in alloy ALMG9," *Journal of Thermal Analysis and Calorimetry*, vol. 133, no. 1, pp. 379–390, 2018.

[6] V. Paranthaman, K. S. Sundaram, and L. Natrayan, "Influence of SiC particles on mechanical and microstructural properties of modified interlock friction stir weld lap joint for automotive grade aluminium alloy," *SILICON*, vol. 1, pp. 1–11, 2021.

[7] J. Wu, N. T. Aboulkhair, M. Degano, I. Ashcroft, and R. J. M. Hague, "Process-structure-property relationships in laser powder bed fusion of permanent magnetic Nd-Fe-B," *Materials & Design*, vol. 209, p. 109992, 2021.

[8] F. Feng, Y. Lian, X. Liu, J. Wang, and Y. Xu, "Effect of high-energy-rate forging on microstructure and properties of W-TaC alloys," *IEEE Transactions on Plasma Science*, vol. 46, no. 6, pp. 2314–2317, 2018.

[9] R. Suryanarayanan, V. G. Sridhar, L. Natrayan et al., "Improvement on mechanical properties of submerged friction stir joining of dissimilar tailor welded aluminum blanks," *Advances in Materials Science and Engineering*, vol. 2021, 6 pages, 2021.

[10] Q. Lin, W. Dong, Z. Wang, and D. Xue, "Research on galling behavior in square cup drawing of high tensile strength steel," in *2010 International Conference on Digital Manufacturing & Automation*, vol. 2, pp. 212–215, Changcha, China, 2010.

[11] V. Paranthaman, K. Shanmuga Sundaram, and L. Natrayan, "Effect of silica content on mechanical and microstructure behaviour of resistance spot welded advanced automotive TRIP steels," *SILICON*, vol. 3, pp. 1–10, 2021.

[12] A. Sharma, M. A. Hoffmann, P. Matthes et al., "Magnetic tunnel junctions: laser annealing versus oven annealing," *IEEE Transactions on Magnetics*, vol. 55, no. 1, pp. 1–4, 2019.

[13] M. Sandeep Kauthsa Sharma, S. Umadevi, Y. Sai Sampath et al., "Mechanical behavior of silica fume concrete filled with steel tubular composite column," *Advances in Materials Science and Engineering*, vol. 2021, Article ID 3632991, 9 pages, 2021.

[14] S. J. Kim, D. H. Yoon, Y. S. Rim, and H. J. Kim, "Low-temperature solution-processed ZrO2 gate insulators for thin-film transistors using high-pressure annealing," *Electrochemical and Solid State Letters*, vol. 14, no. 11, article E35, 2011.

[15] H. Zhao, Z. Zhang, H. Zhang, J. Hu, and J. Li, "Effect of aging time on intergranular corrosion behavior of a newly developed LDX 2404 lean duplex stainless steel," *Journal of Alloys and Compounds*, vol. 672, pp. 147–154, 2016.

[16] D. Veeman, M. S. Sai, P. Sureshkumar et al., "Additive manufacturing of biopolymers for tissue engineering and regenerative medicine: an overview, potential applications, advancements, and trends," *International Journal of Polymer Science*, vol. 2021, Article ID 4907027, 20 pages, 2021.

[17] B. Eggleston, S. Varlamov, and M. Green, "Large-area diode laser defect annealing of polycrystalline silicon solar cells," *IEEE Transactions on Electron Devices*, vol. 59, no. 10, pp. 2838–2841, 2012.

[18] F. He, X. Ma, K. Shen, and C. Wang, "Study on material and energy flow in steel forging production process," *IEEE Access*, vol. 8, pp. 12921–12932, 2020.

[19] M. Terada, M. Saiki, I. Costa, and A. F. Padilha, "Microstructure and intergranular corrosion of the austenitic stainless steel 1.4970," *Journal of Nuclear Materials*, vol. 358, no. 1, pp. 40–46, 2006.

[20] Z. Yuan, F. Tao, J. Wen, and Y. Tu, "The dependence of microstructural evolution and corrosion resistance of a sandwich multi-layers brazing sheets on the homogenization annealing," *IEEE Access*, vol. 7, pp. 121388–121394, 2019.

[21] L. Kosec, Š. Šavli, S. Kožuh et al., "Transformation of austenite during isothermal annealing at 600-900 °C for heat-resistant stainless steel," *Journal of Alloys and Compounds*, vol. 567, pp. 59–64, 2013.

[22] M. V. Klimova, D. G. Shaysultanov, S. V. Zherebtsov, and N. D. Stepanov, "Effect of second phase particles on mechanical properties and grain growth in a CoCrFeMnNi high entropy alloy," *Materials Science and Engineering: A*, vol. 748, pp. 228–235, 2019.

[23] H. Sahlaoui, H. Sidhom, and J. Philibert, "Prediction of chromium depleted-zone evolution during aging of Ni-Cr-Fe alloys," *Acta Materialia*, vol. 50, no. 6, pp. 1383–1392, 2002.

[24] J. Lv, T. Liang, C. Wang, and T. Guo, "Influence of sensitization on passive films in AISI 2205 duplex stainless steel," *Journal of Alloys and Compounds*, vol. 658, pp. 657–662, 2016.

[25] L. Natrayan, P. S. S. Sundaram, and J. Elumalai, "Analyzing the uterine physiological with mmg signals using svm," *International Journal of Pharmaceutical Research*, vol. 11, no. 2, pp. 165–170, 2019.

[26] Z. Zhang, H. Zhao, H. Zhang et al., "Effect of isothermal aging on the pitting corrosion resistance of UNS S82441 duplex

stainless steel based on electrochemical detection," *Corrosion Science*, vol. 93, pp. 120–125, 2015.

[27] W. Zhang and G. S. Frankel, "Transitions between pitting and intergranular corrosion in AA2024," *Electrochimica Acta*, vol. 48, no. 9, pp. 1193–1210, 2003.

[28] D. D. Gorhe, K. S. Raja, S. A. Namjoshi, V. Radmilovic, A. Tolly, and D. A. Jones, "Electrochemical methods to detect susceptibility of Ni-Cr-Mo-W alloy 22 to intergranular corrosion," *Metallurgical and Materials Transactions A, Physical Metallurgy and Materials Science*, vol. 36, no. 5, pp. 1153–1167, 2005.

[29] K. Takahashi, H. Fujishiro, T. Naito, Y. Yanagi, Y. Itoh, and T. Nakamura, "Numerical simulation of electromagnetic and thermal stress in REBaCuO superconducting ring and disk bulks reinforced by stainless steel ring with various widths during field-cooled magnetization," *IEEE Transactions on Applied Superconductivity*, vol. 28, no. 3, pp. 1–5, 2018.

[30] C. S. S. Anupama, L. Natrayan, E. Laxmi Lydia et al., "Deep learning with backtracking search optimization based skin lesion diagnosis model," *Computers, Materials & Continua*, vol. 70, no. 1, pp. 1297–1313, 2022.

[31] L. D. Negro, J. H. Yi, M. Hiltunen et al., "Light-emitting silicon-rich nitride systems and photonic structures," *Journal of Experimental Nanoscience*, vol. 1, no. 1, pp. 29–50, 2006.

[32] M. Forcales, M. Wojdak, M. A. J. Klik et al., "Si nanocrystals as sensitizers for Er PL in SiO2," *MRS Online Proceedings Library*, vol. 770, pp. 119–123, 2003.

[33] Hui Chen, Jingsheng Miao, Jun Yan, Zhicai He, and Hongbin Wu, "Improving organic solar cells efficiency through a two-step method consisting of solvent vapor annealing and thermal annealing," *IEEE Journal of Selected Topics in Quantum Electronics*, vol. 22, no. 1, pp. 66–72, 2016.

[34] Y. Ma, H. Bai, B. Yang, Q. Yu, and Q. Zhang, "Surface modification of carbon steel with plasma chemical vapor deposition for enhancing corrosion resistance in CO_2/brine," *IEEE Transactions on Plasma Science*, vol. 47, no. 5, pp. 2652–2659, 2019.

[35] A. Bahrami and P. Taheri, "A study on the failure of AISI 304 stainless steel Tubes in a Gas Heater Unit," *Metals (Basel)*, vol. 9, no. 9, p. 969, 2019.

[36] C. H. Chen, Y. C. Lin, Y. T. Shih et al., "Evaluation of corrosion resistance of ag-alloy bonding wires for electronic packaging," *IEEE Transactions on Components, Packaging and Manufacturing Technology*, vol. 8, no. 1, pp. 146–153, 2018.

[37] X. Lu, C. Liu, and M. Huang, "Online probabilistic extreme learning machine for distribution modeling of complex batch forging processes," *IEEE Transactions on Industrial Informatics*, vol. 11, no. 6, pp. 1277–1286, 2015.

[38] S. Yogeshwaran, L. Natrayan, G. Udhayakumar, G. Godwin, and L. Yuvaraj, "Effect of waste tyre particles reinforcement on mechanical properties of jute and abaca fiber - epoxy hybrid composites with pre-treatment," *Materials Today: Proceedings*, vol. 37, no. 2, pp. 1377–1380, 2020.

[39] A. Salman, D. Catur, I. Made Septayana, and M. Dani Masterawan, "Tensile strength and bending analysis in producing composites by using vacuum resin infusion (VARI) method for high-voltage insulator application," in *2018 2nd International Conference on Applied Electromagnetic Technology (AEMT)*, pp. 39–43, Lombok, Indonesia, 2018.

[40] S. X. Li, Y. N. He, S. R. Yu, and P. Y. Zhang, "Evaluation of the effect of grain size on chromium carbide precipitation and intergranular corrosion of 316L stainless steel," *Corrosion Science*, vol. 66, pp. 211–216, 2013.

[41] A. Y. Adesina, Z. M. Gasem, and A. S. Mohammed, "Comparative investigation and characterization of the scratch and wear resistance behavior of TiN, CrN, AlTiN and AlCrN cathodic arc PVD coatings," *Arabian Journal for Science and Engineering*, vol. 44, no. 12, pp. 10355–10371, 2019.

[42] F. Alhindawi and S. Altarazi, "Predicting the tensile strength of extrusion-blown high density polyethylene film using machine learning algorithms," in *2018 IEEE International Conference on Industrial Engineering and Engineering Management (IEEM)*, pp. 715–719, Bangkok, Thailand, 2019.

[43] H. Parmar, T. Xiao, Z. Yaoying et al., "Improved corrosion resistance of Co,Al-alloyed NdFeB magnetic nanostructures processed by microwave synthesis techniques," *IEEE Transactions on Magnetics*, vol. 54, no. 11, pp. 1–5, 2018.

[44] T. H. Nguyen, C. Giraud-Audine, B. Lemaire-Semail, G. Abba, and R. Bigot, "Modeling of forging processes assisted by piezoelectric actuators: principles and experimental validation," *IEEE Transactions on Industry Applications*, vol. 50, no. 1, pp. 244–252, 2014.

[45] J. L. Lee, S. Y. Jian, K. N. Kuo, J. L. You, and Y. T. Lai, "Effect of surface properties on corrosion resistance of ZK60 mg alloy microarc oxidation coating," *IEEE Transactions on Plasma Science*, vol. 47, no. 2, pp. 1172–1180, 2019.

[46] Z. Liu, D. Chen, L. Wan, and G. Li, "Micron-scale annealing for ohmic contact formation applied in GaN HEMT gate-first technology," *IEEE Electron Device Letters*, vol. 39, no. 12, pp. 1896–1899, 2018.

[47] X. Lu, B. Fan, and M. Huang, "A novel LS-SVM modeling method for a hydraulic press forging process with multiple localized solutions," *IEEE Transactions on Industrial Informatics*, vol. 11, no. 3, pp. 663–670, 2015.

[48] H. Luo, H. Su, G. Ying, C. Dong, and X. Li, "Applied surface science effect of cold deformation on the electrochemical behaviour of 304L stainless steel in contaminated sulfuric acid environment," *Applied Surface Science*, vol. 425, pp. 628–638, 2017.

[49] Y. Gotoh and N. Takahashi, "Proposal of detecting method of plural cracks and their depth by alternating flux leakage testing: 3-D nonlinear eddy current analysis and experiment," *IEEE transactions on magnetics*, vol. 40, no. 2, pp. 655–658, 2004.

[50] N. K. Banjara and K. Ramanjaneyulu, "Investigations on behaviour of flexural deficient and CFRP strengthened reinforced concrete beams under static and fatigue loading," *Construction and Building Materials*, vol. 201, pp. 746–762, 2019.

[51] S. Yogeshwaran, L. Natrayan, S. Rajaraman, S. Parthasarathi, and S. Nestro, "Experimental investigation on mechanical properties of epoxy/graphene/fish scale and fermented spinach hybrid bio composite by hand lay-up technique," *Materials Today: Proceedings*, vol. 37, no. 2, pp. 1578–1583, 2020.

[52] W. C. Poh, S. N. Piramanayagam, and T. Liew, "Magnetic properties and corrosion resistance studies on hybrid magnetic overcoats for perpendicular recording media," *IEEE Transactions on Magnetics*, vol. 46, no. 4, pp. 1069–1076, 2010.

[53] L. Zhang, J. A. Szpunar, R. Basu, J. Dong, and M. Zhang, "Influence of cold deformation on the corrosion behavior of Ni-Fe-Cr alloy 028," *Journal of Alloys and Compounds*, vol. 616, pp. 235–242, 2014.

[54] H. A. Deore, J. Mishra, A. G. Rao, H. Mehtani, and V. D. Hiwarkar, "Effect of filler material and post process ageing

treatment on microstructure, mechanical properties and wear behaviour of friction stir processed AA 7075 surface composites," *Surface and Coatings Technology*, vol. 374, pp. 52–64, 2019.

[55] I. Zinno, S. Elefante, L. Mossucca et al., "A first assessment of the P-SBAS DInSAR algorithm performances within a cloud computing environment," *IEEE Journal of Selected Topics in Applied Earth Observations and Remote Sensing*, vol. 8, no. 10, pp. 4675–4686, 2015.

[56] H. Kwon, I. S. Han, S. K. Kwon et al., "Effects of high-pressure annealing on random telegraph signal noise characteristic of source follower block in CMOS image sensor," *IEEE Electron Device Letters*, vol. 34, no. 2, pp. 190–192, 2013.

[57] X. Xi, H. Wang, W. Wang, Y. Xiao, Q. Li, and W. Liu, "The study on the relationship of frequency domain spectroscopy of oil-paper insulation with degree of polymerization and tensile strength," in *2018 12th International Conference on the Properties and Applications of Dielectric Materials (ICPADM)*, pp. 801–804, Xi'an, China, 2018.

[58] J. Li, H. Ban, Y. Shi, Y. Wang, and Z. Zhang, "Experimental research on the wearability, corrosion resistance, and life assessment of an aluminum alloy bridge deck," *Tsinghua Science and Technology*, vol. 15, no. 5, pp. 566–573, 2010.

[59] E. Y. Seo, J. Y. Choung, and H. R. Hwang, "The changing patterns of knowledge production of catch-up firms during the forging-ahead period: case study of Samsung Electronics Co. (SEC)," *IEEE Transactions on Engineering Management*, vol. 66, no. 4, pp. 621–635, 2019.

[60] N. C. Barbi and G. Judd, "Microstructure and microsegregation effects in the intergranular corrosion of austenitic stainless steel," *Metallurgical and Materials Transactions B*, vol. 3, no. 11, pp. 2959–2964, 1972.

[61] M. Yeganeh, M. Motamedi, and M. Eskandari, "Comparison of corrosion resistance of nanostructured copper produced in vacuum and electrolytic solution in neutral chloride media," *Micro & Nano Letters*, vol. 6, no. 6, pp. 402–404, 2011.

[62] A. Arutunow and K. Darowicki, "DEIS assessment of AISI 304 stainless steel dissolution process in conditions of intergranular corrosion," *Electrochimica Acta*, vol. 53, no. 13, pp. 4387–4395, 2008.

[63] A. Arutunow and K. Darowicki, "DEIS evaluation of the relative effective surface area of AISI 304 stainless steel dissolution process in conditions of intergranular corrosion," *Electrochimica Acta*, vol. 54, no. 3, pp. 1034–1041, 2009.

[64] S. Iwai, H. Miyazaki, Y. Otani et al., "A conduction-cooled REBCO magnet with a single-stage GM cryocooler and a stainless steel case for storing the coil and covering it from thermal radiation," *IEEE Transactions on Applied Superconductivity*, vol. 27, no. 4, pp. 1–5, 2017.

[65] A. S. Mitko, D. R. Streltsov, P. V. Dmitryakov, A. A. Nesmelov, A. I. Buzin, and S. N. Chvalun, "Evolution of morphology in the process of growth of island poly(p-xylylene) films obtained by vapor deposition polymerization," *Polymer Science, Series A*, vol. 61, no. 5, pp. 555–564, 2019.

[66] S. Xu, Y. Wang, and Y. Tan, "Influence of Discharge Flow of Daily Regulating Hydropower Station on Habitat of Schizothoraxprenanti in Downstream River Channel," *Water Resources and Power*, vol. 1, p. 7, 2013.

[67] X. Zeng and H. Jiang, "In Situ Fabrication and Actuation of Polymer Magnetic Microstructures," *Journal of Microelectromechanical Systems*, vol. 20, no. 4, pp. 785–787, 2011.

[68] T. Li, B. H. Wu, and J. F. Lin, "Effects of pre-strain applied at a polyethylene terephthalate substrate before the coating of TiO_2 film on the coating film quality and optical performance," *Thin Solid Films*, vol. 519, no. 22, pp. 7875–7882, 2011.

[69] T. C. Li, C. F. Han, B. H. Wu, P. T. Hsieh, and J. F. Lin, "Effects of prestrain applied to a polyethylene terephthalate substrate before the coating of al-doped ZnO film on film quality, electrical properties, and pop-in behavior during nanoindentation," *Journal of Microelectromechanical Systems*, vol. 21, no. 5, pp. 1059–1070, 2012.

[70] A. A. Balbola, M. O. Kayed, and W. A. Moussa, "Experimental characterization of the influence of transverse prestrain on the piezoresistive coefficients of heavily doped n-type silicon," *IEEE Transactions on Electron Devices*, vol. 65, no. 11, pp. 5002–5008, 2018.

[71] Y. Zhang, D. W. Hazelton, R. Kelley et al., "Stress-strain relationship, critical strain (stress) and irreversible strain (stress) of IBAD-MOCVD-based 2G HTS wires under uniaxial tension," *IEEE Transactions on Applied Superconductivity*, vol. 26, no. 4, pp. 1–6, 2016.

[72] M. Janecska, Z. Kovacs, A. Pongracz, and M. Tallian, "Correlation study of bulk Si stress and lithography defects using polarized stress imager," *IEEE Transactions on Device and Materials Reliability*, vol. 20, no. 1, pp. 221–223, 2020.

[73] L. Daniel and O. Hubert, "Equivalent stress criteria for the effect of stress on magnetic behavior," *IEEE Transactions on Magnetics*, vol. 46, no. 8, pp. 3089–3092, 2010.

[74] P. Y. Yang, "Effect of gate-line-end-induced stress and its impact on device's characteristics in FinFETs," *IEEE Electron Device Letters*, vol. 37, no. 7, pp. 910–912, 2016.

[75] W. Y. Yong, X. Zhang, T. C. Chai, A. Trigg, N. B. Jaafar, and G. Q. Lo, "In situ measurement and stress evaluation for wire bonding using embedded piezoresistive stress sensors," *IEEE Transactions on Components, Packaging and Manufacturing Technology*, vol. 3, no. 2, pp. 328–335, 2013.

[76] H. Tingting, P. Bo, Z. Yuepu, and Y. Zixuan, "Reliability assessment considering stress drift and shock damage caused by stress transition shocks in a dynamic environment," *Journal of Systems Engineering and Electronics*, vol. 30, no. 5, pp. 1025–1034, 2019.

[77] D. Miyagi, M. Kato, Y. Yoshida, and M. Tsuda, "Influence of a coil bobbin on transient thermal stress in a REBCO pancake coil," *IEEE Transactions on Applied Superconductivity*, vol. 28, no. 4, pp. 1–5, 2018.

Hindawi
Journal of Nanomaterials
Volume 2021, Article ID 8275987, 11 pages
https://doi.org/10.1155/2021/8275987

Research Article

N-Doped Carbon Dots Derived from Melamine and Triethanolamine for Selective Sensing of Fe^{3+} Ions

Sathishkumar Munusamy,[1] **Sathish Sawminathan**,[2] **Thanigaivelan Arumugham**,[3] **Maura Casales Díaz**,[4] **Srinivas Godavarthi**,[5] **and Mohan Kumar Kesarla**[4]

[1]*Institute of Chemical Biology and Nanomedicine, State Key Laboratory of Chemo/Bio-Sensing and Chemometrics, College of Chemistry and Chemical Engineering, Hunan University, Changsha 410082, China*
[2]*Department of Chemistry, School of Advanced Sciences and Vellore Institute of Technology, Vellore 632014, India*
[3]*Department of Chemical Engineering, Khalifa University, 127788 Abu Dhabi, UAE*
[4]*Instituto de Ciencias Físicas, Universidad Nacional Autónoma de México, Avenida Universidad s/n, 62210 Cuernavaca, MOR, Mexico*
[5]*CONACYT–Universidad Juárez Autónoma de Tabasco, Centro de Investigación de Ciencia y Tecnología Aplicada de Tabasco (CICTAT), Cunduacán, C.P. 86690, Mexico*

Correspondence should be addressed to Mohan Kumar Kesarla; mohan@icf.unam.mx

Received 1 June 2021; Revised 22 July 2021; Accepted 15 September 2021; Published 4 October 2021

Academic Editor: Ester Vazquez

Copyright © 2021 Sathishkumar Munusamy et al. This is an open access article distributed under the Creative Commons Attribution License, which permits unrestricted use, distribution, and reproduction in any medium, provided the original work is properly cited.

This work reports nitrogen-doped carbon dots (NCDs) as a selective sensing probe to detect Fe^{3+} in water samples. NCD probes were synthesized via solvothermal method using nitrogen-rich melamine and triethanolamine as precursors. Properties of the resulting NCDs were studied using different characterization techniques, through which N-doping was confirmed. The quantum yield of obtained NCDs was measured to be 21%. When excited at 370 nm, the excellent blue emission property makes this probe adoptable for selectively sensing Fe^{3+} in practical water samples. The limit of detection (LOD) was identified as 216 nM with a good linear range between the concentrations of 0.2-2 μM. The obtained LOD is far less than the World Health Organization (WHO) permissible limits of Fe^{3+} in water. Interference studies reveal that the presence of other competing ions did not alter the sensing of Fe^{3+}, even at the presence of 10 equivalents which indicates the high selectivity of NCDs towards Fe^{3+}. The reversibility studies showed that adding a cheap and readily available EDTA ligand to the NCD results in fluorescence regeneration, leading to exceptional reusability for the detection of Fe^{3+}. So, the synthesized NCDs can be used as a suitable probe for the selective determination of Fe^{3+} in real water samples.

1. Introduction

Among nanocarbon materials, carbon dots (CDs) have been given much attention due to their properties such as low cytotoxicity, robust chemical inertness, and good biocompatibility, which are particularly useful in several areas like sensing, imaging, photodegradation, and theranostic applications [1–6]. On the other hand, modification of electronic structures of CDs by doping heteroatoms such as nitrogen is further beneficial, especially in sensing due to enhanced fluorescence quantum yields [6–17]. Hence, extensive research efforts have been dedicated to their synthesis [18–20]. But, to incorporate a heteroatom in carbon framework requires complicated strategies such as high-temperature carbonization of nitrogen compounds, treatment of carbon materials with ammonia at high temperatures, liquid phase polymerization of nitrogen-containing compounds, and chemical vapor deposition with nitrogen-containing compounds as nitrogen sources. But all the techniques mentioned above have drawbacks such as severe synthetic conditions, high cost, complex, and time-consuming processes [21–23]. Even though many other methods are available to synthesize nitrogen-doped carbon dots (NCDs) [24–26], for example, using biomass via green synthesis methods, -broad PL

emission profiles and high quantum yields remained as challenges in the production of CDs. So, the development of inexpensive and scalable synthesis for the production of NCDs remains a requirement.

Metals play an essential part in the physiological functions of biological systems. Among the different metal ions, iron ions play a crucial role in biochemical reactions, oxygen loading, cellular proliferation, enzyme catalysis, etc. However, a lower or higher concentration of Fe^{3+} may lead to severe health concerns such as anemia, organ dysfunction, and skin diseases [27–30]. Considering the extensive use of iron in the day-to-day life of humans, estimating its quantities in water is vital. In detecting metal ions, fluorescence methods have benefits such as high sensitivity, reusability, onsite usage, and relatively economical, over traditional spectrophotometric approaches, which generally require complex sample preparation procedures and expensive instrumentation [31, 32]. Even though several fluorescent sensors have been reported in the literature [33–37], only very few highly selective and susceptible detection of Fe^{3+} ions with reusability exists [36, 37].

The present study described novel fluorescent NCDs that can detect Fe^{3+} ions. For the first time, water-soluble NCDs were made from readily accessible nitrogen-rich precursors like melamine and triethanolamine together, utilizing a cost-effective and straightforward one-pot solvothermal approach without the need for passivation chemicals. Synthesized NCDs were characterized structurally and optically using TEM, XRD, FT-IR, absorption, and fluorescence spectroscopy. These NCDs were shown to have a high sensitivity and selectivity for Fe^{3+} ions in an aqueous solution with a low detection limit. Moreover, other competing metal ions do not affect the optical property of NCDs. Additionally, the real-time application of Fe^{3+} detection was demonstrated by the quantification of Fe^{3+} in water samples.

2. Experimental

2.1. Materials. Melamine (99%), triethanolamine (99.5%), chloroform, methanol, ethanol, and EDTA were purchased from Sigma Aldrich and used without further purification. Likewise, all the metal salts used for sensing applications were purchased from Sigma Aldrich and utilized as such.

2.2. Synthesis of NCDs. NCDs were synthesized using melamine and triethanolamine together as precursors for carbon and nitrogen. Briefly, 500 mg of melamine was dispersed in 20 mL of ethanol using an ultrasonic bath, and 1 mL of triethanolamine was introduced into the above mixture and stirred for half an hour on a magnetic stirrer. Then, this solution mixture was transferred into Teflon lined autoclave and heated at 160°C for four hours. After four hours, the solution was allowed to cool to room temperature naturally. The crude product was purified by silica gel column chromatography with chloroform and methanol as the eluent (70 : 30), collecting the yellow-green fraction. Finally, the portion was concentrated to get the black solid (~11 mg). The obtained NCDs were redispersed in double distilled water as per the requirement.

2.3. Characterization. The UV-vis spectrum of the purified NCDs and different cations was monitored from 200 to 800 nm using Shimadzu 3300 UV-double beam spectrophotometer. FT-IR spectra of the obtained NCDs were recorded using the Thermo Scientific Nicolet iS10 ATR-FTIR instrument to get surface functionalization information before and after sensing of Fe^{3+}. The size, shape, and SAED patterns of NCDs were obtained using an FEI Technai G2-20 twin high-resolution transmission electron microscope (HRTEM) with an operating acceleration voltage of 200 kV. The sample for HRTEM was prepared by dispersing and sonicating the NCDs in methanol and then dropping them on a Cu grid coated with holey carbon film and allowed to dry. XRD pattern was collected using Bruker D8 Advanced eco with Cu Kα = 1.54 Å in the 2θ range of 10 to 90°. Prior to recording the XRD patterns, the instrument was calibrated with Lanthanum hexaboride (LaB_6). Finally, all the PL measurements including sensing of Fe^{3+} were carried out using a Hitachi F-2000 spectrophotometer.

2.4. Quantum Yield Measurements. Quantum yield (QY) was determined using the below equation

$$\Phi S = \Phi R \frac{A_R(\lambda_R) n_s^2 I_s}{A_S(\lambda_S) n_R^2 I_R}, \quad (1)$$

where ΦS and ΦR are quantum yields of sample and reference, respectively; $A_R(\lambda_R)$ and $A_s(\lambda_s)$ are the absorbance of the reference and sample at excitation wavelengths; n_S and n_R are refractive indices of the sample medium and reference medium, respectively; I_S and I_R are the integrated fluorescence intensities of sample and reference, respectively. Because of the stable luminescent properties of quinine sulfate (Φ = 54% at 340 nm), this was used as a reference in 0.1 M H_2SO_4 to determine the QY of NCDs [22].

2.5. Detection of Metal Ions Using NCDs. To detect metal ions using NCDs, precursors like $Cu(NO_3)_2$, KBr, $NaNO_2$, $MgSO_4$, $MnSO_4$, H_2O, $NiCl_2.6H_2O$, $PbSO_4$, SeS_2, $Sr(NO_3)_2$, $ZnSO_4$. $7H_2O$, $CaSO_4$, $2H_2O$, $BaCl_2$, $HgCl_2$, $FeCl_2.4H_20$, BiOCl, and $FeCl_3$ were used. The ion solution with a concentration of 100 μM was added into 2 mL of predispersed NCDs solution and recorded the PL spectra immediately. All the PL spectra were recorded at an excitation wavelength of 370 nm.

3. Results and Discussion

The solvothermal method was adopted to synthesize NCDs where melamine and triethanolamine together act as carbon and nitrogen sources. Upon solvothermal treatment at 160°C for four hours, the solution turned yellow and emitted greenish-blue when kept under UV light (Scheme 1).

After purification of NCDs by column chromatography using the eluent mixture of chloroform and methanol

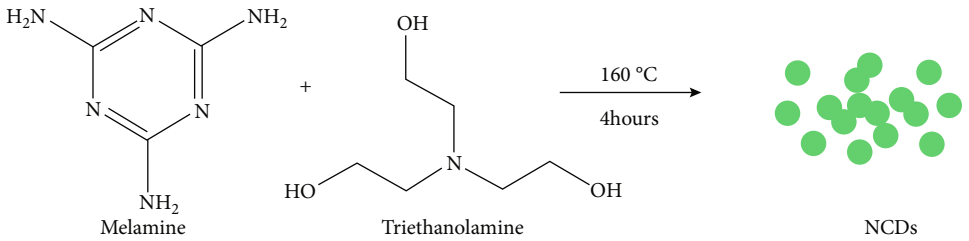

Scheme 1: Synthesis of NCDs by solvothermal methods.

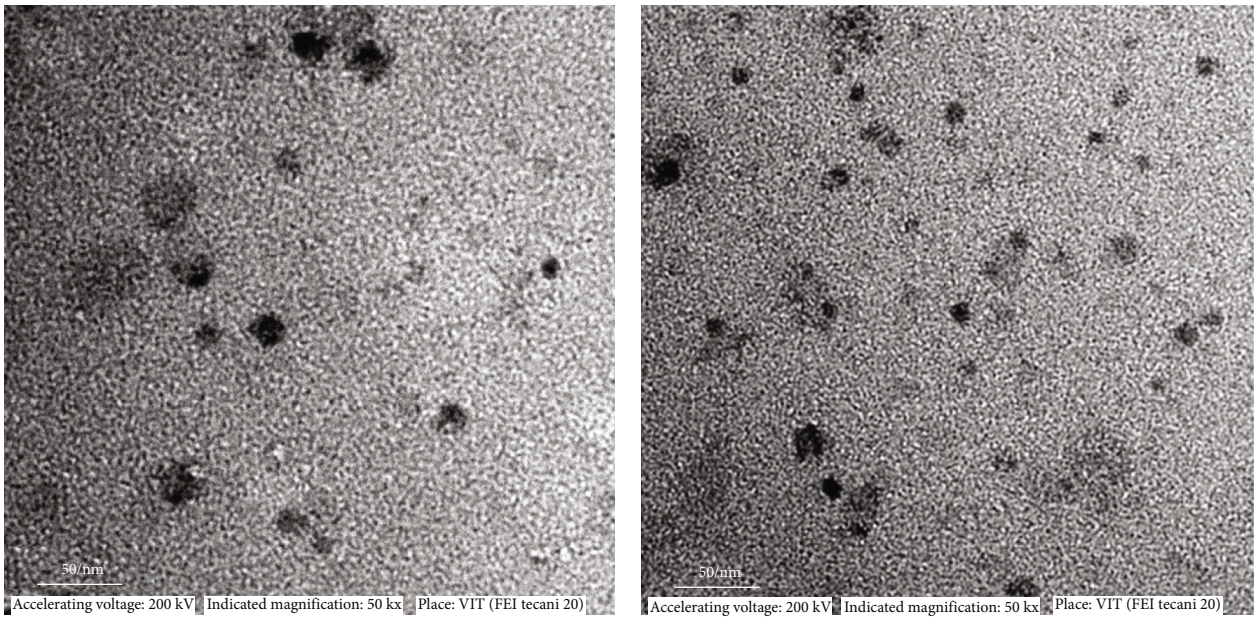

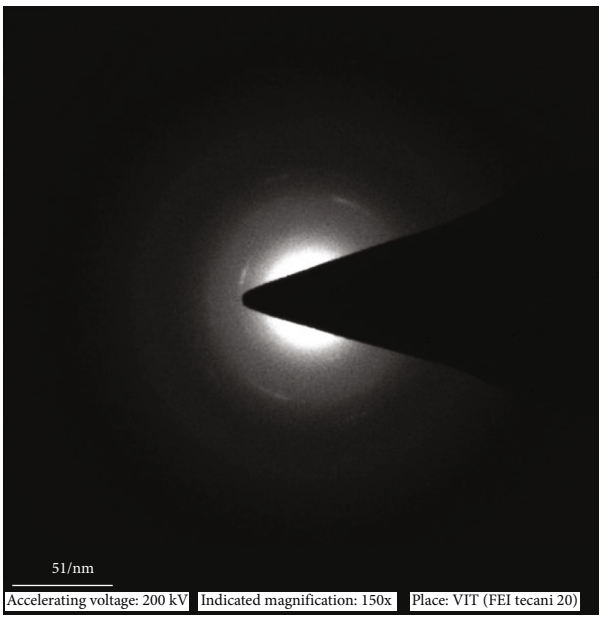

Figure 1: (a) and (b) HRTEM images of synthesized NCDs with scale bar 50 nm and (c) SAED pattern of the obtained NCDs.

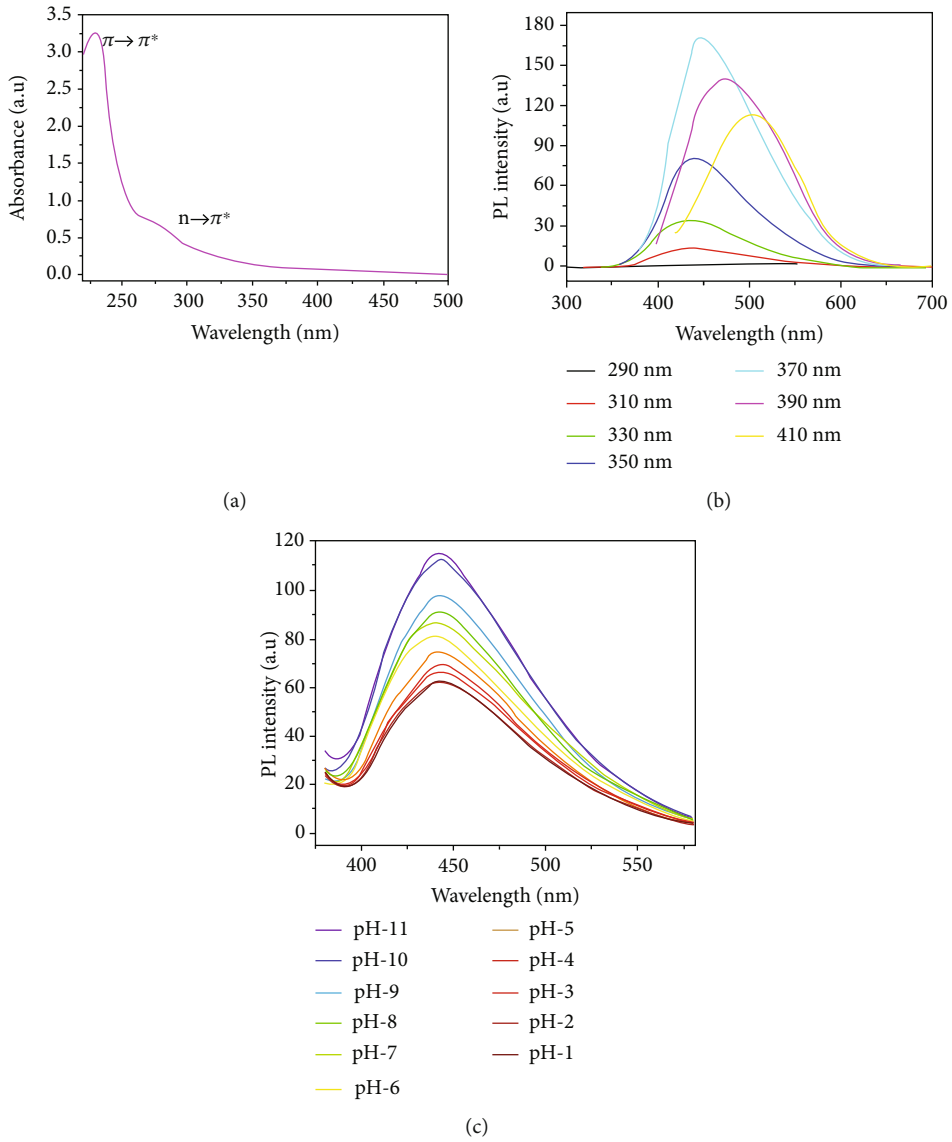

Figure 2: (a) UV-vis spectra of purified NCDs in methanol solution. (b) PL spectra of NCDs under various excitation wavelengths. (c) The effect of pH on fluorescence intensity of NCDs. All the experiments were carried out in a water medium.

(70 : 30), the as-prepared sample showed the relative fluorescence quantum yield of 21% using quinine sulfate reference. The observed high quantum yield was ascribed to nitrogen doping in the carbon framework [19].

Figure S1 of supplementary information shows the X-ray diffraction pattern of the as-obtained NCDs. From the XRD pattern, it is clear that a broad peak is centered at $2\theta = 26.87^{\circ}$, which corresponds to (002), due to the highly disordered graphitic structure associated with NCDs. The weak diffraction peak around 43° is due to the presence of highly disordered amorphous carbon with a fractional extent of graphitization [38]. In general, graphitic carbon appears at 26.5°, and the slight shift in diffraction angle is due to the doping of nitrogen into carbon, which resembles more or less like amorphous carbon nitride [39]. So indirectly, N-doping was confirmed with XRD results.

FT-IR spectra were used to identify the surface functionalization. Figure S2 of supplementary information depicts

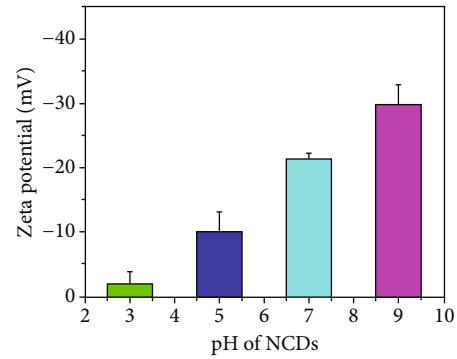

Figure 3: Zeta potential as a function of pH for NCDs.

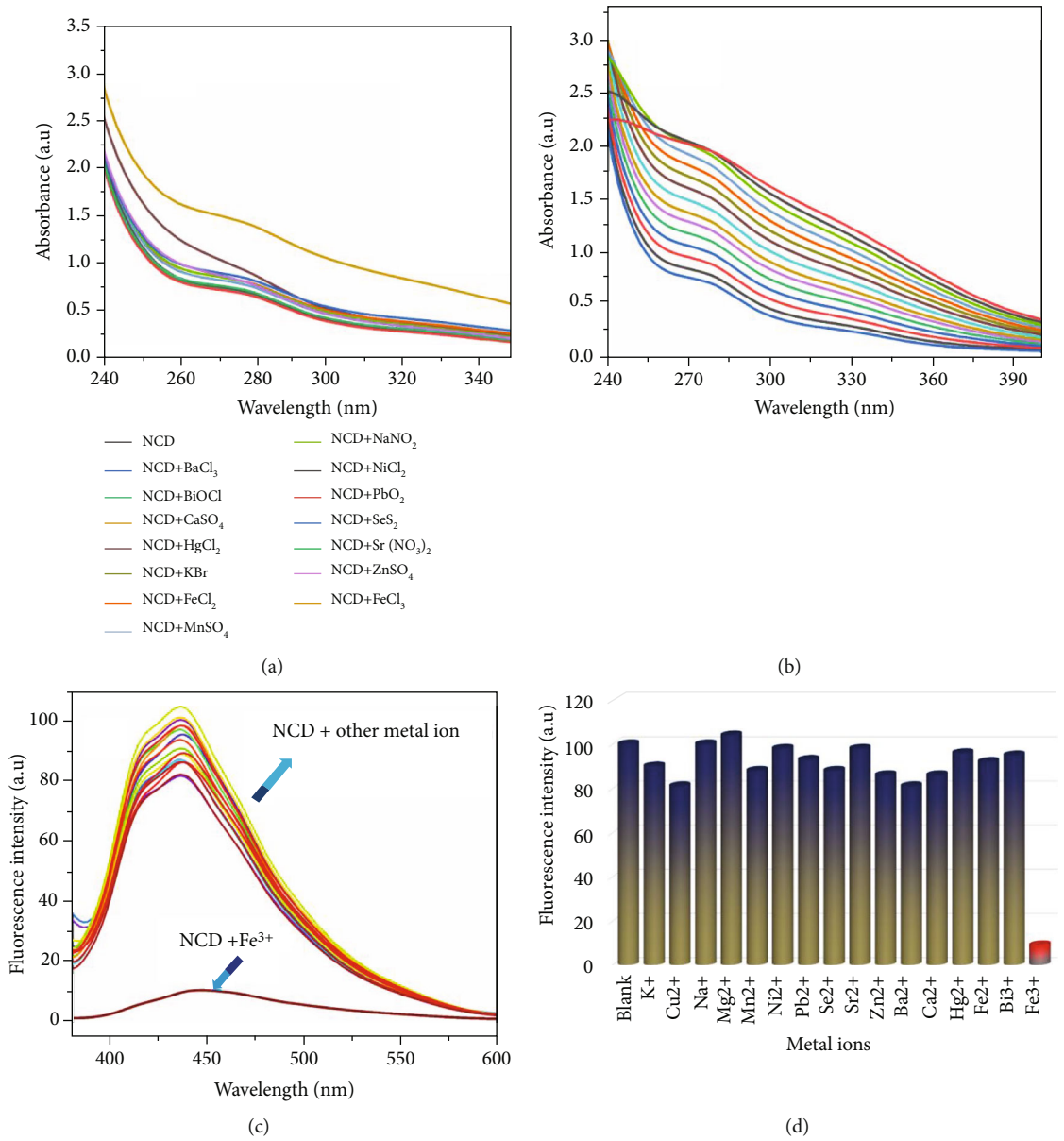

Figure 4: (a) UV-vis spectra of NCDs in the presence of different metal ions. (b) UV-vis spectra of NCDs with the gradual increase in the concentration of Fe^{3+}. (c) PL spectra of NCDs in the presence of various metal ions. (d) Bar diagrams showing selectivity of NCDs towards Fe^{3+} sensing. All the experiments were carried out in a water medium.

FT-IR of the synthesized NCDs. FT-IR shows a broad absorption band at 3323 cm^{-1} which indicates the presence of -OH/-NH_2 groups. The bands around 2830 and 2943 cm^{-1} were due to the -C-H stretching, and the strong band at 1022 cm^{-1} reveals the presence of -C-O stretching vibrations. The peak at 1675 cm^{-1} indicates the stretching of -C=N/-C=O and -C-H deformation appears around 1450 cm^{-1}. The presence of nitrogen in the NCDs was evident from FT-IR, and the surface was functionalized with -OH and -NH_2 groups.

High-resolution transmission electron microscopy of the as-synthesized NCDs were shown in Figures 1(a) and 1(b), and the selected area diffraction patterns (SAED) was shown in Figure 1(c). It is clear from the HRTEM that the NCDs were well dispersed, and the size of the dots was in the range of 5 to 20 nm. The selected area diffraction pattern also reveals the semicrystalline nature of the formed NCDs due to disordered graphitic structure associated with NCDs (Figure 1(c)).

The optical properties of the NCDs were studied using a UV-vis spectrophotometer in double-distilled water (Figure 2(a)). It is very clear from UV-vis spectra, the band around 230 nm appeared due to $\pi \longrightarrow \pi *$ transition of aromatic conjugated sp^2 domains, the shoulder peak at around 275 nm corresponds to the $n \longrightarrow \pi *$ transition of carbonyl groups, and the broad peak centered at approximately 330 nm indicates the surface state defects induced by nitrogen doping [40]. PL spectra of as-synthesized NCDs at various excitation wavelengths are shown in Figure 2(b) at different excitation wavelengths. The synthesized NCDs

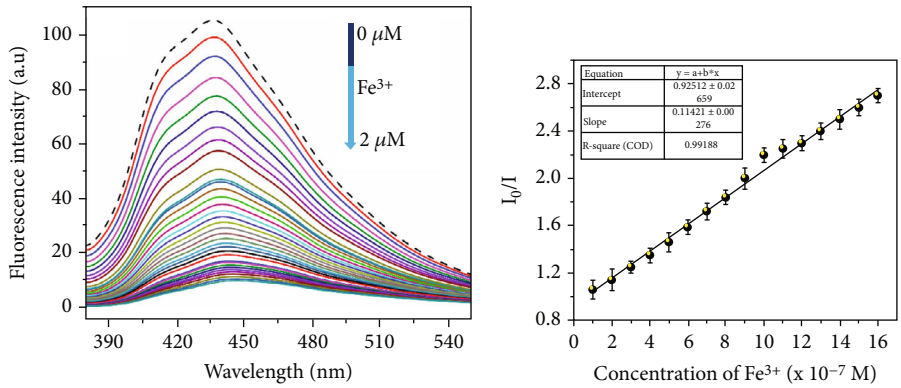

(a) (b)

Figure 5: (a) PL spectra of NCDs with increasing concentration of Fe^{3+} and (b) S-V plot of quenching of NCDs with Fe^{3+}.

exhibit excitation-dependent fluorescence upon increasing the excitation wavelength from 290 to 410 nm; the PL emission peak shifts gradually from 425 nm to 525 nm. The fluorescence intensity under 370 nm excitation shows a maximum emission peak at 435 nm among the various excitation wavelengths. In addition, an apparent redshift was observed with a remarkable decrease in PL intensity when the excitation wavelength was increased beyond 370 nm. The excitation-dependent PL spectra were attributed to the presence of functionalities like (C = O/N, -NH_2), which leads to $\pi * \longrightarrow n$ transitions of surface states. These phenomena occur due to doping of nitrogen hetero atom, leading to defective surface states with a concomitant effect on PL enhancement.

The effect of pH on the fluorescence emission intensity of NCDs solution was also evaluated in the range of 1 to 11 (Figure 2(c)). The pH of the NCDs solution was adjusted to the desired value by adding either 0.1 M HCl or NaOH. Medium with the pH range of 1-4 has shown a significant reduction in the PL. Whereas neutral or basic pH has caused a dramatic increase in the PL intensity. This behavior can be attributed to the different degrees of protonation at lower pH solutions. At lower pH solutions, the primary sites at the surface of NCDs tend to neutralize, generating a lower net surface charge which provides the NCDs with hydrophobic and aggregative properties with subsequent aggregation caused quenching (ACQ) of PL. The NCDs show good PL behavior in basic environments, and it is found that pH 6 to 11 was the best pH values for the sensing system. To further understand the mechanism of NCDs behavior with different pH, their Zeta potentials were determined in acidic, neutral, and alkaline conditions. As shown in Figure 3, in the neutral or basic pH condition, the NCDs showed overall negative surface potential due to free -OH and -NH_2 functional groups, which ensures high colloidal stability due to electrostatic repulsion between NCDs. As the pH of the solution decreases from 9 to 3, the negative zeta potential tends to decrease, which is in accordance with our assumption. The decrease in negative zeta potential is due to the protonation of the surface functional groups. As the pH medium of NCDs after the purification is ~7, there is no need to adjust the pH of the solution before proceeding to metal sensing.

3.1. Selectivity of NCDs towards Fe^{3+} Ions. To figure out which metal ions that NCDs can recognize selectively, NCDs sensing of different metals were monitored by changes in UV-vis and fluorescence spectra in the presence of various metal ions like K^+, Cu^{2+}, Na^+, Mg^{2+}, Mn^{2+}, Ni^{2+}, Pb^{2+}, Se^{2+}, Sr^{2+}, Zn^{2+}, Ca^{2+}, Ba^{2+}, Hg^{2+}, Bi^{3+}, Fe^{2+}, and Fe^{3+} in 100 μM concentration of each element. It is very clear from Figure 4(a); no significant absorbance changes were observed except upon the addition of $FeCl_3$. The intensity of the NCDs absorption peak at around 270 nm showed a substantial increase over the addition of Fe^{3+}, which provided the preliminary insight about pursuing our experiments towards detecting Fe^{3+} selectivity of NCDs towards sensing Fe^{3+} (Figure 4(b)). Moreover, a linear relationship was found between the absorption intensity of NCDs and Fe^{3+} concentration (Figure S3 of supplementary information) between 2 μM and 20 μM concentrations.

The fluorescence response of NCDs with various metal ions (100 μM) was studied at an excitation wavelength of 370 nm. As shown in Figure 4(c), although NCDs exhibit emission at 435 nm, we observed that there are no significant changes in the fluorescence intensities upon introduction of different metal ions like K^+, Cu^{2+}, Na^+, Mg^{2+}, Mn^{2+}, Ni^{2+}, Pb^{2+}, Se^{2+}, Sr^{2+}, Zn^{2+}, Ca^{2+}, Ba^{2+}, Hg^{2+}, Fe^{2+}, and Bi^{3+}. But over the addition of Fe^{3+} ions, it was observed that NCDs suffered a significant quenching in emission. This experiment revealed that the NCDs are very selective towards sensing Fe^{3+} ions. The selective sensing of Fe^{3+} was demonstrated using the bar diagram in Figure 4(d). This observation encouraged us to believe that the NCDs could be used as potential "turn-off" nanosensors for Fe^{3+} in an aqueous medium.

To check the quantitative applicability of NCDs, fluorescence spectrometric titrations were carried out with increasing concentrations of Fe^{3+}. The titration experiment was performed in the medium of pH 7 using phosphate buffer. Figure 5(a) shows the PL behavior of NCDs with an increasing concentration of 0.2 μM Fe^{3+} in every step. Upon increasing the concentration of Fe^{3+}, the emission peak at 435 nm decreases gradually. As the concentration of Fe^{3+} reached 2 μM, NCDs showed very little fluorescence and perturbance. From the Stern-Volmer (S-V) curve, the linear

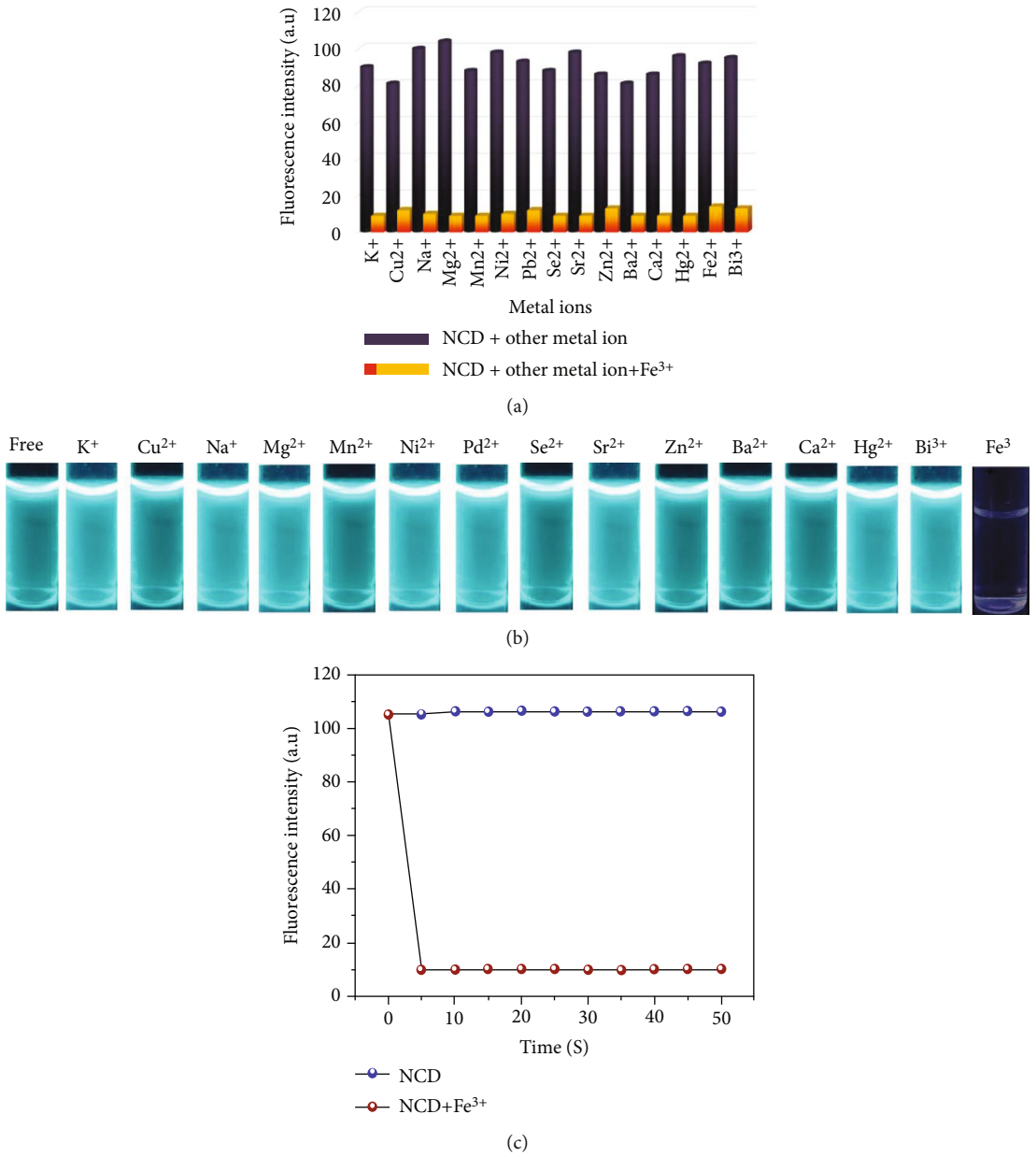

Figure 6: (a) Anti-interference of NCDs in the presence of Fe^{3+} (2 μM) and miscellaneous cations (20 μM) at 435 nm. (b) Fluorescence response time of NCDs over the addition of Fe^{3+}. (c) Photographs of NCDs in the presence of various metals and Fe^{3+} under a UV lamp at 365 nm.

regression was found to be $y = 0.11x + 0.92$. Y and X are Io/I (where Io and I are fluorescence intensity of NCDs without and with Fe^{3+}) and the concentration of Fe^{3+}, respectively. The linear range was displayed for a concentration range of 0.2 to 2 μM with a 0.9925 correlation coefficient (Figure 5(b)). The LOD is determined to be 216 nM/L based on the $3.3\sigma/K$ equation, where σ is the standard deviation and K is the slope of the calibration curve. The obtained LOD is significantly less compared to that of permissible levels of WHO for Fe^{3+} in water (5.36 μmol L^{-1}) [41] and many recent papers (Table S3 of supplementary information). The current observation signifies the use of synthesized NCDs to detect Fe^{3+} with high selectivity and sensitivity.

3.2. Interference and Time Dependence. Interference with the detection of Fe^{3+} with NCDs by other competitive metal ions was investigated. As can be seen from Figure 6(a), the presence of other ions did not disturb the sensing of Fe^{3+}, even at the presence of 10 equivalents, which indicates the high selectivity of NCDs towards Fe^{3+}. Besides, the probe's bright and clear bluish-green emission was completely switched off when viewed under the UV light (Figure 6(b)), whereas other metal ions retained the bluish-green fluorescence. Besides, the fluorescence response time of NCDs to Fe^{3+} was monitored by a time-based fluorescence study. As shown in Figure 6(c), the addition of Fe^{3+} to NCDs caused emissions to quench immediately, and it reached the plateau within 5 seconds. This demonstrates there is an instant

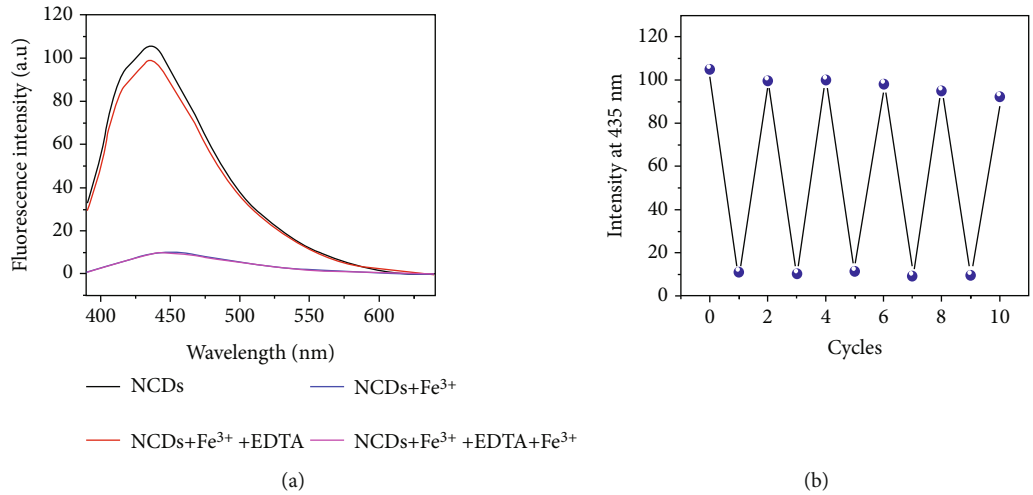

Figure 7: (a) Fluorescence intensity responses of NCD upon addition of Fe^{3+} + EDTA. (b) Number of sequential detections of Fe^{3+} and EDTA.

reaction between NCDs and Fe^{3+}. This indicates that Fe^{3+} can be detected free of culture time with NCDs, which may be used in real-time applications.

3.3. Reversibility Study. Reversibility is the essential parameter of the probe for the real-time application and economic aspect [42]. A fervent complexing agent EDTA has been added to the NCD-Fe^{3+} system to validate NCD sensors' reversibility towards Fe^{3+}. In the beginning, free NCDs show intense fluorescence, and the addition of Fe^{3+} almost completely quenched the emission. Upon the addition of five equivalents of Na_2-EDTA to the above solution, the emission was immediately registered. As shown in Figure 7(a), the addition of EDTA to the NCDs and Fe^{3+} mixture caused nearly immediate recovery of the fluorescence due to the formation of EDTA + Fe^{3+} complex and consequent regeneration of previous intensity of free NCDs. The 'ON-OFF-ON' behavior of the NCDs fluorescence emission at 435nm canbe repeated around five times with a slight decrease in the initial emissionintensity (Figure 7(b)). This experiment suggests that adding a cheap and readily available EDTA ligand to the NCDs results in excellent reusability for the detection of Fe^{3+}.

3.4. Application of NCDs in Practical Water Analysis. To determine the practical utility of NCDs, we performed fluorescence detection of Fe^{3+} using NCDs in water samples collected from various bodies of water throughout the Vellore district, India. First, water samples were spiked with known Fe^{3+} concentrations, and their effect on the fluorescence of NCDs was determined by recording the emission intensity at 435 nm. Then, three consecutive measurements were made to determine the mean Fe^{3+} detection value. As shown in Table 1, a satisfactory recovery and relative standard deviation (R.S.D.) were detected with the spiked Fe^{3+} concentration. These findings suggest that NCDs can detect Fe^{3+} with high selectivity and precise quantification.

Table 1: Estimation of Fe^{3+} ion quantity in collected water samples using NCDs.

Synod	Water samples[a]	Fe^{3+} spiked (μM)	Fe^{3+} found (μM)	Recovery (%)	R.S.D[b] ($n = 3$) (%)
1	Tap water	1×10^{-5}	0.93×10^{-5}	93	.36
2	Lake water	1×10^{-5}	0.95×10^{-5}	95	0.18
3	Well water	1×10^{-5}	0.93×10^{-5}	93	0.21
4	Mineral water	1×10^{-5}	0.96×10^{-5}	96	0.49
5	Distilled water	1×10^{-5}	0.92×10^{-5}	92	0.28
6	Purified water	1×10^{-5}	0.95×10^{-5}	95	0.61

[a]Water samples were collected from throughout the Vellore district, India; [b]relative standard deviation.

3.5. Fluorescence Quenching Mechanism. The fluorescence quenching of NCDs up on the introduction of Fe^{3+} may be explained as follows (Figure 8). When there are no Fe^{3+} ions, upon incidence of the light, NCDs captivate energy, and electrons move from the ground (HOMO) to the excited (LUMO) state. When the electrons fall back to the ground state, radiative recombination of electrons and holes results in fluorescence emission.

As confirmed from FTIR, the surface of NCDs has -NH_2 and -OH groups on their surfaces. The relatively high selectivity of the NCDs towards Fe^{3+} was attributed to the half-filled 3D orbitals, short-range ionic radius, and unique coordinate interaction of Fe^{3+}. Those properties made Fe^{3+} possess greater binding affinity and quicker chelating kinetics for hydroxyl, carboxyl, and amino groups on the surface of N-CDs, which would promote the coordination reaction between N-CDs and Fe^{3+}. Therefore, when Fe^{3+} comes in contact with surface states of NCDs, the five half-filled d

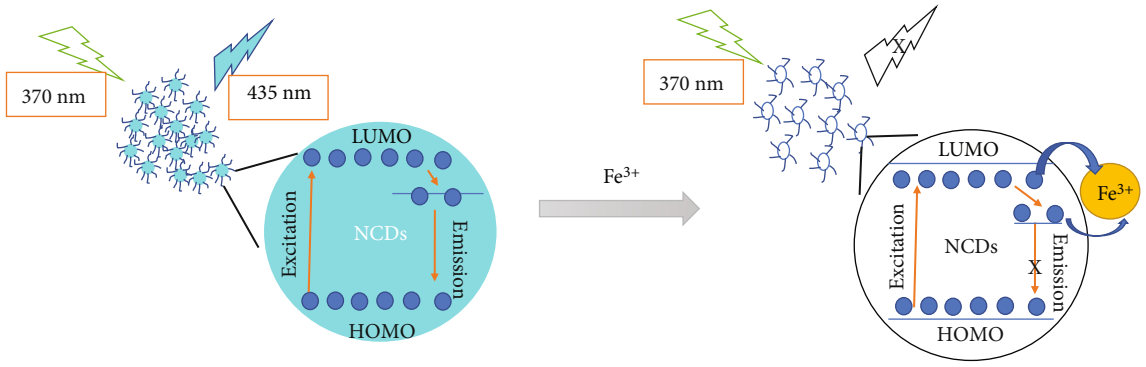

Figure 8: Schematic representation of quenching in emission selectively with Fe^{3+} ions.

orbitals of Fe^{3+} take up the excited electron, forming nonradiative recombination, which simultaneously leads to fluorescence quenching shown in Figure 8. This selective interaction of Fe^{3+} with NCDs was further confirmed by FT-IR analysis (Figure S4 of supplementary information). The NCDs clear vibration peak at 3323 cm^{-1} arising from -OH/NH_2 functional got diminished over the addition of Fe^{3+}. Whereas Cu^{2+} (potential interferant for Fe^{3+}) has significantly less influence on the FT-IR spectra of NCDs (Figure S4).

The S-V plot can also explain the fluorescent quenching mechanism. It denotes the relationship between the fluorescence intensity and the metal ion concentration. In essence, the quenching mechanisms are two types. One is complexation (static quenching), and another one is collisional deactivation (dynamic quenching). The S-V plot can be used to verify the preceding mechanism. The general form of the S-V equation is as follows.

$$\frac{F_0}{F} = 1 + K_{sv}[Q], \tag{2}$$

where F_0 and F are the fluorescence intensity of the NCDs before and after the presence of metal ions. K_{sv} is the S-V constant, and Q is the Quencher concentration. The calibration curve (Figure 5(b)) was obtained from the plot of F_0/F versus the concentration of Fe^{3+}, and it exhibits a linear relationship between x and y-axis over the range of 0-2 μM, which denotes static quenching, resulting in the formation of a nonfluorescent complex formation between Fe^{3+} and NCDs. The plausible explanation for the occurrence of static quenching can be further confirmed by performing the fluorescence sensing experiments at different sets of temperatures, i.e., 25°C, 30°C, and 35°C, maintaining optimal conditions for all other parameters (Figure 9). For each temperature, the S-V calibration curve was drawn. It was noticed that the value of K_{sv} decreased as the temperature increased (as shown in Table 2) because raising temperature tends to reduce the binding interactions result in static quenching. As a result, the findings are consistent with a static quenching process.

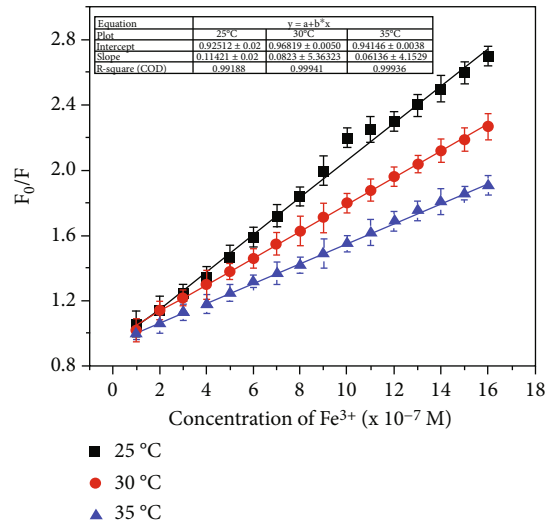

Figure 9: S-V plot for fluorescence quenching of NCDs by Fe^{3+} ions at different temperatures.

Table 2: S-V constant of interaction between NCDs and Fe^{3+} at different temperatures.

S. no	Temperature (°C)	K_{sv} (M^{-1})	R^2
1	25	1.14×10^6	0.9918
2	30	0.82×10^6	0.9994
3	35	0.61×10^6	0.9936

4. Conclusion

Nitrogen-doped carbon dots (NCDs) were synthesized successfully by the solvothermal method using melamine and triethanolamine as carbon/nitrogen precursors with a quantum yield of 21%. Surface functionalization and the presence of nitrogen were confirmed using FTIR. HRTEM results revealed that the NCDs were in the range of 5-15 nm. The excitation-dependent PL nature was observed from PL spectra. PL experiments revealed that the synthesized NCDs show good potential towards sensitive and selective detection of Fe^{3+} with a detection limit of 216 nM/L, far less than WHO permissible limits. Furthermore, a cheap and readily

available ligand can regenerate the emission from the probe leading to its excellent reusability. Applicability in the practical water analysis suggests that NCDs can detect Fe^{3+} with high selectivity and precise quantification.

Data Availability

The data used to support the findings of this study are included within the article and in the supplementary information file.

Conflicts of Interest

The authors declare no conflict of interest.

Acknowledgments

Dr. Kesarla acknowledges the financial support from Programa de Apoyo a Proyectos de Investigación e Innovación Tecnológica (PAPIIT), project no. IA201321. We thank Mr. José Juan Ramos Hernández, Academic Technician, for his continuous support in various characterizations.

Supplementary Materials

Supplementary information file available with Figures S1 to S4 and Tables S1 as referred in the main text. *(Supplementary Materials)*

References

[1] B. B. Chen, M. L. Liu, and C. Z. Huang, "Recent advances of carbon dots in imaging-guided theranostics," *TrAC Trends in Analytical Chemistry*, vol. 134, article 116116, 2021.

[2] P. Jayasekhar Babu, S. Saranya, Y. D. Singh, M. Venkataswamy, A. M. Raichur, and M. Doble, "Photoluminescence carbon nano dots for the conductivity based optical sensing of dopamine and bioimaging applications," *Optical Materials*, vol. 117, article 111120, 2021.

[3] S. Hu, Y. Ding, Q. Chang, J. Yang, and K. Lin, "Chlorine-functionalized carbon dots for highly efficient photodegradation of pollutants under visible-light irradiation," *Applied Surface Science*, vol. 355, pp. 774–777, 2015.

[4] M. Zheng, S. Liu, J. Li et al., "Integrating oxaliplatin with highly luminescent carbon dots: an unprecedented theranostic agent for personalized medicine," *Advanced Materials*, vol. 26, no. 21, pp. 3554–3560, 2014.

[5] X. Tu, Y. Ma, Y. Cao, J. Huang, M. Zhang, and Z. Zhang, "PEGylated carbon nanoparticles for efficient in vitro photothermal cancer therapy," *Journal of Materials Chemistry B*, vol. 2, no. 15, pp. 2184–2192, 2014.

[6] M. Ashrafizadeh, R. Mohammadinejad, S. K. Kailasa, Z. Ahmadi, E. G. Afshar, and A. Pardakhty, "Carbon dots as versatile nanoarchitectures for the treatment of neurological disorders and their theranostic applications: a review," *Advances in Colloid and Interface Science*, vol. 278, article 102123, 2020.

[7] Y. Man, W.-S. Zou, W.-L. Kong et al., "Brightly blue triazine-doped carbon dots for selective determination of Cu(II) in environment and imaging in cell," *Journal of Photochemistry and Photobiology A: Chemistry*, vol. 416, article 113321, 2021.

[8] M. Bonet-San-Emeterio, M. Algarra, M. Petković, and M. del Valle, "Modification of electrodes with N -and S -doped carbon dots. Evaluation of the electrochemical response," *Talanta*, vol. 212, article 120806, 2020.

[9] Z. Zhang and Z. Fan, "Application of cerium-nitrogen co-doped carbon quantum dots to the detection of tetracyclines residues and bioimaging," *Microchemical Journal*, vol. 165, article 106139, 2021.

[10] L. Sun, Y. Liu, Y. Wang et al., "Nitrogen and sulfur co-doped carbon dots as selective and visual sensors for monitoring cobalt ions," *Optical Materials*, vol. 112, article 110787, 2021.

[11] Z. Wang, L. Zhang, Y. Hao et al., "Ratiometric fluorescent sensors for sequential on-off-on determination of riboflavin, Ag^{+} and l-cysteine based on NPCl-doped carbon quantum dots," *Analytica Chimica Acta*, vol. 1144, pp. 1–13, 2021.

[12] C. Lu, D. Chen, Y. Duan et al., "New properties of carbon nanomaterials through zinc doping and application as ∗∗ a∗∗ ratiometric fluorescence pH sensor," *Materials Research Bulletin*, vol. 142, article 111410, 2021.

[13] C. Wang, H. Shi, M. Yang et al., "Biocompatible sulfur nitrogen co-doped carbon quantum dots for highly sensitive and selective detection of dopamine," *Colloids and Surfaces. B, Biointerfaces*, vol. 205, article 111874, 2021.

[14] X. Kou, S. Jiang, S.-J. Park, and L.-Y. Meng, "A review: recent advances in preparations and applications of heteroatom-doped carbon quantum dots," *Dalton Transactions*, vol. 49, no. 21, pp. 6915–6938, 2020.

[15] S. Kaushal, M. Kaur, N. Kaur, V. Kumari, and P. P. Singh, "Heteroatom-doped graphene as sensing materials: a mini review," *RSC Advances*, vol. 10, no. 48, pp. 28608–28629, 2020.

[16] S. Chandra, A. R. Chowdhuri, D. Laha, and S. K. Sahu, "Fabrication of nitrogen- and phosphorous-doped carbon dots by the pyrolysis method for iodide and iron(III) sensing," *Luminescence*, vol. 33, no. 2, pp. 336–344, 2018.

[17] J. Chen, J. Shu, J. Chen, Z. Cao, A. Xiao, and Z. Yan, "Highly luminescent S,N co-doped carbon quantum dots-sensitized chemiluminescence on luminol-H2O2system for the determination of ranitidine," *Luminescence*, vol. 32, no. 3, pp. 277–284, 2017.

[18] N. Li, F. Lei, D. Xu, Y. Li, J. Liu, and Y. Shi, "One-step synthesis of N, P co-doped orange carbon quantum dots with novel optical properties for bio-imaging," *Optical Materials*, vol. 111, article 110618, 2021.

[19] X. Ma, S. Li, V. Hessel, L. Lin, S. Meskers, and F. Gallucci, "Synthesis of N-doped carbon dots via a microplasma process," *Chemical Engineering Science*, vol. 220, article 115648, 2020.

[20] L. Ansari, S. Hallaj, T. Hallaj, and M. Amjadi, "Doped-carbon dots: recent advances in their biosensing, bioimaging and therapy applications," *Colloids and Surfaces. B, Biointerfaces*, vol. 203, article 111743, 2021.

[21] R. Wang, K.-Q. Lu, Z.-R. Tang, and Y.-J. Xu, "Recent progress in carbon quantum dots: synthesis, properties and applications in photocatalysis," *Journal of Materials Chemistry A*, vol. 5, no. 8, pp. 3717–3734, 2017.

[22] D. Kumar, K. Singh, V. Verma, and H. S. Bhatti, "Synthesis and characterization of carbon quantum dots from orange juice," *Journal of Bionanoscience*, vol. 8, no. 4, pp. 274–279, 2014.

[23] J. Xu, T. Lai, Z. Feng, X. Weng, and C. Huang, "Formation of fluorescent carbon nanodots from kitchen wastes and their

application for detection of Fe3+," *Luminescence*, vol. 30, no. 4, pp. 420–424, 2015.

[24] S. Miao, K. Liang, J. Zhu, B. Yang, D. Zhao, and B. Kong, "Hetero-atom-doped carbon dots: doping strategies, properties and applications," *Nano Today*, vol. 33, article 100879, 2020.

[25] Z. Zhang, G. Yi, P. Li et al., "A minireview on doped carbon dots for photocatalytic and electrocatalytic applications," *Nanoscale*, vol. 12, no. 26, pp. 13899–13906, 2020.

[26] L. Đorđević, F. Arcudi, and M. Prato, "Preparation, functionalization and characterization of engineered carbon nanodots," *Nature Protocols*, vol. 14, no. 10, pp. 2931–2953, 2019.

[27] G. Cairo and A. Pietrangelo, "Iron regulatory proteins in pathobiology," *The Biochemical Journal*, vol. 352, no. 2, pp. 241–250, 2000.

[28] M. W. Hentze, M. U. Muckenthaler, B. Galy, and C. Camaschella, "Two to tango: regulation of mammalian iron metabolism," *Cell*, vol. 142, no. 1, pp. 24–38, 2010.

[29] G. Papanikolaou and K. Pantopoulos, "Iron metabolism and toxicity," *Toxicology and Applied Pharmacology*, vol. 202, no. 2, pp. 199–211, 2005.

[30] P. Aisen, M. Wessling-Resnick, and E. A. Leibold, "Iron metabolism," *Current Opinion in Chemical Biology*, vol. 3, no. 2, pp. 200–206, 1999.

[31] D. Gomes, M. Segundo, J. Lima, and A. Rangel, "Spectrophotometric determination of iron and boron in soil extracts using a multi-syringe flow injection system," *Talanta*, vol. 66, no. 3, pp. 703–711, 2005.

[32] C. M. G. van den Berg, "Chemical speciation of iron in seawater by cathodic stripping voltammetry with dihydroxynaphthalene," *Analytical Chemistry*, vol. 78, no. 1, pp. 156–163, 2006.

[33] E. Li, J. Kang, P. Ye, W. Zhang, F. Cheng, and C. Yin, "A prospective material for the highly selective extraction of lithium ions based on a photochromic crowned spirobenzopyran," *Journal of Materials Chemistry B*, vol. 7, no. 6, pp. 903–907, 2019.

[34] R. Wang, L. Diao, Q. Ren, G. Liu, and S. Pu, "New bifunctional diarylethene sensor for multianalyte detection and Al3+ imaging in live cells," *ACS Omega*, vol. 4, no. 1, pp. 309–319, 2019.

[35] A. Kumar, P. R. Sahoo, P. Arora, and S. Kumar, "A light controlled, sensitive, selective and portable spiropyran based receptor for mercury ions in aqueous solution," *Journal of Photochemistry and Photobiology A: Chemistry*, vol. 384, article 112061, 2019.

[36] D. A. Gupta, M. L. Desai, N. I. Malek, and S. K. Kailasa, "Fluorescence detection of Fe^{3+} ion using ultra-small fluorescent carbon dots derived from pineapple (Ananas comosus): Development of miniaturized analytical method," *Journal of Molecular Structure*, vol. 1216, article 128343, 2020.

[37] M. L. Desai, H. Basu, S. Saha, R. K. Singhal, and S. K. Kailasa, "Investigation of silicon doping into carbon dots for improved fluorescence properties for selective detection of Fe^{3+} ion," *Optical Materials*, vol. 96, article 109374, 2019.

[38] S. K. Tammina, Y. Wan, Y. Li, and Y. Yang, "Synthesis of N, Zn-doped carbon dots for the detection of Fe^{3+} ions and bactericidal activity against Escherichia coli and Staphylococcus aureus_," *Journal of Photochemistry and Photobiology. B*, vol. 202, article 111734, 2020.

[39] Y. Kang, Y. Yang, L.-C. Yin, X. Kang, G. Liu, and H.-M. Cheng, "An amorphous carbon nitride photocatalyst with greatly extended visible-light-responsive range for photocatalytic hydrogen generation," *Advanced Materials*, vol. 27, no. 31, pp. 4572–4577, 2015.

[40] X. Gong, W. Lu, M. C. Paau et al., "Facile synthesis of nitrogen-doped carbon dots for Fe^{3+} sensing and cellular imaging," *Analytica Chimica Acta*, vol. 861, pp. 74–84, 2015.

[41] G. Dong, K. Lang, H. Ouyang et al., "Facile synthesis of N, P-doped carbon dots from maize starchviaa solvothermal approach for the highly sensitive detection of Fe3+," *RSC Advances*, vol. 10, no. 55, pp. 33483–33489, 2020.

[42] Z. Yi, X. Li, H. Zhang et al., "High quantum yield photoluminescent N-doped carbon dots for switch sensing and imaging," *Talanta*, vol. 222, p. 121663, 2021.

Hindawi
Journal of Nanomaterials
Volume 2021, Article ID 4741296, 7 pages
https://doi.org/10.1155/2021/4741296

Research Article

Structural Behavior of Nanocoated Oil Palm Shell as Coarse Aggregate in Lightweight Concrete

V. Swamy Nadh,[1] **Chunchubalarama Krishna**,[2] **L. Natrayan**,[3] **KoppulaMidhun Kumar**,[4] **K. J. N. Sai Nitesh**,[5] **G. Bharathi Raja**,[3] **and Prabhu Paramasivam**[6]

[1]*Department of Civil Engineering, Aditya College of Engineering, Surampalem, Andhra Pradesh 533437, India*
[2]*School of Civil Engineering, REVA University, Bangalore 560064, India*
[3]*Department of Mechanical Engineering, Saveetha School of Engineering, SIMATS, Chennai, 602105 Tamil Nadu, India*
[4]*Department of Civil Engineering, Tirumala Engineering College, Andhra Pradesh 522601, India*
[5]*Department of Civil Engineering, Anurag University, Hyderabad, 500088 Telangana, India*
[6]*Department of Mechanical Engineering, College of Engineering and Technology, Mettu University, Ethiopia 318*

Correspondence should be addressed to V. Swamy Nadh; swamynadh09@gmail.com, L. Natrayan; natrayanphd@gmail.com, and Prabhu Paramasivam; prabhuparamasivam21@gmail.com

Received 29 July 2021; Revised 30 August 2021; Accepted 17 September 2021; Published 1 October 2021

Academic Editor: Lakshmipathy R

Copyright © 2021 V. Swamy Nadh et al. This is an open access article distributed under the Creative Commons Attribution License, which permits unrestricted use, distribution, and reproduction in any medium, provided the original work is properly cited.

Oil palm shells (OPS) are mechanical waste that is utilized as coarse aggregates in lightweight concrete. These OPS have shape and strength like conventional aggregates yet the substantial made with these OPS invigorates a limit of 18 MPa. The characteristic strength which must be utilized in structures is seen to be around 25 MPa to 30 MPa. Considering the strength as one of the boundaries for design to be sturdy, the OPS are surface-covered with nanosilane compound. This nanosilane covering goes about as infill on the outside of the aggregates and holds the concrete paste as traditional cement. Operations are permeable in nature; their inner construction has permeable design which makes the aggregates frail. Nanosilane coatings go about as holding between the concrete stage and aggregate stage and hold the substantial solid. In the present examination, mechanical and underlying conduct of nanocovered oil palm shell lightweight concrete is contrasted with that of regular cement. Nanocovered oil palm shell lightweight substantial shows comparative strength as customary cement and decrease in nonsustainable wellspring of energy in oil palm shell lightweight concrete. Supplanting of customary cement with oil palm shell concrete addresses the modern waste which can be utilized for making concrete solid and solid. Morphology and material portrayal of oil palm shell and ordinary aggregates are investigated.

1. Introduction

One the main structure materials in structural designing is primary cement. Lightweight aggregates (LWA) are by and large used, being developed in regions these days which shows monstrous advantages [1]. Thickness contrasts between lightweight concrete (LWC) and normal weight concrete (NWC) are about 28% [2]. Usage of lightweight concrete being developed lessens the seismic effect on the development and thickness contrasts which shows the traditionalist arrangement of essential people like shaft and fragment. Usage of lightweight concrete decreases the utilization of steel in structure. Reduction in thickness of significant saves improvement and transportation cost, which may prompt extension in stories and longer ranges in platforms and abatement size of the essential people. Concrete made with lightweight cement to convey essential concrete should be hidden lightweight concrete and moreover called as lightweight concrete (LWC) [3]. There is liberty of basically lower unit weight than that of conveyed using rock or squashed stone. As side-effects from adventures, for instance, oil palm shells, reused plastic, and reused flexible are similarly used as lightweight sums in making of lightweight cement. Lightweight totals conveyed in turning

Figure 1: Oil palm shells.

broiler are expanded soils; shales should be LECA sums [4]. Lightweight aggregates made by sintering are said to by AGLITE sums. Lightweight aggregates made by water fly or slags stretched out unequivocally should be FOAMED lightweight sums, while sintered squashed fuel flotsam and jetsam sums should be LYTAG aggregates.

Genuine properties of OPS, for instance, water ingestion, surface area, thickness, and influence regard were finished by Barton et al. (1998) (using ACI 211.2, ASTM D3398, and ASTM C127 (ACI 211)). By far, most of the examinations in the past found interstitial change zone (ITZ) or bond direct of complete to network in lightweight concrete with different lightweight sums as uncovered [5]. All the LWA shows assorted lead up on their making cooperation and the conditions. Right when the LWC differentiated from NWC, the bond strength of NWC is higher and stood out from that of LWC [6]. However, few examinations uncovered that there is essentially indistinguishable bond strength among LWC and NWC.

Artificial aggregates like shale and broadened mud and record which are made by rotatory heater measure have been used for numerous years. These lightweight sums helps in the decline in additional weight, decline in sizes of the people, and warm security. Concretes produced with these lightweight aggregates as shown in Figure 1 had thickness of 1400-1750 kg/m^3 with the most outrageous compressive strength of 18-25 MPa. According to ACI 318-R, lightweight concrete conveying more than 25 MPa should be basic lightweight concrete. Aggregates which are used for numerous years cannot make compressive strength more than 25-30 MPa according to trained professionals. Extension of admixtures and blended sums can convey significant strength up to 30-33 MPa [7]. Various experts used fly flotsam and jetsam, GGBS, silica smoke, and rice calm remaining parts as significant replacement of cement. Various experts used coconut shells, egg shells, and various sorts as replacement of coarse aggregate almost completely. All of the assessments address that any displaced constituent material concrete can be used remarkably for building nonessential parts in the turn of events.

Table 1: Physical properties of aggregates used in this research.

Properties	Oil palm shell	Nanocoated oil palm shell	Conventional aggregate [11]
Aggregate size (mm)	12	12	40
Thickness (mm)	0.4–9	0.4–9	—
Bulk density (kg/m^3)	580	580–590	1430–1570
Specific gravity (SSD)	1.27	1.25–1.28	2.60
24 h water absorption (%)	23	8	2–4
Aggregate impact value (%)	29.5	21.6	17.8
Porosity (%)	27%	18%	15%

Bonding of concrete has a critical essential limit when we use a new material. The holding power among concrete and steel is fundamentally a direct result of the grasp between network (cement, sand, and water paste) and aggregate. Cooperation of holding rises up out of crushing of all out stage to harden stick and significant lattice to developing steel, mechanical dock of ribs against the considerable surface as nitty gritty [8]. As made lightweight sums or reused aggregates (RA) have higher flakiness document, it animates more security than standard concrete.

It is represented that open OPS in India can be used as a replacement of coarse absolute in concrete to make the lightweight concrete after genuine treatment of OPS complete as itemized by Swamy Nadh and Muthumani [9]. The place of the assessment is to make surface-treated OPS lightweight concrete with diminished ITZ thickness. Late researchers saw that reused aggregates show higher ITZ thickness than the normal significant which is a direct result of the genuine properties of reused sums used for making of concrete [10]. Smaller than usual essential assessment of treated oil palm shell lightweight concrete and nontreated oil palm shell lightweight concrete are thought of and differentiated and customary concrete. ITZ thickness in all of the three concretes is dissected; mineralogical properties are concentrated with the help of XRD assessment.

2. Materials Used and Methodology

Materials used in this research are OPS, conventional aggregate, cement, sand, and some fillers to make the concrete durable and strong to hold the compressive force acting on that. Nanocoat is used to fill the pores of the OPS aggregate and to create good bonding between the aggregate to cement phase. The physical properties of OPS, nanocoated OPS, and conventional aggregate are given in Table 1. Water absorption of OPS (23%) is higher than conventional concrete (4-5%), whereas nanocoated OPS (8%) has similar water absorption to conventional concrete. This is due to the fact that nanofillers of the coating act as filler on the voids of the OPS aggregate; this reduces the water absorption level in the coated OPS aggregate.

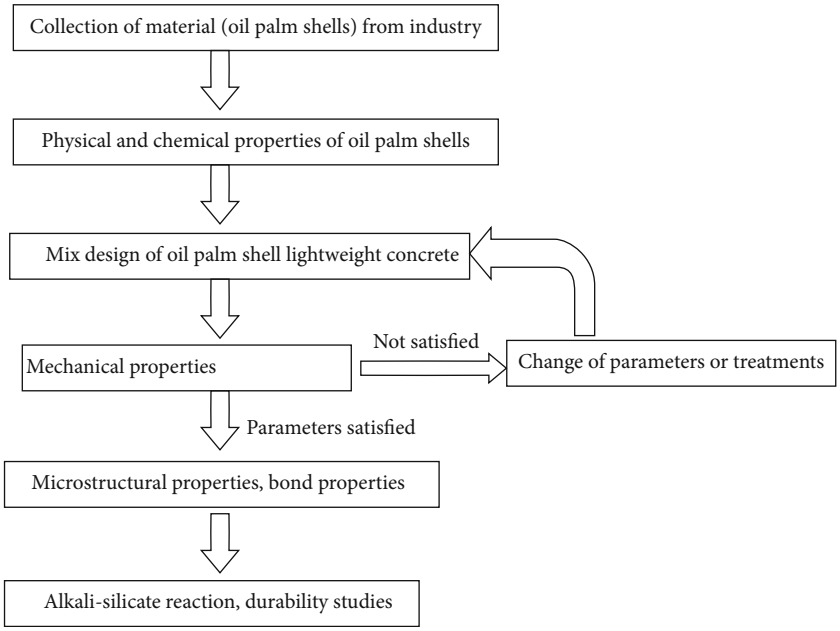

Figure 2: Block scheme diagram.

Table 2: Mix design for OPSC (oil palm shell concrete) and CC (conventional concrete).

Mix	Cement (kg)	Water (liter)	W/C (ratio)	Sand (kg)	Coarse aggregate		Slump (mm)	Density (kg/m^3)
					OPS (kg)	Gravel (kg)		
OPSC	380	152	0.4	750	—	1080	60	2362
CC	480	192	0.4	715	382	—	95	1769

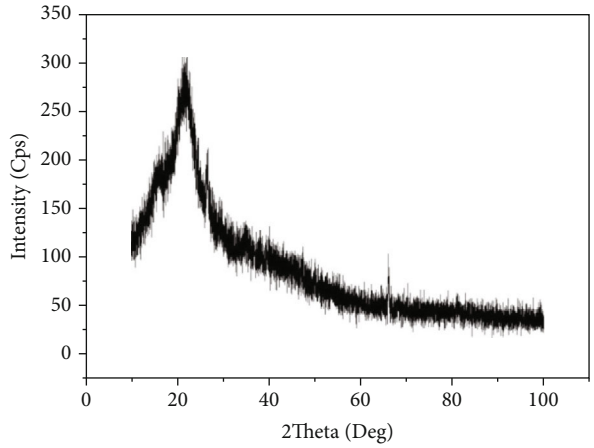

Figure 3: XRD analysis of OPS aggregate.

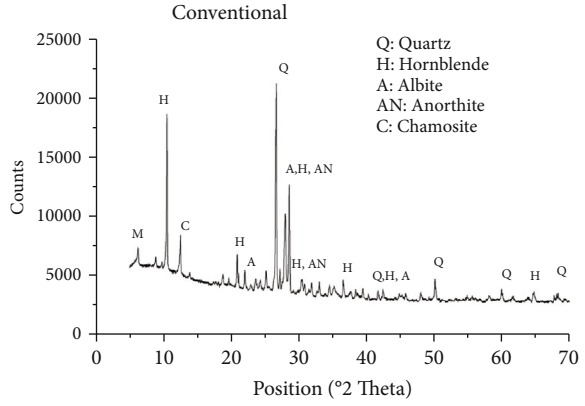

Figure 4: XRD analysis of conventional aggregate.

2.1. Experimental Procedure. Oil palm shells are prone to voids as these are from industrial waste toxic chemicals which are observed on the external part of the shells. For using these OPS as replacement of coarse aggregate in the concrete, it should be treated with water. A unique methodology is adopted in this research paper to use OPS as coarse aggregate in concrete. As shown in Figure 2, a stepwise procedure is conducted to make the OPS concrete strong, durable, and resistant to chemical attack. A special mix design is considered to make the OPS concrete as these absorb more amount of water as mentioned by Vandanapu and Krishnamurthy [12]. OPS aggregates are soaked in water and dried to room temperature. These have very less weight as compared to conventional aggregate as their specific gravity is 1.2. The quantity of aggregates used in OPS concrete is more compared to conventional aggregate.

The concrete made with OPS is dried in room and even in oven temperature to make the concrete completely dry by 28 days. The dried concrete is taken for testing. Once the test results are satisfied, remaining samples were tested under durability aspect. If the results for the above concrete are

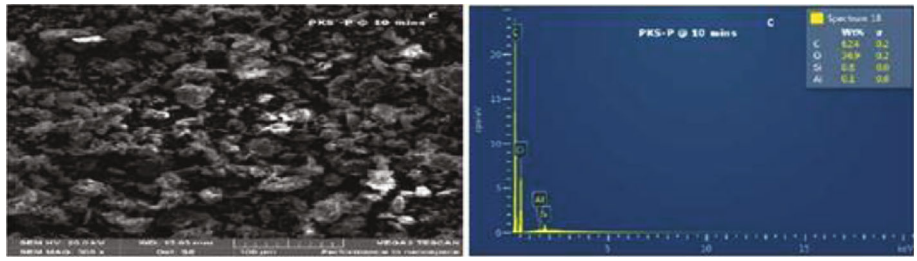

Figure 5: EDX analysis of nanocoated OPS aggregate powder.

not satisfied, reconsideration of mix design and well as special treatments is done accordingly.

Conventional concrete (CC) with natural aggregates is made with water/cement ratio of 0.35. Conventional concrete cubes and cylinders are casted and cured for 28 days. Cured concrete is tested under a compressive testing machine to know the mechanical behavior of concrete. Measured mechanical properties are compared with those of OPS concrete.

Concrete made with OPS is surface dried and examined for surface texture. There is uneven texture of OPS concrete; this is due to the more water absorption of OPS as their internal structure is completely with pores as mentioned by Shafigh et al. [13]. The OPS concrete seen in Figure 2 is leached, and shells are coming out forming the edges. When the concrete is demolded after 28 days of curing, the edges of the OPS concrete are collapsed and the internal structure of the concrete is somewhat wet. As the OPS concrete is tested under UTM capacity of 200 kN, the maximum compressive strength of the concrete is around 15 MPa [14]. This shows how the concrete is poor in compression as compared to conventional concrete.

Variety in concrete substance for OPSC and CC can be seen in Table 2. The same water/concrete proportion is utilized for making OPSC and CC. Expansion in concrete substance in LWC is because of the raised state of the oil palm shells which required greater amount of glue stage to fill the holes in the substantial. So the concrete amount is more when contrasted with ordinary cement [15]. Droop worth of OPSC is 95 mm though in CC it is 60 mm. Varieties in droop esteem are because of the thickness of the substantial and framework content. Thickness of lightweight cement is 28% less when contrasted with ordinary cement.

3. Results and Discussions

3.1. XRD Analysis. Mineralogical properties are carried out for OPS to examine the internal structure. This method is taken into consideration to understand the behavior of the OPS aggregate, as the OPS concrete is shown to have less compressive strength than the ordinary concrete [16]. Examination of OPS is only done because the unknown constituents of the OPS concrete are OPS, as the remaining constituents of the concrete are known and examined by many researchers worldwide [17].

Figure 3 shows the XRD analysis of OPS aggregate; the figure clearly shows the amorphous behavior of aggregate, like glassy structure. This kind of amorphous behavior

Figure 6: Internal structure of nanocoated OPS concrete.

makes the aggregate break easily under compression. The intensity peaks of OPS are only observed in 21.3 2θ angle which represents silicon dioxide. One more peak is observed around 69 2θ angles which represent iron oxide in XRD analysis of OPS aggregate [18]. This results in poor workability and leads to less compressive strength. These peaks in OPS are not crystalline as conventional concrete. Figure 4 shows the XRD analysis of conventional concrete. Several peaks are observed in XRD analysis of conventional concrete; these peaks show different mineralogical properties of conventional aggregate [11]. This type of crystalline peaks leads to higher compressive strength and more durable to environment.

3.2. Nanocoated OPS EDX Analysis. Nanocoating is sprayed on the surface of the OPS aggregate to fill the pores on the surface of the aggregate. Choosing of the nanocoating is finalized after many coatings are made with wax, sintering and applying filler coat on the surface of the OPS aggregate. The aggregates are coated with nanoorganosilane compound which fills the surface aggregate pores and makes proper bonding with cement matrix. This coating is spared at 1 : 10 nanosealer-to-water ratio and evenly sprayed on the surface of the aggregate [19]. These aggregates are dried in room temperature for 24 h and oven dried for 8 h. Nanocoated OPS are examined under EDX analysis, and mineralogical properties are taken out. Figure 5 shows the OPS shell as well as OPS powder, and crystal peaks that formed are observed which represent the elements of conventional aggregate. Carbon, oxygen, calcium, potassium, iron, and magnesium and some other elements are observed in the OPS EDX peak [20].

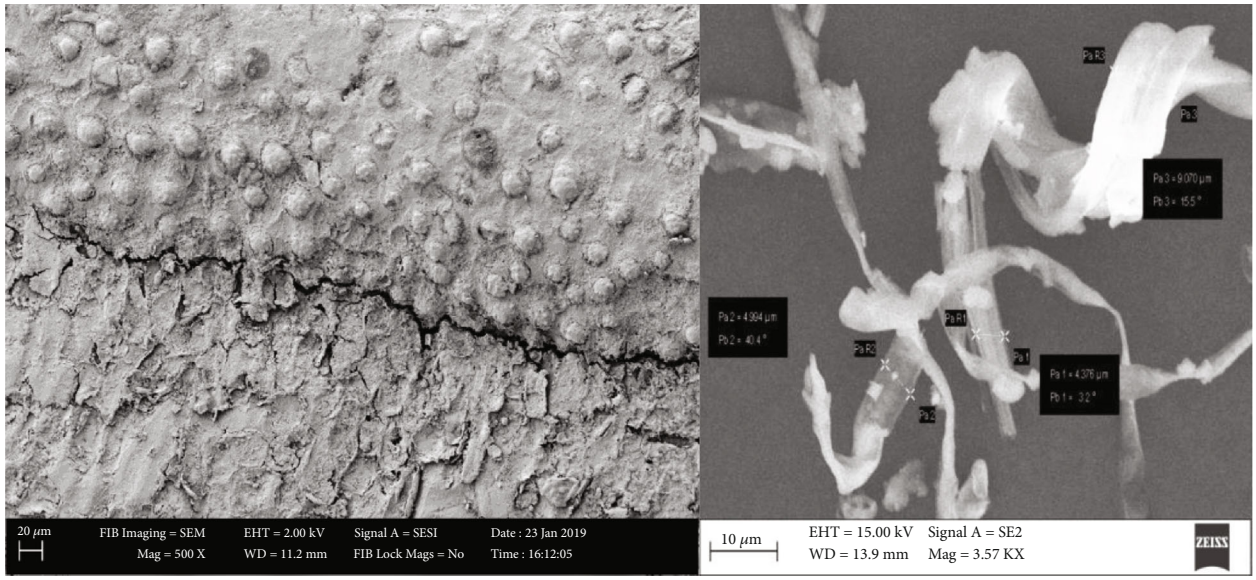

Figure 7: Nanocoated OPS aggregate and size of the OPS fiber.

3.3. Microstructural Analysis of Nanocoated OPS Aggregate and OPS Powder. Observation of the microstructural properties of nanocoated OPS aggregate is carried out to examine the internal bonding between aggregate to the cement paste. Bonding is the major criterion for the concrete to be strong. Scanning electron microscope (SEM) examination has shown the morphology of nanocoated OPS aggregates: conventional concrete with ITZ thickness less than 400 μm, nontreated OPS concrete with ITZ thickness more than 600 μm, and treated OPS concrete with ITZ thickness of maximum 400 μm. Operation aggregates are analyzed with SEM gear under electron high pressure of 300 V to 30 kV at the profundity of 4 to 30 mm [21]. SEM examination of nanocoated OPS totally uncovers the interior design with permeable and heterogeneous construction as displayed in Figure 6. Inward construction is for the most part permeable and has a pore size of 0.5 to 15 micrometers. This offers admittance to the inward surface of the particles to burn-through more water [22].

Microstructural analysis of OPS after coating with nanosiliceous material is shown in Figure 7. This shows that the pores on the surface of the OPS are filled with nanocoatings as shown in Figure 7. Micropores are filled with nanocoating; these pores have a size of 10 micrometers to 12 micrometers. Filled pores are seen on top of the OPS aggregate with bubbles. This improves the bonding between OPS and cement paste. This shows improvement in the interfacial transition zone of the nanocoated OPS concrete [23].

Water absorption of nanocoated oil palm shells is 25% whereas it is 5% for conventional aggregate. The binder is not sufficient to mix with concrete due to higher absorption rate in OPS aggregate. Aggregate impact value of OPS aggregate is not in the range of standards for making the concrete. XRD analysis of OPS aggregate shows a lower percentage of Al_2O_3 as compared to conventional aggregate. Al_2O_3 is a hard material composition which is responsible for the strength of the aggregate and also for aggregate impact value [24]. SEM images of OPS aggregate show the pore diameter of 0.5-15 micrometers whereas conventional aggregate has a pore diameter of 2-5 micrometers.

Table 3: Compressive strength of concrete.

Concrete type	W/C ratio	Compressive strength (MPa)		
		7	14	28
OPS concrete	0.50	7.4	8.7	10.4
	0.55	8.6	9.5	11.6
	0.60	9.7	11.4	13.7
Nanocoated OPS concrete	0.32	16.8	18.1	24.6
	0.38	17.1	22.2	2543
	0.42	15.8	23.4	28.6
Conventional concrete	0.30	15.6	24.3	28.1
	0.42	16.8	24.6	26.6
	0.47	17.5	24.2	28.7

Table 3 shows the mechanical behavior of nanocoated OPS concrete, conventional concrete, and OPS concrete. In conventional concrete, the compressive strength for 28 days is 27 MPa. The compressive strength for nanocoated OPS concrete is 26.7 MPa whereas OPS have a maximum compressive strength of 12.6 MPa. This shows improvement in OPS lightweight concrete after the coating with nanosilane coating. This coating improved the bonding between the OPS aggregate and the cement paste, so there is higher compressive strength noted in coated OPS concrete than in non-coated OPS concrete [25].

3.4. Alkali-Silicate Reaction for Nanocoated OPS Concrete. Materials which are under the effect of environment are exposed to different chemicals; in this, one of the most reacted chemicals in concrete is reactive silica. This reactive silica cracks the concrete due to thermal stresses due to

Figure 8: Alkali-silicate reaction of nanocoated OPS concrete.

Table 4: Expansion of nanocoated OPS concrete samples.

Sample	Aggregate	Expansion after 90 days (mm)
A1	OPS coarse	0.0415
A2	OPS coarse	0.0435
A3	OPS coarse	0.0442
B1	OPS fine	0.031
B2	OPS fine	0.035
B3	OPS fine	0.0325

increase in pH value [26]. This causes expansion of concrete which leads to cracking. As OPS are exposed to environment for years, checking of OPS concrete under alkali-silicate reaction is a must. For motor bars, $200 * 10 * 10$ mm bars are made, and for prism bars, $100 * 100 * 500$ mm bars are made to examine the expansion of concrete under alkali-silicate reaction. As shown in Figure 8, samples are casted and demolded and tested in an expansion bar gauge to understand the reaction in the concrete.

Table 4 shows the expansion of coated OPS aggregate concrete under alkali-silicate reaction. This concrete made with coated OPS is immersed in NaoH solution for 28 days and 90 days to observe the reaction that happens in the concrete [27]. 90-day expansion of nanocoated OPS concrete is 0.04 to 0.03 mm which represents lower expansion rate in the concrete. This expansion of concrete is in ASTM limit; hence, this type of concrete and coatings is recommended to replace the conventional concrete with OPS lightweight concrete.

4. Conclusions

(i) OPS have higher pore size than the conventional aggregate. These pores are of size 10-15 micrometers

(ii) Concrete made with OPS shows lower mechanical behavior than the conventional concrete; this is due to the higher water absorption in OPS concrete

(iii) OPS are treated with nanosilane coating to fill the pores on the surface of the aggregate as well as to maintain the higher bonding between aggregate and cement paste

(iv) Interfacial transition zone shows fewer gaps between the coated OPS aggregate and the cement phase; this shows the bonding between the constituents of the concrete is higher than the nontreated OPS concrete

(v) Mechanical behavior of coated OPS shows 28 MPa compressive strength and 15 MPa in normal OPS concrete

(vi) EDX analysis shows mineralogical properties of coated OPS aggregate with elements in it, whereas not coated OPS shows amorphous peaks which represent crystal behavior

(vii) Alkali-silicate reaction for coated OPS shows much more protection than conventional concrete as the expansion of concrete is below the limit, and hence, coated OPS shows better performance than the conventional concrete

Data Availability

The data used to support the findings of this study are included in the article. Should further data or information be required, these are available from the corresponding author upon request.

Disclosure

The research was performed as part of the authors' employment in Mettu University, Ethiopia.

Conflicts of Interest

The authors declare that there are no conflicts of interest regarding the publication of this paper.

Acknowledgments

The authors thank Aditya College of Engineering, Andhra Pradesh, and Saveetha School of Engineering, SIMATS, Chennai, for the technical assistance. The authors appreciate the supports from Mettu University, Ethiopia.

References

[1] M. Aslam, P. Sha, and M. Zamin, "Oil-palm by-products as lightweight aggregate in concrete mixture: a review," *Journal of Cleaner Production*, vol. 126, pp. 56–73, 2016.

[2] M. Aslam, P. Shafigh, M. Z. Jumaat, and M. Lachemi, "Benefits of using blended waste coarse lightweight aggregates in structural lightweight aggregate concrete," *Journal of Cleaner Production*, vol. 119, pp. 108–117, 2016.

[3] G. Batis, N. Kouloumbi, and P. Pantazopoulou, "Corrosion protection of steel in pumice lightweight mortar by coatings," *Cement and Concrete Composites*, vol. 27, no. 2, pp. 261–267, 2005.

[4] C. O. Edmund, M. S. Christopher, and D. K. Pascal, "Characterization of palm kernel shell for materials reinforcement and water treatment," *Journal of Chemical Engineering and Materials Science*, vol. 5, no. 1, pp. 1–6, 2014.

[5] M. Z. Jumaat, U. J. Alengaram, R. Ahmmad, S. Bahri, and A. B. M. S. Islam, "Characteristics of palm oil clinker as replacement for oil palm shell in lightweight concrete subjected to elevated temperature," *Construction and Building Materials*, vol. 101, pp. 942–951, 2015.

[6] E. Khankhaje, M. R. Salim, J. Mirza, M. W. Hussin, and M. Rafieizonooz, "Properties of sustainable lightweight pervious concrete containing oil palm kernel shell as coarse aggregate," *Construction and Building Materials*, vol. 126, pp. 1054–1065, 2016.

[7] K. H. Mo, U. J. Alengaram, and M. Z. Jumaat, "Bond properties of lightweight concrete - A review," *Construction and Building Materials*, vol. 112, pp. 478–496, 2016.

[8] A. Ben Nakhi and J. M. Alhumoud, "Effects of recycled aggregate on concrete mix and exposure to chloride," *Advances in Materials Science and Engineering*, vol. 2019, Article ID 7605098, 7 pages, 2019.

[9] V. Swamy Nadh and K. Muthumani, "Critical review on structural light weight concrete," *International Journal of Civil Engineering and Technology*, vol. 8, no. 2, pp. 111–127, 2017.

[10] P. Shafigh, H. B. Mahmud, M. Z. B. Jumaat, R. Ahmmad, and S. Bahri, "Structural lightweight aggregate concrete using two types of waste from the palm oil industry as aggregate," *Journal of Cleaner Production*, vol. 80, pp. 187–196, 2014.

[11] J. Baalamurugan, V. G. Kumar, S. Chandrasekaran et al., "Recycling of steel slag aggregates for the development of high density concrete: alternative & environment-friendly radiation shielding composite," *Composites Part B: Engineering*, vol. 216, article 108885, 2021.

[12] S. N. Vandanapu and M. Krishnamurthy, "Seismic performance of lightweight concrete structures," *Advances in Civil Engineering*, vol. 2018, 6 pages, 2018.

[13] P. Shafigh, M. Z. Jumaat, H. B. Mahmud, and U. J. Alengaram, "A new method of producing high strength oil palm shell lightweight concrete," *Materials and Design*, vol. 32, no. 10, pp. 4839–4843, 2014.

[14] J. W. Bang, G. Ganesh Prabhu, Y. I. Jang, and Y. Y. Kim, "Development of ecoefficient engineered cementitious composites using supplementary cementitious materials as a binder and bottom ash aggregate as fine aggregate," *International Journal of Polymer Science*, vol. 2015, Article ID 681051, 12 pages, 2015.

[15] S. Nassiri, Z. Chen, G. Jian et al., "Comparison of unique effects of two contrasting types of cellulose nanomaterials on setting time, rheology, and compressive strength of cement paste," *Cement and Concrete Composites*, vol. 123, article 104201, 2021.

[16] D. C. L. Teo, M. A. A. Mannan, V. J. Kurian, and C. Ganapathy, "Lightweight concrete made from oil palm shell (OPS): structural bond and durability properties," *Building and Environment*, vol. 42, pp. 2614–2621, 2017.

[17] V. Swamynadh and K. Muthumani, "Properties of structural lightweight concrete containing treated oil palm shell as coarse aggregate," *Asian Journal of Civil Engineering*, vol. 19, no. 6, pp. 673–678, 2018.

[18] D. C. L. Teo, M. A. Mannan, and J. V. Kurian, "Flexural behaviour of reinforced lightweight concrete beams made with oil palm shell (OPS)," *Journal of Advanced Concrete Technology*, vol. 4, no. 3, pp. 459–468, 2006.

[19] S. Seal, A. Jeyaranjan, C. J. Neal, U. Kumar, T. S. Sakthivel, and D. C. Sayle, "Engineered defects in cerium oxides: tuning chemical reactivity for biomedical, environmental, & energy applications," *Nanoscale*, vol. 12, no. 13, pp. 6879–6899, 2020.

[20] J. E. Rossen and K. L. Scrivener, "Optimization of SEM-EDS to determine the C-A-S-H composition in matured cement paste samples," *Materials Characterization*, vol. 123, pp. 294–306, 2017.

[21] B. Zhang and C. S. Poon, "Sound insulation properties of rubberized lightweight aggregate concrete," *Journal of Cleaner Production*, vol. 172, pp. 3176–3185, 2018.

[22] Y. Wu, Z. Liu, and F. Ran, "New comprehensions on structure superiority of asymmetric carbon membrane and controlled construction of advanced hierarchical inner-structure for high performance supercapacitors," *Microporous and Mesoporous Materials*, vol. 275, pp. 14–25, 2019.

[23] M. Y. J. Liu, U. J. Alengaram, M. Santhanam, M. Z. Jumaat, and K. H. Mo, "Microstructural investigations of palm oil fuel ash and fly ash based binders in lightweight aggregate foamed geopolymer concrete," *Construction and Building Materials*, vol. 120, pp. 112–122, 2016.

[24] K. Hemalatha, C. James, L. Natrayan, and V. Swamynadh, "Analysis of RCC T-beam and prestressed concrete box girder bridges super structure under different span conditions," *Materials Today: Proceedings*, vol. 37, no. 2, pp. 1507–1516, 2021.

[25] X. Ping and J. J. Beaudoin, "Modification of transition zone microstructure –silica fume coating of aggregate surfaces," *Cement and Concrete Research*, vol. 22, no. 4, pp. 597–604, 1992.

[26] S. Multon, A. Sellier, and M. Cyr, "Chemo-mechanical modeling for prediction of alkali silica reaction (ASR) expansion," *Cement and Concrete Research*, vol. 39, no. 6, pp. 490–500, 2009.

[27] A. A. Patil, H. S. Chore, and P. A. Dodeb, "Effect of curing condition on strength of geopolymer concrete," *Advances in Concrete Construction*, vol. 2, no. 1, pp. 29–37, 2014.

Hindawi
Journal of Nanomaterials
Volume 2021, Article ID 7133154, 10 pages
https://doi.org/10.1155/2021/7133154

Research Article

Synthesis of Cellulose Nanocrystals (CNCs) from Brewer's Spent Grain Using Acid Hydrolysis: Characterization and Optimization

Bisrat Yihun Matebie,[1] Belachew Zegale Tizazu,[1] Aseel A. Kadhem,[2] and S. Venkatesa Prabhu[1]

[1]*Department of Chemical Engineering, Addis Ababa Science and Technology University, 16417 Addis Ababa, Ethiopia*
[2]*Ministry of Education, Wasit Education Directorate, Wasit Governorate, Kut City, Iraq*

Correspondence should be addressed to Belachew Zegale Tizazu; belachew.zegale@aastu.edu.et

Received 30 July 2021; Accepted 3 September 2021; Published 26 September 2021

Academic Editor: Lakshmipathy R

Copyright © 2021 Bisrat Yihun Matebie et al. This is an open access article distributed under the Creative Commons Attribution License, which permits unrestricted use, distribution, and reproduction in any medium, provided the original work is properly cited.

This study is aimed at utilizing brewery's spent grain (BSG) byproduct for the synthesis of cellulose nanocrystals (CNCs) using acid hydrolysis and optimizing the hydrolysis parameters (hydrolysis time, temperature, liquid-solid ratio, and acid concentration). Alkali and bleaching treatment were done to remove hemicellulose and lignin from BSG. Optimization process was performed using central composite design (CCD) to obtain optimum value of cellulose nanocrystal (CNC) yield. The maximum cellulose nanocrystal (CNC) yield of 43.24% was obtained at optimum hydrolysis conditions of 50°C, 51 wt% acid concentration, 41 min, and liquid-solid ratio of 19 ml/g. The raw brewery spent grain; alkali-treated fiber, bleached fiber, and obtained CNC were characterized using scanning electron microscopy (SEM), XRD, particle analyzer, FTIR, and differential scanning calorimeter (DSC). The characterization results indicated that the obtained cellulose nanocrystal (CNC) has rod-like whisker shape with crystallinity of 76.3% and an average particle size of 309.4 nm.

1. Introduction

Currently, cost minimization and environmental awareness issues become a common agenda for researchers [1]. Developing a new green material from renewable biomass is one of a promising ways to solve cost and environmental pollution-related issues. Renewable biomasses commonly have three parts which are cellulose, lignin, and hemicellulose [2]. Cellulose is the most abundantly existing biopolymer which mainly exists in plant cell wall, and it also found in animals such as tunicates, bacteria, sea mosses, and algae [3]. The estimated annual production of cellulose in the world is 1.5×10^{12} ton [1]. Even if cellulose is attractive due to its biodegradable, renewable, and nontoxic properties, it has a limitation towards its use in the area of various applications due to low strength, poor thermal stability, and high-water absorption properties [2].

Currently, nanotechnology is an interesting and promising area to improve the performance and application of cellulose by destroying the amorphous region and such kind of material called cellulose nanocrystals (CNCs) [4]. Different raw materials were used for isolation of nanocrystalline cellulose such as corn husk [5], rice straw [4], and bamboo pulp using acid hydrolysis [1]. For the present study, brewery spent grain (BSG) is a renewable biomass source for cellulose to extract cellulose nanocrystals using acid hydrolysis.

Brewery's spent grain (BSG) is a lignocellulosic residue produced from brewery industry [6]. Beer is the fifth most consumed beverage in the world behind tea, soft drinks, milk, and coffee with the annual world beer production of exceeding 1.34 billion hectoliters [7]. BSG is generated after the raw barley grain passes through the process of malting, mashing, fermentation, and filtration [8]. The common raw materials for brewery's spent grain include barley malt cereals, cereal straws of wheat, buckwheat, and rice [6]. The statistics of FAO shows that the world annual cropping of barely seed is 8.3 million metric tons in 2010 [9]. Barley brewery spent grain mainly composed of cellulose, hemicellulose, lignin,

protein, ash, and extractives [8]. Thus, barely BSG covers 85% of the total beer production byproducts [10]. BSG readily exists with high volume and low cost [11] and has a high potential for the isolation of cellulose for further synthesis of different derivatives such as carboxymethyl cellulose [12] and cellulose nanocomposites [13].

Nanocrystalline cellulose (cellulose nanocrystals) is renewable resource which has short rod like or whisker shape with the size of 2-100 nm diameter and 100-500 nm length with the composition of 100% cellulose in the crystalline region [14]. The world annual mass production of nanocellulose is increasing and estimated up to more than 9×10^3 tons of nanocellulose per year [15]. Currently, the researcher interest is growing up to produce nanocrystalline cellulose due to an excellent property such as better mechanical strength, high surface area and aspect ratio, nontoxicity, crystallinity, biocompatibility, and biodegradability. For this reason, it is a potential renewable green substrate for many applications ranging from medicinal use such as xylitol and pullulan production for dental caries and diabetes treatment [11] to producing of composite materials, food packaging, foams, aerogels, textile, oxygen-barrier layers, and optically transparent functional materials [1].

Different methods have been used to synthesize highly purified nanocrystals from cellulosic materials, including the chemical method, mainly carried out by acid hydrolysis [4], enzyme-assisted hydrolysis [15], and mechanical treatments, such as high-pressure homogenizing [16], grinding [17], and ultrasonication [3] as well as a combination of two or several of the abovementioned methods. In recent years, acid hydrolysis has become a promising method with nanotechnology to modify the physical and chemical properties of cellulose. Acid hydrolysis produces nanocrystalline cellulose by hydrolyzing the hydroxyl functional group of cellulose at specific parametric condition of temperature, time, and acid [18].

This study is aimed at isolating cellulose nanocrystals (CNCs) from a renewable, cheap, and currently underutilized raw material, i.e., barley brewery spent grain (BSG). BSG was pretreated using several mechanical and chemical processes, including grinding, sieving, alkali treatment, and bleaching. Cellulose nanocrystals (CNCs) were produced by sulfuric acid hydrolysis followed by ultrasonication (SNC). The resulting CNC products were characterized by scanning electron microscopy (SEM), X-ray diffraction (XRD), Fourier-transform infrared spectroscopy (FTIR), particle size analyzer, and differential scanning calorimeter (DSC).

2. Materials and Methods

2.1. Materials. Brewery spent grain (BSG) was obtained from local Heineken brewery factory in Addis Ababa, Ethiopia. All analytical grade chemicals such as hydrogen peroxide (30%) for bleaching, sodium hydroxide (98%) for alkali treatment, and sulfuric acid (98%) for synthesis of cellulose nanocrystals were obtained from Himedia, India, and Merck, Germany.

2.2. Isolation of Cellulose from Brewery Spent Grain (BSG). Raw brewery spent grain was washed with distilled water successively and dried using air circulating oven (TD-1315) at 50°C for 12 hours. After drying its size, it was reduced to 0.5 mm using grinder. Oversize spent grain particle was then separated using sieve (500 μm mesh size) for further pretreatment processes such as acid, alkali, and bleaching treatments.

2.3. Acid and Alkali Treatments. The BSG was initially treated with 1.25% (wt/v) sulfuric acid, 120°C for 17 minutes at solid-liquid ratio of 1 : 10 (g : ml) to solubilize the hemicellulose. The acid-treated spent grain was dried using air circulating oven for 12 hours at 50°C. It was then milled using mortar pestle. Following acid treatment, the alkali treatment was employed two times to remove the hemicellulose completely. During alkali treatment, 2% sodium hydroxide with solid-liquid ratio of 1 : 20 (g : ml) was used. This mixture was heated using magnetic heater for 2 hr at 80°C. The mixture was successively washed with distilled water and separated using centrifuge at 4000 rpm to remove the black liquor and to achieve a neutral pH. It was then dried for 12 hours at 50°C in the oven to remove the moisture content [12, 19].

2.4. Bleaching Treatment. Bleaching treatment was done after alkali treatment to remove lignin and the remaining hemicellulose content of the brewery spent grain. The bleaching treatment was done in three steps: (1) 5% hydrogen per oxide and 0.07 M sodium hydroxide with equal parts (1 : 1) was mixed. The solid liquid ratio used during bleaching treatment was 1 : 30 (g : ml). This mixture was heated using magnetic stirrer heater for 40 min at 70°C. It was then successively washed with distilled water and separated using centrifuge at 4000 rpm until a neutral pH was obtained. (2) The above bleaching procedure was repeated. Subsequently, it was dried using oven for 18 hours at 50°C to remove the moisture. (3) 0.25 M sodium hydroxide, at a temperature of 70°C, was mixed with the pulp for one hour at the solid liquid ratio of 1 : 30 (g : ml). It was then repeatedly washed with distilled water and separated using centrifuge at 4000 rpm until a neutral pH was obtained. It was then dried using oven for 18 hours at 50°C to remove the moisture [19].

2.5. Synthesis of Cellulose Nanocrystals (CNCs). CNCs were synthesized from brewery spent grain fiber using acid hydrolysis based on the previous methods reported in the literature with some modification [20, 21]. The brewery spent grain samples were treated with 47, 51, and 55% (wt/v) sulfuric acid, at a temperature of 45, 50, and 55°C and treatment time of 35, 40, and 45 minutes at a solid-liquid ratio of 1 : 15, 1 : 20, and 1 : 25 (g : ml) into 200 ml beaker. The mixture was placed on magnetic stirrer (MS-H280-PRO) at 800 rpm to homogenize it. The hydrolysis reaction was ceased by placing the reaction mixture in an ice bath, and the excessive sulfuric acid was removed by successive distilled water washing and centrifugation (Pro-Analytical C2004) for 10 min at 4000 rpm. The successive centrifugation resulted colloidal suspension. This colloidal suspension

Table 1: Independent variables and levels used in the CCD for acid hydrolysis of BSG cellulose.

Variables	Coding	Unit	Levels		
			-1	0	1
Time	X1	Minute	35	40	45
Sulfuric acid concentration	X2	%	47	51	55
Temperature	X3	˚C	45	50	55
Liquid solid ratio	X4	ml/g	15	20	25

was neutralized using 0.5 N sodium hydroxide to achieve a neutral pH. Sonication was then performed at 60 W for 10 minutes to reduce the aggregation of nanoparticles. The suspension was dried using freeze dryer for two days.

2.6. Experimental Design. The central composite design (CCD) of response surface methodology was used to investigate the effect of and optimize the acid hydrolysis parameters on the yield of CNC production. The yield was investigated depending on four factors, i.e., the upper and lower levels of the parameters, viz., acid concentration, hydrolysis time, temperature, and liquid-solid ratio, were fixed following a preliminary experiment conducted one variable at a time (OVAT) for each parameter as shown in Table 1. Three-level-four-factor central composite design (CCD) was used for optimizing the factors and the response of the experiment in which 26 runs were conducted. After those 26 experiments were conducted, the Design-Expert Software 12.0.0 was used to statistically analyze the data and obtain suitable equation for synthesis of cellulose nanocrystals using acid hydrolysis.

2.7. Analytical Methods

2.7.1. Scanning Electron Microscopy (SEM) Analysis. SEM (FEI INSPECTF50) was used to determine the surface morphology of untreated, alkali treated, bleached BSG, and isolated CNC with an accelerating voltage of 10 kV. Those samples were prepared in dried form and scanned the surfaces with a focus beam of electrons. The samples were placed on black carbon tape, and the image was captured with various magnification level and working distance.

2.7.2. Fourier-Transform Infrared Spectroscopy (FTIR). FTIR (iS50ABX) was used for determination of change in the chemical functional group. FTIR spectra of raw BSG, alkali-treated fiber, bleached fiber, and CNC samples were recorded with range of 400 to 4000 cm^{-1} with 32 resolution. The samples were prepared in powder form for analysis. Then, the prepared samples were pressed into a pellet and analyzed in spectral region.

2.7.3. X-Ray Diffraction (XRD). XRD (BTX-528) was used for the determination of sample crystallinity (which shows cellulose amorphous region is hydrolyzed or not). The samples were dried using oven for 24 h at 50˚C to remove the moisture content completely. After this, the dried samples were prepared in powder form and scanned in 2θ using XRD by varying the range from 5 to 60˚ and operated at an acceleration voltage of 40 kV, using Cu Kα radiation. The crystallinity index can be determined using Equation (1):

$$\%\text{crystallinity}(\text{CI}) = \frac{\text{Area of crystalline peaks}}{\text{Total area of peaks}} \times 100. \quad (1)$$

Crystalline size can be determined using Scherrer equation as follows:

$$D = \frac{\kappa\lambda}{d\cos\theta}, \quad (2)$$

where D is crystalline size, λ is constant radiation with value of 0.154060 nm, k is crystallite shape factor, d is FWHM, and θ is angle (in radian).

2.7.4. Differential Scanning Calorimeter (DSC). The thermal behavior of raw cellulose and extracted cellulose nanocrystals were analyzed using differential scanning calorimeter (SKZ1052B). During measurement, 20 mg of each sample was prepared for analysis. The weighed sample was placed

Table 2: RSM-CCD experimental design matrix and response data.

Std	Run	Time (min)	Temperature (˚C)	Sulfuric acid (wt%)	Liquid-solid ratio (ml/g)	Yield (%)
21	1	40	50	47	20	41.61
19	2	40	45	51	20	41.77
11	3	35	55	47	25	37.89
14	4	45	45	55	25	36.78
9	5	35	45	47	25	36.18
4	6	45	55	47	15	37.83
2	7	45	45	47	15	35.31
25	8	40	50	51	20	43.02
13	9	35	45	55	25	38.34
12	10	45	55	47	25	38.51
24	11	40	50	51	25	42.79
10	12	45	45	47	25	36.91
22	13	40	50	55	20	42.33
8	14	45	55	55	15	36.96
3	15	35	55	47	15	35.73
5	16	35	45	55	15	36.61
7	17	35	55	55	15	36.74
26	18	40	50	51	20	42.95
16	19	45	55	55	25	37.74
18	20	45	50	51	20	41.55
17	21	35	50	51	20	41.14
20	22	40	55	51	20	42.46
6	23	45	45	55	15	37.42
15	24	35	55	55	25	37.58
1	25	35	45	47	15	34.42
23	26	40	50	51	15	42.46

Table 3: ANOVA for quadratic regression model.

Source	SS	DF	MS	*F* value	*P* value	
Model	191.58	14	13.68	75.17	<0.0001	Significant
A-X1	1.07	1	1.07	15.85	0.0340	
B-X2	3.29	1	3.29	18.09	0.0014	
C-X3	2.07	1	2.07	11.39	0.0062	
D-X4	4.74	1	4.74	26.05	0.0003	
AB	0.3108	1	0.3108	21.71	0.0180	
AC	1.39	1	1.39	17.62	0.0186	
AD	1.04	1	1.04	15.69	0.0362	
BC	3.30	1	3.30	18.14	0.0013	
BD	6.250*E*-06	1	6.250*E*-06	25.00	0.00954	
CD	0.7613	1	0.7613	14.18	0.0456	
A^2	13.55	1	13.55	74.42	<0.0001	
B^2	5.99	1	5.99	32.93	0.0001	
C^2	7.19	1	7.19	39.47	<0.0001	
D^2	2.66	1	2.66	14.64	0.0028	
Residual	2.00	11	0.1821			
Lack of fit	2.00	10	0.2000	81.64	0.0859	Not significant
Pure error	0.0025	1	0.0025			
Total	193.58	25				

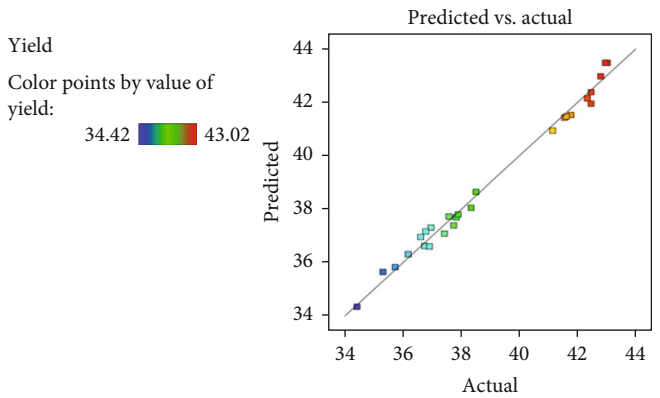

Figure 1: Experimental vs. predicted yield in the regression model.

in platinum crucible and heated from room temperature to 400°C for 40 minutes with a heating rate of 10°C min^{-1}.

2.7.5. Particle Size Analyzer. Malvern zetasizer nano (ZE3600) was used to measure the particle size distribution of obtained cellulose nanocrystals (CNCs). The sample was prepared by diluting the CNC suspension using distilled water, and size distribution measurement was performed at room temperature, and time taken for thermal equilibrium was 170 seconds. The measurements were conducted in triplicate.

3. Results and Discussion

3.1. Cellulose Nanocrystal (CNC) Yield Optimization Using Central Composite Design. Response surface methodology using central composite design was used to modeling, analysis, and optimizing the yield of CNC. RSM was used in the way of determining the level and optimum combination of the relevant factors which gives a desired cellulose nanocrystal yield. Multiple regression equation was performed to express the relationship between factors and performance measures. Each relevant factor (time, temperature, concentration, and liquid solid ratio) has been tested on three levels. The dependent variable used as response parameter was the cellulose nanocrystal yield. All experiment was carried out three times to minimize the experimental error. Synthesis yield of CNC was varied in the range of 34.42-43.02% as shown in Table 2.

The quadratic model was chosen from the several possible models of Design expert12 for the prediction of the given yield. The model equation that relates cellulose nanocrystal

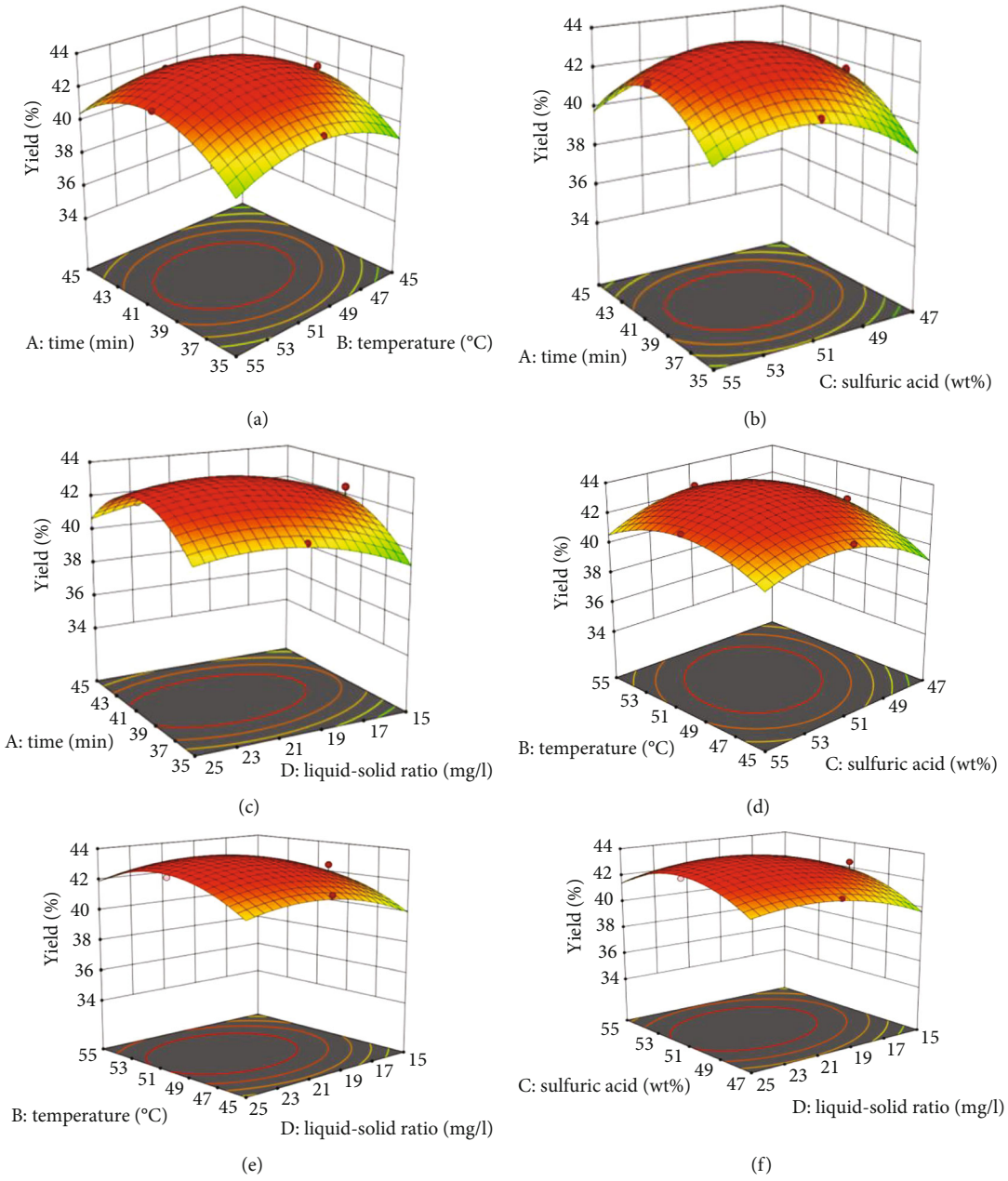

Figure 2: Response surface and contour plots showing interaction effect of parameters on CNC yield.

yield to the acid hydrolysis parameters in terms of coded factors is given in Equation (3). The equation is significant for predicting the given yield and effect of each parameter.

$$\begin{aligned}\text{Yield}(\%) = {} & +43.48 + 0.2433A + 0.4278B + 0.3394C \\ & + 0.5133D + 0.1394AB - 0.2944AC - 0.2544AD \\ & - 0.4544BC + 0.0006BD - 0.2181CD - 2.30A^2 \\ & - 1.53B^2 - 1.67C^2 - 1.02D^2. \end{aligned} \quad (3)$$

Parameters having positive coefficient values increase CNC yield whereas parameters with negative coefficient values decrease CNC yield. Results of analysis of variance (ANOVA) are given in Table 3. The P value less than 0.0500 indicates the model terms are significant. In this case, A, B, C, D, AC, AD, BC, A^2, B^2, C^2, and D^2 are significant model terms. This implies that hydrolysis time, temperature, sulfuric acid concentration, liquid solid ratio, interaction between hydrolysis time and sulfuric acid concentration, interaction between hydrolysis time and liquid solid ratio, and interaction between temperature and sulfuric acid concentration are significant parameters for yield of cellulose nanocrystals produced from BSG. It was observed in Figure 1 that all points are much closed to the line of perfect fit which indicates that the actual and predicted values have closer value.

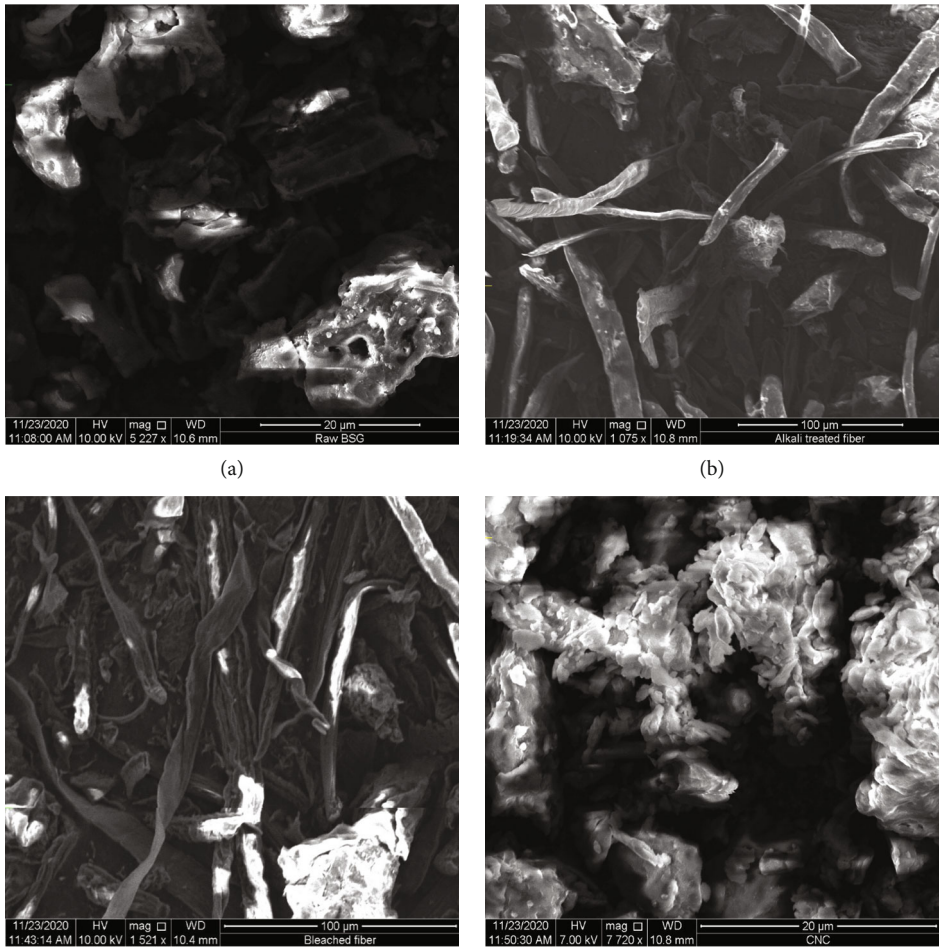

Figure 3: SEM image of (a) BSG fiber, (b) alkali-treated fiber, (c) bleached fiber, and (d) extracted CNCs.

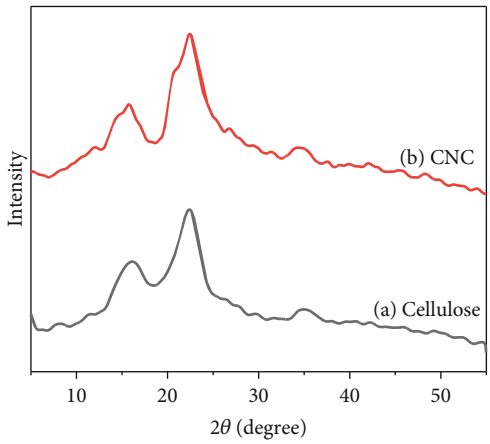

Figure 4: X-ray diffraction (XRD) pattern of (a) raw cellulose and (b) CNCs obtained from BSG.

The significant of the regression model with correlation coefficient was determined by depending on R-square, adjusted R-square, and predicted R-square which have a value of 0.9897, 0.9765, and 0.9399, respectively. The quality of the model developed could be evaluated from their coefficient of relationship. The value shows that the predicted R-square of 0.9399 is in reasonable agreement with the adjusted R-square of 0.9765, i.e., the difference is less than 0.2. The 0.9897 value of R-square shows that 98.97% of total variation in the percentage of yield of cellulose nanocrystals is attributed to experimental variables studied. As the value of R-square is close to unity, the stronger the model predicts the response better. The "Adeq precision" measures the signal to noise ratio. A ratio greater than 4 is desirable. The value of "Adeq precision" for the developed correlation 28.1722 indicates an adequate signal. Thus, the model can be used to navigate the design space.

Cellulose nanocrystal preparation is affected by many parameters starting from sample preparation to bleaching process; the acid hydrolysis process has more relation with independent parameters. Response surface plot and contour plot are the best way to the effect of parameters on the yield of cellulose nanocrystals. In this study, response surface and contour plot were developed using the Design-Expert 12.0.0 software. These plots showed the interaction effect of two parameters on CNC yield by keeping other parameters constant at their middle levels. Circular and elliptical contour

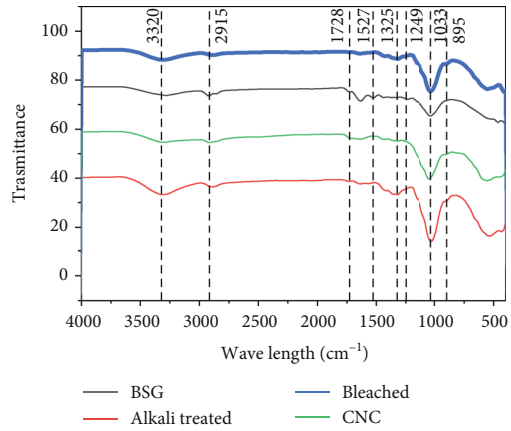

Figure 5: FTIR spectra of raw BSG, alkali-treated fiber, bleached fiber, and CNC.

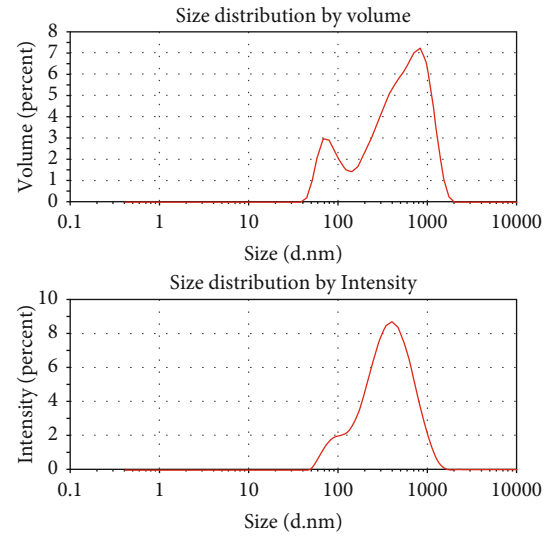

Figure 6: Particle size distribution by volume and intensity.

plot shows whether the interaction of parameters is significant or not, which means that circular contour plot implies parameter interaction is insignificant whereas elliptical contour plot indicates parameter interaction is significant [22]. Figure 2(a) presents the interaction effect of hydrolysis time and temperature with acid concentration and liquid-solid ratio maintained constant at 51% (w/v) and 20 ml/g, respectively. Figure 2(b) also indicates the effect of time and acid concentration on CNC yield at a constant value of liquid solid ratio and temperature. It was observed that the CNC yield was changed, when the time changed from 35 to 40 minutes and acid concentration changed from 47 to 51% (w/v) and the yield of CNC reached higher value, while beyond 40 minutes of time and 51% (w/v) acid concentration, the yield of CNC was gradually decreased. This occurred due to the over degradation of cellulose in to undesired product at high acid concentration and longer hydrolysis time. Figure 2(c) presents the interaction effect of hydrolysis time and liquid-solid ratio with acid concentration and temperature maintained constant at 51% (w/v) and 50°C, respectively. Figure 2(d) shows the effect of temperature and acid concentration interaction at a fixed value of time and liquid-solid ratio. It was observed that yield of CNC increased as temperature and acid concentration increased from 45 to 50°C and 47 to 51%, respectively, while further increasing of both temperature and acid concentration, the value of CNC yield becomes decline due to over degradation of cellulose into undesired product at high temperature and acid concentration. Therefore, conducting many experiments at the center point gives optimum yield. Figure 2(e) indicates the effect of liquid-solid ratio and temperature on CNC yield with time and acid concentration kept constant at 40 min and 51% (w/v), while Figure 2(f) shows the effect of liquid-solid ratio and acid concentration interaction at a fixed value of 40 min of time and 50°C steady temperature. Generally, it can be understood that all four variables have important effect on CNC yield.

The optimization was carried out, and its objective was maximizing cellulose nanocrystal yield in a given design space and range of process parameters. Optimization of different combination of process variables was conducted depending on desirability (D). Numerical optimization and graphical optimization are most common ways for finding optimum response with optimum operating conditions. For this study, numerical optimization and the possible solution of numerical optimization with different interaction of parameters and corresponding desirability value (1.00) were selected. The desirability value helps to identify the maximum and stable response of the experiment. According to numerical optimization solution, the maximum cellulose nanocrystal yield of 43.244% was achieved at the interaction parameters of 41.07 min, 51.088°C, 50.566% (w/v) of acid concentration, and 18.794 ml/g liquid-solid ratio. Hong et al. [1] have isolated CNC from bamboo pulp at optimum parameters of 90 min, 60% (wt/v) acid concentration, 45°C, and 8 ml/g liquid-solid ratio and achieved 32.3% CNC yield. Our study indicates a better yield was achieved with minimum time and acid concentration relative to CNC yield reported in the previous work.

3.2. Scanning Electron Microscope (SEM) Analysis. The morphology of brewery spent grain, alkali-treated fiber, bleached fiber, and CNCs obtained were examined by SEM analysis as shown in Figure 3. Figures 3(a)–3(c) show the SEM micrograph of BSG fiber of untreated, alkali treated, and bleached, respectively. In Figure 3(a), the microstructure of BSG fiber could not be observed clearly. However, the alkali treated and bleached fibers (Figures 3(b) and 3(c)) of the microstructures of the fibers were separately seen. The reason for this was hemicellulose, lignin, and other impurities were successfully removed through chemical treatment. From the image of SEM analysis (Figure 3(d)), it was clearly shown that the microscale cellulose fiber of BSG was effectively reduced to nanoscale through acid hydrolysis and as observed from this image, the extracted cellulose nanocrystals (CNCs) have rod-like whisker-shaped cellulose nanostructure.

3.3. XRD Analysis. The overall crystalline structure of bleached BSG cellulose and extracted CNC samples were

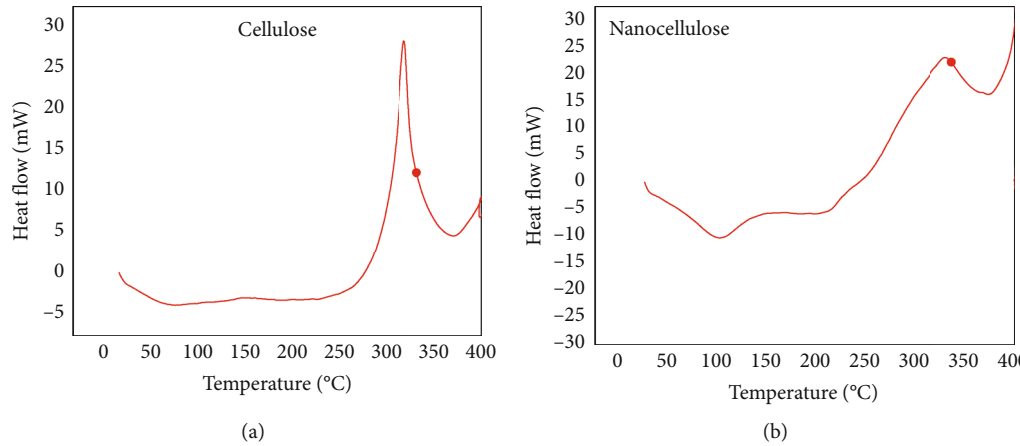

(a) (b)

Figure 7: DSC thermographs for (a) raw cellulose and (b) CNC.

determined by XRD measurement on BTX-528 model diffractometer as shown in Figure 4. The diffraction peak of raw cellulose is relatively broader extracted CNCs. However, the CNC peaks became sharper and narrower due to chemical treatment. According to this pattern, a strong peak appeared at $2\theta = 22.6$ degree was considered for the determination of crystallinity of raw cellulose and CNCs. The crystallinity index and crystal thickness of raw cellulose and CNCs were determined using Equations (1) and (2). The crystallinity of raw cellulose and extracted CNCs as determined by Equation (1) was 64.8% and 76.3%, respectively. The higher crystallinity value of CNCs compared to cellulose can be well understood by the reduction and removal of amorphous region of cellulose during acid hydrolysis. The crystal size of raw cellulose and obtained CNCs as determined by Equation (2) was 3.08 nm and 4.97 nm, respectively. In similar study conducted by Hemmati et al. [23], the crystallinity degree of raw cellulose obtained from cotton and resulting CNCs was 62% and 82%, respectively. Thus, the results of our study were in agreement with this study.

3.4. FTIR Analysis. FTIR analysis of raw BSG, alkali-treated fiber, bleached fiber, and CNCs is given in Figure 5. In the spectrum of all samples, there was a common peak at 3320 −3290 cm^{-1} which is related to OH stretching vibration of cellulose molecules [24]. Comparing the absorption position of bleached fiber and CNCs, the OH stretching vibration absorption band of CNCs moved toward a lower frequency and the absorption frequency was weakened, which shows that part of intermolecular hydrogen bonding was broken after acid treatment, while intermolecular hydrogen was enhanced. The peak appeared at 1728 cm^{-1} in the spectrum of untreated BSG attributed to either hemicellulose groups (acetyl and uronic ester group) or lignin groups (ester linkage of carboxylic group of the ferulic and p-coumeric acids). However, this peak almost missed in the spectrum of bleached fiber which shows the removal of lignin and hemicellulose components from BSG through chemical treatment. The peaks observed at 1249 cm^{-1} and 1527 cm^{-1} in the spectrum of BSG represent C-O-C (aryl-alkyl ether) and C=C aromatic rings of lignin, respectively. These two peaks also vanished after bleaching treatment, which indicates the removal of lignin component from BSG [12]. The peak observed in the spectrum of bleached fiber at 1325 cm^{-1} was attributed to S ring (CH_2 rocking at C_6 in cellulose). This peak almost disappeared in the spectrum of CNC, which indicates the developed hydrogen bonding network through acid hydrolysis in the crystalline structure of CNC decreased shocking movement of CH_2. A weak sulfur peak was observed at 1325 cm^{-1} in CNC, which did not appear in the spectra of BSG bleached fiber. The peaks at 1033 cm^{-1} are associated with the C-O stretching which is directly related to increase in the cellulosic component. The spectrum at 2915 cm^{-1} is associated to symmetric and antisymmetric stretching modes of C-H in methyl and methylene functional groups. The peak at 895 cm^{-1} is associated with the presence of typical structure of cellulose due to β-glycosidic linkage.

3.5. Particle Size Analysis. The particle size measurement was conducted at room temperature with a measurement position of 0.85 mm and count rate of 45.2 kcps. During particle size measurement, glass cuvette was used as cell and a time taken for thermal equilibrium was 170 seconds. It was observed that the average particle size of the obtained cellulose nanocrystals (CNCs) was 309.4 nm. Figure 6 depicts particle size distribution by volume and intensity of obtained CNC. As shown in Figure 6, the obtained cellulose nanocrystals (CNCs) did not present in a uniform size distribution because particles are fragmented during acid hydrolysis [23]. Size distribution by volume shows that CNC particle with smaller size of 86.3 nm is accountable for 26.7% of volume. In similar study, Lu and Hsieh [25] have isolated cellulose nanocrystals (CNCs) from rice husk with an average particle size of 700 nm. Brito et al. [26] have also isolated CNC from bamboo fiber with an average size of 130 nm. The slight difference might be due to variation in raw material used and hydrolysis conditions such as variation in time, temperature, acid type, and liquid-solid ratio.

3.6. Differential Scanning Calorimeter (DSC) Analysis. Figures 7(a) and 7(b) depict the thermal behavior of raw cellulose and extracted cellulose nanocrystals. As shown Figures 7(a)

and 7(b), the thermographs of an endothermic peak appeared from 28 to 150°C due to water evaporation [27]. The exothermic peaks appeared in the thermographs indicate the decomposition point of the raw cellulose and extracted CNC. The exothermic peak of decomposition of raw cellulose shows a sharp peak at 310°C, whereas the extracted CNCs show a sharp peak at 335°C. This indicates that the position of peaks increased after chemical treatment. Thus, the resulting CNCs have high thermal stability as compared to the raw cellulose due to acid hydrolysis treatment. The position of peaks mainly depends on the amount of amorphous present in a sample. As we can be observed from peak position of raw cellulose and CNCs, CNCs show higher peak position and this indicates that the amorphous part was removed and the crystallinity was enhanced through chemical treatment.

4. Conclusion

High value-added cellulose nanocrystals (CNCs) were successfully extracted from brewery spent grain using acid hydrolysis. The hydrolysis parameters time, temperature, acid concentration, and liquid-solid ratio were investigated to obtain the optimum conditions for the production of cellulose nanocrystals from brewery spent grain. Maximum CNC yield of 43.24% was obtained at optimum hydrolysis parameters of 41 min, 50°C, 51 wt% acid concentration, and liquid-solid ratio of 19 ml/g.

Characterization of samples was performed, and the result showed that the obtained cellulose nanocrystals have rod-like shape with an average diameter of 309.4 nm. The FTIR and diffraction scanning calorimeter (DSC) analysis indicated that noncellulosic components were successfully removed during pretreatment process, which resulted better thermal stability. The XRD study evidenced that the amorphous region of cellulose was reduced during acid hydrolysis, and the crystallinity was enhanced from 64.6% to 76.8%. Generally, this study suggested that brewery spent grain can be used as a feedstock for isolation of cellulose nanocrystals for various applications and a better way to minimize environmental effect of brewery spent grain.

Abbreviations

BSG: Brewery's spent grain
CCD: Central composite design
CI: Crystallinity index
CNCs: Cellulose nanocrystals
D: Crystallinity size
DSC: Diffraction scanning calorimeter
FAO: Food and Agriculture Organization
FTIR: Fourier-transform infrared spectroscopy
RSM: Response surface methodology
SEM: Scanning electron microscopy
XRD: X-ray diffraction.

Data Availability

All data are available in the manuscript, and further data availability is requested from the corresponding author.

Conflicts of Interest

Authors declare that they do not have any conflict of interest.

Acknowledgments

Authors would like to thank Addis Ababa Science and Technology University for allowing experimental set-up work and analytical instrument for characterization.

References

[1] B. Hong, F. Chen, and G. Xue, "Preparation and characterization of cellulose nanocrystals from bamboo pulp," *Cellulose Chemistry and Technology*, vol. 50, no. 2, pp. 225–231, 2016.

[2] M. T. Fath and H. Nasution, "Process optimization of manufacturing nanocrystalline cellulose from rattan biomass using sulfuric acid," in *AIP Conference Proceedings*, vol. 2024, 2018no. 1.

[3] Z. Chowdhury and S. B. A. Hamid, "Preparation and characterization of nanocrystalline cellulose using ultrasonication combined with a microwave-assisted pretreatment process," *BioResources*, vol. 11, no. 2, pp. 3397–3415, 2016.

[4] A. Musa, M. Ahmad, M. Z. Hussein, and S. M. Izham, "Acid hydrolysis-mediated preparation of nanocrystalline cellulose from rice straw," *International Journal of Nanomaterials, Nanotechnology and Nanomedicine*, vol. 3, no. 2, pp. 51–56, 2017.

[5] P. Kampeerapappun, "Extraction and characterization of cellulose nanocrystals from corn stover," *Journal of Metals, Materials and Minerals*, vol. 25, no. 1, pp. 19–26, 2015.

[6] S. I. Mussatto and M. Fernandes, "Lignin recovery from brewer's spent grain black liquor," *Carbohydrate Polymers*, vol. 70, no. 2, pp. 218–223, 2007.

[7] L. Fillaudeau, B.-A. Pascal, and G. Daufin, "Water, wastewater and waste management in brewing industries," *Journal of Cleaner Production*, vol. 14, no. 5, pp. 463–471, 2006.

[8] G. Z. Dehnavi, *Fractionation of the Main Components of Barley Spent Grains from a Microbrewery*, University of Borås, 2009.

[9] I. Shahabi-Ghahfarrokhi, F. Khodaiyan, M. Mousavi, and H. Yousefi, "Preparation and characterization of nanocellulose from beer industrial residues using acid hydrolysis/ultrasound," *Fibers and Polymers*, vol. 16, no. 3, pp. 529–536, 2015.

[10] D. Tang, G. Yin, Y.-Z. He et al., "Recovery of protein from brewer's spent grain by ultrafiltration," *Biochemical Engineering Journal*, vol. 48, no. 1, pp. 1–5, 2009.

[11] S. Aliyu and M. Bala, "Brewer' s spent grain : a review of its potentials and applications," *African Journal of Biotechnology*, vol. 10, no. 3, pp. 324–331, 2011.

[12] D. M. Santos, A. L. Bukzem, D. P. R. Ascheri, R. Signini, and G. L. B. Aquino, "Microwave-assisted carboxymethylation of cellulose extracted from brewer's spent grain," *Carbohydrate Polymers*, vol. 131, no. 2015, pp. 125–133, 2015.

[13] A. Sharma, M. Thakur, M. Bhattacharya, T. Mandal, and S. Goswami, "Commercial application of cellulose nanocomposites - A review," *Biotechnology Reports*, vol. 21, p. e00316, 2019.

[14] P. Phanthong, P. Reubroycharoen, X. Hao, G. Xu, A. Abudula, and G. Guan, "Nanocellulose: Extraction and application," *Carbon Resources Conversion*, vol. 1, no. 1, pp. 32–43, 2018.

[15] R. S. A. Ribeiro, B. C. Pohlmann, V. Calado, N. Bojorge, and N. Pereira Jr., "Production of nanocellulose by enzymatic hydrolysis : trends and challenges," *Engineering in Life Sciences*, vol. 19, no. 4, pp. 279–291, 2019.

[16] S. Ren, X. Sun, T. Lei, and Q. Wu, "The effect of chemical and high-pressure homogenization treatment conditions on the morphology of cellulose nanoparticles," *Journal of Nanomaterials*, vol. 2014, Article ID 582913, 11 pages, 2014.

[17] H. Xie, D. Haishun, X. Yang, and S. Chuanling, "Recent strategies in preparation of cellulose nanocrystals and cellulose nanofibrils derived from raw cellulose materials," *International Journal of Polymer Science*, vol. 2018, Article ID 7923068, 25 pages, 2018.

[18] M. Santos, J. J. Jiménez, B. Bartolomé, C. Gómez-Cordovés, and M. J. Del Nozal, "Variability of brewer's spent grain within a brewery," *Food Chemistry*, vol. 80, no. 1, pp. 17–21, 2003.

[19] S. I. Mussatto, G. J. M. Rocha, and I. C. Roberto, "Hydrogen peroxide bleaching of cellulose pulps obtained from brewer's spent grain," *Cellulose*, vol. 15, no. 4, pp. 641–649, 2008.

[20] I. K. Al-khateeb, S. M. Hussin, and Y. M. Al-obaidi, "Extraction of cellulose nano crystalline from cotton by ultrasonic and its morphological and structural characterization," *International Journal of Materials Chemistry and Physics*, vol. 1, no. 2, pp. 99–109, 2019.

[21] S. Maiti, J. Jayaramudu, K. Das et al., "Preparation and characterization of nano-cellulose with new shape from different precursor," *Carbohydrate Polymers*, vol. 98, no. 1, pp. 562–567, 2013.

[22] G. Kandhola, A. Djioleu, K. Rajan et al., "Maximizing production of cellulose nanocrystals and nanofibers from pre-extracted loblolly pine kraft pulp: a response surface approach," *Bioresources and Bioprocessing*, vol. 7, no. 1, 2020.

[23] F. Hemmati, S. M. Jafari, and R. A. Taheri, "Optimization of homogenization-sonication technique for the production of cellulose nanocrystals from cotton linter," *International Journal of Biological Macromolecules*, vol. 137, pp. 374–381, 2019.

[24] M. El Achaby, Z. Kassab, A. Aboulkas, C. Gaillard, and A. Barakat, "Reuse of red algae waste for the production of cellulose nanocrystals and its application in polymer nanocomposites," *International Journal of Biological Macromolecules*, vol. 106, pp. 681–691, 2018.

[25] P. Lu and Y.-L. Hsieh, "Preparation and characterization of cellulose nanocrystals from rice straw," *Carbohydrate Polymers*, vol. 87, no. 1, pp. 564–573, 2012.

[26] B. L. Brito, F. Pereira, J.-L. Putaux, and B. Jean, "Preparation, morphology and structure of cellulose nanocrystals from bamboo fibers," *Cellulose*, vol. 19, no. 5, pp. 1527–1536, 2012.

[27] J. Moran, V. Alvarez, V. Cyras, and A. Vazquez, "Extraction of cellulose and preparation of nanocellulose from sisal fibers," *Cellulose*, vol. 15, no. 1, pp. 149–159, 2008.

Hindawi
Journal of Nanomaterials
Volume 2021, Article ID 4401829, 11 pages
https://doi.org/10.1155/2021/4401829

Review Article

Review on Silver Nanoparticle Synthesis Method, Antibacterial Activity, Drug Delivery Vehicles, and Toxicity Pathways: Recent Advances and Future Aspects

D. Chandra Lekha,[1] R. Shanmugam,[2] K. Madhuri,[3] L. Priyanka Dwarampudi,[4] Mahendran Bhaskaran,[5] Deepak Kongara,[1] Jule Leta Tesfaye,[6,7] N. Nagaprasad,[8] V. L. Nirmal Bhargavi,[9] and Ramaswamy Krishnaraj[7,10]

[1]*Department of Pharmaceutical Analysis, Sree Vidyanikethan College of Pharmacy, Tirupati, Andhra Pradesh, India*
[2]*TIFAC, CORE-HD, Department of Pharmacognosy, JSS College of Pharmacy, JSS Academy of Higher Education & Research, Nilgiris, Ooty, Tamil Nadu, India*
[3]*Pacemach Tech Consultants, London, UK*
[4]*Department of Pharmacognosy, JSS College of Pharmacy, JSS Academy of Higher Education & Research, Nilgiris, Ooty, Tamil Nadu, India*
[5]*.Department of Pharmaceutical, JSS College of Pharmacy, JSS Academy of Higher Education & Research, Mysuru, Karnataka, India*
[6]*Department of Physics, College of Natural and Computational Science, Dambi Dollo University, Ethiopia*
[7]*Centre for Excellence-Indigenous Knowledge, Innovative Technology Transfer and Entrepreneurship, Dambi Dollo University, Ethiopia*
[8]*Department of Mechanical Engineering, ULTRA College of Engineering and Technology, Madurai, 625104 Tamilnadu, India*
[9]*Department of Chemistry, Sri Venkateswara College of Engineering and Technology, 517004, Chittoor, Andhra Pradesh, India*
[10]*Department of Mechanical Engineering, College of Engineering and Technology, Dambi Dollo University, Ethiopia*

Correspondence should be addressed to Ramaswamy Krishnaraj; prof.dr.krishnaraj@dadu.edu.et

Received 10 July 2021; Accepted 15 September 2021; Published 26 September 2021

Academic Editor: Lakshmipathy R

Copyright © 2021 D. Chandra Lekha et al. This is an open access article distributed under the Creative Commons Attribution License, which permits unrestricted use, distribution, and reproduction in any medium, provided the original work is properly cited.

Silver nanoparticles in the range from 1 to 100 nm are widely used in industrial applications as catalysis, electronics, and photonics, and they have unique properties such as optical, electrical, and magnetic characteristics that can be used as antimicrobial, biosensor textile, cosmetics, composite fibers, and electronic components and to amend shelf life of food substances. The main objective of the present review was to focus on formulation methods of silver nanoparticles with recent advances and future aspects. Silver nanoparticle shows very high potential towards biological applications. Several physicals, chemical, and various biological techniques have been employed to synthesize and stabilize silver nanoparticles. For the manufacture of silver nanoparticles, multiple methods, including chemical simplification with different natural and inorganic decreasing agents, physicochemical reduction, electrochemical procedures, and radiolysis, are employed. Silver nanoparticles are the single most manufacturer-identified material that can be used in all nanotechnology products. They can be used in food packing polymers to enhance the shelf lifespan. The present review is aimed at different types of synthesis and details of silver nanoparticles used as drug delivery vehicles, antibacterial activity, toxicity, recent advances, and future aspects.

1. Introduction

In nanotechnology, a nanospeck is defined as a small object or a speck that acts as a whole unit in terms of its conveyed properties. The physical and chemical properties of nanomaterials can alter from those of the same material in colossal bulk class; nanosubatomic particles have one attribute in the reach of 1 to 100 nm. These are utilized in nutrition handling, surgical, promotional material, wound dressing, computing devices, recollection implements, water purifiers, textiles, cosmetics, and contact lens. Silver nanoparticles are the unity most producer-identified material that can be used in all the nanotechnology products. They can be used in food packing polymers to enhance the shelf life of food [1]. Currently, silver nanoparticles (AgNPs) are the most widely used nanoparticles due to their broad antimicrobial activity. Not less than 383 out of 1628 nanotechnology products contain silver nanoparticles [2]. Silver nanoparticles are incorporated into milk to decrease microbial magnification [1]. When reacting with bacteria, silver nanoparticles adhere to both the cell wall and cell membrane and inhibit replication, leading to cell death. When silver dissolves in the cytosol, it ionizes to engender nanoparticles that increase the bactericidal activity [3]. Therefore, the design and development of superficial, one-step, reliable, low-cost, nontoxic, complex fibers, cryogenic superconducting materials, electronic components [4, 5], and ecocordial technique for prevarication multifunctional silver nanoparticles is the greatest consequentiality to expand their biomedical applications [3]. Silver nanoparticles show an incipient optical place, which is observed in bulk metals or molecules [6]. This review article focused in detail on various types of synthesis of silver nanoparticles, such as physical, chemical, and biological approaches. The article briefly discusses the antibacterial activity of silver nanoparticles, where silver acts as a toxic agent against microorganisms which showed good wound healing activity. This review also highlights silver nanoparticles used as drug delivery vehicles, toxicity pathways, recent advances, and future aspects of silver nanoparticles.

2. Review on Synthesis of Silver Nanoparticles

2.1. Physical Approach. Metal nanoparticles are generated physically by a desiccation condensate technique, which might be performed by using a vacuum tube shell at the force of the atmosphere per unit area. The source fabric, centered on a boat, is vaporized into the carrier gas. By using vaporization techniques, nanoparticles of diverse components like Ag, Gold, Pb, and fullerene have already been manufactured [7–9]. The production of tube furnaces by AgNP has some disadvantages; however, since tube ovens occupy a more extended area, they consume a lot of push while raising environmental temperatures from around. It will require a long time for the source material to achieve thermal stability. A standard tube oven needs over several kilowatts of energy and several 10 minutes of preheating to ensure a constant operating temperature. Silver nanoparticles were additionally generated with precision optical maser removal of metallic mass materials [10–12]. This approach can be used to manufacture pure colloids that will be underlying for further applications [13]. In essence, the physical synthesis of AgNP's customarily leverages the physical energies to create AgNP's with proximately restricted size distribution. The physical methodology may sanction significantly copious amounts of sampling of AgNP in one procedure, which is also the most excellent subsidiary method for producing AgNP powder. Nevertheless, primary expenditures for equipment investment should be taken into account.

2.2. Photochemical Approach. The synthetic strategy induced by exposure has also been established. Huang and coworkers generated AgNPs in multilayer synthetic clay suspensions using light reduction in AgNO3, which functions as a stabilizing agent to prevent nanoparticles from assembly. Irradiation dissolved AgNP into a short lifespan with a single-mode until the distribution was reasonably steady in size and diameter [14]. The limitation of this approach is the need for high-cost instruments and a laboratory environment.

2.3. Biological Approach. Biosynthetic approaches using natural reduction components, like polysaccharides, biological microorganisms, bacteria, funguses, plant extraction, and green chemistry, were recently developed as a feasible and straightforward alternative to more complicated synthetic chemistry processes. Bacteria could alternatively intracellularly or extracellularly generate inorganic compounds. This makes them possible biofabrics for nanoparticles such as gold and silver. Silver stands out categorically for its biotic qualities. Vilchis-Genus Nestor et al. employed green tea extract to reduce gold-silver nanoparticles in an aqueous solution under environmental conditions as a stabilizing agent [15]. The AgNPs generated are pretty stable, and this process benefits from other ways because the organism employed here is a nonpathogenic bacterium. The biological approach provides various resources in which silver nanoparticles are produced and is viewed as a process of synthesis of nanoparticles having benefits over standard synthetic chemical routes and an ecologically friendly gliding path and as an initial cost strategy. In addition, Kalishwaralal et al. 2008 noted the AgNP's synthesis by reducing the aqueous Ag + ions and Bacillus licheniform is supernatant culture [16].

2.4. Bacterial Triggered Synthesis. The lactobacillus fermentum eliminates the development of Pseudomonas aeruginosa in the manufacture of biogenic silver nanoparticles and inhibits the generation of biofilm. B. flexus nanoparticles produced spherical nanoparticles (12 nm) and triangle nanoparticles (61 nm) anisotropic nanoparticles [17]. For AgNP to use B. cereus, an incubation duration of 3–5 days is required at an atmospheric temperature [18]. The durability and production of AgNP depended on psychrophilic bacteria's cell-free culture supernatants [19]. Bacillus thuringiensis spore crystal fusion is used to generate AgNP's of a 15 nm (cube and Hexagonal) commixed shape [20]. The dimension of the AgNP-synthesized parameters such as temperature, pH, and concentration using Escherichia coli, Klebsiella pneumonia, and the combination between Plectonema boryanium UTEX 485 and aqueous AgNO3 caused the spherical silver nanoparticles to precipitate 28 days [21]. Only with the incorporation of the Entero bacteriaceae

cell filtrate in the silver nitrate solution, the silver ions decrease quickly within 5 minutes [22]. The size and form of produced silver nanoparticles using microorganisms are influenced by the relationship between silver ions and microbes [23, 24]. Pseudomonas stutzeri AG259 extracted derived through silver mine excellently, possibly the best silver nanoparticles and distinctive morphology inside the periplasmic area [25]. The various applications of silver nanoparticles are illustrated in Figure 1.

2.5. Fungal-Derived Synthesis. Polydispersed spherical Agnips ranging in dimension from 17–33 nm were produced utilizing Helminthosporium tetramer cell-free filtration and demonstrated substantial antibacterial activity [26]. Escherichia coli has been reported to become more vulnerable than S. aureus to silver nanoparticles [27]. The Humicola sp thermophilic fungus responded with Ag (+) ions, reduced the precursor solution, and caused extracellular nanoparticles [28] to develop. In order to synthesize AgNPs from Aspergillus niger, optimal circumstances such as temperature 37°C, pH of 6.0, and membrane quantity of 2,0 mm silver nitrate were needed [29]. However, one essential effort was the synthesis of the use of wet biomass of Trichoderma reesei funguses by AgNP (5-50 nm) at 28°C after 120 hours with constant shaking [30]. Bipolaris nodulosa was formed of spherical, semipentagonal, and hexahedral shapes (10-60 nm) of silver nanoparticles [31]. Pseudomonas aeruginosa and Escherichia coli were superior antibacterial in nanoparticles created by utilizing Pleurotus sajor caju, relative to Staphylococcus aureus [32]. The result was the treatment of aquatic silver nitrate resolution using fungus Fusarium semitectum [33]. These were extraordinarily durable and crystalline silver nanoparticles. Extracellular mycosynthesis from Fusarium acuminatum isolated from contaminated ginger developed sizing nanoparticles of 5-40 nm of operational size in a period of 15-20 minutes. Nanocrystalline AgNPs of 13 to 18 nm were produced adopting Trichoderma asperellum cell-free leaf extracts within five full days of development [34, 35]. Aspergillus flavus acquired silver nanoparticles on its cell membrane in 72 hours; although, ultrasonication was observed to dislocate [36]. [Ag (NH3)2] + speedy reduction to Ag actually took place topographically whenever a quantity of -OH has been supplied into the Aeromonas bacteria [37]. Within few hours, an extraordinary synthesis of AgNPs with a dispersion of 525 nm was obtained when Aspergillus fumigates were subjected to the silver ion [38]. The production of silver nanoparticles used for Fusarium oxysporum produced in agglomeration [39]. In contrast, AgNP's typical halogen tungsten lamp technique was generated in less than an hour [40]. The degradation of silver is caused by the enzyme located on the Verticillium surface, and the electric cell was observed to multiply even after the creation of AgNP [41]. Through the microbial manufacture of silver nanoparticles, the biomimetic tube to plant mintage has been established. The enzymes present in the microbes cause silver ions constituting silver nanoparticles to be reduced [42]. These species are vulnerable to increased silver ion concentrations. Therefore, nanosilver generated by microorganisms has specific problems when used in biomedical applications [24].

2.6. Plant-Mediated Synthesis. A variety of plant compounds with the size of nanosilver particles were extracted by incorporating different extracts (Piper pedicellatum (2-3 nm), Centella asiatica L. (30–50 nm), Boswellia serrate, Pomegranate tree seed (30 nm), (Myrmecodia pendans (10-20 nm), Alternaria alternate (27–79 nm), Citrus maxima (2.5–5.7 nm), Desmodium gangeticum (18–39 nm) Tectona grandis (30–40 nm), Syzygium cumini (10–15 nm), Rhynchotechum ellipticum (51–73 nm), the latex of genus Thevetia peruviana (10–30 nm), Lycopersicon esculentum Mill (30–40 nm), Mentha piperita (90 nm), Murraya koenigii (10–25 nm), and so forth as capping agents) [43]. A study conducted using antioxidant ingredients from blackberry, blueberry, and pomegranate, as well as turmeric peels discovered that the dimension of silver nanoparticles generated by utilizing these extracts ranged within 20 and 500 nm in dimension, based on their nature and the technique of formulation [44]. It was discovered to be an effective catalyst for the production of the response, which resulted in the rapid generation of AgNPs in a shorter duration of 24 hours with such a molecular dimension of 59 nm [45]. The zeta potential (18 mV) of AgNPs produced with Delonix elata following 24-hour confinement is used to determine the stability of the material [46]. The SILAR (successive ionic layer adsorption and reaction) approach [47] was used to produce AgNP thin films with a significant amount of volumetric area using guava leaf extract. In this study, Potamogeton pectinatus L was used to synthesis nanotriangles and hexagon-shaped AgNPs, and the silver nitrate percentage was increased over time under constant magnification resulted in polydispersity in the final product. In the laboratory, polyphenol-rich extracts of Rumex hymenosepalus were used in the synthesis, resulting in the coalescence of face-centered cubic and hexagonal structured AgNPs with sizes ranging from 2 to 40 nm [48–50]. The presence of dihydrogen monoxide soluble organics inside the natural sources was the most critical factor in the degradation of silver ions to AgNPs. It was discovered that AgNPs generated using Prunus armeniaca (apricot) plant extracts had around 50% free radical scavenging activity when tested in a DPPH and an ABTS assay, respectively. In a study using the root extract of Coleus forskohlii, needle-shaped AgNPs with such a size of 82.46 nm were discovered [51–54].

Researchers discovered that Malva parviflora produces monodispersed AgNPs in such a shorter time frame compared to Beta vulgaris, A. graveolens, Allium kurrat, and Capsicum frutescens, and that this is the case even when compared to other plants. Fermentation at 150 rpm in a very shaker in dark settings is recommended, and dihydrogen monoxide soluble compounds such as saponins observed in the extraction from the plant of Memecylon edule have been found to be associated with lowering of silver ions, with the majority of the AgNPs in size range of 50–90 nm in square shape [55, 56]. Acrylamide nanoparticles (AgNPs) of spherical shape (average size of 18.2 8.9 nm) were synthesized using the methanolic plant extraction of Vitex negundo. They demonstrated antibacterial efficacy either towards Gram-positive as well as Gram-negative bacteria. AgNP production in protein-depleted fractions was shown to be altered, with the size distribution of AgNPs changing and the rate of AgNP synthesis decreasing,

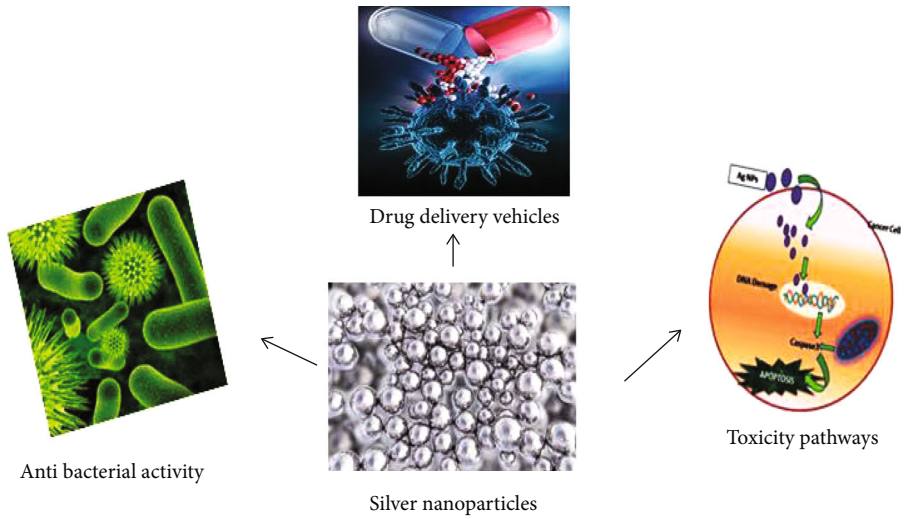

Figure 1: Silver nanoparticles and its applications.

confirming that cellular proteins in the unicellular algae Chlamydomonas reinhardtii were involved in the manufacture of AgNPs. In this study, the decrease of AgNO3 induced by eugenol embedded in the garlic leaf extracts was attributed to the evidential impact of methoxy and allyl substances situated at the ortho and para locations of the proton relinquishing -OH band from one particle of eugenol stored in the garlic clove extract. As a result, the creation of a resonant pattern in the elemental state of eugenol follows shortly after. The polyol and liquid heterocyclic elements discovered in Cinnamomum camphora's leaf broth are responsible for the degeneration of silver ions in the environment of silver ions, and these components are also found in the plant's leaves. Silver and gold nanoparticles with diameters varied between 10 and 20 nm as well as 15–25 nm, respectively, have been synthesized with the assistance of a derivative from the herb Emblica officinalis. The nanoparticles were shown to be highly stable and trustworthy. In the existence of lowering sugars and terpenoids in the A. indica leaf broth, the decrease of metal ions led to the development of clean silver, gold, and bimetallic nanostructures, which were then cleaned [57–62].

2.7. Review on Antibacterial Activity of Silver Nanoparticles. The highest antimicrobial activity was defined for silver nanoparticles (AgNP's) since silver shows low toxicity to mammalian cells and high toxicity towards microorganisms than various other metals, and the sequence is in the order Ag > Hg > Cu > Cd > Cr > Pb > Co > AU > Zn > Fe > Mn > Mo > Sn [63]. Silver nanoparticles exhibit even more antimicrobial activity than silver ions and salts [64, 65]. Silver nanoparticles have a decrease tendency to induce microbial impedance than several germicide agents [66, 67], which resulted in an application to a wide range of antimicrobial agents to prevent infection, burns, traumatic wound dressings, coating of catheters, diabetic ulcers, dental works, and medical equipment [65–69]. AgNPs are also used in various sanitary items, such as water purification systems, the linings of washing machines, dishwashers, freezers, and toilet seats, among other things [65, 67], to treat tropical diseases $1'$ that promote wound healing process turmeric-loaded nanoparticles was created. Turmeric is a spice obtained from the roots of Curcuma longa, which is a member of the Zingiberaceae family and is used to flavor food. The primary curcuminoid in turmeric is often regarded as the herb's main active component [70, 71]. Curcumin is a curcuminoid that has been shown to have anti-inflammatory properties. Silver is the most commonly used in the nitrate condition to elicit an antibacterial action in bacteria. The nanoscale size of AgNPs also increases the perforation potential of the silver nanoparticles, allowing for more efficient utilization of metal characteristics [72], which is beneficial. The nanoparticles connect to the cell surface and perforate the bacterial membrane that contains sulfur-containing protein as they travel through the cell. Specifically, AgNPs bind with proteins in the cell and phosphorus-containing substances such as DNA and forming complexes. After entering the bacterial cell, AgNPs form a low molecular content area in the middle of the bacteria, which eventually causes the bacteria to succumb to cell death. With a surface area of around 2 m^2 and a blood supply accounting for around one-third of all blood circulating throughout the body, skin is a three-layered structure consisting of the epidermis, dermis, and subcutaneous tissue layer [73], and the drug should cross through the layers of stratum corneum cuticle and dermis via various barriers for an effective drug delivery of the dosage form [74].

2.8. Review on Silver Nanoparticles as Drug Delivery Vehicles. Traditionally, gold and other molecules [75–78] have been used in nanoparticle-predicted drug delivery applications, but the use of silver has been restricted due to the complexity in synthesis; when functionalized using the classic salt aging procedure, there was a reduction in durability, and there were worries regarding silver toxicity in the past. Clinical application of silver nanoparticles as beneficial antibacterial treatments in wound care and also current in vivo studies showing that systemic exposure to silver nanoparticles is safe to have sparked interest in biomedical research involving silver nanoparticles. In a 2008 rat study, it was revealed because even in the diagnosis of severe oral AgNps at doses

larger than 300 mg/kg/day during 28 days, there was a greater preponderance of above 300 mg/kg/day throughout 28 days [79], and there was only a minor induction of secondary indicators of liver injury. Reports of the safety and absence of side-effects associated with silver nanoparticles administered at "moderate" doses [80] may instill greater preponderant confidence in the suitability of AgNPs for in vivo studies that aim to lower the threshold of effective AgNPs daily dosage by integrating their drug load potential and electromagnetic field research amplifying properties. Enhanced biocompatibility of AgNPs as a result of surface alteration, as well as outstanding optical characteristics [81, 82], has increased the suitability of AgNPs for drug delivery applications.

Silver nanoparticles have distinctive field properties, such as having a light scattering cross-section nearly ten times greater than that of a comparably sized gold nanoparticle [77, 81], which has sparked interest in their use as sensors [83, 84], biological labels, and substrates for surface-enhanced absorption, fluorescence, and photochemistry [77, 81]. AgNPs also have greater extinction coefficients and blue-shifted plasmon resonant peaks than other metallic nanomaterials, making them an excellent choice for photocontrolled drug delivery uses and potential surface-enhanced photochemistry of caged substances, such as nitro benzyl derivatives and among other applications [82]. The optical properties and biocompatibility of AgNPs are well described, and they have distinct blood plasma relative absorption maxima at ~420 nm [83, 84]. This difference is difficult to determine the role of plasmon in the nitrophenylethyl (NPE), which can be incorporated into microRNA (miRNA) complexes. The nonthermal component is likely related to intense electrical fields in the oscillating open plasmon region interacting with ions and mote, thus reducing the energizing energy of the reaction [85, 86]. Metal enhanced fluorescence has been described with silver nanostructures. In contrast, the resonance state of the coupled photon is shared between a photoactive molecule and the metal nanomaterial resulting in more efficient photon conversion [87].

2.9. Review on Toxicity Pathways of Silver Nanoparticles. Recent studies on the therapeutic utilization of silver nanoparticles utilizing drug distribution have addressed the toxicity and adverse effects of silver nanomaterials. Concerns of the impact of silver nanoparticles on cell health include decreased mitochondrial function and evocation of apoptosis, the mitochondria being a sensitive objective of cytotoxicity of AgNP's. While the mechanism of AgNP's toxicity was not well characterized, they may involve surface binding (depletion) of thiol-containing proteins, including glutathione and key component enzymes of the cells antioxidant mechanism, which leads to increased reactive oxygen species (ROS) propagation, oxidative damage [88], and apoptosis, an involute programmed cell death pathway. Particle surface electrostatic interactions with charged biomolecules might additionally attribute to the toxic properties often observed for "naked" silver nanoparticles at high concentrations. Mechanisms to enhance biocompatibility include functionalizing the metal nanoparticles with polyethylene glycol (PEG) radical, lipids, polymers, and minute peptides. The surface modification of silver nanoparticles with thiol-modified biomolecules improved silver biocompatibility and intracellular uptake [89–93]. The phospholipid-protected silver nanoparticles were distributed into 3T3 fibroblast cells and platelet cells with minimal toxic effects.

3. Discussion

Due to recent breakthroughs in the knowledge of silver nanoparticles' biocidal mechanisms of action, this one has been established that silver nanoparticles can be used to treat a wide range of infections, including virulent and bactericidal infections, as well as to promote wound healing [94, 95]. It has been demonstrated that silver nanoparticle and biopolymer-based biomaterial have good biocompatibility and low toxicity in physiological settings and may be used as a wound dressing material to heal a wide range of wounds. The current strategy for improving the efficacy of antibiotics is to combine them with silver nanoparticles in order to control microbial infections, as confirmed by the damage action of silver nanoparticles on microbial deoxyribonucleic acid [95]. This review focused in detail on various types of synthesis of silver nanoparticles which are categorized as physical, chemical, and biological approaches that are safe and environmentally friendly. This article also highlights the antibacterial activity of silver nanoparticles; when nanoparticles release silver atoms into the bacterial cell, it enhances their bactericidal activity and shows good wound healing activity [14, 15]. The benefits of these procedures are pretty crucial to utilize silver nanoparticles for checking diligence owing to nontoxicity. Because of this, these technologies may be applied to the large-scale industrial production of stable colloid silver nanoparticles, which have been used in various sectors, including digital manufacturing of electronic circuits and medicinal applications [96]. The use of traditional microbicidal medicines to combat the epidemic has been associated with an appropriate therapeutic index, insufficient drug bioavailability, the establishment of multiple drug resistance, and significant systemic side effects, among other things. It has been discovered that germicidal silver nanoparticles are effective against infection because of their ultra-diminutive controlled size as heights surface area and increased the responsiveness with active functional structure [97]. The phospholipid-protected silver nanoparticles that can decrease toxicity were distributed into 3T3 fibroblast and platelet cells [36, 37]. The previous review paper contains preliminary insights into pharmacological uses like anticancer, larvicidal, medicinal fabrics, and contrivances involving silver nanoparticles, all of which are now under investigation. In this way, the use of these biogenically generated silver nanoparticles will bring in a significant reward for the domain of bio nanomedicine [98].

3.1. Future Prospects. Due to the various potent activities of silver nanoparticles can be used in powerful disinfectants for preventing microbial infections [99, 100], silver nanoparticles can be employed in magnetic disinfection systems to treat waterborne infections, which is a new development. Magnetic disinfection [101] includes magnetic oxide as an active ingredient. Using silver nanoparticles as a sorbent and driving force for removing ecological contamination

has been shown to be effective [102, 103]. Nanosilver-based disinfection solutions have the potential to be helpful in decontaminating surfaces, instruments in kindergartens and schools, various types of equipment, and computers, which could lead to the development of nanosilver-based consumer items in the future. Silver-based nanocomposites have the potential to be ecologically beneficial, and they may be used in the development of unique product applications [104, 105].

3.2. Patent Methods. Raghuraman and Katti [106] had patented the method of producing silver nanoparticles. When silver salts react with phosphene amino acid, it makes silver nanoparticles with a temperature less than 40°C and a time period of fewer than 30 mins. These nanoparticles can be stored for a more extended period without agglomeration [107]. Mohd Rais Ahmad [108] patented a method for preparing silver nanoparticles; when commixing silver salt and pentaerythritol in polar resolution, it catalyzes the reduction process of silver ion clusters. Silver nanoparticles should be precipitated and washed with a solution, and finally, silver nanoparticles should be dried off [109].

3.3. Patent Formulations. Oh et al. [110] patented the preparation of silver nanoparticles and silver alloyed with factors like platinum, palladium, gold, aluminum, cadmium, and sulfur in surfactant solvents. The surfactant has the intrinsic property to adsorb into the interface, which is composed of two different phases. Thus, the surfactant molecules would adsorb into the open nuclei in the solvent. The adsorbed surfactant molecules from the solution prevent the coalescence of particles and control the rate of particle exaggeration. By choosing the proper kind or concentration of the surface active agent, the size of particles composed in the solution can be contained on a nanometer scale [111–117]. A process patent has been granted to Li and Ong [118] for the preparation of silver nanoparticles and the formation of molecules of an initial stabilizer on the surface of the nanoparticles, as well as the mixing of a replacement stabilizer composed mainly of a carboxylic acid also with composition to substitute at least a portion of the primary stabilizer with the replacement stabilizer, resulting in molecules of the initial stabilizer on the surface of the nanoparticles [119–130].

4. Conclusion

The methods for producing silver nanoparticles and their practical applications have been discussed in detail in this previous section. These methods help reduce the cost of silver nanoparticles, save energy, and practice safely. Recent research on silver nanoparticles is in the field of food maintenance and handling, and silver nanoparticles can be used as drug delivery vehicles and exhibit high antibacterial activity. In the drug delivery system, AgNPs often improve solubility, stability, and biodistribution, increasing efficacy. Since drug absorption increases multifold in the presence of nanoparticles, AgNPs can be used as a drug delivery system. With their unique properties, AgNPs stand out in various innovations, including biomedical materials and optical and antimicrobial coatings. They have proven their applicability in many fields such as medicine, catalysis, materials science, biotechnology, nanotechnology, and bioengineering. They have also been used in electronics, optics, and water treatment.

In addition, AgNPs exhibit antibacterial activity against microbial infections and are commonly used as an antimicrobial component in a wide variety of consumer goods. Due to their small size, nanoparticles have a large surface area, making them suitable candidates for various applications, while the morphology is also controllable. While NPs are beneficial for a variety of uses, they can pose health risks due to their uncontrolled use and release into the natural environment, which must be taken into account to make NP use more practical and environmentally acceptable. There is a wide range of applications for AgNPs in nanotoxicology studies, which is why they are so popular. The main trend in the development of silver nanomaterials is to make them multifunctional and programmable by external signals or the local environment, transforming them into nanodevices. For the benefit of future researchers, the continuous increase in the number of publications on the above subject has been examined. Since the influence of AgNPs on the environment and human health could be a problem in their widespread application, further investigations on the accumulation and mechanism of action of AgNPs in the human body are needed. However, more research is needed to use the particles outside of the lab.

Data Availability

The data used to support the findings of this study are included within the article.

Conflicts of Interest

The authors declare that there are no conflicts of interest.

References

[1] K. R. P. Biswas and D. Subhadip, "Effects and applications of silver nanoparticles in different fields," *International Journal of Recent Scientific Research*, vol. 6, pp. 5880–5883, 2015.

[2] L. Mulfinger, S. D. Solomon, M. Bahadory, A. V. Jeyarajasingam, S. A. Rutkowsky, and C. Boritz, "Synthesis and study of silver nanoparticles," *Journal of chemical education*, vol. 84, no. 2, p. 322, 2007.

[3] P. Hemalatha and A. Premnath, "Study on silver nanoparticle encapsulated curcumin for anticancer activity," *World Journal of Pharmaceutical Research*, vol. 5, pp. 958–973, 2016.

[4] S. Senapati, *Biosynthesis and immobilization of nanoparticles and their applications*, vol. 6, University of pune, India, 2005.

[5] T. Klaus-Joerger, R. Joerger, E. Olsson, and C. G. Granqvist, "Bacteria as workers in the living factory: metal-accumulating bacteria and their potential for materials science," *Trends in Biotechnology*, vol. 19, no. 1, pp. 15–20, 2001.

[6] C. Y. Xing, T. F. Ma, J. S. Guo et al., "Bacterially self-assembled encapsulin nanocompartment for removing silver from water," *Water Research*, vol. 191, article 116800, 2021.

[7] G. J. Zhao and S. E. Stevens, "Multiple parameters for the comprehensive evaluation of the susceptibility of Escherichia coli to the silver ion," *Bimetals*, vol. 11, pp. 27–32, 1998.

[8] C. N. Lok, C. M. Ho, R. Chen et al., "Proteomic analysis of the mode of antibacterial action of silver nanoparticles," *Journal of proteome research*, vol. 5, no. 4, pp. 916–924, 2006.

[9] M. Rai, A. Yadav, and A. Gade, "Silver nanoparticles as a new generation of antimicrobials," *Biotech Advances*, vol. 27, pp. 76–83, 2009.

[10] J. S. Kim, E. Kuk, K. N. Yu et al., "Antimicrobial effects of silver nanoparticles," *Nanomedicine: Nanotechnology, biology and medicine*, vol. 3, no. 1, pp. 95–101, 2007.

[11] S. Silver, L. T. Phung, and G. Silver, "Silver as biocides in burn and wound dressings and bacterial resistance to silver compounds," *Journal of Industrial Microbiology and Biotechnology*, vol. 33, no. 7, pp. 627–634, 2006.

[12] N. Law, S. Ansari, F. R. Livens, J. C. Renshaw, and J. R. Lloyd, "Formation of nanoscale elemental silver particles via enzymatic reduction by Geobacter sulfurreducens," *Applied and environmental microbiology*, vol. 74, no. 22, pp. 7090–7093, 2008.

[13] V. Thomas, M. M. Yallapu, B. Sreedhar, and S. K. Bajpai, "A versatile strategy to fabricate hydrogel–silver nanocomposites and investigation of their antimicrobial activity," *Journal of colloid and interface science*, vol. 315, no. 1, pp. 389–395, 2007.

[14] N. Choudhary and B. S. Sekhon, "Potential therapeutic effect of curcumin-an update," *Journal of Pharmaceutical Education and Research*, vol. 3, no. 2, p. 64, 2012.

[15] X. H. Vu, T. T. T. Duong, T. T. H. Pham, D. K. Trinh, X. H. Nguyen, and V. S. Dang, "Synthesis and study of silver nanoparticles for antibacterial activity against Escherichia coli and Staphylococcus aureus," *Advances in Natural Sciences: Nanoscience and Nanotechnology*, vol. 9, no. 2, article 025019, 2018.

[16] S. Prabhu and E. K. Poulose, "Silver nanoparticles: mechanism of antimicrobial action, synthesis, medical applications, and toxicity effects," *International nano letters*, vol. 2, no. 1, pp. 1–10, 2012.

[17] R. H. Muller, M. Radtke, and S. A. Wissing, "Solid lipid nanoparticles (SLN) and nanostructured lipid carriers (NLC) in cosmetic and dermatological preparations," *Advanced drug delivery reviews*, vol. 54, pp. S131–S155, 2002.

[18] C. R. Behl, G. L. Flynn, T. Kurihara et al., "Hydration and percutaneous absorption: Influence of hydration on alkanol permeation through hairless mouse skin,," *Journal of Investigative Dermatology*, vol. 75, no. 4, pp. 346–352, 1980.

[19] C. M. Agrawal, K. A. Athanasiou, and J. D. Heckman, "Biodegradable PLA-PGA polymers for tissue engineering in orthopaedics," *In Materials Science Forum*, vol. 250, pp. 115–128, 1997.

[20] N. L. McKnight and J. A. Frangos, "Strain rate mechanotransduction in aligned human vascular smooth muscle cells," *Annals of biomedical engineering*, vol. 31, no. 3, pp. 239–249, 2003.

[21] M. Li, M. J. D. Glawe, H. Green, D. K. Mills, M. J. McShane, and B. K. Gale, "Effect of high-aspect-ratio microstructures on cell growth and attachment," *Medicine and Biology Proceedings*, pp. 531–536, 2000.

[22] T. Sun, N. C. Harris, and C. H. Kiang, "Phase transition and optical properties of DNA gold nanoparticle assemblies," *Plasmonics*, vol. 2, no. 4, pp. 193–199, 2007.

[23] Y. S. Kim, J. S. Kim, H. S. Cho et al., "Twenty-eight-day oral toxicity, genotoxicity, and gender-related tissue distribution of silver nanoparticles in Sprague-Dawley rats," *Inhalation toxicology*, vol. 20, no. 6, pp. 575–583, 2008.

[24] D. K. Tiwari, T. Jin, and J. Behari, "Dose-dependent in-vivo toxicity assessment of silver nanoparticle in Wistar rats," *Toxicology mechanisms and methods*, vol. 21, no. 1, pp. 13–24, 2011.

[25] J. Yguerabide and E. E. Yguerabide, "Light-scattering submicroscopic particles as highly fluorescent analogs and their use as tracer labels in clinical and biological applications: II Experimental characterization," *Analytical biochemistry*, vol. 262, no. 2, pp. 157–176, 1998.

[26] O. J. Clarke and I. J. Burgess, "Electrodeposited gold nanodaggers on conductive metal oxide films provide substrates for dual-modality surface sensitive vibrational spectroscopy," *The Journal of Physical Chemistry C*, vol. 124, no. 24, pp. 13356–13364, 2020.

[27] D. G. Thompson, A. Enright, K. Faulds, W. E. Smith, and D. Graham, "Ultrasensitive DNA detection using oligonucleotide– silver nanoparticle conjugates," *Analytical chemistry*, vol. 80, no. 8, pp. 2805–2810, 2008.

[28] D. Graham, K. Faulds, D. Thompson et al., "Functionalized nanoparticles for bioanalysis by SERRS," *Biochemical Society Transactions*, vol. 37, no. 4, pp. 697–701, 2009.

[29] R. A. Wolkow and M. Moskovits, "Enhanced photochemistry on silver surfaces," *The Journal of chemical physics*, vol. 87, no. 10, pp. 5858–5869, 1987.

[30] P. V. Asha Rani, G. L. K. Mun, M. P. Hande, and S. Valiyaveettil, "Cytotoxicity and genotoxicity of silver nanoparticles in human cells," *ACS Nano*, vol. 3, no. 2, pp. 279–290, 2009.

[31] S. Link and M. A. El-Sayed, "Size and temperature dependence of the plasmon absorption of colloidal gold nanoparticles," *The Journal of Physical Chemistry B*, vol. 103, no. 21, pp. 4212–4217, 1999.

[32] L. Zhang, L. Laug, W. Munchgesang et al., "Reducing stress on cells with apoferritin-encapsulated platinum nanoparticles," *Nano Letters*, vol. 10, no. 1, pp. 219–223, 2010.

[33] W. H. Hung, M. Aykol, D. Valley, W. Hou, and S. B. Cronin, "Plasmon resonant enhancement of carbon monoxide catalysis," *Nano Letters*, vol. 10, no. 4, pp. 1314–1318, 2010.

[34] T. Ung, L. M. Liz-Marzan, and P. Mulvaney, "Redox catalysis using Ag@ SiO2 colloids," *The Journal of Physical Chemistry B*, vol. 103, no. 32, pp. 6770–6773, 1999.

[35] M. H. Chowdhury, K. Aslan, S. N. Malyn, J. R. Lakowicz, and C. D. Geddes, "Metal-enhanced chemiluminescence: Radiating plasmons generated from chemically induced electronic excited states," *Applied physics letters*, vol. 88, no. 17, article 173104, 2006.

[36] F. Persano and S. Leporatti, "Current Overview of inorganic nanoparticles for the treatment of central nervous system (CNS) diseases," *Current Nanomaterials*, vol. 5, no. 2, pp. 92–110, 2020.

[37] Y. C. Chung, I. H. Chen, and C. J. Chen, "The surface modification of silver nanoparticles by phosphoryl disulfides for improved biocompatibility and intracellular uptake," *Biomaterials*, vol. 29, pp. 1807–1816, 2008.

[38] A. S. Gurav, T. T. Kodas, L. M. Wang, E. I. Kauppinen, and J. Joutsensaari, "Generation of nanometer-size fullerene

particles via vapor condensation," *Chemical physics letters*, vol. 218, no. 4, pp. 304–308, 1994.

[39] F. E. Kruis, H. Fissan, and B. Rellinghaus, "Sintering and evaporation characteristics of gas-phase synthesis of size-selected PbS nanoparticles," *Materials Science and Engineering: B*, vol. 69, pp. 329–334, 2000.

[40] M. H. Magnusson, K. Deppert, J. O. Malm, J. O. Bovin, and L. Samuelson, "Gold nanoparticles: production, reshaping, and thermal charging," *Journal of Nanoparticle Research*, vol. 1, no. 2, pp. 243–251, 1999.

[41] F. Mafune, J. Y. Kohno, Y. Takeda, T. Kondow, and H. Sawabe, "Formation and size control of silver nanoparticles by laser ablation in aqueous solution," *The Journal of Physical Chemistry B*, vol. 104, no. 39, pp. 9111–9117, 2000.

[42] A. V. Simakin, V. V. Voronov, N. A. Kirichenko, and G. A. Shafeev, "Nanoparticles produced by laser ablation of solids in liquid environment," *Applied Physics A*, vol. 79, no. 4, pp. 1127–1132, 2004.

[43] J. P. Sylvestre, A. V. Kabashin, E. Sacher, M. Meunier, and J. H. Luong, "Stabilization and size control of gold nanoparticles during laser ablation in aqueous cyclodextrins," *Journal of the American Chemical Society*, vol. 126, no. 23, pp. 7176-7177, 2004.

[44] T. Tsuji, K. Iryo, N. Watanabe, and M. Tsuji, "Preparation of silver nanoparticles by laser ablation in solution: influence of laser wavelength on particle size," *Applied surface science*, vol. 202, no. 1-2, pp. 80–85, 2002.

[45] H. Huang and Y. Yang, "Preparation of silver nanoparticles in inorganic clay suspensions," *Composites Science and Technology*, vol. 68, no. 14, pp. 2948–2953, 2008.

[46] A. R. Vilchis-Nestor, V. Sanchez-Mendieta, M. A. Camacho-Lopez, R. M. Gomez-Espinosa, M. A. Camacho-Lopez, and J. A. Arenas-Alatorre, "Solventless synthesis and optical properties of Au and Ag nanoparticles using Camellia sinensis extract," *Materials letters*, vol. 62, no. 17-18, pp. 3103–3105, 2008.

[47] K. Kalishwaralal, V. Deepak, S. Ramkumarpandian, H. Nellaiah, and G. Sangiliyandi, "Extracellular biosynthesis of silver nanoparticles by the culture supernatant of _Bacillus licheniformis_," *Materials Letters*, vol. 62, no. 29, pp. 4411–4413, 2008.

[48] M. Zhang, K. Zhang, B. De Gusseme, W. Verstraete, and R. Field, "The antibacterial and anti-biofouling performance of biogenic silver nanoparticles by lactobacillus fermentum," *Biofouling*, vol. 30, no. 3, pp. 347–357, 2014.

[49] S. Sunkar and C. V. Nachiyar, "Biogenesis of antibacterial silver nanoparticles using the endophytic bacterium Bacillus cereus isolated from Garcinia xanthochymus," *Asian Pacific Journal of Tropical Biomedicine*, vol. 2, no. 12, pp. 953–959, 2012.

[50] S. Shivaji, S. Madhu, and S. Singh, "Extracellular synthesis of antibacterial silver nanoparticles using psychrophilic bacteria," *Process Biochemistry*, vol. 46, no. 9, pp. 1800–1807, 2011.

[51] D. Jain, S. Kachhwaha, R. Jain, G. Srivastava, and S. L. Kothari, "Novel microbial route to synthesize silver nanoparticles using spore crystal mixture of Bacillus thuringiensis," *Indian Journal of Experimental Biology*, vol. 48, no. 11, pp. 1152–1156, 2010.

[52] S. Gurunathan, K. Kalishwaralal, R. Vaidyanathan et al., "Biosynthesis, purification and characterization of silver nanoparticles using Escherichia coli," *Colloids and Surfaces B: Biointerfaces*, vol. 74, no. 1, pp. 328–335, 2009.

[53] A. R. Shahverdi, S. Minaeian, H. R. Shahverdi, H. Jamalifar, and A. A. Nohi, "Rapid synthesis of silver nanoparticles using culture supernatants of Enterobacteria: a novel biological approach," *Process Biochemistry*, vol. 42, no. 5, pp. 919–923, 2007.

[54] A. Panacek, M. Kolar, R. Vecerova et al., "Antifungal activity of silver nanoparticles against _Candida_ spp.," *Biomaterials*, vol. 30, no. 31, pp. 6333–6340, 2009.

[55] J. R. Morones, J. L. Elechiguerra, A. Camacho et al., "The bactericidal effect of silver nanoparticles," *Nanotechnology*, vol. 16, no. 10, article 2346, 2005.

[56] T. Klaus, R. Joerger, E. Olsson, and C. G. Granqvist, "Silver-based crystalline nanoparticles, microbially fabricated," *Proceedings of the National Academy of Sciences*, vol. 96, no. 24, pp. 13611–13614, 1999.

[57] G. B. Shelar and A. M. Chavan, "Fungus-mediated biosynthesis of silver nanoparticles and its antibacterial activity," *Archives of applied science research*, vol. 6, pp. 111–114, 2014.

[58] T. Ahmad, I. A. Wani, N. Manzoor, J. Ahmed, and A. M. Asiri, "Biosynthesis, structural characterization and antimicrobial activity of gold and silver nanoparticles," *Colloids and Surfaces B: Biointerfaces*, vol. 107, pp. 227–234, 2013.

[59] A. Syed, S. Saraswati, G. C. Kundu, and A. Ahmad, "Biological synthesis of silver nanoparticles using the fungus Humicola sp. and evaluation of their cytoxicity using normal and cancer cell lines," *Spectrochimica Acta Part A: Molecular and Biomolecular Spectroscopy*, vol. 114, pp. 144–147, 2013.

[60] M. Sangappa and P. Thiagarajan, "Mycobiosynthesis and characterization of silver nanoparticles from Aspergillus niger: a soil fungal isolate," *International Journal of Life Sciences Biotechnology and Pharma Research*, vol. 1, no. 2, pp. 282–289, 2012.

[61] V. Khabat, G. A. Mansoori, and S. Karimi, "Biosynthesis of silver nanoparticles by fungus Trichoderma Reesei," *Insciences journal*, vol. 1, no. 1, pp. 65–79, 2011.

[62] S. Saha, J. Sarkar, D. Chattopadhyay, S. Patra, A. Chakraborty, and K. Acharya, "Production of silver nanoparticles by a phytopathogenic fungus Bipolaris nodulosa and its antimicrobial activity," *Digest Journal of Nanomaterials and Biostructures*, vol. 5, no. 4, pp. 887–895, 2010.

[63] R. Nithya and R. Ragunathan, "Synthesis of silver nanoparticle using Pleurotus sajor caju and its antimicrobial study," *Digest Journal of Nanomaterials and Biostructures*, vol. 4, no. 4, pp. 623–629, 2009.

[64] S. Basavaraja, S. D. Balaji, A. Lagashetty, A. H. Rajasab, and A. Venkataraman, "Extracellular biosynthesis of silver nanoparticles using the fungus Fusarium semitectum," *Materials Research Bulletin*, vol. 43, no. 5, pp. 1164–1170, 2008.

[65] A. Ingle, A. Gade, S. Pierrat, C. Sonnichsen, and M. Rai, "Mycosynthesis of silver nanoparticles using the fungus fusarium acuminatum and its activity against some human pathogenic bacteria," *Current Nanoscience*, vol. 4, no. 2, pp. 141–144, 2008.

[66] A. Mukherjee, M. Roy, B. P. Mandal et al., "Green synthesis of highly stabilized nanocrystalline silver particles by a non-pathogenic and agriculturally important fungus T. asperellum," *Nanotechnology*, vol. 19, no. 7, article 075103, 2008.

[67] N. Vigneshwaran, N. M. Ashtaputre, P. V. Varadarajan, R. P. Nachane, K. M. Paralikar, and R. H. Balasubramanya,

"Biological synthesis of silver nanoparticles using the fungus _Aspergillus flavus_," *Materials Letters*, vol. 61, no. 6, pp. 1413–1418, 2007.

[68] F. U. Mouxing, L. I. Qingbiao, S. U. N. Daohua et al., "Rapid preparation process of silver nanoparticles by bioreduction and their characterizations," *Chinese Journal of Chemical Engineering*, vol. 14, no. 1, pp. 114–117, 2006.

[69] K. C. Bhainsa and S. F. D'souza, "Extracellular biosynthesis of silver nanoparticles using the fungus _Aspergillus fumigatus_ ," *Colloids and surfaces B: Biointerfaces*, vol. 47, no. 2, pp. 160–164, 2006.

[70] N. Duran, P. D. Marcato, O. L. Alves, G. I. De Souza, and E. Esposito, "Mechanistic aspects of biosynthesis of silver nanoparticles by several Fusarium oxysporum strains," *Journal of nanobiotechnology*, vol. 3, no. 1, pp. 1–7, 2005.

[71] A. Mohammadian, S. A. Shojaosadati, and M. H. Rezaee, "Fusarium oxysporum mediates photogeneration of silver nanoparticles," *Scientia Iranica*, vol. 14, no. 4, pp. 323–326, 2010.

[72] P. Mukherjee, A. Ahmad, D. Mandal et al., "Fungus-mediated synthesis of silver nanoparticles and their immobilization in the mycelial matrix: a novel biological approach to nanoparticle synthesis," *Nano Letters*, vol. 1, no. 10, pp. 515–519, 2001.

[73] K. Kalimuthu, R. S. Babu, D. Venkataraman, M. Bilal, and S. Gurunathan, "Biosynthesis of silver nanocrystals by Bacillus licheniformis," *Colloids and surfaces B: Biointerfaces*, vol. 65, no. 1, pp. 150–153, 2008.

[74] B. Kassa, J. Leta Tesfaye, B. Bulcha et al., "Effect of Manganese Ions on Spectroscopic and Insulating Properties of Aluminophosphate Glasses," *Advances in Materials Science and Engineering*, vol. 2021, Article ID 6253069, 11 pages, 2021.

[75] M. N. Nadagouda, N. Iyanna, J. Lalley, C. Han, D. D. Dionysiou, and R. S. Varma, "Synthesis of silver and gold nanoparticles using antioxidants from blackberry, blueberry, pomegranate, and turmeric extracts," *ACS Sustainable Chemistry& Engineering*, vol. 2, no. 7, pp. 1717–1723, 2014.

[76] A. Annamalai, V. L. P. Christina, V. Christina, and P. T. V. Lakshmi, "Green synthesis and characterisation of Ag NPs using aqueous extract of Phyllanthus maderaspatensis L," *Journal of Experimental Nanoscience*, vol. 9, no. 2, pp. 113–119, 2014.

[77] C. K. Sathiya and S. Akilandeswari, "Fabrication and characterization of silver nanoparticles using Delonix elata leaf broth," *Spectrochimica Acta Part A: Molecular and Biomolecular Spectroscopy*, vol. 128, pp. 337–341, 2014.

[78] N. M. Shinde, A. C. Lokhande, J. S. Bagi, and C. D. Lokhande, "Biosynthesis of large area (30×30 cm 2) silver thin films," *Materials science in semiconductor processing*, vol. 22, pp. 28–36, 2014.

[79] J. Das and P. Velusamy, "Biogenic synthesis of antifungal silver nanoparticles using aqueous stem extract of banana," *Nano Biomedicine and Engineering*, vol. 5, no. 1, pp. 34–38, 2013.

[80] A. A. Abdel Hamid, M. A. Al-Ghobashy, M. Fawzy, M. B. Mohamed, and M. M. Abdel-Mottaleb, "Phytosynthesis of Au, Ag, and Au–Ag bimetallic nanoparticles using aqueous extract of sago pondweed (Potamogeton pectinatus L.)," *ACS Sustainable Chemistry & Engineering*, vol. 1, no. 12, pp. 1520–1529, 2013.

[81] E. Rodriguez-Leon, R. Iniguez-Palomares, R. E. Navarro et al., "Synthesis of silver nanoparticles using reducing agents obtained from natural sources (Rumex hymenosepalus extracts)," *Nanoscale research letters*, vol. 8, no. 1, pp. 1–9, 2013.

[82] M. Vanaja, G. Gnanajobitha, K. Paulkumar, S. Rajeshkumar, C. Malarkodi, and G. Annadurai, "Phytosynthesis of silver nanoparticles by Cissus quadrangularis: influence of physicochemical factors," *Journal of Nanostructure in Chemistry*, vol. 3, no. 1, pp. 1–8, 2013.

[83] M. Shu, F. He, Z. Li et al., "Biosynthesis and antibacterial activity of silver nanoparticles using yeast extract as reducing and capping agents," *Nanoscale Research Letters*, vol. 15, no. 1, pp. 1–9, 2020.

[84] P. Dauthal and M. Mukhopadhyay, "In vitro free radical scavenging activity of biosynthesized gold and silver nanoparticles using Prunus armeniaca (apricot) fruit extract—nanomaterials in energy, health and environmen," *Journal of Nanoparticle Research*, vol. 15, p. 1366, 2013.

[85] C. Baskaran and V. R. Bai, "Green synthesis of silver nanoparticles using Coleus forskohlii roots extract and its antimicrobial activity against bacteria and fungus," *International Journal of Drug Development and Research*, vol. 5, pp. 114–119, 2013.

[86] M. F. Zayed, W. H. Eisa, and A. A. Shabaka, "Malva parviflora extract assisted green synthesis of silver nanoparticles," *Spectrochimica Acta Part A: Molecular and Biomolecular Spectroscopy*, vol. 98, pp. 423–428, 2012.

[87] T. Elavazhagan and K. D. Arunachalam, "Memecylon edule leaf extract mediated green synthesis of silver and gold nanoparticles," *International Journal of Nanomedicine*, vol. 6, p. 1265, 2011.

[88] M. Zargar, A. A. Hamid, F. A. Bakar et al., "Green synthesis and antibacterial effect of silver nanoparticles using Vitex negundo L," *Molecules*, vol. 16, no. 8, pp. 6667–6676, 2011.

[89] I. Barwal, P. Ranjan, S. Kateriya, and S. C. Yadav, "Cellular oxido-reductive proteins of Chlamydomonas reinhardtii control the biosynthesis of silver nanoparticles," *Journal of nanobiotechnology*, vol. 9, no. 1, pp. 1–12, 2011.

[90] A. Nabikhan, K. Kandasamy, A. Raj, and N. M. Alikunhi, "Synthesis of antimicrobial silver nanoparticles by callus and leaf extracts from saltmarsh plant Sesuvium portulacastrum L," *Colloids and surfaces B: Biointerfaces*, vol. 79, no. 2, pp. 488–493, 2010.

[91] A. K. Singh, M. Talat, D. P. Singh, and O. N. Srivastava, "Biosynthesis of gold and silver nanoparticles by natural precursor clove and their functionalization with amine group," *Journal of Nanoparticle Research*, vol. 12, no. 5, pp. 1667–1675, 2010.

[92] J. Huang, Q. Li, and D. Sun, "Biosynthesis of silver and gold nanoparticles by novel sundried Cinnamomum camphora leaf," *Nanotech*, vol. 18, article 10504, 2007.

[93] H. H. Lara, E. N. Garza-Trevino, L. Ixtepan-Turrent, and D. K. Singh, "Silver nanoparticles are broad-spectrum bactericidal and virucidal compounds," *Journal of nanobiotechnology*, vol. 9, no. 1, pp. 1–8, 2011.

[94] S. S. D. Kumar, N. K. Rajendran, N. N. Houreld, and H. Abrahamse, "Recent advances on silver nanoparticle and biopolymer-based biomaterials for wound healing applications," *International journal of biological macromolecules*, vol. 115, pp. 165–175, 2018.

[95] J. Natsuki, T. Natsuki, and Y. Hashimoto, "A review of silver nanoparticles: synthesis methods, properties and

applications," *International journal of materials science and applications*, vol. 4, no. 5, pp. 325–332, 2015.

[96] A. K. Mandal, "Silver nanoparticles as drug delivery vehicle against infections," *Global Journal of Nanomedicine*, vol. 3, no. 2, article 555607, 2017.

[97] M. J. Firdhouse and P. Lalitha, "Biosynthesis of silver nanoparticles and its applications," *Journal of Nanotechnology*, vol. 2015, 18 pages, 2015.

[98] A. T. Le, T. T. Le, H. H. Tran, D. A. Dang, Q. H. Tran, and D. L. Vu, "Powerful colloidal silver nanoparticles for the prevention of gastrointestinal bacterial infections," *Advances in Natural Sciences: Nanoscience and Nanotechnology*, vol. 3, no. 4, article 045007, 2012.

[99] K. Chamakura, R. Perez-Ballestero, Z. Luo, S. Bashir, and J. Liu, "Comparison of bactericidal activities of silver nanoparticles with common chemical disinfectants," *Colloids and Surfaces B: Biointerfaces*, vol. 84, no. 1, pp. 88–96, 2011.

[100] G. A. Kurian, A. Vivek Vishnu, N. Subhash, and A. Shakilabanu, "Characterization and biological evaluation of silver nanoparticles synthesized by aqueous root extract of Desmodium gangeticum for its antioxidant, antimicrobial and cytotoxicity," *International Journal of Pharmacy and Pharmaceutical Sciences*, vol. 7, no. 1, pp. 182–186, 2014.

[101] J. Dong, Z. Xu, and S. M. Kuznicki, "Synthesis of Luminescent ZrO_2: Eu^{3+} Nanoparticles and Their Holographic Sub-Micrometer Patterning in Polymer Composites," *Advanced Functional Materials*, vol. 19, pp. 12–68, 2009.

[102] M. Yoosefian and M. Jahani, "A molecular study on drug delivery system based on carbon nanotube for the novel norepinephrine prodrug, Droxidopa," *Journal of Molecular Liquids*, vol. 284, pp. 258–264, 2019.

[103] L. Yildirimer, N. T. Thanh, M. Loizidou, and A. M. Seifalian, "Toxicology and clinical potential of nanoparticles," *Nano Today*, vol. 6, no. 6, pp. 585–607, 2011.

[104] A. Figoli, J. Hoinkis, S. A. Altinkaya, and J. Bundschuh, *Application of nanotechnology in membranes for water treatment*, vol. 45, article 8989, CRC Press, 2017.

[105] E. Abaie, L. Xu, and Y. X. Shen, "Bioinspired and biomimetic membranes for water purification and chemical separation: A review," *Frontiers of Environmental Science & Engineering*, vol. 15, no. 6, pp. 1–33, 2021.

[106] K. Raghuraman and K. K. Katti, "US Patent for Methods for producing silver nanoparticles," Patent (Patent # 9,005,663) - The Curators of the University of Missouri, 2004.

[107] S. K. Shukla, J. Anusha, H. Ramaiya, J. Lee, and H. Al Sadeq, "Application of nanotechnology in membrane-based wastewater treatment: a critical review," *Membrane-Based Hybrid Processes for Wastewater Treatment*, pp. 119–145, 2021.

[108] M. R. Ahmad, "Preparation of silver nanoparticles WO2012074355A1," 2010.

[109] R. Singh, V. Y. Patade, Sanchita, and A. Singh, "Antimicrobial potential of silver nanoparticles biosynthesized using aerial yam bulbils for control of selected phytopathogens," *Archives of Phytopathology and Plant Protection*, vol. 67, pp. 1–19, 2021.

[110] S.-G. Oh, S. C. Yi, S. I. Shin, D. W. Kim, and S. H. Jeong, "Preparation of silver and silver alloyed nanoparticles in surfactant solutions," US6660058B1 US Grant, 2000.

[111] R. K. Bachheti, Y. Godebo, A. Bachheti, M. O. Yassin, and A. Husen, "Root-based fabrication of metal/metal-oxide nanomaterials and their various applications," *Nanomaterials for Agriculture and Forestry Applications*, vol. 134, pp. 135–166, 2020.

[112] D. Tripathi, A. Modi, G. Narayan, and S. P. Rai, "Green and cost effective synthesis of silver nanoparticles from endangered medicinal plant Withania coagulans and their potential biomedical properties," *Materials Science and Engineering: C*, vol. 100, pp. 152–164, 2019.

[113] B. Pannerselvam, P. Durai, D. Thiyagarajan et al., "Facile synthesis of silver nanoparticles using Asian spider flower and its in vitro cytotoxic activity against human breast carcinoma cells," *Processes*, vol. 8, no. 4, p. 430, 2020.

[114] S. Abel, J. L. Tesfaye, R. Shanmugam et al., "Green synthesis and characterizations of zinc oxide (ZnO) nanoparticles using aqueous leaf extracts of coffee (Coffea arabica) and its application in environmental toxicity reduction," *Journal of Nanomaterials*, vol. 2021, 6 pages, 2021.

[115] L. T. Jule, K. Ramaswamy, B. Bekele, A. Saka, and N. Nagaprasad, "Experimental investigation on the impacts of annealing temperatures on titanium dioxide nanoparticles structure, size and optical properties synthesized through sol-gel methods," *Materials Today: Proceedings*, vol. 45, pp. 5752–5758, 2021.

[116] L. T. Jule, R. Krishnaraj, N. Nagaprasad, B. Stalin, V. Vignesh, and T. Amuthan, "Evaluate the structural and thermal analysisof solid and cross drilled rotor by using finite element analysis," *Materials Today: Proceedings*, vol. 47, 2021.

[117] T. Amuthan, N. Nagaprasad, R. Krishnaraj, V. Narasimharaj, B. Stalin, and V. Vignesh, "Experimental study of mechanical properties of AA6061 and AA7075 alloy joints using friction stir welding," *Materials Today: Proceedings*, vol. 46, 2021.

[118] Y. Li and B. S. Ong, "Silver-containing nanoparticles with replacement stabilizer," US20080085594A1 US Application, 2006.

[119] S. Abel, J. Leta Tesfaye, R. Kiran et al., "Studying the Effect of Metallic Precursor Concentration on the Structural, Optical, and Morphological Properties of Zinc Sulfide Thin Films in Photovoltaic Cell Applications," *Advances in Materials Science and Engineering*, vol. 2021, Article ID 7443664, 6 pages, 2021.

[120] S. Abel, J. L. Tesfaye, B. Fikadu et al., "Application of Titanium Dioxide Nanoparticles Synthesized by Sol-Gel Methods in Wastewater Treatment," *Journal of Nanomaterials*, vol. 2021, 6 pages, 2021.

[121] B. Bulcha, J. L. Jule, A. Degefa et al., "Synthesis of zinc oxide nanoparticles by hydrothermal methods and spectroscopic investigation of ultraviolet radiation protective properties," *Journal of Nanomaterials*, vol. 2021, 2021.

[122] B. Bulcha, A. Degefa, F. Tesgera et al., "Green Synthesis, Characterization of Zinc Oxide Nanoparticles, and Examination of Properties for Dye-Sensitive Solar Cells Using Various Vegetable Extracts," *Journal of Nanomaterials*, vol. 2021, 9 pages, 2021.

[123] E. K. Subramaniam, M. Sakthivel, K. Kanthavel, R. Krishnaraj, M. G. Deepan Marudachalam, and R. Palani, "Overall resource effectiveness, cycle time reduction & capacity improvements," *International Journal of Scientific and Engineering Research*, vol. 2, no. 8, pp. 1–5, 2011.

[124] R. Sathiyamoorthy and R. Krishnaraj, "Optimization of cellular layout under dynamic demand environment by simulated annealing," *International Journal of Scientific and Engineering Research*, vol. 3, no. 10, pp. 1–7, 2012.

[125] V. M. M. Thilak, R. Krishnaraj, M. Sakthivel, K. Kanthavel, M. Marudachalam, and R. Palani, "Transient thermal and structural analysis of the rotor disc of disc brake," *International Journal of Scientific and Engineering Research*, vol. 2, no. 8, pp. 2–5, 2011.

[126] S. Varatharajan, R. Krishnaraj, M. Sakthivel, K. Kanthavel, M. G. Deepan Marudachalam, and R. Palani, "Design and analysis of single disc machine top and bottom cover," *International Journal of Scientific and Engineering Research*, vol. 2, no. 8, pp. 1–6, 2011.

[127] C. M. Balamurugan, R. Krishnaraj, M. Sakthivel, K. Kanthavel, D. Marudachalam, and R. Palani, "Computer aided modeling and optimization of crankshaft," *International Journal of Scientific and Engineering Research*, vol. 2, no. 8, pp. 2–7, 2011.

[128] M. Vyshakh, R. Krishnaraj, A. P. Sayooj, and M. Afzal, "Experimental investigation on aluminium gravity die casting," *International Journal of Applied Environmental Sciences*, vol. 9, no. 2, pp. 213–222, 2014.

[129] M. Deepu, R. Krishnaraj, D. Karthik, and N. M. Binoj, "Cycle time optimization of rubber floor mat die," *International Journal of Applied Environmental Sciences*, vol. 9, no. 2, pp. 229–237, 2014.

[130] V. S. Arun, R. Krishnaraj, M. N. Rohit, and V. Mohan, "Optimising rejection rate of laser diamond sawing using Taguchi method," *International Journal of Applied Environmental Sciences*, vol. 9, no. 2, pp. 223–228, 2014.

Hindawi
Journal of Nanomaterials
Volume 2021, Article ID 8617290, 10 pages
https://doi.org/10.1155/2021/8617290

Research Article

Synthesis of Zinc Oxide Nanoparticles by Hydrothermal Methods and Spectroscopic Investigation of Ultraviolet Radiation Protective Properties

Bekele Bulcha,[1] Jule Leta Tesfaye,[2] Degefa Anatol,[3] R. Shanmugam,[4] L. Priyanka Dwarampudi,[5] N. Nagaprasad,[6] V. L. Nirmal Bhargavi,[7] and Ramaswamy Krishnaraj[2,8]

[1]*Department of Physics, College of Natural and Computational Science, Dambi Dollo University, Ethiopia*
[2]*Centre for Excellence-Indigenous Knowledge, Innovative Technology Transfer and Entrepreneurship, Dambi Dollo University, Ethiopia*
[3]*Department of Mathematics, College of Natural and Computational Science, Dambi Dollo University, Ethiopia*
[4]*TIFAC CORE HD, Department of Pharmacognosy, JSS Academy of Higher Education and Research, JSS College of Pharmacy, Ooty, Tamilnadu, India*
[5]*Department of Pharmacognosy, JSS Academy of Higher Education and Research, JSS College of Pharmacy, Ooty, Tamilnadu, India*
[6]*Department of Mechanical Engineering, ULTRA College of Engineering and Technology, Madurai, 625 107 Tamil Nadu, India*
[7]*Department of Chemistry, Sri Venkateswara College of Engineering and Technology, 517004, Chittoor, Andhra Pradesh, India*
[8]*Department of Mechanical Engineering, Dambi Dollo University, Ethiopia*

Correspondence should be addressed to Ramaswamy Krishnaraj; prof.dr.krishnaraj@dadu.edu.et

Received 20 June 2021; Revised 9 August 2021; Accepted 1 September 2021; Published 23 September 2021

Academic Editor: Lakshmipathy R

Copyright © 2021 Bulcha Bekele et al. This is an open access article distributed under the Creative Commons Attribution License, which permits unrestricted use, distribution, and reproduction in any medium, provided the original work is properly cited.

Ultraviolet radiation causes damages to the human body, such as skin ageing, skin cancer, and allergies throughout the world. Applying zinc oxide nanoparticles (ZnO NPs) in sunscreen products (like cloths or textiles) to protect human skin by absorbing the ultraviolet radiations that emerged from the sun. The main aim of this study is to investigate both absorbance and transmittance characteristics of the untreated and treated cotton textiles. For ZnO NPs using hydrothermal methods, they were made from $Zn(NO_3)_2{\cdot}6H_2O$ and NaOH at a constant annealing temperature of 300°C. Fourier transform infrared (FT-IR), X-ray diffraction (XRD), scanning electron microscopy (SEM), and UV-vis spectroscopy were used to analyze the produced ZnO NPs. From the FT-IR result, ZnO NPs were observed in the region of 400-600 cm^{-1}. Wurtzite hexagonal structure of ZnO NPs with the average crystal size 32 ± 49 nm was observed from XRD results. Flowers in the shape of synthesized ZnO NPs were observed from SEM images. The UV-vis penetration peaks were identified at 264 nm and 376 nm, with energy band gaps of 4.68 and 3.536 eV, respectively. When compared to bulk ZnO, the energy band gap of ZnO NPs was blue-shifted due to the impact of quantum confinement. The peaks in UV-vis absorption were caused by an electronic transition from the valiancy to the conduction bands. The high energy band shows high absorbance of the synthesis sample in the case of 264 nm. The ZnO NPs were manufactured and applied to 100% of raw cotton to impart sunscreen action to both untreated and treated cotton fabrics. The performance of treatment has been evaluated utilizing UV-vis spectroscopy through quantifying ultraviolet protective factors (UPF) and percentage of transmitted (%T) radiations. The treated cotton textiles have 61.50% UPF while 2.65% ultraviolet radiations were transmitted. In other words, untreated cotton textiles have 1.63% UPF while 74.56% ultraviolet radiation was transmitted. Therefore, the treated cotton textiles have excellent protection categories when compared to untreated cotton textiles.

1. Introduction

Nanotechnology is a new field of study that deals with the discovery and use of nanoparticles containing structural differences among the nanomaterials with their bulk counterparts. It also refers to the art and science of creating and using nanoparticles having fundamental properties and functions [1]. Nanoparticles are microscopic particles with a diameter of 1 to 100 nanometers that are used in current textile technology. Nanoparticles also have a wide range of applications in life science [1, 2], biomedical [3, 4], healthcare [4], and security [5] as well as the energy generation [6], farming [7], sustainable energy [6, 7], energy storage [6, 8], infrastructure [9], and building and constructions [10]. Because of their capacity to transfer charges and give fast responses, as well as their ease of use and inexpensive cost, ZnO NPs are a popular choice among nanoparticles for a range of applications. According to the literature [2–4, 7, 11], ZnO NPs can be used in textiles as UV blocking properties, antifungal, antibacterial activities, solar screening, cosmetics, food packaging, biomedical, self-cleaning, water, and air cleaning, sterilizing surroundings, and photocatalyst due because of its one-of-a-kind physical and chemical characteristics such as high electrochemical coupling coefficient, more chemical stability, a diverse range of absorbing radiation, huge excitonic binding energy (60 meV), large energy band gap (3.37 eV), and high mechanical and thermal stability. ZnO NPs have a number of great qualities, including ease of synthesis, controllable shape and size, nontoxicity, the existence of extrinsic and intrinsic at the emission centre, and the ability to emit a variety of hues (violet, blue, green, yellow, and red) [12–14].

UV radiation protection is one of the most critical challenges in the textiles industry because of ozone depletion and the greenhouse effect. Ultraviolet radiation penetrates from the sun to the earth in the form of energy having fifty percent visible lights, forty-five percent infrared, and five percent ultraviolet radiations [15]. UV radiation can be classified into three wavelength regions based on its wavelength: UVA (400 nm-320 nm), UV-B (320 nm-280 nm), and UV-C (280 nm–200 nm) [3, 5, 7]. At this time, the ozone layer has completely absorbed UV-C. From all UV radiation, the most damaging types of radiation are UV-A and UV-B. It has high energy and a short wavelength [4–6, 15]. In order to reduce such effects, ZnO NPs must be synthesized for textiles industries. Cubic rock salt, cubic zinc blende, and hexagonal are the three most common structures of ZnO NPs. Under normal environmental circumstances, hexagonal structures are thermodynamically stable [7]. Nanowire, nanoflower, nanocombs, nanobelts, nanocages, nanosprings, nanoring, needle-like, nanoflake, spherical, nanohelix, sheet, bullet-like, hexagonal plate, polyhedral, nanotube, nanorod, pyramid shape, doughnut-like, malty sphere, nanobows, nanoleafs, star, spike, and multipods, smashed stone-like, cylinder-like, and ellipsoid are morphological forms of ZnO NPs derived from SEM [5–8, 12–16]. UV radiation absorbance by semiconductive, whether significantly refractive or dispersing radiations, is closely related to the UV blocking characteristics of ZnO NPs. The chemical composition of ZnO NPs has a direct impact on their protective actions [11, 16]. Furthermore, particle shapes, sizes, crystals, and crystalline forms all have a role [9–13]. When textiles are subjected to UV radiation, they experience direct transmittance, absorption, and scattering [13]. Skin damage is caused by UV radiation that is emitted, as well as reflection and fibre dye [10–13]. UV radiation absorption is measured inside ultraviolet protective factors (UPF). The UPF value of treated fabrics evaluates their blocking qualities, and the greater the UPF value, the much more protective they are [10]. For the production of ZnO NPs, a range of preparation techniques have been reported, including chemical precipitation, spray-pyrolysis, hydrothermal, sol-gel, photochemical, and electrospanning methods [13, 14, 16–20]. As reported in several kinds of literature [6], ZnO NPs were prepared for textile application through hydrothermal methods using different solvents (distilled water, ethanol, and methanol) results from 20 to 9 nm sizes with high UPF of UV-A and UV-B. Recently, ZnO NPs were prepared for UV absorber properties of cotton textiles using zinc acetate $(CH_3COO)_2{\cdot}2H_2O$) and NaOH precursor by adding surfactant (cetyl trimethyl ammonium/CTAB) was seen in literature [12]. Yadav et al. [21] prepared ZnO NPs with an average diameter of less than 35 nm for cotton textiles results from an increment of UPF and antimicrobial activities. Another group of researchers leads by Ibrahim et al. [22] also prepared ZnO NPs by sol-gel technique for cotton textiles found 359 nm of particle size which provides durable multifunctional fishing (UV protection and antimicrobial activities).

Several kinds of literature use sol-gel methods to prepare ZnO NPs rather than hydrothermal methods, and there are no clear methods to prepare ZnO NPs using hydrothermal processes. Previously, no literature reports on the comparison of absorbance of untreated and treated cotton textiles and a transmittance of untreated and treated cotton textiles. Furthermore, a comparison of transmittance with an absorbance of treated and untreated cotton textiles was not clearly reported previously. Therefore, this research gives detail information on synthesis methods and UV-protective properties of nanoparticles in terms of absorbance and transmittance. ZnO NPs were prepared using $Zn(NO_3)_2{\cdot}6H_2O$ and NaOH precursors. The produced samples were FT-IR analyzed and utilized to identify contaminants. The XRD results demonstrate that the ex situ produced nanoparticles [17], which have been deposited onto bleached cotton fibers, had an average weight of 33 nm, as reported in various literature. SEM is used to analyze the shape of the nanoparticles, and a UV-vis is accustomed to evaluate the absorption spectrum of untreated and treated cotton textiles [18–46]. As a result, the goal of this study is to synthesize, characterize, contrast, and compare untreated and treated cotton textiles.

2. Experimental Details

Sodium hydroxide (NaOH), zinc nitrate hexahydrate $(Zn(NO_3)_2{\cdot}6H_2O)$, and ethanol were acquired from a local supplier (used without further purification). ZnO NPs were made utilising a hydrothermal method that included the use of $Zn(NO_3)_2{\cdot}6H_2O$ and NaOH precursors, as described

in the literature [18]. For this situation, a 0.6 M aqueous ethanol solution of $Zn(NO_3)_2{\cdot}6H_2O$ were maintained with constant stirring for 45 minutes with a mild magnetic stirrer to thoroughly dissolve the zinc nitrate hexahydrate, and a 1 M aqueous ethanol solution of NaOH was likewise made exactly the same as 45 minutes of agitation. After the zinc nitrate hexahydrate was completely dissolved, 1 M NaOH mixture was prepared by slowly adding drop by drop for 25 minutes without touching the container's wall, while magnetic stirring was kept at high speed. The process was permitted to continue for 1 hour after the aqueous solution of NaOH was added, and the container was sealed at this temperature for 1 hour. Afterward, the sample was transferred to settle for an overnight period before the resultant liquid was carefully separated. The precipitate was removed after 15 minutes of centrifugation. ZnO NPs were precipitated and rinsed four times with the double distilled water and ethanol before being dried in an air environment at roughly 90°C. Zn $(OH)_2$ was totally transformed to ZnO NPs at this time, and the existence of nanoparticles and other functional groups was determined by Fourier transform infrared spectroscopy (FT-IR). The size, shape, optical, and structural properties of the produced ZnO NPs were all measured. An X-ray diffractometer (panalytical) was used to record the X-ray diffraction (XRD) pattern of manufactured ZnO NPs using Cu-K radiation with a wavelength of ($\lambda = 0.1541$ nm) in the scan range of 2theta = 10°–80°. A scanning electron microscope (SEM) with (EDXA, SIRION) for the morphology of the specimen was examined using compositional analysis of generated ZnO NPs. Using a UV-vis spectrophotometer (Hitachi, U-3010), the optical transmission/absorption spectra of ZnO NPs distributed in water were recorded as follows. The solution was dipped in a quartz cuvette and taken into a UV-vis spectrophotometer with around 0.3 g of ZnO NPs dissolved in deionized water. In such a process, the absorbance/transmittance spectra of ZnO NPs were measured. Finally, ZnO NPs were brought into the application as follows. White 100% cotton fabrics were purchased from the local market of Dambi Dollo Town, Oromia Regional State. A piece of cotton textiles with a surface area of 10 cm × 10 cm and a mass for every unit surface of 60 g m^{-2} were prepared and washed five times using deionized water. Then, the fibre was soaked by ZnO NPs solution for 10 min by a gentle magnetic stirrer. The cloth was dried in the oven at 130°C for 15 min to remove the excessive dispersion. UV/absorption and transmission were then used to determine the efficiency of the shielding against UV radiation.

3. Results and Discussion

This current research includes the development of nanoparticles by hydrothermal approaches that aid in the management of surface energy. FT-IR, XRD, SEM, and UV-visible spectroscopy were used to characterize the functionalized nanoparticles. The nano and other potential functional groups of produced ZnO NPs were investigated using Fourier transform infrared (FT-IR). FT-IR transmission spectra of ZnO NPs in the 400–4000 cm^{-1} range were measured, as shown in Figure 1 below. The stretching vibration of O-H has appeared at 3428 cm^{-1}, and this is maybe due to the oscillation of water molecules [14, 17, 19, 21]. The peak observed at 2924 cm^{-1} was related to –CH2 vibration [21, 23]. The transmission peaks were observed at 1557 cm^{-1} due to C=O symmetric stretching [22]. The transmission peaks observed at 1391 cm^{-1} and 1278 cm^{-1} were bending, and the vibrational mode of CO_2 was related to CO_2 is from the real environment [18]. The peak observed at 1055 cm^{-1} was associated with H-O-H bending vibration was due to the presence of water of crystallization [25]. The band observed at 810 cm^{-1} was also due to the deformation vibration of water molecules [21–23]. The transmission band observed at 466 cm^{-1} was due to Zn-O stretching mode [27].

The XRD diffraction spectra of prepared ZnO NPs were shown in Figure 2 below. ZnO NPs were prepared from zinc nitrate hexahydrate ($Zn(NO_3)_2{\cdot}6H_2O$) and sodium hydroxide (NaOH) through hydrothermal methods. A broad and well-defined spectral peaks show that the synthesized substances incorporate particles in the nanoscale range. Intensity, full-width at half-maxima, size, and position were determined from XRD result analysis. About nine diffraction peaks were observed at 21.77°, 24.43°, 26.26°, 37.55°, 46.62°, 52.88°, 56.40°, 57.97°, and 59.1° with their corresponding crystal plane of (100), (002), (101), (102), (110), (103), (200), (112), and (201), respectively. Broad diffraction and most intense peak peaks without peak shift were observed at (101) peaks. Randomly oriented crystallites were seen from these several peaks.

The average crystallite size (D) of produced ZnO NPs were estimated via the Debye-Scherrer formula (1).

$$D = \frac{0.89\,\lambda}{\beta \cos\theta}, \tag{1}$$

where D is the crystallite size, λ is the X-ray transmittance wavelength ($\lambda = 0.15418$ nm), β is full-width at half-maximum (FWHM) in radians, and θ represents the angle of diffraction [20]. Table 1 displays the average particle size distribution of produced ZnO NPs, which was about 32.49 nm.

The produced material has a size range of 1 nm to 100 nm and is suitable for use in the textile industry [21]. The measured "D" values for ZnO nanopowder or synthesized nanomaterials have crystallized in a hexagonal wurtzite structure, as shown in Table 1, are also in excellent accordance with all those obtained from Joint Committee on Powder Diffraction Guideline (JCPDS) card document data for ZnO nanopowder or synthesized nanomaterials [5, 9].

The lattice spacing (d) were derived from Braggs equation:

$$d = \frac{\lambda}{2\sin\theta} \tag{2}$$

The lattice parameters c and a were determined from

$$a = \sqrt{\frac{1}{3}}\frac{\lambda}{\sin\theta}, \tag{3}$$

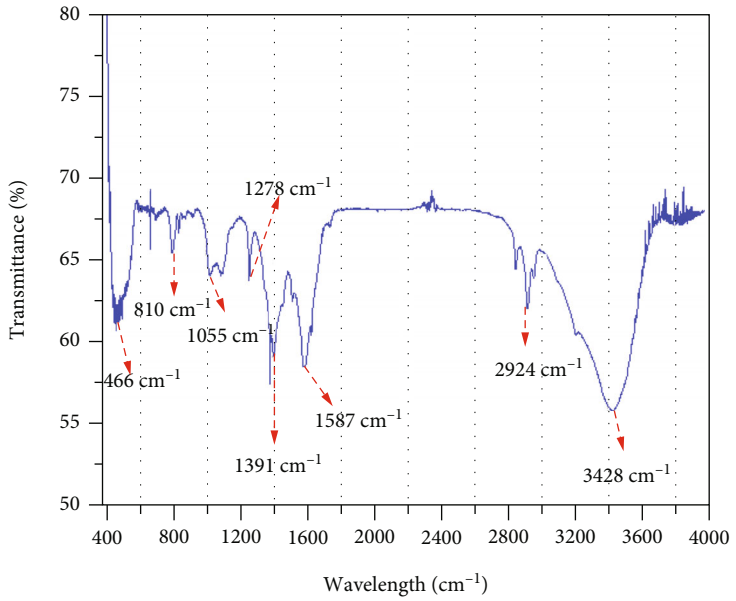

Figure 1: Fourier transform infrared (FT-IR) spectral analysis of prepared ZnO NPs.

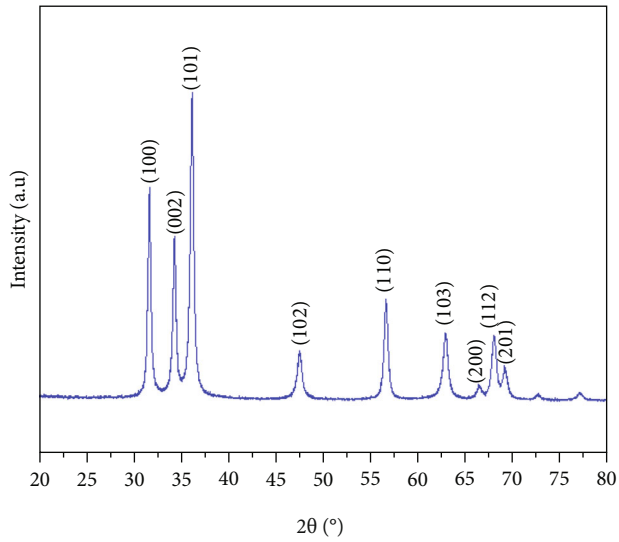

Figure 2: X-ray diffraction (XRD) pattern of prepared ZnO NPs.

Table 1: Diffraction angle (2theta), FWHM (β), and average crystallite size (D) of prepared ZnO NPs.

No.	2theta (degree)	Cos2θ (radian)	β (radian)	β (Cos2θ)	Crystallite size (nm)	Average D (nm)
1	21.77	0.0162	0.269	0.0043	31.90	
2	24.43	0.0159	0.278	0.0044	31.18	
3	26.26	0.0156	0.298	0.0046	29.82	
4	37.55	0.0138	0.365	0.0050	27.44	
5	46.62	0.0119	0.355	0.0042	32.67	32.49
6	52.88	0.0105	0.417	0.0043	31.90	
7	56.40	0.0096	0.377	0.0036	38.11	
8	57.97	0.0096	0.426	0.0040	34.30	
9	59.10	0.0089	0.442	0.0039	35.17	

Table 2: Lattice parameters, lattice spacing, unit cell volume, grain size, and dislocation density of prepared ZnO NPs.

Hkl	Lattice parameter			Lattice spacing	Unit cell volume (nm)	Grain size (δ)	Dislocation density (ε)
	a (nm)	c (nm)	c/a (nm)				
101	0.3617	0.3899	1.0779	0.339	0.0442	0.0668	7.1063

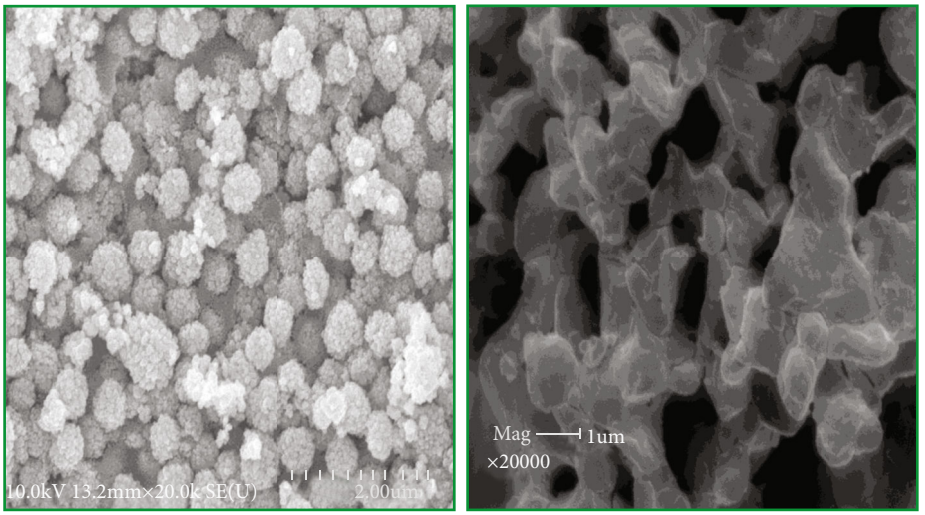

Figure 3: Scanning electron microscopy (SEM) images of synthesized ZnO NPs with different magnifications.

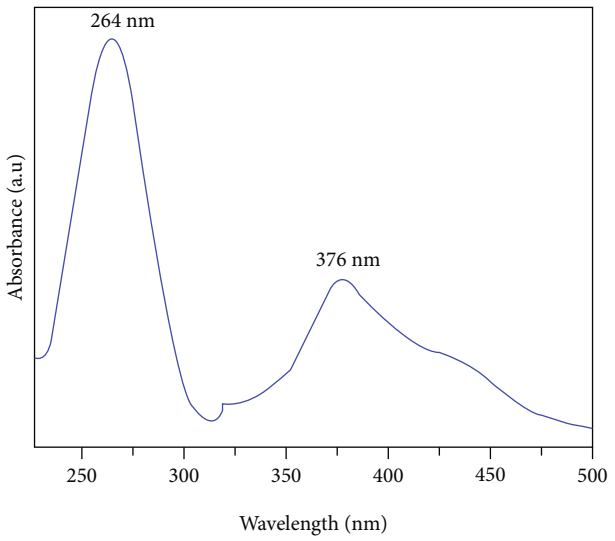

Figure 4: Absorption spectral analysis of synthesized ZnO NPs.

$$c = \frac{\lambda}{\sin\theta}. \quad (4)$$

The unit cell volume (V)

$$V = \frac{\sqrt{3}}{2}a^2c. \quad (5)$$

The grain size (δ) of synthesized particles were evaluated by using the following formula:

$$\varepsilon = \frac{\beta\mathrm{Cos}\theta}{4}. \quad (6)$$

The dislocation density (δ) is used to determine the defects in crystallite were determined from Small man's and Williamson formula.

$$\delta = \frac{15\varepsilon}{ad}. \quad (7)$$

The grain size and dislocation density of the synthesized sample were obtained from peak of XRD and summarized in

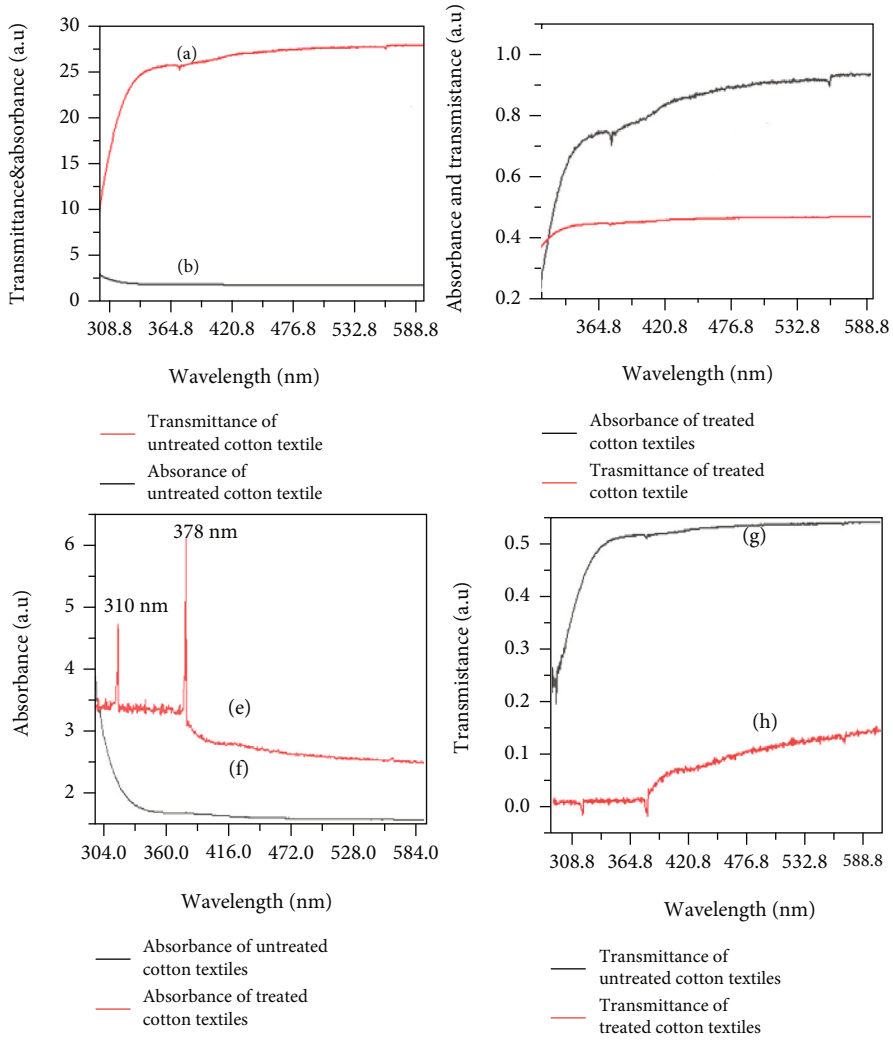

FIGURE 5: UV-vis spectral analysis: transmittance and absorbance of untreated cotton textiles (a, b) and nanotreated cotton textiles (c, d). The absorbance of treated and untreated textiles (e, f) and transmittance of untreated and treated textiles (g, h).

Table 2 above. As described in JCPDS card number 36-1451, all X-ray diffraction peaks of manufactured ZnO NPs are carefully categorized of wurtzite structure with lattice parameters of $a = b = 0.3249$ nm and $c = 0.5206$ nm. For (101) peaks, the lattice parameters 'a' and 'c,' spacing distance (d), and volume cell of ZnO NPs were computed, and there was a minor variance in the lattice parameter values. The variation could be caused by a minor shift throughout the position of its peaks as a result of a fault [22, 23]. Lattice imperfection of synthesized nanoparticles was observed from dislocation density and strain. Figure 3 represents the SEM image of prepared ZnO NPs at a constant annealing temperature of 300°C. The particle morphology is homogenous and well spread, with a flower-like shape. This shows that ZnO NPs may be successfully produced utilising zinc salt precursors in the nanoscale range.

The UV-vis absorbance spectrum of produced ZnO NPs at a fixed heating rate of 300°C is depicted in Figure 4. These uptake peaks were found at 264 nm and 376 nm. The strong absorption peak was observed at 264 nm. This indicates that a high ability to absorb ultraviolet radiation. Furthermore, synthesized nanoparticles have high absorption abilities in the region of 200-300 nm and 350-450 nm.

The technique of UV-vis absorption spectroscopy is commonly adapted to investigate the optical characteristics of particles that are in nanosize [33]. The ZnO nanoparticles, which are substantially underneath the bandgap frequency of 376 nm, give rise to an excitonic maximum absorption at roughly 264 nm ($E_g = 3.29$ eV). The fact that considerable sharp absorption of ZnO implies that the nanoparticle dispersion is monodispersed [7]. The bandgap energy of the synthesized samples was computed by using the absorption edge relationship equation (8) [24–27].

$$E_g = h\nu_g = \frac{hc}{\lambda_g}, \tag{8}$$

where $h = 4.14 \times 10^{-15}$evs, $C = 2.99 \times 10^{8}$m s^{-1}, and its wavelength.

The E_g values for samples were 4.68 and 3.13 eV, which are in good accordance with the literature. In comparison to

Table 3: UV blocking qualities of the handcrafted cotton fabrics.

Specimens	Transmittance (%)	UPF	Protection categories
Treated	2.65	61.50	Excellent
Untreated	74.56	1.63	Neat

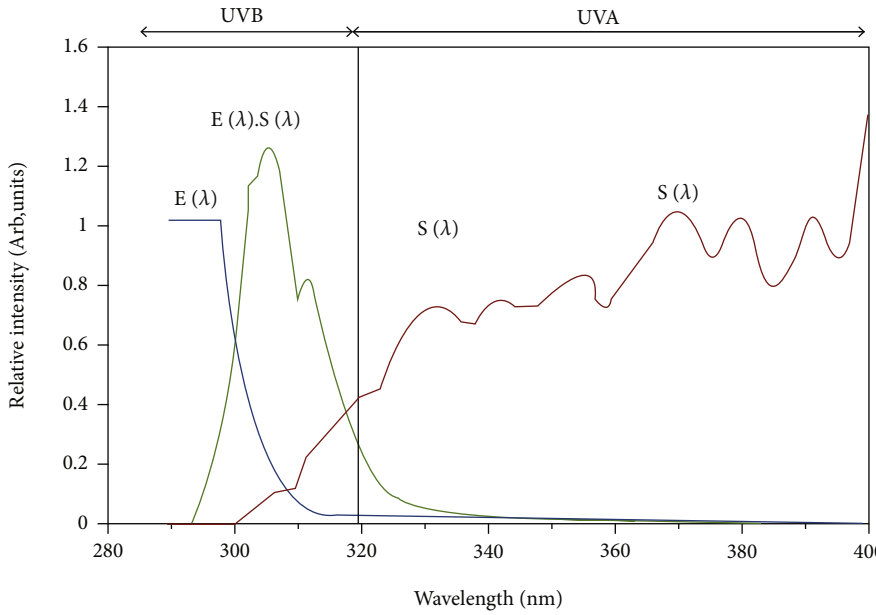

Figure 6: Graph of relative erythermal action spectrum, $E(\lambda)$, standard solar spectral irradiance, $S(\lambda)$, and $E(\lambda) \cdot S(\lambda)$ in the ultraviolet light region.

bulk ZnO, the quantum confinement impact pushed its energy band gap of ZnO nanoparticles to the blue. Peaks have been caused due to electronic transition from the valence band to the conduction band. The use of nanosized ZnO NPs on 100 percent cotton fabrics enhances UV/radiation absorption. ZnO NPs have been applied to the surface of cotton fibres. The ability of ZnO NPs to absorb UV rays was successfully transferred to fabric products. The absorbance and transmittance spectra of untreated and treated cotton fabric in the 200-500 nm range are shown in Figure 5. Highly transmitted ultraviolet radiation was observed from untreated cotton textiles, as shown in Figures 5 and 5(b). As shown in Figures 5(c) and 5(d), more ultraviolet radiation was absorbed rather than transmitted. A small amount of radiation was transmitted through nanocotton textiles that have been treated [47].

The absorption ability of treated and untreated textiles was shown in Figures 5(e) and 5(f). Higher values of ultraviolet absorbance were obtained when cotton textiles were treated with ZnO NPs. The sensitivity of treated cotton fabrics was shown to be higher at 378 nm and 297 nm, which are both in the UV range, while untreated cotton textile (see Figure 5(f)) does not absorb ultraviolet radiation. The transmittance ability of untreated and treated cotton textiles was observed in Figures 5(g) and 5(h), and a low ultraviolet radiation spectrum was transmitted through nanocoated cotton textiles. The wash withstanding ability of nanoparticles is an intriguing feature of their treatment. After 25 washes, the treated fabrics were examined again because there was no discernible difference in their sunscreen activity. This clearly shows that even without the application of a binder, the nanoparticles are strongly attached to the cloth surface. A binder, on the other hand, can be employed when a higher degree of wash fastness is necessary [14, 16, 24–27]. As shown in Table 3, the UV protection parameter (UPF) and percent transmittances (%T) were determined using equations (9) and (10), respectively.

$$\text{UPF} = \int_{\lambda 1}^{\lambda 2} \frac{E(\lambda).S(\lambda)}{E(\lambda).S(\lambda).T(\lambda)} d\lambda, \quad (9)$$

$$\%\text{Transmition} = \sum_{\lambda 1}^{\lambda 2} \frac{T(\lambda)}{\lambda 2 - \lambda 1}. \quad (10)$$

In this case, $E(\lambda)$ is relatively erythermic spectral efficiency, $S(\lambda)$ in $\text{Wm}^{-2}\,\text{nm}^{-1}$ is a specimen of spectrum transmittance produced from UV spectrometric tests, and $E(\lambda)$ and $S(\lambda)$ were acquired at the national database of sea surface temperature administration (NOAA), [18, 29], which is shown in Figure 6 [31–35].

Tests for UV-A and UV-B are generally conducted in the UVA and UVB zones. However, $E(\lambda)$ has very tiny UV-A values and is substantially large in the UV-B field, as seen

in Figure 6. Therefore, the UPF value indicates mostly UVB protection rather than a wide range of protection against UVA-UVB [36–43].

The use of ready ZnO NPs on cotton fabrics improves the absorption and transmission of UV light. This means that UV radiation shields are effectively absorbed by ZnO NP UV radiation upon its cotton textile surface. As ZnO NPs treat cotton has a small percentage of the transmission, untreated materials have a high percentage of the transmission (Table 3).

It was proven by the variety of cotton textiles that, compared to cotton-treating textiles, a considerable % of transmittance in unprocessed textiles having a low ability to block ultraviolet light, i.e., unprocessed cotton textiles absorb ultraviolet radiation. In comparison with untreated cotton textiles, the low spectrum in the transmission of cotton textiles has shown a significant UV blocking capability [16, 22, 30].

4. Conclusion

Sodium hydroxide and zinc nitrate hex-hydrate were used to create ZnO NPs using a hydrothermal technique. Different characterization tools were used to characterize the produced ZnO NPs. These instruments are Fourier transform infrared (FT-IR), X-ray diffraction (XRD), UV-vis spectroscopy, and scanning electron microscopy (SEM). The presence of nanoparticles and other functional groups were observed from FT-IR results. Utilizing Debye-Scherer's equation, the outcome from the XRD investigation shows that the materials generated were on the nanoscale scale with a mean particle size of 32.49 nm. The absorbance maximum of produced nanoparticles was 264 nm and 376 nm, respectively, as determined by UV-vis spectroscopy. UV-vis spectroscopy was also used to investigate the optical characteristics of nanoparticles. The morphology of prepared ZnO NPs was evaluated by SEM shows flower images. Through the use of ZnO NPs on the surface of cotton textiles, the good performance of ZnO NPs as ultraviolet absorbers may be efficiently transferred to cotton textiles. The increase in UV absorption capacity of ZnO NP-treated cotton textiles, according to the ultraviolet-visible tests. The absorption capability of ZnO NPs on the surface of cotton textiles ensures that UV light is effectively shielded. The UV protection factor (UPF) and percentage of transmittance (percent T) values that have been computed reflect the protection offered by ZnO nanoparticles treated fabrics against ultraviolet light. This finding could be used to shield the body from the harmful effects of UV light.

Data Availability

The data used to support the findings of this study are included within the article.

Conflicts of Interest

The authors declare no conflict of interest.

References

[1] S. A. Noorian, N. Hemmatinejad, and J. A. Navarro, "Ligand modified cellulose fabrics as support of zinc oxide nanoparticles for UV protection and antimicrobial activities," *International Journal of Biological Macromolecules*, vol. 154, pp. 1215–1226, 2020.

[2] N. A. Ibrahim, A. A. Nada, B. M. Eid, M. Al-Moghazy, A. G. Hassabo, and N. Y. Abou-Zeid, "Synthesis, characterization and application of zinc oxide nanoparticles for textile materials against ultra violet radiation," *International Journal of Innovative Science and Research Technology*, vol. 9, article 035014, 2018.

[3] A. A. M. Attia, M. S. Antonious, M. A. H. Shouman, A. A. A. Nada, and K. M. Abas, "Processing and fundamental characterization of carbon fibers and cellulose nanocrystals derived from bagasse," *Carbon Letters*, vol. 29, no. 2, pp. 145–154, 2019.

[4] A. Rahdar, M. R. Hajinezhad, V. S. Sivasankarapillai, F. Askari, M. Noura, and G. Z. Kyzas, "Synthesis, characterization, and intraperitoneal biochemical studies of zinc oxide nanoparticles in Rattus norvegicus," *Applied Physics A*, vol. 126, no. 5, pp. 1–9, 2020.

[5] B. Abebe, B. Bulcha, and A. R. C. Reddy, "Effects of temperature and polyvinyl alcohol concentrations in the synthesis of zinc oxide nanoparticles," *Journal of Nanotechnology and Materials Science*, vol. 5, no. 1, pp. 44–50, 2018.

[6] M. E. el-Naggar, S. Shaarawy, and A. A. Hebeish, "Multifunctional properties of cotton fabrics coated with in situ synthesis of zinc oxide nanoparticles capped with date seed extract," *Carbohydrate Polymers*, vol. 181, pp. 307–316, 2018.

[7] A. Fouda, S. el-Din Hassan, S. S. Salem, and T. I. Shaheen, "_In-Vitro_ cytotoxicity, antibacterial, and UV protection properties of the biosynthesized Zinc oxide nanoparticles for medical textile applications," *Microbial Pathogenesis*, vol. 125, pp. 252–261, 2018.

[8] A. V. Abramova, V. O. Abramov, V. M. Bayazitov et al., "A sol-gel method for applying nanosized antibacterial particles to the surface of textile materials in an ultrasonic field," *Ultrasonics Sonochemistry*, vol. 60, p. 104788, 2020.

[9] W. Zhang, X. Chen, Y. Ma et al., "Positive aging effect of ZnO nanoparticles induced by surface stabilization," *The Journal of Physical Chemistry Letters*, vol. 11, no. 15, pp. 5863–5870, 2020.

[10] A. Awad, A. I. Abou-Kandil, I. Elsabbagh, M. Elfass, M. Gaafar, and E. Mwafy, "Polymer nanocomposites part 1," *Journal of Thermoplastic Composite Materials*, vol. 28, no. 9, pp. 1343–1358, 2015.

[11] A. Verbic, M. Gorjanc, and B. Simoncic, "Zinc oxide for functional textile coatings: recent advances," *Coatings*, vol. 9, no. 9, p. 550, 2019.

[12] B. S. Butola and A. Kumar, "Green chemistry based in-situ synthesis of silver nanoparticles for multifunctional finishing of chitosan polysaccharide modified cellulosic textile substrate," *International Journal of Biological Macromolecules*, vol. 152, pp. 1135–1145, 2020.

[13] H. Y. Phin, Y. T. Ong, and J. C. Sin, "Effect of carbon nanotubes loading on the photocatalytic activity of zinc oxide/carbon nanotubes photocatalyst synthesized via a modified sol-gel method," *Journal of Environmental Chemical Engineering*, vol. 8, no. 3, p. 103222, 2020.

[14] K. F. Hasan, H. Wang, S. Mahmud, and C. Genyang, "Coloration of aramid fabric via in-situ biosynthesis of silver

nanoparticles with enhanced antibacterial effect," *Inorganic Chemistry Communications*, vol. 119, p. 108115, 2020.

[15] U. Manzoor, M. Islam, L. Tabassam, and S. U. Rahman, "Quantum confinement effect in ZnO nanoparticles synthesized by co-precipitate method," *Physica E: Low-dimensional Systems and Nanostructures*, vol. 41, no. 9, pp. 1669–1672, 2009.

[16] A. H. Alrajhi, N. M. Ahmed, M. al Shafouri, M. A. Almessiere, and A. ahmed Mohammed al-Ghamdi, "Green synthesis of zinc oxide nanoparticles using salvia officials extract," *Materials Science in Semiconductor Processing*, vol. 125, p. 105641, 2021.

[17] A. K. Dikshit, P. Banerjee, N. Mukherjee, and P. Chakrabarti, "Theoretical optimization of double dielectric back reflector layer for thin c-Si based advanced solar cells with notable enhancement in MAPD," *Superlattices and Microstructures*, vol. 149, p. 106747, 2021.

[18] M. Fiedot-Toboła, M. Ciesielska, I. Maliszewska et al., "Deposition of zinc oxide on different polymer textiles and their antibacterial properties," *Materials*, vol. 11, no. 5, p. 707, 2018.

[19] J. A. Delezuk, D. E. Ramírez-Herrera, B. Esteban-Fernández de Ávila, and J. Wang, "Chitosan-based water-propelled micromotors with strong antibacterial activity," *Nanoscale*, vol. 9, no. 6, pp. 2195–2200, 2017.

[20] S. Nourbakhsh, "Self-cleaning and antibacterial properties of ZnO nanoparticles on cotton fabric treated with maleic acid," *Materials Science*, vol. 27, no. 1, pp. 90–95, 2021.

[21] A. Yadav, V. Prasad, A. A. Kathe et al., "Functional finishing in cotton fabrics using zinc oxide nanoparticles," *Bulletin of Materials Science*, vol. 29, no. 6, pp. 641–645, 2006.

[22] N. A. Ibrahim, A. A. Nada, B. M. Eid, M. Al-Moghazy, A. G. Hassabo, and N. Y. Abou-Zeid, "Nano-structured metal oxides: synthesis, characterization and application for multifunctional cotton fabric," *Advances in Natural Sciences: Nanoscience and Nanotechnology*, vol. 9, no. 3, p. 035014, 2018.

[23] R. Pandimurugan and S. Thambidurai, "UV protection and antibacterial properties of seaweed capped ZnO nanoparticles coated cotton fabrics," *International Journal of Biological Macromolecules*, vol. 105, Partt 1, pp. 788–795, 2017.

[24] J. A. Shirley, S. E. Florence, B. S. Sreeja, G. Padmalaya, and S. Radha, "Zinc oxide nanostructure-based textile pressure sensor for wearable applications," *Journal of Materials Science: Materials in Electronics*, vol. 31, no. 19, pp. 16519–16530, 2020.

[25] S. M. Costa, D. P. Ferreira, A. Ferreira, F. Vaz, and R. Fangueiro, "Multifunctional flax fibres based on the combined effect of silver and zinc oxide (Ag/ZnO) nanostructures," *Nanomaterials*, vol. 8, no. 12, p. 1069, 2018.

[26] M. T. Noman, N. Amor, M. Petru, A. Mahmood, and P. Kejzlar, "Photocatalytic behaviour of zinc oxide nanostructures on surface activation of polymeric Fibres," *Polymers*, vol. 13, no. 8, p. 1227, 2021.

[27] M. S. Choi, H. G. Na, G. S. Shim et al., "Simple and scalable synthesis of urchin-like ZnO nanoparticles via a microwave-assisted drying process," *Ceramics International*, vol. 47, no. 10, pp. 14621–14629, 2021.

[28] A. H. Patil, S. A. Jadhav, V. B. More et al., "A new method for single step sonosynthesis and incorporation of ZnO nanoparticles in cotton fabrics for imparting antimicrobial property," *Chemical Papers*, vol. 75, no. 3, pp. 1247–1257, 2021.

[29] D. Asmat-Campos, D. Delfín-Narciso, and L. Juarez-Cortijo, "Textiles functionalized with ZnO nanoparticles obtained by chemical and green synthesis protocols: evaluation of the type of textile and resistance to UV radiation," *Fibers*, vol. 9, no. 2, p. 10, 2021.

[30] M. Turemen, A. Demir, and Y. Gokce, "The synthesis and application of chitosan coated ZnO nanorods for multifunctional cotton fabrics," *Materials Chemistry and Physics*, vol. 268, p. 124736, 2021.

[31] S. Abel, L. Tesfaye Jule, F. Belay et al., "Application of Titanium Dioxide Nanoparticles Synthesized by Sol-Gel Methods in Wastewater Treatment," *Journal of Nanomaterials*, vol. 2021, p. 6, 2021.

[32] D. Kundu, C. Hazra, A. Chatterjee, A. Chaudhari, and S. Mishra, "Extracellular biosynthesis of zinc oxide nanoparticles using _Rhodococcus pyridinivorans_ NT2: Multifunctional textile finishing, biosafety evaluation and _in vitro_ drug delivery in colon carcinoma," *Journal of Photochemistry and Photobiology B: Biology*, vol. 140, pp. 194–204, 2014.

[33] A. Javed, J. Wiener, A. Tamuleviciene et al., "One step in-situ synthesis of zinc oxide nanoparticles for multifunctional cotton fabrics," *Materials*, vol. 14, no. 14, p. 3956, 2021.

[34] M. Afsharpour and S. Imani, "Preventive protection of paper works by using nanocomposite coating of zinc oxide," *Journal of Cultural Heritage*, vol. 25, pp. 142–148, 2017.

[35] M. Wasim, M. R. Khan, M. Mushtaq, A. Naeem, M. Han, and Q. Wei, "Surface modification of bacterial cellulose by copper and zinc oxide sputter coating for UV-resistance/antistatic/antibacterial characteristics," *Coatings*, vol. 10, no. 4, p. 364, 2020.

[36] S. Preethi, A. Anitha, and M. Arulmozhi, "A comparative analysis of the properties of zinc oxide (ZnO) nanoparticles synthesized by hydrothermal and sol–gel methods," *Indian Journal of Science and Technology*, vol. 9, no. 40, pp. 1–6, 2016.

[37] G. Baskar, J. Chandhuru, K. S. Fahad, and A. S. Praveen, "Mycological synthesis, characterization and antifungal activity of zinc oxide nanoparticles," *Asian Journal of Pharmacy and Technology*, vol. 3, no. 4, pp. 142–146, 2013.

[38] M. D. Jayappa, C. K. Ramaiah, M. A. P. Kumar et al., "Green synthesis of zinc oxide nanoparticles from the leaf, stem and in vitro grown callus of Mussaenda frondosa L.: characterization and their applications," *Applied Nanoscience*, vol. 10, no. 8, pp. 3057–3074, 2020.

[39] B. Siripireddy and B. K. Mandal, "Facile green synthesis of zinc oxide nanoparticles by _Eucalyptus globulus_ and their photocatalytic and antioxidant activity," *Advanced Powder Technology*, vol. 28, no. 3, pp. 785–797, 2017.

[40] G. Sangeetha, S. Rajeshwari, and R. Venckatesh, "Green synthesis of zinc oxide nanoparticles by _aloe barbadensis miller_ leaf extract: Structure and optical properties," *Materials Research Bulletin*, vol. 46, no. 12, pp. 2560–2566, 2011.

[41] M. M. AbdElhady, "Preparation and characterization of chitosan/zinc oxide nanoparticles for imparting antimicrobial and UV protection to cotton fabric," *International Journal of Carbohydrate Chemistry*, vol. 2012, Article ID 840591, 6 pages, 2012.

[42] S. M. Taghizadeh, N. Lal, A. Ebrahiminezhad et al., "Green and economic fabrication of zinc oxide (ZnO) nanorods as a broadband UV blocker and antimicrobial agent," *Nanomaterials*, vol. 10, no. 3, p. 530, 2020.

[43] S. Abel, J. L. Tesfaye, R. Shanmugam et al., "Green synthesis and characterizations of zinc oxide (ZnO) nanoparticles using

aqueous leaf extracts of coffee (Coffea arabica) and its application in environmental toxicity reduction," *Journal of Nanomaterials*, vol. 2021, Article ID 3413350, 6 pages, 2021.

[44] A. Degefa, B. Bekele, L. T. Jule et al., "Green Synthesis, Characterization of Zinc Oxide Nanoparticles, and Examination of Properties for Dye-Sensitive Solar Cells Using Various Vegetable Extracts," *Journal of Nanomaterials*, vol. 2021, Article ID 3941923, 9 pages, 2021.

[45] A. M. Awwad, M. W. Amer, N. M. Salem, and A. O. Abdeen, "Green synthesis of zinc oxide nanoparticles (ZnO-NPs) using Ailanthus altissima fruit extracts and antibacterial activity," *Chemistry International*, vol. 6, no. 3, pp. 151–159, 2020.

[46] T. I. Shaheen, M. E. El-Naggar, A. M. Abdelgawad, and A. Hebeish, "Durable antibacterial and UV protections of in situ synthesized zinc oxide nanoparticles onto cotton fabrics," *International Journal of Biological Macromolecules*, vol. 83, pp. 426–432, 2016.

[47] R. K. Sharma and R. Ghose, "Synthesis of zinc oxide nanoparticles by homogeneous precipitation method and its application in antifungal activity against _Candida albicans_," *Ceramics International*, vol. 41, no. 1, pp. 967–975, 2015.

Hindawi
Journal of Nanomaterials
Volume 2021, Article ID 4927607, 9 pages
https://doi.org/10.1155/2021/4927607

Research Article

Impact of Big Data Analysis on Nanosensors for Applied Sciences Using Neural Networks

S. Shitharth,[1] **Pratiksha Meshram**,[2] **Pravin R. Kshirsagar**,[3] **Hariprasath Manoharan**,[4] **Vineet Tirth**,[5,6] **and Venkatesa Prabhu Sundramurthy**[7]

[1]*Department of CSE, Vardhaman College of Engineering, Hyderabad, India*
[2]*Department of IT, SVKM's NMIMS, Mukesh Patel School of Technology Management & Engineering, India*
[3]*Department of ECE, AVN Institute of Engineering & Technology, Hyderabad, India*
[4]*Department of Electronics and Communication Engineering, Panimalar Institute of Technology, Poonamallee 600123, Chennai, India*
[5]*Mechanical Engineering Department, College of Engineering, King Khalid University, 61411 Abha, Asir, Saudi Arabia*
[6]*Research Centre for Advanced Materials Science (RCAMS), King Khalid University, P.O. Box 9004, 61413 Abha, Asir, Saudi Arabia*
[7]*Department of Chemical Engineering, Addis Ababa Science and Technology University, Ethiopia*

Correspondence should be addressed to Venkatesa Prabhu Sundramurthy; venkatesa.prabhu@aastu.edu.et

Received 6 August 2021; Revised 25 August 2021; Accepted 28 August 2021; Published 21 September 2021

Academic Editor: Lakshmipathy R

Copyright © 2021 S. Shitharth et al. This is an open access article distributed under the Creative Commons Attribution License, which permits unrestricted use, distribution, and reproduction in any medium, provided the original work is properly cited.

In the current-generation wireless systems, there is a huge requirement on integrating big data which can able to predict the market trends of all application systems. Therefore, the proposed method emphasizes on the integration of nanosensors with big data analysis which will be used in healthcare applications. Also, safety precautions are considered when this nanosensor is integrated where depth and reflection of signals are also observed using different time samples. In addition, to analyze the effect of nanosensors, six fundamental scenarios that provide good impact on real-time applications are also deliberated. Moreover, for proving the adeptness of the proposed method, the results are equipped in both online and offline analyses for investigating error measurement, sensitivity, and permeability parameters. Since nanosensors are introduced, the efficiency of the projected technique is increased by implementing media access control (MAC) protocol with recurrent neural network (RNN). Further, after observing the simulation results, it is proved that the proposed method is more effective for an average percentile of 67% when compared to the existing methods.

1. Big Data and Nanotechnology: An Introduction

The introduction of wireless sensors in human life has changed the entire life activities of humans as they can able to monitor any parameters that are relevant to different applications in their remote locations. However, as ages grow, the size of each component becomes very small which changed the standard networks to nanonetworks, and in recent time, industry has created a great revolution with such nanoparticles. In addition, the working functionality of nanosensors is equivalent to standard sensors, thus providing high reliability, security, and performance. Since the electronic community is growing in a fast manner, it is necessary to update each element that is present inside it. Therefore, nanotechnology paves a new way of monitoring parameters that are relevant to different applications.

One of the important features of nanomaterials is that it can able to store huge amount of data when compared to standard networks. Moreover, nanotechnology is having a wide surface for interacting with different materials; thus, if any blockage occurs, then materials cannot interact with surrounding materials. However, only surface can interact with other materials where it provides a new way of creating opportunities in medical field with system on chip-enabled technologies that can minimize the damage of tissues inside

the human body. Furthermore, these nanosensors provide great advantage as they are flexible, stretchable, and bendable; thus, it can be easily integrated with any applications using the Internet of Things.

2. Literature Survey

In this section, recent literatures that provide relevant information about big data with nanosensors are examined and their pros and cons are discussed. The convention of nanodevice has been increased in current-generation networks where a separate effect on piezoelectric devices has been analyzed [1] using semiconductor devices. This type of research enhancement provides a good opportunity for enhancing the design and regulation of nanosensors for different applications where day-to-day problems can be easily solved. By using the underlying concept of nanosensors, both effect and characterization of silver nanoparticles have been analyzed [2] using physical and chemical properties of materials. This type of enhanced introduction provides valuable information about different environmental threats and way to control such threats. Even intrabody research on nanosensors has been considered to determine the amount of electromagnetic radiation with difference channel capacity [3]. Such type of networks can able to identify different diseases within a short span of time. In recent time, there is huge necessity of using nanosensors to identify coronavirus disease as it has spread over the entire country [4]. Since big data is needed for this type of analysis, a knowledge decision-making system is required. In addition, since big data varies from day-to-day as the number of patients is higher, a data analysis tool can be used. But when data tools are introduced, a manual time of operation is required which increases the time of estimation. Also, in order to analyze the effect of big data in another application that differs from healthcare, a social media consumer behavior with high number of data has been provided [5]. The major reason of experimentation is to use the same preprocessing technique where more number of data errors can be avoided. However, the model has not been established under real-time operations because it is tested with only 20 percent of testing data. The authors [6] have also investigated about different characteristics of big data with six different techniques that include collaborative, associative, high dimensional, deep, precision, and separation where geometrical associations of different parameters have been integrated.

Since more parameters are represented in all six different types, it will be beneficial to design the simulation if a less parameter is used. Moreover, if big data conception is evaluated, then, mathematical data have to run into a simulation model; therefore, better understanding about insight mathematics in interdisciplinary applications should be known [7]. By using Laplace transform and eigenvalue problems, the nanosensors can be applied for detection of different diseases, and finally, clustering of data should be processed. But only basic problems can be identified using clustering analysis; however, design of nanosensors is not possible using such techniques. Instead of such basic insights, an edge intelligence model can be designed using deep learning methods [8]. This type of advanced intelligence model uses Raspberry Pi as a hardware platform which provides much high storage of data and it can even be expanded. Further, the same model can be extended when a network is rationalized to sixth generation with high data security measures. The same method can be used for monitoring the activities of different persons [9] where data can be collected with blending techniques. In the aforementioned method, a distributed database has to be used by following hierarchy of data.

A survey on big data analysis has been sort out by including current technologies, opportunities, and different challenges that support the expansion of optimum techniques using nanosensors [10]. In the aforementioned method, a continuous life cycle methodology has been provided for big data where huge growth can be perceived. Even though information is extracted correctly, usage of big data in various applications still remains as an incomplete trail. Therefore, to confer the application part introduced, an expression method has been introduced that works with the help of big data using machine learning algorithm [11] where in each step, a search process has been activated. Further, logical reasoning is also presented that determines the widespread feature of application process. Another application is emphasized on healthcare technologies which are used to detect the presence of coronavirus in many conflict zones [12–14]. However, only challenges have been discussed, but diagnosis and early treatment methods are not projected which leads to high state of confusion in application sequence. Since basic resources are introduced, it will not be efficient to detect the presence of terminal diseases by using investigation panes. Furthermore, Vitabile et al. [15] suggest a natural method using artificial intelligence for all healthcare applications where the perception of locating affected individuals has been examined with big data storage [16, 17]. In these case studies, it is possible to evaluate the presence of diseases using wireless sensors, but if the same has been changed to nanosensors, then, accuracy of identical process will increase to a higher extent [13, 14].

In the present day-to-day changes, new innovations in healthcare diligence are much important since the growth of human life is increasing with high potential risks [18]. In line with the above concern, the authors have addressed the necessity of big data in healthcare applications which can able to save the life of each individual. Even Punith Kumar and Pasha [19] incorporated a model that combines the data from different sources where a significant impact on distribution of materials to healthcare industry has been identified. The major source of data for the abovementioned method will grow progressively since physiological data has been integrated. In view of an imaginary aspect, more valuable information is gathered from Shu [20] which provides a high impact on human life with a systematic review process. Since big data analytics is not developed with corresponding software, a standard mechanism for retrieving the sensitive data has been provided.

3. Research Gap and Motivation

All the literatures have used different formulations for monitoring the condition of every individual, but all the methods

have their individual drawbacks. Also, there are few measures that are able to decipher these challenging errands. Therefore, there is a need to overcome all the drawbacks by combining different methods. Even a lot of authors have used different algorithms, but only some of the projected algorithms delivered accurate results. In addition, most of the researchers have considered only standard sensors for evaluation purpose without introducing nanosensors.

In this article, the authors have formulated a new flanged method using big data for monitoring the health condition of each individual with nanosensors and different parameters are monitored. The results are observed via online monitoring system and they are finally plotted using MATLAB. Also, an efficient RNN algorithm has been implemented with the objective parameters.

3.1. Objectives. The proposed work on nanosensors to analyze the impact on the body of different individuals will focus primarily on the following three major objectives.

(i) To examine big data incorporation using nanosensors for use in medical applications where more number of infections from different people can be identified in an easy way

(ii) To reduce the error measurements of standard sensors by introducing nanomaterials that can be safely inserted in the human body

(iii) To acquaint with RNN and noiseless channel protocols for transferring big data by creating an individual application

3.2. System Model. In this section, a mathematical model of big data analysis for multimedia networks with wireless sensors has been designed. The major fragment of this model consists of a linear interpreter where data points are implemented for receiving different variables that provides high-end support for implementation of sensors. Whenever data points are located, then, information about individuals crossing a particular sensor point will be immediately monitored without delay. The mathematical model for prediction of data using a linear method can be given as follows:

$$l_i = \omega_1 + \omega_2 \alpha_{i1} + \cdots + \omega_i \alpha_{ii}, \tag{1}$$

where $\omega_1 \cdots \omega_n$ denotes that data will be collected in a single vector matrix which is of same size. $\alpha_{i1} \cdots \alpha_{ii}$ indicates the dot product of each variable at each data point.

Equation (1) denotes that dot product of each variable should be multiplied with variable values where data size should be uniform in length. The main reason for indication of uniform length is that behavior of each individual should be known within a short period of time. Since the proposed method focuses on detection of various infectious diseases, it is necessary to create a hub of central database where each station will be connected with each other using a high-end server. For this high-end server, the sensor needs to be galvanized and it can be represented using Equation (2).

$$\delta(i) = \begin{cases} 0 \text{ if error} \geq 0, \\ 1 \text{ if error} < 0, \end{cases} \tag{2}$$

where $\delta(i)$ indicates that input function can be transformed and activation will be performed based on input error values.

From Equation (2), all error values of incorporated sensors should be less than zero which indicates that sensors can be activated within a less period of time. If more nanoparticles are found, it is very difficult for sensors to detect them, and as a result, the error values are much higher. Therefore, sensitivity parameter for percentage of errors can be given as follows:

$$S_i = \frac{(A_0 - A_i)/A_{0i}}{P_r - P_i}, \tag{3}$$

where A_0 and A_i denotes the measurement of area that is present under 0^{th} and i^{th}curve. P_r and P_i represents the reference and investigated parametric values.

Equation (3) indicates that difference between values under area of curve between 0^{th} and i^{th} sensors should be measured and it should be alienated under a complete area. Also, the reference parametric and investigated parametric values should be considered for making decision on precise sensitivity values. If sensitivity values are calculated appropriately, then, permeability values of sensors can be measured using the following equation:

$$\vartheta = \vartheta_0 (1 - S_i) \vartheta_i + S_i \left(\frac{\mu_0}{\mu_i} \right), \tag{4}$$

where ϑ_0 and ϑ_i denote the maximum ability of nanosensing signals that can penetrate inside the human body. μ_0 and μ_i represent the initial and absolute void volumes of nanoparticles that can be accessible from either end of sensors.

It is to be eminent that from Equation (4) since the nanosensors are installed inside the human body, the signal permeability should be minimized without causing any effect to other parts of the system. In addition, to provide a clear view about nanoparticle transport, Equation (5) is framed.

$$T(i) = (\epsilon_i C_i D_i \times \nabla_i) + R_i, \tag{5}$$

where ϵ_i, C_i, and D_i denote the saturation, concentration, and dispersion states of sensors. R_i represents the rate of failure of detection of sensors.

Equation (5) indicates that resistance temperature detector will be used for installing sensors for measuring thermal dispersion. Moreover, net rate loss in case of failure detection will also be monitored. This indicates that saturation, concentration, and dispersion values have to be calculated in equal proportion for proper discovery of nanoparticles in the human body. In case if there is a situation that more number of nanosensors needs to be installed, then, distance of measurement should be known. This can be formulated using the following equation:.

$$d_i = \sum_{i=1}^{n} \frac{t_i * s_i}{2}, \tag{6}$$

where t_i and s_i denote the time of measurement and sound of air which is equal to 340 m/s.

Thus, the objective function can be framed using Equations (1)–(5) as follows:

$$O_i = \min \sum_{i=1}^{n} \delta_i S_i \vartheta_i. \tag{7}$$

Equation (7) indicates the minimization problem where a tri-objective case study has been formed using minimized values of error, sensitivity, and permeability values. If the aforementioned values are minimized, then, big data analysis using linear prediction can be evaluated and nanoparticles that are present inside individuals can be easily identified using nanosensors.

4. Optimization Algorithm

In this section, set of rules for data transfer process using nanosensors and corresponding algorithm that can support the protocols and incorporated system model has been deliberated. Since nanoparticles are evaluated, media access control (MAC) protocols are used. Also, the channels that are used for sensor estimation should be free from noise which leads to minimization of error. Therefore, a sliding window protocol has been considered where window size will be selected and corresponding data will be sent by checking the sequence number of data. Also, a pipelining mechanism should be implemented for selecting the transmitter window size and its efficiency can be mathematically given as follows:

$$E_i = \sum_{i=1}^{n} \frac{1}{(1+2)(t_s/t_t)}, \tag{8}$$

where t_s and t_t denote the time period of sending and receiving frames.

If efficiency that is provided in Equation (8) is augmented, then, data transfer process throughput will be increased with higher number of bits. Therefore, the number of required bits for transferring information through nanosensors can be given as follows:

$$b_i = \log_2(N_i + 1), \tag{9}$$

where N_i represents the total number of packets that are present for data transfer process in layer 2.

After determining the efficiency of MAC protocol, corresponding vector size has to be fixed and it can be completed using a type of neural network which is termed as recurrent neural network (RNN). The major reason for using RNN in the proposed method is that there is no size determination when inputs are given to nanosensors.

Since big data related to medical care of the human body is analyzed, it is necessary to remember all past data and decisions should be compared with previous one. The main advantage of RNN in the proposed method is that since big data is needed for evaluation purpose, there is a requisite that previous inputs need to be stored. Hence, RNN has been introduced where information about previous inputs that are supplied to nanosensors have been stored with bidirectional data transfer mode. Moreover, pixels of all neighborhood layers can be extended since many-to-many communication is possible in RNN [21]. The aforementioned process will be added as an advantage if RNN is implemented. In addition, precise decision can be made within a short period of time by using less number of parameters since the parameters can be shared in RNN. Thus, the parametric formulations can be given as follows:

$$\Delta(i) = \sum_{i=1}^{n} \widehat{\Delta_{\text{in}}} (\log_2 \Delta_{\text{in}}), \tag{10}$$

where $\widehat{\Delta_{\text{in}}}$ and Δ_{in} denote the past and previous prediction probability values of RNN.

Since the nanosensors are injected inside the body, a bidirectional full duplex communication is established. Therefore, an internal context is required for such transmission process and it can be given using conventional forward propagation equations as follows:

$$\widehat{\Delta_i} = \sum_{i=1}^{n} W_{\text{in}} h_{\text{in}}, \tag{11}$$

where W_{in} denotes the corresponding weight that is present between input and output states. h_{in} represents the hidden layer which is acting as a channel between input and output states.

Since different weight vectors and layers are introduced with wireless sensing device, it is necessary to optimize the cost of the proposed method by integrating Equation (6) as follows:

$$\complement_i = \sum_{i=1}^{n} [\Delta_i \wedge (W_i - h_i)]^2. \tag{12}$$

Equation (11) indicates that cost function is calculated using difference between corresponding weights and hidden layer weight which is reproduced with propagation values. For a clear view of integration, a step-by-step evaluation of the proposed method is necessary. Therefore, a flow chart of the proposed model is given in Figure 1.

5. Results and Discussions

In this section, analysis of big data has been carried out using recurrent neural networks where MAC has been applied by considering a noiseless channel. In addition, most of the literatures [1–12, 15, 18–20] have only measured the performance of standard sensors, but nanosensors have been developing in current trends for all applications. Therefore,

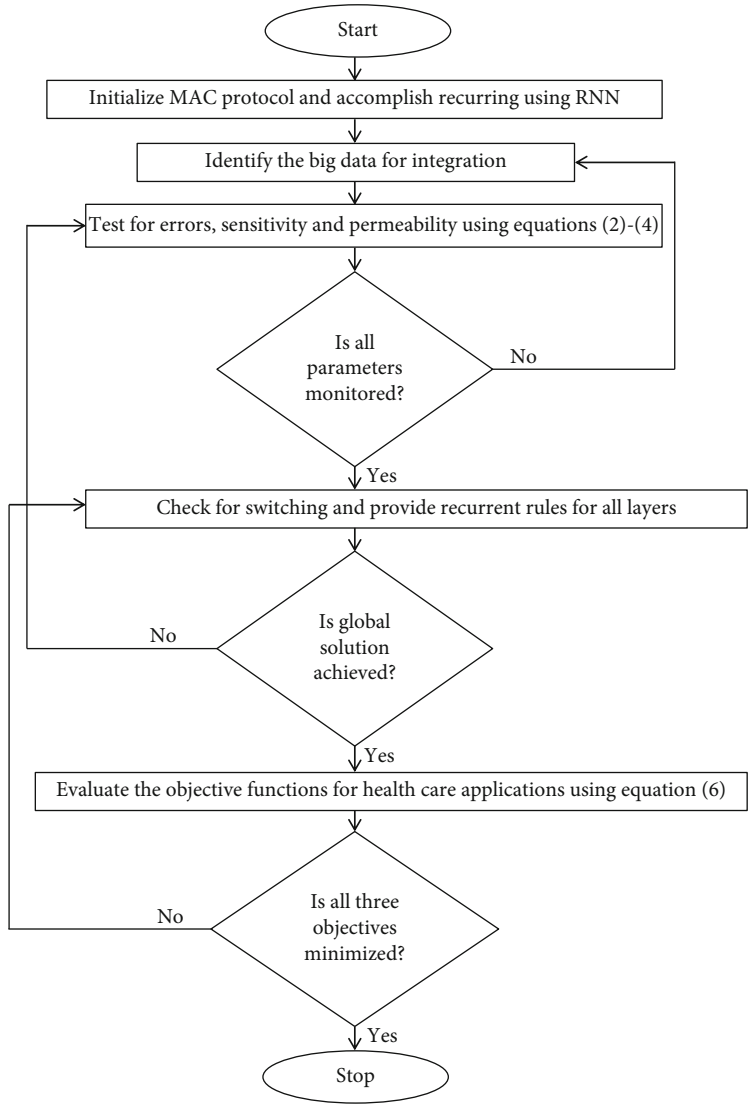

Figure 1: Flow chart of the proposed RNN with MAC.

integration of nanosensors and their performance is measured using six significant scenarios as follows:

(1) Scenario 1: Minimization of error

(2) Scenario 2: Level of sensitivity

(3) Scenario 3: Intricacy of permeability

(4) Scenario 4: Cost of implementation

(5) Scenario 5: Energy consumption of nodes

(6) Scenario 6: Response time of connected signals

5.1. Scenario 1. In this scenario, accuracy and prediction level of nanosensors have been deliberated where a mathematical model is used for calculating the identified error values as given in Equation (2). Since the accuracy of prediction is much important, nanosensors should produce the error rate and it should not contain any negative values. If negative values are present, then it indicates that accuracy is much lesser and immediate action has to be taken to reduce the errors. Since nanosensors are mostly used in healthcare application, it should be installed at proper position to provide high accurate values. In the proposed method, error values are established by comparing the existing big data with probable values using node red as an online platform. The same values have been considered and they are plotted in MATLAB for offline analysis.

Figure 2 shows the error values of nanosensors which are measured in nanometers. For detecting the accuracy, 100-500 nanosensors are considered and their corresponding ranges are measured. After calculating the sensing ranges, the sensed values are compared with existing big data that is stored already. From the sensed values, difference in error values is distinguished and it can be observed that negative value of error is present in the existing method which indicates that accuracy of detection is much lesser when compared to the projected method. For example, if sensing range is 20000 and the number of nanosensors in this case is 200, then, the projected method provides 3 nm as

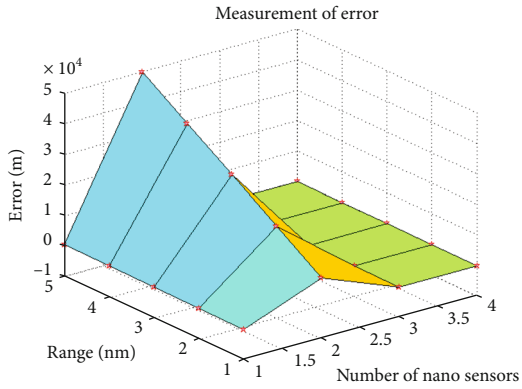

Figure 2: Amount of error in harmony with arrays.

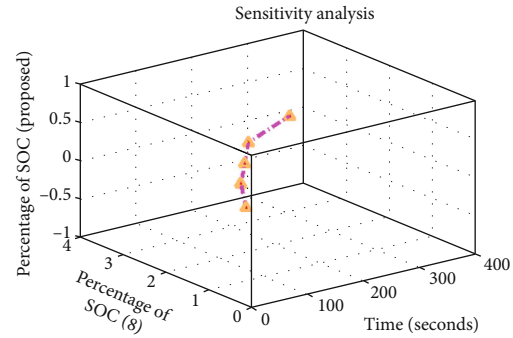

Figure 3: Percentage of SOC with reverence to time.

maximum error range which can be neglected since percentage of recognition is much lesser. But for the same circumstance, the existing method [11] provides negative error value which is detected as -2. This proves that accuracy of the proposed method is much higher when nanosensors are installed in healthcare applications.

5.2. Scenario 2. Once error values are calculated in the next phase level of sensitivity, it should be known for achieving a steady-state operating conditions. If error values are much higher, then, sensitivity level of nanosensors will be protracted which affects both wavelength and phase. Therefore, to make all data to travel at same wavelength, it is necessary to reduce the sensitivity level of nanosensors. In addition, if sensitivity level is much higher, then, difficulty in sensing the targets will be much higher for all indoor applications. In the proposed method, the sensitivity level of nanosensors is calculated using Equation (3) by considering an area curve using orientation of big data. The observed operational values are directly plotted in MATLAB for providing accurate analysis on sensitivity case study.

Figure 3 deliberates the observed compassion values of nanosensors which are calculated by considering different time periods. In the scenario, time period is considered since at proper response time, only the nanosensors will provide sensitivity outcomes. Moreover, for incorporated nanosensors, error values are lesser; therefore, as a consequence, the sensitivity values are also lesser. For example, if the response time period of nanosensor is 180 seconds, then, the proposed method provides less sensitive value which is observed to be 0.2 percent of original datagram. But for same time period, the existing method [11] provides high sensitivity value which is observed to be 2.5 percent which is much higher than the proposed method.

5.3. Scenario 3. In this scenario, the quality of installed nanosensors is observed and it is calculated using Equation (4). Since the proposed method provides a solution to install nanosensor in the human body, it is necessary to evaluate the penetration level. If a sensor is installed in the human body, then, it should have low permeability limits as higher reflection of sensors deep inside the body will cause a serious damage and it should be avoided. Even though nanosensors can be easily injected in the human body due to its small size, the depth of installation should be identified. In this scenario, nanosensors are installed at 1 mm depth and corresponding permeability is simulated and shown in Figure 4.

From Figure 4, it can be observed that different frequency ranges of signals are considered for 1 mm depth which varies between 1 and 200 GHz. The permeability level for corresponding frequency ranges is indicated in Henry per meter (H/m) and it should be less than 100. This value is obtained from prespecified big data, and it is evident from simulation result that the proposed method provides permeability values within 100. For example, if maximum frequency range of nanosensor is 200 GHz, then, permeability of the existing method is found to be 99 H/m which is almost reaching the settled maximum limit. But for same 200 GHz frequency range at a depth of 1 mm, the proposed method provided permeability values which are equal to 78 H/m. This proves that using the proposed methodology, nanosensors can be installed at less propagation limits.

5.4. Scenario 4. The cost of installing nanosensors is an important case study, and it should be conversed in this scenario as RNN is considered in the projected method. Even though a lot of sensors are used in real-time application, it should provide sustenance to each individual in terms of quality, quantity, and cost. If cost of installation is much higher, then, most of the individuals will not purchase and real-time application of nanosensors will be reduced. Therefore, in this scenario, the cost values are simulated by installing the nodes of corresponding areas which are similar to the areas considered in scenario 2. The cost values are calculated from Equation (12) and the same has been plotted in Figure 5.

From Figure 5, it can be observed that implementation of cost using different weights in all layers varies and it is not remaining constant as the number of sensor nodes varies. Therefore, the number of nodes is considered between 100 and 500 where for each sensor node, corresponding built-up and setting up costs are considered. Even during cost implementation using RNN, the proposed method provides better performance; for example, if the number of sensor nodes is considered to be 300, then, total cost of implementation will be 29800 which is provided in INR. But for the

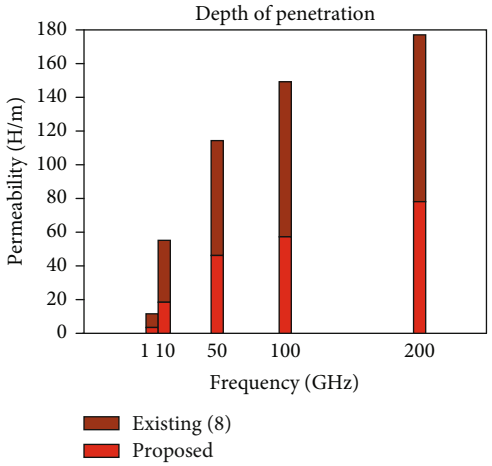

Figure 4: Competence of dissemination.

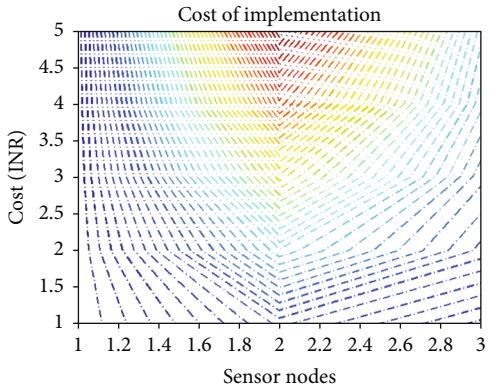

Figure 5: Implementation cost of nanosensors with RNN.

same number of nodes, the existing method [11] provides 69000 as installation cost for all layers and weights are much higher. Also, the weights installed in the existing method are not applicable to all applications; therefore, the weights can be reduced as complexity of process in big data is not considered.

5.5. Scenario 5. Since nanosensors are introduced for monitoring different parameters, it is indispensable to understand the amount of energy consumed by each node. Therefore, in this scenario, energy consumed by each node is observed which is measured in Joules. Even though energy consumption of all branches should remain same, it will always vary due to environmental conditions and the way of installation. In addition, if few sensors are integrated, then, energy consumption can be higher as expected, but if more number of sensors are implemented, then, it is enforced that consumption of energy by each node should be reduced. Therefore, consumption of energy by each node is observed in real time using online analysis and it is plotted using MATLAB in Figure 6.

From Figure 6, it can be observed that n number of nodes from 0 to 4000 is considered for standard evaluation of nanosensors. The data cursor part represents that best

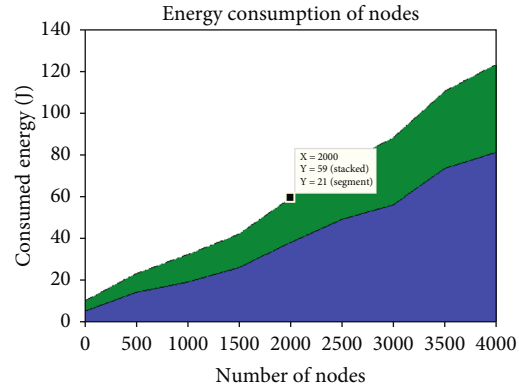

Figure 6: Consumed energy of nodes.

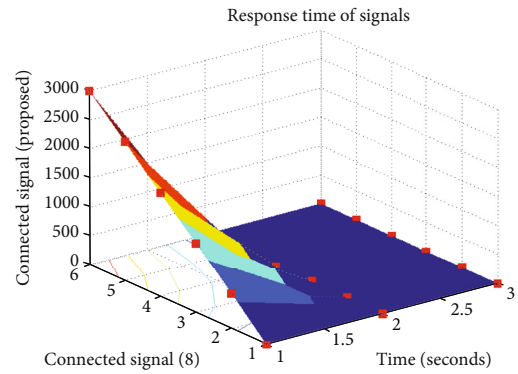

Figure 7: Response time of connected signal.

segments are observed where more amount of energy is saved which leads to reduction in wastage of energy. For example, if the number of nodes is 3500, then, energy consumed by the proposed method is 37 Joules, whereas with the same number of nodes, the existing [8] method consumed 73 Joules which is much higher than expected energy. As mentioned previously, if more number of nanosensors is implemented, then, energy consumption should be lesser which is proved by incorporating the proposed method.

5.6. Scenario 6. To detect the signals that are distributed in nanosensors, response time should be calculated which is separated into transient and steady-state response time. For observing different parameters, it is always required that response time should be much faster so that decisions can be made very quickly and in turn it will be sent to central operator since the proposed method uses only single hop network. For a virtuous network to achieve a steady-state response, the values should be greater than 1. If the value drops below the prescribed value, then, transient response will be observed which makes the network to go into foulest state.

Figure 7 provides information on simulation results that are plotted for observed response time in seconds. It can be observed in Figure 7 that when signals are passed in nanosensors within the corresponding response time, a steady-

state response with values greater than 1 can be observed. For example, if response time is 600 seconds, then, steady-state response is observed which is equal to 1.2. Then, after this corresponding period, a constant steady-state response has been observed which makes the performance and reliability of the network to be higher.

6. Conclusions

In this proposed work, applications of big data analysis using nanosensors have been procreated by considering six different scenarios. In future, big data plays a vital role and is needed for providing training to all machines. Therefore, in this article, a RNN algorithm is considered with MAC protocol for determining the size of nanosensors to inject it in the human body. In addition, complexity of big data process is much higher and it is not considered, but weights of all hidden layers have been added. If nanosensors are applied in healthcare applications, then, all parametric values can be easily monitored at remote locations and this type of sensors will provide more efficiency when compared to standard sensors as nanosensors are having the ability to be installed inside the body but penetration level of signals is much lesser. Moreover, to prove the efficiency of the proposed method, simulation results are carried out in both online and offline where results prove that the proposed method using big data, RNN, and MAC is much efficient when compared to the existing methods.

Data Availability

There is no data used to support this study.

Conflicts of Interest

The authors declare that they have no conflicts of interest.

Acknowledgments

The authors thankfully acknowledge the Deanship of Scientific Research, King Khalid University, Abha, Asir, Kingdom of Saudi Arabia, for funding the project under the grant number (R.G.P1./74/42).

References

[1] R. Bao, J. Tao, C. Pan, and Z. L. Wang, "Piezophototronic effect in nanosensors," *Small Science*, vol. 1, no. 6, article 2000060, 2021.

[2] S. Dawadi, S. Katuwal, A. Gupta et al., "Current research on silver nanoparticles: synthesis, characterization, and applications," *Journal of Nanomaterials*, vol. 2021, Article ID 6687290, 23 pages, 2021.

[3] M. A. Akkaş, "Nano-sensor modelling for intra-body nano-networks," *Wireless Personal Communications*, vol. 118, no. 4, pp. 3129–3143, 2021.

[4] T. Liu, T. Wu, M. Wang, M. Fu, J. Kang, and H. Zhang, "Recurrent neural networks based on LSTM for predicting geomagnetic field," in *2018 IEEE International Conference on Aerospace Electronics and Remote Sensing Technology (ICARES)*, pp. 56–60, Bali, Indonesia, 2018.

[5] P. Liu, X. Qiu, and H. Xuanjing, "Recurrent neural network for text classification with multi-task learning," 2016, http://arxiv.org/abs/1605.05101.

[6] P. Galetsi, K. Katsaliaki, and S. Kumar, "Big data analytics in health sector: theoretical framework, techniques and prospects," *International Journal of Information Management*, vol. 50, pp. 206–216, 2020.

[7] G. Chen and M. Islam, "Big data analytics in healthcare," in *Proc. -2019 2nd Int. Conf. Saf. Prod. Informatiz. IICSPI 2019*, pp. 227–230, China, 2019.

[8] S. L. Garapati and S. Garapati, "Application of big data analytics: an innovation in health care," *International Journal of Computational Intelligence Research*, vol. 14, no. 1, pp. 15–27, 2018.

[9] I. E. Agbehadji, B. O. Awuzie, A. B. Ngowi, and R. C. Millham, "Review of big data analytics, artificial intelligence and nature-inspired computing models towards accurate detection of COVID-19 pandemic cases and contact tracing," *International Journal of Environmental Research and Public Health*, vol. 17, no. 15, p. 5330, 2020.

[10] O. B. da'ar, M. Haji, and H. Jradi, "Coronavirus disease 2019 (COVID-19): potential implications for weak health systems and conflict zones in the Middle East and North Africa region," *The International Journal of Health Planning and Management*, vol. 35, no. 5, pp. 1240–1245, 2020.

[11] R. Hu, H. M. Zhao, and H. Xu, "A big data intelligence analysis expression method based on machine learning," *Cluster Computing*, vol. 22, no. S4, pp. 8017–8024, 2019.

[12] M. Wada and N. Tanaka, "Infrared spectroscopy of metal-MgO single crystalline composite films," *Japanese Journal of Applied Physics*, vol. 29, Part 2, 8, pp. L1497–L1499, 1990.

[13] P. R. Kshirsagar, H. Manoharan, F. Al-Turjman, and K. Kumar, "Design and testing of automated smoke monitoring sensors in vehicles," *IEEE Sensors Journal*, 2020.

[14] P. R. Kshirsagar and S. G. Akojwar, "Prediction of neurological disorders using optimized neural network," in *2016 International Conference on Signal Processing, Communication, Power and Embedded System (SCOPES)*, pp. 1695–1699, Paralakhemundi, India, 2016.

[15] S. Vitabile, M. Marks, D. Stojanovic et al., *Medical Data Processing and Analysis for Remote Health and Activities Monitoring*, Springer International Publishing, 2019.

[16] H. Manoharan, Y. Teekaraman, P. R. Kshirsagar, S. Sundaramurthy, and A. Manoharan, "Examining the effect of aquaculture using sensor-based technology with machine learning algorithm," *Aquaculture Research*, vol. 51, no. 11, pp. 4748–4758, 2020.

[17] S. Sundaramurthy, C. Saravanabhavan, and P. Kshirsagar, "Prediction and classification of rheumatoid arthritis using ensemble machine learning approaches," in *2020 International Conference on Decision Aid Sciences and Application (DASA)*, pp. 17–21, Sakheer, Bahrain, 2020.

[18] S. U. Amin and M. S. Hossain, "Edge intelligence and Internet of Things in healthcare: a survey," *IEEE Access*, vol. 9, pp. 45–59, 2021.

[19] D. N. Punith Kumar and A. Pasha, "Insights of mathematics for big data," *International Journal of Engineering and Advanced Technology*, vol. 8, no. 5, pp. 207–213, 2019.

[20] H. Shu, "Big data analytics: six techniques," *Geo-spatial Information Science*, vol. 19, no. 2, pp. 119–128, 2016.

[21] S. G. Akojwar and P. R. Kshirsagar, "Performance evolution of optimization techniques for mathematical benchmark functions," *International Journal of Computers*, vol. 1, pp. 231–236, 2016.

Hindawi
Journal of Nanomaterials
Volume 2021, Article ID 5840645, 21 pages
https://doi.org/10.1155/2021/5840645

Review Article

Sustainable Development of Carbon Nanocomposites: Synthesis and Classification for Environmental Remediation

Dhinakaran Veeman,[1] **M. Varsha Shree**,[1] **P. Sureshkumar**,[2] **T. Jagadeesha**,[3] **L. Natrayan**,[4] **M. Ravichandran**,[5] **and Prabhu Paramasivam**[6]

[1]*Centre for Additive Manufacturing, Chennai Institute of Technology, -600069, Chennai, India*
[2]*Department of Mechanical Engineering, Ramco Institute of Technology, Rajapalayam, Virudhunagar, Tamil Nadu, India*
[3]*Department of Mechanical Engineering, National Institute of Technology, Calicut, India*
[4]*Department of Mechanical Engineering, Saveetha School of Engineering, SIMATS, Chennai, Tamil Nadu 602105, India*
[5]*Department of Mechanical Engineering, K. Ramakrishnan College of Engineering, Tiruchirappalli, 621 112 Tamil Nadu, India*
[6]*Department of Mechanical Engineering, College of Engineering and Technology, Mettu University, Ethiopia -318*

Correspondence should be addressed to Dhinakaran Veeman; dhinakaranv@citchennai.net, L. Natrayan; natrayanphd@gmail.com, and Prabhu Paramasivam; prabhuparamasivam21@gmail.com

Received 12 July 2021; Revised 7 August 2021; Accepted 27 August 2021; Published 20 September 2021

Academic Editor: Lakshmipathy R

Copyright © 2021 Dhinakaran Veeman et al. This is an open access article distributed under the Creative Commons Attribution License, which permits unrestricted use, distribution, and reproduction in any medium, provided the original work is properly cited.

Composite materials with carbon nanotube and graphene attachments have been regarded as promising prospects. Carbon nanocomposites have gained considerable interest in different fields including biomedical applications due to its exceptional structural dimensions and outstanding mechanical, electrical, thermal, optical, and chemical characteristics. The significant advances made in carbon nanocomposite over past years along with the discovery of new nanocomposite processing technologies to improvise the functional impact of nanotube and graphene composites by providing proper methods of synthesis and improving the production of diverse composite based on carbon nanomaterials are discussed. Carbon nanocomposites are applied in various fields such as aviation, batteries, chemical industry, fuel cell, optics, power generation, space, solar hydrogen, sensors, and thermoelectric devices. The recent design, fabrication, characteristics, and applications of carbon nanocomposites such as active carbon, carbon black, graphene, nanodiamonds, and carbon nanotubes are explained in detail in this research. It is found that unlike traditional fiber composites, Van der Waals force interfacial compounds have an important effect on the mechanical performance of carbon nanomaterial-based composites.

1. Introduction

The incessant demand for the commercial usage of engineered carbon-based nanomaterials are increasing in the field of modern technology, medicine, environment, and agriculture; the distinctive properties of carbon-based nanomaterials have engrossed great concentration by the researchers and industrialists which have stimulated the expansion and innovation techniques for significant industrial production [1]. Carbon is among the stimulating elements, with the capacity to produce wide range of arrangements, habitually with diverse characteristics [2]. Some of the significant allotropes of carbon encompass "hard" diamond and "soft" graphite [3]. The innovative constituents that are carbon nanotubes (CNTs), fullerenes, graphene, and engrossed high contemplation from scientific industries which exhibit varieties of exceptional features as encouraging resources for abundant application fields due to their special capabilities, they were recurrently labelled as "wonder materials" [4]. The allotropical carbon transition, known as fullerenes, is generally a chemical component of carbon, or carbon particles. Here, carbon atoms naturally exist in the form of sp^2-hybrid and are bound by covalent bonds. Fullerene (C60) is a highly symmetrical spherical compound with 60 carbon atoms, at the tip of 20 hexagons and 12 pentagons [5, 6]. Carbon nanotubes (CNT) are the most notable of carbon-based nanomaterials;

CNTs are one of the carbon allotropes with excellent mechanical properties, characterized by tubular structures with a width of only a few nanometres, consisting of rolled graphene sheets and often varying in chirality, diameter, and weight [7, 8]. Graphene is a 2D allotropic carbon group consisting of "single layers of sp2-hybridized carbon atoms" in a 0.142 nm outcrop of 2D hexagonal crystal lattice between adjacent hexagonal carbon atoms [9]. It has various physicochemical properties, such as unusually high structural rigidity and higher thermal stability, and the electrical properties of graphene are very different from those of 3 dimensional products [10]. Intensively developed the discovery of carbon-based nanomaterials and their study of superior characteristics, synthesis methods, culminating in the basic component called carbon vapour, which manipulates the production of carbon nanomaterials [11]. The buoyant physical and chemical characteristics of carbon-based nanomaterials influence various applications that, in effect, allow their production to intensify [12]. Figure 1 displays the variations of the carbon nanocomposites. Carbon nanostructures contain numerous low-dimensional allotropes of carbon including carbon black (CB), carbon fiber, carbon nanotubes (CNTs), fullerene, and graphene.

By achieving several thousand tons of products [14], the carbon nanotubes have resulted in industrial development being the broadest area of operation. Due to the mechanical features of CNT such as high tensile strength and improved stability, they are integrated into polymers and other resources to manufacture structural and composite materials with innovative properties as required by their application and specification [15]. Carbon nanocomposites have exhibited exceptional catalytic activity in organic chemical processes due to their shape-dependent physical and chemical properties and thickness, primarily metal nanostructures or carbon materials consisting of graphene and carbon nanotubes [16]. The catalytic yield from the use of carbon nanocomposites in various fields, including nutritional, pharmaceutical, and materials sciences for biotechnology [17], has been found to be of great value. The catalytic products produced using carbon nanocomposites are considered of great value in various fields, particularly in medicinal, biomedical, agricultural, and material sciences [18, 19]. Consequently, demand for carbon nanocomposites has increased rapidly and therefore the development of new methods of preparation deserves a high degree of interactivity [20]. Nanocomposite benefits involve module enhancement, flexural strength, thermal distortion, barrier effects, and other advantages and, unlike conventional mineral-reinforced systems, are with no typical impact and visibility trade-offs.

2. Methods of Synthesis of Carbon Nanocomposites

2.1. Covalent Functionalization. Covalent functionality uses covalent connection of functional elements to the carbon scaffold of the nanotube. It can be of two forms, covalent side-wall functionalization and defect functionalization, depending on the location of contact. The functioning of the direct covalent sidewall implies a shift in hybridisation

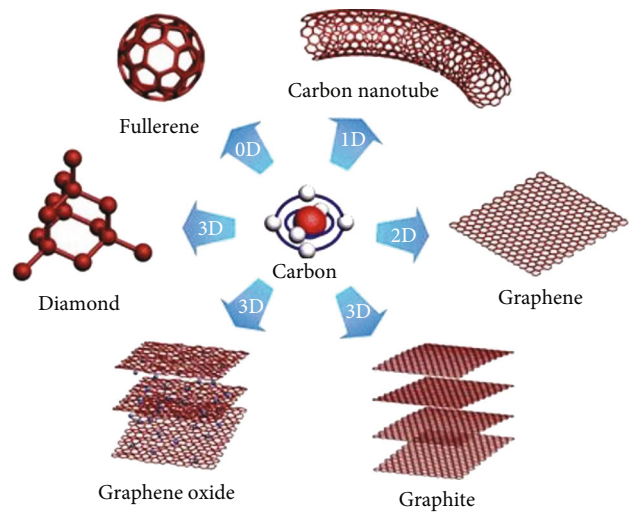

Figure 1: Classification of carbon nanocomposites [13].

from sp^2 to sp^3 and conjugation loss [21]. Functionalization of defects is based on the already existing site modifications [22]. Defect sites may include the open ends and the sidewall holes ended in hexagonal graphene framing, e.g., by functional groups and defects in stone/wales (5–7 faults). Oxidative purification also includes oxygenated sites produced as faults. SWCNTs have poor dispersibility and are shown as bundles [23]. The use of a highly reactive reagent for the covalent bond creation of the walls is guaranteed in this circumstance. It cannot be said in advance whether such additional reactions are most likely to occur at defective locations or intact hexagonal areas of the edge [24]. Several covalent methods, such as oxidative purification, amidation, esterification, thiolation, halogation, hydrogenation, and electrochemical functionality, have been adopted for covalent functionalization [25].

2.2. Noncovalent Functionalization. The noncovalent functionalization also known as supramolecular correlations is found across all types of materials which are exposed to attractive or repulsive forces, common in both organic and inorganic structures [26]. In the case of graphene, assigning defects or irregularities arising from the transition from sp^2 carbon to sp^3 carbon, though combining multiple relations, is technically useful [27]. Graphene materials and energy dissociation of less than $50\,kJ\,mol^{-1}$ [28] have a prevailing relationship. A major component to be addressed in graphene and graphene oxide (GO) systems is solvation and hydrophobic effects induced by various interactions, as they affect not only their dispersibility but also the identification of associations that can be used to classify them [29]. Graphene has two forms of interactions that influence its compatibility with other nanomaterials or stimulants between electron-rich and electron-poor regions [30]. This is often seen on both face-to-face arrangement and edge-to-face arrangement [31]. Also present in biologically relevant molecules such as DNA, RNA, and porphyrins through electron interactions. In addition, these interactions are found in small molecules and are transmitted to GO and G systems

where they can be used to process and modify properties [32]. The effective dispersion of graphene was accomplished by noncovalent functionalization with amine-packed and fully packed polymers [33]. Reduced graphene in nonsolvents could be spread by noncovalent grafting with an end-functional PS–NH_2 polymer [34]. For noncovalent functionalization, numerous nonsolvents for reduced graphene, benzene, hexane, oxylene, and dichloromethane, which are immiscible with the aqueous process, were used [35]. The remaining carboxylate groups effectively provided the noncovalent functionalization locations to the protonated amine terminals of end-functional polymers after the chemical reduction of graphene oxide [36]. The noncovalent functionality promoted the transmission of graphene sheets from the water phase to the organic phase through simple sonication [37]. Figure 2 displays the noncovalent functionalization of carbon nanocomposites. Here, chitosan is packed more firmly when covalently connected to the surface of CNTs than when noncovalently functionalized CNTs. Atomic force microscopy (AFM) might be used to assess the efficacy of macromolecule coating. This figure shows Chit-f-CNT preparation (top), AFM height images (middle), and profile measurements (bottom) for pure CNT (left), Chit noncovalent functionalized CNT (centre), and Chit covalent connected CNT (right).

2.3. Wet Synthesis. Metal oxide nanoparticles are an important class of nanomaterials which find numerous scientific and technological applications. The selective surface design, step, size, and shape of nanoparticles of metal oxides can be achieved by the use of wet chemical propagation which contributes to the collection of desired properties [39]. Developments in the synthesis of metal oxide nanoparticles are noteworthy due to their use in the electronics and optics as metal oxide nanoparticles and nanocomposites are becoming more popular in applied ecology, particularly as adsorbents and photo catalysts, and also a resource for the fabrication of environmental monitoring systems [40] and catalytic and energy storage industries [41]. Metal oxides are naturally capable of isolating the metal oxide charges [42]. Nanomaterial synthesis is split into two types: top-down approach and bottom-up approach [43]. In the top-down process, a large part of the substance is broken up into nanosized bodies [44].

It takes a complicated, costly, extremely energy-intensive, and sophisticated system to sustain precise conditions such as atmosphere, heat, and temperature [46]. Top-down methodology creates nonuniform, surface-defected nanomaterials that obstruct practical application [47]. From the bottom up, the atomic or molecular agents for the formation of nanostructures are incorporated into the process. The downstream approach is largely based on humid chemicals being processed fairly scalable and flexibility [48]. The method of wet chemical synthesis has made great progress as it benefits from using a kinetic and thermodynamic provision that can alter the scale, structure, and formulation of the electronic, optical, and interface properties [49]. Wet chemical processing methods for replicating desirable shape and size of metal oxide nanoparticles have been implemented. To generate ultrafine, extremely homogenous, and high purity powders, wet chemical techniques such as sol–gel, coprecipitation, and hydrothermal synthesis were developed [50]. The control of shape and size is accomplished by a better understanding of the fundamental events, the cycle by transforming the precursor, the surface stabilizing factor, and the reagent of the system and its interaction with the rate of proliferation and nucleation [51, 52]. A standard conventional batch technique will produce nanoparticles with a total scaling capacity of 10 mg/m [53]. The synthesis process should be versatile in terms of product quality and quantity to meet industrial specifications in order to understand the profitable functioning of colloidal metal oxide [54]. Figure 3 represents the chemical, physical, and biological approach for the synthesis of nanocomposites.

2.4. Dry Synthesis. The dry synthesis is known to be an extremely effective and adequate process for carbon nanocomposite propagation. The main benefits of this strategy are its versatility, enhanced adherence, and the advantages of the least design variables [55]. The dry synthesis has been described as the method ideally suited for the carbon decoration of metal nanoparticles [56]. The functional oxygen groups can bridge the metal nanoparticles and the carbon resources [57] through. Carbon materials with no usable surface groups may also be used consistently in carbon nanocomposite processing [58].

Nguyen-Tri et al. have established a method of quick and less dry solvent synthesis for the production of carbon nanocomposite [60]. A two-step direct process involves dry mixing of the metal precursor salt with carbon materials (CNTs or GO), followed by inert atmospheric heating [61]. No solvent, no additional reducing agents, or applied electric current are needed for the mechanochemical cycle [62]. Studies find that the mechanochemical method typically applies not only to CNTs but also to other carbon products with a high thermal conductivity, such as graphene, GO, and activated carbon [63]. The mechanochemical approach is considered rapid, adaptable, and ultimately versatile, allowing it to be used in various applications [64] for further usage. It covers possible uses in fields such as anticorrosion, antiwear, super hydrophobic area, self-cleaning, antifouling, antibacterial area, and electronics, as it is close to carbon nanocoating and it is represented in Figure 4 [65].

3. Classification of Carbon Nanocomposite

3.1. Carbon Black Nanocomposite. Polyaniline or carbon black (PANI/CB) nanocomposite structures and properties are particularly sensitive to chemical synthesis constraints [66]. It was found when the derived structures shifted from globular to a multitude of globular and nanofiber-like configurations by altering aniline and CB composition [67]. Complex nanostructures and synergistic capabilities [68] have been shown to produce the synthesis of conductive polymers and carbon-based substances. PANI/CB nanocomposites have better radiative stability and greater electrical conductivity compared to graphene-based nanotubes or nanocomposites [69]. The lightest PANI nanostructures

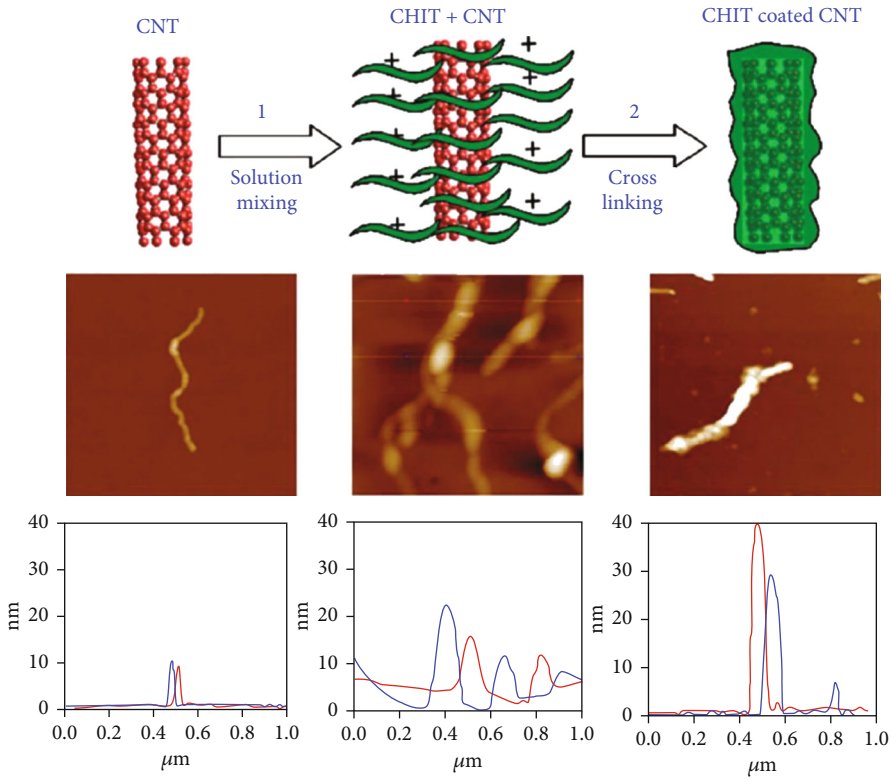

Figure 2: Noncovalent functionalisation of carbon [38].

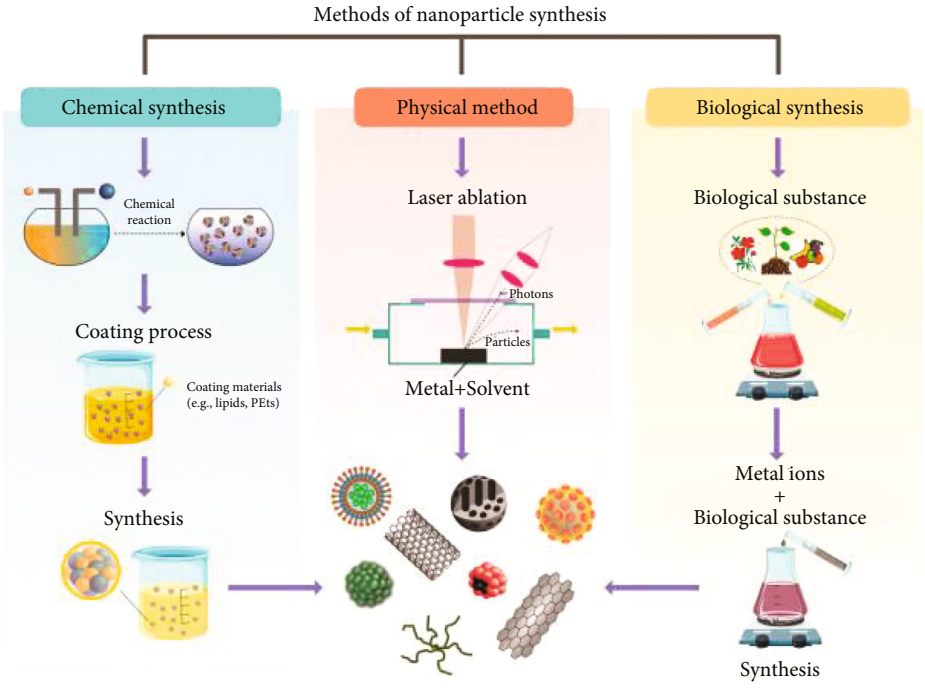

Figure 3: Wet synthesis of nanocomposites [45].

would have a significant number of heterogeneous crystallization sites to strengthen, avoid assembly, and increase nano particular nucleation dispersion [70]. In addition to carbon black (CB), carbon fibers, melamine fibers, and mica numerous reinforcement fillers have been used to enhance the mechanical properties of the finished products. Indeed, CB still retains the most significant global contribution [71]. Nanofillers, especially nanoclay (NC), have replaced

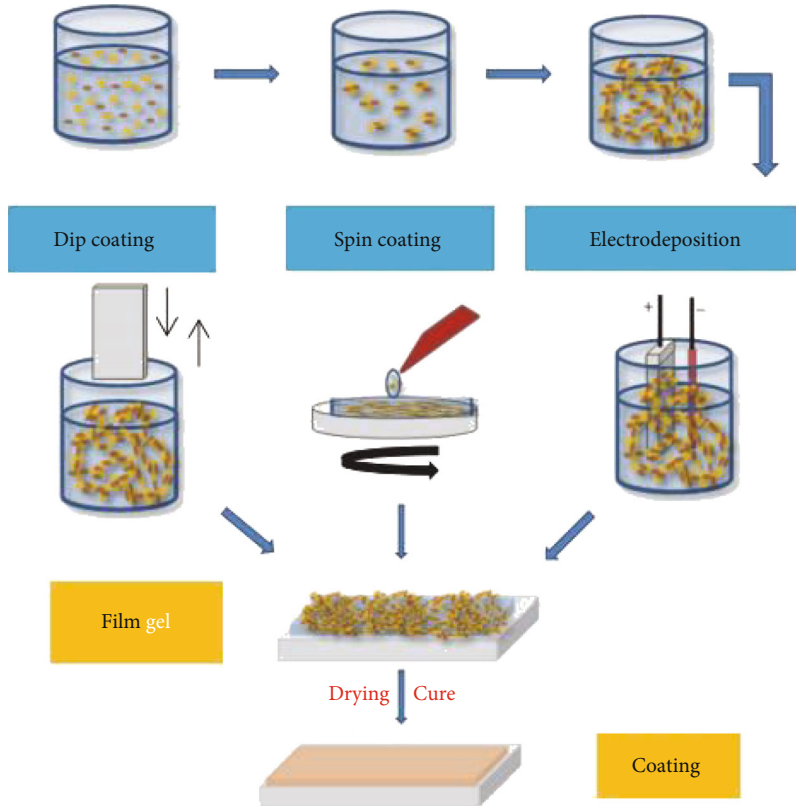

Figure 4: Dry synthesis of carbon nanocomposites [59].

traditional micro fillers in modern times by providing a higher surface area which correlates in much better interaction between molecular fillers [72, 73].

Based on the mechanical behaviour of nanocomposites [75], the feasible formulation of a dual filler frame in NBR matrix is researched. The impact of NC and NBR matrix interfacial communication on synergistic influence of NC and CB is explored [76]. Studies have also shown that involvement with CB, greater dispersal of NC in natural rubber, and rubber with styrene butadiene may be achieved [77]. Nanocomposites based on NBR/CB/NC and the mechanical and microstructural tests of subsequent hybrid systems have been configured to use NC and CB simultaneously [78, 79]; Figure 5 highlights methods for the synthesis of black carbon nanocomposite. The effects of heat treatment on carbon black (CB) nanocomposites are shown in Table 1.

3.2. Composites Based on Carbon Nanotubes. In the last few decades, the scope and application of nanotechnology have had an extraordinary effect on carbon nanomaterials. The university has been flush with fresh ideas, innovations, and many attempts to identify the ultimate uses for such amazing nanostructures, starting with the finding of fullerenes and going through the CO_2 era to graphene and other double-dimensional (2D) materials [81]. In this section, one such application which looked close to incorporating these materials when initially presented, but which did not meet expectations for different reasons: composite materials. In particular, the problem of whether mechanical reinforcing structures like carbon nanotubes and graphene are the correct option remained largely unsolved and was prominently reinforced in composite matrices due to their mechanical characteristics. In addition, careful assessment and thinking are needed in the field of functionality to be obtained by inserting nanotubes against graph in a matrix [82]. Although the two are sp^2 allotropes, their structure, morphology, and dimensionality, and the nature of their interactions, with the surrounding matrix, are actually extremely different [83]. The overall mechanical composite behaviour of these two reinforcing units could therefore be distinctive [84]. It would certainly be helpful to have selection procedures in composite applications, however, in nanocomposites with CNT or graphene phases such logical techniques are not developed.

Nanostructured composite polymer materials have created new insights for multipurpose materials. Carbon nanotubes (CNTs) directly provide possible applications for the enhancement of mechanical and electrical performance in aerospace laminates [86, 87]. A new composite substance with enhanced electromagnetic properties forms the combination of epoxy resin with double-walled carbon nanotubes [88]. Documentation of nanotubes distributed in polymer matrix was intended to improve the electrical and mechanical properties of polymer composites [89, 90]. The covalent and noncovalent functionalization processes have been suggested as one of the options for improved nanotube distribution [91]. Molecular modification of the nanotube

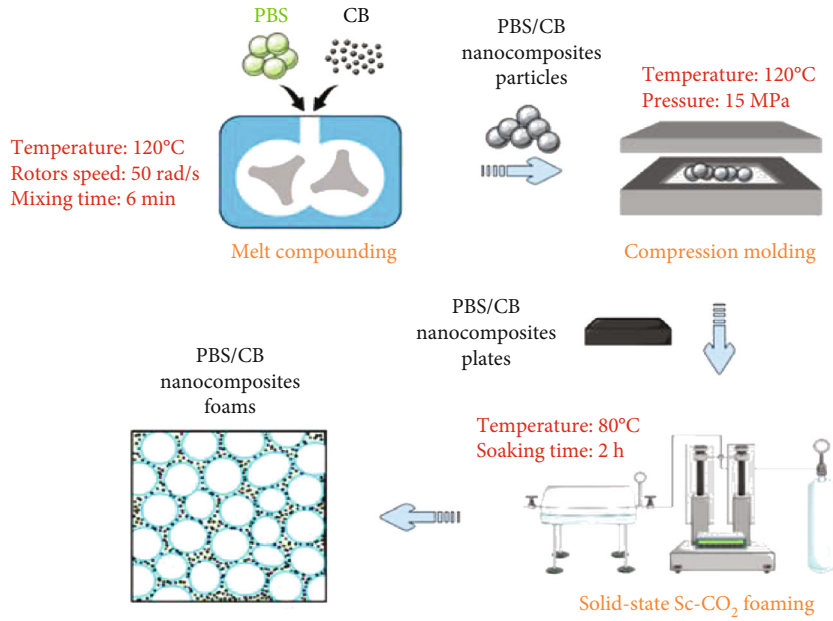

Figure 5: Synthesis of carbon black nanocomposite [74].

Table 1: Effects of heat treatment on carbon black (CB) nanocomposites [80].

CB sample	NSA (m^2/g)	STSA (m^2/g)	O (%)	N (%)	H (%)	S (%)	C (%)	Lc (nm)	d002 (nm)
N234, untreated	126.4	120.3	2.21	0.145	0.337	0.924	93.7	1.19	0.365
N234, 900°C	134.7	124.7	1.28	0.158	0.250	0.932	95.9	1.15	0.361
N234, 1000°C	129.6	129.6	0.204	0.064	0.130	0.916	96.7	1.40	0.361
N234, 1200°C	129.0	132.8	0.128	0.041	0.021	0.790	98.7	1.44	0.355
N660, untreated	36.4	35.2	0.576	0.082	0.339	1.84	95.9	1.78	0.352
N660, 1000°C	36.4	37.3	0.110	0.056	0.141	1.78	96.8	1.59	0.355

substratum by covalent functionalization decreases the aspect ratio with the formation of carbon atoms sp^3 on the nanotube layer [92]. That reduces the power conductivity of nanotubes [93]. The cylindrical CNT specification allows them to obtain a so-called electronic conjugate framework which reflects their distinctive behaviour in electronic transport [94]. Composites incorporated in a polymer host were used for microwave operations [95] as well as for electromagnetic interference shielding (EMI) or microwave absorbers such as antireflection [96]. The advent of CNTs as filler components has contributed to the production of CNT-polymer nanocomposites as the sophisticated structural material of the next century [97]. The A polyacrylonitrile (PAN)/polyvinylidene fluoride (PVDF) nanofibers achieved a high CO_2 absorption of 2.21 wt percent and demonstrated efficiency in reversible CO_2 capture under flow gas pressures [98]. Magnetic composites based on carbon nanotubes (CNTs) have huge potential for the discovery and use of magnetic solid-phase extraction (MSPE) technology [99, 100]. Figure 6 represents the classification of carbon nanotubes based on their structural arrangements.

3.3. Graphene-Based Carbon Nanocomposites. Graphene is one of the world's finest materials and has developed considerable interest in physics, materials science, chemistry, and biology. Graphene has a very high conductivity in electricity and thermal efficiency, making it the best incentives for thermally conductive composites [101]. Films used as the heating element are more smart than conventional heating elements because of lower environmental pollution, easy to use on various surface areas, and have the characteristics of lightweight [102]. At the forefront of nanotechnology are carbon-based nanomaterials from earlier C60 and carbon nanotubes into graphene [103].

The monolayer graphene is dense on a single surface and can be separated from graphite using adhesive by standard graphite flake exfoliation [105]. Classification and detachment of substantial lateral dimension of pristine graphene at high solvent concentrations are difficult. Tiny layer of graphene is containing roughly 2–10 sheets of graphene atoms, like flakes [106]. This was a by-product that was created during attempts to render monolayer graphene. Ultrathin graphite is a graphite substance greater than 3–5 nm in diameter but less than 100 nm [107]. Graphene oxide is a strongly oxidized graphene produced by intense crystal graphite oxidation followed by sonication or some other dispersion phase, typically in aqueous absorption, forming a monolayer material [108]. Reduced graphene oxide is the

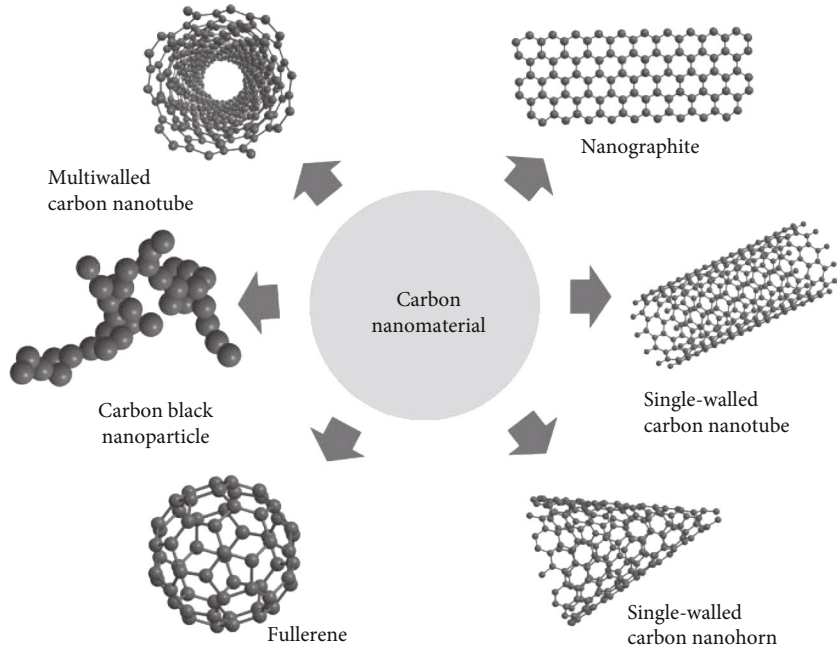

Figure 6: Classification of carbon nanotubes based on their structures [85].

substance produced by treating GO under reduced conditions, such as thermal processing at high temperatures [109]. Decreasing GO also influences many of its properties, such as reducing its oxygen content [110], increasing its hydrophobicity, creating CO/CO_2 emission holes or defects in the carbon lattice [111], and reducing its surface load and water supply [112]. Also, the basal planes contain unchanged, hydrophobic, and capable graphene domains of $\pi - \pi$ interactions associated with dye molecules or other drugs adsorption [113]. Figure 7 displays graphene nanocomposite structure.

The van der Waals binding of the walls of carbon nanotubes to individual layers of multilayer graphic must also be considered in layered reinforcement. Compared to the strong covalent bonding of the graph layers, this link is rather weak [114]. Therefore, when multiwalled carbon nanotube (MWNT) and multilayer graphene are employed in composites, their capacity to strengthen is restricted by simple cuts between the walls or between the layers [115]. The inner stress transmission between the nanotube walls of carbon and the graph layers may be monitored by variations in the Raman-related stress band [116]. Imperfect stress transmission occurs during deformation as the Raman band is extended, and the Raman band shift is lowness compared to the single-wall or single-level material. Comparing Raman bands stress shifts in epoxy nanocomposites for single walled carbon nanotube (SWNT) and MWNT indicate that efficiency for transferring stress from interwalls for MWNTs is only approximately 70% [117]. Compared to the large number of research on CNT and graphene reinforced polymer matrix composites, the focus on ceramic or metal composites was significantly less, maybe because of limited production [118]. Furthermore, in polymer-based composites, mechanical strengthening effects are more evident. CNTs or ceramic graphic composites are driven primarily by increased toughness or resistance to fracture formation because ceramics are already stiff and solid [119]. The major toughening process is the higher energy dissipation owing to graphene nanosheet pull for graphene-enhanced ceramic composites [120]. Other difficult processes discovered include crack deflection and crack bridging on the matrix reinforcement interface. In CNT-reinforced ceramic composites, similar toughening mechanisms were also reported. Improved thermal and electrical conduction is also possible [121]. Graphene plays a vital role in removal of heavy material; they are shown in Table 2.

3.4. Activated Carbon Nanocomposites. Activated carbon, also known as activated charcoal, is a type of carbon treated with small, lower volume holes that enhance the area of the surface [123]. Because of its significant degree of microporosity, one gram of activated carbon has an area of more than $3{,}000\,m^2/g$, as calculated by gas adsorption [124]. ZnO or activated carbon nanocomposites are produced by physically combining the ZnO nanoparticles produced with activated carbon [125]. The proportion of nanoparticles to activated charcoal for the adsorption of Cd^{2+} from aqueous solutions was standardized (9 : 1) [126]. These carbon nanocomposites are produced by mechanically combining the ZnO nanomaterials excreted above with activated carbon [127]. The concentration scope of activated carbon nanocomposites of 0.15–1.5 mg/ml has been used to evaluate Cd^{2+} formulated at concentrations between 10 and 100 ppm [128]. A sonicator probe has been used to create agitation for the adsorption of cadmium ions through vibration energy [129]. The higher adsorption power and good magnetic segregation efficiency of magnetic activated carbon are Fe_3O_4 [130] and can be used as possible sorbents for the extraction of multiple toxic contaminants from wastewater [131]. The M versus H curves for Fe_2O_3 nanoparticles and Fe_3C

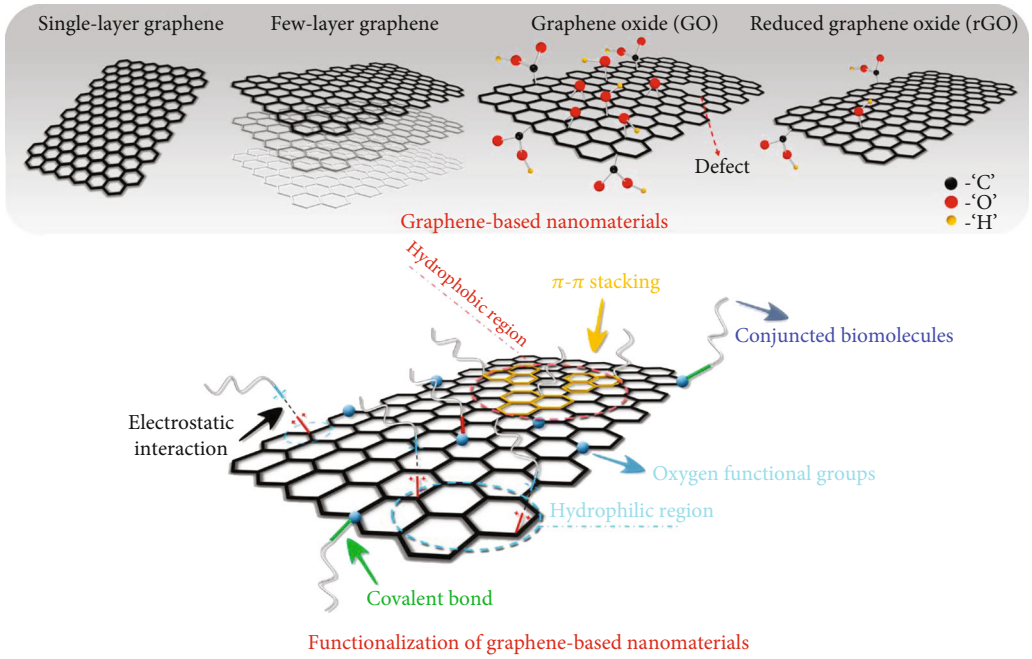

Figure 7: Structure of graphene-based nanocomposite [104].

Table 2: Graphene nanocomposites for heavy metal removal [122].

Adsorbent	Adsorbate	Maximum adsorption capacity ($mg.g^{-1}$)
Functionalised GOCA beads	Pb (II), Hg (II), and Cd (II)	602, 374, and 181
GO/PAMAMs	Pb (II), Cd (II), Cu (II), and Mn (II)	568.18, 253.81, 68.68, and 18.29
CS/GO-SH	Pb (II), Cd (II), Cu (II)	425, 447, and 177
MMSP-GO	Pb (II), Cd (II)	333 and 167
PVK-GO	Pb (II)	887.98
$MnFe_2O_4$/GO	Pb (II), As (II), and As (V)	673, 146, and 207
EDTA-mGO	Pb (II), Hg (II), Cu (II)	508.4, 268.4, and 301.2
Go/L-Trp	Cu (II) and Pb (II)	588 and 222
PAH-GO	Cu (II)	349.04
GO-CD-PPY NC	Cr (VI)	666.67
RGO/NiO	Cr (VI)	198
PAS-GO	U (VI) and Eu (VI)	310.63 and 243.90
Chitosan/GO	Cr(VI), Cu (II), and Pb (II)	461.3, 4238, and 310.4

MWCNT is shown in Figure 8. The adsorption process in activated carbon is distinct for organic and inorganic impurities. Activated carbon has the maximum removal effect for most organic contaminants. When activated carbon-quartz sand combination procedures were used, organic contaminants species and overall peak area may be decreased at the same time. However, the effects of phthalates, esters, and aldehydes were not substantially the same as dimethyl phthalate and di-nbutyl phthalate [132].

A basic progressive impregnation approach has been used to obtain some transition metal hexacyanoferrate [134], also known as microporous activated carbon composites [135] where in activated carbons are recognized as effective for many contaminants collected, having high surface area and formed porosity [120]. An activated carbon and iron oxide nanocomposite was developed and defined by the methods of X-ray diffraction and scanning electron microscopy [136]. Figure 9 represents the nanocomposite based on active carbon.

In order to synthesise polysulfone- (PSF-) activated nanocomposites, a melt-mixing method was utilised. This study examined the properties of thermal, mechanical, magnetic, morphological, and carbon dioxide capturing and utilised 2-wt% activated carbon (CA, CA-Ni, and CO-Co) as a filler. The pyrolysis of the sawdust wood produced carbon compounds activated by Co and/or Ni Salt. The heat degradation and metal amount of carbon compounds were investigated. Thermogravimetric analysis is an effective method of measuring the polymer material thermal stability [137]. With the addition of metal-activated carbons, the beginning

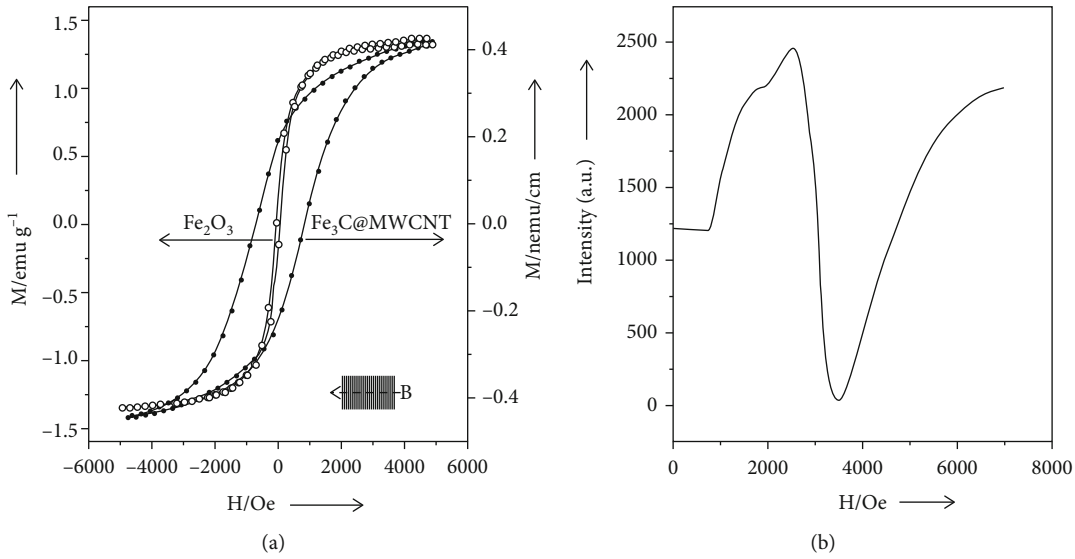

Figure 8: M versus H curves for Fe_2O_3 nanoparticles and Fe_3C MWCNT [133].

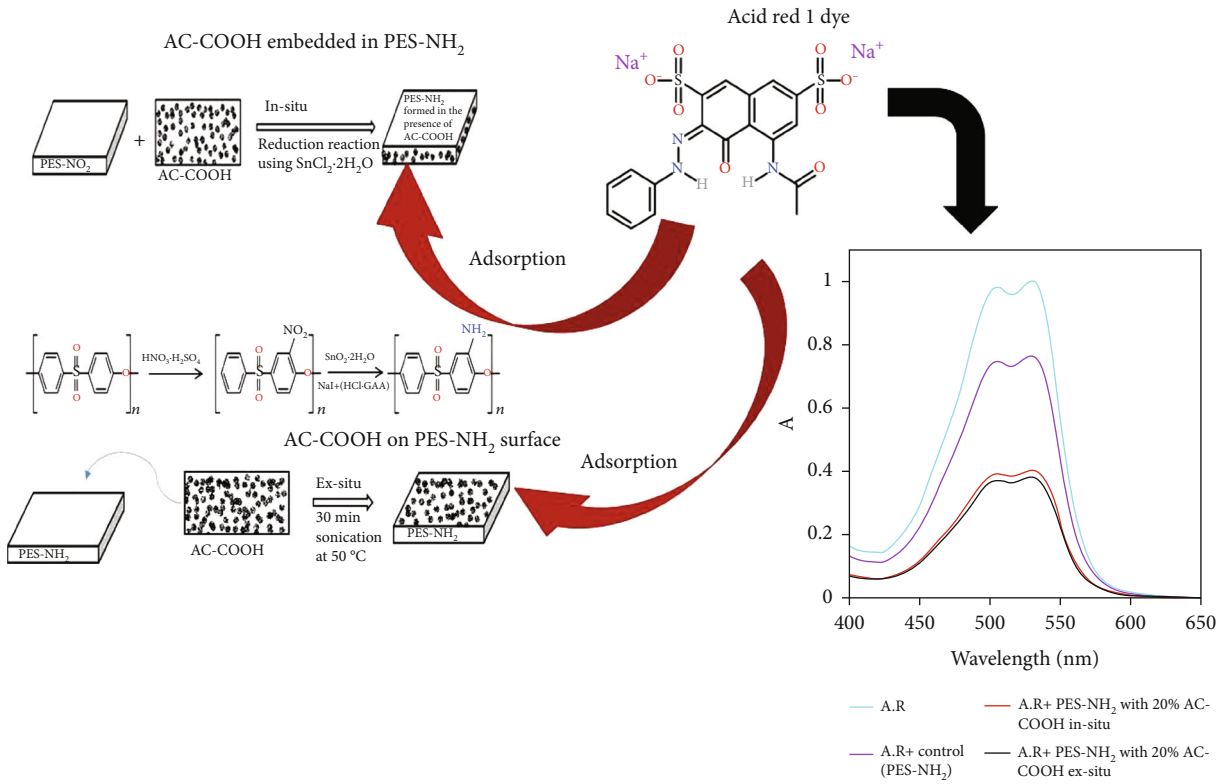

Figure 9: Nanocomposite based on active carbon [142].

deterioration temperature has decreased to 4°C, which may improve to 3°C by the highest degradation temperature [138]. For pure PSF and its nanocomposites, Tg values measured with differential calorimetry scanners are almost comparable. The nanocomposite elasticity modulus exhibits a 17 percent increase in the clean PSF [139]. With the addition of the fillers, the water contact angle revealed a reduction in the hydrophilicity of the composite. In contrast to the nanocomposite, the carbon dioxide sorbent capacity shows an increase of about 10% [140]. With the injection of 20 wt percent metal-carbonized filler, the ferromagnetic behaviour of a thermoplastic nanocomposite was observed. Extraordinary magnetic characteristics make it attractive in many industrial applications for a thermoplastic polymer such as polysulfone [141]. The applications of activated carbon for are shown in Table 3.

Table 3: Applications of activated carbon [145].

Types of AC	Shape/particle size	Application
Powder AC (fine powder)	Pulverized carbon/less than 0.18 mm	Recovery of liquid and gas
Granular AC (coarse particles)	Irregular shaped/0.6-4.0 mm	Recovery, separation of liquid and gas
Extruded AC (cylindrical particles)	Cylindrical shaped/large than 4.0 mm	Natural gas storage, off-gases from wastewater control
Activated carbon fiber (threadlike piece)	Fabrication flexibility/narrower pore size compound distribution	Removal of volatile organic compound
Activated carbon cloths	Fabrication flexibility/uniform microporosity	Removal of volatile organic compound

A chemical binding on activated carbon powder (AC) nanoparticles was used for synthesising the magnetic Fe_3O_4 activated carbon nanocomposites with high surface area as recovered adsorbents [143]. In this nanocomposite, the component AC and Fe_3O_4 are amorphous nongraphic and cubic crystal structure each. Superparamagnetic characteristics were detected in all composite samples. $Fe_3O_{4/}$AC nanocomposite magnetised saturation was considerably less than that of bare Fe_3O_4 particles, showing that the AC was really bound to Fe_3O_4. The picture of the microstructure showed Fe_3O_4 particles were spread evenly throughout AC surfaces and hence kept a highly specific surface area. Methyl orange (MO) somewhat decreased its adsorption capacity at 30°C from 384 mg/g for AC ponding to 324 mg/g for Fe_3O_4/C, a reduction of 15 percent following magnet manufacturing. On Fe_3O_4/AC nanocomposites, MO adsorption was shown to follow the pseudosecond-order kinetic model and Langmuir models could describe the isotherm. The simple recovery of magnetic adsorbents from water proved their use potential for eliminating harmful contaminants in the treatment of waste water [144].

3.5. Nanodiamonds. Nanodiamonds offer outstanding mechanical and optical characteristics and are adjustable to the surface. They are also nontoxic, making them suitable for biomedical uses. Nanodiamonds are made from explosive molecules that offer carbon source and conversion energy [146]. The approach for the disposal of obsolete weapons such as composition B, while other explosives may also be employed, is ecologically and economically feasible. The detonation occurs in a confined chamber with a "dry" or "wet" synthesis, or inert gas or water (ice) as shown in Figure 10 [147]. The resulting product soot exposure is a 4-5 nm diamond combination with various carbohydrates and contaminants. Depending on cooling medium, the carbon output is 4-10% of the weight of the explosive, during that explosion Danilenko found the formation of nanodiamonds [148]. Bouget's pressures and heat are not sufficiently enough to make liquid carbon in bulk, but are high enough to generate nanoscale liquid carbon. The liquid carbon area is moved to lower nanocarbon temperatures, while the nanodiamond region is moved slightly into higher pressures. It is therefore hypothesised that nanodiamonds develop via the condensation and crystallization of the liquid carbon in volume of the super saturated carbon vapour [149]. Other approaches (such the use of shock waves to generate graphite nanodiamonds) yield crystallite-sized nanodiamonds of more than 10 nm. The soot detonation, apart from the diamonds phase, includes both graphics (25%-80% wt) and incombustible impurities (1%-8% metals and oxides). The distinctive property of nanodiamonds is that many different functional groups are bonded to their surface compared to carbon nanotubes and other graphic nanoparticles, thereby permitting advanced surface functionality without sacrificing the beneficial characteristics of the diamond core [150].

However, it is equally important to understand how these groups interact with their environment and minimize harmful consequences (such as aggregation). While commercial nanodiamond powders may be utilised for the covalent functionality of different functional groups, the usage of air purification or ozone-generated carboxylated nanodiamonds and then the rich chemistry of COOH groups are more easy to start with. Nanodiamond is a good filler for composites due to its superior mechanical and thermal characteristics and the rich surface chemical properties of diamond nanoscale particles. The diamond core's biocompatibility and chemical stability make them extremely suitable for biomedical use. The addition of tiny quantities of nanodiamond generated transparent polyvinyl alcohol nanocomposites with enhanced mechanical characteristics [152]. Surface chemistry can influence the interactions between the nanoparticles of the diamonds and the matrix, as well as the dispersion of the nanoparticles in the matrix. Table 4 shows the biomedical applications of nanodiamond composites.

4. Industrial Applications of Carbon Nanocomposites

4.1. Super Capacitors. As an electricity collection system, super condenser finds desirable applications in consumer product and alternative energy sources due to its increased energy density, rapid discharge and charge time, lower heating, protection, long-term operating reliability, and no removable components [154]. In particular, CNTs are desirable electrode resources for the production of high-performance super condensers due to its innovative characteristics of high conductivity, high specific volume, high charging power, high mesoporosity, and high electrolyte functionality [155]. These are an appealing choice for applications for energy storage in compact or remote devices [156] where electrodes and traditional condensers must be overdimensioned due to unfavourable power-to-energy ratio [157]. Carbon aerogel (CA) or any other types of carbon

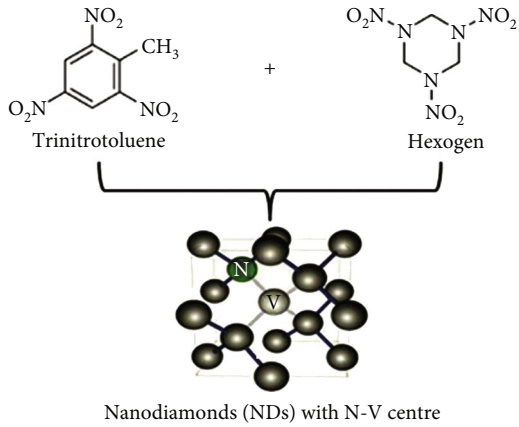

Figure 10: Synthesis of nanodiamond [151].

products such as black carbon or carbon cloth are commonly used in these super condensers [158]. Two essential parts for a CNT super capacitor are the electrodes and the electrolyte [159]. Capacity of traditional carbon electrodes will slowly decrease as current discharge density increases [160]. Specific capacitance of nanocomposite electrode with-grown single-walled CNTs, pure PPY, and single-walled CNT-polypyrrole (PPY) is a result of discharged current densities [161].

The performance of today's super capacitors in terms of power density must be significantly increased, yet maintaining a long life cycle to satisfy the demanding demands of electric hybrid and large-scale industry applications [162]. In order to increase the efficiency of supercapacitors, nanocarbon materials from first generation are employed as electrode materials. MWCNTs as electrodes are in regular, box-like form, with a capacitance up to 120 FG1 and a pure electrostatic attraction characteristic (the value depends on the scanning rate). A gravimetric capacitance of 20 to 300 F/g is displayed for EDLCs with a SWCNT electrode. Graphene-processed supercapacitors do not improve performance considerably. The biggest drawback for super capacitors is the limited specific surface area of such nanocarbons [163].

4.2. Biosensors. The integration of observable traits into analytical instruments, particularly in medical research, is becoming a prerequisite for early detection of various diseases [164]. Carbon nanotubes (CNTs) are pseudoone-dimensional carbon allotropes, especially identified as a system of carbon atoms arranged into one or more levels of smooth cylinders with either open or closed edges [165]. CNTs have quite wide specific surface area which enables for the immobilization of a substantial number of operational units such as biosensing receptor moieties [166]. CNTs possess special optical intrinsic properties such as near-infrared photoluminescence (NIR) [167]. The biocompatibility and biodegradability were increased by turning the layer of pristine CNTs into hydrophilic f-CNTs [168]. Such biosensors analyse a broad variety of genetic markers of cancer by conjugating DNA or proteins, peptides, enzymes [169], and electrochemical biosensors for the early diagnosis of genetic markers of cancer [170]. Microspecificity of the enzymatic reaction is used by CNT-based enzymatic electrochemical nanomaterials to guide electrical transfer among biomolecules [171]. CNT paste was produced of brumoform, and the electrode was designed with superior enactment over all other carbon electrodes [172]. Bioaffinity electrochemical biosensors are very robust complexes [173] in CNT-DNA electrochemical biosensors have been designed to acquire a simple, cheap, fast sensor [174]. Figure 11 shows the applications of biosensors from nanocomposite. For example, the synthesis of 3-methoxy phenol sensor used for biotech applications made from Fe_3O_4.CNT NCs/GCE, and its calculation is shown in Table 5.

Although the study of carbon nanotubes in biological applications is still in its early stages, it has enormous potential. Carbon is a particularly biocompatible substance since it makes up a large portion of the human body [176]. Cell growth on CNTs has been proven; hence, they do not appear to be harmful. The cells also do not attach to the CNTs, which opens the door to uses such as antifouling coatings for ships and prosthetic coatings [177]. The ability to functionalize (chemically alter) the sidewalls of carbon nanotubes (CNTs) opens the door to biological applications such as neuron development and regeneration and vascular stents. It has also been shown that a single strand of DNA may be linked to a nanotube and then efficiently implanted into a cell [178].

4.3. Solar Cells. A new type of solar cell, dye-sensitized solar cells (DSSCs), based on nanocrystalline TiO2 electrodes, has captured the attention of industry and academia [179]. DSSCs offer lower manufacturing costs relative to commercial silicon-based solar cells and provide similar advantages for amorphous silicon solar cells [180]. CNTs will have a possible high-field direction that interpenetrates DSSC electrodes along. The hypothesis was that carbon nanotubes would effectively increase the electrode's electrical conductivity and thus improve the solar system's light conversion performance [181]. Due to extreme CNT aggregation [182], the expansion of the CNT charge will impair the efficiency of DSSC cells. Dye-sensitized solar cells (DSCs) consisting of colouring molecules, nanocrystalline metal oxides, and natural liquid electrolytes have valuable high-performance characteristics in energy conversion and low energy and manufacturing costs [183]. The carbon cloth (CC) altered MWCNT-MnO_2/PPy nanocomposite electrode has a good biocompatibility resulting in a well-recognized moderator for the production of bioelectricity in wastewater with less MFCs [184]. Microbial fuel cells (MFCs) generate electricity for the oxidation of organic materials such as acetate, lactate, and glucose from exo electrogenic substances [185]. MFCs have applications in the fields of renewable energy recovery, remotely controlled power supplies, nanomaterials and biofilm testing, hydrogen production, and chemical fermentation systems due to their flexibility in processing various bacterial sources [186].

4.4. Radar Absorbing Materials. The curiosity in radar-absorbing materials (RAM) has extended to the business

Table 4: Biomedical applications of nanodiamonds [153].

Nanodiamond kind	System	Cells	Toxicity
Fluorescent nanodiamonds prepared by detonation method	Fluorescence nanodiamond PCL fibers	Human lens epithelial cell line	Nontoxic and the scaffold can support in vitro cell growth
Nanodiamonds	Particle	Hepatocyte cells	Nontoxic less than 10 μg ml
Nanodiamonds	Particle	Lymphocytes and cervical cancer cells in vitro	Toxic
Nanodiamonds	Particle	Three kinds of mammalian cells	It is possible an effect in noncovalent adsorption between NDs and serum proteins in culture medium
Nanodiamonds	Natural polymers-BG composite coating by electrophoretic deposition	Human osteosarcoma cell line	Improving cellular behaviour

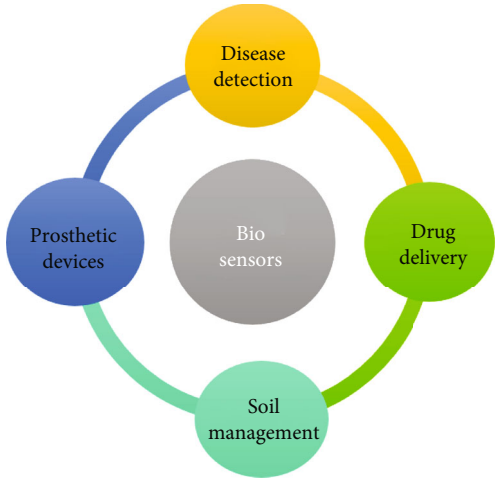

Figure 11: Applications of biosensors from nanocomposite.

sector as they can be used to minimize electromagnetic interference due to recent developments in electromagnetic devices entering the RF frequency range [187]. Short carbon fiber reinforced composites (CFRC) are ideally suited for the development of thin multipurpose RAM [188]. Owing to their high execution of electrical and thermal qualities at comparatively low concentration, composites dependent on polymers and carbon nanofillers have received significant interest in both academic and industrial societies [189]. Extraordinary interest has been given to carbon nanostructure-filled polymer nanocomposites as electromagnetic absorbers in both military and civil applications [190] in terms of their ability to modify electromagnetic and molecular properties at comparatively low quantities of nanofiller extraordinary interest has been given to carbon nanostructure-filled polymer nanocomposites as electromagnetic absorbers in both military and civil applications [191] in terms of their ability to modify electromagnetic and molecular properties at comparatively low quantities of nanofillers and their light weight, outstanding thermal tolerance and high mechanical characteristics and their light weight, and outstanding thermal tolerance and high mechanical characteristics [192].

4.5. Energy Storage. The intrinsic characteristics of CNT make them two fast-growing technologies the ideal material to be used as electrodes in condensers and batteries. The electrical conductivity of CNTs is high, and their area of exceptionally high surface (~1000 m^2/g) is particularly accessible to the electrolyte because of their linear geometries. Research has shown that CNTs have the largest reversible capacity for usage in lithium-ion batteries with any carbon material [193]. In addition, the CNTs are ideal materials for electrodes with supercapacitors and are readily available for sale. Moreover, CNTs are used in several components of the fuel cell. They have various features, such as high thermal conductivity and surface area, and are important in PEM fuel cells as electrode catalyst support [194]. They also may be utilised in gas diffusion layers, in addition to current collectors, due to their high electrical capacity [195]. CNTs are also able to demonstrate great strength and toughness to weight as part of composites in fuel cells that are utilised in transportation applications where durability is essential [196].

4.6. Field Emission Applications. CNTs are the best-known source of any substance in the area. It is comprehensible because of its great electrical performance and the incredible sharpness of its tip (when the curvature radius of the tip is reduced, the electric area will be concentrated, resulting in enhanced emissions from the field, this is because of the sharp lightning rods) [197]. Moreover, the sharpness of the tip also suggests that they emit at a very low voltage, which is a critical attribute for creating low-power electrical devices [198]. CNTs may be quite current, perhaps up to 1013 A/cm^2. CNT's are very high. The current is also quite steady. This characteristic is implemented immediately and attracts great interest in field-emission flat panel displays. CNT-based displaying uses a distinct electron gun (or perhaps several of them) for every pixel in the view, as opposed to traditional cathode ray tube display with a single electron gun [199]. CNTs have low turn-off and operating voltages, a large current density, and constant, long-lived behaviour, which make this application highly desirable. Other applications using CNT's field emission properties are general low-

Table 5: Calculation of 3-methoxy phenol sensor with Fe_3O_4.CNT NCs/GCE [175].

Samples	Observed current (μA)				Conc. (μM)	SD ($n = 3$)
	R1	R2	R3	Average		
Industrial effluent	7.09	5.27	4.91	5.75	23.76	1.17
PC baby bottle	7.73	5.25	4.42	5.80	23.96	1.72
PC bottle	1.66	4.14	3.85	3.22	13.30	1.36
PVC food packaging bag	4.18	3.08	2.77	3.34	13.80	0.74
Red sea water	4.33	3.31	2.58	3.41	14.09	0.88
Tape water	3.54	2.66	2.31	2,83	11.71	0.63

voltage cold cathode light sources, electron microscope sources, and lightning arresters [200].

4.7. Conductive Plastic. Plastics have been used in many cases as a metal replacement. Polymers have improved enormously for structural applications but not where electrical conductivity is essential, as plastics are particularly strong electrical insulators [201]. The filling of polymers with lever fillers like as carbon black and bigger graphite fibers can prevent this deficit (the ones used to make golf clubs and tennis rackets) [202]. However, the loading needed is generally considerable, resulting in hefty parts and plastic parts which have a high degraded construction characteristic, in order to give the requisite conductivity via traditional fillers [203]. As the load needed for a certain conductivity is reduced as the filling particle aspect ratio is higher. For this reason, CNT is excellent since it has the greatest carbon fiber aspect ratio. In addition, their intrinsic inclination to shape cords provides naturally very lengthy leading routes even at extremely low loads [204]. This characteristic of CNT is used in applications such as electrostatic dissipation (ESD), composite EMI (electromagnetic interference), shielding, gasket, enclosure, and other usage coatings, low-observance radar absorption materials, and conductive (even transparent) antistatic and material coatings [205].

4.8. Future Scope. Significant improvements in the preparation of carbon nanotube-polymer composites with remarkable mechanical and physical characteristics have been achieved. In this area, a great deal of study is still required until these remarkable characteristics are completely realised in a macroscopic nanometric medium. In addition, experiments have to be done in order to identify disintegration or recycling mechanisms for carbon nanocomposites in order to create something new at the end of their life cycle (recycle). Furthermore, research has not progressed much while attempting to produce naturally enhanced compounds using biologically degradable polymer matrix, as the creation of such "green composites" poses a number of obstacles. They are regarded as the most ecologically sound material but issues such as poor adherence to the fiber matrix, difficulty in fiber orientation, and the attainment of nanoscale dimensions halt those materials in search of appropriate applications. In this regard, some limitations include insulating individual nanofiber composites to evaluate the nanofibers tensile characteristics and adhere them to a load tester which is yet difficult. Electro spun nanofiber, atomistic modelling, and continuum mechanism methods remain a major challenge to theoretical approaches in prediction of the mechanical behaviour of CNTs implanted in electro spun fibers.

5. Conclusion

Carbon nanocomposites assisted by metal nanoparticles have been observed to perform a substantial role in a broad array of potential applications in science and technologies. In this research work, the prominent enhancements have been made in formulating carbon nanotube polymer composite materials with excellent mechanical and thermodynamic properties are studied. The carbon nanotube functionalization improves the diffusion status of carbon nanotubes and to change the properties of the device and boost the attributes of polymer nanocomposite products, particularly material properties. The incessant demand for the commercial usage of engineered carbon-based nanomaterials is increasing in the field of modern technology, medicine, environment, and agriculture; the distinctive properties of carbon-based nanomaterials have engrossed great concentration by the researchers and industrialists which has stimulated the expansion and innovation techniques for significant industrial production.

(i) The advanced production techniques for carbon nanocomposites (primarily graphene or graphene oxide and CNTs) and their usage in organic processes have been discussed

(ii) Layered nanocomposites are the most widely used materials for increasing the barrier character of polymer nanocomposites in packaging applications

(iii) Nanocomposites also serve as organic photovoltaic sheets in solar panels. These films may be utilised as flexible semitransparent modules and are exceptionally light in weight. The other advantages of these films are continuous production for different light and climatic conditions

(iv) Nanocomposites based on graphene oxide (GO) can make a substantial contribution to the treatment of waste water by removing heavy metals

(v) Due to characteristics such as long-term durability, better sensitivity, stronger order conductivity, and easy production, carbon nanocomposites are used in construction of sensors

Conflicts of Interest

The author(s) declare(s) that they have no conflicts of interest.

References

[1] N. M. Julkapli and S. Bagheri, "Graphene supported heterogeneous catalysts: an overview," *International Journal of Hydrogen Energy*, vol. 40, no. 2, pp. 948–979, 2015.

[2] D. Deng, L. Xiao, I.-M. Chung, I. S. Kim, and M. Gopiraman, "Industrial-quality graphene oxide switched highly efficient Metal- and solvent-free synthesis of β-ketoenamines under feasible conditions," *ACS Sustainable Chemistry & Engineering*, vol. 5, no. 2, pp. 1253–1259, 2017.

[3] O. Zaytseva and G. Neumann, "Carbon nanomaterials: production, impact on plant development, agricultural and environmental applications," *Chemical and Biological Technologies in Agriculture*, vol. 3, no. 1, p. 17, 2016.

[4] P. O'Brien, R. Nuzzo, H. Kroto, and J. Rocha, *Hierarchical nanostructures for energy devices*, Royal Society of Chemistry, 2014.

[5] B. C. Yadav and R. Kumar, "Structure, properties and applications of fullerenes," *International Journal of Nanotechnology and Applications*, vol. 2, no. 1, pp. 15–24, 2008.

[6] R. Taylor and D. R. M. Walton, "The chemistry of fullerenes," *Nature*, vol. 363, no. 6431, pp. 685–693, 1993.

[7] R. Zhang, Y. Zhang, Q. Zhang, H. Xie, W. Qian, and F. Wei, "Growth of half-meter long carbon nanotubes based on Schulz–Flory distribution," *ACS Nano*, vol. 7, no. 7, pp. 6156–6161, 2013.

[8] A. M. K. Esawi, K. Morsi, A. Sayed, M. Taher, and S. Lanka, "Effect of carbon nanotube (CNT) content on the mechanical properties of CNT- reinforced aluminium composites," *Composites Science and Technology*, vol. 70, no. 16, pp. 2237–2241, 2010.

[9] X.-M. Liu, Z. Huang, S. Oh et al., "Carbon nanotube (CNT)-based composites as electrode material for rechargeable Li-ion batteries: a review," *Composites Science and Technology*, vol. 72, no. 2, pp. 121–144, 2012.

[10] R. Khare and S. Bose, "Carbon nanotube based composites-a review," *Journal of Minerals and Materials Characterization and Engineering*, vol. 4, no. 1, pp. 31–46, 2005.

[11] W. Krätschmer, "The story of making fullerenes," *Nanoscale*, vol. 3, no. 6, pp. 2485–2489, 2011.

[12] K. Morsi and A. Esawi, "Effect of mechanical alloying time and carbon nanotube (CNT) content on the evolution of aluminum (Al)–CNT composite powders," *Journal of Materials Science*, vol. 42, no. 13, pp. 4954–4959, 2007.

[13] S. H. Chae and Y. H. Lee, "Carbon nanotubes and graphene towards soft electronics," *Nano Convergence*, vol. 1, no. 1, pp. 1–26, 2014.

[14] M. F. L. de Volder, S. H. Tawfick, R. H. Baughman, and A. J. Hart, "Carbon nanotubes: present and future commercial applications," *science*, vol. 339, no. 6119, pp. 535–539, 2013.

[15] K. Ahmad and W. Pan, "Microstructure-toughening relation in alumina based multiwall carbon nanotube ceramic composites," *Journal of the European Ceramic Society*, vol. 35, no. 2, pp. 663–671, 2015.

[16] X. Zang, Q. Zhou, J. Chang, Y. Liu, and L. Lin, "Graphene and carbon nanotube (CNT) in MEMS/NEMS applications," *Microelectronic Engineering*, vol. 132, pp. 192–206, 2015.

[17] A. K. Geim and K. S. Novoselov, "The rise of graphene," *Nature Mater. 6.*, vol. 183, no. 2007, p. 109, 2010.

[18] M. Kang, M. W. Song, and C. H. Lee, "Catalytic carbon monoxide oxidation over CoO_x /CeO_2 composite catalysts," *Applied Catalysis A: General*, vol. 251, no. 1, pp. 143–156, 2003.

[19] D. Vairavapandian, P. Vichchulada, and M. D. Lay, "Preparation and modification of carbon nanotubes: review of recent advances and applications in catalysis and sensing," *Analytica Chimica Acta*, vol. 626, no. 2, pp. 119–129, 2008.

[20] D. S. Su and R. Schlögl, "Nanostructured carbon and carbon nanocomposites for electrochemical energy storage applications," *ChemSusChem: Chemistry & Sustainability Energy & Materials*, vol. 3, no. 2, pp. 136–168, 2010.

[21] R. J. Chen, S. Bangsaruntip, K. A. Drouvalakis et al., "Noncovalent functionalization of carbon nanotubes for highly specific electronic biosensors," *Proceedings of the National Academy of Sciences*, vol. 100, no. 9, pp. 4984–4989, 2003.

[22] Y.-L. Zhao and J. F. Stoddart, "Noncovalent functionalization of single-walled carbon nanotubes," *Accounts of chemical research*, vol. 42, no. 8, pp. 1161–1171, 2009.

[23] J. Zhao, J. P. Lu, J. Han, and C.-K. Yang, "Noncovalent functionalization of carbon nanotubes by aromatic organic molecules," *Applied Physics Letters*, vol. 82, no. 21, pp. 3746–3748, 2003.

[24] V. Georgakilas, J. N. Tiwari, K. C. Kemp et al., "Noncovalent functionalization of graphene and graphene oxide for energy materials, biosensing, catalytic, and biomedical applications," *Chemical Reviews*, vol. 116, no. 9, pp. 5464–5519, 2016.

[25] N. Nakayama-Ratchford, S. Bangsaruntip, X. Sun, K. Welsher, and H. Dai, "Noncovalent functionalization of carbon nanotubes by fluorescein– polyethylene glycol: supramolecular conjugates with pH-dependent absorbance and fluorescence," *Journal of the American Chemical Society*, vol. 129, no. 9, pp. 2448-2449, 2007.

[26] J. Chen and C. P. Collier, "Noncovalent functionalization of single-walled carbon nanotubes with water-soluble porphyrins," *The Journal of Physical Chemistry B*, vol. 109, no. 16, pp. 7605–7609, 2007.

[27] P. Petrov, F. Stassin, C. Pagnoulle, and R. Jérôme, "Noncovalent functionalization of multi-walled carbon nanotubes by pyrene containing polymers," *Chemical Communications*, vol. 23, no. 23, pp. 2904-2905, 2003.

[28] A. Ghosh, K. . V. Rao, S. . J. George, and C. . N. . R. Rao, "Noncovalent functionalization, exfoliation, and solubilization of graphene in water by employing a fluorescent coronene carboxylate," *Chemistry–A European Journal*, vol. 16, no. 9, pp. 2700–2704, 2010.

[29] R. Tian, X. Jia, J. Yang, Y. Li, and H. Song, "Large-scale, green, and high-efficiency exfoliation and noncovalent functionalization of fluorinated graphene by ionic liquid crystal," *Chemical Engineering Journal*, vol. 395, article 125104, 2020.

[30] J. Kim, J. Cha, B. Chung, S. Ryu, and S. H. Hong, "Fabrication and mechanical properties of carbon fiber/epoxy nanocomposites containing high loadings of noncovalently

functionalized graphene nanoplatelets," *Composites Science and Technology*, vol. 192, article 108101, 2020.

[31] N. Alzate-Carvajal, L. M. Bolivar-Pineda, V. Meza-Laguna, V. A. Basiuk, E. V. Basiuk, and E. A. Baranova, "Oxygen evolution reaction on single-walled carbon nanotubes noncovalently functionalized with metal phthalocyanines," *ChemElectroChem*, vol. 7, no. 2, pp. 428–436, 2020.

[32] Z. Ju, X. Yao, Z. Luo, M. Cao, and W. Xiao, "Theoretical studies on the noncovalent interaction of fructose and functionalized ionic liquids," *Carbohydrate Research*, vol. 487, article 107882, 2020.

[33] M. Karimi, N. Solati, M. Amiri et al., "Carbon nanotubes part I: preparation of a novel and versatile drug-delivery vehicle," *Expert opinion on drug delivery*, vol. 12, no. 7, pp. 1071–1087, 2015.

[34] R. S. Ribeiro, A. M. T. Silva, J. L. Figueiredo, J. L. Faria, and H. T. Gomes, "Catalytic wet peroxide oxidation: a route towards the application of hybrid magnetic carbon nanocomposites for the degradation of organic pollutants. A review," *Applied Catalysis B: Environmental*, vol. 187, pp. 428–460, 2016.

[35] X. Zhou, Z. Dai, J. Bao, and Y.-G. Guo, "Wet milled synthesis of an Sb/MWCNT nanocomposite for improved sodium storage," *Journal of Materials Chemistry A*, vol. 1, no. 44, pp. 13727–13731, 2013.

[36] S. H. S. Zein, L.-C. Yeoh, S.-P. Chai, A. R. Mohamed, and M. E. M. Mahayuddin, "Synthesis of manganese oxide/carbon nanotube nanocomposites using wet chemical method," *Journal of materials processing technology*, vol. 190, no. 1-3, pp. 402–405, 2007.

[37] M. N. Rumyantseva, V. V. Kovalenko, A. M. Gaskov et al., "Nanocomposites SnO_2/Fe_2O_3: wet chemical synthesis and nanostructure characterization," *Sensors and Actuators B: Chemical*, vol. 109, no. 1, pp. 64–74, 2005.

[38] Y. Zhou, Y. Fang, and R. P. Ramasamy, "Non-covalent functionalization of carbon nanotubes for electrochemical biosensor development," *Sensors*, vol. 19, no. 2, p. 392, 2019.

[39] K. Shameli, M. B. Ahmad, W. Z. Yunus, N. A. Ibrahim, and M. Darroudi, "Synthesis and characterization of silver/talc nanocomposites using the wet chemical reduction method," *International journal of nanomedicine*, vol. 5, p. 743, 2010.

[40] C. Chae, K. W. Kim, S. J. Kim et al., "3D intra-stacked CoO/-carbon nanocomposites welded by Ag nanoparticles for high-capacity, reversible lithium storage," *Nanoscale*, vol. 7, no. 23, pp. 10368–10376, 2015.

[41] J. Dong, W. Liu, H. Li, X. Su, X. Tang, and C. Uher, "*In situ* synthesis and thermoelectric properties of PbTe–graphene nanocomposites by utilizing a facile and novel wet chemical method," *Journal of Materials Chemistry A*, vol. 1, no. 40, pp. 12503–12511, 2013.

[42] W.-C. Du, Y.-X. Yin, X.-X. Zeng et al., "Wet chemistry synthesis of multidimensional nanocarbon–sulfur hybrid materials with ultrahigh sulfur loading for lithium–sulfur batteries," *ACS Applied Materials & Interfaces*, vol. 8, no. 6, pp. 3584–3590, 2016.

[43] S. Yogeshwaran, L. Natrayan, G. Udhayakumar, G. Godwin, and L. Yuvaraj, "Effect of waste tyre particles reinforcement on mechanical properties of jute and abaca fiber-epoxy hybrid composites with pre-treatment," *Materials Today: Proceedings*, vol. 37, no. 2, pp. 1377–1380, 2021.

[44] S. Li, Y. Wang, C. Lai et al., "Directional synthesis of tin oxide@ graphene nanocomposites via a one-step upscalable wet-mechanochemical route for lithium ion batteries," *Journal of Materials Chemistry A*, vol. 2, no. 26, pp. 10211–10217, 2014.

[45] M. Jeyaraj, S. Gurunathan, M. Qasim, M.-H. Kang, and J.-H. Kim, "A comprehensive review on the synthesis, characterization, and biomedical application of platinum nanoparticles," *Nanomaterials*, vol. 9, no. 12, p. 1719, 2019.

[46] R. Ramachandran, M. Saranya, A. N. Grace, and F. Wang, "MnS nanocomposites based on doped graphene: simple synthesis by a wet chemical route and improved electrochemical properties as an electrode material for supercapacitors," *RSC advances*, vol. 7, no. 4, pp. 2249–2257, 2017.

[47] M. Gich, C. Fernández-Sánchez, L. C. Cotet, P. Niu, and A. Roig, "Facile synthesis of porous bismuth–carbon nanocomposites for the sensitive detection of heavy metals," *Journal of Materials Chemistry A*, vol. 1, no. 37, pp. 11410–11418, 2013.

[48] L. Gan, S. Shang, C. Mei, L. Xu, L. Tan, and E. Hu, "Wet functionalization of carbon nanotubes and its applications in rubber composites," *Carbon-Based Nanofillers and Their Rubber Nanocomposites*, vol. 3, pp. 77–108, 2019.

[49] S. A. Mirzaee, N. Jaafarzadeh, H. T. Gomes, S. Jorfi, and M. Ahmadi, "Magnetic titanium/carbon nanotube nanocomposite catalyst for oxidative degradation of Bisphenol A from high saline polycarbonate plant effluent using catalytic wet peroxide oxidation," *Chemical Engineering Journal*, vol. 370, pp. 372–386, 2019.

[50] G. Pandey, D. Rawtani, and Y. K. Agrawal, "Aspects of nanoelectronics in materials development," in *Nanoelectronics and Materials Development*, IntechOpen, 2016.

[51] H.-W. Tien, Y.-L. Huang, S.-Y. Yang, J.-Y. Wang, and C. C. M. Ma, "The production of graphene nanosheets decorated with silver nanoparticles for use in transparent, conductive films," *Carbon*, vol. 49, no. 5, pp. 1550–1560, 2011.

[52] N. Yang, S. Zhu, D. Zhang, and S. Xu, "Synthesis and properties of magnetic Fe_3O_4-activated carbon nanocomposite particles for dye removal," *Materials Letters*, vol. 62, no. 4-5, pp. 645–647, 2008.

[53] S. E. A. S. El-Deen and F. Zhang, "Synthesis of Nanocomposite for the Recovery of as (V) from Wastewater," *Procedia Environmental Sciences*, vol. 16, pp. 378–390, 2012.

[54] A. Ślosarczyk, M. Barełkowski, S. Niemier, and P. Jakubowska, "Synthesis and characterisation of silica aerogel/carbon microfibers nanocomposites dried in supercritical and ambient pressure conditions," *Journal of Sol-Gel Science and Technology*, vol. 76, no. 1, pp. 227–232, 2015.

[55] T.-H. Ko, S. Radhakrishnan, M.-K. Seo, M.-S. Khil, H.-Y. Kim, and B.-S. Kim, "A green and scalable dry synthesis of $NiCo_2O_4$/graphene nanohybrids for high-performance supercapacitor and enzymeless glucose biosensor applications," *Journal of Alloys and Compounds*, vol. 696, pp. 193–200, 2017.

[56] S.-L. Chou, J.-Z. Wang, H.-K. Liu, and S.-X. Dou, "Rapid synthesis of Li4Ti5O12Microspheres as anode materials and its binder effect for lithium-ion battery," *The Journal of Physical Chemistry C*, vol. 115, no. 32, pp. 16220–16227, 2011.

[57] S. Kalathil, M. M. Khan, A. N. Banerjee, J. Lee, and M. H. Cho, "A simple biogenic route to rapid synthesis of Au@

TiO 2 nanocomposites by electrochemically active biofilms," *Journal of Nanoparticle Research*, vol. 14, no. 8, p. 1051, 2012.

[58] S. Kellici, J. Acord, A. Vaughn et al., "Calixarene assisted rapid synthesis of silver-graphene nanocomposites with enhanced antibacterial activity," *ACS Applied Materials & Interfaces*, vol. 8, no. 29, pp. 19038–19046, 2016.

[59] P. Nguyen-Tri, T. A. Nguyen, P. Carriere, and C. Ngo Xuan, "Nanocomposite coatings: preparation, characterization, properties, and applications," *International Journal of Corrosion*, vol. 2018, Article ID 4749501, 19 pages, 2018.

[60] S. Yogeshwaran, L. Natrayan, S. Rajaraman, S. Parthasarathi, and S. Nestro, "Experimental investigation on mechanical properties of Epoxy/graphene/fish scale and fermented spinach hybrid bio composite by hand lay-up technique," *Materials Today: Proceedings*, vol. 37, no. 2, pp. 1578–1583, 2021.

[61] V. Vergaro, I. Pisano, R. Grisorio et al., "CaCO3 as an environmentally friendly renewable material for drug delivery systems: uptake of HSA-CaCO3 nanocrystals conjugates in cancer cell lines," *Materials*, vol. 12, no. 9, p. 1481, 2019.

[62] L. M. G. da Silva, H. G. Lemos, S. F. Santos, R. A. Antunes, and E. C. Venancio, "Polyaniline/carbon black nanocomposites: the role of synthesis conditions on the morphology and properties," *Materials Today Communications*, vol. 16, pp. 14–21, 2018.

[63] K. H. Wu, Y. C. Chang, C. C. Yang, Y. J. Gung, and F. C. Yang, "Synthesis, infrared stealth and corrosion resistance of organically modified silicate-polyaniline/carbon black hybrid coatings," *European Polymer Journal*, vol. 45, no. 10, pp. 2821–2829, 2009.

[64] E. Esmizadeh, G. Naderi, and S. M. R. Paran, "Preparation and characterization of hybrid nanocomposites based on NBR/nanoclay/carbon black," *Polymer Composites*, vol. 38, pp. E181–E188, 2017.

[65] K. H. Wu, T. H. Ting, G. P. Wang, W. D. Ho, and C. C. Shih, "Effect of carbon black content on electrical and microwave absorbing properties of polyaniline/carbon black nanocomposites," *Polymer Degradation and Stability*, vol. 93, no. 2, pp. 483–488, 2008.

[66] S. Tolooei, G. Naderi, S. Shokoohi, and S. Soltani, "Elastomer nanocomposites based on NBR/BR/nanoclay: morphology and mechanical properties," *Journal of Polymer Engineering*, vol. 33, no. 2, pp. 133–139, 2013.

[67] S. H. Jafari, A. Asadinezhad, A. K. Vahid, H. A. Khonakdar, U. Wagenknecht, and G. Heinrich, "Polypropylene/poly (trimethylene terephthalate) blend nanocomposite: a thermal properties study," *Polymer-Plastics Technology and Engineering*, vol. 51, no. 7, pp. 682–688, 2012.

[68] K. Chrissafis, K. M. Paraskevopoulos, S. Y. Stavrev, A. Docoslis, A. Vassiliou, and D. N. Bikiaris, "Characterization and thermal degradation mechanism of isotactic polypropylene/carbon black nanocomposites," *Thermochimica Acta*, vol. 465, no. 1-2, pp. 6–17, 2007.

[69] T. Liu, S. Jia, T. Kowalewski, K. Matyjaszewski, R. Casado-Portilla, and J. Belmont, "Water-dispersible carbon black nanocomposites prepared by surface-initiated atom transfer radical polymerization in protic media," *Macromolecules*, vol. 39, no. 2, pp. 548–556, 2006.

[70] Q. Li, Siddaramaiah, N. H. Kim, G.-H. Yoo, and J. H. Lee, "Positive temperature coefficient characteristic and structure of graphite nanofibers reinforced high density polyethylene/-carbon black nanocomposites," *Composites Part B: Engineering*, vol. 40, no. 3, pp. 218–224, 2009.

[71] X. Liu, C. Li, Y. Pan, D. W. Schubert, and C. Liu, "Shear-induced rheological and electrical properties of molten poly(-methyl methacrylate)/carbon black nanocomposites," *Composites Part B: Engineering*, vol. 164, pp. 37–44, 2019.

[72] J. du, Z. Zhang, D. Liu, T. Ren, D. Wan, and H. Pu, "Triple-stimuli responsive shape memory effect of novel polyolefin elastomer/lauric acid/carbon black nanocomposites," *Composites Science and Technology*, vol. 169, pp. 45–51, 2019.

[73] Z. Li, H. Xu, X. Xia, Y. Song, and Q. Zheng, "Energy dissipation accompanying Mullins effect of nitrile butadiene rubber/carbon black nanocomposites," *Polymer*, vol. 171, pp. 106–114, 2019.

[74] Z. Chen, J. Hu, J. Ju, and T. Kuang, "Fabrication of poly (butylene succinate)/carbon black nanocomposite foams with good electrical conductivity and high strength by a supercritical CO2 foaming process," *Polymers*, vol. 11, no. 11, p. 1852, 2019.

[75] T. H. Wu, A. Foyet, A. Kodentsov, L. G. J. van der Ven, R. A. T. M. van Benthem, and G. de With, "Curing and percolation for carbon black-epoxy-amine nanocomposites," *Composites Science and Technology*, vol. 181, article 107672, 2019.

[76] C. Yan, L. Guo, D. Ren, and P. Duan, "Novel composites based on geopolymer for removal of Pb(II)," *Materials Letters*, vol. 239, pp. 192–195, 2019.

[77] V. A. Silva, L. d. C. Folgueras, G. M. Cândido, A. L. de Paula, M. C. Rezende, and M. L. Costa, "Nanostructured composites based on carbon nanotubes and epoxy resin for use as radar absorbing materials," *Materials Research*, vol. 16, no. 6, pp. 1299–1308, 2013.

[78] C. Zhu, D. Liu, Z. Chen, L. Li, and T. You, "An ultra-sensitive aptasensor based on carbon nanohorns/gold nanoparticles composites for impedimetric detection of carbendazim at picogram levels," *Journal of Colloid and Interface Science*, vol. 546, pp. 92–100, 2019.

[79] Y.-J. Heo, Y. Zhang, K. Y. Rhee, and S.-J. Park, "Synthesis of PAN/PVDF nanofiber composites-based carbon adsorbents for CO_2 capture," *Composites Part B: Engineering*, vol. 156, pp. 95–99, 2019.

[80] C. G. Robertson and N. J. Hardman, "Nature of carbon black reinforcement of rubber: perspective on the original polymer nanocomposite," *Polymers*, vol. 13, no. 4, p. 538, 2021.

[81] S. S. Suner, S. Demirci, B. Yetiskin et al., "Cryogel composites based on hyaluronic acid and halloysite nanotubes as scaffold for tissue engineering," *International Journal of Biological Macromolecules*, vol. 130, pp. 627–635, 2019.

[82] H. Lee, D. Lee, J. Cho et al., "Super-insulating, flame-retardant, and flexible poly(dimethylsiloxane) composites based on silica aerogel," *Composites Part A: Applied Science and Manufacturing*, vol. 123, pp. 108–113, 2019.

[83] E. Galata, E. A. Georgakopoulou, M.-E. Kassalia, N. Papadopoulou-Fermeli, and E. A. Pavlatou, "Development of smart composites based on doped-TiO2 nanoparticles with visible light anticancer properties," *Materials*, vol. 12, no. 16, p. 2589, 2019.

[84] A. G. Rosenberger, D. C. Dragunski, E. C. Muniz et al., "Electrospinning in the preparation of an electrochemical sensor based on carbon nanotubes," *Journal of Molecular Liquids*, vol. 298, article 112068, 2020.

[85] X. Yuan, X. Zhang, L. Sun, Y. Wei, and X. Wei, "Cellular toxicity and immunological effects of carbon-based

nanomaterials," *Particle and Fibre Toxicology*, vol. 16, no. 1, pp. 1–27, 2019.

[86] G. R. Mitchell, F. J. Davis, S. Mohan, and M. Nazhipkyzy, "Highly Anisotropic Polymer Composites Based on Carbon Nanotubes," in *Carbon Nanotubes-Recent Progress*, IntechOpen, 2017.

[87] F. Inam, D. W. Y. Wong, M. Kuwata, and T. Peijs, "Multiscale hybrid micro-nanocomposites based on carbon nanotubes and carbon fibers," *Journal of Nanomaterials*, vol. 2010, Article ID 453420, 12 pages, 2010.

[88] A. Eatemadi, H. Daraee, H. Karimkhanloo et al., "Carbon nanotubes: properties, synthesis, purification, and medical applications," *Nanoscale Research Letters*, vol. 9, no. 1, p. 393, 2014.

[89] M. S. Dresselhaus, G. Dresselhaus, P. C. Eklund, and A. M. Rao, "Carbon nanotubes," in *The physics of fullerene-based and fullerene-related materials*, pp. 331–379, Springer, Dordrecht, 2000.

[90] G. Dresselhaus, G. Dresselhaus, P. Eklund, and R. Saito, "carbon nanotubes," *World scientific*, vol. 11, no. 1, pp. 33–38, 1998.

[91] N. Saifuddin, A. Z. Raziah, and A. R. Junizah, "Carbon nanotubes: a review on structure and their interaction with proteins," *Journal of Chemistry*, vol. 2013, Article ID 676815, 18 pages, 2013.

[92] S. Pattnaik, K. Swain, and Z. Lin, "Graphene and graphene-based nanocomposites: biomedical applications and biosafety," *Journal of Materials Chemistry B*, vol. 4, no. 48, pp. 7813–7831, 2016.

[93] D. G. Papageorgiou, I. A. Kinloch, and R. J. Young, "Mechanical properties of graphene and graphene-based nanocomposites," *Progress in Materials Science*, vol. 90, pp. 75–127, 2017.

[94] V. Dhand, K. Y. Rhee, H. Ju Kim, and D. Ho Jung, "A comprehensive review of graphene nanocomposites: research status and trends," *Journal of Nanomaterials*, vol. 2013, Article ID 763953, 14 pages, 2013.

[95] Y. Liang, D. Wu, X. Feng, and K. Müllen, "Dispersion of graphene sheets in organic solvent supported by ionic interactions," *Advanced Materials*, vol. 21, no. 17, pp. 1679–1683, 2009.

[96] H. L. Guo, X. F. Wang, Q. Y. Qian, F. Wang, and X. Xia, "A green approach to the synthesis of graphene nanosheets," *ACS Nano*, vol. 3, no. 9, pp. 2653–2659, 2009.

[97] T. Yamada, J. Kim, M. Ishihara, and M. Hasegawa, "Low-temperature graphene synthesis using microwave plasma CVD," *Journal of Physics D: Applied Physics*, vol. 46, no. 6, article 063001, 2013.

[98] G. Williams, B. Seger, and P. V. Kamat, "TiO2-graphene nanocomposites. UV-assisted photocatalytic reduction of graphene oxide," *ACS nano*, vol. 2, no. 7, pp. 1487–1491, 2008.

[99] R. J. Young, I. A. Kinloch, L. Gong, and K. S. Novoselov, "The mechanics of graphene nanocomposites: a review," *Composites Science and Technology*, vol. 72, no. 12, pp. 1459–1476, 2012.

[100] K. M. F. Shahil and A. A. Balandin, "Graphene–multilayer graphene nanocomposites as highly efficient thermal interface materials," *Nano letters*, vol. 12, no. 2, pp. 861–867, 2012.

[101] H.-B. Zhang, W.-G. Zheng, Q. Yan et al., "Electrically conductive polyethylene terephthalate/graphene nanocomposites prepared by melt compounding," *polymer*, vol. 51, no. 5, pp. 1191–1196, 2010.

[102] Y. Li, L. Tang, and J. Li, "Preparation and electrochemical performance for methanol oxidation of Pt/graphene nanocomposites," *Electrochemistry Communications*, vol. 11, no. 4, pp. 846–849, 2009.

[103] S. Dul, L. Fambri, and A. Pegoretti, "Fused deposition modelling with ABS-graphene nanocomposites," *Composites Part A: Applied Science and Manufacturing*, vol. 85, pp. 181–191, 2016.

[104] H. P. Bei, Y. Yang, Q. Zhang et al., "Graphene-based nanocomposites for neural tissue engineering," *Molecules*, vol. 24, no. 4, p. 658, 2019.

[105] Y.-W. Chen, Y. L. Su, S.-H. Hu, and S.-Y. Chen, "Functionalized graphene nanocomposites for enhancing photothermal therapy in tumor treatment," *Advanced Drug Delivery Reviews*, vol. 105, pp. 190–204, Part B, 2016.

[106] S. N. Tripathi, G. S. S. Rao, A. B. Mathur, and R. Jasra, "Polyolefin/graphene nanocomposites: a review," *RSC Advances*, vol. 7, no. 38, pp. 23615–23632, 2017.

[107] K. Singh, A. Ohlan, and S. K. Dhaw, "Polymer-graphene nanocomposites: preparation, characterization, properties, and applications," in *Nanocomposites-New Trends and Developments*, pp. 37–72, IntechOpen, 2012.

[108] H. Sharififard, F. Pepe, M. Soleimani, P. Aprea, and D. Caputo, "Iron-activated carbon nanocomposite: synthesis, characterization and application for lead removal from aqueous solution," *RSC Advances*, vol. 6, no. 49, pp. 42845–42853, 2016.

[109] L. Yang and A. Merneedi, "Experimental investigation on wear behaviour of bio-waste reinforced fusion fiber composite laminate under various conditions," *Materials Today: Proceedings*, vol. 37, no. 2, pp. 1486–1490, 2021.

[110] L.-J. Xie, J.-F. Wu, C.-M. Chen et al., "A novel asymmetric supercapacitor with an activated carbon cathode and a reduced graphene oxide-cobalt oxide nanocomposite anode," *Journal of Power Sources*, vol. 242, pp. 148–156, 2013.

[111] R. Li, Y. Liu, L. Cheng, C. Yang, and J. Zhang, "Photoelectrochemical aptasensing of kanamycin using visible light-activated carbon nitride and graphene oxide nanocomposites," *Analytical Chemistry*, vol. 86, no. 19, pp. 9372–9375, 2014.

[112] J. Xu, P. Xin, Y. Gao et al., "Magnetic properties and methylene blue adsorptive performance of $CoFe_2O_4$/activated carbon nanocomposites," *Materials Chemistry and Physics*, vol. 147, no. 3, pp. 915–919, 2014.

[113] E. Altintig and S. Kirkil, "Preparation and properties of Ag-coated activated carbon nanocomposites produced from wild chestnut shell by $ZnCl_2$ activation," *Journal of the Taiwan Institute of Chemical Engineers*, vol. 63, pp. 180–188, 2016.

[114] T. A. Saleh, K. O. Sulaiman, S. A. AL-Hammadi, H. Dafalla, and G. I. Danmaliki, "Adsorptive desulfurization of thiophene, benzothiophene and dibenzothiophene over activated carbon manganese oxide nanocomposite: with column system evaluation," *Journal of Cleaner Production*, vol. 154, pp. 401–412, 2017.

[115] Y.-F. Lee, K.-H. Chang, C.-C. Hu, and K.-M. Lin, "Synthesis of activated carbon-surrounded and carbon-doped anatase TiO_2 nanocomposites," *Journal of Materials Chemistry*, vol. 20, no. 27, pp. 5682–5688, 2010.

[116] D. Deng, B.-S. Kim, M. Gopiraman, and I. S. Kim, "Needle-like MnO_2/activated carbon nanocomposites derived from human hair as versatile electrode materials for supercapacitors," *RSC Advances*, vol. 5, no. 99, pp. 81492–81498, 2015.

[117] B. B. Zhang, J. C. Xu, P. H. Xin et al., "Magnetic properties and adsorptive performance of manganese-zinc ferrites/activated carbon nanocomposites," *Journal of Solid State Chemistry*, vol. 221, pp. 302–305, 2015.

[118] J. Matos, P. S. Poon, R. Montaña et al., "Photocatalytic activity of P-Fe/activated carbon nanocomposites under artificial solar irradiation," *Catalysis Today*, vol. 356, pp. 226–240, 2020.

[119] D. N. Sangeetha, D. Krishna Bhat, and M. Selvakumar, "h-MoO_3/Activated carbon nanocomposites for electrochemical applications," *Ionics*, vol. 25, no. 2, pp. 607–616, 2019.

[120] G. Sharma, D. D. Dionysiou, S. Sharma et al., "Highly efficient Sr/Ce/activated carbon bimetallic nanocomposite for photoinduced degradation of rhodamine B," *Catalysis Today*, vol. 335, pp. 437–451, 2019.

[121] G. Bharath, K. Rambabu, F. Banat, A. Hai, A. F. Arangadi, and N. Ponpandian, "Enhanced electrochemical performances of peanut shell derived activated carbon and its Fe_3O_4 nanocomposites for capacitive deionization of Cr(VI) ions," *Science of the Total Environment*, vol. 691, pp. 713–726, 2019.

[122] J. Yang, B. Hou, J. Wang et al., "Nanomaterials for the removal of heavy metals from wastewater," *Nanomaterials*, vol. 9, no. 3, p. 424, 2019.

[123] F. Keyvani, S. Rahpeima, and V. Javanbakht, "Synthesis of EDTA-modified magnetic activated carbon nanocomposite for removal of permanganate from aqueous solutions," *Solid State Sciences*, vol. 83, pp. 31–42, 2018.

[124] F. Cao, M. Zhao, Y. Yu et al., "Synthesis of two-dimensional CoS1. 097/nitrogen-doped carbon nanocomposites using metal–organic framework nanosheets as precursors for supercapacitor application," *Journal of the American Chemical Society*, vol. 138, no. 22, pp. 6924–6927, 2016.

[125] Y. Peng, Z. Chen, J. Wen et al., "Hierarchical manganese oxide/carbon nanocomposites for supercapacitor electrodes," *Nano Research*, vol. 4, no. 2, pp. 216–225, 2011.

[126] C. Yang, M. Zhou, and Q. Xu, "Three-dimensional ordered macroporous MnO 2/carbon nanocomposites as high-performance electrodes for asymmetric supercapacitors," *Physical Chemistry Chemical Physics*, vol. 15, no. 45, pp. 19730–19740, 2013.

[127] H. Li, L. Jiang, Q. Cheng et al., "MnO_2 nanoflakes/hierarchical porous carbon nanocomposites for high-performance supercapacitor electrodes," *Electrochimica Acta*, vol. 164, pp. 252–259, 2015.

[128] Y. Yan, Q. Cheng, Z. Zhu, V. Pavlinek, P. Saha, and C. Li, "Controlled synthesis of hierarchical polyaniline nanowires/ordered bimodal mesoporous carbon nanocomposites with high surface area for supercapacitor electrodes," *Journal of Power Sources*, vol. 240, pp. 544–550, 2013.

[129] J.-S. Ye, H. F. Cui, X. Liu, T. M. Lim, W.-D. Zhang, and F.-S. Sheu, "Preparation and characterization of aligned carbon nanotube–ruthenium oxide nanocomposites for supercapacitors," *Small*, vol. 1, no. 5, pp. 560–565, 2005.

[130] J. Shi, B. Jiang, C. Li et al., "Review of transition metal nitrides and transition metal nitrides/carbon nanocomposites for supercapacitor electrodes," *Materials Chemistry and Physics*, vol. 245, article 122533, 2020.

[131] P. Liu, J. Yan, Z. Guang, Y. Huang, X. Li, and W. Huang, "Recent advancements of polyaniline-based nanocomposites for supercapacitors," *Journal of Power Sources*, vol. 424, pp. 108–130, 2019.

[132] X. Zhong, X. Li, Y. Zhuo, Y. Chai, and R. Yuan, "Synthesizing anode electrochemiluminescent self-catalyzed carbon dots-based nanocomposites and its application in sensitive ECL biosensor for microRNA detection," *Sensors and Actuators B: Chemical*, vol. 305, p. 127490, 2020.

[133] V. Gupta and R. K. Kotnala, "Multifunctional ferromagnetic carbon-nanotube arrays prepared by pulse-injection chemical vapor deposition," *Angewandte Chemie International Edition*, vol. 51, no. 12, pp. 2916–2919, 2012.

[134] Z. Wei, H. Wang, Z. Ma, and H. Han, "Amperometric biosensor of matrix metalloproteinase-7 enhanced by Pd-functionalized carbon nanocomposites," *Nanoscale Research Letters*, vol. 13, no. 1, p. 375, 2018.

[135] S. Selvarajan, A. Suganthi, and M. Rajarajan, "Fabrication of g-C_3N_4/NiO heterostructured nanocomposite modified glassy carbon electrode for quercetin biosensor," *Ultrasonics Sonochemistry*, vol. 41, pp. 651–660, 2018.

[136] S. Shrivastava, N. Jadon, and R. Jain, "Next-generation polymer nanocomposite-based electrochemical sensors and biosensors: a review," *TrAC Trends in Analytical Chemistry*, vol. 82, pp. 55–67, 2016.

[137] R. Madhu, V. Veeramani, S.-M. Chen, P. Veerakumar, S.-B. Liu, and N. Miyamoto, "Functional porous carbon–ZnO nanocomposites for high-performance biosensors and energy storage applications," *Physical Chemistry Chemical Physics*, vol. 18, no. 24, pp. 16466–16475, 2016.

[138] Q. Zhang, Y. Qing, X. Huang, C. Li, and J. Xue, "Synthesis of single-walled carbon nanotubes-chitosan nanocomposites for the development of an electrochemical biosensor for serum leptin detection," *Materials Letters*, vol. 211, pp. 348–351, 2018.

[139] A. Şavk, H. Aydın, K. Cellat, and F. Şen, "A novel high performance non-enzymatic electrochemical glucose biosensor based on activated carbon-supported Pt-Ni nanocomposite," *Journal of Molecular Liquids*, vol. 300, article 112355, 2020.

[140] A. Hassanein, N. Salahuddin, A. Matsuda, G. Kawamura, and M. Elfiky, "Fabrication of biosensor based on Chitosan-ZnO/Polypyrrole nanocomposite modified carbon paste electrode for electroanalytical application," *Materials Science and Engineering: C*, vol. 80, pp. 494–501, 2017.

[141] N. Kaur, H. Thakur, and N. Prabhakar, "Conducting polymer and multi-walled carbon nanotubes nanocomposites based amperometric biosensor for detection of organophosphate," *Journal of Electroanalytical Chemistry*, vol. 775, pp. 121–128, 2016.

[142] N. A. Alenazi, M. A. Hussein, K. A. Alamry, and A. M. Asiri, "Nanocomposite-based aminated polyethersulfone and carboxylate activated carbon for environmental application. A real sample analysis," *C—Journal of Carbon Research*, vol. 4, no. 2, p. 30, 2018.

[143] F. O. Gomes, L. B. Maia, C. Delerue-Matos, I. Moura, J. J. G. Moura, and S. Morais, "Third-generation electrochemical biosensor based on nitric oxide reductase immobilized in a multiwalled carbon nanotubes/1- *n*-butyl-3-methylimidazolium tetrafluoroborate nanocomposite for nitric oxide detection," *Sensors and Actuators B: Chemical*, vol. 285, pp. 445–452, 2019.

[144] A. T. Lawal, "Synthesis and utilization of carbon nanotubes for fabrication of electrochemical biosensors," *Materials Research Bulletin*, vol. 73, pp. 308–350, 2016.

[145] S. Chaemsanit, N. Matan, and N. Matan, "Activated carbon for food packaging Application: Review," *Walailak Journal of Science and Technology (WJST)*, vol. 15, no. 4, pp. 255–271, 2018.

[146] I. Heras, M. Krause, G. Abrasonis et al., "Advanced characterization and optical simulation for the design of solar selective coatings based on carbon: transition metal carbide nanocomposites," *Solar Energy Materials and Solar Cells*, vol. 157, pp. 580–590, 2016.

[147] H. Hou, H. Shao, X. Zhang, G. Liu, S. Hussain, and G. Qiao, "RGO-loaded flower-like $ZnCo_2O_4$ nanohybrid as counter electrode for dye-sensitized solar cells," *Materials Letters*, vol. 225, pp. 5–8, 2018.

[148] K. Xiong, W. Nie, P. Yu, L. Zhu, and X. Xiao, "Flower-like $CuCo_2O_4$@RGO nanohybrid as an effective counter electrode for dye-sensitized solar cells," *Materials Letters*, vol. 204, pp. 69–72, 2017.

[149] I. M. A. Mohamed, V.-D. Dao, A. S. Yasin et al., "Physicochemical and photo-electrochemical characterization of novel N-doped nanocomposite ZrO_2/TiO_2 photoanode towards technology of dye-sensitized solar cells," *Materials Characterization*, vol. 127, pp. 357–364, 2017.

[150] M. Q. Hamzah, A. H. Jabbar, S. O. Mezan, A. N. Tuama, and M. A. Agam, "Fabrications of PS/TiO2 nanocomposite for solar cells applications," *AIP Conference Proceedings*, vol. 2151, no. 1, article 020011, 2019.

[151] S. Chauhan, N. Jain, and U. Nagaich, "Nanodiamonds with powerful ability for drug delivery and biomedical applications: recent updates on in vivo study and patents," *Journal of Pharmaceutical Analysis*, vol. 10, no. 1, pp. 1–12, 2020.

[152] M. Karimi-Nazarabad and E. K. Goharshadi, "Highly efficient photocatalytic and photoelectrocatalytic activity of solar light driven WO_3/g-C_3N_4 nanocomposite," *Solar Energy Materials and Solar Cells*, vol. 160, pp. 484–493, 2017.

[153] S.-A. Martel-Estrada, *Recent progress in biomedical applications of nanodiamonds*, Instituto de Arquitectura Diseño y Arte, 2018.

[154] R. Zentel, "Polymer coated semiconducting nanoparticles for hybrid materials," *Inorganics*, vol. 8, no. 3, p. 20, 2020.

[155] A. Kausar, "Polydimethylsiloxane-based nanocomposite: present research scenario and emergent future trends," *Polymer-Plastics Technology and Materials*, vol. 59, no. 11, pp. 1148–1166, 2020.

[156] A. V. Penkova, S. F. A. Acquah, L. B. Piotrovskiy, D. A. Markelov, A. S. Semisalova, and H. W. Kroto, "Fullerene derivatives as nano-additives in polymer composites," *Russian Chemical Reviews*, vol. 86, no. 6, pp. 530–566, 2017.

[157] P. Senthil Kumar, P. R. Yaashikaa, and S. Ramalingam, "Efficient removal of nitrate and phosphate using graphene nanocomposites," in *A New Generation Material Graphene: Applications in Water Technology*, pp. 287–307, Springer, Cham, 2019.

[158] I. M. A. Mohamed, V.-D. Dao, C. Liu, N. A. M. Barakat, and H.-S. Choi, "Synthesis of electrospun 1D-photoanode nanocomposite based on electrospinning followed by hydrothermal treatment for highly efficient liquid-junction photovoltaic devices," *Journal of Sol-Gel Science and Technology*, vol. 91, no. 2, pp. 342–352, 2019.

[159] P. S. Nagasree, K. Ramji, K. K. Murthy, M. Kannam Naidu, and T. Haritha, "Fibre reinforced polymer (FRP) nanocomposites for radar absorption application in the X-band," in *Recent Trends in Mechanical Engineering*, pp. 409–418, Springer, Singapore, 2020.

[160] A. Munir, "Microwave radar absorbing properties of multi-walled carbon nanotubes polymer composites: a review," *Advances in Polymer Technology*, vol. 36, no. 3, pp. 362–370, 2017.

[161] B. K. Nagesha, V. Dhinakaran, M. Varsha Shree, K. P. Manoj Kumar, and T. Jagadeesha, "A review on weldability of additive manufactured titanium alloys," *Materials Today: Proceedings*, vol. 33, pp. 2964–2969, 2020.

[162] S. Tyagi, V. S. Pandey, H. B. Baskey et al., "RADAR absorption study of $BaFe_{12}O_{19}/ZnFe_2O_4$/CNTs nanocomposite," *Journal of Alloys and Compounds*, vol. 731, pp. 584–590, 2018.

[163] N. Rezazadeh and A. Kianvash, "Flexible radar absorbing nanocomposites based on co-ferrite/nano carbon/polymeric epoxy resin," *Journal of Electrical and Computer Engineering Innovations*, vol. 5, no. 1, pp. 53–57, 2017.

[164] V. Dhinakaran, N. Suraj Khope, S. Shanmugam, and K. Sankaranarayanasamy, "Numerical prediction of weld bead geometry in plasma arc welding of titanium sheets using COMSOL," in *Proceedings of the 2014 COMSOL Conference in Bangalore*, pp. 13-14, Bangalore, India, 2014.

[165] S.-E. Lee, W.-J. Lee, K. S. Oh, and C.-G. Kim, "Broadband all fiber-reinforced composite radar absorbing structure integrated by inductive frequency selective carbon fiber fabric and carbon-nanotube- loaded glass fabrics," *Carbon*, vol. 107, pp. 564–572, 2016.

[166] V. Dhinakaran, K. V. Surendar, M. S. Hasunfur Riyaz, and M. Ravichandran, "Review on study of thermosetting and thermoplastic materials in the automated fiber placement process," *Materials Today: Proceedings*, vol. 27, pp. 812–815, 2020.

[167] L. Sha, P. Gao, T. Wu, and Y. Chen, "Chemical Ni–C bonding in Ni–carbon nanotube composite by a microwave welding method and its induced high-frequency radar frequency electromagnetic wave absorption," *ACS Applied Materials & Interfaces*, vol. 9, no. 46, pp. 40412–40419, 2017.

[168] S.-H. Chen, W.-S. Kuo, and R.-B. Yang, "Microwave absorbing properties of a radar absorbing structure composed of carbon nanotube papers/glass fabric composites," *International Journal of Applied Ceramic Technology*, vol. 16, no. 5, pp. 2065–2072, 2019.

[169] H. Karimi-Maleh, Y. Orooji, F. Karimi et al., "A critical review on the use of potentiometric based biosensors for biomarkers detection," *Biosensors and Bioelectronics*, vol. 184, article 113252, 2021.

[170] S. A. Abid, A. Ahmed Muneer, I. M. S. al-Kadmy et al., "Biosensors as a future diagnostic approach for COVID-19," *Life Sciences*, vol. 273, article 119117, 2021.

[171] P. Li, G.-H. Lee, S. Y. Kim, S. Y. Kwon, H.-R. Kim, and S. Park, "From diagnosis to treatment: recent advances in patient-friendly biosensors and implantable devices," *ACS Nano*, vol. 15, no. 2, pp. 1960–2004, 2021.

[172] R. Antiochia, "Developments in biosensors for CoV detection and future trends," *Biosensors and Bioelectronics*, vol. 173, article 112777, 2021.

[173] J. Min, J. R. Sempionatto, H. Teymourian, J. Wang, and W. Gao, "Wearable electrochemical biosensors in North

America," *Biosensors and Bioelectronics*, vol. 172, article 112750, 2021.

[174] X. Zheng, F. Zhang, K. Wang et al., "Smart biosensors and intelligent devices for salivary biomarker detection," *TrAC Trends in Analytical Chemistry*, vol. 140, article 116281, 2021.

[175] M. M. Rahman, M. M. Hussain, and A. M. Asiri, "Fabrication of 3-methoxyphenol sensor based on Fe3O4 decorated carbon nanotube nanocomposites for environmental safety: real sample analyses," *PLoS One*, vol. 12, no. 9, article e0177817, 2017.

[176] L. Qian, S. Durairaj, S. Prins, and A. Chen, "Nanomaterial-based electrochemical sensors and biosensors for the detection of pharmaceutical compounds," *Biosensors and Bioelectronics*, vol. 175, article 112836, 2021.

[177] T. Yu, D. Liu, and Y. Xianyu, "Recent advances in gold nanoparticles-based biosensors for food safety detection," *Biosensors and Bioelectronics*, vol. 179, article 113076, 2021.

[178] Y. Nasu, Y. Shen, L. Kramer, and R. E. Campbell, "Structure- and mechanism-guided design of single fluorescent protein-based biosensors," *Nature Chemical Biology*, vol. 17, no. 5, pp. 509–518, 2021.

[179] A. A. Ansari, M. K. Nazeeruddin, and M. M. Tavakoli, "Organic-inorganic upconversion nanoparticles hybrid in dye-sensitized solar cells," *Coordination Chemistry Reviews*, vol. 436, article 213805, 2021.

[180] D. Zhang, M. Stojanovic, Y. Ren et al., "A molecular photosensitizer achieves a V_{oc} of 1.24 V enabling highly efficient and stable dye-sensitized solar cells with copper(II/I)-based electrolyte," *Nature communications*, vol. 12, no. 1, article 1777, pp. 1–10, 2021.

[181] D. Vikraman, S. Hussain, S. A. Patil et al., "Engineering MoSe2/WS2Hybrids to replace the scarce platinum electrode for hydrogen evolution reactions and dye-sensitized solar cells," *ACS Applied Materials & Interfaces*, vol. 13, no. 4, pp. 5061–5072, 2021.

[182] N. Vlachopoulos, A. Hagfeldt, I. Benesperi et al., "New approaches in component design for dye-sensitized solar cells," *Sustainable Energy & Fuels*, vol. 5, no. 2, pp. 367–383, 2021.

[183] J. Weerasinghe, S. Sen, J. M. K. W. Kumari et al., "Efficiency enhancement of low-cost metal free dye sensitized solar cells via non-thermal atmospheric pressure plasma surface treatment," *Solar Energy*, vol. 215, pp. 367–374, 2021.

[184] G. Fu, E. J. Cho, X. Luo et al., "Enhanced light harvesting in panchromatic double dye-sensitized solar cells incorporated with bilayered TiO_2 thin film-based photoelectrodes," *Solar Energy*, vol. 218, pp. 346–353, 2021.

[185] M. Dhonde, K. Sahu, and V. V. S. Murty, "Cu-doped TiO_2 nanoparticles/graphene composites for efficient dye-sensitized solar cells," *Solar Energy*, vol. 220, pp. 418–424, 2021.

[186] H. Zhou, J.-M. Ji, and H. K. Kim, "Porphyrin sensitizers with acceptor structural engineering for dye-sensitized solar cells," *Dyes and Pigments*, vol. 187, article 109082, 2021.

[187] C. Kim and M. Kim, "Intrinsically conducting polymer (ICP) coated aramid fiber reinforced composites for broadband radar absorbing structures (RAS)," *Composites Science and Technology*, vol. 211, article 108827, 2021.

[188] M.-S. Jang, J.-H. Choi, W.-H. Jang, Y.-W. Nam, and C.-G. Kim, "Effects of dot-type electroless nickel plating on the mechanical properties of glass/epoxy used for radar-absorbing structures," *Composite Structures*, vol. 257, article 113165, 2021.

[189] V. Joy, V. G. Padwal, H. Singh, and R. U. Nair, *Optimization of Multilayered Radar Absorbing Structures (RAS) Using Nature Inspired Algorithm*, CRC Press, 2021.

[190] S. M. Baek and W. J. Lee, "Design method for radar absorbing structures using reliability-based design optimization of the composite material properties," *Composite Structures*, vol. 262, article 113559, 2021.

[191] A. F. N. Boss, H. R. Ferreira, F. L. Braghiroli et al., "Investigation of sustainable porous carbon as radar absorbing material," *Matéria (Rio de Janeiro)*, vol. 26, no. 2, 2021.

[192] Y. R. Denny, A. Trenggono, T. Firmansyah, I. Revaldi, Y. Taryana, and S. Aritonang, "Effect of filler concentration and time sonication of ZnO composite for radar absorbing material applications," *Materials Science Forum*, vol. 1028, pp. 249–254, 2021.

[193] Y. Xie, P. Li, J. Tang et al., "Highly thermally conductive and superior electromagnetic interference shielding composites via in situ microwave-assisted reduction/exfoliation of expandable graphite," *Composites Part A: Applied Science and Manufacturing*, vol. 149, article 106517, 2021.

[194] D. V. Baker, C. Bao, and W. S. Kim, "Highly conductive 3D printable materials for 3D structural electronics," *ACS Applied Electronic Materials*, vol. 3, no. 6, pp. 2423–2433, 2021.

[195] E. Ragni, C. Perucca Orfei, A. Bidossi et al., "Superior osteoinductive and osteo-conductive properties of trabecular titanium vs. PEEK scaffolds on human mesenchymal stem cells: a proof of concept for the use of fusion cages," *International journal of molecular sciences*, vol. 22, no. 5, article 2379, 2021.

[196] B. Zhao, Q. Chen, G. da, J. Yao, Z. Shao, and X. Chen, "A Highly stretchable and anti-freezing silk-based conductive hydrogel for application as a self-adhesive and transparent ionotronic skin," *Journal of Materials Chemistry C*, vol. 9, no. 28, pp. 8955–8965, 2021.

[197] V. Katseli, A. Economou, and C. Kokkinos, "Smartphone-addressable 3D-printed electrochemical ring for nonenzymatic self-monitoring of glucose in human sweat," *Analytical Chemistry*, vol. 93, no. 7, pp. 3331–3336, 2021.

[198] J. Chen, Y. Zhu, J. Huang et al., "Advances in responsively conductive polymer composites and sensing applications," *Polymer Reviews*, vol. 61, no. 1, pp. 157–193, 2021.

[199] D. Serban and C. G. Opran, "Influence of the surface microstructure of conductive polymer composite bipolar plate on the fuel cell performance," *Macromolecular Symposia*, vol. 396, no. 1, article 2000324, 2021.

[200] Y. Guan, F. Xu, X. Wang et al., "Implementation of hybrid PDMS-graphite/Ag conductive material for flexible electronic devices and microfluidic applications," *Microelectronic Engineering*, vol. 235, article 111455, 2021.

[201] S.-M. Yong, S. J. Lee, J. Park, J. Hong, J. H. Jung, and Y. Kim, "Fiber-reinforced plastic material with de-icing capability for radome application," *Materials Letters*, vol. 284, article 128943, 2021.

[202] D. Kim, Y. Hirayama, Z. Liu, H. Kwon, M. Kobashi, and K. Takagi, "Highly conductive Al/Al interfaces in ultrafine grained Al compact prepared by low oxygen powder metallurgy technique," *Nanomaterials*, vol. 11, no. 5, p. 1182, 2021.

[203] Q. Zou, S.-w. Xiong, M.-y. Jiang et al., "Highly thermally conductive and eco-friendly OH-h-BN/chitosan nanocomposites by constructing a honeycomb thermal network," *Carbohydrate Polymers*, vol. 266, article 118127, 2021.

[204] N. Zavanelli and W.-H. Yeo, "Advances in screen printing of conductive nanomaterials for stretchable electronics," *ACS Omega*, vol. 6, no. 14, pp. 9344–9351, 2021.

[205] A. Wang, Y. Wang, B. Zhang et al., "Hydrogen-bonded network enables semi-interpenetrating ionic conductive hydrogels with high stretchability and excellent fatigue resistance for capacitive/resistive bimodal sensors," *Chemical Engineering Journal*, vol. 411, article 128506, 2021.

Hindawi
Journal of Nanomaterials
Volume 2021, Article ID 8082522, 7 pages
https://doi.org/10.1155/2021/8082522

Research Article

Synthesis of $CuAl_2O_4$ Nanoparticle and Its Conversion to CuO Nanorods

V. Andal,[1] **G. Buvaneswari**,[2] **and R. Lakshmipathy**[1]

[1]*Department of Chemistry, KCG College of Technology, Chennai, 600097 Tamil Nadu, India*
[2]*Materials Division, School of Advanced Sciences, VIT University, Vellore, 632014 Tamil Nadu, India*

Correspondence should be addressed to R. Lakshmipathy; lakshmipathy.che@kcgcollege.com

Received 27 May 2021; Revised 20 July 2021; Accepted 22 August 2021; Published 7 September 2021

Academic Editor: P. Davide Cozzoli

Copyright © 2021 V. Andal et al. This is an open access article distributed under the Creative Commons Attribution License, which permits unrestricted use, distribution, and reproduction in any medium, provided the original work is properly cited.

The molten salt approach was used to convert $CuAl_2O_4$ nanoparticles to CuO nanorods in this study. Molten hydroxide (NaOH) synthesis was chosen over molten salts (NaCl/KCl) for removing aluminium oxide from copper aluminate at low temperatures. The molten salt process is environmentally beneficial. Polymeric precursors were used to make nanosized copper aluminates. Alginic acid polymer is used to gel aqueous solutions of copper acetate and aluminium nitrate, yielding precursor after further heating. The precursor provides 14 nm nanosized copper aluminates after being heated at 900°C for 5 hours. XRD, FTIR, SEM, and TEM were used to characterize the nanosized copper aluminate powder. Solid state mixing and solution technique were used to investigate molten hydroxide treatment of spinel $CuAl_2O_4$. The products of the reaction were identified using XRD. FTIR and SEM are also used to analyze the sample. Using UV-DRS absorbance spectrum analysis, the optical characteristics of $CuAl_2O_4$ and CuO nanorods were examined. Using the Tauc plot method, the band gaps of $CuAl_2O_4$ and CuO were calculated to be 4.3 and 3.93 eV.

1. Introduction

Spinel oxides are interesting due to their various physical and chemical properties [1, 2]. They are applied widely in different fields such as multiferroics, spintronics, superconductors, optoelectronics, and cathodes for rechargeable lithium batteries [3–7]. Among them, transition metal aluminates having spinel structure are of current importance due to their technological applications in various fields such as catalysis, refractories, heat-resistant pigment, and degradation of organic compounds [8–13]. Reduction in the size of their metal aluminates yields improved properties such as lower temperature sinterability, greater thermal stability, increased hardness, better diffusion, and ductility [14]. Generally, nanostructured transition metal aluminates are prepared by different routes such as sol-gel, microemulsion, templating process, hydrothermal, coprecipitation, and solution combustion [10, 14–18]. However, these methods have some drawbacks, such as the utilisation of expensive metal alkoxide precursors, effective templating agents, homogeneity, stoichiometric control, and high temperatures.

Copper aluminate is an inverse spinel with a low band gap which makes it a potential candidate as photocatalyst [19]. Various methods such as coprecipitation, sol-gel, hydrothermal, and combustion have been reported for the synthesis of nanosized $CuAl_2O_4$ [20–22]. Weizhong et al. synthesized nanosized copper aluminate spinel by precursor approach with the help of ultrasound irradiation in the presence of argon atmosphere [11]. In the present study, we synthesized nanosized copper aluminate by alginate precursor approach without using argon atmosphere and ultrasonic irradiation.

CuO nanostructures have excellent applications such as electrode materials for lithium batteries, catalyst, and adsorbent [22]. In particular, CuO nanostructures are prepared by hydrothermal, microwave, and solvothermal, at high temperatures and complex methods. So there is a requirement for simple and low-temperature method of preparation of CuO nanostructure.

Few reports are available on the conversion of spinel oxides to metal and metal oxide in which the spinel oxide can be considered as a precursor. Yang et al. reported on

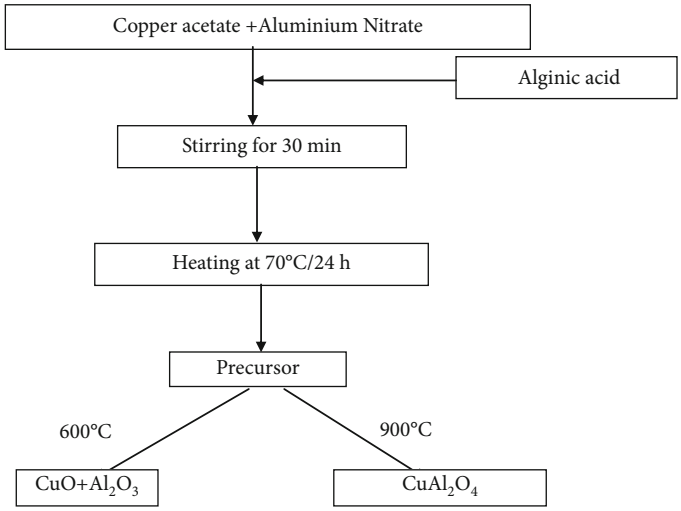

Figure 1: Experimental procedures for the synthesis of nano-$CuAl_2O_4$.

the preparation of nanocrystalline "Cu" from rod-like $CuFe_2O_4$ [23]. Ribeiro et al. reported the formation of surface "Ni" nanoparticles from $NiAl_2O_4$ during CO_2 reforming of methane [24]. $CuMn_2O_4$ catalyst showed high reactivity in water gas shift reaction due to its reduction to Cu/MnO in the presence of H_2 atmosphere at 350-400°C [25]. Formation of "Cu" on the surface of $CuCr_2O_4$ makes the system an active catalyst for the selective hydrogenation of furfural to furfuryl alcohol [26]. Similarly, Ni metal dispersed on the surface of nickel spinel oxide catalyst results in stable performance in ethanol steam reforming [27]. Spinel $CuFe_2O_4$ has been studied as a precursor for copper catalyst by Kameoka et al. [28]. Nillohit et al. synthesized mesoporous CuO nanoparticles from $Cu(OOCPh)_2Lut_2$ precursor complex by annealing at 450°C [29]. Precursors already reported for synthesizing CuO nanoparticles are $Cu_2(OH)_3Br$, CuS, etc. [30, 31]. So far, no reports are available for the synthesis of CuO from $CuAl_2O_4$ precursor. However, the regeneration process of Cu or CuO from copper containing spinel oxides has not been investigated thoroughly.

Molten salt syntheses are effective low-temperature synthesis without using expensive precursors and toxic elements, and they do not require any specialized equipment for synthesizing metal oxides. Molten hydroxide synthesis is a type of molten salt synthesis in which hydroxides are used instead of salts which produces single-phase and controlled morphology [32, 33]. Due to its advantages, molten hydroxide synthesis is considered to be the most promising one, and hence, it is applied to prepare simple metal oxide from complex metal oxide.

The development of new methods for preparation of cupric oxide with various morphologies has always been important because cupric oxide is a significant metal oxide. From the literature reports, it was prominent that the synthesis will have an effect on size and morphology of the particles [34]. To the best of our knowledge, no work has been done to synthesize $CuAl_2O_4$ particles by polymeric precursor method using alginic acid as a complexing agent and its conversion to CuO by molten hydroxide method. Therefore, the aim of this study is to prepare nanostructured $CuAl_2O_4$ powders and CuO nanopowder at low temperature and to calculate its band gap.

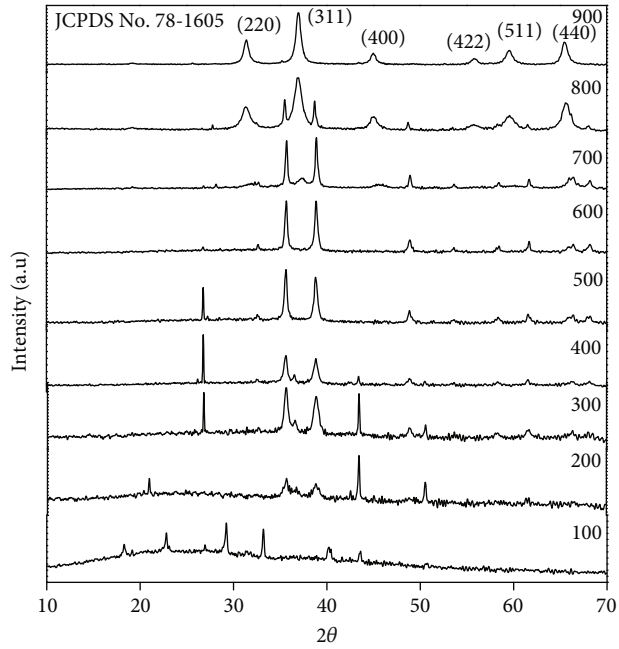

Figure 2: XRD pattern of $CuAl_2O_4$ powder obtained on heating the precursor from 100-900°C.

2. Experimental

2.1. Materials. The regents used were of analytical grade. Aluminium nitrate (98%) and alginic acid (19-25%) were procured from SD Fine-Chemical Limited, India. Cuprous acetate (99%) was from Sisco Lab and NaOH from Qualigens.

2.2. Synthesis of $CuAl_2O_4$ by Polymeric Precursor Method. Nanosized copper aluminate spinel particles are synthesized

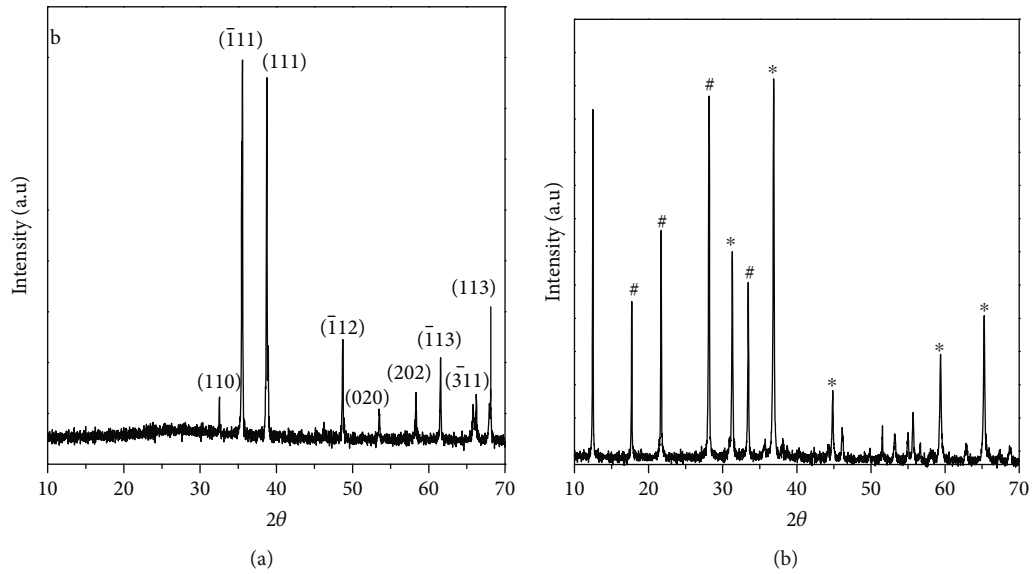

Figure 3: (a) XRD pattern of CuO (CAI). (b) XRD pattern of CAII: ∗ indicates $CuAl_2O_4$; # indicates Al_2O_3.

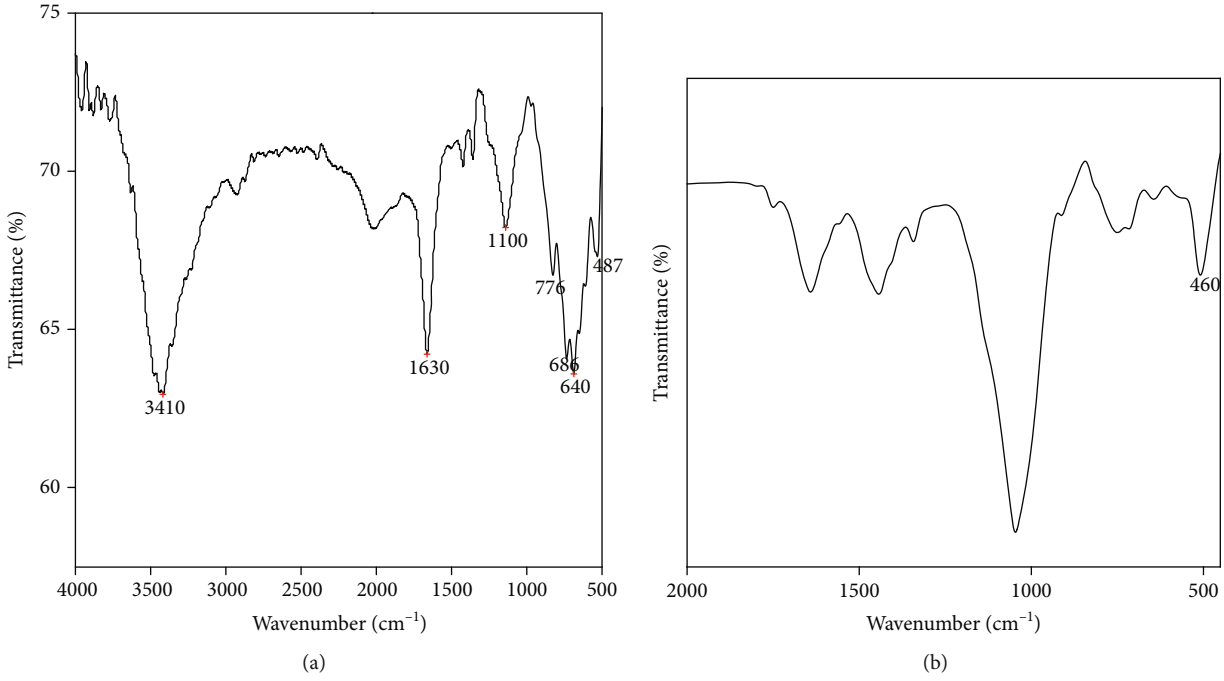

Figure 4: (a) FTIR spectrum of $CuAl_2O_4$. (b) FTIR spectrum of CuO (CAI).

by polymeric precursor approach. The elaborate experimental procedure for the synthesis of $CuAl_2O_4$ is shown in Figure 1.

The synthesis of polymeric precursor was carried out as follows. The two solutions cuprous acetate and aluminium nitrate were stirred thoroughly to get a homogeneous solution. Secondly, 60 ml of 20% alginic acid is added and kept to stirring at 70°C for 24 h till a dark blue gel formed. The gel on continuous heating gets converted to black powder. The black powder or precursor was then calcined at different (100°C, 300°C, 500°C, and 700°C) temperatures for 12 h and 900°C/5 h to produce nanosized $CuAl_2O_4$ particles.

2.3. Molten Hydroxide Synthesis. Synthesized $CuAl_2O_4$ nanomaterial was treated with NaOH (molten hydroxide) by two approaches

(i) Solid state reaction

(ii) Solution reaction method

2.4. Solid State Reaction. $CuAl_2O_4$ and alkali (NaOH) are mixed well in a mortar in the ratio of 1 : 10. After thorough grinding for 5 min, the slurry was immediately put into a

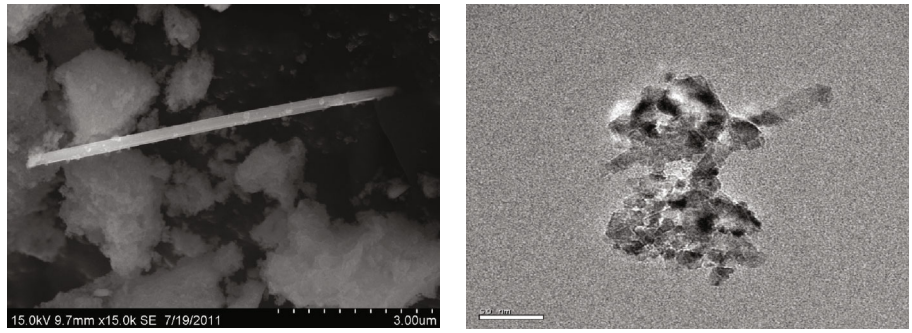

(a) (b)

Figure 5: (a) SEM image of $CuAl_2O_4$. (b) TEM image of $CuAl_2O_4$.

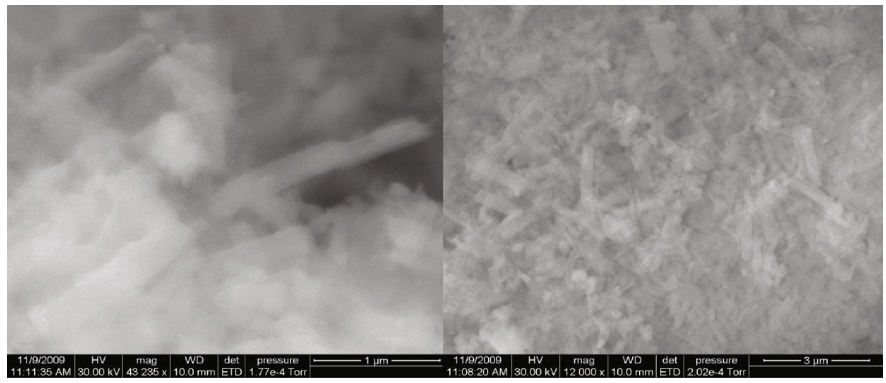

Figure 6: SEM images of CuO (CAI).

crucible and heated at 100°C for 24 hours. After 24 h, a dark blue-coloured layer formed on the substance. The product was then washed multiple times with water to eliminate any sodium aluminate that had generated in the process. The powder (CAI) is then dried and tested.

2.5. Solution Reaction Method. $CuAl_2O_4$ (0.235 g) is dissolved in 10 ml water and mixed thoroughly to get a homogenous dispersion. The sodium hydroxide solution (10 ml, 2.35 g) is added to the dispersion and refluxed in an oil bath at 100°C for 24 hours. The mixture is then filtered, rinsed, and analyzed (CAII).

2.6. Characterization. Powder X-ray diffraction was used to describe the phase present in the $CuAl_2O_4$ precursor and alkali-treated copper aluminate (CAI and CAII) as manufactured powders at room temperature in a Bruker instrument (D8 Advance) using Cu *Kα* radiation (=1.54). The Debye-Scherrer formula was used to calculate the average particle size of the final product. The KBr disc approach was used to record the infrared spectra (FTIR spectrometer, JASSCO Model 4100). The FEI QUANTA FEG 200 HR scanning electron microscope was used to perform scanning electron microscopic analysis on the sample. TEM pictures were captured using a Philips CM 200 with a 20-200 kV working voltage. The optical properties of the powders are measured using DR UV-VIS instrument.

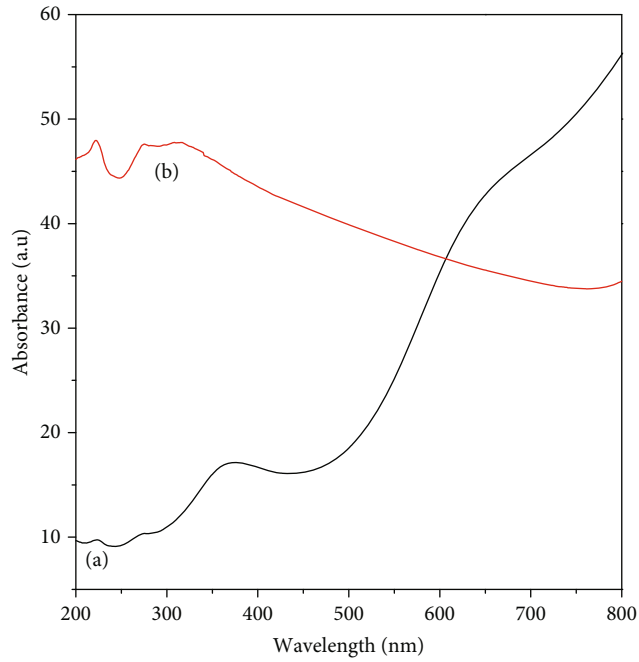

Figure 7: UV-DRS diffuse reflectance spectra of (a) $CuAl_2O_4$ and (b) CuO (CAI).

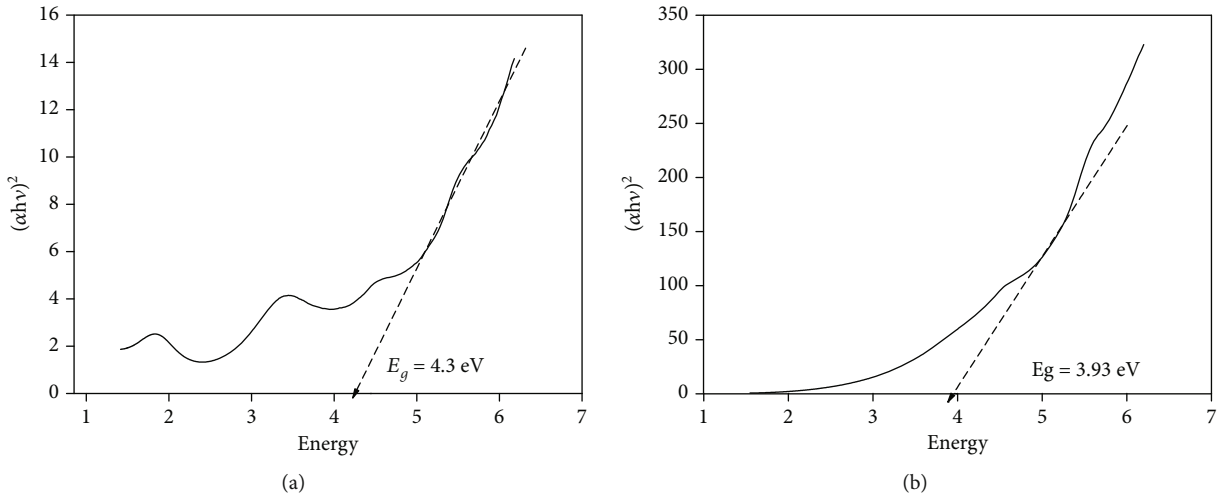

FIGURE 8: Tauc plot of direct allowed transition of (a) $CuAl_2O_4$ and (b) CuO.

3. Results and Discussion

The XRD pattern of $CuAl_2O_4$ precursor heated at different temperatures is shown in Figure 2. At each temperature, the sample is heated for 12 h in air to evaluate the formation of pure phase. The precursor on heat treated at 600°C/12 h yields pure CuO phase with monoclinic structure in agreement with JCPDS No. 45-0397 [35]. On further heating to 700°C, weak intense $CuAl_2O_4$ peak and more intense CuO were obtained. The relative peak intensity of CuO decreased on further heating. On heating at 900°C/5 h, the precursor yields normal spinel $CuAl_2O_4$. The XRD peaks of $CuAl_2O_4$ are in good agreement with JCPDS No. 78-1605. From the XRD data, the crystallite size of as-prepared $CuAl_2O_4$ was calculated to be 14 nm using the Debye-Scherrer equation

$$D = \frac{K\lambda}{\beta \cos\theta}, \quad (1)$$

where β is the full width maximum, K is the shape factor (0.9), and λ is the wavelength of X-ray source. $CuAl_2O_4$ is formed at higher temperature, and CuO is formed at 600°C.Niasari et al. synthesized nanocrystalline $CuAl_2O_4$ at 800°C by modified sol-gel method. Our results are in good agreement with their reports [10].

The XRD peaks of "CAI" (Figure 3(a)) are in good agreement to pure monoclinic CuO (JCPDS No. 45-0937) whereas the XRD peaks of "CAII" (Figure 3(b)) contain $CuAl_2O4$, Al_2O_3, and AlOH. This shows that $CuAl_2O_4$ does not react with NaOH solution even when it was refluxed for 12 h.

FTIR analyses were used to identify the functional groups of nanosized spinel $CuAl_2O_4$ and interaction of $CuAl_2O_4$ with NaOH. The vibrations at 3419 cm^{-1} and 1641 cm^{-1} (Figure 4(a)) are due to the longitudinal and bending vibration of water. A broad peak centered at 640 cm^{-1} is due to the Cu-O, Al-O, and Al-O-Al longitudinal vibrations in $CuAl_2O_4$ [36, 37]. The IR absorption spectrum of NaOH-treated $CuAl_2O_4$ (Figure 4(b)) shows a different pattern from the spinel. On treatment with NaOH, a broad peak centered at 640 cm^{-1} disappears and a small peak appeared at 460 cm^{-1} which confirms the formation of Cu-O. Also, the vibrations due to alumina are not observed which further indicates the complete conversion of $CuAl_2O_4$ into CuO [38].

The size and the morphology of synthesized nanosized $CuAl_2O_4$ were examined by SEM and TEM techniques. Figures 5(a) and 5(b) show the SEM and TEM images of nanosized $CuAl_2O_4$, respectively. The SEM image exhibits a variety of morphologies, including nanosized rod production and porous spherical particles. Thus, the homogeneity in shape is not achieved using alginate precursor. The surface area of the synthesized $CuAl_2O_4$ is 27.6 m^2g.

The TEM image (Figure 5(b)) was done by ultrasonicating the $CuAl_2O_4$ powder in acetone. The TEM image indicates that the particles are of diameter 50 nm. From the TEM image, we can further confirm that the obtained nanocrystals are not dispersed well and the cubes aggregated to form different shapes such as rods and triangles. Thus, the homogeneity in shape is not achieved using an alginate precursor.

The SEM image of CuO (CAI) formed from solid state reaction (Figure 6) shows the rod morphology which is observed in $CuAl_2O_4$. The morphology of $CuAl_2O_4$ persists on further treatment with alkali. Similar to the spinel, the rods are agglomerated and the porosity gets reduced. Similar to the reported literatures, the surface area of the synthesized CuO is 3.59 m^2g.

With reference to the results obtained, the nano-$CuAl_2O_4$ is transformed to pure nano-CuO by solid state reaction with alkali. It is well known that $CuAl_2O_4$ on heating at higher temperature results in a mixture of $CuAlO_2$ and CuO [39]. The mechanism that exists in the formation of CuO from $CuAl_2O_4$ by alkali treatment is mentioned below in the form of equations.

$$\begin{aligned} CuAl_2O_4 + 2NaOH &\longrightarrow Cu(OH)_2 + Na_2Al_2O_4 \\ Cu(OH)_2 &\xrightarrow{100^oC} CuO \end{aligned} \quad (2)$$

$CuAl_2O_4$ on alkali treatment by solid state reaction forms a metastable phase copper hydroxide. The produced copper hydroxide decomposes at low temperature 100°C to form CuO and sodium aluminate. Since sodium aluminate is soluble in water, it is removed in washings with water and pure CuO nanorods obtained. Our reports are in good agreement with the result of Yannick et al. that $Cu(OH)_2$ easily undergoes dehydration on heating to form stable CuO [40].

3.1. Optical Properties of $CuAl_2O_4$ and CuO. The UV-DRS diffuse reflectance spectra of $CuAl_2O_4$ and CuO were measured in the wavelength range of 200-800 nm shown in Figure 7 to investigate optical properties. The UV-VIS absorption spectrum of the synthesized $CuAl_2O_4$ nanostructure is shown in Figure 7(a). There is an absorption band centered at 364 nm with two small shoulders at 269 and 224 nm. The absorption band for CuO is at 294 nm with a shoulder at 221 nm (Figure 7(b)) which was similar to the reported literature [41].

Tauc approach (Figure 8) was applied to calculate the band gap (E_g) of $CuAl_2O_4$ and CuO using the below equation

$$(ahv)^{1/n} = A\left(hv - E_g\right). \tag{3}$$

The optical band gap of $CuAl_2O_4$ nanoparticles annealed at 900°C was evaluated as 4.3 eV. Similarly, for CuO, it was estimated as 3.93 eV, respectively.

4. Conclusion

Nano-$CuAl_2O_4$ with a particle size of 20-50 nm was synthesized using the alginate precursor method. Various experimental techniques were used to characterize $CuAl_2O_4$ that was synthesized. $CuAl_2O_4$ has an optical band gap of 4.3 eV, whereas CuO has an optical band gap of 3.93 eV due to the absence of aluminium oxide. Molten hydroxide was used to transform $CuAl_2O_4$ into pure CuO nanorods at a lower temperature. This procedure can also be used to achieve controlled morphology. The activity of spinel $CuAl_2O_4$ as a precursor for the production of CuO is demonstrated in this study.

Data Availability

All data used to support the findings of this study are included within the article.

Conflicts of Interest

The authors declare that they have no conflicts of interest.

Acknowledgments

The authors thank VIT University for providing all required facilities to carry out the experiments.

References

[1] M. L. Huggins, "Electronic Structures of the Spinels," *Physics Review*, vol. 21, no. 5, pp. 509–516, 1923.

[2] E. J. W. Verwey and E. L. Heilmann, *The Journal of Chemical Physics*, vol. 15, p. 174, 1947.

[3] Y. Yamaski, S. Miyasaka, Y. Kaneko, J.-P. He, T. Arima, and Y. Tokura, *Physical Review Letters*, vol. 96, 2006.

[4] U. Lüders, G. Herranz, M. Bibes et al., "Hybrid perovskite-spinel magnetic tunnel junctions based on conductive ferrimagnetic $NiFe_2O_4$," *Journal of Applied Physics*, vol. 99, no. 8, article 08K301, 2006.

[5] S. Satpathy and R. M. Martin, "Electronic structure of the superconducting oxide spinel $LiTi_2O_4$," *Physical Review B*, vol. 36, no. 13, pp. 7269–7272, 1987.

[6] D. Segev and S.-H. Wei, "Structure-derived electronic and optical properties of transparent conducting oxides," *Physical Review B*, vol. 71, no. 12, article 125129, 2005.

[7] J. Kim and A. Manthiram, "Low temperature synthesis and electrode properties of $Li_4Mn_5O_{12}$," *Journal of the Electrochemical Society*, vol. 145, L53, 1998.

[8] L. Ji, S. Tang, H. C. Zeng, J. Lin, and K. L. Tan, "CO_2 reforming of methane to synthesis gas over sol–gel-made Co/γ-Al_2O_3 catalysts from organometallic precursors," *Applied Catalysis A: General*, vol. 207, no. 1-2, pp. 247–255, 2001.

[9] M. H. Amin, A. Kazemzadeh, B. Arfaei, N. S. Chaudhury, and V. Sahajwalla, "Investigations of calcium aluminate slag penetration to MgO monolithic refractories in steelmaking process," *International Journal of ISSI*, vol. 3, no. 2, pp. 34–42, 2006.

[10] M. S. Niasari, M. F. Khouzani, and F. Davar, "Bright blue pigment $CoAl_2O_4$ nanocrystals prepared by modified sol–gel method," *Journal of Sol-Gel Science and Technology*, vol. 52, pp. 321–327, 2009.

[11] L. V. Weizhong, B. Liu, Q. Qiu et al., "Synthesis, characterization and photocatalytic properties of spinel $CuAl_2O_4$ nanoparticles by a sonochemical method," *Journal of Alloys and Compounds*, vol. 479, pp. 480–483, 2009.

[12] K. Ajay, P. B. Chauke, S. Zahra et al., "Microwave-mediated fabrication of mesoporous Bi-doped $CuAl_2O_4$ Nanocomposites for Antioxidant and Antibacterial Performances," *Materials Today: Proceedings*, vol. 15, pp. 454–463, 2019.

[13] R. G. Chaudhary, V. N. Sonkusare, and G. S. Bhusari, "Microwave-mediated synthesis of spinel $CuAl_2O_4$ nanocomposites for enhanced electrochemical and catalytic performance," *Research on Chemical Intermediates*, vol. 44, pp. 2039–2060, 2018.

[14] F. Meyer, R. Hempelmann, S. Mathur, and M. Veith, "Microemulsion mediated sol-gel synthesis of nano-scaled MAl_2O_4 (M=Co, Ni, Cu) spinels from single-source heterobimetallic alkoxide precursors," *Journal of Materials Chemistry*, vol. 9, pp. 1755–1763, 1999.

[15] L. Zou, F. Li, X. Xiang, D. G. Evans, and X. Duan, "Self-generated template pathway to high-surface-area zinc aluminate spinel with mesopore network from a single-source inorganic precursor," *Chemistry of Materials*, vol. 18, pp. 5852–5859, 2006.

[16] Z. Chen, E. Shi, Y. Zheng, W. Li, N. Wu, and W. Zhong, "Synthesis of mono-dispersed $ZnAl_2O_4$ powders under hydrothermal conditions," *Materials Letters*, vol. 56, p. 601, 2002.

[17] M. A. Valenzuela, J. P. Jacobs, P. Bosch, S. Reijne, and B. Zapata, "The influence of the preparation method on the

surface structure of $ZnAl_2O_4$," *Brongersma HH Appl Catal A Gen*, vol. 148, p. 315, 1997.

[18] K. C. Patil, S. T. Aruna, and S. Ekambaram, "Combustion synthesis," *Current Opinion in Solid State & Materials Science*, vol. 2, p. 158, 1997.

[19] Y. Y. Jiang, J. G. Li, X. T. Sui et al., "$CuAl_2O_4$ powder synthesis by sol-gel method and its photodegradation property under visible light irradiation," *Journal of Sol-Gel Science and Technology*, vol. 42, pp. 41–45, 2007.

[20] U. Kameswari and C. N. Pillai, "Reaction of piperidine with formaldehyde over alumina and spinel aluminates," *Catalysis Letters*, vol. 38, pp. 53–56, 1996.

[21] T. Mimani, "Instant synthesis of nanoscale spinel aluminates," *Journal of Alloys and Compounds*, vol. 315, p. 123, 2001.

[22] A.-m. Cao, J. D. Monnell, C. Matranga, J.-m. Wu, L.-l. Cao, and J. Di Gao, "Hierarchical nanostructured copper oxide and its application in arsenic removal," *The Journal of Physical Chemistry C*, vol. 111, pp. 18624–18628, 2007.

[23] S. C. Yang, W. N. Su, S. D. Lin et al., "Preparation of nanosized Cu from a rod-like $CuFe_2O_4$: suitable for high performance catalytic applications," *Applied Catalysis B: Environmental*, vol. 106, pp. 650–656, 2011.

[24] F. P. N. Ribeiro, R. C. R. Neto, S. F. Moya, M. V. M. Souza, and M. Schmal, "Synthesis of $NiAl_2O_4$ with high surface area as precursor of Ni nanoparticles for hydrogen production," *International Journal of Hydrogen Energy*, vol. 35, pp. 11725–11732, 2010.

[25] Y. Tanaka, T. Utaka, R. Kikuchi, T. Takeguchi, K. Sasaki, and K. Eguchi, "Water gas shift reaction for the reformed fuels over Cu/MnO catalysts prepared via spinel-type oxide," *Journal of Catalysis*, vol. 215, no. 2, p. 271, 2003.

[26] R. Prasad and P. Singh, "Applications and preparation methods of copper chromite catalysts: a review," *Bulletin of Chemical Reaction Engineering & Catalysis*, vol. 6, no. 2, pp. 63–113, 2011.

[27] H. Muroyama, R. Nakase, T. Matsui, and K. Eguchi, "Ethanol steam reforming over Ni-based spinel oxide," *International Journal of Hydrogen Energy*, vol. 35, pp. 1575–1581, 2010.

[28] S. Kameoka, T. Tanabe, and A. P. Tsai, "Spinel $CuFe_2O_4$: a precursor for copper catalyst with high thermal stability and activity," *Catalysis Letters*, vol. 100, pp. 89–93, 2005.

[29] S. K. Maji, N. Mukherjee, A. Mondal, B. Adhikary, and B. Karmakar, "Chemical synthesis of mesoporous CuO from a single precursor: Structural, optical and electrical properties," *Journal of Solid State Chemistry*, vol. 183, pp. 1900–1904, 2010.

[30] J.-Y. Li, S. Xiong, B. Xi, X.-G. Li, and Y.-T. Qian, "Synthesis of CuO perpendicularly cross-bedded microstructure via a precursor-based route," *Crystal Growth & Design*, vol. 9, no. 9, pp. 4108–4115, 2009.

[31] C. Mu and J. He, "Confined conversion of CuS nanowires to CuO nanotubes by annealing-induced diffusion in nanochannels," *Nanoscale Research Letters*, vol. 6, 2011.

[32] T. Lusiola, F. Bortolani, Q. Zhang, and R. A. Dorey, "Molten hydroxide synthesis as an alternative to molten salt synthesis for producing $K_{0.5}Na_{0.5}NbO_3$ lead free ceramics," *Journal of Materials Science*, vol. 47, pp. 1938–1942, 2012.

[33] J. T. Zeng, K. W. Kwok, and H. L. W. Chan, "$K_xNa_{1-x}NbO_3$ powder synthesized by molten-salt process," *Materials Letters*, vol. 61, pp. 409–411, 2007.

[34] S. A. Hassanzadeh-Tabrizi, "Optimization of the synthesis parameters of high surface area ceria nanopowder prepared by surfactant assisted precipitation method," *Applied Surface Science*, vol. 257, no. 24, pp. 10595–10600, 2011.

[35] D. Keyson, D. P. Volanti, L. S. Cavalcante, A. Z. Simoes, J. A. Varela, and E. Longo, "CuO urchin-nanostructures synthesized from a domestic hydrothermal microwave method," *Materials Research Bulletin*, vol. 43, pp. 771–775, 2008.

[36] J. Yanyan, L. Jinggang, S. Xiaotao, N. Guiling, W. Chengyu, and G. Xiumei, "$CuAl_2O_4$ powder synthesis by sol-gel method and its photodegradation property under visible light irradiation," *Journal of Sol-Gel Science and Technology*, vol. 42, pp. 41–45, 2007.

[37] M. Salavati-Niasari, F. Davar, and M. Farhadi, "Synthesis and characterization of spinel-type $CuAl_2O_4$ nanocrystalline by modified sol–gel method," *Journal of Sol-Gel Science and Technology*, vol. 51, pp. 48–52, 2009.

[38] T. Sato, "Low-Frequency Vibration to aluminas," *Shigen to Sozhai*, vol. 114, pp. 987–990, 1998.

[39] C.-Y. Hu, K. Shih, and J. O. Leckie, "Formation of copper aluminate spinel and cuprous aluminate delafossite to thermally stabilize simulated copper-laden sludge," *Journal of Hazardous Materials*, vol. 181, pp. 399–404, 2010.

[40] Y. Cudennec and A. Lecerf, "The transformation of $Cu(OH)_2$ into CuO, revisited," *Solid State Sciences*, vol. 5, no. 11-12, pp. 1471–1474, 2003.

[41] V. K. J. KavithaGanesan, A. Natarajan, A. Rajaram, S. Ravichandran, and SatishRamalingam, "Green synthesis of copper oxide nanoparticles decorated with graphene oxide for anticancer activity and catalytic applications," *Arabian Journal of Chemistry*, vol. 13, pp. 6802–6814, 2020.

Hindawi
Journal of Nanomaterials
Volume 2021, Article ID 3039761, 6 pages
https://doi.org/10.1155/2021/3039761

Research Article

Application of Titanium Dioxide Nanoparticles Synthesized by Sol-Gel Methods in Wastewater Treatment

Saka Abel,[1] Leta Tesfaye Jule,[1,2] Fikadu Belay,[3] R. Shanmugam,[4] L. Priyanka Dwarampudi,[5] N. Nagaprasad,[6] and Ramaswamy Krishnaraj[2,7]

[1]*Dambi Dollo University, Department of Physics, College of Natural and Computational Science, Ethiopia*
[2]*Centre for Excellence-Indigenous Knowledge, Innovative Technology Transfer and Entrepreneurship, Dambi Dollo University, Ethiopia*
[3]*Dambi Dollo University, Department of Mathematics, College of Natural and Computational Science, Ethiopia*
[4]*TIFAC CORE HD, Department of Pharmacognosy, JSS Academy of Higher Education and Research, JSS College of Pharmacy Ooty, Tamil Nadu, India*
[5]*Department of Pharmacognosy, JSS Academy of Higher Education and Research, JSS College of Pharmacy Ooty, Tamil Nadu, India*
[6]*Department of Mechanical Engineering, ULTRA College of Engineering and Technology, Madurai, Tamil Nadu, India*
[7]*Department of Mechanical Engineering, College of Engineering and Technology, Dambi Dollo University, Ethiopia*

Correspondence should be addressed to Ramaswamy Krishnaraj; prof.dr.krishnaraj@dadu.edu.et

Received 9 July 2021; Accepted 11 August 2021; Published 29 August 2021

Academic Editor: Lakshmipathy R

Copyright © 2021 Saka Abel et al. This is an open access article distributed under the Creative Commons Attribution License, which permits unrestricted use, distribution, and reproduction in any medium, provided the original work is properly cited.

Nanotechnology from titanium dioxide has been deposited, and its application in desalination and water treatment has been investigated by using sol-gel methods. Homogeneously dispersed sphere shapes of titanium dioxide nanoparticles were observed from scanning electron microscope micrographs and decrease in size as aging time increases from 40 min to 60 min. SEM micrographs of highly transparent nanopowders show that they are detected in the visible region from UV/visible and that their red shift around maximum wavelength increases with increasing aging time due to an increase in water quality. The energy band gap of the generated nanosheet has narrowed as the aging time has increased, which is related to the red shift of the absorption spectrum edge in the sheet. The structural behaviors of deposited nanoparticles have also been investigated, which confirms the existence of anatase as well as rutile levels in the liquid phase. The findings of the PL allowed us to determine the total strength of the intensity. This shows that applying photodegradation by a solar absorber could play a vital role in desalination and water treatment.

1. Introduction

The important thing for human life is clean water which is a critical feedstock in a variety of key productions including electronics, pharmaceuticals, and nutrition [1]. The biosphere is encrusted with difficult challenges in consultation rising difficulties of pure water as obtainable provisions of freshwater are declining because of lengthy droughts, resident's growth, more rigorous health-based protocols, and contending demands from multiplicity of customers. As reports show, only three percent of all existing water on earth is actually freshwater; seawater is the most abundant obtainable foundation of drinking water as well as water for manufacture use in several regions and novelties in the growth of new [2]. The welfares of nanotechnology in case of water treatment claim have been intensive in 3 main sites: cure and remediation, sensor and recognition, and waste control. It has produced massive advancement in numerous fields like the engineering of electronics, telecommunications, and medicals. Nanotechnology has a vital role in addressing essential issues of the atmosphere and sectors of water. Nanotechnology apparatuses used to desalinate water are highly exhilarating as well as hopeful [3].

The charge of desalination, either heating or thermal, is enormously high. Improvements in nanoscale technology and engineering have created an unparalleled opportunity to produce more cost-effective as well as environmentally favourable acceptable water refinement systems [4, 5]. Developments in nanotechnology recommend that several of the current difficulties concerning water quality can be determined or greatly perfected by using nanocatalysts, nanosorbents, bioactive nanoparticles, nanostructured catalytic sheaths, and nanoparticle which improved clarification from other yields and procedures subsequent from the improvement of nanotechnology [6]. Moreover, nanotechnology derivative merchandises that minimize the concentrations of poisonous amalgams to sub-ppb stages can support in the accomplishment of water quality values and healthiness advisories [7]. There are very few wastewater treatment reports as general in sol-gel method. For the first time, titanium dioxide nanosheet or nanomembrane is used in application of desalination and water treatment. Throughout this work, we technologically advanced novel nanomaterials and procedures for treatment of surface water contaminated with toxic metal ions, organic and inorganic solutes, bacteria, and viruses [8]. In addition, we discuss some of the risks and challenges associated with the development of cost-effective and environmentally acceptable functional nanomaterials for water purification. Since the last few years, desalination technology has been used progressively all over the world to yield pure drinking water from briny groundwater and seawater, to recover the feature of prevailing provisions of freshwater for consumption and engineering dedications, agricultural needs and luxury manufacturing [9–12].

TiO_2 nanosheets were prepared by using CBD. The maximum resistivity and less optical transmission of such tools limit their application as optical ingredients for thermoelectric materials, requiring the essential to grow their optical as well as electrical behaviors. In addition, there is a shortage of information on the properties of TiO_2 nanoparticles in a chemical medium. Nanosheets prepared in alkaline have environmental pollution; usually, they yield hydroxides, which can reduce the quality of nanosheet prepared. It would be difficult to depose the maximum quality of TiO_2 nanoparticles intimate of an alkaline chemical immerse environment unless the challenge of TiO_2 preparation is overcome [13–18]. The influence of hydroxide is diminished when TiO_2 is prepared in an acidic bath. The most metallic ions are widely utilised in chemical bath deposition procedures; it is correct to generalise that no hydroxide exists in these conditions and that synthesis occurs via an ion by ion procedure. The objective of the current study was to synthesize and characterize TiO_2 nanoparticle sheets as solar absorber and study its application in wastewater treatment and desalination, deposited under different aging times at 40 min, 50 min, and 60 min. It is employed in the synthesis of tints, fabrics, sheets, polymers, cosmetic, and foodstuffs, as well as in the production of dyes. The biomediated TiO_2 nanoparticles have a wide range of purposes including illness diagnosis, therapy, manufacture of medical equipment, regenerative medicine, imaging, detection, energy production, and farming [19–25].

Sol- (solution-) gel (molten) systems are from the most encouraging and effective methods used in nanoparticle fabrication. This technique yields high crystal oxides by permitting regulator in nanoparticles size and surface morphology as well as phase configuration in different concentration precursors, and it is easy to operate. The present study is aimed at desalinating and treating water by using TiO_2 nanoparticle sheets as solar absorber with varying aging times at 40 min, 50 min, and 60 min.

2. Materials and Methodology

2.1. Materials. Titanium isopropoxide, hydrochloric acid (HCl), double-distilled water, ethanol, etc. were gained from chemical shop best chemicals Ltd., Addis Ababa, Ethiopia. Deionized water was used to make aqueous mixtures of essential concentrations. Completely, the chemicals were served as expected from the providers without any desalination [7].

2.2. Production of Titanium Dioxide Nanoparticles. The laboratory setup involves a magnetic stirrer. The reaction solution was regained at a constant temperature of 32°C with the magnetic stirrer revolving at 300 rpm. In this study, TiO_2 NPs were produced through sol-gel techniques; for that, 10 milliliters of titanium tetraisopropoxide was added into 120 milliliters of ethanol in a bath container with volume 500 milliliters. And total solution was agitated for 25 min by using a magnetic stirrer. In case of hydrolysis mixture, 5 milliliters of distilled water and 4 milliliters of HCl were mixed to the reaction by small drops. The reaction mixture was stirred constantly for hours to get a uniform solution. The pH of the total solutions was kept in the acidic medium of pH 5; after 20 hours of development, the gels generated were dehydrated and heated in an oven at 300°C. Lastly, the prepared nanoparticle changed to molten state by using double-distilled water; then, coated substrate was used to get TiO_2 nanosheet for the solar panel absorber.

2.3. Photodegradation of Wastewater Using Prepared TiO_2 Nanoparticle Sheet as Solar Panel. All the experiments have been performed at a constant volume of 100 wastewater liter by using the aqueous solution concentration. The solar power used is 80 W. Photodegradation has been investigated as shown in Figure 1. The initial pH of the solution has been observed as 5, and the acidity effect of pH was achieved. All the experiments were performed for a period of 160 min, and samples were taken out at different time ranges of 40 min, 50 min, and 60 min for further analysis.

3. Result and Discussions

A photodegradation experiment of wastewater was carried out by pouring 100 ml in a bottle and leaving it overnight. The effect of the amount of catalyst panes on the performance of degradation was being investigated in this experiment by altering the desalination time. All sheets have an area of $10 \times 20\ cm^2$. Wastewater without substance was used as control laboratory conditions [8]. Through the laboratory experiment, the water bottle was protected by a transparent acrylic to evade the influence of vaporizations on the

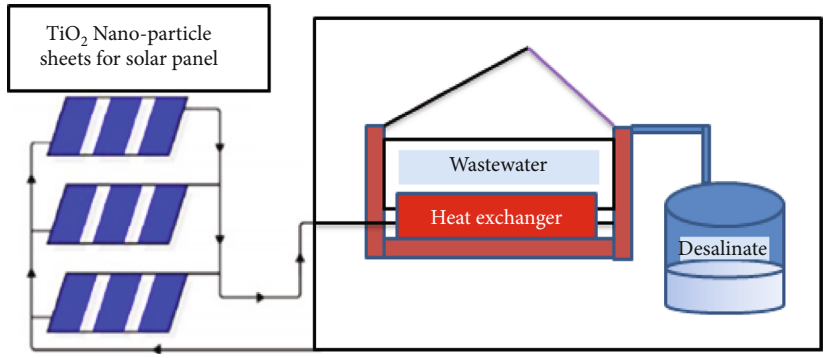

Figure 1: The schematic diagram of application of TiO_2 nanoparticles as nanosheet for desalination and water treatment.

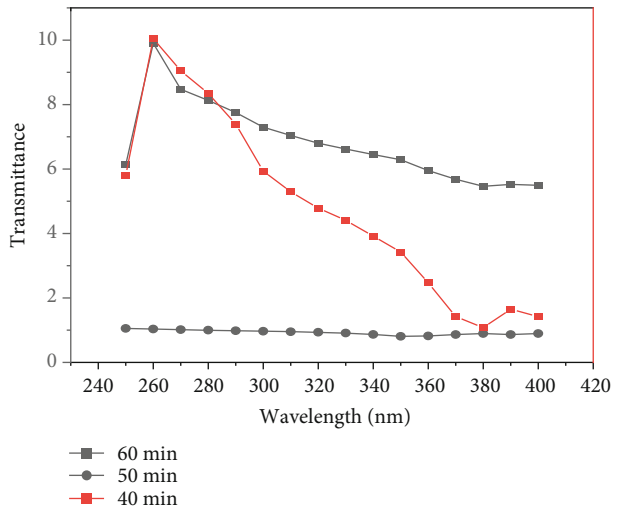

Figure 2: Transmittances of TiO_2 nanoparticle with varying aging times at 40 min, 50 min, and 60 min.

photodegradation solution wavelength in the range of UV-V which is until visible light. Even as ultraviolet-visible spectrum demonstrates, photons in the visible spectrum are required to elicit the photocatalytic reaction. Acrylic transmission peaks are shown in Figure 2 together with the experimental setup and lighting conditions. It was discovered that measuring the absorbance of a solution may be used to investigate the decolorization procedure of substances contained in wastewater. The concentration of a mixture is directly proportional to the generosity of the absorption spectra according to the Lambert-Beer principles. The reduction in the maximum absorption spectra of a solution throughout the degradation cycle implies a reduction in the concentration of waste in the water [12], which is supported by other research. As shown in Figure 2, the UV-Vis absorption spectra of batik sewage without and with a catalyst may be observed.

Photoluminescence is also used to describe the optical properties of TiO_2 nanoparticles that have been produced and characterized. The wavelength range between 350 and 650 nm with lower temperature is depicted in the figure. The photoluminescence (PL) spectra of the produced materials were examined in step three. When the annealing temperature is raised between 400 and 100-degree Celsius, the mean strength of photoluminescence falls as the amount of time spent aging the sample rises. The majority of the highest PL hardness is because of self-trapped exciton recombination, which is produced from particle size and is referred to as defect centres. For all elevated temperatures, the PL intensity drops instantaneously as a function of the aging time [9–24]. In comparison, the photoluminescence intensity for wavelengths of higher wavelength for 60 min and 50 min is smaller than 40 min for wavelength intensity for higher aging time. The anatase and rutile structures that have been discovered are mostly responsible for this effect.

The anatase phase is assigned to the secondary band spectra experienced at a length of 500 nm as shown in Figure 3, whilst the rutile phase is assigned to the peaks between 500 and 550 nm. When compared to the manufacturing of electron states throughout the band gap, associated faults are much more energetically attractive, and they are shaped also during description of the TiO_2 nanoparticle anatase stage and the 500 nm band gap happens once the structure is a combination of anatase and rutile phases at a reduced oxygen flow ratio [11–25]. The highest peak observed shows that at maximum aging the desalination of water has the highest quality.

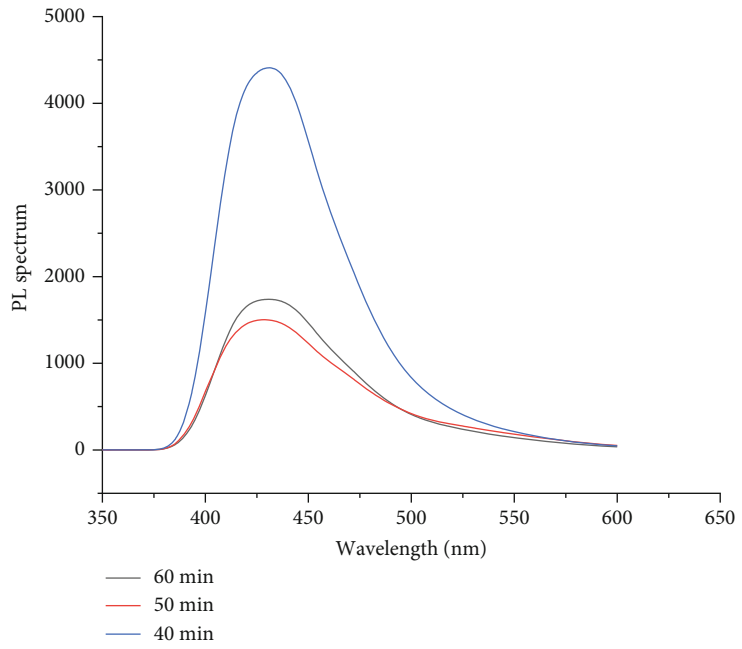

Figure 3: Photoluminescence spectrum of TiO_2 nanoparticles at different aging times at 40 min, 50 min, and 60 min.

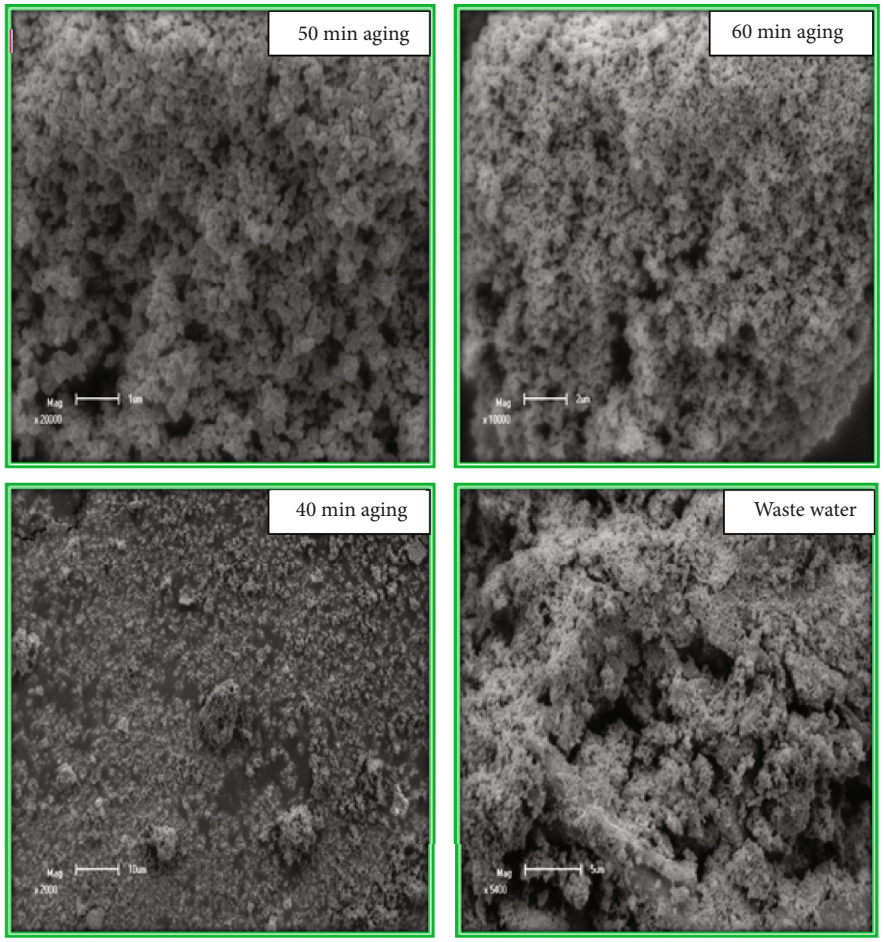

Figure 4: SEM analysis of TiO_2 nanoparticles for desalination and water treatment at different aging time at 40 min, 50 min, and 60 min.

The titanium nanoparticles were analyzed by a scanning electron microscope. The micrograph results reveal that sphere-like structure of titanium nanoparticles having 50-60 nm diameter, as explained in Figure 4. As aging time increased from 40 min to 60 min, the shape obtained confirms the pureness of water and this result is in good agreement with that previously reported [12–45].

4. Conclusions

In this research, we have successfully prepared nanoparticle of TiO_2 and its application in desalination and water treatment with related photodegradation of technologically advanced photocatalytic covering with acrylic by inserting a solution of visible light-receptive titanium dioxide nanoparticles at different aging times. We verified the possibility of solar absorber coating by sol-gel on a commercially available ITO substrate. Succeeding treatment with UV photo light occasioned on heterogeneous surface with intercalating long aging time. Our nanosheet could recuperate the fluidity upon visible light treatment. We qualified this to the photodegradation of the collected wastewater when applied visible light treatment. We contrived a device that empowered the constant departure and desalination of water mixture that was melted with organic substances that were adsorbed. It was established that the nanosheet prepared from TiO_2 has a potential to absorb photo light and able to recover its infuse flux in situ when applied under visible light treatment. We visualized that our nanosheet would have numerous applications, like wastewater treatment, fuel purification, and desalinating drinking water and water in industry. We also conclude that TiO_2 nanosheet has a wide range of uses, including wastewater treatment, fuel purification, desalination of drinking water and industrial water.

Data Availability

The data used to support the findings of this study are included within the article.

Disclosure

The research was performed as a part of employment of the authors from Dambi Dollo University Ethiopia.

Conflicts of Interest

The authors declare that there are no conflicts of interest.

References

[1] M. Batool, A. Shafeeq, B. Haider, and N. M. Ahmad, "TiO_2 nanoparticle filler-based mixed-matrix PES/CA nanofiltration membranes for enhanced desalination," *Membranes*, vol. 11, no. 6, p. 433, 2021.

[2] Y. S. Khoo, W. J. Lau, Y. Y. Liang, M. Karaman, M. Gursoy, and A. F. Ismail, "Eco-friendly surface modification approach to develop thin film nanocomposite membrane with improved desalination and antifouling properties," *Journal of Advanced Research*, 2021.

[3] B. Shrestha, M. Ezazi, and G. Kwon, "Engineered nanoparticles with decoupled photocatalysis and wettability for membrane-based desalination and separation of oil-saline water mixtures," *Nanomaterials*, vol. 11, no. 6, p. 1397, 2021.

[4] G. Ma, Z. Almansoori, and B. Khorshidi, "Development of antifouling thin film nanocomposite polyamide membrane using ITO nanoparticles," *Journal of Material Sciences & Engineering*, vol. 10, 2021.

[5] A. Ghaffar, S. Kiran, M. A. Rafique et al., "Citrus paradisi fruit peel extract mediated green synthesis of copper nanoparticles for remediation of disperse yellow 125 dye," *Desalination and Water Treatment*, vol. 212, pp. 368–375, 2021.

[6] O. N. Borisova, I. G. Doronkina, and V. M. Feoktistova, "Resource-saving nanotechnologies in waste water treatment," *Nanotechnologies in Construction*, vol. 13, no. 2, 2021.

[7] D. A. Tatarinov, S. R. Sokolnikova, and N. A. Myslitskaya, "Applying of chitosan-TiO_2 nanocomposites for photocatalytic degradation of anthracene and pyrene," *Journal of Biomedical Photonics & Engineering*, vol. 7, no. 1, 2021.

[8] E. L. Shafey, A. M. Abdel-Latif, and H. M. Abd El-Salam, "The facile synthesis of poly(acrylate/acrylamide) titanium dioxide nanocomposite for groundwater ammonia removal," *Desalination and Water Treatment*, vol. 212, pp. 61–70, 2021.

[9] A. Juliani, S. Rahmawati, and M. Yoneda, "Heavy metal characteristics of wastewater from batik industry in Yogyakarta area, Indonesia," *International Journal*, vol. 20, no. 80, pp. 59–67, 2021.

[10] E. Wibowo, M. Rokhmat, D. Y. Rahman, R. Murniati, and M. Abdullah, "Batik wastewater treatment using TiO2 nanoparticles coated on the surface of plastic sheet," *Procedia engineering*, vol. 170, pp. 78–83, 2017.

[11] B. M. P. Pereira and B. P. Backx, "Nanotechnology in water treatment: an optimistic perspective for the near future," *Journal of Nanotechnology and Nanomaterials*, vol. 2, pp. 51–56, 2021.

[12] K. R. Reyes and D. B. Robinson, *WO_3/TiO_2 Nanotube Photoanodes for Solar Water Splitting with Simultaneous Wastewater Treatment*, Sandia National Laboratories, Springfield, 2013.

[13] S. Roa, M. Sandoval, and S. Suarez, "Rutherford backscattering spectroscopy analysis of the growth quality of chemical bath deposited PbSe thin films," *Solid State Sciences*, vol. 113, p. 106545, 2021.

[14] S. Roa, M. Sandoval, M. J. C. Burgos, P. Manidurai, and S. Suarez, "Potential photovoltaic properties of thin film solar cells based on chemically deposited ZnO/PbSe junctions," *Journal of Alloys and Compounds*, vol. 871, p. 159559, 2021.

[15] M. H. Jang, E. R. Hoglund, P. M. Litwin et al., "Photoconductive mechanism of IR-sensitive iodized PbSe thin films via strong hole–phonon interaction and minority carrier diffusion," *Applied Optics*, vol. 59, no. 33, pp. 10228–10235, 2020.

[16] J. T. Harrison, E. Pantoja, M. H. Jang, and M. C. Gupta, "Laser sintered PbSe semiconductor thin films for Mid-IR applications using nanocrystals," *Journal of Alloys and Compounds*, vol. 849, p. 156537, 2020.

[17] C. K. Bandoh, I. Nkrumah, F. K. Ampong, R. K. Nkum, and F. Boakye, "Effect of annealing on the structure and optical properties of lead selenide and cadmium selenide thin film prepared by chemical bath deposition," *Chalcogenide Letters*, vol. 18, no. 2, 2021.

[18] B. B. Jin, S. Y. Kong, G. Q. Zhang et al., "Voltage-assisted SILAR deposition of CdSe quantum dots to construct a high

performance of ZnS/CdSe/ZnS quantum dot-sensitized solar cells," *Journal of Colloid and Interface Science*, vol. 586, pp. 645-646, 2021.

[19] I. A. Kariper, "Amorphous PbSe thin film produced by chemical bath deposition at pH of 5–8," *Surface Review and Letters*, vol. 27, no. 4, p. 1950128, 2020.

[20] K. Ravi and V. Chitra, "Characteristics of lead selenide (PbSe) thin films deposited by CBD," *In AIP Conference Proceedings*, vol. 2224, article 050003, 2020.

[21] L. N. Maskaeva, V. M. Yurk, A. V. Belceva, I. V. Zarubin, A. D. Kutyavina, and V. F. Markov, "Experimental verification of the deposition regions of PbSe by sodium selenosulfate and selenourea in the presence of various ligands," *Chemical bath synthesis of metal chalcogenide films*, vol. 60, pp. 88–90, 2019.

[22] T. Hemati and B. Weng, "Experimental study of the size-dependent photoluminescence emission of CBD-grown PbSe nanocrystals on glass," *Nano Express*, vol. 1, no. 1, article 010030, 2020.

[23] A. Kassim, H. S. Min, S. Monohorn, and S. Nagalingam, "Synthesis of PbSe thin film by chemical bath deposition and its characterization using XRD, SEM and UV-VIS spectrophotometer," *Makara Journal of Science*, vol. 14, pp. 117–120, 2011.

[24] A. Kassim, T. W. Tee, H. S. Min, S. Monohorn, and S. Nagalingam, "Effect of bath temperature on the chemical bath deposition of PbSe thin films," *Kathmandu University Journal of Science, Engineering and Technology*, vol. 6, pp. 126–132, 2010.

[25] S. Roa, M. Sandoval, and M. Sirena, "Chemical bath deposition of high structural and morphological quality PbSe thin films with potential optoelectronic properties for infrared detection applications," *Materials Chemistry and Physics*, vol. 264, p. 124479, 2021.

[26] S. S. Peled, M. Perez, D. Meron et al., "Morphology control of perovskite films: a two-step, all solution process for conversion of lead selenide into methylammonium lead iodide," *Materials Chemistry Frontiers*, vol. 5, no. 3, pp. 1410–1417, 2021.

[27] C. S. Diko, Y. Qu, Z. Henglin, Z. Li, N. A. Nahyoon, and S. Fan, "Biosynthesis and characterization of lead selenide semiconductor nanoparticles (PbSe NPs) and its antioxidant and photocatalytic activity," *Arabian Journal of Chemistry*, vol. 13, no. 11, pp. 8411–8423, 2020.

[28] L. T. Jule, R. Krishnaraj, N. Nagaprasad, B. Stalin, V. Vignesh, and T. Amuthan, "Evaluate the structural and thermal analysis of solid and cross drilled rotor by using finite element analysis," *Materials Today: Proceedings*, 2021.

[29] N. Nagaprasad, B. Stalin, V. Vignesh, M. Ravichandran, N. Rajini, and O. Ismail, "Effect of cellulosic filler loading on mechanical and thermal properties of date palm seed/vinyl ester composites," *International Journal of Biological Macromolecules*, vol. 147, pp. 53–66, 2020.

[30] N. Nagaprasad, B. Stalin, V. Vignesh, M. Ravichandran, N. Rajini, and O. Ismail, "Applicability of cellulosic-based Polyalthia longigolia seed filler reinforced vinyl ester biocomposites on tribological performance," *Polymer Composites*, vol. 42, no. 2, pp. 791–804, 2021.

[31] B. Kassa, J. Leta Tesfaye, B. Bulcha, and R. Krishnaraj, "Effect of manganese icons on spectroscopic and insulating properties of aluminophosphate glasses," *Advances in Materials Science and Engineering*, vol. 2021, 11 pages, 2021.

[32] S. Abel, J. Leta Tesfaye, R. Kiran et al., "Studying the effect of metallic precursor concentration on the structural, optical, and morphological properties of zinc sulfide thin films in photovoltaic cell applications," *Advances in Materials Science and Engineering*, vol. 2021, 6 pages, 2021.

[33] L. Tesfaye, B. Bekele, A. Saka, N. Nagaprasad, K. Sivaramasundaram, and R. Krishnaraj, "Investigating spectroscopic and structural properties of Cr doped TiO2 NPs synthesized through sol gel deposition technique," *Tierarztliche Prax*, vol. 41, pp. 860–872, 2021.

[34] L. Tesfaye Jule, K. Ramaswamy, N. Nagaprasad, V. Shanmugam, and V. Vignesh, "Design and analysis of serial drilled hole in composite material," *Materials Today: Proceedings*, vol. 45, pp. 5759–5763, 2021.

[35] T. Amuthan, N. Nagaprasad, R. Krishnaraj, V. Narasimharaj, B. Stalin, and V. Vignesh, "Experimental study of mechanical properties of AA6061 and AA7075 alloy joints using friction stir welding," *Materials Today: Proceedings*, 2021.

[36] E. K. Subramaniam, M. Sakthivel, K. Kanthavel, R. Krishnaraj, M. G. Deepan Marudachalam, and R. Palani, "Overall resource effectiveness, cycle time reduction & capacity improvements," *International Journal of Scientific and Engineering Research*, vol. 2, no. 8, 2011.

[37] R. Sathiyamoorthy and R. Krishnaraj, "Optimization of cellular layout under dynamic demand environment by simulated annealing," *International Journal of Scientific and Engineering Research*, vol. 3, no. 10, 2012.

[38] V. M. M. Thilak, R. Krishnaraj, M. Sakthivel, K. Kanthavel, M. Marudachalam, and R. Palani, "Transient thermal and structural analysis of the rotor disc of disc brake," *International Journal of Scientific and Engineering Research*, vol. 2, no. 8, pp. 2–5, 2011.

[39] S. Varatharajan, R. Krishnaraj, M. Sakthivel, K. Kanthavel, M. G. Deepan Marudachalam, and R. Palani, "Design and analysis of single disc machine top and bottom cover," *International Journal of Scientific and Engineering Research*, vol. 2, no. 8, 2011.

[40] C. M. Balamurugan, R. Krishnaraj, M. Sakthivel, K. Kanthavel, D. Marudachalam, and R. Palani, "Computer aided modeling and optimization of crankshaft," *International Journal of Scientific and Engineering Research*, vol. 2, no. 8, pp. 2–7, 2011.

[41] M. Vyshakh, R. Krishnaraj, A. P. Sayooj, and M. Afzal, "Experimental investigation on aluminium gravity die casting," *International Journal of Applied Environmental Sciences*, vol. 9, no. 2, pp. 213–222, 2014.

[42] M. Deepu, R. Krishnaraj, D. Karthik, and N. M. Binoj, "Cycle time optimization of rubber floor mat die," *International Journal of Applied Environmental Sciences*, vol. 9, no. 2, pp. 229–237, 2014.

[43] V. S. Arun, R. Krishnaraj, M. N. Rohit, and V. Mohan, "Optimising rejection rate of laser diamond sawing using Taguchi method," *International Journal of Applied Environmental Sciences*, vol. 9, no. 2, pp. 223–228, 2014.

[44] R. Krishnaraj, "Investigation on the effect of thermo physical properties on heat and mass transfer–review," *International Journal of Applied Environmental Sciences*, vol. 9, no. 4, pp. 1893–1900, 2014.

[45] C. N. Anil Kumar, R. Krishnaraj, M. Sakthivel, and M. Arularasu, "Implementation of safety education program for material handling equipment in construction sites and its effectiveness analysis using T-test," *International Journal of Applied Environmental Sciences*, vol. 8, no. 15, pp. 1961–1969, 2013.